SELF-ORGANIZED CRITICALITY, THREE DECADES LATER

EDITED BY: Subhrangshu Sekhar Manna, Attilio L. Stella, Peter Grassberger and Ronald Dickman

PUBLISHED IN: Frontiers in Physics

frontiers Research Topics

frontiers

ISSN 1664-8714
ISBN 978-2-88974-219-6
DOI 10.3389/978-2-88974-219-6

About Frontiers

Frontiers is more than just an open-access publisher of scholarly articles: it is a pioneering approach to the world of academia, radically improving the way scholarly research is managed. The grand vision of Frontiers is a world where all people have an equal opportunity to seek, share and generate knowledge. Frontiers provides immediate and permanent online open access to all its publications, but this alone is not enough to realize our grand goals.

Frontiers Journal Series

The Frontiers Journal Series is a multi-tier and interdisciplinary set of open-access, online journals, promising a paradigm shift from the current review, selection and dissemination processes in academic publishing. All Frontiers journals are driven by researchers for researchers; therefore, they constitute a service to the scholarly community. At the same time, the Frontiers Journal Series operates on a revolutionary invention, the tiered publishing system, initially addressing specific communities of scholars, and gradually climbing up to broader public understanding, thus serving the interests of the lay society, too.

Dedication to Quality

Each Frontiers article is a landmark of the highest quality, thanks to genuinely collaborative interactions between authors and review editors, who include some of the world's best academicians. Research must be certified by peers before entering a stream of knowledge that may eventually reach the public - and shape society; therefore, Frontiers only applies the most rigorous and unbiased reviews.
Frontiers revolutionizes research publishing by freely delivering the most outstanding research, evaluated with no bias from both the academic and social point of view. By applying the most advanced information technologies, Frontiers is catapulting scholarly publishing into a new generation.

What are Frontiers Research Topics?

Frontiers Research Topics are very popular trademarks of the Frontiers Journals Series: they are collections of at least ten articles, all centered on a particular subject. With their unique mix of varied contributions from Original Research to Review Articles, Frontiers Research Topics unify the most influential researchers, the latest key findings and historical advances in a hot research area! Find out more on how to host your own Frontiers Research Topic or contribute to one as an author by contacting the Frontiers Editorial Office: frontiersin.org/about/contact

SELF-ORGANIZED CRITICALITY, THREE DECADES LATER

Topic Editors:
Subhrangshu Sekhar Manna, S.N. Bose National Centre for Basic Sciences, India
Attilio L. Stella, University of Padua, Italy
Peter Grassberger, Julich Research Center, Helmholtz Association of German Research Centres (HZ), Germany
Ronald Dickman, Federal University of Minas Gerais, Brazil

Citation: Manna, S. S., Stella, A. L., Grassberger, P., Dickman, R., eds (2022). Self-Organized Criticality, Three Decades Later. Lausanne: Frontiers Media SA. doi: 10.3389/978-2-88974-219-6

Table of Contents

frontiers in Physics

REVIEW
published: 04 September 2020
doi: 10.3389/fphy.2020.00333

Feedback Mechanisms for Self-Organization to the Edge of a Phase Transition

Victor Buendía[1,2,3], *Serena di Santo*[4], *Juan A. Bonachela*[5] *and Miguel A. Muñoz*[1]*

[1] Departamento de Electromagnetismo y Física de la Materia and Instituto Carlos I de Física Teórica y Computacional, Universidad de Granada, Granada, Spain, [2] Dipartimento di Matematica, Fisica e Informatica, Università di Parma, Parma, Italy, [3] Istituto Nazionale di Fisica Nucleare (INFN), Gruppo Collegato di Parma, Parma, Italy, [4] Morton B. Zuckerman Mind Brain Behavior Institute, Columbia University, New York, NY, United States, [5] Department of Ecology, Evolution, and Natural Resources, Rutgers University, New Brunswick, NJ, United States

OPEN ACCESS

Edited by:
Ronald Dickman,
Federal University of Minas Gerais, Brazil

Reviewed by:
Bikas K. Chakrabarti,
Saha Institute of Nuclear Physics (SINP), India
Manish Dev Shrimali,
Central University of Rajasthan, India

***Correspondence:**
Miguel A. Muñoz
mamunoz@onsager.ugr.es

Specialty section:
This article was submitted to Interdisciplinary Physics, a section of the journal Frontiers in Physics

Received: 04 June 2020
Accepted: 17 July 2020
Published: 04 September 2020

Citation:
Buendía V, di Santo S, Bonachela JA and Muñoz MA (2020) Feedback Mechanisms for Self-Organization to the Edge of a Phase Transition. Front. Phys. 8:333. doi: 10.3389/fphy.2020.00333

Scale-free outbursts of activity are commonly observed in physical, geological, and biological systems. The idea of self-organized criticality (SOC), introduced back in 1987 by Bak, Tang, and Wiesenfeld suggests that, under certain circumstances, natural systems can seemingly self-tune to a critical state with its concomitant power-laws and scaling. Theoretical progress allowed for a rationalization of how SOC works by relating its critical properties to those of a standard non-equilibrium second-order phase transition that separates an active state in which dynamical activity reverberates indefinitely, from an absorbing or quiescent state where activity eventually ceases. The basic mechanism underlying SOC is the alternation of a slow driving process and fast dynamics with dissipation, which generates a feedback loop that tunes the system to the critical point of an absorbing-active continuous phase transition. Here, we briefly review these ideas as well as a recent closely-related concept: self-organized bistability (SOB). In SOB, the very same type of feedback operates in a system characterized by a discontinuous phase transition, which has no critical point but instead presents bistability between active and quiescent states. SOB also leads to scale-invariant avalanches of activity but, in this case, with a different type of scaling and coexisting with anomalously large outbursts. Moreover, SOB explains experiments with real sandpiles more closely than SOC. We review similarities and differences between SOC and SOB by presenting and analyzing them under a common theoretical framework, covering recent results as well as possible future developments. We also discuss other related concepts for "imperfect" self-organization such as "self-organized quasi-criticality" and "self-organized collective oscillations," of relevance in e.g., neuroscience, with the aim of providing an overview of feedback mechanisms for self-organization to the edge of a phase transition.

Keywords: self-organized criticality, scaling, scale invariance, phase transitions, avalanches, self-organization

1. INTRODUCTION

The seminal work of Bak, Tang, and Wiesenfeld in which the idea of "self-organized criticality" was first introduced [1], which has been cited thousands of times in the scientific literature and beyond, opened a whole research field and triggered a huge avalanche of scientific excitement in Statistical physics. Fractals [2] can be considered as precursors of these ideas, and scale-free complex networks [3] successors in the timeline of waves of scientific interest.

Bak and collaborators developed the groundbreaking idea that scaling behavior is observed in Nature owing to self-organization mechanisms that tune systems to the vicinity of critical points [4]. Thus, self-organized criticality (SOC) helped shed light onto why scale-invariant phenomena (both in space and time) are so commonly observed in natural systems, in spite of the fact that criticality, i.e., second-order phase transitions, with their associated power-laws and scaling, occur only at singular (critical) points of parameter spaces [1, 4, 5] (for pedagogical reviews and detailed accounts of SOC, we refer to [6–12]).

The most succesful and archetypical examples of SOC are sandpile toy models [1, 13–17][1]. In sandpiles, "grains" —which represent in an abstract way some token of "stress" or "energy" [19]—are slowly added into a system (usually a lattice or another type of network), and locally redistributed on a fast way whenever an instability threshold is overcome. This redistribution triggers avalanches of topplings, eventually dissipating some of these grains at the system's open boundaries. Upon iteration, these dynamics result in the self-organization of the system to a critical stationary state that exhibits power-law avalanche distributions and obeys finite-size scaling [4, 6–9, 11, 20–23].

The observation of scale invariance and other features characteristic of criticality without the need for parameter fine tuning prompted an enormous interest in these simple models. As a word of caution, let us remark that it was also soon realized that sandpile models bear little resemblance with the physics of actual sandpiles as experimentally analyzed in the laboratory. In actual sandpiles, ingredients such as inertia, gravity, and stickiness (typically absent in standard SOC models) play important roles, and scale invariance is not easily observed [8, 9, 11]. Empirical evidence of SOC is more easily found in ricepiles or in superconductors [see [8] for an account on experimental realizations as well as for other general aspects of SOC]. Let us just highlight that compelling evidence of SOC has been recently found in an ultracold atomic gas [24, 25]. This discovery illustrates that, more than 30 years after its birth, SOC is still a powerful, relevant and pervading concept.

On the theoretical side, a key ingredient of the mechanism for self-organization in sandpiles is the fact that driving and dynamics operate at two broadly separated timescales (i.e., slow-fast dynamics) [4, 6, 7, 22]. An infinite separation of timescales is usually achieved by driving the system only when all activity has stopped, but not during avalanches ("*infinitely slow*" or "*offline*" *driving*); if this is not the case, a finite characteristic (time/size) scale appears [22, 26, 27]. Similarly, *conservative dynamics* in the bulk of the system are also key to SOC, because bulk dissipation leads necessarily to the emergence of characteristic spatio-temporal scales, thus preventing the possibility of scale-invariance [22, 28–32]. We refer to [22] for a more in depth theoretical discussion on the emergence of generic scale invariance, conservation laws, and SOC.

A large variety of sandpile models, with diverse microscopic rules, were investigated after the original proposal of Bak and colleagues (see a compilation of prototypical SOC models in [33] and [6–8]). The main additional ingredient was the introduction of stochasticity in the redistribution rules, replacing the fully deterministic updating rules of the original sandpile [13]. Given the diversity of models, a compelling question emerged as to whether there is universality in SOC (i.e., models/systems that share the same scaling features) [34, 35]. From the computational viewpoint it soon became clear that, in spite of preliminary evidence, the original (deterministic) sandpile model of Bak, Tang, and Wiesenfeld (BTW) does not obey clean scaling behavior but rather some type of multiscaling or anomalous scaling [36–39]. This anomaly stems from the breaking of ergodicity [16], and the existence of many conservation laws associated with the deterministic nature of its updating rules[2]. On the other hand, sandpiles with some level of stochasticity (such as the Manna model [13] or the Oslo ricepile model [14]) exhibit standard and universal scaling behavior, even though large-scale simulations and careful computational analyses were required to reach such a conclusion (see e.g., [33, 40–43]).

Because criticality and universality are hallmarks of second-order phase transitions, diverse attempts were made to map the behavior emerging in SOC systems to that of standard (continuous or second-order) phase transitions. In particular:

- A first proposal mapped sandpiles to the pinning-depinning transition of interfaces moving in random media [44–48]. In this approach, the height of the interface at a given location corresponds to the number of times that such a site has toppled in the sandpile. This successful mapping has profound physical implications, as pinning-depinning transitions are also related to the dynamics of magnetic domain walls in random media, the Barkhausen effect, and $1/f$ noise, which had long been studied and are known to display scale invariance [49–51].
- A second proposal, on which we focus here, connected SOC with reaction-diffusion systems exhibiting absorbing-active phase transitions [9, 33, 52–56]. The mapping was proposed on general symmetry and conservation principles, and afterward refined in an exact formal way [57].

These two apparently disparate approaches were found to be fully equivalent to each other, first using heuristic and numeric arguments [58–60] and then with more rigorous analyses [61].

[1] Alternative models and mechanisms such as for example, the celebrated Bak-Sneppen model for punctuated evolution relying on "extremal dynamics" [18] were also proposed to achieve scaling in a self-organized way, but we will not discuss them here.

[2] Let us remark that there exist very powerful theoretical tools for deterministic (Abelian) sandpiles [20, 21], a theoretical endeavor complementary to the type of analyses for stochastic sandpiles discussed here.

In order to scrutinize how SOC behavior is related to standard phase transitions, the notion of "fixed-energy sandpiles" (FESs) was introduced, an idea similar in spirit to an early suggestion by Tang and Bak [19, 62]. The key idea was to "regularize" sandpiles by switching off both slow driving and boundary dissipation, with the total number of sandgrains in the system thus becoming fixed, i.e., a conserved quantity, suitable to be considered a control parameter [9, 52–54, 63]. Thus, the state of a FES is described by two quantities: the total number of sandgrains in the system (control parameter) and the total number of sites that are above the threshold of instability (order parameter). The latter is based on the fact that, in a sandpile, sandgrains can be either "active" if they happen to be above threshold (ready to topple and be redistributed), or "inactive" otherwise. Inactive grains can, however, contribute to future activations. Using a more general and abstract language, "**energy**" hereon refers to the mean accumulated stress (e.g., total number of sandgrains per site on the sandpile) while "**activity**" describes the number of sandgrains above the instability threshold.

Not surprisingly, FESs exhibit two distinct phases depending on the value of their energy E: either they are in an "active" phase with ceaseless redistribution of activity for sufficiently large values of E, or they are in an absorbing or quiescent phase in which all activity ceases and the dynamics are frozen [64–66] (see **Figure 1**, left panel). Thus, there exists a *continuous* absorbing-to-active phase transition at a critical energy value E_c. Let us note that the existence of such a phase transition in FESs has only recently been demonstrated mathematically [67, 68].

This observation allowed for a rationalization of SOC as a dynamical feedback mechanism that tunes the system to the edge of an absorbing-to-active phase transition through (slow) driving and (fast) bulk dynamics, occurring at infinitely separated timescales with boundary dissipation [9, 33, 53, 54, 69–71]. In other words, the steady state reached spontaneously by the SOC dynamics is characterized by an average steady-state energy E^{SOC} such that $E^{SOC} = E_c$. As a consequence, the scaling features of SOC systems can be inferred from those of their corresponding fixed-energy counterparts using the powerful set of theoretical tools available for standard non-equilibrium phase transition.

Non-equilibrium phase transitions into absorbing states have long been studied, and it is well-established that most of them share the same type of universal behavior, belonging to the so-called "directed percolation" (DP) universality class [64–66, 72]. As in some DP systems, in FESs there is not one but many absorbing states. Any configuration with vanishing activity and arbitrary values of the energy is absorbing [73]. However, in FESs there is an additional conservation law that might be relevant for universality issues (see below).

To help clarify this and other issues, here we use the formalism of Langevin equations to review classic and state-of-the-art theoretical aspects of SOC. This formalism follows the philosophy of the extremely successful approach of Landau and Ginzburg to equilibrium phase transitions and critical points [74–76], as well as its extension to dynamical problems (as reviewed by [77]). For each case, we will present the simplest (Langevin) equation, including the main symmetries, conservation laws, and stochastic effects present in the system, and neglecting irrelevant terms [74–76]. This approach places the focus on universal scaling features, leaving aside unimportant microscopic details. Thus, such Langevin equations constitute an ideal starting point for further theoretical analyses (such as renormalization group calculations and other field theoretical approaches) and even for numerical studies. After presenting and discussing the theory of SOC, we move on to discussing related theories of self-organization to the edge of a phase transition. We next describe the theory for the self-organization to the edge of a discontinuous phase transition with bistability, and finally we discuss theories for "imperfect self-organization" either to a continuous or to a discontinuous transition. The latter can be of more relevance than the original self-organization theories to describe real-world situations.

2. THEORY OF SELF-ORGANIZED CRITICALITY (SOC)

Let us start by discussing the simplest possible SOC system [78]. For a macroscopic (mean-field) description of a sandpile, two relevant variables are needed: the overall energy E (which represents the total density of sandgrains in sandpiles and is conserved in the bulk), and the overall activity ρ (i.e., the density of sites which are above threshold). To analyze the possible connection between sandpiles and standard non-equilibrium phase transitions at a mean-field level, let us consider the simplest possible equation describing a continuous absorbing-active phase transition for the overall density ρ:

$$\dot{\rho}(t) = a\rho(t) - b\rho^2(t) \tag{1}$$

where a and $b > 0$ are constants, and the fine-tuning of a controls the behavior of the system. This equation exhibits an absorbing phase with vanishing activity ($\rho = 0$) below the critical point, i.e., for $a < a_c = 0$, and an active phase with steady-state density $\rho = a/b \neq 0$ for $a > a_c = 0$.

To establish the connection with SOC, let us start by linking the equation above with FESs. To that end, it is required an additional conserved energy (or energy density) E such that it fosters the creation of activity (i.e., increases a in Equation 1). Thus, in first approximation we can write:

$$\dot{\rho}(t) = (a + \omega E)\rho(t) - b\rho^2(t) \tag{2}$$

where $\omega > 0$ is simply a proportionality constant. Observe that, since E is a conserved quantity (i.e. $\dot{E} = 0$), it can be used as a control parameter keeping a fixed. In particular, the critical point lies now at $E_c = -a/\omega$. Equation (2) constitutes the mean-field description of fixed energy sandpiles: a dynamical equation for the overall activity, $\rho(t)$, whose steady state is determined by the control parameter, the energy density E in the system.

On the other hand, in the SOC version of sandpiles E becomes a dynamical variable $E(t)$, which increases by external driving (at an arbitrarily small rate h) and decreases owing to activity-dependent dissipation (at a rate $\epsilon\rho$). This can be summarized by

the equation:

$$\dot{E}(t) = h - \epsilon\rho(t). \tag{3}$$

In the double limit $h, \epsilon \to 0^+$ (infinitely separated timescales), or if $h/\epsilon \to 0$ (energy conservation), the steady-state solution of the system represented by Equations (2) and (3) is $\rho = h/\epsilon \to 0^+$ and $E^{SOC} = (bh/\epsilon - a)/\omega \to E_c$ (see **Figure 1**, left). In other words, the system self-organizes to the critical point of a standard absorbing-active phase transition, i.e., the critical state is a dynamical attractor of the system [19].

Observe that the key to the SOC mechanism lies on the feedback created by the dynamics of the control parameter E (see **Figure 1**). Its dynamics strongly depend on the system state/phase: if activity vanishes, $\rho = 0$ and $\dot{E} = h$, leading to an increase in E that shifts the system toward its supercritical phase. If, on the other hand, $\rho > 0$, since $\epsilon \gg h$, then $\dot{E} \approx -\epsilon\rho$ and E decreases, pushing the system toward the subcritical phase. This feedback loop necessarily drives the system to the vicinity of the critical point, and exactly to the critical point if the separation of timescales is infinite, as shown above. In more general terms: *the existence of a control mechanism that acts differentially on each phase—i.e., at each side of the phase transition—creates a feedback loop that self-organizes the system to the very edge of the transition* [9, 26, 33] (see [79] for a discussion of this general idea in the context of control theory).

In order to go beyond this simple mean-field description, we need to extend the theory to make it spatially explicit and stochastic, i.e., shift from mean-field theory to stochastic field theory [75, 76]. The simplest possible equation describing absorbing phase transitions is the so-called Reggeon field theory (or DP theory), which can be written as the following Langevin equation [66, 80, 81]:

$$\partial_t\rho(\vec{x},t) = a\rho(\vec{x},t) - b\rho^2(\vec{x},t) + D\nabla^2\rho(\vec{x},t) + \sigma\sqrt{\rho(\vec{x},t)}\eta(\vec{x},t) \tag{4}$$

where $\rho(\vec{x},t)$ is the activity field, a and $b > 0$ are constants, and D and σ are the diffusion and noise constants, respectively. $\eta(\vec{x},t)$ is a zero-mean Gaussian noise with $\langle\eta(\vec{x},t)\eta(\vec{x'},t)\rangle = \delta(\vec{x} - \vec{x'})\delta(t - t')$ which, together with the prefactor $\sqrt{\rho(\vec{x},t)}$, accounts for demographic fluctuations in particle numbers. Importantly, the noise term vanishes in the absorbing state $\rho(\vec{x},t) = 0$.

In analogy with the mean-field approach, we now use the equation above to represent FESs, for which we need to add another equation for the (conserved) energy coupled linearly with the activity [9, 53, 54]:

$$\begin{aligned}\partial_t\rho(\vec{x},t) &= (a + \omega E(\vec{x},t))\rho - b\rho^2 + D\nabla^2\rho + \sigma\sqrt{\rho(\vec{x},t)}\eta(\vec{x},t)\\ \partial_t E(\vec{x},t) &= \nabla^2\rho(\vec{x},t)\end{aligned} \tag{5}$$

where $E(\vec{x},t)$ is the energy field. Some dependencies on $(\vec{x},t)$ have been omitted for the sake of simplicity. Note that the equation for the energy is diffusive, describing the redistribution of energy among neighboring locations with no loss in the presence of activity. Thus, the system-averaged energy per site (i.e., the spatial integral of the energy field divided by the system volume) $\overline{E}$ is constant in FESs and can be taken as a control parameter. As in the case of the mean-field theory, Equation (5) exhibit a phase transition at a particular value of the average energy density: for $\overline{E} > E_c$ there are continuous ongoing redistributions of activity and energy, while for $\overline{E} < E_c$ the system eventually falls into the absorbing state $\rho(\vec{x},t) = 0$ (see e.g., [82]). The set of equations for FESs, Equation (5), was proposed on phenomenological grounds [53, 54] (see also [83]) and later derived from a discrete reaction-diffusion model with many absorbing states and a local conservation law [56]. Only recently has it been derived in a rigorous way from the microscopic rules of a stochastic (fixed-energy) sandpile [57].

Equation (5) can be integrated "a la SOC," e.g., by adding at the initial time and after each avalanche a discrete amount of energy and activity ("infinitely slow" or "offline" driving), and considering open boundary conditions (i.e., allowing for boundary dissipation). The resulting self-organized system converges to the critical point of Equation (5). Alternatively, a continuous version can be achieved by including in Equation (5) an explicit ("online") driving and a dissipation term:

$$\begin{aligned}\partial_t\rho(\vec{x},t) &= (a + \omega E(\vec{x},t))\rho - b\rho^2 + D\nabla^2\rho + \sigma\sqrt{\rho(\vec{x},t)}\eta(\vec{x},t),\\ \partial_t E(\vec{x},t) &= \nabla^2\rho(\vec{x},t) - \epsilon\rho(\vec{x},t) + h(\vec{x},t).\end{aligned} \tag{6}$$

Note that the small driving $h(\vec{x},t)$ could also be added to the activity in order to avoid the absorbing state (in which the dynamics stop). Otherwise, a small seed of activity needs to be added to slightly perturb the system every time the absorbing state is reached. Note that this "online" methods are slightly different from the "offline" driving since the average energy field changes during avalanches and not only between them.

As in the mean-field theory, this system of equations converges to Equation (5) in the limit $h/\epsilon \to 0$ (**Figure 2**, upper-left panel). Although the equivalence of Equation (5) at criticality and its SOC counterpart Equation (6) is very challenging to prove analytically, it has been consistently demonstrated by means of extensive computational analyses [33]. Such numerical analyses are possible owing to an exact algorithm to integrate this type of Langevin equations with multiplicative (square-root) noise [82][3]. **Figures 2–4** (upper-left panels) show results from the numerical integration of these equations. In particular, **Figure 3** (upper-left) shows the probability distribution to find the system in a state with average energy density $\overline{E}$ in the SOC version of the dynamics. This distribution becomes progressively more peaked around E_c as the system is enlarged (since dissipation and driving become arbitrarily small as the system size is increased), converging to a Dirac delta function at $\overline{E} = E_c$ in the infinite-system-size limit.

Some aspects of this mapping have generated long-lasting controversies in the past:

- The first one regards the conclusion of the above theory that the value to which the self-organization mechanism leads the system, E^{SOC}, coincides with the critical point of the standard phase transition in the FES model, E_c. This

[3]Details of the algorithm, a description of an improvement over the original formulation [84], and a code for its implementation can be found in Github: https://github.com/pvillamartin/Dornic_et_al_integration_class.

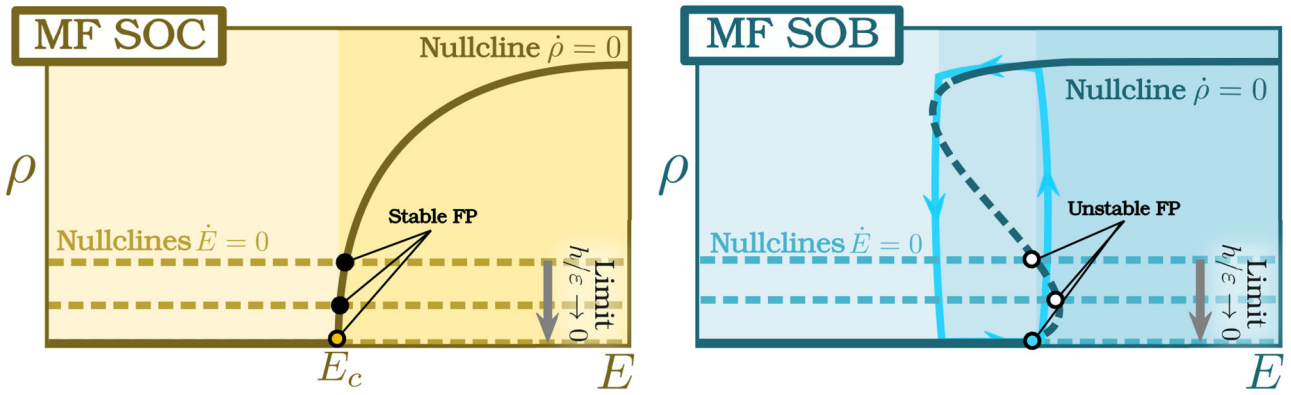

FIGURE 1 | Mean-field (MF) pictures of SOC and SOB. Sketch of the nullclines associated with the two dynamical mean-field equations defining self-organized criticality [SOC, **(Left)**] and self-organized bistability [SOB, **(Right)**]. In both cases, the nullcline for the second (feedback) equation is plotted for three different values of the ratio h/ϵ. **(Left)** In the case of SOC, nullclines intersect at a stable fixed point, which becomes closer and closer to the critical point as the limit of infinite separation of timescales $h/\epsilon \to 0$ is approached (see gray arrow). **(Right)** In the case of SOB, for sufficiently low values of h/ϵ the intersection between nullclines occurs on the so-called spinodal line (dashed dark line). Points located in the spinodal line are unstable, and the system presents a stable, fixed-amplitude limit cycle sketched by the cyan trajectory.

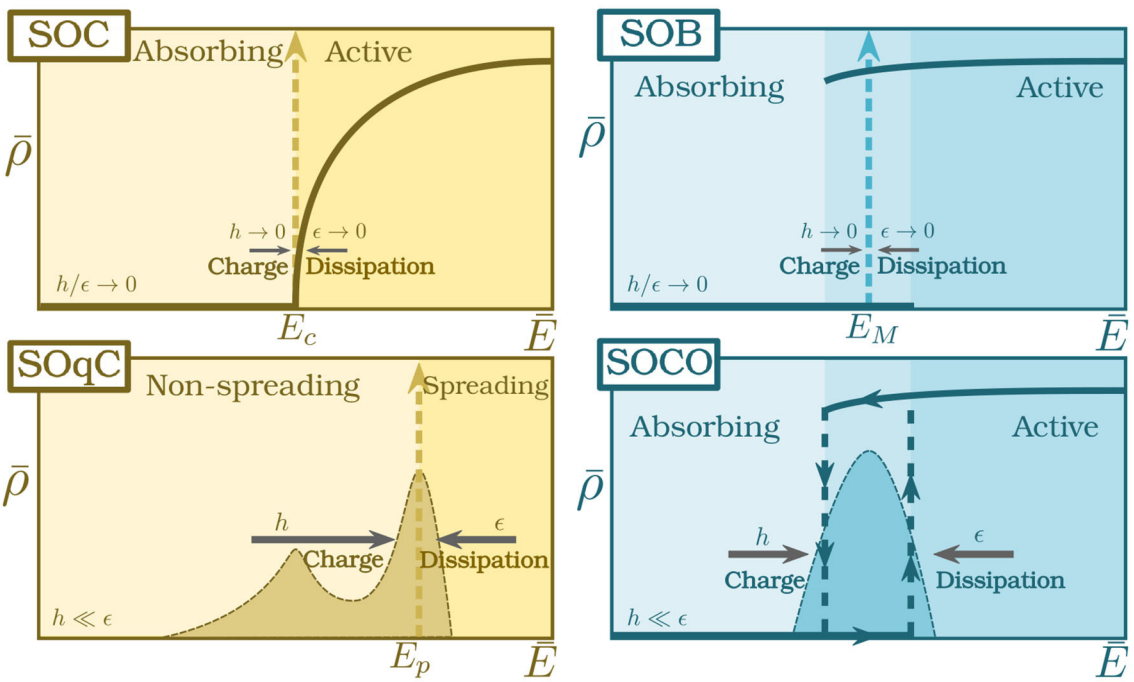

FIGURE 2 | Sketch of the different types of self-organization mechanisms discussed here. The four panels illustrate, respectively, the mechanisms for self-organization to a continuous phase transition with criticality (left panels) and to a discontinuous transition (right panels), for both the "perfect" conserved case (top panels) and the "approximated" or "imperfect" non-conserved case (bottom panels). In all cases the steady-state average activity is plotted as a function of the control parameter (the average "energy" or "stress"). The SOC and SOB mechanisms change dynamically the control parameter to a precise value (either E_c or E_M, respectively), meaning that the system becomes perfectly self-organized to the edge of a phase transition (either a continuous one for SOC or discontinuous one for SOB) in the thermodynamic limit. On the other hand, their corresponding "imperfect" or non-conserved counterparts—that we call "self-organized quasi-criticality" (SOqC) and "self-organized collective oscillations" (SOCO)—give rise to broad distributions of possible energy values, even in the thermodynamic limit, typically around the edge of the transition point (shown as an area enclosed by dashed lines). The thin arrows in the upper panels illustrate the fact that dissipation and driving rates are very small ($h \to 0$, $\epsilon \to 0$ with $h/\epsilon \to 0$), while the thick ones indicate that such a strict limit is not taken, but still ($h \ll \epsilon$).

was questioned by using a possible counterexample [85]. In particular, for the original BTW deterministic sandpile model in some particular types of lattices is was shown that $E_c^{SOC} \neq E_c$ (for example, for a square lattice $E^{SOC} = 2.1252...$ [85] but the analytical prediction is $E_c = 2.125$ [86], i.e., there is a deviation in the fourth decimal digit). This result, criticized

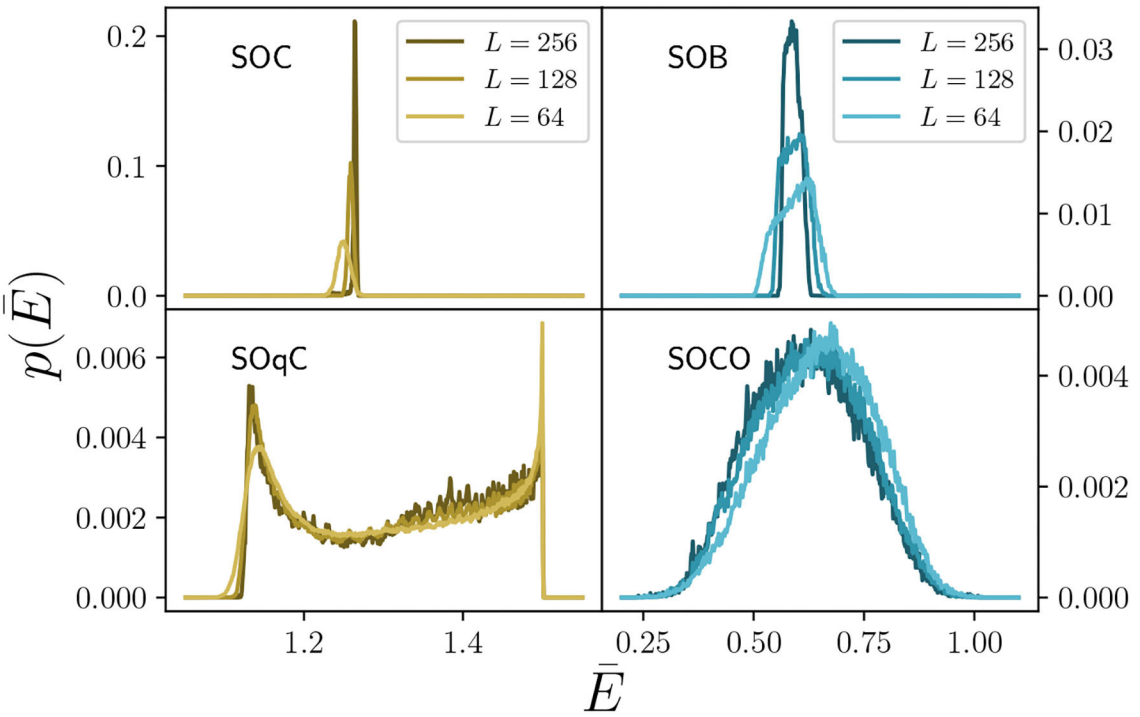

FIGURE 3 | Distribution of average energy density $\bar{E}$ at the stationary state in the different types of self-organization mechanisms for finite system sizes. In the case of SOC and SOB (upper panels), the (unimodal) distribution of energy values becomes progressively more peaked at the transition point as the system size is enlarged, converging as $N \to \infty$ to perfect self-organization to the transition point (either a critical point E_c for SOC, or the Maxwell point E_M for SOB). In the absence of a conservation law, i.e., in the presence of non-vanishing dissipation term (bottom panels), the distribution remains broad even in the $N \to \infty$ limit, reflecting the presence of excursions of $\bar{E}$ to both sides of the transition: both in SOqC and in SOCO, the system continuously shifts between the active and absorbing regimes, even in the limit of infinitely-large system sizes. In the case of SOqC, the distribution is broad and bimodal. In the case of SOCO, the broad distribution results from the presence of ongoing oscillations from one phase to the other. In all cases, we simulated the corresponding Langevin equations as described in the text [e.g., Equation (5) with updating rules (11) for SOC, etc.]. For the conserved cases, $\epsilon = 0$, while for non-conserved ones we employed the "offline" charge rules described by Equation (11). See **Table A1** for a list of all parameter values.

in [87, 88], stems from the previously-mentioned lack of ergodicity of deterministic sandpiles, and it does not apply to standard stochastic (ergodic) sandpiles, where the equality $E_c^{SOC} = E_c$ has been consistently verified numerically to hold (see e.g., [33]).

- The second one concerns the universality class of stochastic SOC models. The numerical values of the exponents are close to those of DP, which led some researchers to claim that SOC models (and FES theory) are in the directed percolation class [89–91]. However, the following observations support the existence of a universality class *per se*, the so-called C-DP (*conserved* directed percolation) or Manna class (see e.g., [82]):

  1. In Equation (5) there is an additional equation with respect to the DP theory that includes a conservation law. The latter constitutes a relevant perturbation in the renormalization group sense at the DP fixed point [54].
  2. There is a mapping from SOC to interfaces moving in random media, whose universality is different from DP (as known from numerical as well as from analytical renormalization group approaches; see [58–61] and references therein).
  3. Numerical estimates of critical exponent values for this class with one- and two-dimensional systems are distinct from those of DP [33, 35, 41, 43, 56, 92]. Recent large-scale numerical analyses (of the one-dimensional Oslo sandpile [14]) closed the debate even on more firm bases by confirming the discrepancy with the DP scaling and conjecturing rational values for some of the exponents [42]. As a side note, let us highlight that obtaining critical exponents numerically in SOC is challenging because there is a very slow decay from initial conditions in the background or energy field, which makes observing true asymptotic behavior necessitate large system sizes and long computer simulations [91]. Indeed, in the stationary state of SOC and FES, as first pointed out in [91] (see also [93–95]) the energy field is "hyper-uniform" (i.e., the standard deviation of field values in a region of size N decays faster than $\sqrt{N}$ [42, 96]). Given the critical slow decay of correlations, a convenient strategy to observe numerically clean exponents consists in preparing initial conditions that preserve hyperuniformity (or naturally obtained from the system's dynamics) [42]. Another powerful strategy to discriminate between DP and C-DP consists in perturbing

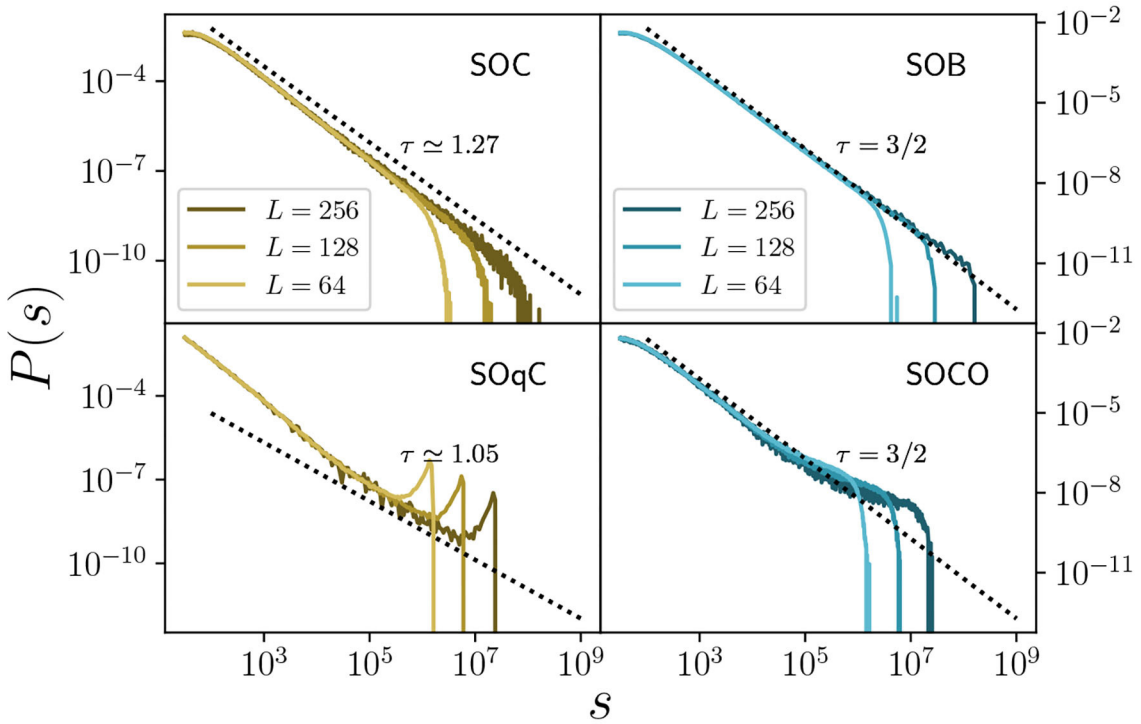

FIGURE 4 | Avalanche size distributions for the four different types of self-organization mechanisms in two dimensional lattices. For the cases of SOC and SOB (upper panels) the distribution can be fitted by a power law in an exact way in the thermodynamic limit, while it is truncated—in a scale-invariant way—in finite systems. For SOC, the distributions show scaling that belongs to the C-DP or Manna class. In the case of SOB, power-laws are also obtained, and show mean-field exponents (including logarithmic corrections to scaling as the upper critical dimension is 2, see main text); also, note the bump at the end of the distribution, due to "king" events, effect that can be made more apparent by increasing the value of b in the Langevin equation (i.e., making the jump at the discontinuity of the phase transition more abrupt). For the cases of imperfect self-organization (i.e., non-conserved) either SOqC or SOCO (lower panels), the distributions can be fitted by power-laws only in an approximate way. This is a consequence of the fact that, in these cases, the control parameter does not settle to a precise (critical) value but keeps hovering around the edge of the transition even in the thermodynamic limit. Parameter values are as in **Table A1**, except for SOB, for which b was reduced to $b = -0.7$ to avoid excessively large "king" events.

the system introducing walls or anisotropy, because systems in the DP class and in the C-DP class respond very differently to these perturbations [43]. Finally, not only critical exponents but also some correlators have been shown to be different in DP and C-DP with remarkable numerical accuracy [35, 60].

Another important point is the lingering (and frustrating) lack of a working renormalization group approach to study analytically the large-scale behavior of the C-DP field theory (Equation 5). Thorough attempts to renormalize the theory have been made in the literature (see e.g., [54, 97–99]), but a sound solution to this problem has yet to be found.

Notwithstanding, as already mentioned the C-DP universality class can be exactly mapped into the pinning-depinning transition of linear interfaces moving in a random media [61], also called the quenched-Edwards-Wilkinson class [100]. This mapping enables an additional route to understanding the scaling features of SOC systems, providing us with an excellent workbench to check for consistency in computational results. Moreover, given that a working (functional) renormalization group solution exists for the interfaces in random media [100–103], this connection could be used as an inspiration for theoreticians to tackle the renormalization problem of Equation (5).

In summary, there exists a full stochastic theory of SOC that explains how a mechanism relying on slow driving and dissipation—operating at infinitely separated timescales—is able to self-organize a system to the edge of a non-equilibrium continuous phase transition. At the critical point of this absorbing state transition, marginal propagation of activity in the form of scale-free outbursts occurs. From a more technical point of view, such a critical point is in the C-DP or Manna class, equivalent to the quenched-Edwards-Wilkinson class, and different from DP. Some theories, however, suggest that noise could be optimized to help the system reach the self-organized steady state even in the absence of perfect timescale separation, a phenomenon called "Steady State Stochastic Resonance" [104].

3. THEORY OF SELF-ORGANIZED BISTABILITY (SOB)

SOC describes the self-organization of a system to the edge of a continuous (or second-order) phase transition. Thus, one could

wonder whether there exists a similar mechanism for the self-organization of a system to the edge of a discontinuous (or first order) phase transition, with a region of bistability between active and absorbing phases. This idea, recently scrutinized, has led to the concept of "self-organized bistability (SOB)" [105] (see also [106]).

Let us start, once again, by considering the minimal form of a discontinuous absorbing-to-active transition in the simplest possible mean-field terms:

$$\dot{\rho}(t) = a\rho - b\rho^2 - \rho^3 \tag{7}$$

where now $b < 0$ and $c > 0$. Indeed, as illustrated in **Figure 1** (right panel), the stationary solution of Equation (7) exhibits a regime of bistability between an absorbing and an active state. Coupling this dynamical equation to one for an energy field as in SOC, $\dot{E} = h - \epsilon\rho$, introduces a feedback loop that leads the system to exhibit a limit cycle (the loop in **Figure 1**). Indeed, the nullcline of this second equation is $\rho = h/\epsilon$ which, for small h/ϵ, intersects the other nullcline at an unstable point, thus leading to the creation of a limit cycle [105, 107]. Therefore, a mechanism identical to that of SOC is able to self-organize a mean-field system that exhibits a discontinuous transition to generating periodic bursts of activity.

In order to go beyond this mean-field picture, a simple modification of the theory above leads to the following set of Langevin equations describing self-organization to the edge of a discontinuous transition in spatially extended systems [105]:

$$\begin{aligned} \partial_t \rho(\vec{x},t) &= (a + \omega E(\vec{x},t))\rho - b\rho^2 - c\rho^3 + D\nabla^2\rho \\ &\quad + \sigma\sqrt{\rho(\vec{x},t)}\eta(\vec{x},t) \\ \partial_t E(\vec{x},t) &= \nabla^2\rho(\vec{x},t) \end{aligned} \tag{8}$$

where all the terms are as in Equation (5) except the coefficient of the quadratic term, negative here (i.e., $b < 0$), and the additional cubic term (with coefficient $c > 0$), which needs to be added to preserve stability.

Numerical integration of Equation (8) can be performed using the same integration scheme as with SOC. The system can be initialized with either low or high homogeneous values of the density, ρ, which enables the system to reach different homogeneous steady states (provided that $|b|$ is larger than a certain (tricritical) value[4]), thus confirming explicitly that the fixed-energy equations above exhibit a full region of bistability with hysteresis on two-dimensional lattices [105]. In addition, within the bistable region there exists a *Maxwell point* ($\overline{E} = E_M$ at which both phases are equally stable) that defines the edge of phase coexistence. The latter is computationally verified by considering as initial condition half a system in the active state and the other half in the absorbing state; right at $\overline{E} = E_M$, the flat interface separating these two halves does not move on average (i.e., none of the two phases is more stable than the other).

[4]Let us remark that, for relatively small (in absolute value) b, the transition becomes continuous even if the mean-field approximation predicts a discontinuous one. As discussed in [108], fluctuation effects typically soften the discontinuity, shrink bistability regions, and can even alter the order of the phase transition, leading to noise-induced criticality.

The mechanism enabling self-organization to the edge of bistability (SOB) is constructed, as in SOC, by adding slow ("offline") driving and boundary dissipation to the previous equations. In particular, the system is set into an absorbing state and is locally perturbed to trigger avalanches of activity, which are eventually dissipated at the system boundaries. By iterating this process, the system self-organizes to values of $\overline{E}$ close to E_M (converging exactly to E_M in the thermodynamic limit). Alternatively, again as in the SOC case, we can obtain a similar behavior by considering "online" driving and dissipation, i.e., by replacing the second equation in (8) with:

$$\partial_t E(\vec{x},t) = \nabla^2\rho(\vec{x},t) - \epsilon\rho(\vec{x},t) + h(\vec{x},t) \tag{9}$$

in the limit $h/\epsilon \to 0$ (see **Figure 2**, upper-right panel).

Remarkably, avalanches of broadly different scales with signatures of scale invariance also emerge in SOB, in spite of the lack of a critical point [105]. However, the avalanche size and duration probability distributions are different from their SOC counterparts in two important ways:

- The probability distributions for both avalanche size and duration are bimodal: small avalanches coexist with extremely large ones that span the whole system. These latter "anomalous" outbursts of activity, which are also called "king" (or "dragon king") avalanches in the literature [105, 109], occur in an almost periodic way. They represent waves of activity that propagate almost deterministically (i.e., ballistically) starting from a localized seed, and span through most of the system until they are dissipated at the open boundaries, leaving the system depleted of "energy." Let us also emphasize that such system-wide episodes are reminiscent of what happens in the mean-field counterpart, in which activity cyclically "waxes and wanes" the system.
- Smaller standard avalanches have sizes and durations distributed as power laws with exponents $\tau = 3/2$ (size, see **Figure 4** upper-right panel) and $\alpha = 2$ (duration). These values coincide with those of the mean-field branching process, which is also equivalent to compact directed percolation and the voter model [64–66, 72, 110]. This type of scaling emerges because the system becomes self-organized to the Maxwell point E_M (see **Figure 3**, upper-right panel), where the two phases are equally stable (or "neutral" [111, 112]). In this way, clusters of active sites in a non-active environment are equally likely to expand or shrink through fluctuations; this marginality is tantamount to criticality and generates scale invariance. In this sense, the system behaves as an effective voter model (or compact directed percolation) with two symmetric states in which none of them is favored. Indeed, the voter model exhibits a critical point for the propagation of activity with the mean-field behavior mentioned above. In two dimensions, upper critical dimension for these systems, logarithmic corrections to scaling appear [66, 113].

As discussed in detail in [105], the larger the value of $|b|$—which defines the jump or discontinuity at the phase transition—the stronger the weight and frequency of anomalous avalanches. Thus, for relatively small jumps, clean scaling can be observed

for many decades (as in **Figure 4**, upper-right panel), while for large values of $|b|$ the statistics are more prominently dominated by large anomalous avalanches. In the latter case, larger system sizes are needed to observe clearly the power-law scaling of standard avalanches.

For the sake of completeness, let us mention that it is also possible to construct sandpile models with SOB phenomenology [105]. The key difference with respect to standard SOC sandpiles is the presence of a "facilitation" mechanism such that activity (i.e., sites above threshold) amplifies in a non-linear way the creation of additional activity. This type of facilitation mechanism is well-known to be at the origin of discontinuous transitions, leading to bistability (see e.g., [108]). The phenomenology of sandpiles with facilitation coincides remarkably well with what we just described for SOB; in particular, they exhibit scale-free avalanches with mean-field exponents together with king avalanches [105]. Moreover, in experimental results for real-life sandpiles [114] small avalanches coexist with much larger ones, the global energy experiences large excursions, and the empirically determined avalanche distributions are remarkably similar to those of SOB. Furthermore, it seems that inertia in the dynamics of real sandgrains plays a role similar to facilitation. All these observations together suggest that SOB is potentially a more adequate theory to describe real sandpiles than SOC. Similarly, SOB could also be at the origin of the "self-organized avalanche oscillator" found in microfracture experiments [115]. Finally, in the context of neurodynamics, models of neuronal activity regulated by the level of synaptic resources—very similar in essence to SOB—can reproduce scale-free avalanches coexisting with anomalous large waves of activity in agreement with empirical observations [116] (see next sections for more details on neural dynamics).

4. THEORIES FOR IMPERFECT SELF-ORGANIZATION

The theories of SOC and SOB rely heavily onto conservative (bulk) dynamics as well as onto infinite separation of timescales between driving and (boundary) dissipation. These ingredients, as we have extensively discussed, are essential to achieving a precise and exact self-organization to either a critical point (SOC) or to the point of phase coexistence (SOB). On the other hand, there is a large variety of natural phenomena that exhibit scale invariance (at least approximately) and in which some form of (bulk) dissipation is inevitably present and/or timescales are not perfectly separated. As an illustrative example, let us discuss the case of neuronal dynamics in the cerebral cortex. Seminal experiments revealed that the dynamics of actual neural networks are bursty, and that critical-like scale-free avalanches of activity can be measured experimentally under generic experimental conditions [117]. It has been argued that such a critical-like state induces important functional advantages for information processing and transmission in the cortex [118–125] (for a recent review, see [126]). This caught the attention of physicists, who readily tried to describe neural networks in terms of SOC [127–131]. However, neurons are "leaky," as there is no conserved quantity in their dynamics (for instance, the membrane voltage decays spontaneously to some baseline level in the absence of inputs). Moreover, timescales in the brain are not infinitely fast/slow. Therefore, the scaling behavior of cortical networks observed empirically cannot be exactly ascribed neither to SOC [132] nor SOB [107]. In order to understand this type of scaling, a more general theory that does not rely on infinite separation of timescales and conservation laws is needed.

Alternative mechanisms for alleged self-organization to criticality in the absence of conservation have long been studied [22]. Indeed, some of the archetype models of self-organized criticality (other than sandpiles) are non-conserved. Prominent examples are earthquake models [133, 134] and forest-fire models [135–137]. These are non-trivial models with a rich and complex phenomenology showing power-laws and scaling for at least some decades. However, the lack of theoretical arguments as solid as the ones discussed above for conserving systems led to a long-standing controversy regarding the existence of true generic scale-invariance in these non-conserving systems. It is not our scope here to review this controversy, but let us just to summarize the main conclusion: none of the studied self-organizing non-conserved models is truly critical but, instead, they exhibit some sort of "approximate" or "relaxed" criticality [see e.g., [138–144], as well as [33] for further discussions and references].

In what follows, we use our unified theoretical framework to briefly introduce and discuss versions of SOC and SOB, respectively, in which the strict conditions of conservation and infinite separation of timescales are relaxed.

4.1. Theory of Self-Organized Quasi Criticality (SOqC)

To provide non-conserved systems alleged to be SOC with a general theoretical background, some of us proposed a modified version of the SOC theory, Equation (5), that includes explicitly a non-vanishing energy-dissipation term:

$$\begin{aligned}\partial_t \rho(\vec{x},t) &= (a+\omega E(\vec{x},t))\rho - b\rho^2 + D\nabla^2\rho + \sigma\sqrt{\rho(\vec{x},t)}\eta(\vec{x},t)\\ \partial_t E(\vec{x},t) &= \nabla^2\rho(\vec{x},t) - \epsilon\rho(\vec{x},t),\end{aligned} \tag{10}$$

that is, Equation (6) with $h = 0$, and where now $\epsilon > 0$ is not necessarily small and does not vanish in the large-system-size limit. This equation can be complemented with the following "offline" updating rule, inspired in the charging mechanism in models of forest fires and earthquakes [33]: every time the system reaches the absorbing state, a small "seed" of activity is placed at a randomly chosen site, and the energy of all sites is increased:

$$\begin{aligned}\rho(\vec{x}_0,0) &\to h\\ E(\vec{x},0) &\to E(\vec{x},0) + \gamma(E_{\max} - \overline{E})\end{aligned} \tag{11}$$

where γ is an external driving, $E_{\max}$ the maximum allowed energy in the system, $\overline{E}$ the system average energy density, and $\vec{x}_0$ a random position in the lattice. Note that this "offline" updating rule has been used for the $\epsilon \neq 0$ cases in **Figures 3**, **4**. These modifications with respect to the SOC case lead to the following results [33]:

- First, the leakage (i.e., dissipative) term prevents the existence of a true self-sustained active phase. This can be easily seen by integrating formally the second equation and plugging the result into the first one, thus generating a non-Markovian term $-\epsilon\rho(\vec{x},t)\int_0^t dt'\rho(\vec{x},t')$, which is characteristic of *dynamical percolation* [73, 145–147]. This makes it impossible to have a steady state with $\rho(\vec{x}) \neq 0$ in the long-time limit. Moreover, Equation (11) exhibit a transition at some value of the initial energy, $E_p > E_c$, that separates a *spreading* phase (in which local perturbations of activity can propagate by percolating transiently through the system without reaching a steady state) from a non-spreading phase where perturbations cannot span the whole system.
- As a consequence of the previous argument, scaling features in this type of models are related to dynamical percolation when using "offline" driving, rather than to C-DP [33]. In other words, bulk dissipation (i.e., breaking the bulk-conservation law) is a relevant perturbation in the renormalization group sense [146]. See Appendix for further details.
- An analytical and computational study of Equation (10) revealed that, in this case, increasing $\overline{E}$ through the addition of energy like in sandpiles shifts progressively the systems into the dynamical-percolating phase beyond its critical point E_p [33]. If an avalanche occurs, the associated strong dissipation depletes the system of energy, thus pushing it deep into the non-percolating phase. Therefore, the system does not self-organize exactly to the edge of a phase transition as in the conserved cases above but, instead, it keeps hovering around it, with excursions of finite amplitude to both sides of the (dynamical percolation) transition point, E_p (see **Figures 2**, **3**, lower-left panels). In other words, the average energy does not self-tune to a critical value but keeps on alternating between subcritical and supercritical values, even for infinitely large systems. Numerical results reveal that this sweeping though the phase transition point might suffice to induce approximate or "dirty" scaling behavior, but not strict "*bona fide*" scale invariance [33, 148, 149].

This mechanism, accounting generically for non-conservative self-organized systems, has been termed "*self-organized quasi-criticality*" (SOqC) [33][5]. Several remarks are in order:

- In systems in which driving does not occur "offline" (i.e., at an arbitrarily slow timescale, where both the activity and the energy are perturbed only between avalanches) one needs to include explicitly a continuous "online" driving term in Equation (10), so that the second equation becomes $\partial_t E(\vec{x},t) = \nabla^2\rho(\vec{x},t) - \epsilon\rho(\vec{x},t) + h$, where h is the (arbitrarily large) charging or driving rate; alternatively:

$$\partial_t E(\vec{x},t) = \nabla^2\rho(\vec{x},t) - \epsilon\rho(\vec{x},t) + h(E_{max} - E) \qquad (12)$$

  if there is a maximum possible level of charging given by E_{max}. These alternative charging mechanisms may change the previously described phenomenology. The "online" driving parameters can be fine-tuned to effectively compensate for dissipation, and a steady state with $\rho \neq 0$ can be achieved. In this case the system phenomenology is controlled by the C-DP transition even if the system does not become truly critical (it just hovers around the critical point, E_c); energy is conserved on average, and an approximated or "dirty" C-DP-like behavior emerges. However, dynamical percolation dominates for sufficiently large systems if "offline" charge is used because, during avalanches, energy can only be dissipated, i.e. bulk conservation is not present during the dynamics. The system will always deplete the available energy until falling again into the absorbing state, when the system is charged to restart the dynamics (see **Figure 4**, lower-left panel).
- It is important to underline that, in spite of its name reminiscent of SOC, SOqC does not describe true "self-organization" to a unique dynamical state. The ratio between dissipation and driving constants h/ϵ (and also E_{max}) determines the system state, thus acting as a true control parameter. If dissipation dominates strongly, the system is subcritical (a case sometimes called "*self-organized subcriticality*"). If driving is strong, then the system becomes supercritical ("*self-organized supercriticality*") [33, 132]. Finally, for a broad range of intermediate situations, the system hovers around a critical point ("self-organized quasi criticality"). Thus, unlike the SOC case, the choice of parameters (and not only system size) can determine the "cleanliness" of the observed scaling behavior.

For more detailed explanations of all this phenomenology we refer to [33, 132] and, for applications in neuroscience, to [151–161].

4.2. Theory of Self-Organized Collective Oscillations (SOCO)

To close the loop, we now discuss self-organization in the case of non-conservative systems exhibiting a discontinuous phase transition (see **Figures 2**–**4**, lower-right panels).

A theory for this case can be written combining the activity equation in Equation (8) with a second equation analogous to Equation (12) for the non-conserved energy ("online" driving and dissipation). Alternatively, the "online" driving component can be replaced by the ("offline") rule in Equation (11) to "charge" between avalanches. However, in order to make the presentation more appealing, we will instead discuss the recently introduced Landau-Ginzburg theory for cortical dynamics in the presence of synaptic resources [162], which fits perfectly our purposes here. The theory is defined by the following set of equations (considered on e.g., a two-dimensional lattice [162]):

$$\begin{aligned} &\partial_t\rho(\vec{x},t) = (a + \omega E(\vec{x},t))\rho - b\rho^2 - c\rho^3 \\ &+D\nabla^2\rho + \sigma\sqrt{\rho(\vec{x},t)}\eta(\vec{x},t) \\ &\partial_t E(\vec{x},t) = \nabla^2\rho(\vec{x},t) - \epsilon E\rho + h(E_{max} - \overline{E}) \end{aligned} \qquad (13)$$

with $b < 0$ and $c > 0$. In the context of neural dynamics, $\rho(\vec{x},t)$ represents the density of neuronal activity in a coarse-grained

[5]The concept on "weak criticality," proposed more recently, bears strong resemblance to SOqC [149]; see also the slightly different definition of quasi-critical employed in [150].

region of the cortex, while the energy field represents the level of synaptic resources at a given location (with E_{max} its maximum level at any given location). These equations are similar to those for SOB (Equation 8), but note the presence of a dissipative term in the second equation (similar to, but different from, that in the SOqC theory, Equation 10), as well as a driving term (as in Equation 12) that "charges" the energy field. The diffusion term in the second equation could be safely removed as it is irrelevant in this case [107], and was actually absent/omitted in the original neural-dynamic model [162].

As commented for SOqC, because the dynamics are not conserved, the system is not really "self-organized" to a unique type of behavior [162]. Indeed, the free parameter E_{max} becomes a control parameter, regulating the system output:

- If E_{max} is exceedingly small, the system "self-organizes" into an absorbing configuration with no activity.
- If E_{max} is sufficiently large, the system "self-organizes" into a homogeneous active state where individual sites alternate between the active and the inactive state; the latter occurs in an incoherent or "asynchronous" way, thus keeping an overall fixed stationary density of activity.
- In the more interesting case between the two regimes above, there is an intermediate phase in which quasi-oscillatory dynamics emerge. This regime is described by waves of activity traveling through the system, generating co-activation of many units within a relatively small time window [we refer to [162] for more details and videos of these rich dynamics]. These events bear strong resemblance with the system-spanning avalanches—or anomalous waves—described in SOB.

By fine-tuning E_{max}, it is possible to find a critical point that separates the phase of global oscillations ("synchronous phase") from the active phase in which units do not oscillate in unison ("asynchronous phase"). In other words, these systems exhibit a synchronization phase transition [162].

Finally, let us remark that, in the limit in which the driving and dissipation parameters ϵ and h converge to 0 (keeping the usual separation of timescales), the system approaches true self-organization. Not surprisingly, in this limit one recovers all the phenomenology of SOB, including scale-free avalanches coexisting with anomalously large waves of activity [107].

SUMMARY AND DISCUSSION

More than three decades after the creation of the concept of self-organized criticality, SOC continues to attract interest of theoretical and applied scientists. The original prototypical models such as sandpiles rely on a rather general type of feedback mechanism that, acting differentially at both sides of the phase transition, allows for the self-organization to the edge of the transition. As profusely discussed here, such a feedback mechanism depends crucially on a large separation of timescales between a slow driving and the intrinsic fast dynamics, conserved in the bulk. Note that the feedback mechanism is "just" a way to reach the neighborhood of a phase transition, but it is the intrinsic dynamics that determines the universality class that the system belongs to. Thus, there is no "self-organized universality class," but instead phase transitions that belong to specific universality classes (BTW, C-DP...) and that may be reached through the described self-organization mechanism.

Although other mechanisms for self-organization to criticality that do not depend on such a type of feedback were originally proposed (e.g., extremal dynamics [18]), in this mini-review paper we have focused instead on this feedback mechanism to provide the reader with a concise and systematic overview of field theoretical or, equivalently, Langevin approaches to SOC. This formalism—in the spirit of Landau-Ginzburg and Hohenberg-Halperin—constitutes, in our opinion, an excellent framework to underline the generality of the discussed phenomenology, stressing the key aspects and neglecting as much as possible specific model-dependent details.

Thus, we reviewed the Langevin approach to SOC and described how and why the system self-organizes to the edge of a standard (non-equilibrium) continuous phase transition separating an active from an absorbing phase. In the limit of an infinite separation of timescales and conservative bulk dynamics, the systems self-organizes perfectly to the phase transition, i.e., to criticality. On the other hand, when some of these stringent conditions are relaxed (i.e., if the separation of timescales is not perfect and/or the system is not perfectly conservative), then there is instead approximate or "imperfect" self-organization to the vicinity of the transition point, with the system's control parameter hovering around it and excursions into both the subcritical and the supercritical phases (SOqC). Forest-fire and earthquake models—as well as models of neural dynamics—can much better be ascribed to SOqC than to actual SOC. It is, however, important to underline that tuning the parameters associated with driving and dissipation is required for the system to self-organize either to the subcritical or the supercritical regimes. Thus, SOqC systems do not really self-organize to the vicinity of a transition in a strict sense, but rather there are broad ranges of parameter values for which the system hovers around criticality and exhibits approximate scale invariance.

We also reviewed the recently proposed concept of SOB, explaining how a feedback mechanism similar to that of SOC may operate to self-organize a system to the edge of a first-order, discontinuous, phase transition. As for SOC, in the limit of infinite separation of timescales and conservative bulk dynamics, the self-organization to the transition is exact. Unlike for SOC, however, small avalanches coexist with anomalously large ones. Furthermore, avalanches belong to the voter model universality class, which results from the existence of bistability (i.e., two equivalent states as in the voter model class) at the self-organized Maxwell point. We also defined an "imperfect" self-organization mechanism for a family of systems exhibiting a discontinuous phase transition. As in SOqC, there is not "true" self-organization. Instead, the non-conserved equivalent of SOB shows a broad range of parameter values for which the system exhibits collective oscillations, alternating between regimes of high activity and quiescent ones (hence the name "self-organized collective oscillations," SOCO).

All the mechanisms discussed above lead to the self-organization to the vicinity of a non-equilibrium absorbing-active phase transition. Nevertheless, similar mechanisms have also been described in other contexts, such as self-organization to the edge of a synchronization phase transition in the context of models of neuronal dynamics [163–165]. This mechanism is similar in spirit to those above, operating differentially in the two alternative phases; in particular, the synaptic strengths (which play the role of "energy variable") tend to be reinforced when the system is in the asynchronous phase and weakened when it is exceedingly synchronous (which is achieved by a synaptic plasticity mechanism such as "spike-time dependent plasticity" [166]), thus, leading the system to the edge of a synchronization phase transition in a self-organized way. The concept of "imperfect self-organization" can also potentially shed some light on other biological systems where controversy remains as to whether they show critical behavior, such as the emergence of marginal orientational order in flocks of birds and insect swarms [126, 167–170], as well as on other ordering transitions emerging in the lively research field on active matter [171]. In fact, the concepts discussed here can be re-interpreted in terms of homeostatic mechanisms allowing systems (e.g., brain), organisms, or collectives to self-regulate to an operational regime that is close to optimal.

It is indeed in the realm of living systems, where self-organization and optimization are habitual, where we foreshadow SOC will find some of its most exciting future challenges. Although during the last decades the idea of SOC has been widely and successfully used to conceptualize the dynamical behavior of natural systems, there exist many biological systems that appear to display critical properties [126] and, therefore, are susceptible to being studied from the SOC viewpoint. The theory of SOC, along with its current generalizations, are a powerful tool to conceptually understand these and other phenomena. For example, as already discussed here, SOC, SOqC, as well as SOB, have been argued to play a relevant role in neuronal dynamics (see e.g., the review paper by Kinouchi et al. in this same special issue and [132, 172]); a Langevin approach as the one presented here could potentially help develop a renormalization-group approach to describe the scale-invariant behavior of brain activity [107, 162]. In addition, evolutionary processes can be seen as the driving force that allows biological systems to self-organize to an optimal critical-like point [18]. Concepts such as "self-evolved criticality" [173, 174] could thus be used to explain the evolutionary pathway of specific organisms and/or the emergence of specific traits, or adaptive responses to short- or long-term perturbations. The latter would provide important insight on the resilience of key biological systems, as it could help assess whether the self-organizing mechanisms present in a focal system are robust enough for it to cope with the rapid environmental changes occurring in the anthropocene.

In summary, we have reviewed within a common and unified framework different types of mechanisms for the self-organization to the the vicinity of phase transitions. We hope that this work help clarify the—sometimes confusing or contradictory—literature on the subject, and contribute to pave the road for new and exciting developments in physics, but also other disciplines. This could be especially important in biology, where the idea that living systems can obtain important functional advantages by operating at the edge of two alternative/complementary types of phases/states has attracted a great deal of attention and excitement [126, 170].

AUTHOR CONTRIBUTIONS

MM, JB, and SS designed the research. JB and VB performed the simulations. VB prepared the figures. All authors contributed to writing and reviewing the manuscript.

FUNDING

We acknowledge the Spanish Ministry and Agencia Estatal de investigación (AEI) through grant *FIS*2017−84256−*P* European Regional Development Fund (ERDF), as well as the Consejería de Conocimiento, Investigación y Universidad, Junta de Andalucía and ERDF, $A-FQM-175-UGR18$ and $SOMM17/6105/UGR$ and for financial support. We also thank Cariparma for their support through the TEACH IN PARMA project.

ACKNOWLEDGMENTS

We are very thankful to Ronald Dickman, Guillermo B. Morales, Johannes Zierenberg, Matteo Sireci for comments and a critical reading of initial versions of the manuscript.

REFERENCES

1. Bak P, Tang C, Wiesenfeld K. Self-organized criticality: an explanation of the 1/f noise. *Phys Rev Lett*. (1987) **59**:381. doi: 10.1103/PhysRevLett.59.381
2. Mandelbrot BB. *The Fractal Geometry of Nature*. Vol. 173. New York, NY: Macmillan (1983).
3. Albert R, Barabási AL. Statistical mechanics of complex networks. *Rev Mod Phys*. (2002) **74**:47–97. doi: 10.1103/RevModPhys.74.47
4. Bak P. *How Nature Works: The Science of Self-Organized Criticality*. New York, NY: Copernicus (1996). doi: 10.1007/978-1-4757-5426-1
5. Bak P, Chen K. Self-organized criticality. *Sci Am*. (1991) **264**:46–53. doi: 10.1038/scientificamerican0191-46
6. Jensen HJ. *Self-Organized Criticality: Emergent Complex Behavior in Physical and Biological Systems*. Cambridge: Cambridge University Press (1998). doi: 10.1017/CBO9780511622717
7. Christensen K, Moloney N. *Complexity and Criticality*. London: Imperial College Press (2005). doi: 10.1142/p365
8. Pruessner G. *Self-Organised Criticality: Theory, Models and Characterisation*. Cambridge: Cambridge University Press (2012).
9. Dickman R, Mu noz M, Vespignani A, Zapperi S. Paths to self-organized criticality. *Braz J Phys*. (2000) **30**:27–41. doi: 10.1590/S0103-97332000000100004
10. Watkins NW, Pruessner G, Chapman SC, Crosby NB, Jensen HJ. 25 years of self-organized criticality: concepts and controversies. *Space Sci Rev*. (2015) **198**:3–44. doi: 10.1007/s11214-015-0155-x

11. Turcotte DL. Self-organized criticality. *Rep Prog Phys*. (1999) **62**:1377. doi: 10.1088/0034-4885/62/10/201
12. Marković D, Gros C. Power laws and self-organized criticality in theory and nature. *Phys Rep*. (2014) **536**:41–74. doi: 10.1016/j.physrep.2013.11.002
13. Manna SS. Two-state model of self-organized criticality. *J Phys A*. (1991) **24**:L363–9. doi: 10.1088/0305-4470/24/7/009
14. Christensen K, Corral A, Frette V, Feder J, Jossang T. Tracer dispersion in a self-organized critical system. *Phys Rev Lett*. (1996) **77**:107–10. doi: 10.1103/PhysRevLett.77.107
15. Zhang YC. Scaling theory of self-organized criticality. *Phys Rev Lett*. (1989) **63**:470. doi: 10.1103/PhysRevLett.63.470
16. Grassberger P, Manna S. Some more sandpiles. *J Phys*. (1990) **51**:1077–98. doi: 10.1051/jphys:0199000510110107700
17. Maslov S, Zhang YC. Exactly solved model of self-organized criticality. *Phys Rev Lett*. (1995) **75**:1550. doi: 10.1103/PhysRevLett.75.1550
18. Bak P, Sneppen K. Punctuated equilibrium and criticality in a simple model of evolution. *Phys Rev Lett*. (1993) **71**:4083. doi: 10.1103/PhysRevLett.71.4083
19. Tang C, Bak P. Critical exponents and scaling relations for self-organized critical phenomena. *Phys Rev Lett*. (1988) **60**:2347. doi: 10.1103/PhysRevLett.60.2347
20. Dhar D. The Abelian sandpile and related models. *Phys A*. (1999) **263**:4–25. doi: 10.1016/S0378-4371(98)00493-2
21. Dhar D. Theoretical studies of self-organized criticality. *Phys A*. (2006) **369**:29–70. doi: 10.1016/j.physa.2006.04.004
22. Grinstein G. Generic scale invariance and self-organized criticality. In: McKane A, Droz M, Vannimenus J, Wolf D, editors. *Scale Invariance, Interfafaces, and Non-equilibrium Dynamics*. Vol. 344 of NATO Advanced Study Institute, Series B: Physics. New York, NY: Plenum Press (1995). p. 261–293. doi: 10.1007/978-1-4899-1421-7_11
23. Laurson L, Alava MJ, Zapperi S. Power spectra of self-organized critical sandpiles. *J Stat Mech*. (2005) **2005**:L11001. doi: 10.1088/1742-5468/2005/11/L11001
24. Helmrich S, Arias A, Lochead G, Wintermantel T, Buchhold M, Diehl S, et al. Signatures of self-organized criticality in an ultracold atomic gas. *Nature*. (2020) **579**:E13. doi: 10.1038/s41586-020-2091-5
25. Schiró M. Rydberg atoms on fire. *Physics*. (2020) **13**:70. doi: 10.1103/Physics.13.70
26. Grinstein G, Lee DH, Sachdev S. Conservation laws, anisotropy, and "self-organized criticality in noisy nonequilibrium systems. *Phys Rev Lett*. (1990) **64**:1927. doi: 10.1103/PhysRevLett.64.1927
27. Socolar J, Grinstein G, Jayaprakash C. On self-organized criticality in nonconserving systems. *Phys Rev E*. (1993) **47**:2366. doi: 10.1103/PhysRevE.47.2366
28. Bak P. Self-organized criticality in non-conservative models. *Phys A*. (1992) **191**:41–6. doi: 10.1016/0378-4371(92)90503-I
29. Hwa T, Kardar M. Avalanches, hydrodynamics, and discharge events in models of sandpiles. *Phys Rev A*. (1992) **45**:7002. doi: 10.1103/PhysRevA.45.7002
30. Hwa T, Kardar M. Dissipative transport in open systems: an investigation of self-organized criticality. *Phys Rev Lett*. (1989) **62**:1813. doi: 10.1103/PhysRevLett.62.1813
31. Drossel B. Complex scaling behavior of nonconserved self-organized critical systems. *Phys Rev Lett*. (2002) **89**:238701. doi: 10.1103/PhysRevLett.89.238701
32. Malcai O, Shilo Y, Biham O. Dissipative sandpile models with universal exponents. *Phys Rev E*. (2006) **73**:056125. doi: 10.1103/PhysRevE.73.056125
33. Bonachela JA, Mu noz MA. Self-organization without conservation: true or just apparent scale-invariance? *J Stat Mech*. (2009) **2009**:P09009. doi: 10.1088/1742-5468/2009/09/P09009
34. Ben-Hur A, Biham O. Universality in sandpile models. *Phys Rev E*. (1996) **53**:R1317–20. doi: 10.1103/PhysRevE.53.R1317
35. Bonachela JA. Ph. D Thesis: Universality in Self-Organized Criticality. Granada: Universidad de Granada; 2008.
36. Ktitarev D, Lübeck S, Grassberger P, Priezzhev V. Scaling of waves in the Bak-Tang-Wiesenfeld sandpile model. *Phys Rev E*. (2000) **61**:81. doi: 10.1103/PhysRevE.61.81
37. Tebaldi C, De Menech M, Stella AL. Multifractal scaling in the Bak-Tang-Wiesenfeld sandpile and edge events. *Phys Rev Lett*. (1999) **83**:3952. doi: 10.1103/PhysRevLett.83.3952
38. De Menech M, Stella AL. From waves to avalanches: two different mechanisms of sandpile dynamics. *Phys Rev E*. (2000) **62**:R4528. doi: 10.1103/PhysRevE.62.R4528
39. Bagnoli F, Cecconi F, Flammini A, Vespignani A. Short-period attractors and non-ergodic behavior in the deterministic fixed-energy sandpile model. *Europhys Lett*. (2003) **63**:512. doi: 10.1209/epl/i2003-00561-8
40. Christensen K, Moloney NR, Peters O, Pruessner G. Avalanche behavior in an absorbing state Oslo model. *Phys Rev E*. (2004) **70**:67101. doi: 10.1103/PhysRevE.70.067101
41. Huynh HN, Pruessner G, Chew LY. The Abelian Manna model on various lattices in one and two dimensions. *J Stat Mech*. (2011) **2011**:P09024. doi: 10.1088/1742-5468/2011/09/P09024
42. Grassberger P, Dhar D, Mohanty P. Oslo model, hyperuniformity, and the quenched Edwards-Wilkinson model. *Phys Rev E*. (2016) **94**:042314. doi: 10.1103/PhysRevE.94.042314
43. Bonachela JA, Mu noz MA. Confirming and extending the hypothesis of universality in sandpiles. *Phys Rev E*. (2008) **78**:041102. doi: 10.1103/PhysRevE.78.041102
44. Narayan O, Middleton AA. Avalanches and the renormalization group for pinned charge-density waves. *Phys Rev B*. (1994) **49**:244. doi: 10.1103/PhysRevB.49.244
45. Paczuski M, Boettcher S. Universality in sandpiles, interface depinning, and earthquake models. *Phys Rev Lett*. (1996) **77**:111. doi: 10.1103/PhysRevLett.77.111
46. Nunes Amaral LA, Lauritsen KB. Universality classes for rice-pile models. *Phys Rev E*. (1997) **56**:231–4. doi: 10.1103/PhysRevE.56.231
47. Alava MJ, Lauritsen KB. Quenched noise and over-active sites in sandpile dynamics. *Europhys Lett*. (2001) **53**:563. doi: 10.1209/epl/i2001-00189-8
48. Pruessner G. Oslo rice pile model is a quenched Edwards-Wilkinson equation. *Phys Rev E*. (2003) **67**:030301. doi: 10.1103/PhysRevE.67.030301
49. Sethna JP, Dahmen KA, Myers CR. Crackling noise. *Nature*. (2001) **410**:242–50. doi: 10.1038/35065675
50. Perković O, Dahmen K, Sethna JP. Avalanches, Barkhausen noise, and plain old criticality. *Phys Rev Lett*. (1995) **75**:4528. doi: 10.1103/PhysRevLett.75.4528
51. Zapperi S, Cizeau P, Durin G, Stanley HE. Dynamics of a ferromagnetic domain wall: avalanches, depinning transition, and the Barkhausen effect. *Phys Rev B*. (1998) **58**:6353. doi: 10.1103/PhysRevB.58.6353
52. Dickman R, Vespignani A, Zapperi S. Self-organized criticality as an absorbing-state phase transition. *Phys Rev E*. (1998) **57**:5095. doi: 10.1103/PhysRevE.57.5095
53. Vespignani A, Dickman R, Mu noz MA, Zapperi S. Absorbing-state phase transitions in fixed-energy sandpiles. *Phys Rev E*. (2000) **62**:4564. doi: 10.1103/PhysRevE.62.4564
54. Vespignani A, Dickman R, Mu noz M, Zapperi S. Driving, conservation, and absorbing states in sandpiles. *Phys Rev Lett*. (1998) **81**:5676. doi: 10.1103/PhysRevLett.81.5676
55. Pastor-Satorras R, Vespignani A. Field theory of absorbing phase transitions with a nondiffusive conserved field. *Phys Rev E*. (2000) **62**:R5875–8. doi: 10.1103/PhysRevE.62.R5875
56. Rossi M, Pastor-Satorras R, Vespignani A. Universality class of absorbing phase transitions with a conserved field. *Phys Rev Lett*. (2000) **85**:1803–6. doi: 10.1103/PhysRevLett.85.1803
57. Wiese KJ. Coherent-state path integral versus coarse-grained effective stochastic equation of motion: from reaction diffusion to stochastic sandpiles. *Phys Rev E*. (2016) **93**:042117. doi: 10.1103/PhysRevE.93.042117
58. Alava M, Mu noz MA. Interface depinning versus absorbing-state phase transitions. *Phys Rev E*. (2002) **65**:026145. doi: 10.1103/PhysRevE.65.026145
59. Bonachela JA, Chaté H, Dornic I, Mu noz MA. Absorbing states and elastic interfaces in random media: two equivalent descriptions of self-organized criticality. *Phys Rev Lett*. (2007) **98**:155702. doi: 10.1103/PhysRevLett.98.155702
60. Bonachela JA, Alava M, Mu noz MA. Cusps, self-organization, and absorbing states. *Phys Rev E*. (2009) **79**:050106. doi: 10.1103/PhysRevE.79.050106

61. Le Doussal P, Wiese KJ. Exact mapping of the stochastic field theory for manna sandpiles to interfaces in random media. *Phys Rev Lett*. (2015) **114**:110601. doi: 10.1103/PhysRevLett.114.110601
62. Tang C, Bak P. Mean field theory of self-organized critical phenomena. *J Stat Phys*. (1988) **51**:797–802. doi: 10.1007/BF01014884
63. Dickman R, Alava M, Mu noz MA, Peltola J, Vespignani A, Zapperi S. Critical behavior of a one-dimensional fixed-energy stochastic sandpile. *Phys Rev E*. (2001) **64**:056104. doi: 10.1103/PhysRevE.64.056104
64. Hinrichsen H. Non-equilibrium critical phenomena and phase transitions into absorbing states. *Adv Phys*. (2000) **49**:815–958. doi: 10.1080/00018730050198152
65. Marro J, Dickman R. *Nonequilibrium Phase Transitions in Lattice Models*. Collection Aléa-Saclay. Cambridge University Press (2005). Available online at: http://books.google.it/books?id=80YF69jbczYC
66. Henkel M, Hinrichsen H, Lübeck S. *Non-Equilibrium Phase Transitions: Absorbing Phase Transitions. Theoretical and Mathematical Physics*. Berlin: Springer London (2008).
67. Sidoravicius V, Teixeira A. Absorbing-state transition for stochastic sandpiles and activated random walks. *Electron J Probabil*. (2017) **22**:1–35. doi: 10.1214/17-EJP50
68. Dickman R, Rolla LT, Sidoravicius V. Activated random walkers: facts, conjectures and challenges. *J Stat Phys*. (2010) **138**:126–42. doi: 10.1007/s10955-009-9918-7
69. Vespignani A, Zapperi S. Order parameter and scaling fields in self-organized criticality. *Phys Rev Lett*. (1997) **78**:4793. doi: 10.1103/PhysRevLett.78.4793
70. Sornette D, Johansen A, Dornic I. Mapping self-organized criticality onto criticality. *J Phys I*. (1995) **5**:325–35. doi: 10.1051/jp1:1995129
71. Bröker HM, Grassberger P. SOC in a population model with global control. *Phys A*. (1999) **267**:453–70. doi: 10.1016/S0378-4371(99)00042-4
72. Ódor G. *Universality in Nonequilibrium Lattice Systems: Theoretical Foundations*. Singapore: World Scientific (2008). doi: 10.1142/6813
73. Mu noz M, Grinstein G, Dickman R, Livi R. Critical behavior of systems with many absorbing states. *Phys Rev Lett*. (1996) **76**:451. doi: 10.1103/PhysRevLett.76.451
74. Binney JJ, Dowrick NJ, Fisher AJ, Newman MEJ. *The Theory of Critical Phenomena*. Oxford: Oxford University Press (1993).
75. Le Bellac M. *Quantum and Statistical Field Theory*. Oxford: Clarendon Press (1991).
76. Amit DJ, Martin-Mayor V. *Field Theory, the Renormalization Group, and Critical Phenomena: Graphs to Computers*. 3rd Edition. Singapore: World Scientific Publishing Company (2005). doi: 10.1142/5715
77. Hohenberg PC, Halperin BI. Theory of dynamic critical phenomena. *Rev Modern Phys*. (1977) **49**:435. doi: 10.1103/RevModPhys.49.435
78. Zapperi S, Lauritsen KB, Stanley HE. Self-organized branching processes: mean-field theory for avalanches. *Phys Rev Lett*. (1995) **75**:4071. doi: 10.1103/PhysRevLett.75.4071
79. Moreau L, Sontag E. Balancing at the border of instability. *Phys Rev E*. (2003) **68**:020901. doi: 10.1103/PhysRevE.68.020901
80. Grassberger P. On phase transitions in Schlögl second model. In: Vidal C, and Pacault A, editors. *Nonlinear Phenomena in Chemical Dynamics*. Berlin; Heidelberg: Springer (1981). p. 262. doi: 10.1007/978-3-642-81778-6_49
81. Janssen HK. On the nonequilibrium phase transition in reaction-diffusion systems with an absorbing stationary state. *Z Phys B Condens Matter*. (1981) **42**:151–4. doi: 10.1007/BF01319549
82. Dornic I, Chaté H, Mu noz MA. Integration of Langevin equations with multiplicative noise and the viability of field theories for absorbing phase transitions. *Phys Rev Lett*. (2005) **94**:100601. doi: 10.1103/PhysRevLett.94.100601
83. Paczuski M, Maslov S, Bak P. Field theory for a model of self-organized criticality. *Europhys Lett*. (1994) **27**:97. doi: 10.1209/0295-5075/27/2/004
84. Weissmann H, Shnerb NM, Kessler DA. Simulation of spatial systems with demographic noise. *Phys Rev E*. (2018) **98**:022131. doi: 10.1103/PhysRevE.98.022131
85. Fey A, Levine L, Wilson DB. Driving sandpiles to criticality and beyond. *Phys Rev Lett*. (2010) **104**:145703. doi: 10.1103/PhysRevLett.104.145703
86. Caracciolo S, Sportiello A. Exact integration of height probabilities in the Abelian Sandpile model. *J Stat Mech*. (2012) **2012**:P09013. doi: 10.1088/1742-5468/2012/09/P09013
87. Jo HH, Jeong HC. Comment on "driving sandpiles to criticality and beyond". *Phys Rev Lett*. (2010) **105**:019601. doi: 10.1103/PhysRevLett.105.019601
88. Poghosyan SS, Poghosyan VS, Priezzhev VB, Ruelle P. Numerical study of the correspondence between the dissipative and fixed-energy abelian sandpile models. *Phys Rev E*. (2011) **84**:066119. doi: 10.1103/PhysRevE.84.066119
89. Mohanty PK, Dhar D. Generic sandpile models have directed percolation exponents. *Phys Rev Lett*. (2002) **89**:104303. doi: 10.1103/PhysRevLett.89.104303
90. Mohanty P, Dhar D. Critical behavior of sandpile models with sticky grains. *Phys A*. (2007) **384**:34–8. doi: 10.1016/j.physa.2007.04.117
91. Basu M, Basu U, Bondyopadhyay S, Mohanty P, Hinrichsen H. Fixed-energy sandpiles belong generically to directed percolation. *Phys Rev Lett*. (2012) **109**:015702. doi: 10.1103/PhysRevLett.109.015702
92. da Cunha SD, da Silva LR, Viswanathan GM, Dickman R. Activity, diffusion, and correlations in a two-dimensional conserved stochastic sandpile. *J Stat Mech*. (2014) **2014**:P08003. doi: 10.1088/1742-5468/2014/08/P08003
93. Hexner D, Levine D. Hyperuniformity of critical absorbing states. *Phys Rev Lett*. (2015) **114**:110602. doi: 10.1103/PhysRevLett.114.110602
94. Dickman R, da Cunha SD. Particle-density fluctuations and universality in the conserved stochastic sandpile. *Phys Rev E*. (2015) **92**:020104. doi: 10.1103/PhysRevE.92.020104
95. Garcia-Millan R, Pruessner G, Pickering L, Christensen K. Correlations and hyperuniformity in the avalanche size of the Oslo model. *Europhys Lett*. (2018) **122**:50003. doi: 10.1209/0295-5075/122/50003
96. Torquato S, Stillinger FH. Local density fluctuations, hyperuniformity, and order metrics. *Phys Rev E*. (2003) **68**:041113. doi: 10.1103/PhysRevE.68.041113
97. van Wijland F. Universality class of nonequilibrium phase transitions with infinitely many absorbing states. *Phys Rev Lett*. (2002) **89**:190602. doi: 10.1103/PhysRevLett.89.190602
98. Janssen HK, Stenull O. Directed percolation with a conserved field and the depinning transition. *Phys Rev E*. (2016) **94**:042138. doi: 10.1103/PhysRevE.94.042138
99. Pruessner G. A field theory for self-organised criticality. In: *Proceedings of the European Conference on Complex Systems 2012*. Cambridge: Springer (2013). p. 79–86. doi: 10.1007/978-3-319-00395-5_13
100. Nattermann T, Stepanow S, Tang LH, Leschhorn H. Dynamics of interface depinning in a disordered medium. *J Phys II*. (1992) **2**:1483–8. doi: 10.1051/jp2:1992214
101. Leschhorn H, Nattermann T, Stepanow S, Tang LH. Driven interface depinning in a disordered medium. *Ann Phys*. (1997) **509**:1–34. doi: 10.1002/andp.19975090102
102. Chauve P, Le Doussal P, Wiese KJ. Renormalization of pinned elastic systems: how does it work beyond one loop? *Phys Rev Lett*. (2001) **86**:1785. doi: 10.1103/PhysRevLett.86.1785
103. Le Doussal P, Wiese KJ, Chauve P. Two-loop functional renormalization group theory of the depinning transition. *Phys Rev B*. (2002) **66**:174201. doi: 10.1103/PhysRevB.66.174201
104. Kuehn C. Time-scale and noise optimality in self-organized critical adaptive networks. *Phys Rev E*. (2012) **85**:026103. doi: 10.1103/PhysRevE.85.026103
105. di Santo S, Burioni R, Vezzani A, Mu noz MA. Self-organized bistability associated with first-order phase transitions. *Phys Rev Lett*. (2016) **116**:240601. doi: 10.1103/PhysRevLett.116.240601
106. Gil L, Sornette D. Landau-Ginzburg theory of self-organized criticality. *Phys Rev Lett*. (1996) **76**:3991. doi: 10.1103/PhysRevLett.76.3991
107. Buendía V, di Santo S, Villegas P, Burioni R, Mu noz MA. Self-organized bistability and its possible relevance for brain dynamics. *Phys Rev Res*. (2020) **2**:013318. doi: 10.1103/PhysRevResearch.2.013318
108. Villa Martín P, Bonachela JA, Levin SA, Mu noz MA. Eluding catastrophic shifts. *Proc Natl Acad Sci USA*. (2015) **112**:E1828–36. doi: 10.1073/pnas.1414708112
109. Sornette D, Ouillon G. Dragon-kings: mechanisms, statistical methods and empirical evidence. *Eur Phys J Spec Top*. (2012) **205**:1–26. doi: 10.1140/epjst/e2012-01559-5

110. Mu noz M, Dickman R, Vespignani A, Zapperi S. Avalanche and spreading exponents in systems with absorbing states. *Phys Rev E*. (1999) **59**:6175–9. doi: 10.1103/PhysRevE.59.6175
111. Pinto OA, Munoz MA. Quasi-neutral theory of epidemic outbreaks. *PLoS ONE*. (2011) **6**:e21946. doi: 10.1371/journal.pone.0021946
112. Martinello M, Hidalgo J, Maritan A, di Santo S, Plenz D, Mu noz MA. Neutral theory and scale-free neural dynamics. *Phys Rev X*. (2017) **7**:041071. doi: 10.1103/PhysRevX.7.041071
113. Dornic I, Chaté H, Chave J, Hinrichsen H. Critical coarsening without surface tension: the universality class of the voter model. *Phys Rev Lett*. (2001) **87**:045701. doi: 10.1103/PhysRevLett.87.045701
114. Yoshioka N. A sandpile experiment and its implications for self-organized criticality and characteristic earthquake. *Earth Planets Space*. (2003) **55**:283–9. doi: 10.1186/BF03351762
115. Papanikolaou S, Dimiduk DM, Choi W, Sethna JP, Uchic MD, Woodward CF, et al. Quasi-periodic events in crystal plasticity and the self-organized avalanche oscillator. *Nature*. (2012) **490**:517–21. doi: 10.1038/nature11568
116. de Arcangelis L. Are dragon-king neuronal avalanches dungeons for self-organized brain activity? *Eur Phys J Spec Top*. (2012) **205**:243–57. doi: 10.1140/epjst/e2012-01574-6
117. Beggs JM, Plenz D. Neuronal avalanches in neocortical circuits. *J Neurosci*. (2003) **23**:11167–77. doi: 10.1523/JNEUROSCI.23-35-11167.2003
118. Plenz D, Niebur E. *Criticality in Neural Systems*. Weinheim: John Wiley & Sons (2014). doi: 10.1002/9783527651009
119. Chialvo DR. Emergent complex neural dynamics. *Nat Phys*. (2010) **6**:744–50. doi: 10.1038/nphys1803
120. Cocchi L, Gollo LL, Zalesky A, Breakspear M. Criticality in the brain: a synthesis of neurobiology, models and cognition. *Prog Neurobiol*. (2017) **158**:132–52. doi: 10.1016/j.pneurobio.2017.07.002
121. Shew WL, Plenz D. The functional benefits of criticality in the cortex. *Neuroscientist*. (2013) **19**:88–100. doi: 10.1177/1073858412445487
122. Beggs JM. The criticality hypothesis: how local cortical networks might optimize information processing. *Philos Trans R Soc A*. (2008) **366**:329–43. doi: 10.1098/rsta.2007.2092
123. Massobrio P, de Arcangelis L, Pasquale V, Jensen HJ, Plenz D. *Criticality as a Signature of Healthy Neural Systems: Multi-Scale Experimental and Computational Studies*. Lausanne: Frontiers in Systems Neuroscience (2015) p. 4. doi: 10.3389/978-2-88919-503-9
124. Kinouchi O, Copelli M. Optimal dynamical range of excitable networks at criticality. *Nat Phys*. (2006) **2**:348–51. doi: 10.1038/nphys289
125. Boedecker J, Obst O, Lizier JT, Mayer NM, Asada M. Information processing in echo state networks at the edge of chaos. *Theory Biosci*. (2012) **131**:205–13. doi: 10.1007/s12064-011-0146-8
126. Mu noz MA. Colloquium: Criticality and dynamical scaling in living systems. *Rev Modern Phys*. (2018) **90**:031001. doi: 10.1103/RevModPhys.90.031001
127. Levina A, Herrmann JM, Geisel T. Dynamical synapses causing self-organized criticality in neural networks. *Nat Phys*. (2007) **3**:857–60. doi: 10.1038/nphys758
128. de Arcangelis L, Perrone-Capano C, Herrmann HJ. Self-organized criticality model for brain plasticity. *Phys Rev Lett*. (2006) **96**:028107. doi: 10.1103/PhysRevLett.96.028107
129. Millman D, Mihalas S, Kirkwood A, Niebur E. Self-organized criticality occurs in non-conservative neuronal networks during 'up' states. *Nat Phys*. (2010) **6**:801–5. doi: 10.1038/nphys1757
130. Cowan J, Neuman J, Kiewiet B, Van Drongelen W. Self-organized criticality in a network of interacting neurons. *J Stat Mech*. (2013) **2013**:P04030. doi: 10.1088/1742-5468/2013/04/P04030
131. Hesse J, Gross T. Self-organized criticality as a fundamental property of neural systems. *Front Comput Neurosci*. (2014) **8**:1–14. doi: 10.3389/fnsys.2014.00166
132. Bonachela J, de Franciscis S, Torres JJ, Mu noz MA. Self-organization without conservation: are neuronal avalanches generically critical? *J Stat Mech*. (2010) **2010**:P02015. doi: 10.1088/1742-5468/2010/02/P02015
133. Olami Z, Feder HJS, Christensen K. Self-organized criticality in a continuous, nonconservative cellular automaton modeling earthquakes. *Phys Rev Lett*. (1992) **68**:1244. doi: 10.1103/PhysRevLett.68.1244
134. Bak P, Tang C. Earthquakes as a self-organized critical phenomenon. *J Geophys Res*. (1989) **94**:15635. doi: 10.1029/JB094iB11p15635
135. Bak P, Chen K, Tang C. A forest-fire model and some thoughts on turbulence. *Phys Lett A*. (1990) **147**:297–300. doi: 10.1016/0375-9601(90)90451-S
136. Drossel B, Schwabl F. Self-organized critical forest-fire model. *Phys Rev Lett*. (1992) **69**:1629. doi: 10.1103/PhysRevLett.69.1629
137. Clar S, Drossel B, Schwabl F. Scaling laws and simulation results for the self-organized critical forest-fire model. *Phys Rev E*. (1994) **50**:1009. doi: 10.1103/PhysRevE.50.1009
138. Grassberger P. Efficient large-scale simulations of a uniformly driven system. *Phys Rev E*. (1994) **49**:2436. doi: 10.1103/PhysRevE.49.2436
139. Wissel F, Drossel B. Transient and stationary behavior of the Olami-Feder-Christensen model. *Phys Rev E*. (2006) **74**:066109. doi: 10.1103/PhysRevE.74.066109
140. Grassberger P, Kantz H. On a forest fire model with supposed self-organized criticality. *J Stat Phys*. (1991) **63**:685–700. doi: 10.1007/BF01029205
141. Grassberger P. On a self-organized critical forest-fire model. *J Phys A*. (1993) **26**:2081. doi: 10.1088/0305-4470/26/9/007
142. Bröker HM, Grassberger P. Random neighbor theory of the Olami-Feder-Christensen earthquake model. *Phys Rev E*. (1997) **56**:3944. doi: 10.1103/PhysRevE.56.3944
143. Grassberger P. Critical behaviour of the Drossel-Schwabl forest fire model. *N J Phys*. (2002) **4**:17. doi: 10.1088/1367-2630/4/1/317
144. Zierenberg J, Wilting J, Priesemann V, Levina A. Description of spreading dynamics by microscopic network models and macroscopic branching processes can differ due to coalescence. *Phys Rev E*. (2020) **101**:022301. doi: 10.1103/PhysRevE.101.022301
145. Cardy JL, Grassberger P. Epidemic models and percolation. *J Phys A*. (1985) **18**:L267. doi: 10.1088/0305-4470/18/6/001
146. Janssen HK. Renormalized field theory of dynamical percolation. *Z Phys B Condens Matter*. (1985) **58**:311–7. doi: 10.1007/BF01303673
147. Grassberger P. On the critical behavior of the general epidemic process and dynamical percolation. *Math Biosci*. (1983) **63**:157–72. doi: 10.1016/0025-5564(82)90036-0
148. Sornette D. Sweeping of an instability: an alternative to self-organized criticality to get powerlaws without parameter tuning. *J Phys I*. (1994) **4**:209–21. doi: 10.1051/jp1:1994133
149. Palmieri L, Jensen HJ. The emergence of weak criticality in SOC systems. *Europhys Lett*. (2018) **123**:20002. doi: 10.1209/0295-5075/123/20002
150. Williams-García RV, Moore M, Beggs JM, Ortiz G. Quasicritical brain dynamics on a nonequilibrium Widom line. *Phys Rev E*. (2014) **90**:062714. doi: 10.1103/PhysRevE.90.062714
151. Wang SJ, Ouyang G, Guang J, Zhang M, Wong KYM, Zhou C. Stochastic oscillation in self-organized critical states of small systems: sensitive resting state in neural systems. *Phys Rev Lett*. (2016) **116**:018101. doi: 10.1103/PhysRevLett.116.018101
152. de Andrade Costa A, Copelli M, Kinouchi O. Can dynamical synapses produce true self-organized criticality? *J Stat Mech*. (2015) **2015**:P06004. doi: 10.1088/1742-5468/2015/06/P06004
153. Campos JaGF, Costa AdA, Copelli M, Kinouchi O. Correlations induced by depressing synapses in critically self-organized networks with quenched dynamics. *Phys Rev E*. (2017) **95**:042303. doi: 10.1103/PhysRevE.95.042303
154. Brochini L, de Andrade Costa A, Abadi M, Roque AC, Stolfi J, Kinouchi O. Phase transitions and self-organized criticality in networks of stochastic spiking neurons. *Sci Rep*. (2016) **6**:35831. doi: 10.1038/srep35831
155. Costa A, Brochini L, Kinouchi O. Self-organized supercriticality and oscillations in networks of stochastic spiking neurons. *Entropy*. (2017) **19**:399. doi: 10.3390/e19080399
156. Kinouchi O, Brochini L, Costa AA, Campos JGF, Copelli M. Stochastic oscillations and dragon king avalanches in self-organized quasi-critical systems. *Sci Rep*. (2019) **9**:1-12. doi: 10.1038/s41598-019-40473-1
157. Priesemann V, Wibral M, Valderrama M, Pröpper R, Le Van Quyen M, Geisel T, et al. Spike avalanches in vivo suggest a driven, slightly subcritical brain state. *Front Syst Neurosci*. (2014) **8**:108. doi: 10.3389/fnsys.2014.00108
158. Zierenberg J, Wilting J, Priesemann V. Homeostatic plasticity and external input shape neural network dynamics. *Phys Rev X*. (2018) **8**:031018. doi: 10.1103/PhysRevX.8.031018

159. Das A, Levina A. Critical neuronal models with relaxed timescale separation. *Phys Rev X*. (2019) **9**:021062. doi: 10.1103/PhysRevX.9.021062
160. Saeedi A, Jannesari M, Gharibzadeh S, Bakouie F. Coexistence of stochastic oscillations and self-organized criticality in a neuronal network: sandpile model application. *Neural Comput*. (2018) **30**:1132–49. doi: 10.1162/neco_a_01061
161. Moosavi SA, Montakhab A, Valizadeh A. Coexistence of scale-invariant and rhythmic behavior in self-organized criticality. *Phys Rev E*. (2018) **98**:022304. doi: 10.1103/PhysRevE.98.022304
162. Di Santo S, Villegas P, Burioni R, Mu noz MA. Landau-Ginzburg theory of cortex dynamics: scale-free avalanches emerge at the edge of synchronization. *Proc Natl Acad Sci USA*. (2018) **115**:E1356–65. doi: 10.1073/pnas.1712989115
163. Mikkelsen K, Imparato A, Torcini A. Emergence of slow collective oscillations in neural networks with spike-timing dependent plasticity. *Phys Rev Lett*. (2013) **110**:208101. doi: 10.1103/PhysRevLett.110.208101
164. Matias FS, Carelli PV, Mirasso CR, Copelli M. Self-organized near-zero-lag synchronization induced by spike-timing dependent plasticity in cortical populations. *PLoS ONE*. (2015) **10**:e140504. doi: 10.1371/journal.pone.0140504
165. Khoshkhou M, Montakhab A. Spike-timing-dependent plasticity with axonal delay tunes networks of Izhikevich neurons to the edge of synchronization transition with scale-free avalanches. *Front Syst Neurosci*. (2019) **13**:73. doi: 10.3389/fnsys.2019.00073
166. Dan Y, Poo Mm. Spike timing-dependent plasticity of neural circuits. *Neuron*. (2004) **44**:23–30. doi: 10.1016/j.neuron.2004.09.007
167. Toner J, Tu Y. Flocks, herds, and schools: a quantitative theory of flocking. *Phys Rev E*. (1998) **58**:4828. doi: 10.1103/PhysRevE.58.4828
168. Bialek W, Cavagna A, Giardina I, Mora T, Silvestri E, Viale M, et al. Statistical mechanics for natural flocks of birds. *Proc Natl Acad Sci USA*. (2012) **109**:4786–4791. doi: 10.1073/pnas.1118633109
169. Chaté H, Mu noz MA. Insect swarms go critical. *Physics*. (2014) **7**:120. doi: 10.1103/Physics.7.120
170. Mora T, Bialek W. Are biological systems poised at criticality? *J Stat Phys*. (2011) **144**:268–302. doi: 10.1007/s10955-011-0229-4
171. Ramaswamy S. Active matter. *J Stat Mech*. (2017) **2017**:054002. doi: 10.1088/1742-5468/aa6bc5
172. Plenz D, Niebur E. *Criticality in Neural Systems*. New York, NY: John Wiley & Sons (2014). doi: 10.1002/9783527651009
173. Rand D, Keeling M, Wilson H. Invasion, stability and evolution to criticality in spatially extended, artificial host-pathogen ecologies. *Proc R Soc Lond Ser B*. (1995) **259**:55–63. doi: 10.1098/rspb.1995.0009
174. Buendía V, Muñoz MA, Manrubia S. Limited role of spatial self-structuring in emergent trade-offs during pathogen evolution. *Sci Rep*. (2018) **8**:1–13. doi: 10.1038/s41598-018-30945-1

Conflict of Interest: The authors declare that the research was conducted in the absence of any commercial or financial relationships that could be construed as a potential conflict of interest.

APPENDICES

TABLE WITH PARAMETER VALUES

TABLE A1 | Parameters used in the numerical simulations for **Figures 1**, **2**.

Parameter	SOC	SOqC	SOB	SOCO
a	−1.00	−1.00	−1.00	−1.00
b	1.00	1.00	−1.50	−1.50
c	–	–	1.50	1.50
ω	1.00	1.00	1.00	1.00
h	1.00	0.10	1.00	1.00
γ	0.00	0.10	0.00	0.02
ϵ	0.00	0.10	0.00	0.10
E_{max}	–	1.50	–	1.30
D	1.00	1.00	1.00	1.00
D_E	1.00	0.10	1.00	1.00
σ	1.00	1.00	1.00	1.00

Dashes indicate that the corresponding parameter is not present in the model.

C-DP APPROXIMATE SCALING IN SOqC

Although the case of the SOqC has been argued to be belong, in general, to the dynamical percolation universality class, it is possible to select parameter values such that avalanches present a scaling controlled, at least transiently (i.e. for small sizes and durations) by C-DP (see **Figure A1**, and [33] for more details). For instance, in the case of "offline" driving, if the driving is not strong enough as to bringing the system above the critical point for spreading, the averaged energy $\overline{E}$ hovers around the C-DP critical point E_c, as shown in [33]. Actually, there is a value of the charge rate, γ_s, that allows the system to enter into the spreading phase leading to dynamical-percolation type of scaling. Similarly, "online" driving can effectively compensate for dissipation so that an steady state can be reached: as discussed in the main text, this state can be either sub-critical, supercritical, or near critical, depending on the relative strengths of driving and dissipation. In the near-critical case the critical-like features are expected to be controlled by the C-DP point due to the dynamic "online" addition of energy, which perturbs the dynamical-percolation (dissipative) behavior.

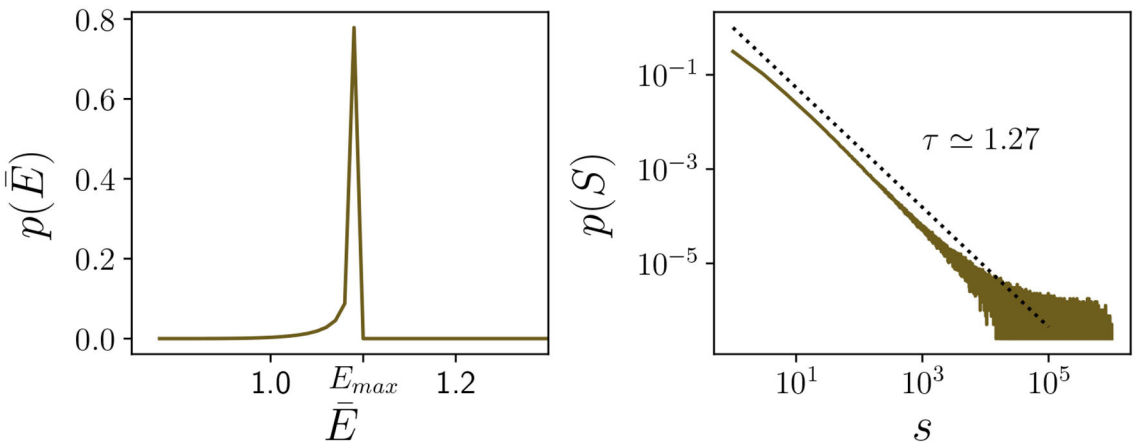

FIGURE A1 | Simulations of the SOqC theory may exhibit scaling similar to that of C-DP. **(Left)** The probability distribution of the average energy is peaked around E_c, but it is much more sprread that the SOC case, owing to oscillations around the critical point. **(Right)** Distributions of avalanche sizes in this case. The C-DP exponent is shown for comparison. Although a change in trend can be seen around $s \sim 10^4$, larger sizes are required in order to clearly see the exponent corresponding asymptotic scaling (controlled by dynamical percolation, as discussed in the main text). Parameter values are: $a = 0.423$, $b = \omega = 1$, $D = D_E = 0.25$, $\sigma = \sqrt{2}$, $\gamma = 0.1$, $h = 1.0$, $\epsilon = 0.1$, $E_{max} = 1.1$, $L = 256$.

frontiers in Physics

ORIGINAL RESEARCH
published: 04 September 2020
doi: 10.3389/fphy.2020.00257

The Forest Fire Model: The Subtleties of Criticality and Scale Invariance

Lorenzo Palmieri[1]* *and Henrik Jeldtoft Jensen*[1,2]

[1] *Department of Mathematics, Centre for Complexity Science, Imperial College London, London, United Kingdom,* [2] *Institute of Innovative Research, Tokyo Institute of Technology, Yokohama, Japan*

Amongst the numerous models introduced with SOC, the Forest Fire Model (FFM) is particularly attractive for its close relationship to stochastic spreading, which is central to the study of systems as diverse as epidemics, rumors, or indeed, fires. However, since its introduction, the nature of the model's scale invariance has been controversial, and the lack of scaling observed in many studies diminished its theoretical attractiveness. In this study, we analyse the behavior of the tree density, the average cluster size and the largest cluster and show that the model could be of high practical relevance for the activation dynamics seen in brain and rain studies. From this perspective, its peculiar scaling properties should be regarded as an asset rather than a limitation.

Keywords: forest fire model, critical density, residence times, largest cluster, scale invariance, cluster size distribution, average cluster size, data collapse

OPEN ACCESS

Edited by:
Subhrangshu Sekhar Manna, S.N. Bose National Centre for Basic Sciences, India

Reviewed by:
Mahendra Verma, Indian Institute of Technology Kanpur, India
Alberto Rosso, Centre National de la Recherche Scientifique (CNRS), France

***Correspondence:**
Lorenzo Palmieri
l.palmieri16@imperial.ac.uk

Specialty section:
This article was submitted to Interdisciplinary Physics, a section of the journal Frontiers in Physics

Received: *13 May 2020*
Accepted: *09 June 2020*
Published: *04 September 2020*

Citation:
Palmieri L and Jensen HJ (2020) The Forest Fire Model: The Subtleties of Criticality and Scale Invariance. Front. Phys. 8:257. doi: 10.3389/fphy.2020.00257

1. INTRODUCTION

Soon after the seminal paper introducing Self-Organised Criticality (SOC) [1], it was suggested that examples of SOC could include models describing the spread of activation in a manner reminiscent of forest fires or infectious diseases. The degree to which these models were examples of scale invariance and criticality instantly became a subject of intense debate, see, e.g., [2, 3]. Despite the controversy and indications that the Drossel-Schwabl Forest Fire Model [2] lacks scale invariance [4, 5], the dynamics of the model is of a type that seems of direct relevance to many real systems such as the brain [6] and precipitation [7]. So if for no other reason, it is still worthwhile to develop a better understanding of the behavior generated by this kind of stochastic spreading and relaxation dynamics and to develop ways to probe the dynamics which can be applied to data from real systems.

SOC focuses on criticality in the sense of equilibrium statistical mechanics, and for this reason, one typically looks for scale invariance and dynamics that can tune sharply to a critical point. Conversely, broad crossover behavior is not seen as properly belonging to the SOC paradigm. However, the relevance of a theoretical scientific framework is, in the end, determined by how useful it is for the description and analysis of real systems. Seen from this perspective, it is of importance to bear in mind that exact fine-tuning to a completely scale-invariant state is not always observed in systems that exhibit SOC-like behavior. This is demonstrated, e.g., by the studies of the size distribution of rain showers [7], and the bursts of brain activity measured during fMRI scans [6]. Indeed, neither study finds sharp critical behavior but, despite the systems being of totally different microscopic nature, both identify similar indications of critical behavior in terms of approximate power laws and even features reminiscent of peaked, or perhaps diverging, fluctuations or susceptibilities. Moreover, both studies find that the dynamics pulls the systems into a crossover region of large fluctuations within which one most frequently finds configurations to reside. In other words, in both cases, the distribution of residence times,

i.e., the amount of time spent at a certain value of the control parameter, is found to exhibit a broad peak centered about what appears to be a critical-like value of the control parameter. From our experience with equilibrium critical phenomena, one would expect a broad peak for small system sizes only, and that the width of the peak will shrink with increasing system size. Therefore, for systems as big as the atmosphere or with as many components as the brain, broad peaks would not be expected.

The experimental observations in [6, 7] suggest that the dynamics couples the control parameter to the fluctuations in a way that makes the system move around in a critical region, rather than tuning to a critical point. This is similar to suggestions previously put forward, such as [8, 9]. Intuitively, one may imagine something like the following in the case of precipitation: nucleation of drops can happen at a particular value of the vapor content. The vapor in the atmosphere over the ocean gradually builds up toward that value, and sometimes overshooting may even occur before nucleation is seeded. When precipitation events occur, a significant amount of vapor is removed from the atmosphere, and one observes oscillations between subcritical and supercritical regions. For some reason, the coupling between the driving (vapor formation) and the response (precipitation) produces such large fluctuations that a precise tuning to the critical value of the control parameter is excluded. A parallel situation may take place in the brain as neurones have to go through a refractory period before they are able to fire again after discharge.

A link between the behavior observed in brain activity and rainfalls [6, 7] and the Forest Fire Model was already suggested in [10]. Inspired by these studies, we analyse in detail the residence time distribution (which corresponds to the tree density distribution in the FFM) and its relationship to the order parameters used in standard percolation [11] and the brain study [6], namely the average cluster size and the normalized size of the largest cluster. We find that there is indeed a critical-like region where the fluctuations peak up and where the system seems to spend most of the time, exactly like in the brain and rain observations. Furthermore, analyzing the distribution of the non-normalized largest cluster, we find that it displays scale invariance for our reachable system sizes and that its first moment seemingly grows superlinearly with the activity θ, in a way that reminds the superlinear growth of the instantaneous correlation length observed in [12].

2. MODEL DESCRIPTION

As reported in [3], the original forest fire model proposed in [13] was revised in [2] and became known in the literature as the Drossel-Schwabl Forest Fire Model (DS-FFM), despite the resulting model coinciding with the one introduced a few years before in [14] as *Self-organised percolation*. In the following, we will analyse the model proposed in [2, 14] and refer to it simply as forest fire model (FFM). The FFM consists of a dissipative dynamic that involves the occupation of empty sites (planting of trees) and the removing of clusters of trees (burning of a forest). In the following, we will restrict our simulations to a two-dimensional square grid with periodic boundary conditions and side length L. Our implementation follows [4, 10, 12, 15–17], and is summarized by the following pseudocode [10]. An efficient implementation of the FFM can be found at [18].

Algorithm 1: Forest Fire Model

```
while True do
  for i = 1:θ do
    select randomly a site s
    if s is empty then
      s becomes occupied
    end if
  end for
  select randomly a site s
  if s is occupied then
    collect statistics
    burn the cluster connected to s
  end if
end while
```

Clusters are computed considering 4 neighbors for each site (2 horizontal and 2 vertical). In order to avoid finite-size effects, θ has to be tuned, taking into account the system size L^2. In our simulations, we keep fixed the ratio $k = \frac{\theta}{L^2}$ as in [12]. The great majority of the simulations are done at $k = 10^{-3}$, but we also present results for smaller values of k in **Figures 3**, **10**. Since the model is known for taking a long time to thermalize, we performed $5 \cdot 10^6$ burning steps for thermalization and 10^6 to collect the statistics as in [4]. The only exception is for the heatmaps in **Figures 7**, **8**, where 10^7 datapoints were used to produce the statistics.

3. RESULTS

3.1. The Distribution of Densities

To compute the distribution of the densities $P(\rho)$, we assign one spatially averaged density ρ to each generated configuration and sample the distribution over the ensemble. In this way, we obtain an object that is equivalent to the distribution of residence times in [6, 7]. In the early studies of the FFM, the average density of trees $\langle\rho\rangle$ was assumed to behave as

$$\langle\rho\rangle = \rho_\infty - a\theta^{-b} \tag{1}$$

Where ρ_∞ is the supposedly asymptotic density of trees and a and b are two constants. The value of the power was estimated as $b = 0.47$ in [19, 20] and $b = 0.5$ in [15]. However, it was noted in [5] that for $\theta \gtrsim 10^4$ the average density starts to deviate dramatically from the estimates made at lower values, ending up to be more than 100 standard deviations higher than the expected value for $\theta \sim 10^5$, and seemingly growing as a pure power law for $\theta \gtrsim 10^4$. Assuming that the power law behavior holds asymptotically in θ, it was estimated in [5] that the tree density would reach the percolation density ($\rho_p \simeq 0.5927\ldots$) for $\theta \sim 10^{40}$.

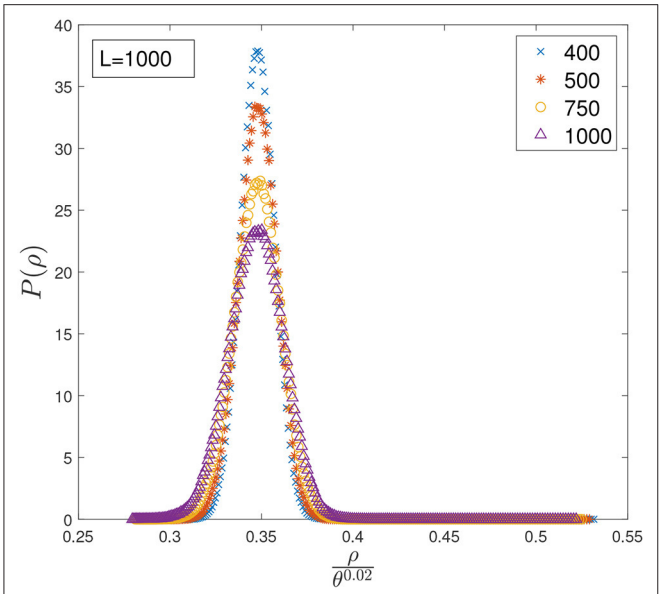

FIGURE 1 | Distribution of densities $P(\rho)$ computed at different values of θ and fixed $L = 1,000$. The x-axis has been rescaled by $\theta^{0.02}$ to align the peaks.

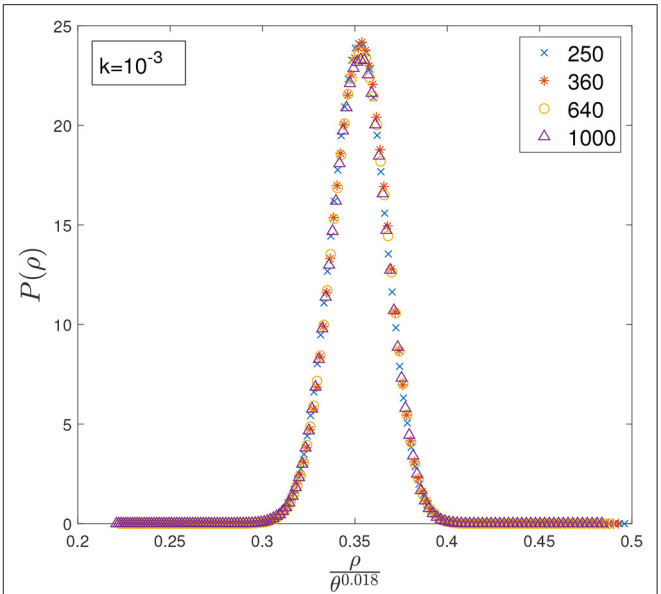

FIGURE 2 | Distribution of densities $P(\rho)$ computed at different values of θ and $k = 10^{-3}$. Although rescaling the x-axis by $\theta^{0.018}$ seems to make it possible to perform a data collapse for $\theta \in [250, 1000]$, this does not hold for larger values of θ.

To avoid finite-size effects, in [5] the values of θ and L were chosen as follows: for every value of θ, several simulations were carried out at different system sizes, and it was verified that the distribution of the rms radius, cluster sizes, and burning time were independent of L. The distribution of densities, on the other hand, depends strongly on the system size. For a fixed value of θ, increasing the system size would make the variance of the distribution decrease as L^{-2} in the absence of finite size effects [4]. Conversely, fixing L and increasing θ would lead to an increase in the standard deviation and $\langle\rho\rangle$, as can be seen in **Figure 1**. In the following, we will focus our attention on the behavior of $P(\rho)$ for increasing system sizes and fixed values of k.

In **Figures 2**, **3** we plot the distribution of densities rescaling the x-axis by θ^{ν}, and tune ν to align the peaks of the distributions computed at different values of θ. Interestingly, in both cases the curves seem to collapse on the same shape for quite a wide range of θ, suggesting that the distribution has reached a stationary state and that increasing θ would imply only a shift of $\langle\rho\rangle$. However, increasing θ even further clearly shows that the asymptotic behavior suggested by the data collapse is only transient, as the curves start to deviate considerably from the shape observed at lower values of θ, as can be seen in **Figure 4**. Rescaling ρ by $\theta^{0.005}$ one can align the position of the peaks in **Figure 4** for $\theta \gtrsim 10^4$, but it is clear that, in order to perform a data collapse, the y-axis must be rescaled as well, as the height of the peaks decreases with θ.

For a fixed θ, we found that $P(\rho)$ is well fitted by a Gaussian distribution. In **Figure 5**, we plot the mean and standard deviations of $P(\rho)$ for $k = 10^{-3}$ and find that the average density seemingly increases as a power-law for $\theta \gtrsim 10^4$, in agreement with the numerics presented in [5]. Although the mean $\mu(\theta)$ seems to enter an asymptotic regime after $\theta \gtrsim 10^4$, it is less convincing whether the standard deviation $\sigma(\theta)$ has reached its asymptotic form.

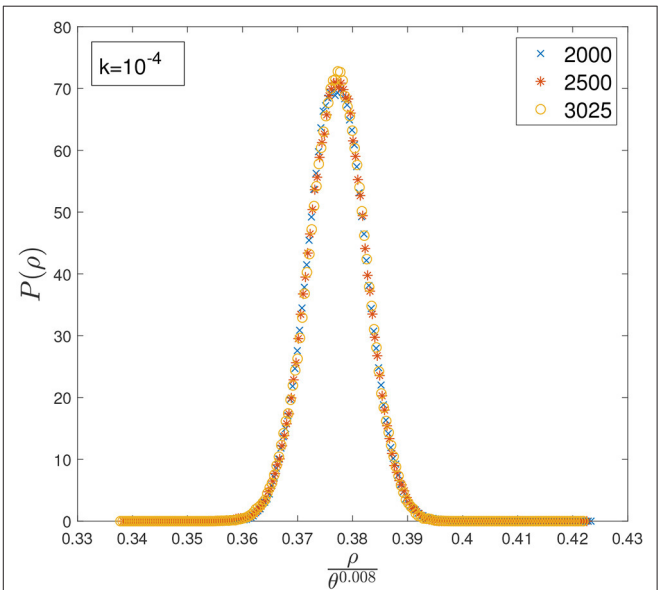

FIGURE 3 | Distribution of densities $P(\rho)$ computed at different values of θ and $k = 10^{-4}$. Although rescaling the x-axis by $\theta^{0.008}$ seems to make it possible to perform a data collapse for $\theta \in [2000, 3025]$, this does not hold for larger values of θ.

If we assume a Gaussian behavior for $P(\rho)$ and that the mean and the standard deviation behave as

$$\mu = a\theta^{\nu_\mu} \text{ and } \sigma = b\theta^{\nu_\sigma}. \tag{2}$$

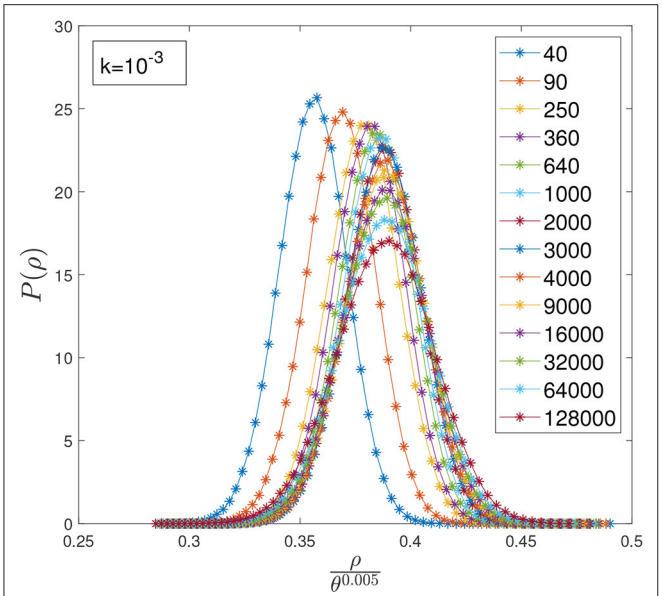

FIGURE 4 | Distribution of densities $P(\rho)$ computed at different values of θ and $k = 10^{-3}$. The x-axis has been rescaled by $\theta^{0.005}$ to align the position of the peaks at large values of θ.

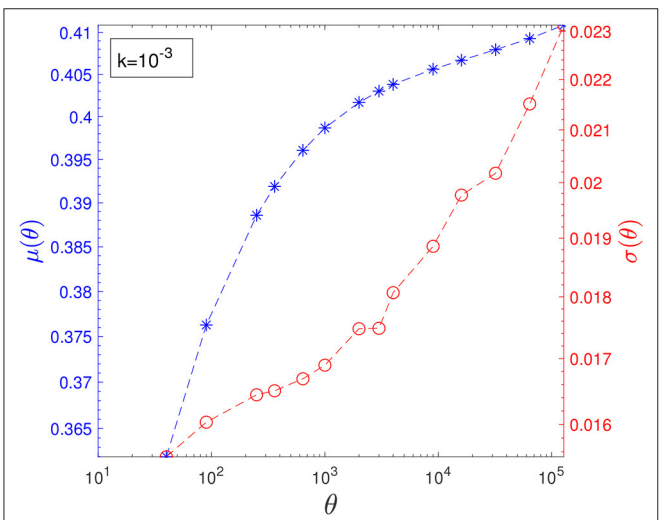

FIGURE 5 | Log-log plot of the mean and standard deviation of $P(\rho)$ as a function of θ.

then plotting $P(\rho)\sigma(\theta)$ vs. $\frac{\rho-\mu}{\sigma}$ should produce a standard normal distribution for systems at $\theta \gtrsim 10^4$. To estimate the asymptotic behavior, we used the last six data points for $\mu(\theta)$ and the last three data points for $\sigma(\theta)$ in **Figure 5**, finding

$$a = 0.388 \pm 0.001 \text{ and } \nu_\mu = 0.0049 \pm 0.0003$$

and

$$b = 0.007 \pm 0.004 \text{ and } \nu_\sigma = 0.099 \pm 0.047$$

using 95% confidence bounds.

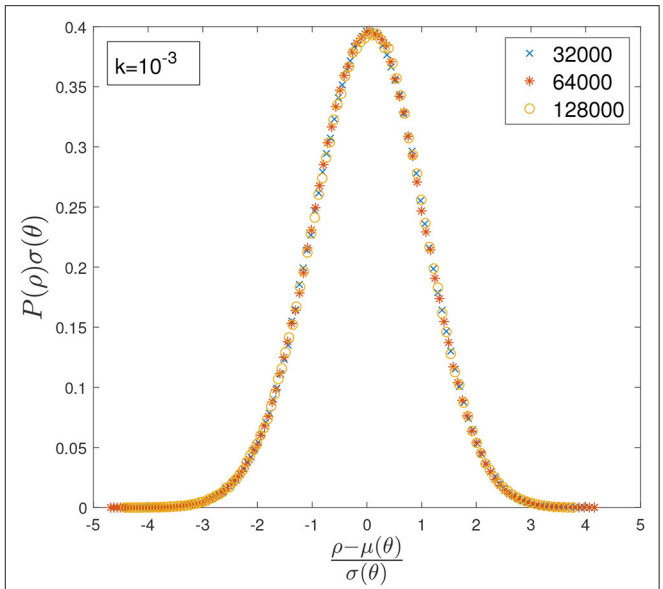

FIGURE 6 | Data collapse for the distribution of densities $P(\rho)$ and $k = 10^{-3}$ obtained by inputting the estimated values of μ and σ into a Gaussian distribution. The x-axis and the y-axis have been rescaled in order to make all the curves collapse on a standard normal distribution.

Using these estimates, we find that a data collapse seems to hold well for very large values of θ, as can be seen in **Figure 6**. However, such extrapolations have to be taken with great care, firstly because of the small data available for the fit and the not so convincing behavior of $\sigma(\theta)$, and secondly because the average density can never exceed 1, meaning that the apparent power-law growth has to stop at some point.

Since $\nu_\sigma > \nu_\mu$, the fluctuations grow at a faster rate than the average, as one would expect for a system close to criticality. From the ratio $\frac{\sigma(\theta)}{\mu(\theta)} \sim 0.018 \cdot \theta^{0.094}$, one can obtain a crude estimate for when the fluctuations would become of the same order of magnitude as the average. This would happen at $\theta \sim 10^{18}$ and $\langle\rho\rangle \simeq 0.478$. However, this argument can hardly hold, as it would imply that within two standard deviations, we would have values of the densities that exceed $\rho = 1$, which is, of course, impossible. Therefore, we can conclude that for $k = 10^{-3}$ and within the Gaussian approximation, we can expect the standard deviation to be smaller than the average, despite growing at a faster rate.

As a reference, we computed a rough estimate of the value θ^* that would correspond to an average density equal to the percolation threshold $\mu(\theta^*) = \rho_p$. This gives $\theta^* \sim 10^{37}$, which is consistent with the estimate made in [5] once the confidence bounds on a and ν_μ are taken into account for both datasets. However, there is no reason why the asymptotic density of the FFM should be the same as the critical percolation density, as even for very large systems the clusters would still be correlated and therefore intrinsically different from a percolation process.

Like previous studies of the FFM, we are unable to settle the true asymptotic scaling behavior of the model, which is still unreachable with today's computers. However, we showed

that *effectively*, the distribution of densities remains Gaussian for very large system sizes and significant ranges of θ. In the next section, we will study the relationship between $P(\rho)$ and the order parameters used in percolation and in [6], and show that $P(\rho)$ defines a wide region where one can observe critical-like behavior.

3.2. The Most Frequently Visited Region

Even though the studies of precipitation [7] and brain activity [6] related their findings to critical behavior, both observed a remarkable broad onset of the order parameter, which is certainly not the behavior seen as one approaches the critical point of a second-order phase transition of an infinite system. The absence of a sharp onset of the order parameter is remarkable because, for system sizes like the earth atmosphere or the human brain, one would not expect any significant finite-size effect if the usual phenomenology of equilibrium phase transitions were any guidance.

While the activation dynamics characteristic of precipitation and brain phenomena are not at all similar to thermal equilibrium dynamics, both systems are at least at a schematic qualitative level similar to the dissipative dynamics of the FFM, with its cycles of loading and discharging. Here we want to investigate further the relationship between the distribution of residence times and the order parameter suggested in [10] and to determine to what extent the FFM exhibits an onset region similar to those observed in rain and brain. If that is the case, we may perhaps take this as indicative of a kind of "universality" different from the stringent universality definition we know from equilibrium systems and more of a pragmatic nature. Needless to say, could such a universality be established, it may be a great help in attempts to classify the behavior of activation dynamics in complex systems. Furthermore, it could be taken as indicative of a level of emergent behavior that is independent of the microscopic details, since rain and brain clearly do operate on totally different substrates.

We are of course just repeating the original hope of SOC research and suggesting that systems of entirely different nature may indeed exhibit similar emergent collective behavior, even if the dynamics does not operate in a critical state, but rather is found to inhabit a broad region of approximately scale-free nature. Crucial for our suggestion is the observation that the true asymptotic behavior of the FFM appears to happen for such enormous systems sizes that they hardly are of relevance to real macroscopic systems. In contrast, the quasi-scale free behavior observed in the FFM for intermediate system sizes [4, 5] may very well be helpful for the understanding of observations such as those presented in [6, 7].

To investigate the presence of a critical-like region in the FFM, we focus on the onset of measures that characterize the clusters of trees and keep track of the frequencies at which the system visits different regions of the parameter space. The order parameter for precipitation [7] was taken to be the precipitation rate and for the brain [6], the normalized size of the largest cluster of activated voxels in the fMRI scans—a choice that appears very natural in the light of ordinary percolation analysis.

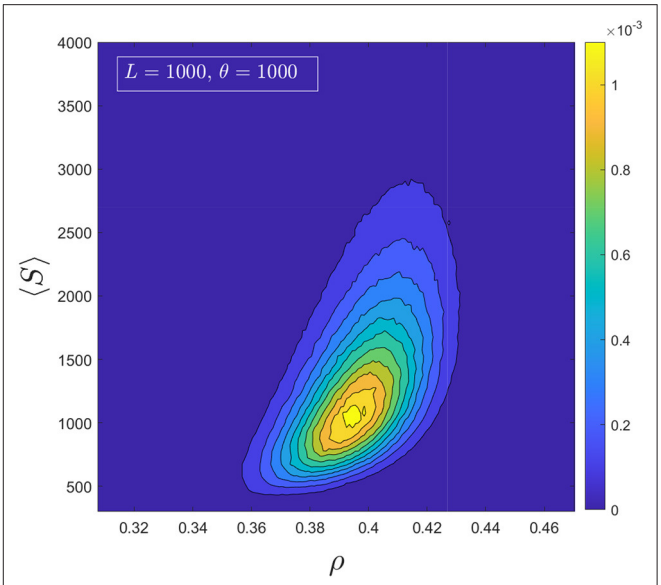

FIGURE 7 | Heatmap representing the bivariate histogram of the average cluster size and the density.

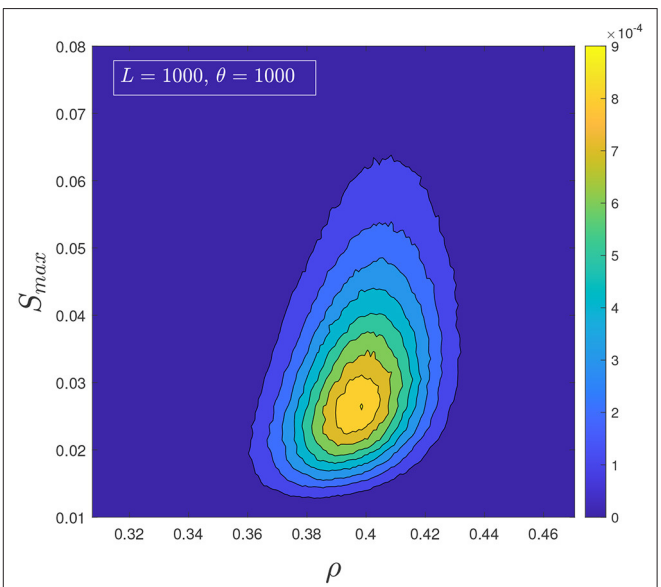

FIGURE 8 | Heatmap representing the bivariate histogram of the normalized largest cluster and the density.

In **Figures 7**, **8** we present the contour plot of the bivariate histograms of the average cluster size [11] $\langle S \rangle$ vs. the density ρ, and of the largest cluster normalized to the number of trees S_{max} vs. ρ. The color map represents the probability of observing a certain point in the parameter space, which is the same as the proportion of time spent by the system at that point. To create the heatmaps, we sampled 10^7 configurations and grouped points with similar probabilities for better visual representation. Therefore, the histograms are not perfectly normalized. The

study of both the average cluster size $\langle S \rangle$ and the normalized largest cluster S_{max} is inspired by the resemblance between the clusters of sites occupied by trees and the ordinary geometrical percolation transition. In percolation, either $\langle S \rangle$ or S_{max} are used to construct an order parameter.

It is clear from the heat-maps that the density around $\rho^* \simeq 0.4$ stands out and that precisely like in the precipitation study [7], and even more so in the brain study [6], ρ^* is indicative of an onset of the order parameter. Furthermore, the region over which the creation of large events happens is very broad, and the system spends a significant fraction of time in the *critical* region. We know from the Gaussianity of $P(\rho)$, see **Figure 6**, that this region stays broad for any reachable system size and values of θ. This very much suggests that the FFM's quasi-tuning to a critical region is a stylistic feature of important relevance.

3.3. The Distribution of the Largest Cluster

We now turn our attention to the non-normalized largest cluster, which we indicate with Λ to distinguish it from S_{max}. For a fixed system size and θ, we find that the distribution of the largest cluster $P(\Lambda)$ is very well fitted by a Fréchet distribution, which corresponds to the class of extreme value statistics with a power-law tail. The good agreement of $P(\Lambda)$ with a Fréchet distribution implies that the correlations between consecutive configurations generating the clusters are sufficiently weak to be ignored.

Although the distribution of cluster sizes does not obey simple scaling [4, 5], it was found in [12] that the distribution of instantaneous correlation lengths is scale-invariant for $k = 10^{-3}$ and system sizes at least as big as $\theta = 9,000$. Given that $P(\lambda)$ is fat-tailed, we now turn our attention to its scaling properties and see if simple scaling applies.

In order to measure Λ, one has to maintain and keep track of all clusters at all times, which makes the task more computationally intensive than just sampling the density ρ. For this reason, we analyzed systems sizes that are smaller than those used for the analysis of $P(\rho)$. In our simulations, we used $k = 10^{-3}$ and values of θ up to 4000, but we also checked the scaling for $k = 5 \cdot 10^{-4}$.

Assuming that simple scaling holds, we can expect $P(\Lambda)$ to follow

$$P(\Lambda) = aG\left(\frac{\Lambda}{\Lambda_c(\theta)}\right)\Lambda^{-\tau} \tag{3}$$

for $\Lambda_0 \ll \Lambda \ll \Lambda_c$, where Λ_0 is a constant lower cutoff and Λ_c is an upper cutoff that diverges with θ. In Equation (3), a is a constant metric factor, τ is the critical exponent, and G is a universal function that decays quickly for $\Lambda \gg \Lambda_c$. The form that is usually assumed for the upper cutoff is $\Lambda_c = b\theta^{\nu}$, where b is another constant metric factor and ν is the spatial dimensionality of the observable Λ [3].

If the data are consistent with the simple scaling ansatz, then it is possible to perform a data collapse by plotting $P(\Lambda)\Lambda^{\tau}$ vs. the rescaled variable $\frac{\Lambda}{\Lambda_c}$ for different values of θ. In **Figure 9**, we performed a data collapse using $\nu = 1.055$ and $\tau = 1.04$. We also estimated the critical exponents analyzing the first two

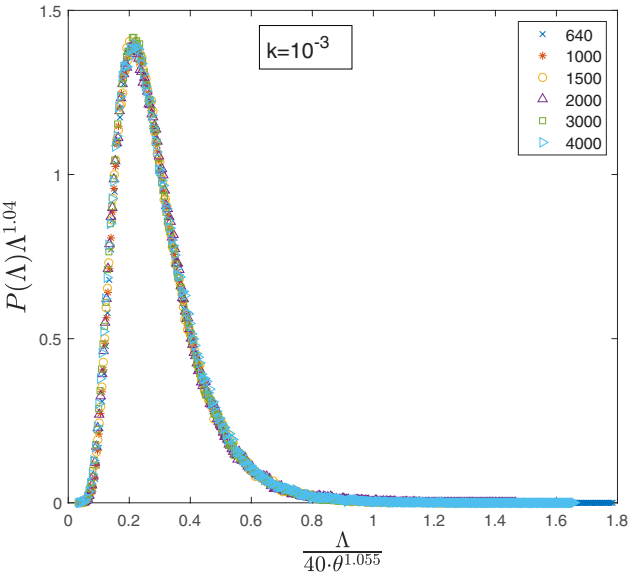

FIGURE 9 | Data collapse for the distribution of the largest cluster $P(\Lambda)$ at $k = 10^{-3}$.

moments of Equation (3) and fitting the data with $\langle \Lambda \rangle = c_1\theta^{\alpha_1}$ and $\langle \Lambda^2 \rangle = c_2\theta^{\alpha_2}$, obtaining

$$c_1 = 10.7 \pm 0.8 \text{ and } \alpha_1 = 1.04 \pm 0.01$$

and

$$c_2 = 110 \pm 36 \text{ and } \alpha_2 = 2.11 \pm 0.04$$

using 95% confidence bounds.

From the exponents of the first two moments one can easily recover ν and τ using Equation (3):

$$\nu = \alpha_2 - \alpha_1 \quad \tau = 2 - \frac{\alpha_1}{\nu} \tag{4}$$

Using our estimates for α_1 and α_2, we get

$$\nu = 1.07 \pm 0.04 \quad \tau = 1.03 \pm 0.04 \tag{5}$$

using 95% confidence bounds.

These estimates for ν and τ are consistent with the ones obtained via data collapse and that have been used in **Figure 9**. Finally, we applied the whole procedure a second time using a smaller value of k, namely $k = 5 \cdot 10^{-4}$ and θ up to 2000. From the data collapse in **Figure 10** we obtained an estimate of $\nu = 1.065$ and $\tau = 1.04$, while fitting the first two moments we obtained:

$$c_1 = 12.0 \pm 0.7 \text{ and } \alpha_1 = 1.05 \pm 0.01$$

and

$$c_2 = 148 \pm 15 \text{ and } \alpha_2 = 2.12 \pm 0.02$$

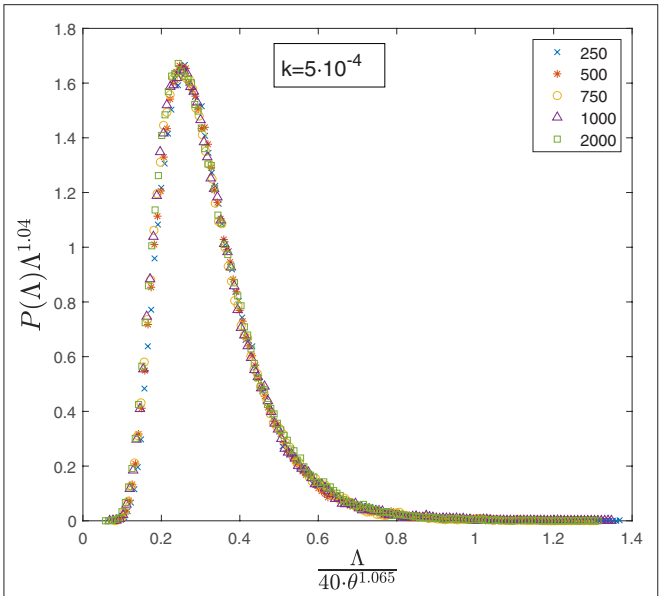

FIGURE 10 | Data collapse for the distribution of the largest cluster $P(\Lambda)$ at $k = 5 \cdot 10^{-4}$.

which are consistent with the data collapse and with those estimated for $k = 10^{-3}$.

Although we had to restrict our simulations to values of $\theta < 10^4$, we observe a very robust scaling for the largest cluster Λ, which is not observed in the distribution of cluster sizes $P(S)$ over the same range of θ [4]. Interestingly, we found that $\langle \Lambda \rangle \sim \theta^{1.04}$, a super-linear growth which indicates that the correlations in the system increase rapidly with θ. This behavior is consistent with the analysis of the distribution of instantaneous correlation lengths $P(\xi)$ performed in [12], where it was found that the average instantaneous correlation length grows as $\langle \xi \rangle \sim \theta^{0.56}$ over the same range of θ.

4. DISCUSSION

SOC was very much inspired by the successes of the renormalization group studies of equilibrium critical phenomena of the 1970-ties and its phenomenal understanding of the origin of universality classes. Initially, the discussions of SOC focused on accurately establishing the scaling behavior and related scaling exponents of the various models thought to represent the SOC phenomenology. The original sandpile model [1] was disappointingly far from simple scaling, and also the FFM turned out to behave very differently from the familiar scaling observed in equilibrium models such as the Ising model or geometrical percolation. Though there is at least one class of SOC models that exhibits clear scaling, namely the class represented by the Manna model [21], the beauty of strict scaling and universality classes defined by scaling exponents seems not to really capture the less than ideal critical behavior frequently observed in real systems, such as our two examples from rain and brain.

There is no doubt that the studies of the emergent dynamics of real complex systems from biology, geophysics, astrophysics, economics and more [22–24] keep identifying behavior which is qualitatively in the spirit of the hopes and dreams behind SOC, namely the lack of one characteristic scale in time and space, large fluctuations and no need for specific external tuning. So if the beauty of strict scaling and exact power laws does not carry over from equilibrium critical phenomena, the question is how we establish a systematic classification of the emergent phenomena observed in completely different systems. The study of the FFM and its comparison with the behavior of real systems suggests it is possible to establish a useful phenomenological understanding and classification reaching beyond the usual strict classification of universality classes defined in terms of shared scaling exponents.

The study presented here confirms earlier investigations of the behavior of the density ρ, and the change in the behavior of $\langle \rho \rangle$ for very large system sizes. Although we observed that the Gaussian behavior of $P(\rho)$ holds at least until $\theta = 10^5$, we also showed that it is possible to obtain very good but deceitful data collapses for $P(\rho)$ at different ranges of θ. If, on the one hand, this should serve as a warning for the analysis of the asymptotic scaling behavior of the FFM and other out of equilibrium systems, on the other hand, it shows that such *effective* scaling could be of guidance in the understanding and analysis of real systems that show similar dynamics.

Analyzing the average cluster size and the normalized largest cluster, we found that the FFM exhibits very similar behavior to the one observed in experimental studies of rain and brain [6, 7]. In particular, both studies and the FFM display a *critical region* over which both the residence time distribution and the order parameter peak up, meaning that the system spends most of the time in a highly susceptible state.

From the study of the largest cluster Λ it emerges that, although the FFM displays broken scaling in the distribution of cluster sizes, the distribution $P(\Lambda)$ appears to be scale-invariant at least for $\theta < 10^4$. Furthermore, $P(\Lambda)$ displays a super-linear growth of the first moment similar to the one observed for the average instantaneous correlation length in [12]. It is clear from the anomalous behavior of the density ρ that such results should be taken with care, as the model seems to enter a new regime when $\theta \gtrsim 10^4$. However, the robust scaling observed both in the largest cluster and in the instantaneous correlation length suggests that at least for system sizes below $\theta = 10^4$ there is a fast and scale-free growth of the correlations with the *activity* θ.

Although the FFM does not display the reassuring scaling observed in equilibrium models, its phenomenology appears to summarize elegantly and robustly the emergent dynamics of spreading and recharging seen in such disparate phenomena as rain precipitation and brain dynamics. Moreover, examples of broken scaling and non-exact powerlaws are ubiquitous in nature and in the scientific literature [25] and, for this reason, we believe that the characteristic behavior of the FFM should be seen as an asset rather than a limitation of the model.

DATA AVAILABILITY STATEMENT

The original contributions presented in the study are included in the article/**Supplementary Material**, further inquiries can be directed to the corresponding author.

AUTHOR CONTRIBUTIONS

LP performed the numerical simulations and analyses and produced the figures. Both authors discussed the results of the simulations and jointly wrote the manuscript.

FUNDING

LP gratefully acknowledges an EPSRC-Roth scholarship (Award Reference No. 1832407) from EPSRC and the Department of Mathematics at Imperial College London.

ACKNOWLEDGMENTS

LP thankfully acknowledges the High-Performance Computing facilities provided by the Imperial College Research Computing Service (DOI: 10.14469/hpc/2232).

SUPPLEMENTARY MATERIAL

The Supplementary Material for this article can be found online at: https://www.frontiersin.org/articles/10.3389/fphy.2020.00257/full#supplementary-material

REFERENCES

1. Bak P, Tang C, Wiesenfeld K. Self-organized criticality: an explanation of the 1/f noise. *Phys Rev Lett*. (1987) **59**:381–4. doi: 10.1103/PhysRevLett.59.381
2. Drossel B, Schwabl F. Self-organized critical forest-fire model. *Phys Rev Lett*. (1992) **69**:1629–32. doi: 10.1103/PhysRevLett.69.1629
3. Pruessner G. *Self-Organised Criticality: Theory, Models and Characterisation*. Cambridge: Cambridge University Press (2012).
4. Pruessner G, Jensen HJ. Broken scaling in the forest-fire model. *Phys Rev E*. (2002) **65**:056707. doi: 10.1103/PhysRevE.65.056707
5. Grassberger P. Critical behaviour of the Drossel-Schwabl forest fire model. *N J Phys*. (2002) **4**:17. doi: 10.1088/1367-2630/4/1/317
6. Tagliazucchi E, Balenzuela P, Fraiman D, Chialvo D. Criticality in large-scale brain fMRI dynamics unveiled by a novel point process analysis. *Front Physiol*. (2012) **3**:15. doi: 10.3389/fphys.2012.00015
7. Peters O, Neelin JD. Critical phenomena in atmospheric precipitation. *Nat Phys*. (2006) **2**:393–6. doi: 10.1038/nphys314
8. Sornette D. Critical phase transitions made self-organized : a dynamical system feedback mechanism for self-organized criticality. *J Phys I France*. (1992) **2**:2065–73.
9. Zapperi S, Lauritsen KB, Stanley HE. Self-organized branching processes: mean-field theory for avalanches. *Phys Rev Lett*. (1995) **75**:4071–4. doi: 10.1103/PhysRevLett.75.4071
10. Palmieri L, Jensen HJ. The emergence of weak criticality in SOC systems. *Europhys Lett*. (2018) **123**:20002. doi: 10.1209/0295-5075/123/20002
11. Christensen K, Moloney NR. *Complexity and Criticality*. London: Imperial College Press (2005).
12. Palmieri L, Jensen HJ. Investigating critical systems via the distribution of correlation lengths. *Phys Rev Res*. (2020) **2**:013199. doi: 10.1103/PhysRevResearch.2.013199
13. Bak P, Chen K, Tang C. A forest-fire model and some thoughts on turbulence. *Phys Lett A*. (1990) **147**:297–300. doi: 10.1016/0375-9601(90)90451-S
14. Henley CL. Self-organized percolation: a simpler model. *Bull Am Phys Soc*. (1989) **34**:838.
15. Grassberger P. On a self-organized critical forest-fire model. *J Phys A Math Gen*. (1993) **26**:2081–9. doi: 10.1088/0305-4470/26/9/007
16. Clar S, Drossel B, Schwabl F. Scaling laws and simulation results for the self-organized critical forest-fire model. *Phys Rev E*. (1994) **50**:1009–18. doi: 10.1103/PhysRevE.50.1009
17. Schenk K, Drossel B, Clar S, Schwabl F. Finite-size effects in the self-organized critical forest-fire model. *Eur Phys J B Condens Matter Complex Syst*. (2000) **15**:177–85. doi: 10.1007/s100510051113
18. Pruessner G, Jensen HJ. Efficient algorithm for the forest fire model. *Phys Rev E*. (2004) **70**:066707. doi: 10.1103/PhysRevE.70.066707
19. Honecker A, Peschel I. Length scales and power laws in the two-dimensional forest-fire model. *Phys A Stat Mech Appl*. (1997) **239**:509–30.
20. Pastor-Satorras R, Vespignani A. Corrections to scaling in the forest-fire model. *Phys Rev E*. (2000) **61**:4854–9. doi: 10.1103/PhysRevE.61.4854
21. Manna SS. Two-state model of self-organized criticality. *J Phys A Math Gen*. (1991) **24**:L363–9. doi: 10.1088/0305-4470/24/7/009
22. Ball P. *Critical Mass. How One Thing Leads to Another*. New York, NY: Farrar, Straus and Giroux (2004).
23. West G. *Scale: The Universal Laws of Life and Death in Organisms, Cities and Companies*. London: The Orion Publishing Group (2018).
24. Krakauer DC, editor. *Worlds Hidden in Plain Sight*. Santa Fe, NM: The Santa Fe Institute Press (2019).
25. Clauset A, Shalizi CR, Newman MEJ. Power-law distributions in empirical data. *SIAM Rev*. (2009) **51**:661–703. doi: 10.1137/070710111

Conflict of Interest: The authors declare that the research was conducted in the absence of any commercial or financial relationships that could be construed as a potential conflict of interest.

frontiers in Physics

ORIGINAL RESEARCH
published: 20 November 2020
doi: 10.3389/fphy.2020.581126

Pattern Formation and Tropical Geometry

Nikita Kalinin [1,2]*

[1] Faculty of Mathematics and Computer Sciences, Saint Petersburg State University, Saint Petersburg, Russia,
[2] Laboratory of Game Theory and Decision Making, Higher School of Economics, National Research University Higher School of Economics, Saint Petersburg, Russia

Sandpile models exhibit fascinating pattern structures: patches, characterized by quadratic functions, and line-shaped patterns (also called solitons, webs, or linear defects). It was predicted by Dhar and Sadhu that sandpile patterns with line-like features may be described in terms of tropical geometry. We explain the main ideas and technical tools—tropical geometry and discrete superharmonic functions—used to rigorously establish certain properties of these patterns. It seems that the aforementioned tools have great potential for generalization and application in a variety of situations.

Keywords: tropical curves, pattern formation, solitons, sandpile, discrete harmonic analysis

OPEN ACCESS

Edited by:
Subhrangshu Sekhar Manna, S.N. Bose National Centre for Basic Sciences, India

Reviewed by:
Deepak Dhar, Indian Institute of Science Education and Research, Pune, India
Tridib Sadhu, Tata Institute of Fundamental Research, India

***Correspondence:**
Nikita Kalinin
nikaanspb@gmail.com

Specialty section:
This article was submitted to Interdisciplinary Physics, a section of the journal Frontiers in Physics

Received: *07 July 2020*
Accepted: *26 August 2020*
Published: *20 November 2020*

Citation:
Kalinin N (2020) Pattern Formation and Tropical Geometry. Front. Phys. 8:581126. doi: 10.3389/fphy.2020.581126

1. PATTERN FORMATION AND CELLULAR AUTOMATA

Animals show beautiful skin and wing patterns. Explaining how these come about has been a longstanding puzzle. In line with the Darwinian paradigm, an evolutionary biologist may suggest that formations of patterns on the skin of animals are visual traces of certain biological mechanisms that help survival in terms of natural selection.

In his seminal book, however, Thomson [1] argues that the geometry of patterns may be mainly dictated by chemical forces, albeit it is known that patterns may benefit their owners in certain cases. In his famous paper on morphogenesis [2], Turing speculated on the mechanism behind pattern formation on the skin of animals and proposed the famous reaction diffusion system, which consists of an inhibitor and an activator with different diffusion rates. Historically, this was the first explicit model of pattern formation, though it is purely theoretical.

An important example of self-oscillating patterns in the real world was discovered soon after, see the Belousov-Zhabotinsky reaction [3, 4]. Both the Turing model and the Belousov-Zhabotinsky reaction produce beautiful spatiotemporal patterns with quasi-ordered strips and spots, see a popular concise exposition of both topics in Ball [5]. A recent discussion about parallels in emerging complexities and patterns in biological systems and physical glass-like models can be found in Wolf et al. [6].

A possibility to obtain all sorts of patterns starting from local interactions suggests trying relatively simple models to explore patterns by pure or computer mathematics. Assuming that on a big scale all coarse grained functions are smooth and continuous, one may use differential equations in the study of patterns; see comprehensive reviews [7, 8]. But, appealing to the discrete nature of pattern formation, we shift our attention to cellular automata.

Historically, cellular automata were introduced to "abstract the logical structure of life" in 1948 by J. von Neumann and S. Ulam [9, 10]. Since then, cellular automata were used with great success to analyze complexity [11], pattern formation [12], self-organized criticality [13], and segregation [14]. Recent examples of using cellular automata for pattern prediction in biology include marine angelfish [15], seashells [16], and lizard skin [17]; see also a survey [18].

In this article we focus on so-called *sandpile models*, and firstly, discuss in section 2 how the patterns in that model were obtained in experimental computer physics, and secondly, we survey the main ideas permitting to study these patterns with mathematical rigor: discrete harmonic analysis (section 3), tropical geometry (section 4), toppling function (section 5), and the most technical part of the proofs, the lower bound (section 6). We mention open problems and new research directions when appropriate.

2. PATTERN FORMATION IN SANDPILES

2.1. Definitions

A sandpile model, which we consider here, consists of the standard integer lattice grid inside a compact convex domain $\Omega \subset \mathbb{R}^2$, i.e., the graph $\Gamma = \Omega \cap \mathbb{Z}^2$.

A *state* of a sandpile model is a function $\varphi(i,j)$, representing the number of grains of sand at the vertex $(i,j) \in \Gamma$. A state, thus, is an integer-valued function $\varphi : \Gamma \to \mathbb{Z}_{\geq 0}$.

A vertex (i,j) is *unstable* if there are four or more grains of sand at (i,j), i.e., $\varphi(i,j) \geq 4$. The evolution proceeds as follows: any unstable vertex (i,j) *topples* by sending one grain of sand to each of its four neighbors $(i+1,j+1), (i+1,j-1), (i-1,j+1), (i-1,j-1)$. The sand, falling outside Ω, disappears from the system. Vertices outside of Ω (formally they do not even belong to Γ) and stable vertices are never toppled. Equivalently, one may think that all the lattice points outside of Ω are sinks; sand, falling to sinks, disappears. Given an initial state φ, the state φ° denotes the stable state reached after all possible topplings have been performed. It is a classical fact that φ° does not depend on the order of topplings [19, 20].

2.2. Line-Shaped Patterns in the Literature

Line-shaped patterns [which can also go under different names: solitons, linear defects, and (p,q)-webs] can be found in the pictures in Liu et al. [21] and Ostojic [22], but the main subject of the latter article was quadratic patches, recently explained in Pegden and Smart [23, 24] and Levine at al. [25, 26] using Apollonian circle packings.

Let us put three grains in all the vertices of the intersection between the standard grid $\mathbb{Z}^2$ and a planar domain Ω. Let us choose several vertices and add one more grain to each of them. An example of the relaxation of such a state for Ω being a square is shown in **Figure 1**. We sequentially drop grains to blue points, performing a relaxation after each dropping (thus we have one blue point on the first pictures and four blue points on the fourth picture, where blue points indicate the positions of additional grains). One may easily guess a graph with straight edges along non-white parts of the pictures. With each new blue point such a graph changes, but its edges always pass through the blue points. In **Figure 2** we added grains to all blue points simultaneously and took snapshots of the subsequent relaxation (since the order of topplings does not influence the final picture, we might add grains sequentially).

Line-shaped patterns, clearly recognizable in **Figures 1**, **2** along straight edges of the imaginable graph, explicitly came in the sight of researchers in Dhar et al. [27] and Dhar and Sadhu [28] with an emphasis on a proportional growth phenomenon, and later, in Caracciolo et al. [29] (see also [30, 31]). These papers performed the analysis from the point of view of theoretical physics and explained the pictures based on experimental evidence.

The use of tropical geometry was predicted in Sadhu and Dhar [32] and later implemented with rather involved mathematical proofs in a series of articles [33–35]. A certain limit of the sandpile model gives a continuous limiting piece-wise linear model that also exhibits power-law behavior [36]; the statistical properties of the latter model can be found in Kalinin and Prieto [37]. Line-shaped patterns may be viewed as spacetime diagrams of two incoming particles that join to form one particle. It turns out that we can associate the "energy of the particle" with each world line such that total energy is conserved in these collisions. As it was recently shown (experimentally), quadratic patches may be thought of as a limit of many line-shaped patterns coming together during a relaxation [38].

2.3. Our Main Problem: Small Perturbation of the Maximal Stable State

Let us formalize the observations in **Figure 1** in the following way. Let Ω be a non-degenerate compact domain with non-empty interior and P be a finite non-empty subset of Ω. For each $N \in \mathbb{N}$ consider a set $\Gamma_N = \Omega \cap \frac{1}{N}\mathbb{Z}^2$, i.e., the intersection of Ω with the lattice of mesh $\frac{1}{N}$. Define the state $\varphi_N = (3 + \sum_{p \in P} \delta_p)^\circ$ on Γ_N, i.e., we put three grains everywhere on Γ_N and dropped one additional grain to each of the points $p \in P$ or to a near vertex in Γ_N if $p \notin \Gamma_N$, and then we performed a relaxation. Define the *deviation* set

$$C_N = \{v \in \Gamma_N | \varphi_N(v) < 3\} \subset \Omega.$$

Experimental evidence suggests that when N grows, the sets $C_N \subset \Omega$ converge to a thin balanced graph (see **Figure 1**).

Theorem 1. announced in [33] and proven in [33–35] *The sequence of sets $C_N \subset \Omega$ converges (in the Hausdorff sense) to a set $\tilde{C}_{\Omega,P}$. The set $\tilde{C}_{\Omega,P}$ is a planar graph passing through the points P. Each edge of $\tilde{C}_{\Omega,P}$ is a straight segment with a rational slope.*

At least in this setting, we have proven that the limiting/asymptotic patterns exist, though there is no close description of the shape and exact amount of grains for the pattern in the direction $(p,q) \in \mathbb{Z}^2$.

More intricate instances of the line-shaped patterns, namely, in the identity element of the sandpile group of Ω, await an explanation. Recall that the recurrent states of a sandpile model on a given graph form an Abelian group, the sandpile group of a graph [19, 39]. In **Figure 3**, the identity of the sandpile group for a cylinder consists of linear-shaped patterns. In **Figure 4**, we see similar patterns (along with quadratic patches) on the identity of the sandpile group for a non-convex domain. It has not yet been mathematically proven that the sandpile identity of such graphs indeed contains these linear patterns. A remarkably simple pattern for the identity on a circular base was found by Melchionna [40] [see Figures 7, 10 in [40]], the sandpile identity on ellipses of certain type consists of a unique pattern, up to "linear defects."

In the further text we briefly explain the main ideas behind the proof of Theorem 2. All the details of the actual proofs,

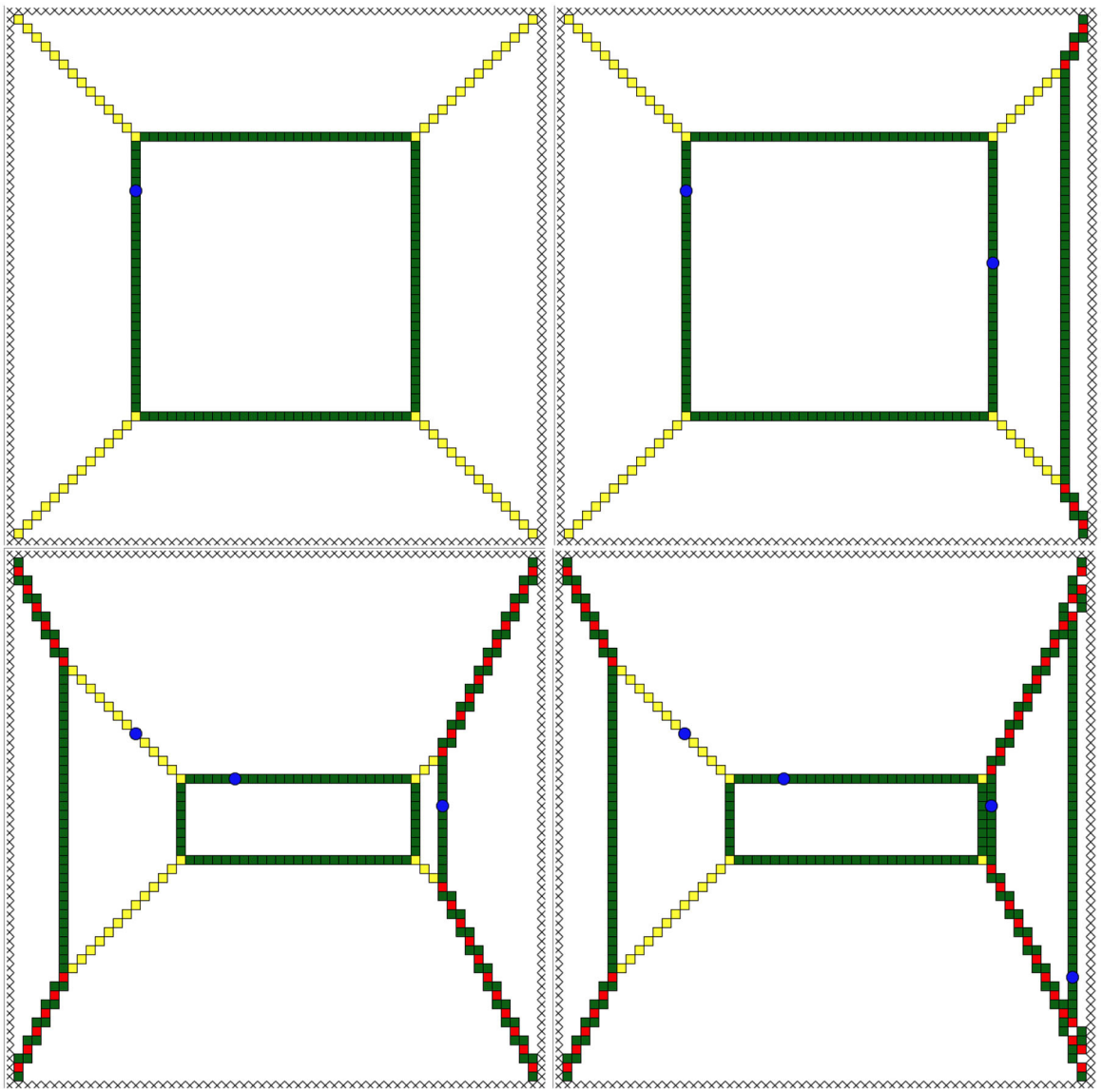

FIGURE 1 | Ω is a square $[0, 100] \times [0, 100]$, we put 3 grains at every vertex of the lattice inside Ω and drop 1 additional grain to each blue point (sequentially). The result of the relaxation after one additional grain is on the top-left picture. Then we added a grain of sand to the second blue point and performed a relaxation, the result of which is the top-right picture. The third picture is the bottom left one, and the last one is the bottom right one. White is three grains, green is two, yellow is one, and red is zero. Crosses mark the sinks in the model.

exact notation, omitted conditions, etc., can be found in Kalinin and Shkolnikov [33–35]. We believe that our tools are worth generalizing for other situations and can be used to prove the aforementioned appearance of linear patterns in different setups.

3. DISCRETE HARMONIC ANALYSIS

The laplacian ΔF of a function $F : \mathbb{Z}^2 \to \mathbb{Z}$ is defined as

$$(\Delta F)(i,j) = -4F(i,j) + F(i+1,j) + F(i-1,j) + F(i,j+1) + F(i,j-1).$$

A function $F : \Gamma \to \mathbb{Z}$ is harmonic (resp., superharmonic) if $\Delta F = 0$ (resp., $\Delta F \leq 0$) at every point of $\Gamma \subset \mathbb{Z}^2$ where ΔF is defined. Recall the Liouville theorem: a non-negative harmonic function on $\mathbb{Z}^2$ must be a constant (for several proofs see Theorem 9.24 in [41]).

Assume that Γ is an intersection of a big convex subset $\Omega \subset \mathbb{R}^2$ with $\mathbb{Z}^2$. Fix an arbitrary linear function $L : \mathbb{Z}^2 \to \mathbb{Z}$. The following lemmata are close in spirit to Buhovsky et al. [42] where an improvement of the Liouville theorem is presented.

Lemma 1. A positive integer-valued harmonic function F which is less than L on a large enough subdomain Γ' of Γ, is linear itself

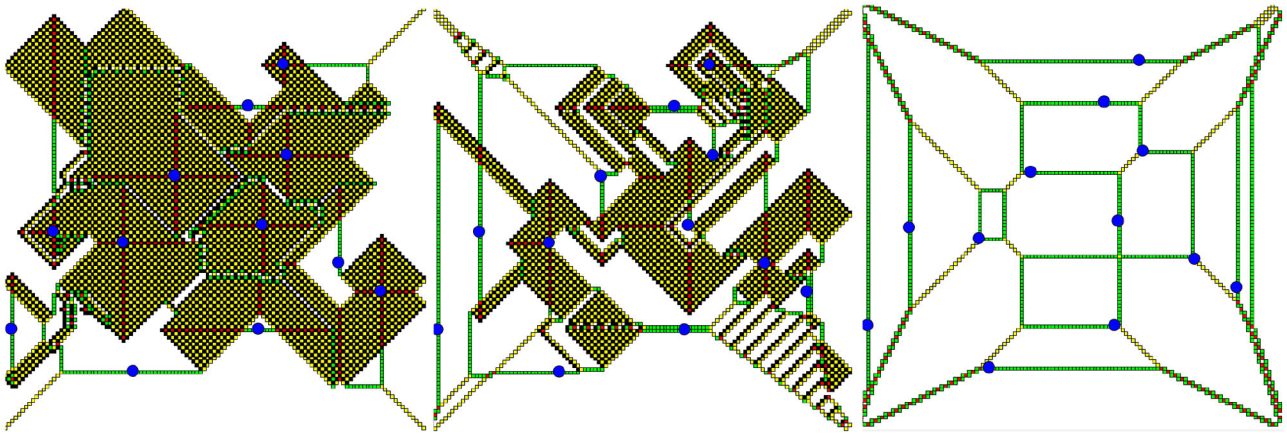

FIGURE 2 | Ω is a square $[0, 100] \times [0, 100]$, and we put 3 grains at every vertex of the lattice inside Ω and drop 1 additional grain to each blue point. On the left we see the initial phase of the relaxation. The central picture shows an intermediate phase. On the right we see the final result.

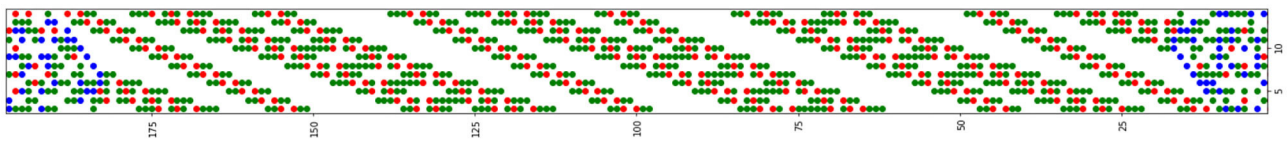

FIGURE 3 | The identity of the sandpile group on a skewed cylinder is presented, that is, we took the standard lattice in the rectangle $[0, 200] \times [0, 12]$ and identified each point $(x, 0)$ with $(x + 5, 12)$ for $x \in [0, 195]$. Let sinks be the vertices with less than four neighbors. The picture presents the identity of the sandpile group of this graph. White is three, green is two, red is one, and blue is zero. If we would take a flat cylinder, i.e., we would identify $(x, 0)$ with $(x, 12)$, then, in the picture for the identity of the sandpile group, we would have 3 everywhere except several green vertical lines, i.e., columns with two grains.

on a (smaller, but still large) subdomain Γ'' of Γ', i.e., there exists $\Gamma'' \subset \Gamma'$ such that

$$F(x, y)|_{\Gamma''} = ix + jy + a_{ij}, \text{where } i, j, a_{ij} \in \mathbb{Z}.$$

Lemma 2. Fix a constant $c > 0$. Consider a positive integer-valued superharmonic function F such that the sum of its laplacian at points in $\Gamma' \subset \Gamma$ linearly depends on the diameter of Γ' with an a priori bound c, i.e.,

$$\sum_{v \in \Gamma'} \Delta F(v) < c \cdot diam(\Gamma').$$

Then, if F is less than L and the domain is large enough then F is linear itself on a large subdomain $\Gamma'' \subset \Gamma'$.

In other words, given an upper estimate of a natural-valued function F by a linear function L, we may deduce that F is linear on a large subdomain provided F is harmonic or almost harmonic. Precise formulations can be found in Kalinin and Shkolnikov [34]. The two main ideas used in the proofs are as follows.

- The green function (harmonic at all points except one) on the plane grows as the logarithm.
- For a positive discrete harmonic function F on a ball of radius R with the center O, the discrete derivative of F at O (i.e., $F(O) - F(O')$ for a neighbor O' of O) is at most the maximum of F on the ball, divided by R. If F has only integer values, then $|F(O) - F(O')| < 1$ implies that $F(O) = F(O')$.

We conjecture that the line-shaped patterns show up in the relaxation of a perturbation of the maximal stable state in the sandpile model on a certain graph, if there is a notion of a linear function on such a graph and both lemmata above hold. To perform a "scaling" one needs a graph that is self-similar on different scales, such as $\mathbb{Z}^2$. A natural candidate is a Cayley graph of a group.

Recall that given a group G and a set S of its generators, one may construct the so-called Cayley graph of G, whose vertices are elements of G and two vertices $u, v \in G$ are connected by an edge if $u^{-1}v$ or $v^{-1}u$ belongs to S. If $G = \mathbb{Z}^2, S = \{(1, 0), (0, 1)\}$, then the Cayley graph is the standard grid $\mathbb{Z}^2$ with all vertices of valency four. If $G = \mathbb{Z}^2, S = \{(1, 0), (0, 1), (1, 1)\}$ then the Cayley graph is $\mathbb{Z}^2$ and each vertex (i, j) is connected by edges to $(i \pm 1, j), (i, j \pm 1), (i + 1, j + 1), (i - 1, j - 1)$.

On a Cayley graph, the generators of the group play the role of coordinates [modulo relations, as $(1, 0) + (0, 1) = (1, 1)$ in the example above] so the notion of a linear function can be easily extended. The discrete harmonic function theory is quite developed for several classes of groups [43–46].

Question. Do Lemmata 1,2 hold for the harmonic and superharmonic functions on Cayley graphs of amenable groups?

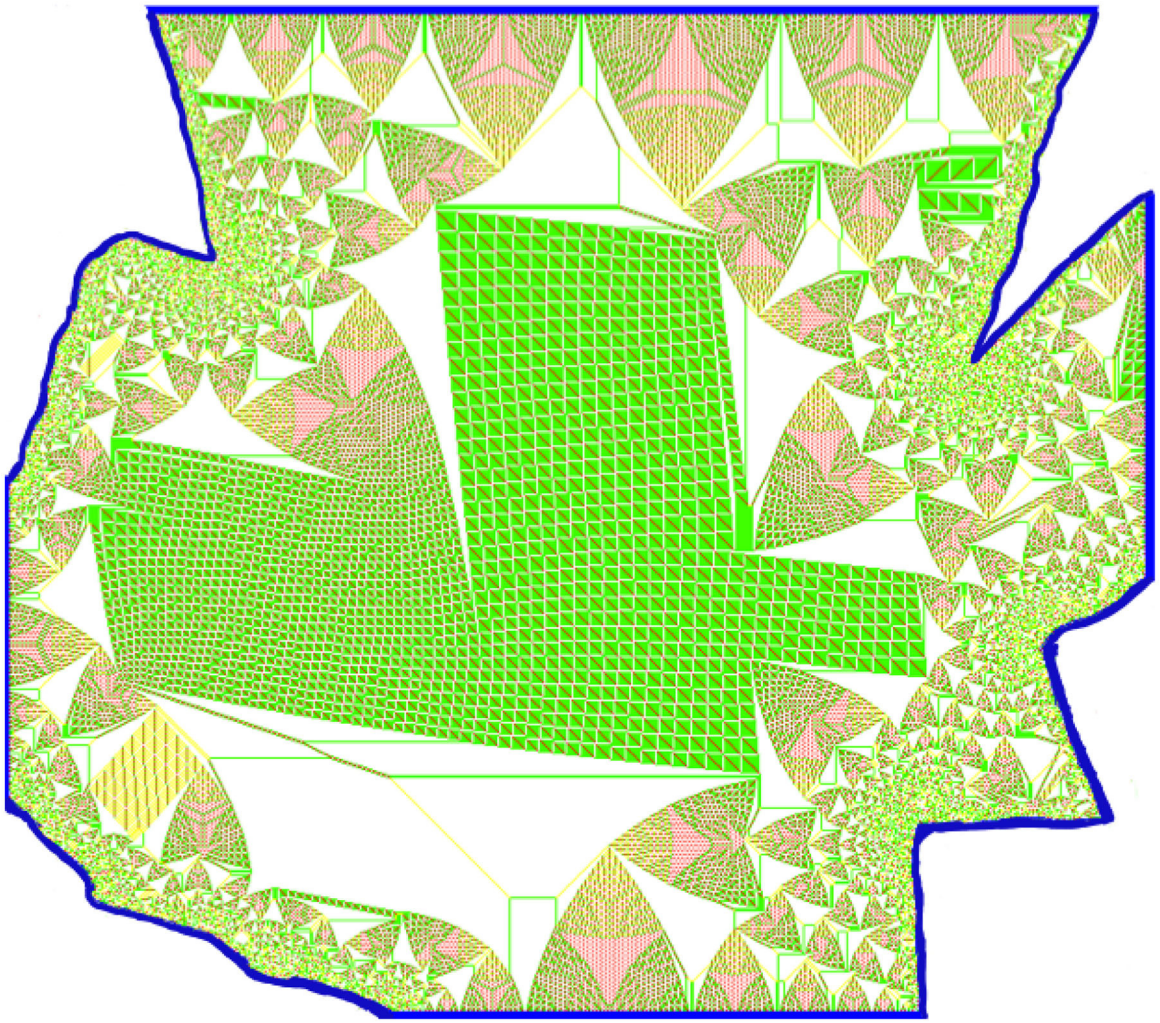

FIGURE 4 | The blue points mark the sinks. The identity of the remaining part of the lattice is presented. Note the presence of the linear patterns, the same as in the previous pictures. Colors are the same as in **Figure 1**.

If yes, then, under an appropriately chosen scaling procedure, one should be able to prove convergence of the deviation sets of the relaxations of a slightly perturbed maximal stable states (on a big bounded polygonal-shaped part of the Cayley graph) to the corner locus of a piecewise linear function on the scaling limit of these polygonal shaped parts of the Cayley graphs. The first thing to prove is that the toppling function has a piecewise linear estimate from above.

The Cayley graphs of abelian groups are composed of $\mathbb{Z}^k$ and cylinders as in **Figure 3**. The simplest non-abelian group, which is not much different from $\mathbb{Z}^3$, is the Heisenberg group.

Question. Are there any patterns in the sandpile for the Cayley graph of the Heisenberg group H?

$$H = \{H_{a,b,c} | a, b, c \in \mathbb{Z}\} \text{ where } H_{a,b,c} = \begin{pmatrix} 1 & a & b \\ 0 & 1 & c \\ 0 & 0 & 1 \end{pmatrix}.$$

Two generators $H_{1,0,0}, H_{0,1,0}$ of the group commute; the Cayley graph of H therefore looks like a collection of standard lattices $\mathbb{Z}^2$ with additional edges corresponding to the third generator $H_{0,0,1}$. Consider the intersection of this Cayley graph with a large cube, e.g., let $\Gamma = \{H_{a,b,c} | 0 \leq a, b, c \leq 100\}$. Then, all vertices $v \in \Gamma$ have a valency of six, since they are connected to $v \cdot H_{\pm 1,0,0}, v \cdot H_{0,\pm 1,0}, v \cdot H_{0,0,\pm 1}$, and all the vertices of $\mathbb{Z}^3$ outside of Γ are treated as sinks.

Consider a maximal stable state (i.e., 5 grains at every vertex) and add one grain to several vertices. One expects that the relaxation of such a state on Γ should be not a very complicated "extension" of a relaxation of a perturbation of the maximal stable sandpile on domains in $\mathbb{Z}^2$.

4. TROPICAL CURVES

A *tropical polynomial* is a piecewise linear function $f : \mathbb{R}^2 \to \mathbb{R}$ of the form

$$f(x, y) = \min\{ix + jy + a_{ij} | (i, j) \in A\},$$

where A is a finite subset of $\mathbb{Z}^2$ and $a_{ij} \in \mathbb{R}$ are coefficients. Each term $ix + jy + a_{ij}$ is called a *monomial* and should be thought of $\log(t^{a_{ij}}x^i y^j)$, f should be thought of the limit of a certain logarithmic rescaling of

$$f_t(x, y) = \sum_{(i,j)\in A} t^{a_{ij}} x^i y^j.$$

To each tropical polynomial f there is a corresponding tropical curve $C(f)$, which, by definition, is the *corner locus* of f, i.e., the set of points (x, y) where f is not smooth. An equivalent definition follows.

Definition 3. $C(f) = \{(x, y) \in \mathbb{R}|$the minimum among $ix + jy + a_{ij}$ is attainedat least twice$\}$.

More on algebra-geometric aspects of tropical curves can be found in Brugallé et al. [47], Itenberg and Mikhalkin [48], and Maclagan and Sturmfels [49] along with recent applications in symplectic topology [50–53]. In this set-up, tropical curves should be thought of Riemann surfaces, and each vertex A of a tropical curve corresponds to a small surface S_A with the boundary, the valency of A is equal to the number of the boundary components of S_A, and each edge AB of the tropical curve corresponds to a very long thin cylinder connecting small surfaces S_A and S_B. Unfortunately, we found no connection between tropical curves in sandpiles and tropical curves in algebraic or symplectic geometry.

4.1. Tropical Series

Pick a convex compact set $\Omega \subset \mathbb{R}^2$ with non-empty interior. Let P be a finite subset of Ω.

Definition 4. Kalinin and Shkolnikov [35] an Ω-tropical series is a piecewise linear function in Ω given by the following:

$$F(x, y) = \inf_{(i,j)\in\mathcal{A}} (a_{ij} + ix + jy), \tag{1}$$

where the set $\mathcal{A}$ is not necessarily finite and $F|_{\partial\Omega} = 0$. See an example in **Figure 5**.

Consider the family $\mathcal{F}_P$ of Ω-tropical series that are not smooth at every point of P.

Note that all functions in $\mathcal{F}_P$ are concave and thus superharmonic. Let F_P be the pointwise minimum of functions in $\mathcal{F}_P$. In Kalinin and Shkolnikov [35] it is proven that this pointwise minimum exists (that is easy) and belongs to $\mathcal{F}_P$ (a bit more involved, because it may be not continuous or not a tropical series).

For each $F \in \mathcal{F}_P$ we may consider the set

$$C(F) = \{(x, y) \in \Omega|(\Delta F)(x, y) \neq 0\}.$$

It is easy to see that $C(F)$ is the corner locus of the function F, i.e., exactly those points where F is not linear but changes its slope. The set $C(F)$ is called the Ω-tropical curve defined by F, and $C(F)$ is a planar graph with straight edges of rational directions, the sum of directions of outgoing edges is zero for every vertex, and this is called *the balancing condition*.

Theorem 2. (elaboration) The sequence of sets $C_N \subset \Omega$ converges (in the Hausdorff sense) to the Ω-tropical curve $C(F_P)$.

Let Ω be a disk $\{x^2 + y^2 \leq 1\}$. An example of an Ω-tropical series is $\min\{ix + jy + a_{ij}|(i, j) \in \mathbb{Z}^2\}$ with $|a_{ij}| = \sqrt{i^2 + j^2}$ is presented on the left in **Figure 5**, and its corresponding Ω-tropical curve, which is an infinitely branching tree, is presented on the right. See details in Kalinin and Shkolnikov [54].

Question. The sum of the values of the above Ω-tropical series for a circle (or other plane curve) gives interesting formulae in number theory [54] which are related to Mordell-Tornheim and Witten zeta functions [55, 56]. These formulae take as input the coefficients of the equations of the tangent lines to a given plane curve, and they are thus easy to compute and may provoke interesting questions in the experimental computer mathematics. However, no analogs of these formulae for three dimensional bodies are known.

5. TOPPLING FUNCTION

To understand the appearance of tropical geometry in sandpiles, consider the *toppling function* $H(v)$ defined for every v in Γ_N as follows: given an initial state φ on Γ and its relaxation φ°, the value $H(v)$ equals the number of times that the vertex v toppled in the process taking φ to φ°.

The toppling function is clearly non-negative on Γ and vanishes at the boundary of Γ. The Laplacian ΔH of H completely determines the final state φ° by the formula [22]:

$$\varphi^\circ(v) = \varphi(v) + \Delta H(v). \tag{2}$$

It can be shown by induction that the toppling function H satisfies the *Least Action Principle* [57, 58]: if $\varphi(v) + \Delta F(v) \leq 3$ is stable, then $F(v) \geq H(v)$. Ostojic noticed that $H(i, j)$ is a piecewise quadratic function if we drop a lot of sand in the origin of the otherwise empty plane [22].

5.1. Piecewise Linearity of the Toppling Function in Our Main Problem

Consider a state φ_P, which consists of three grains of sand at every vertex, except at a finite family of points $P = \{p_1, \ldots, p_r\}$ where we have four grains of sand:

$$\varphi := \langle 3\rangle + \delta_{p_1} + \cdots + \delta_{p_r} = \langle 3\rangle + \delta_P. \tag{3}$$

The state φ° and the evolution of the relaxation can be described by means of tropical geometry. This was discovered in Caracciolo et al. [29]. The crucial (experimental) observation is that the toppling function H of the state φ is almost harmonic everywhere since $\varphi^\circ = \varphi$ almost everywhere (see **Figure 1**). Even better, in this case the toppling function H is piecewise linear on the most part of Ω and the line-shaped patterns belong to a finite neighborhood of the *corner locus* of H (in the next section we give a more detailed statement). It is easy to observe but tricky to prove.

We provide an upper bound H_u and a lower bound H_l for H, which are close to H. These tight bounds force the set

$$\{v \in \Gamma|\varphi(v) + \Delta H_u(v) \neq 3\}$$

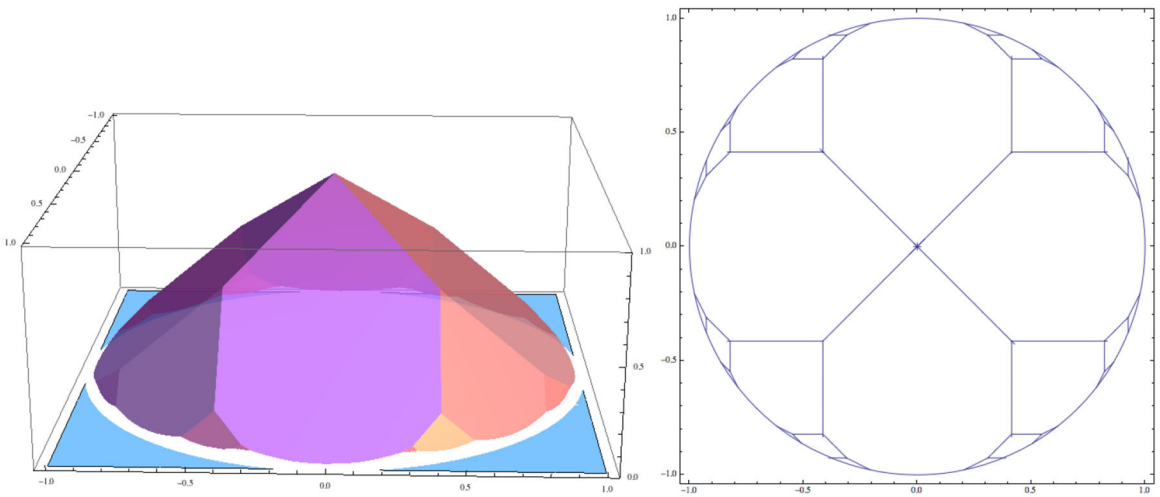

FIGURE 5 | An Ω-tropical series and the corresponding Ω-tropical curve.

to belong to a small neighborhood of the set

$$\{v \in \Gamma | \varphi(v) + \Delta H(v) \neq 3\}.$$

The upper bound H_u is a piece-wise linear function, φ is equal to 3 everywhere except a small set P of points, the laplacian of a function is zero on the domains of its linearity. The set $\Delta H_u(v) \neq 0$ (the corner locus of a piece-wise linear function) is thus close to the set $\Delta H \neq 0$, the deviation locus of φ°. This concludes the proof of the theorem.

5.2. Upper Bound for the Toppling Function

Denote by $H(\varphi_N)$ the toppling function of the state $\varphi_N = \langle 3 \rangle + \sum \delta_{p_i}$ on Γ_N. Abusing notation we will write $H(x, y) = \frac{1}{N} H(\varphi_N)(x, y) : \Omega \to \mathbb{R}$ for the rescaled toppling function without specifying N. Consider the pointwise minimal function F_P in $\mathcal{F}_P$. Then $F_P \geq H(\varphi_N)$ by the Least Action Principle (since $\Delta F_P \leq 0, \Delta F_P(p_i) < 0$ for each i). Thus, $F_P \geq H$.

Corollary. The total defect $\sum_{v \in \Gamma_N} (3 - \varphi^\circ(v))$ grows linearly in N.

Indeed, the total defect is equal to the amount of the sand fallen outside of the system, which, in turn, is equal to the sum of $H(\varphi_N)$ near the boundary, which can be estimated as $N \cdot \int_{\partial \Omega_{1/N}} N F_P$, i.e., N times the integral of F_P over the $1/N$-neighborhood of the boundary of Ω.

In order to study the dependence of the deviation set $\{\varphi^\circ \neq 3\}$ on Ω and P (positions of points where we added grains), one may study F_P because it determines the tropical curve. The dependence of F_P on P is in no sense continuous: when P passes through degenerate configurations (e.g., several points on a vertical line), F_P and the corresponding tropical curve drastically change. Similar phenomenon appears when we keep P fixed and change Ω: no meaningful results about stability of the resulting picture are known.

6. LOWER BOUND. WAVE OPERATORS

Let φ be a sandpile state on a graph Γ. Given a fixed vertex $p \in \Gamma$, we define the *wave operator* W_p acting on a sandpile state φ as the following:

$$W_p(\varphi) := (T_p(\varphi + \delta_p) - \delta_p)^\circ,$$

where T_p is the operator that topples once the state φ at p if it is possible ([59–61]) (see **Figure 6**). In a computer simulation, the application of this operator looks like one wave of topplings spreading from p, while each vertex topples at most once.

The first important property of W_p is that, for the initial state $\varphi := \langle 3 \rangle + \delta_P$, we can achieve the final state φ° by successive applications of the operator $W_{p_1} \circ \cdots \circ W_{p_r}$ a large but finite number of times (we write ∞ in spite of the notation):

$$\varphi^\circ = (W_{p_1} \cdots W_{p_r})^\infty \varphi + \delta_P.$$

This is not a deep theorem but a rather useful description of a relaxation. We thus decompose the total relaxation $\varphi \mapsto \varphi^\circ$ into layers of controlled avalanching

$$\varphi \to W_{p_1}^{k_1} \varphi = \varphi_1 \to W_{p_2}^{k_2} \varphi_1 \to \dots$$

These layers, in turn, can be described by means of tropical geometry. We only need to prove that the linear-shaped patterns, visible in the pictures, move toward the point where we apply a wave operator.

6.1. Construction of Solitons

For each direction $(p, q) \in \mathbb{Z}^2, gcd(p, q) = 1$ we construct a function $F_{p,q}$ whose laplacian coincides with the linear pattern in the direction (p, q). To do that, consider a function

$$\tilde{F} : \mathbb{Z}^2 \to \mathbb{Z}, \tilde{F}(x, y) = \min(0, qx - py).$$

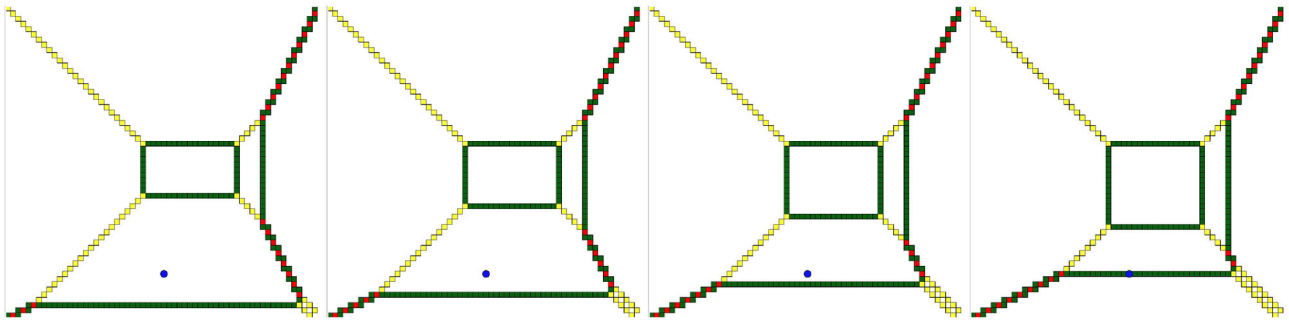

FIGURE 6 | For a given sandpile state we apply several times the wave operator at the blue point p. One can see that the line-shaped pattern around p point creeps toward p until it belongs to one on them. Recall that white cells contain 3 grains, so the deviation set is the green, yellow, and red cells, which belong to a small neighborhood of a certain tropical curve. Let us present this tropical curve as a corner locus of a pointwise minimum of several linear functions (cf. **Figure 5**), i.e., as an Ω-tropical series F. The planar graph is then the projection of edges of a three-dimensional polytope (the graph of F). Then the action of the wave operator corresponds to shifting one of the faces of this polytope, i.e., increasing by one the constant coefficient of the linear function, defining this face. On the level of planar graphs, we take the linear function in F (see Equation 1), which is the minimal at p, and increase its constant coefficient until p belongs to the corner locus of the new piecewise linear function.

Note that the corner locus l (the set of points in $\mathbb{R}^2$ where $\min(0, qx - py)$ is not smooth) of $\tilde{F}$ is a line of direction (p, q). Next, consider all the integer-valued superharmonic functions on $\mathbb{Z}^2$, which coincide with $\tilde{F}$ outside of a finite neighborhood of l. A non-trivial fact is that there exists a pointwise minimum $F_{p,q}$ among this family of functions [34].

The idea of the proof is as follows: instead of taking the pointwise minimum at once, we first prove that we can achieve it by "smoothings," namely, by a sequence of steps $\tilde{F} = F_0 \to F_1 \to F_2 \to \ldots$; in each step $F_k \to F_{k+1}$ we subtract the characteristic function of a certain set in a finite neighborhood of l (thus, a kind of inverse operator to the wave operator) and $0 \le F_k - F_{k+1} \le 1$. Then, since $\tilde{F}$ is periodic, we may factor the plane by the action of the vector (p, q) and reduce the problem to a cylinder.

Then we use lemmata about superharmonic functions: if it would be possible to perform smoothings an infinite number of times, then Lemma 1 would imply that F_k is linear with integer slope in a compact neighborhood of l, hence there exists a linear function with integer slope which is less than $\tilde{F}$ only on a finite neighborhood of the corner locus. This function would be periodic with respect to the shift on (p, q) and would therefore be like $k(qx - py) + c$ (since $gcd(p, q) = 1$), but any such function (with an integer k) is less than $\tilde{F}$ outside of a finite neighborhood of l, which is a contradiction. Then we cannot perform smoothings an infinite number of times, and thus there is a pointwise minimum in the aforementioned family.

Once proved that the pointwise minimum exists, we may define solitons.

Definition 4. A *soliton* [a linear-shaped pattern in the direction (p, q)] is $\varphi_{pq} = \langle 3 \rangle + \Delta F_{p,q}$.

Then, from the Least Action principle and the minimality of $F_{p,q}$ it easily follows that sending a wave from one side of the deviation set of φ_{pq} translates it [i.e., for certain p', q' we have $W_x \varphi_{pq}(i, j) = \varphi_{pq}(i + p', j + q')$ for all (i, j)], otherwise not changing. This is why we call them solitons.

The same can be done for three solitons of direction $(p_1, q_1), (p_2, q_2), (p_3, q_3)$, meeting at a point, provided that $\sum p_i = \sum q_i = 0$ and the triangle $(p_1, q_1), (p_2, q_2), (p_3, q_3)$ does not contain lattice points except vertices. The ideas of the proof are the same, we use Lemma 2 and the final step is that if a linear function $px + qy$ is less than $\min(p_1 y - q_1 x, p_2 y - q_2 x, p_3 y - q_3 x)$ only in a compact neighborhood of the apex of the latter function, then $(p, q) \in \mathbb{Z}^2$ must belong to the triangle $(p_1, -q_1), (p_2, -q_2), (p_3, -q_3)$, which is a contradiction.

We summarize the results as follows: there are certain functions $f_{p,q,\ldots}$ ("at infinity" being described by piecewise functions, i.e., tropical functions), pointwise minimal in special families of superharmonic functions, such that $\langle 3 \rangle + \Delta f_{p,q,\ldots}$ models solitons, and three or four solitons coming to a point.

The crucial property of the wave operator W_p is that its action on a state $\varphi = \langle 3 \rangle + \Delta f_{p,q,\ldots}$ has an interpretation in terms of tropical geometry; see the next section.

6.2. Tropical Wave Operators and the Lower Bound

Whenever, "at infinity" f is a piecewise linear function with integral slopes that, in a neighborhood of p, is expressed as $a_{i_0 j_0} + i_0 x + j_0 y$, then

$$W_p(\langle 3 \rangle + \Delta f) = \langle 3 \rangle + \Delta W(f),$$

where $W(f)$, another piece-wise linear "at infinity" function, has the same coefficients a_{ij} as f, except one, namely $a'_{i_0 j_0} = a_{i_0 j_0} + 1$. This is to emulate the fact that the support of the wave (the set of vertices that toppled during the wave) is exactly the part of the plane where $a_{i_0 j_0} + i_0 x + j_0 y$ is the leading part of f.

Consider an Ω-tropical series f. We will write $G_p := W_p^{\infty}$ to denote the operator that "applies W_p to $\langle 3 \rangle + \Delta f$ until p lies in the corner locus of f"; i.e., G_p increases the coefficient a_{ij}, corresponding to a neighborhood of p, by lifting the plane lying above p in the graph of f by integral steps until p belongs to the

corner locus of $G_p f$. Thus, G_p has the effect of pushing the tropical curve closer toward p until it contains p (see **Figure 6**).

From the properties of the wave operators, it follows immediately that (recall that F_P is the upper bound):

$$F_P = \left(G_{p_1} \cdots G_{p_r}\right)^{\infty} 0,$$

where 0 is the function which is identically zero on Ω.

Now we are ready to provide a lower bound in the main theorem.

Note that the upper bound can be obtained by (possibly infinite) series of applying tropical wave operators (which are nothing else but repetitive increasing of coefficients on linear parts in a piecewise linear function). Then, by the properties of the solitons, this can be emulated in the sandpile model, where wave operators are performed on the sandpile level, and instead of piecewise linear functions we have pictures as in **Figure 6**.

In other words, we choose an approximation of F_P by a finite composition $G_{p_1} G_{p_2} \ldots$ of tropical wave operators, and we then choose an N big enough before starting from a state on Γ_N with a tropical series and a collection of solitons, representing the corresponding Ω-tropical curve. Then we perform the sandpile wave operators $W_{p_1} W_{p_2} \ldots$ as prescribed by tropical wave operators (see **Figure 6**). Since N is big enough we have full control on the picture and know that the solitons move exactly as edges of the tropical curve on the tropical pictures. By the nature of the construction, this will give us a lower bound for the relaxation of φ (constructed by the wave decomposition), which is close to the upper bound (given by an Ω-tropical series) with any prescribed accuracy. The deviation set of φ_N° consequently converges to the Ω-tropical curve defined by F_P.

7. DISCUSSION

We surveyed several mathematical tools which have been used for a concrete problem of sandpiles on a part of $\mathbb{Z}^2$. These tools may be generalized in several directions. One may consider sandpiles on other graphs, e.g., parts of the Cayley graphs for amenable groups. Also, one can take a part of hyperbolic tessellation [62] or other tiling of the plane [63] and ask similar questions about patterns and rescaling procedures.

It seems that the only tool to describe explicitly the picture for the sandpile identity is to compute the toppling function with high precision and controlled error. Above, we explained that the "smoothing" procedure allows us to show that there exists a pointwise minimal function in certain classes of superharmonic functions, and certain localization techniques (tropical geometry) could then be applied based of the properties of harmonic or almost harmonic functions on big domains with an explicit linear upper bound.

Tropical series for planar domains are connected to certain zeta functions. It would be nice to (at least, experimentally) compute series, similar to Kalinin and Shkolnikov [54], for higher dimensions with a good precision and guess what kind of numbers (e.g., polynomials in π if we start with a round sphere) will be obtained.

It would be interesting to find another decomposition of a relaxation into waves of higher magnitude, i.e., such a decomposition will allow us to control the change of not only linear-shaped pattern but the quadratic patches too.

Similar to Sadhu and Dhar [32] it would be nice to run the same research, and in particular, to establish continuity properties for the toppling functions of sandpiles on Cayley graphs and see whether one can get a kind of balancing conditions out of that.

DATA AVAILABILITY STATEMENT

The original contributions presented in the study are included in the article, further inquiries can be directed to the corresponding author.

AUTHOR CONTRIBUTIONS

The author confirms being the sole contributor of this work and has approved it for publication.

ACKNOWLEDGMENTS

NK was supported in part by Young Russian Mathematics award. Support from the Basic Research Program of the National Research University Higher School of Economics was gratefully acknowledged.

REFERENCES

1. Thompson DW. *On Growth and Form*. Cambridge: Cambridge University Press (1942).
2. Turing AM. The chemical basis of morphogenesis. *Philos Trans R Soc Lond B Biol Sci*. (1952) 237:37–72. doi: 10.1098/rstb.1952.0012
3. Belousov BP. Periodicheski deistvuyushchaya reaktsia i ee mekhanism [Periodically acting reaction and its mechanism]. In: *Sbornik Referatov po Radiotsionnoi Meditsine, 1958 [Collection of Abstracts on Radiation Medicine, 1958]*. Moscow: Medgiz (1959). p. 145–7.
4. Kiprijanov KS. Chaos and beauty in a beaker: the early history of the Belousov-Zhabotinsky reaction. *Ann Phys*. (2016) 528:233–7. doi: 10.1002/andp.201600025
5. Ball P. Forging patterns and making waves from biology to geology: a commentary on Turing (1952) 'the chemical basis of morphogenesis'. *Philos Trans R Soc B Biol Sci*. (2015) 370:20140218. doi: 10.1098/rstb.2014.0218
6. Wolf YI, Katsnelson MI, Koonin EV. Physical foundations of biological complexity. *Proc Natl Acad Sci USA*. (2018) 115:E8678–87. doi: 10.1073/pnas.1807890115
7. Cross MC, Hohenberg PC. Pattern formation outside of equilibrium. *Rev Mod Phys*. (1993) 65:851. doi: 10.1103/RevModPhys.65.851
8. Koch A, Meinhardt H. Biological pattern formation: from basic mechanisms to complex structures. *Rev Mod Phys*. (1994) 66:1481. doi: 10.1103/RevModPhys.66.1481
9. Von Neumann J. The general and logical theory of automata. In: Jeffress LA, editor. *Cerebral Mechanisms in Behavior; The Hixon Symposium*. Wiley (1951). p. 1–41.
10. Ulam S. Random processes and transformations. In: *Proceedings of the International Congress on Mathematics*. Cambridge: Citeseer (1952). p. 264–75.

11. Wolfram S. Cellular automata as models of complexity. *Nature*. (1984) 311:419–24. doi: 10.1038/311419a0
12. Ermentrout GB, Edelstein-Keshet L. Cellular automata approaches to biological modeling. *J Theor Biol*. (1993) 160:97–133. doi: 10.1006/jtbi.1993.1007
13. Bak P, Tang C, Wiesenfeld K. Self-organized criticality. *Phys Rev A*. (1988) 38:364. doi: 10.1103/PhysRevA.38.364
14. Schelling TC. *Micromotives and Macrobehavior*. WW Norton & Company (2006). p. 252.
15. Kondo S, Asai R. A reaction–diffusion wave on the skin of the marine angelfish pomacanthus. *Nature*. (1995) 376:765–8. doi: 10.1038/376765a0
16. Fowler DR, Meinhardt H, Prusinkiewicz P. Modeling seashells. *ACM SIGGRAPH Comput Graph.* (1992) 26:379–87. doi: 10.1145/142920.134096
17. Manukyan L, Montandon SA, Fofonjka A, Smirnov S, Milinkovitch MC. A living mesoscopic cellular automaton made of skin scales. *Nature*. (2017) 544:173–9. doi: 10.1038/nature22031
18. Rietkerk M, Van de Koppel J. Regular pattern formation in real ecosystems. *Trends Ecol Evol*. (2008) 23:169–75. doi: 10.1016/j.tree.2007.10.013
19. Dhar D. Self-organized critical state of sandpile automaton models. *Phys Rev Lett*. (1990) 64:1613–6. doi: 10.1103/PhysRevLett.64.1613
20. Dhar D. Theoretical studies of self-organized criticality. *Phys A*. (2006) 369:29–70. doi: 10.1016/j.physa.2006.04.004
21. Liu S, Kaplan T, Gray L. Geometry and dynamics of deterministic sand piles. *Phys Rev A*. (1990) 42:3207. doi: 10.1103/PhysRevA.42.3207
22. Ostojic S. Patterns formed by addition of grains to only one site of an abelian sandpile. *Phys A*. (2003) 318:187–99. doi: 10.1016/S0378-4371(02)01426-7
23. Pegden W, Smart CK. Convergence of the Abelian sandpile. *Duke Math J*. (2013) 162:627–42. doi: 10.1215/00127094-2079677
24. Pegden W, Smart CK. Stability of patterns in the abelian sandpile. *Ann Henri Poinc*. (2020) 21:1383–99. doi: 10.1007/s00023-020-00898-1
25. Levine L, Pegden W, Smart CK. Apollonian structure in the Abelian sandpile. *Geom Funct Anal*. (2016) 26:306–36. doi: 10.1007/s00039-016-0358-7
26. Levine L, Pegden W, Smart CK. The Apollonian structure of integer superharmonic matrices. *Ann Math*. (2017) 186:1–67. doi: 10.4007/annals.2017.186.1.1
27. Dhar D, Sadhu T, Chandra S. Pattern formation in growing sandpiles. *Europhys Lett*. (2009) 85:48002. doi: 10.1209/0295-5075/85/48002
28. Dhar D, Sadhu T. A sandpile model for proportionate growth. *J Stat Mech Theory Exp*. (2013) 2013:P11006. doi: 10.1088/1742-5468/2013/11/P11006
29. Caracciolo S, Paoletti G, Sportiello A. Conservation laws for strings in the abelian sandpile model. *Europhys Lett*. (2010) 90:60003. doi: 10.1209/0295-5075/90/60003
30. Caracciolo S, Paoletti G, Sportiello A. Deterministic abelian sandpile and square-triangle tilings. In: *Combinatorial Methods in Topology and Algebra*. Cham: Springer International Publishing (2015). p. 127–36. doi: 10.1007/978-3-319-20155-9_23
31. Paoletti G. *Deterministic Abelian sandpile models and patterns* (Springer Theses), Springer, Cham, Switzerland (2014).
32. Sadhu T, Dhar D. Pattern formation in fast-growing sandpiles. *Phys Rev E*. (2012) 85:021107. doi: 10.1103/PhysRevE.85.021107
33. Kalinin N, Shkolnikov M. Tropical curves in sandpiles. *Comptes Rendus Math*. (2016) 354:125–30. doi: 10.1016/j.crma.2015.11.003
34. Kalinin N, Shkolnikov M. Sandpile solitons via smoothing of superharmonic functions. (2017) *arXiv[Preprint].arXiv:1711.04285*. doi: 10.1007/s00220-020-03828-8
35. Kalinin N, Shkolnikov M. Introduction to tropical series and wave dynamic on them. *Discrete Contin Dyn Syst A*. (2018) 38:2843–65. doi: 10.3934/dcds.2018120
36. Kalinin N, Guzmán-Sáenz A, Prieto Y, Shkolnikov M, Kalinina V, Lupercio E. Self-organized criticality and pattern emergence through the lens of tropical geometry. *Proc Natl Acad Sci USA*. (2018) 115:E8135–42. doi: 10.1073/pnas.1805847115
37. Kalinin N, Prieto Y. Statistics for tropical sandpile model. (2015) *arXiv[Preprint].arXiv:1906.02802*.
38. Lang M, Shkolnikov M. Harmonic dynamics of the abelian sandpile. *Proc Natl Acad Sci USA*. (2019) 116:2821–30. doi: 10.1073/pnas.1812015116
39. Creutz M. Abelian sandpiles. *Comput Phys*. (1991) 5:198–203. doi: 10.1063/1.168408
40. Melchionna A. The sandpile identity element on an ellipse. (2020) *arXiv[Prerpint].arXiv:2007.0579*.
41. Lyons R, Peres Y. *Probability on Trees and Networks*, Vol. 42. Cambridge: Cambridge University Press (2017).
42. Buhovsky L, Logunov A, Malinnikova E, Sodin M. A discrete harmonic function bounded on a large portion of z^2 is constant. (2017) *arXiv[Preprint].arXiv:1712.07902*.
43. Hua B, Jost J, Li-Jost X. Polynomial growth harmonic functions on finitely generated abelian groups. *Ann Glob Anal Geom*. (2013) 44:417–32. doi: 10.1007/s10455-013-9374-0
44. Meyerovitch T, Perl I, Tointon M, Yadin A. Polynomials and harmonic functions on discrete groups. *Trans Am Math Soc*. (2017) 369:2205–29. doi: 10.1090/tran/7050
45. Meyerovitch T, Yadin A. Harmonic functions of linear growth on solvable groups. *Israel J Math*. (2016) 216:149–80. doi: 10.1007/s11856-016-1406-6
46. Benjamini I, Duminil-Copin H, Kozma G, Yadin A. Minimal growth harmonic functions on lamplighter groups. (2016) *arXiv[Preprint].arXiv:1607.00753*.
47. Brugallé E, Itenberg I, Mikhalkin G, Shaw K. Brief introduction to tropical geometry. In: *Proceedings of the Gökova Geometry-Topology Conference (GGT)*, Gökova (2015). p. 1–75.
48. Itenberg I, Mikhalkin G. Geometry in the tropical limit. *Math Semesterb*. (2012) 59:57–73. doi: 10.1007/s00591-011-0097-7
49. Maclagan D, Sturmfels B. *Introduction to Tropical Geometry, Graduate Studies in Mathematics*, Vol. 161. Providence, RI: American Mathematical Society (2015).
50. Matessi D. Lagrangian pairs of pants. *Int Math Res Notices*. (2018) rnz126. doi: 10.1093/imrn/rnz126
51. Sheridan N, Smith I. Lagrangian cobordism and tropical curves. (2018) *arXiv.[Preprint].arXiv:1805.07924*.
52. Mikhalkin G. Examples of tropical-to-Lagrangian correspondence. *Eur J Math*. (2018) 5:1033–66. doi: 10.1007/s40879-019-00319-6
53. Hicks J. Tropical lagrangians and homological mirror symmetry. (2019) *arXiv[Preprint].arXiv:1904.06005*.
54. Kalinin N, Shkolnikov M. Tropical formulae for summation over a part of $SL(2;\mathbb{Z})$. *Eur J Math*. (2019) 5:909–28. doi: 10.1007/s40879-018-0218-0
55. Matsumoto K. On analytic continuation of various multiple zeta-functions. In: *Surveys in Number Theory: Papers from the Millennial Conference on Number Theory*. AK Peters; CRC Press (2002). p. 169.
56. Romik D. On the number of n-dimensional representations of Su(3), the Bernoulli numbers, and the Witten zeta function. (2015) *arXiv[Preprint].arXiv:1503.03776*.
57. Fey A, Levine L, Peres Y. Growth rates and explosions in sandpiles. *J Stat Phys*. (2010) 138:143–59. doi: 10.1007/s10955-009-9899-6
58. Sadhu T, Dhar D. The effect of noise on patterns formed by growing sandpiles. *J Stat Mech Theory Exp*. (2011) 2011:P03001. doi: 10.1088/1742-5468/2011/03/P03001
59. Ivashkevich EV, Ktitarev DV, Priezzhev VB. Waves of topplings in an Abelian sandpile. *Phys A*. (1994) 209:347–60. doi: 10.1016/0378-4371(94)90188-0
60. Dhar D, Manna S. Inverse avalanches in the Abelian sandpile model. *Phys Rev E*. (1994) 49:2684. doi: 10.1103/PhysRevE.49.2684
61. Ktitarev D, Lübeck S, Grassberger P, Priezzhev V. Scaling of waves in the Bak-Tang-Wiesenfeld sandpile model. *Phys Rev E*. (2000) 61:81. doi: 10.1103/PhysRevE.61.81
62. Kalinin N, Shkolnikov M. Sandpiles on the heptagonal tiling. *J Knot Theory Ramif*. (2016) 25:1642005. doi: 10.1142/S0218216516420050
63. Fersula J, Noûs C, Perrot K. Sandpile toppling on penrose tilings: identity and isotropic dynamics. (2020) *arXiv[Preprint].arXiv:2006.06254*.

Conflict of Interest: The author declares that the research was conducted in the absence of any commercial or financial relationships that could be construed as a potential conflict of interest.

frontiers in Physics

REVIEW
published: 23 December 2020
doi: 10.3389/fphy.2020.583213

Mechanisms of Self-Organized Quasicriticality in Neuronal Network Models

Osame Kinouchi[1]*, *Renata Pazzini*[1] *and Mauro Copelli*[2]

[1]*Laboratório de Física Estatística e Biologia Computacional, Faculdade de Filosofia, Ciências e Letras de Ribeirão Preto, Departmento de Física, Universidade de São Paulo, Ribeirão Preto, Brazil,* [2]*Departamento de Física, Universidade Federal de Pernambuco, Recife, Brazil*

The critical brain hypothesis states that there are information processing advantages for neuronal networks working close to the critical region of a phase transition. If this is true, we must ask how the networks achieve and maintain this critical state. Here, we review several proposed biological mechanisms that turn the critical region into an attractor of a dynamics in network parameters like synapses, neuronal gains, and firing thresholds. Since neuronal networks (biological and models) are not conservative but dissipative, we expect not exact criticality but self-organized quasicriticality, where the system hovers around the critical point.

Keywords: self-organized criticality, neuronal avalanches, self-organization, neuronal networks, adaptive networks, homeostasis, synaptic depression, learning

OPEN ACCESS

Edited by:
Attilio L. Stella,
University of Padua, Italy

Reviewed by:
Srutarshi Pradhan,
Norwegian University of Science and Technology, Norway
Ignazio Licata,
Institute for Scientific Methodology (ISEM), Italy

***Correspondence:**
Osame Kinouchi
osame@ffclrp.usp.br

Specialty section:
This article was submitted to Interdisciplinary Physics, a section of the journal Frontiers in Physics

Received: *14 July 2020*
Accepted: *19 October 2020*
Published: *23 December 2020*

Citation:
Kinouchi O, Pazzini R and Copelli M (2020) Mechanisms of Self-Organized Quasicriticality in Neuronal Network Models. Front. Phys. 8:583213. doi: 10.3389/fphy.2020.583213

1 INTRODUCTION

Thirty-three years after the initial formulation of the self-organized criticality (SOC) concept [1] (and 37 years after the self-organizing extremal invasion percolation model [2]), one of the most active areas that employ these ideas is theoretical neuroscience. However, neuronal networks, similar to earthquakes and forest fires, are nonconservative systems, in contrast to canonical SOC systems like sandpile models [3, 4]. To model such systems, one uses nonconservative networks of elements represented by cellular automata, discrete time maps, or differential equations. Such models have distinct features from conservative systems. A large fraction of them, in particular neuronal networks, have been described as displaying self-organized quasi-criticality (SOqC) [5–7] or weak criticality [8, 9], which is the subject of this review.

The first person that made an analogy between brain activity and a critical branching process probably was Alan Turing, in his memorable paper *Computing machinery and intelligence* [10]. Decades later, the idea that SOC models could be important to describe the activity of neuronal networks was in the air as early as 1995 [11–16], eight years before the fundamental 2003 experimental article of Beggs and Plenz [17] reporting neuronal avalanches. This occurred because several authors, working with models for earthquakes and pulse-coupled threshold elements, noticed the formal analogy between such systems and networks of integrate-and-fire neurons. Critical learning was also conjectured by Chialvo and Bak [18–20]. However, in the absence of experimental support, these works, although prescient, were basically theoretical conjectures. A historical question would be to determine in what extent this early literature motivated Beggs and Plenz to perform their experiments.

Since 2003, however, the study of criticality in neuronal networks developed itself as a research paradigm, with a large literature, diverse experimental approaches, and several problems addressed theoretically and computationally (some reviews include Refs. [7, 21–27]). One of the main results is

that information processing seems to be optimized at a second-order absorbing phase transition [28–42]. This transition occurs between no activity (the absorbing phase) and nonzero steady-state activity (the active phase). Such transition is familiar from the SOC literature and pertains to the directed percolation (DP) or the conservative-DP (C-DP or Manna) universality classes [7, 42–45].

An important question is how neuronal networks self-organize toward the critical region. The question arises because, like earthquake and forest-fire models, neuronal networks are not conservative systems, which means that in principle they cannot be exactly critical [5, 6, 45, 46]. In these networks, we can vary control parameters like the strength of synapses and obtain subcritical, critical, and supercritical behavior. The critical point is therefore achieved only by fine-tuning.

Over time, several authors proposed different biological mechanisms that could eliminate the fine-tuning and make the critical region a self-organized attractor. The obtained criticality is not perfect, but it is sufficient to account for the experimental data. Also, the mechanisms (mainly based on dynamic synapses but also on dynamic neuronal gains and adaptive firing thresholds) are biologically plausible and should be viewed as a research topic *per se*.

The literature about these homeostatic mechanisms is vast, and we do not intend to present an exhaustive review. However, we discuss here some prototypical mechanisms and try to connect them to self-organized quasicriticality (SOqC), a concept developed to account for nonconservative systems that hover around but do not exactly sit on the critical point [5–7].

For a better comparison between the models, we will not rely on the original notation of the reviewed articles, but will try to use a universal notation instead. For example, the synaptic strength between a presynaptic neuron j and a postsynaptic neuron i will be always denoted by W_{ij} (notice the convention in the order of the indexes), the membrane potential is V_i, the binary firing state is $s_i \in \{0, 1\}$, the gain of the firing function is Γ_i, and the firing threshold is θ_i. To prevent an excess of index subscripts as is usual in dynamical systems, like $W_{ij,t}$, we use the convention $W_{ij}(t)$ for continuous time and $W_{ij}[t]$ for discrete time.

Last, before we begin, a few words about the fine-tuning problem. Even perfect SOC systems are in a sense fine-tuned: they must be conservative and require infinite separation of time scales with driving rate $1/\tau \to 0^+$ and dissipation rate $u \to 0^+$ with $1/(\tau u) \to 0$ [3, 4, 7, 43, 45]. For homeostatic systems, we turn a control parameter like the coupling W into a time-dependent slow variable $W[t] = \langle W_{ij}[t] \rangle$ by imposing a local dynamics in the individual W_{ij}. This dynamics could depend on new parameters (here called hyperparameters) which need some tuning (in some cases, this tuning can be very coarse in the large τ case). Have we exchanged the fine tuning on W by several tuning operations on the homeostatic hyperparameters? Not exactly, as nicely discussed by Hernandez-Urbina and Herrmann [47]:

> **To Tune or Not to Tune**
>
> In this article, we have shown how systems self-organize into a critical state through [homeostasis]. Thus, we became relieved from the task of fine-tuning the control parameter W, but instead, we acquire a new task: that of estimating the appropriate values for parameters A, B, C, and D. Is there no way to be relieved from tuning any parameter in the system?
>
> The issue of tuning or not tuning depends mainly on what we understand by control parameter. (. . .) a control parameter can be thought of a knob or dial that when turned the system exhibits some quantifiable change. We say that the system self-organizes if nobody turns that knob but the system itself. In order to achieve this, the elements comprising the system require a feedback mechanism to be able to change their inner dynamics in response to their surroundings. (. . .) The latter does not require an external entity to turn the dial for the system to exhibit critical dynamics. However, its internal dynamics are configured in a particular way in order to allow feedback mechanisms at the level of individual elements.
>
> Did we fine-tune their configuration? Yes. Otherwise, we would have not achieved what was desired, as nothing comes out of nothing. Did we change control parameter from W to A, B, C, and D? No, the control parameter is still intact, and now it is "in the hands" of the system. (. . .) Last and most importantly, the new configuration stresses the difference between global and local mechanisms. The control parameter W (the dial) is an external quantity that observes and governs the global (i.e., the collective), whereas [homeostasis] provides the system with local mechanisms that have an effect over the collective. This is the main feature of a complex system.

2 PLASTIC SYNAPSES

Consider an absorbing-state second-order phase transition where the activity is $\rho = 0$ below a critical point E_c and

$$\rho \simeq C\left(\frac{E - E_c}{E_c}\right)^{\beta}, \tag{1}$$

for $E \gtrsim E_c$, where E is a generic control parameter (see **Figures 1A,B**). For topologies such as random and complete graphs, one typically obtains $\beta = 1$, which is consistent with a transition in the mean-field directed percolation (DP) class (or perhaps, the compact-DP (Manna) class usual in SOC models, which has the same mean-field exponents but different ones below the upper critical dimension; see Refs. 3, 7, 42, 48).

The basic idea underlying most of the proposed mechanism for homeostatic self-organization is to define a slow dynamics in the individual links $E_i(t)$ $(i = 1, \ldots, N)$ such that if the network is in the subcritical state, their average value $E(t) = \langle E_i(t) \rangle$ grows toward E_c, but if the network is in the supercritical state, $E(t)$

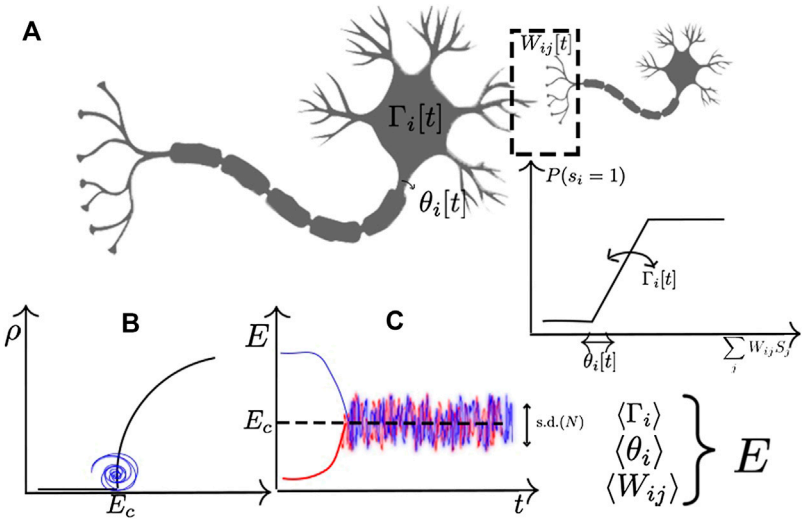

FIGURE 1 | Example of homeostatic mechanisms in a stochastic neuron with firing probability $P(s_i = 1)$. **(A)** Scheme of the loci for homeostatic mechanisms: synapses W_{ij}, neuronal gain Γ_i, and firing threshold θ_i. Inset: Firing probability with homeostatic variables. **(B)** Bifurcation diagram for the activity ρ as a function of a generic control parameter $\boldsymbol{E}$. The critical point is E_c, but the homeostatic fixed point (a focus) is slightly supercritical. **(C)** Self-organization of the generic "control" parameter $E(t)$, where the standard deviation of the stochastic oscillations around the fixed point depends on system size as $s.d. \propto N^{-a}$.

decreases toward E_c (see **Figure 1C**). Ideally, these mechanisms should be local, that is, they should not have access to global network information such as the density of active sites ρ (the order parameter) but rather only to the local firing of the neurons connected by E_i. In the following, we give several examples from the literature.

2.1 Short-Term Synaptic Plasticity

Markram and Tsodyks [49, 50] proposed a short-term synaptic model that inspired several authors in the area of self-organization to criticality. The Markram–Tsodyks (MT) dynamics is

$$\frac{dJ_{ij}(t)}{dt} = \frac{1}{\tau}\left[\frac{A}{u(t)} - J_{ij}(t)\right] - u(t)J_{ij}(t)\delta\left(t - \hat{t}_j\right), \qquad (2)$$

$$\frac{du(t)}{dt} = \frac{1}{\tau_u}\left[U - u(t)\right] + U\left[1 - u(t)\right]\delta\left(t - \hat{t}_j\right), \qquad (3)$$

where J_{ij} is the available neurotransmitter resources, u is the fraction used after the presynaptic firing at time $\hat{t}_j$ (so that the effective synaptic efficacy is $W_{ij}(t) = u(t)J_{ij}(t)$), A and U are baseline constants (hyperparameters), and τ and τ_u are recovery time constants.

In an influential article, Levina, Herrmann, and Geisel (LHG) [51] proposed to use depressing–recovering synapses. In their model, we have leaky integrate-and-fire (LIF) neurons in a complete-graph topology. As a self-organizing mechanism, they used a simplified version of the MT dynamics with constant u, that is, only **Eq. 2**. They studied the system varying A and found that although we need some tuning in the hyperparameter A, any initial distribution of synapses $P(W_{ij}(t = 0))$ converges to a stationary distribution $P^*(W_{ij})$ with $\langle W^*_{ij} \rangle \approx W_c$. We will refer to **Eq. 2** with constant u as the LHG dynamics. These authors found quasicriticality for $1.7 < A < 2.3, u \in]0, 1]$ and $\tau \propto N$. Levina et al. also studied synapses with the full MT model in Refs. 52, 53.

Bonachela et al. [6] studied in depth the LHG model and found that, like forest-fire models, it is an instance of SOqC. The system presents the characteristic hovering around the critical point in the form of stochastic sawtooth oscillations in the $W(t)$ that do not disappear in the thermodynamic limit. Using the same model, Wang and Zhou [54] showed that the LHG dynamics also works in hierarchical modular networks, with an apparent improvement in SOqC robustness in this topology.

Note that the LHG dynamics can be written in terms of the synaptic efficacy $W_{ij} = uJ_{ij}$ by multiplying **Eq. 2** by u, leading to

$$\frac{dW_{ij}(t)}{dt} = \frac{1}{\tau}\left[A - W_{ij}(t)\right] - uW_{ij}(t)\delta\left(t - \hat{t}_j\right). \qquad (4)$$

Brochini et al. [55] studied a complete graph of stochastic discrete time LIFs [56, 57] and proposed a discrete time LHG dynamics:

$$W_{ij}[t+1] = W_{ij}[t] + \frac{1}{\tau}\left(A - W_{ij}[t]\right) - uW_{ij}[t]s_j[t], \qquad (5)$$

where the firing index $s_j[t] \in \{0, 1\}$ denotes spikes. Kinouchi et al. [58], in the same system, studied the stability of the fixed points of the joint neuronal LHG dynamics. They found that, for the average synaptic value W, the fixed point is $W^* = W_c + \mathcal{O}((A-1)/\tau u)$, meaning that for large τu, the

systems approach the critical point W_c if $A > 1$. However, since it is not biologically plausible to assume an infinite recovering time τ, one always obtains a system which is slightly supercritical. This work also showed that the fixed point is a barely stable focus, around which the system is excited by finite size (demographic) noise, leading to the characteristic sawtooth oscillations of SOqC. A similar scenario was already found by Grassberger and Kantz for forest-fire models [59].

The discrete time LHG dynamics was also studied for cellular automata neurons in random networks with an average of K neighbors connected by probabilistic synapses $P_{ij} \in [0, 1]$ (Costa et al. [60], Campos et al. [61] and Kinouchi et al. [58]):

$$P_{ij}[t+1] = P_{ij}[t] + \frac{1}{\tau}\left(\frac{A}{K} - P_{ij}[t]\right) - uP_{ij}[t]s_j[t]\,, \tag{6}$$

with an upper limit $P_{\max} = 1$. Multiplying by K and summing over i, we get an equation for the local branching ratio:

$$\sigma_j[t+1] = \sigma_j[t] + \frac{1}{\tau}\left(A - \sigma_j[t]\right) - u\sigma_j[t]s_j[t]\,. \tag{7}$$

It has been found that such depressing synapses induce correlations inside the synaptic matrix, affecting the global branching ratio $\sigma[t] = \langle \sigma_j[t] \rangle$, so that criticality does not occur at the branching ratio $\sigma_c = 1$ but rather when the largest eigenvalue of the synaptic matrix is $\lambda_c = 1$, with $\sigma^* = K\langle P_{ij}^* \rangle \approx 1.1$ [61].

After examining this diverse literature, it seems that any homeostatic dynamics of the form

$$W_{ij}[t+1] = W_{ij}[t] + R\left(W_{ij}[t]\right) - D\left(W_{ij}, s_j[t]\right) \tag{8}$$

can self-organize the networks, where R and D are the recovery and depressing processes, for example:

$$W_{ij}[t+1] = W_{ij}[t] + \frac{1}{\tau}W_{ij}[t] - uW_{ij}[t]s_j[t]\,. \tag{9}$$

In particular, the simplest mechanism would be

$$W_{ij}[t+1] = W_{ij}[t] + \frac{1}{\tau} - us_j[t]\,, \tag{10}$$

a usual dynamics in SOC models [5, 7]. This means that the full LHG dynamics, and also the full MT dynamics, is a sufficient but not a necessary condition for SOqC.

The average $W = \langle W_{ij} \rangle$ for this dynamics is

$$W[t+1] = W[t] + \frac{1}{\tau} - u\rho[t]\,, \tag{11}$$

where $\rho[t] = \langle s_i[t] \rangle$ is the time-dependent network activity. The stationary state is $\rho^* = 1/(\tau u)$, and if τu is large, this means that $\rho^* = \mathcal{O}(1/(\tau u)) \to \rho_c = 0^+$. Also, if we use **Eq. 1**, we get $W^* = W_c + \mathcal{O}(1/(\tau u))$. The dissipative term u should also be small, meaning that, if we desire absolute separation of time scales, we need $1/\tau \to 0^+, u \to 0^+, 1/(\tau u) \to 0$, as is usual in other SOC systems [3, 5, 7, 43, 45].

Here, for biological plausibility, it is better to assume a large but finite recovery time, say $\tau \in [100, 10, 000]$ ms, in comparison with 1 ms for spikes. Also, to obtain SOqC, u need not be small. We must have $A > 1$ because $A < 1$ produces subcritical activity [6, 51, 58]. So, moderate $A \in [1, 2]$, $u \in\ ]0, 1]$, and large $\tau > 1000$ seem to be the coarse tuning conditions for homeostasis. This produces the hovering of the average value $W[t] = \langle W_{ij}[t] \rangle$ around the critical point W_c, with the characteristic sawtooth oscillations of SOqC and power-law avalanches for some decades.

We observe that the original LHG model [6, 51] had $\tau \propto N$ to produce the infinite separation of time scales in the large-N limit. This, however, did not prevent the SOqC hovering stochastic oscillations in the thermodynamic limit. Moreover, a recovery time proportional to N is a very unrealistic feature for biological synapses. Curiously, if we use a finite τu instead, the oscillations are damped in the thermodynamic limit because the fixed point $\rho^* = \mathcal{O}(1/(\tau u))$, $W^* = W_c + \mathcal{O}(1/(\tau u))$ continues to be an attractive focus, but the demographic noise vanishes. On the other hand, when we use $\tau u \to \infty$, the fixed point loses its stability and continues to be perturbed even by the $N \to \infty$ vanishing fluctuations [58].

As early as 1998, Kinouchi [62] proposed the synaptic dynamics:

$$W_{ij}[t+1] = W_{ij}[t] + \frac{1}{\tau}W_{ij}[t] - us_j[t]\,, \tag{12}$$

with small but finite τ and u. The difference here from the former mechanisms is that, like in **Eq. 10**, depression is not proportional to W_{ij} (but recovery is). He also discussed the several concepts of SOC at the time, and called these homeostatic system as self-tuned criticality, which is equivalent to a SOqC system with finite separation of time scales.

Hsu and Beggs [63] studied a model for the activity $A_i(t)$ of the local field potential at electrode i:

$$A_i[t+1] = H_i[t] + \sum_j P_{ij}[t]s_j[t]\,, \tag{13}$$

where $H_i(t)$ is a spontaneous activity used to prevent the freezing of the system in the absorbing state (this is similar to a time-dependent SOC drive term h). The probabilistic coupling is $P_{ij} \in [0, 1]$. Firing-rate homeostasis and critical homeostasis are achieved by increasing or decreasing H and P if the firing rate is too low or too high compared to a target firing rate $s_0 = 1/\tau_0$:

$$H_i[t+1] = \exp[-k_S(\langle s_i[t] \rangle - s_0)]H_i[t]\,, \tag{14}$$

$$P_{ij}[t+1] = \exp[-k_P(\langle s_i[t] \rangle - s_0)]P_{ij}[t]\,, \tag{15}$$

where $\langle \ldots \rangle$ represents a moving average over a memory widow τ_m.

Hsu and Beggs found that for $k_S/k_P \approx 0.5$, this dynamics leads to a critical branching ratio $\sigma = 1$. They also found that the target firing rate s_0 can be maintained by this homeostasis. **Equation 15** reminds us of the depressing–recovering synaptic rule of **Eq. 9**. Indeed, if we examine the small k_P limit (as used by the authors), we have

$$P_{ij}[t+1] \simeq P_{ij}[t] + \frac{1}{\tau}P_{ij}[t] - uP_{ij}[t]\langle s_i[t]\rangle\,, \tag{16}$$

where now $\tau = 1/(k_P s_0)$ and $u = k_P$. A similar reasoning applies to the equation for $H[t]$, which could be identified with the homeostatic threshold **Eq. 60** discussed in **Section 4**, with $H[t] = -\theta[t]$.

In another article, Hsu et al. [64] extended the model to include distance-dependent connectivity and Hebbian learning [64]. Changing the homeostasis equations to our standard notation, we have

$$\frac{dH_i(t)}{dt} = \frac{1}{\tau_S}\left(1-\eta_i(t)\right)H_i(t) - u_S H_i(t)\left(\langle s_i\rangle - s_0\right), \tag{17}$$

$$\frac{dP_{ij}(t)}{dt} = \frac{1}{\tau}\left(1-\eta_i(t)\right)P_{ij}(t) - uP_{ij}(t)\left(\langle s_i\rangle - s_0\right) - u_D D_{ij}P_{ij}(t)\,, \tag{18}$$

where $H_i \in [0,1]$ is now a probability of spontaneous firing, s_0 is a target average activity, and D_{ij} is the distance between electrodes i and j. The input ratio is $\eta_i(t) = \sum_j P_{ij}(t)$. Remember that, for a critical branching process, $\langle \eta_i\rangle = 1$. These values were chosen as homeostatic targets.

Shew et al. [65] studied experimentally the visual cortex of the turtle and proposed a (complete graph) self-organizing model for the input synapses Ω_i and the cortical synapses W_{ij}. The stochastic neurons fire with a linear saturating function:

$$\text{Prob}\left(s_i[t+1]=1\right) = \begin{cases} V_i[t] & \text{if} \quad V<1\,, \\ \\ 1 & \text{if} \quad V>1\,, \end{cases} \tag{19}$$

$$V_i[t] = \Omega_i[t]H_i[t] + \frac{1}{N}\sum_j W_{ij}[t]s_j[t]\,, \tag{20}$$

where, like in **Eq. 13**, H_i accounts for external stimuli. For both types of synapses, they used the discrete time LHG dynamics, **Eq. 5**, and concluded that the computational model accounts very well for the experimental data.

Hernandez-Urbina and Herrmann [47] studied a discrete time IF model where they define a local measure called node success:

$$\phi_j[t] = \frac{\sum_i A_{ij}s_i[t+1]}{\sum_i A_{ij}}\,, \tag{21}$$

where A is the adjacency matrix of the network, with $A_{ij} = 1$ if j projects onto i ($A_{ij} = 0$ otherwise). Note that we reversed the indices as compared with the original notation [47]. Observe that ϕ_j measures how many postsynaptic neurons are excited by the presynaptic neuron j.

The authors then define the node success–driven plasticity (NSDP):

$$W_{ij}[t+1] = W_{ij}[t] + \frac{1}{\tau}\exp\left(-\phi_j(t)/B\right) - u\,\exp\left(-\Delta t_j/D\right), \tag{22}$$

where $\Delta t_j = t - \widehat{t}_j$ is the time difference between the spike of node j occurring at current time step t and its previous spike which occurred at $\widehat{t}_j$ (the last spike), while B and D are constants. Notice that the drive term is larger if the node success is small and the dissipation term is larger if the firing rate (inferred locally as $\widehat{\rho} = 1/\Delta t_j$) is large [compare with **Eq. 8**].

They analyzed the relation among the avalanche critical exponents, the largest eigenvalue Λ associated to the weight matrix, and the data collapse of the shape of avalanches for several network topologies. All results are compatible with (quasi-)criticality. They also found that if they stop NSDP and introduce STDP, the criticality vanishes, but if the two dynamics are done together, criticality survives.

Levina et al. [66] proposed a model in a complete graph in which the branching ratio σ is estimated as the local branching σ_i of a neuron that initiates an avalanche. The homeostatic rule is to increase the synapses if $\sigma_i < 1$ and decreasing them if $\sigma_i > 1$. The network converges, with SOqC oscillations, to $\sigma^* \approx \sigma_c = 1$.

2.2 Meta-Plasticity

Peng and Beggs [67] studied a square lattice ($K = 4$) of IF neurons with open boundary conditions. A random neuron receives a small increment of voltage (slow drive). If the voltage of presynaptic neuron j is above a threshold $\theta = 1$, we have

$$V_j[t+1] = V_j[t] - 1\,, \tag{23}$$

$$s_j[t+1] = \Theta\left(V_j[t+1] - \theta\right), \tag{24}$$

$$V_i[t+1] = V_i[t] + \frac{1}{K}W_{ij}[t]s_j[t]\,, \tag{25}$$

where Θ is the Heaviside function. The self-organization is made by a LHG dynamics plus a meta-plasticity term:

$$W_{ij}[t+1] = W_{ij}[t] + \frac{1}{\tau}\left(A - W_{ij}[t]\right) - uW_{ij}[t]s_j[t]\,, \tag{26}$$

$$u_{a+1} = u_a - (1 - X_a)/N\,, \tag{27}$$

where X_a is the total fraction of neurons at the boundary that fired during the a-th avalanche and u_{a+1} is the updated value of u after the avalanche. Notice that the meta-plasticity term differs from the MT model of **Eq. 3**, because the hyperparameter u is updated in a much slower time scale. Peng and Beggs show that this dynamics converges automatically to good values for the parameter u; that is, we no longer need set the u value in advance. We observe, however, that X_a is a nonlocal variable.

2.3 Hebbian Synapses

Ever since Donald Hebb's proposal that neurons that fire together wire together [68–70], several attempts have been made to implement this idea in models of self-organization. However, a pure Hebbian mechanism can lead to diverging synapses, so that some kind of normalization or decay needs also be included in Hebbian plasticity.

In 2006, de Arcangelis, Perrone-Capano, and Herrmann introduced a neuronal network with Hebbian synaptic dynamics [71] that we call the APH model. There are several small variations in the models proposed by de Arcangelis et al.,

but perhaps the simplest one [72] is given by the following neuronal dynamics on a square lattice of $L \times L$ neurons: If at time t a presynaptic neuron j has a membrane potential above a firing threshold, $V_j[t] > \theta$, it fires, sending neurotransmitters to all its (nonrefractory) neighbors:

$$V_i[t+1] = V_i[t] + \overline{W}_{ij} V_j[t], \tag{28}$$

where $\overline{W}_{ij} = W_{ij} / \sum_l^{nn} W_{lj}$. Then, neuron j enters in a refractory period of one time step. The synaptic self-organizing dynamics is given by

$$W_{ij}[t+1] = W_{ij}[t] + \frac{1}{\theta} \overline{W}_{ij} V_j[t] \quad \text{(active synapses)}, \tag{29}$$

$$W_{ij} \leftarrow W_{ij} - \frac{1}{N_B} \sum_{ij} \delta W_{ij} \quad \text{(inactive synapses, after avalanche)}, \tag{30}$$

where N_B is the total number bonds and active (inactive) synapses are the ones used (not used) in **Eq. 28**. The sum in **Eq. 30** is over all synaptic modifications $\delta W_{ij}[t+1] = W_{ij}[t+1] - W_{ij}[t]$, a step which involves nonlocal information and amounts to a kind of synaptic rescaling. If the synaptic strength falls below some threshold, the synapse is deleted (pruning), so that this mechanism sculpts the network architecture. So, co-activation of pre- and postsynaptic neurons makes the synapse grow, and inactive synapses are depressed, which means that it is a Hebbian process. Several authors explored the APH model in different contexts, including learning phenomena [72–80].

Çiftçi [81] studied a neuronal SIRs model on the *C. elegans* neuronal network topology. The spontaneous activation rate (the drive) is $h = 1/\tau \to 0^+$, and the recovery rate to the susceptible state is q. The author studied the system as a function of q/h (separation of time scales $q \gg h$). The probability that a neuron j activates its neighbor i is P_{ij} ($g_{ij} = 1 - P_{ij}$ is the probability of synaptic failure in the author notation). The synaptic update occurs after an avalanche (of size S) and affects two neighbors that are active at the same time (Hebbian term):

$$P_{ij}[t+1] = \begin{cases} P_{ij}[t] + \frac{1}{\tau}\frac{1}{S}\left(1 - P_{ij}[t]\right) & \text{if the synapse was not used}, \\ P_{ij}[t] - u\left(1 - \frac{1}{S}\right) P_{ij}[t] & \text{if the synapse was used}. \end{cases} \tag{31}$$

Ciftçi found robust self-organization to quasicriticality. The author notes, however, that S is nonlocal information.

Uhlig et al. [82] considered the effect of LHG synapses in the presence of an associative Hebb synaptic matrix. They found that, although the two processes are not irreconcilable, the critical state has detrimental effects to the attractor recovery. They interpret this as a suggestion that the standard paradigm of memories as fixed point attractors should be replaced by more general approaches like transient dynamics [83].

2.4 Spike Time–Dependent Plasticity

Rubinov et al. [84] studied a hierarchical modular network of LIF neurons with STDP plasticity. The synapses are modeled by double exponentials:

$$\frac{dV_i(t)}{dt} = -(V_i(t) - E) + I + I_i^{\text{syn}}(t), \tag{32}$$

$$I_i^{\text{syn}}(t) = \sum_j W_{ij} V_0 \sum_{\widehat{t}_j} \left[\exp\left(-\frac{t - \widehat{t}_j}{\tau_1} \right) - \exp\left(-\frac{t - \widehat{t}_j}{\tau_2} \right) \right], \tag{33}$$

where $\{\widehat{t}_j\}$ are the presynaptic firing times. Synaptic weight changes at every spike of a presynaptic neuron, following the STDP rule:

$$\Delta W_{ij} = \begin{cases} A_+\left(W_{ij}\right) \exp\left(-\widehat{t}_j - \widehat{t}_i \tau_+ \right) \text{if } \widehat{t}_j < \widehat{t}_i, \\ -A_-\left(W_{ij}\right) \exp\left(-\widehat{t}_j - \widehat{t}_i \tau_- \right) \text{if } \widehat{t}_j \geq \widehat{t}_i, \end{cases} \tag{34}$$

where $A_+(W_{ij})$ and $A_-(W_{ij})$ are weight-dependent functions (see Ref. 84 for details). The authors show an association among modularity, low cost of wiring, STDP, and self-organized criticality in a neurobiologically realistic model of neuronal activity.

Del Papa et al. [85] explored the interaction between criticality and learning in the context of self-organized recurrent networks (SORN). The ratio between inhibitory to excitatory neurons is $N^I/N^E = 0.2$. These neurons interact via W^{EE}, W^{IE}, and W^{EI} synapses (no inhibitory self-coupling). Synapses are dynamic, and also the excitatory thresholds θ_i^E. The neurons evolve as

$$s_i^E[t+1] = \Theta\left(\sum_j^{N^E} W_{ij}^{EE}[t] s_j^E[t] - \sum_k^{N^I} W_{ik}^{EI} s_j^I[t] - \theta_i^E[t] + I_i[t] + \eta_i^E[t] \right), \tag{35}$$

$$s_i^I[t+1] = \Theta\left(\sum_j^{N^E} W_{ij}^{IE} s_j^E[t] - \theta_i^I + \eta_i^I[t] \right), \tag{36}$$

where $\eta_i[t]$ represents membrane noise. Synapses and thresholds evolve following five combined dynamics:

$$W_{ij}^{EE}[t+1] = W_{ij}^{EE}[t] + \frac{1}{\tau_{\text{STDP}}} \left[s_i^E[t+1] s_j^E[t] - s_j^E[t+1] s_i^E[t] \right] \text{ excitatory STDP}, \tag{37}$$

$$W_{ij}^{EI}[t+1] = W_{ij}^{EI}[t] - \frac{1}{\tau_{\text{iSTDP}}} s_j^I[t] \left[1 - s_i^E[t+1] \left(1 + 1/\mu_{\text{IP}} \right) \right] \text{ inhibitory STDP}, \tag{38}$$

$$W_{ij}[t+1] \leftarrow \frac{W_{ij}[t+1]}{\sum_j W_{ij}[t+1]} \text{ synaptic normalization (SN)}, \tag{39}$$

$$p\left(N^E\right) = \frac{N^E\left(N^E - 1\right)}{N(N-1)} p(N) \text{ structural plasticity (SP)}, \tag{40}$$

$$\theta_i^E[t+1] = \theta_i^E[t] + \frac{1}{\tau_{\mathrm{IP}}}\left[s_i^E[t] - \mu_{\mathrm{IP}}\right] \ \text{intrinsic plasticity (IP)}, \tag{41}$$

where μ_{IP} is the desired activity level. In the structural plasticity process, excitatory synapses are added with probability $p(N^E)$. The authors found that this SORN model presents well-behaved power-law avalanche statistics and that the plastic mechanisms are necessary to drive the network to criticality, but not to maintain it critical; that is, the plasticity can be turned off after the networks reach the critical region. Also, they found that noise was essential to produce the avalanches, but degrade the learning performance. From this, they conclude that the relation between criticality and learning is more complex, and it is not obvious if criticality optimizes learning.

Levina et al. [86] studied the combined effect of LHG synapses, homeostatic branching parameter W_h, and STDP:

$$W_{ij}(t) = uJ_{ij}(t)W_h(t)W_{\mathrm{STDP}}(t). \tag{42}$$

They found that there is cooperativity of these mechanisms in extending the robustness of the critical state to variations on the hyperparameter A (see **Eq. 2**).

Stepp et al. [87] examined a LIF neuronal network which has both Markram–Tsodyks dynamics and spiking time–dependent plasticity STDP (both excitatory and inhibitory). They found that, although MT dynamics produces some self-organization, the STDP mechanism increases the robustness of the network criticality.

Delattre et al. [88] included in the STDP synaptic change ΔW_+ a resource depletion term:

$$\Delta W'_+ = \gamma(\eta(t))\Delta W_+, \tag{43}$$

$$\gamma(\eta(t)) = \frac{1 - \exp\left(\frac{\eta^* - \eta(t)}{m}\right)}{1 + \exp\left(\frac{\eta^* - \eta(t)}{m}\right)}, \tag{44}$$

where resource availability $\eta(t)$ evolves as

$$\frac{d\eta(t)}{dt} = \frac{1}{\tau_\eta} - \frac{\eta(t)}{\eta_0(\alpha(t))\tau_\eta}. \tag{45}$$

Here, $\alpha(t)$ is a continuous estimator of the network firing rate, τ_η is the recovery time of the resources availability, and the term $\eta_0(\alpha(t)) = (1 + \alpha/\mathrm{k})^{-1}$ in the denominator ensures that depletion is fast and recovery is slow ($k = 20$ Hz). They called this mechanism as network spiking–dependent plasticity and showed that, in contrast to pure STDP, it leads to power-law avalanches with branching ratio around one.

2.5 Homeostatic Neurite Growth

Kossio et al. [89] studied IF neurons randomly distributed in a plane, with neurites distributed within circles of radii R_i that evolved according to

$$\frac{dR_i}{dt} = \frac{1}{\tau} - u\sum_{t_i}\delta(t - t_i), \tag{46}$$

where $\{t_i\}$ are the spike times of neuron i, with τ and u constants. Since the connections are given by $W_{ij} = gO_{ij}$, where g is a constant and O_{ij} are the overlapping areas of the synaptic discs, **Eq. 46** is not much different from the simple synaptic dynamics of **Eq. 10**, with constant drive and decay due to spikes.

Tetzlaff et al. [90] studied experimentally neuronal avalanches during the maturation of cell cultures, finding that criticality is achieved in a third stage of the dendrites/axons growth process. They modeled the system using neurons with membrane potential $V_i(t) < 1$ and calcium dynamics $C_i(t)$:

$$\frac{dV_i(t)}{dt} = -\frac{V_i(t) - V_0}{\tau_V} + \sum_j k_j^{\pm} W_{ij}(t)\,\Theta\left(V_j(t) - \eta_j(t)\right), \tag{47}$$

$$\frac{dC_i(t)}{dt} = -\frac{1}{\tau_C}C_i(t) + \beta\,\Theta\left(V_i(t) - \eta_i(t)\right), \tag{48}$$

where $k^+ > 0$ ($k^- < 0$) defines excitatory (inhibitory) neurons, and $\eta_j(t) \in [0, 1]$ is a random number. Dendritic and axonal spatial distributions are again represented by their radii R_i and A_i, whose dynamics are governed by calcium dynamics as

$$\frac{dR_i(t)}{dt} = -\frac{1}{\tau_R}\left(C_i(t) - C_{\mathrm{target}}\right), \tag{49}$$

$$\frac{dA_i(t)}{dt} = \frac{1}{\tau_A}\left(C_i(t) - C_{\mathrm{target}}\right). \tag{50}$$

Finally, the effective connection is defined as

$$W_{ij}(t) = \left[\gamma_1(t) - \frac{1}{2}\sin\left(2\gamma_1(t)\right)\right]A_j^2(t) + \left[\gamma_2(t) - \frac{1}{2}\sin\left(2\gamma_2(t)\right)\right]R_j^2(t), \tag{51}$$

$$\gamma_1(t) = \arccos\left(\frac{A_j^2(t) + D_{ij}^2 - R_i^2(t)}{2A_j(t)D_{ij}}\right), \tag{52}$$

$$\gamma_2(t) = \arccos\left(\frac{R_i^2(t) + D_{ij}^2 - A_j^2(t)}{2R_i(t)D_{ij}}\right),$$

where D_{ij} is the distance between the neurons. This essentially represents the overlap of the axonal and dendritic zones, which can be understood as an abstract representation for the probability of synapse formation.

3 DYNAMIC NEURONAL GAINS

For all-to-all topologies as used in Refs. 6, 51, 53, 55, the number of synapses is $N(N-1)$, which means that simulations become impractical for large N. Brochini et al. [55] discovered that, in their model with stochastic neurons, adaptation in a single parameter per neuron (the dynamic gain) is sufficient to self-

organize the network. This reduces the number of dynamic equations from $\mathcal{O}(N^2)$ to $\mathcal{O}(N)$, enabling large-scale simulations.

The stochastic neuron has a probabilistic firing function, say, a linear saturating function or a rational function:

$$\begin{aligned} P(s=1|V) &= \Phi(V) \\ &= \Gamma(V-\theta)\,\Theta(V-\theta)\,\Theta(1-\Gamma(V-\theta)) \\ &\quad + \Theta(\Gamma(V-\theta)-1)\,, \end{aligned} \tag{53}$$

$$P(s=1|V) = \Phi(V) = \frac{\Gamma(V-\theta)}{1+\Gamma(V-\theta)}\,\Theta(V-\theta)\,, \tag{54}$$

where $s = 1$ means a spike, V is the membrane potential, θ is the threshold, and Γ is the neuronal gain.

Now, let us assume that each neuron i has its neuronal gain Γ_i. Several adaptive dynamics work, similar to LHG and even simpler:

$$\Gamma_i(t+1) = \Gamma_i(t) + \frac{1}{\tau}\left[A - \Gamma_i(t)\right] - u\Gamma_i(t)s_i(t)\,, \tag{55}$$

$$\Gamma_i(t+1) = \Gamma_i(t) + \frac{1}{\tau}\Gamma_i(t) - u\Gamma_i(t)s_i(t)\,, \tag{56}$$

$$\Gamma_i(t+1) = \Gamma_i(t) + \frac{1}{\tau} - us_i(t)\,. \tag{57}$$

Costa et al. [91] and Kinouchi et al. [58] studied the stability of the fixed points of mechanisms given by **Eqs 55** and **56** and concluded that the fixed point solution (ρ^*, Γ^*) is of the form $\rho^* = 0^+ + \mathcal{O}(1/\tau)$, $\Gamma^* = \Gamma_c + \mathcal{O}(1/\tau)$. The fixed point is a barely stable focus for large τ, which means that demographic noise creates the hovering around the critical point (the sawtooth SOqC stochastic oscillations). The peaks of theses oscillations correspond to large excursions in the supercritical region, producing the so-called dragon king avalanches [77].

Zierenberg et al. [92] considered a cellular automaton neuronal model with binary states s_i and probabilistic synapses $P_{ij}[t] = \alpha_i[t]W_{ij}$, where $\alpha_i[t]$ is a homeostatic scaling factor. The homeostasis is given by a negative feedback:

$$\alpha_i[t+1] = \alpha_i[t] + \frac{1}{\tau_{\mathrm{hp}}}\left(r^* - s_i[t]\right), \tag{58}$$

where τ_{hp} is the time constant of the homeostatic process and r^* is a target level. Notice that this mechanism depends only on the activity of the postsynaptic neuron i, not the presynaptic neuron j as in the LHG model. So, $\alpha_i[t]$ plays the same role of the neuronal gain $\Gamma_i[t]$ discussed above.

Indeed, for a cellular automata model similar to [60, 61], a probabilistic synapse with neuronal gains could be written as $P_{ij}[t] = \Gamma_i[t]W_{ij}$. In order to compare with the neuronal gain dynamics, we rewrite **Eq. 58** as

$$\Gamma_i[t+1] = \Gamma_i[t] + \frac{1}{\tau} - us_i[t]\,, \tag{59}$$

where $\tau = \tau_{\mathrm{hp}}/r^*$ and $u = 1/\tau_{\mathrm{hp}}$. So, in Zierenberg et al., we have a neuronal gain dynamics similar to **Eq. 10**, with hovering around the critical point and the ubiquitous sawtooth oscillations in $\alpha[t] \equiv \langle \alpha_i[t] \rangle$.

4 ADAPTIVE FIRING THRESHOLDS

Girardi-Schappo et al. [93] examined a network with $N_E = pN = 0.8N$ excitatory and $N_I = qN = 0.2N$ inhibitory stochastic LIF neurons. They found a phase diagram very similar to that of the Brunel model [94], with synchronous regular (SR), asynchronous regular (AR), synchronous irregular (SI), and asynchronous irregular (AI) states. Close to the balanced state $g = W^{II}/W^{EE} = p/q = 4$ they found an absorbing-active second-order phase transition with a critical point $g_c = p/q - 1/(q\Gamma W^{EE})$. The self-organization of the W^{II} and W^{EI} inhibitory synapses was accomplished by a LHG dynamics.

They noticed, however, that for these stochastic LIF systems, the critical point requires also a zero field $h = I - (1-\mu)\theta$, where I is the external input and μ is the leakage parameter. While setting $h = 0$ for the critical point of spin systems is natural, obtaining zero field in this case demands self-organization, which is done by an adaptive firing threshold:

$$\theta_i[t+1] = \theta_i[t] - \frac{1}{\tau_\theta}\theta_i[t] + u_\theta\theta_i[t]s_i[t]\,. \tag{60}$$

Notice the plus signal in the last term, since if the postsynaptic neuron fires ($s_i = 1$) then the threshold must increase to hinder new firings. This mechanism is biologically plausible and also explains classical firing rate adaptation. Remembering that $\rho = \langle s_i \rangle \propto h^{1/\delta_h}$ in the critical point, where δ_h is the field critical exponent, from **Eq. 60**, we have $h \propto 1/(\tau_\theta u_\theta)^{\delta_h} \approx 0$ for large $\tau_\theta u_\theta$.

As already seen, Del Pappa et al. [85] considered a similar threshold dynamics, **Eq. 41**. Bienenstock and Lehmann [95] also studied, at the mean field level, the joint evolution of firing thresholds and dynamic synapses (see **Section 6.3**).

5 TOPOLOGICAL SELF-ORGANIZATION

Consider a cellular automata model [29, 32, 60, 61] in a network with average degree K and average probabilistic synaptic weights $P = \langle P_{ij} \rangle$. The critical branching ratio is $\sigma = PK = 1$; that is, critical average weight $P_c = 1/K$. Notice that we can study networks with any K, even the complete graph, where $P_c = 1/(N-1)$. In this network, what is critical is the activity, which does not depend on the topology (the degree K).

In another sense, we call a network topology critical if there is a barely infinite percolating cluster, which for a random network occurs for $K_c = 2$. Several authors, starting in 2,000 with Bornholdt and Rohlf [96], explored the self-organization toward this type of topological criticality [22, 97–104].

So, we can have a critical network with a W_c and any K or a topologically critical network with a well-defined K_c. The two concepts (activity criticality and topological criticality) are different, but sometimes a topological criticality also presents a phase transition with power-law avalanches and critical

phenomena. The topological phase transition is continuous and has a critical point, related to the formation of a percolating cluster of nodes, but in the Bornholdt and Rohlf (BR) model, it is related to an order-chaos phase transition, not to an absorbing state phase transition.

We present here a more advanced version of the BR model [97]. It follows the idea of deleting synapses from correlated neurons and increasing synapses of uncorrelated neurons. The correlation over time T is calculated as

$$C_{ij}[T] = \frac{1}{T+1}\sum_{t=t_0}^{t_0+T} s_i[t]s_j[t]\,, \tag{61}$$

where the stochastic neurons evolve as

$$V_i[t+1] = \sum_j W_{ij}s_j[t]\,, \tag{62}$$

$$\mathrm{Prob}\,(s_i[t+1] = +1) = \Phi\,(V_i)\,, \tag{63}$$

$$\mathrm{Prob}\,(s_i[t+1] = -1) = 1 - \Phi\,(V_i), \tag{64}$$

$$\Phi[V_i] = \frac{1}{1+\exp(-2\Gamma\,(V_i-\theta_i))}. \tag{65}$$

The self-organization procedure is as follows:

Choose at random a pair (i,j) of neurons.
Calculate the correlation $C_{ij}(T)$.
Define a threshold α. If $C_{ij}(T) > \alpha$, i receives a new link W_{ij} randomly drawn from a uniform distribution on $[-1,1]$ from site j, and if $C_{ij} < \alpha$, the link is deleted.
Then, continue updating the network state $\{s_i\}$ and self-organizing the network.

Interesting analytic results for this class of topological models were obtained by Droste et al. [105]. The self-organized connectivity is about $K_c \approx 2$, where the order-chaos transition occurs. We must notice, however, that $K = 2$ seems to be a very low degree for biological neuronal networks. Kuehn [106] studied how the topological dynamics time scale τ and noise level D affect the BR model, finding that optimal convergence to the critical point occurs for finite values of $\tau_{\mathbf{opt}}$ and $D_{\mathbf{opt}}$.

Zeng et al. [107] combined the rewiring rules of the BR model with the neuronal dynamics of the APH model. They obtained an interesting result: the final topology is a small-world network with a large number of neighbors, say $\langle K\rangle \approx 100$. This avoids the criticism made above about the low number $K \approx 2$ of the BR model.

6 SELF-ORGANIZATION TO OTHER PHASE TRANSITIONS

6.1 First-Order Transition

Mejias et al. [108] studied a neuronal population model with firing rate $\nu(t)$, which can be written in terms of the firing density $\rho = \nu/\nu_{\max}$:

$$\tau_\rho \frac{d\rho}{dt} = -\rho + S\big(W(t)\rho - \theta\big) + D_\eta \eta(t)\,, \tag{66}$$

where $S(z) = (1/2)[1+\tanh(z)]$ is a (deterministic) firing function, $\eta(t)$ is a zero-mean Gaussian noise, and D_η is a noise amplitude. They used a depressing average synaptic weight inspired by a noisy LHG model:

$$\frac{dW(t)}{dt} = \frac{1}{\tau}[1 - W(t)] - uW(t)\rho(t) + D_W\eta(t)\,, \tag{67}$$

where D_W is the synaptic noise amplitude. Within a certain range of noise, they observed up–down states with irregular intervals, leading to a distribution of permanence times T in the upstate as $P(T) \propto T^{-3/2}$. Notice that this model already starts with the mean-field equations; it is not a microscopic model (although a microscopic model perhaps could be constructed from it).

Millman et al. [109] obtained similar results at a first-order phase transition, but now in a random network of LIF neurons with average of K neighbors and chemical synapses. The synapses follow the LHG mechanism:

$$\frac{dW_{ij}(t)}{dt} = \frac{1}{\tau}\big[A - W_{ij}(t)\big] - uW_{ij}(t)s_j(t)\,, \tag{68}$$

where $W_{ij}(t) = p_r U_{ij}(t)$ in the authors notation (p_r for probability of releasing vesicles, $U_{ij}(t)$ for synaptic resources) and $A = p_r$. They found that the branching ratio is close to one in the upstate, with power-law avalanches with size exponent 3/2 and lifetime exponent 2.

Di Santo et al. [110, 111] and Buendía et al. [7, 46] studied the self-organization toward a first-order phase transition (called self-organized bistability or SOB). The simplest self-organizing dynamics was used in a two-dimensional model:

$$\frac{d\rho\left(\vec{x},t\right)}{dt} = \Big[a + \omega E\left(\vec{x},t\right)\Big]\rho\left(\vec{x},t\right) - b\rho^2\left(\vec{x},t\right) - \rho^3\left(\vec{x},t\right) + D\nabla^2\rho\left(\vec{x},t\right) + \eta\left(\vec{x},t\right), \tag{69}$$

$$\frac{dE\left(\vec{x},t\right)}{dt} = \nabla^2\rho\left(\vec{x},t\right) + \frac{1}{\tau}\Big[A - E\left(\vec{x},t\right)\Big] - u\rho\left(\vec{x},t\right), \tag{70}$$

where $\omega, a > 0, b < 0$ are constants, A is the maximum level of charging, D is the diffusion constant, and $\eta(\vec{x},t)$ is a zero-mean Gaussian noise with amplitude ρ. The authors' original notation is $h = 1/\tau, \epsilon = u$, and E is a (former) control parameter. In the limit $1/\tau \to 0^+, u \to 0^+, 1/(\tau u) \to 0$, this self-organization is conservative and can produce a tuning to the Maxwell point with power-law avalanches (with mean-field exponents) and dragon-king quasi-periodic events.

Relaxing the conditions of infinite separation of time scales and bulk conservation, the authors studied the model with an LHG dynamics [7, 46, 111]:

$$\frac{d\rho\left(\vec{x},t\right)}{dt} = \Big[a + W\left(\vec{x},t\right)\Big]\rho\left(\vec{x},t\right) - b\rho^2\left(\vec{x},t\right) - \rho^3\left(\vec{x},t\right) + I + D\nabla^2\rho\left(\vec{x},t\right) + \eta\left(\vec{x},t\right), \tag{71}$$

$$\frac{dW\left(\vec{x},t\right)}{dt}=\frac{1}{\tau}\left[A-W\left(\vec{x},t\right)\right]-uW\left(\vec{x},t\right)\rho\left(\vec{x},t\right), \quad (72)$$

where W is the synaptic weight and I a small input. They found that this is the equivalent SOqC version for first-order phase transitions, obtaining hysteretic up–down activity, which has been called self-organized collective oscillations (SOCOs) [7, 46, 111]. They also observed bistability phenomena.

Cowan et al. [112] also found hysteresis cycles due to bistability in an IF model from the combination of an excitatory feedback loop with anti-Hebbian synapses in its input pathway. This leads to avalanches both in the upstate and in the downstate, each one with power-law statistics (size exponents close to 3/2). The hysteresis loop leads to a sawtooth oscillation in the average synaptic weight. This is similar to the SOCO scenario.

6.2 Hopf Bifurcation

Absorbing-active phase transitions are associated to transcritical bifurcations in the low-dimensional mean-field description of the order parameter. Other bifurcations (say, between fixed points and periodic orbits) can also appear in the low-dimensional reduction of systems exhibiting other phase transitions, such as between steady states and collective oscillations. They are critical in the sense that they present phenomena like critical slowing down (power-law relaxation to the stationary state) and critical exponents. Some authors explored the homeostatic self-organization toward such bifurcation lines.

In what can be considered a precursor in this field, Bienenstock and Lehmann [95] proposed to apply a Hebbian-like dynamics at the level of rate dynamics to the Wilson–Cowan equations, having shown that the model self-organizes near a Hopf bifurcation to/from oscillatory dynamics.

The model has excitatory and inhibitory stochastic neurons. The neuronal equations are

$$V_i^E(t)=\sum_j W_{ij}^{EE}s_j^E(t)+\sum_j W_{ij}^{EI}s_j^I(t)-\theta_i^E, \quad (73)$$

$$V_i^I(t)=\sum_j W_{ij}^{IE}s_j^E(t)+\sum_j W_{ij}^{EI}s_j^I(t)-\theta_i^I, \quad (74)$$

where, as before, the binary variable $s\in\{0,1\}$ denotes the firing of the neuron. The update process is an asynchronous (Glauber) dynamics:

$$P(s=1|V)=\frac{1}{2}\left[1+\tanh\left(\Gamma V(t)\right)\right], \quad (75)$$

where Γ is the neuronal gain.

The authors proposed a covariance-based regulation for the synapses W^{EE} and W^{IE} and a homeostatic process for the firing thresholds $\theta^E(t),\theta^I(t)$. The homeostatic mechanisms are

$$\frac{dW^{EE}(t)}{dt}=\frac{1}{\tau_{EE}}\left(c^{EE}(t)-\Theta^{EE}\right), \quad \frac{dW^{IE}(t)}{dt}=-\frac{1}{\tau_{IE}}\left(c^{IE}-\Theta^{IE}\right), \quad (76)$$

$$\frac{d\theta^E(t)}{dt}=\frac{1}{\tau_E}\left(\rho^E(t)-\Theta^E\right), \quad \frac{d\theta^I(t)}{dt}=\frac{1}{\tau_I}\left(\rho^E(t)-\Theta^I\right), \quad (77)$$

where $c^{EE}\equiv\left(\rho^E(t)-\langle\rho^E(t)\rangle\right)^2$ is the variance of the excitatory activity $\rho^E(t)$, $c^{IE}\equiv\left(\rho^E(t)-\langle\rho^E\rangle\right)\left(\rho^I(t)-\langle\rho^I\rangle\right)$ is the excitatory–inhibitory covariance, $\tau_{EE},\tau_{IE},\tau_E,\tau_I$ are time constants, and $\Theta^{EE},\Theta^{IE},\Theta^E,\Theta^I$ are target constants.

The authors show that there are Hopf and saddle-node lines in this system and that the regulated system self-organizes at the crossing of these lines. So, the system is very close to the oscillatory bifurcation, showing great sensibility to external inputs.

As commented, this article is a pioneer in the sense of searching for homeostatic self-organization at a phase transition in a neuronal network in 1998, well before the work of Beggs and Plenz [17]. However, we must recognize some deficiencies that later models tried to avoid. First, all the synapses and thresholds have the same value, instead of an individual dynamics for each one, as we saw in the preceding sections. Most importantly, the network activities ρ^E and ρ^I are nonlocal quantities, not locally accessible to **Eqs 76** and **77**.

Magnasco et al. [113] examined a very stylized model of neural activity with time-dependent anti-Hebbian synapses:

$$\frac{dV_i(t)}{dt}=\sum_j W_{ij}(t)V_j(t), \quad (78)$$

$$\frac{dW_{ij}(t)}{dt}=\frac{1}{\tau}\left(\delta_{ij}-V_i(t)V_j(t)\right), \quad (79)$$

where δ_{ij} is the Kronecker delta. They found that the system self-organizes around a Hopf bifurcation, showing power-law avalanches and hovering phenomena similar to SOqC.

6.3 Edge of Synchronization

Khoshkhou and Montakhab [114] studied a random network with $K=\langle K_i\rangle$ neighbors. The cells are Izhikevich neurons described by

$$\frac{dV_i(t)}{dt}=0.04V_i^2(t)+5V_i(t)+140-u_i(t)+I+I_i^{\text{syn}}(t), \quad (80)$$

$$\frac{du_i(t)}{dt}=a\left(bV_i(t)-u_i(t)\right), \quad (81)$$

$$\text{if } V_i\geq 30 \text{ then} V_i\leftarrow c, u_i\leftarrow u_i+d. \quad (82)$$

The parameters a, b, c, and d are chosen to have regular spiking excitatory neurons and fast spiking inhibitory neurons. The synaptic input is composed of chemical double-exponential pulses with time constants τ_s and τ_f:

$$I_i^{\text{syn}}=\frac{V_0-V_i}{K_i\left(\tau_s-\tau_f\right)}\sum_j W_{ij}\left[\exp\left(-\frac{t-\left(t_j+\tau_{ij}\right)}{\tau_s}\right)-\exp\left(-\frac{t-\left(t_j+\tau_{ij}\right)}{\tau_f}\right)\right], \quad (83)$$

where τ_{ij} are axonal delays from j to i, V_0 is the reversal potential of the synapses, and K_i is the in-degree of node i.

The inhibitory synapses are fixed, but the excitatory ones evolve with a STDP dynamics. If the firing difference is $\Delta t = t_{\mathbf{post}} - t_{\mathbf{pre}}$, when the postsynaptic neuron i fires, the synapses change by

$$\Delta W_{ij} = \begin{cases} A_+\left(W_{\max} - W_{ij}\right)\exp\left(-\dfrac{\Delta t - \tau_{ij}}{\tau_+}\right) & \textbf{if} \quad \Delta t > \tau_{ij}, \\ A_-\left(W_{\max} - W_{ij}\right)\exp\left(-\dfrac{\Delta t - \tau_{ij}}{\tau_-}\right) & \textbf{if} \quad \Delta t \le \tau_{ij}. \end{cases} \tag{84}$$

This system presents a transition from out-of-phase to synchronized spiking. The authors show that a STDP dynamics self-organizes in a robust way the system to the border of this transition, where critical features like avalanches (coexisting with oscillations) appear.

7 CONCLUDING REMARKS

In this review, we described several examples of self-organization mechanisms that drive neuronal networks to the border of a phase transition (mostly a second-order absorbing phase transition, but also to first-order, synchronization, Hopf, and order-chaos transitions). Surprisingly, for all cases, it is possible to detect neuronal avalanches with mean-field exponents similar to those obtained in the experiments of Beggs and Plenz [17].

By using a standardized notation, we recognized several common features between the proposed homeostatic mechanisms. Most of them are variants of the fundamental drive-dissipation dynamics of SOC and SOqC and can be grouped into a few classes.

Following Hernandez-Urbina and Herrmann [47], we stress that the coarse tuning on hyperparameters of homeostatic SOqC is not equivalent to the fine-tuning of the original control parameter. This homeostasis is a *bona-fide* self-organization, in the same sense that the regulation of body temperature is self-organized (although presumably there are hyperparameters in that regulation). The advantage of these explicit homeostatic mechanisms is that they are biologically inspired and could be studied in future experiments to determine which are more relevant to cortical activity.

Due to nonconservative dynamics and the lack of an infinite separation of time scales, all these mechanisms lead to SOqC [5–7], not SOC. In particular, conservative sandpile models should not be used to model neuronal avalanches because neurons are not conservative. The presence of SOqC is revealed by stochastic sawtooth oscillations in the former control parameter, leading to large excursions in the supercritical and subcritical phases. However, hovering around the critical point seems to be sufficient to account for the current experimental data. Also, perhaps the omnipresent stochastic oscillations could be detected experimentally (some authors conjecture that they are the basis for brain rhythms [91]).

One suggestion for further research is to eliminate nonlocal variables in the homeostatic mechanisms. Another is to study how the branching ratio σ, or better, the synaptic matrix largest eigenvalue λ, depends on the self-organization hyperparameters (as done in Ref. [61]). As several results in this review have shown, the dependence of criticality on the hyperparameters is always weaker than the dependence on the original control parameter. Finally, one could devise local metaplasticity rules for the hyperparameters, similarly to Peng and Beggs [67] (which, however, is unfortunately nonlocal). An intuitive possibility is that, at each level of metaplasticity, the need for coarse tuning of hyperparameters decreases and criticality will turn out more robust.

AUTHOR CONTRIBUTIONS

OK and MC contributed to conception and design of the study; RP organized the database of revised articles and made **Figure 1**; OK and MC wrote the manuscript. All authors contributed to manuscript revision, and read and approved the submitted version.

FUNDING

This article was produced as part of the activities of FAPESP Research, Innovation, and Dissemination Center for Neuromathematics (Grant No. 2013/07699-0, São Paulo Research Foundation). We acknowledge the financial support from CNPq (Grant Nos. 425329/2018-6, 301744/2018-1 and 2018/20277-0), FACEPE (Grant No. APQ-0642-1.05/18), and Center for Natural and Artificial Information Processing Systems (CNAIPS)-USP. Support from CAPES (Grant Nos. 88882.378804/2019-01 and 88882.347522/2010-01) and FAPESP (Grant Nos. 2018/20277-0 and 2019/12746-3) is also gratefully acknowledged.

ACKNOWLEDGMENTS

The authors thank Miguel Muñoz for discussions and advice.

REFERENCES

1. Bak P, Tang C, Wiesenfeld K. Self-organized criticality: an explanation of the 1/fnoise. *Phys Rev Lett* (1987) 59:381. doi:10.1103/physrevlett.59.381
2. Wilkinson D, Willemsen JF. Invasion percolation: a new form of percolation theory. *J Phys A Math Gen* (1983) 16:3365. doi:10.1088/0305-4470/16/14/028
3. Jensen HJ. *Self-organized criticality: emergent complex behavior in physical and biological systems*. Vol. 10. Cambridge: Cambridge University Press (1998)

4. Pruessner G. *Self-organised criticality: theory, models and characterization*. Cambridge: Cambridge University Press (2012).
5. Bonachela JA, Muñoz MA. Self-organization without conservation: true or just apparent scale-invariance? *J Stat Mech* (2009) 2009:P09009. doi:10.1088/1742-5468/2009/09/P09009
6. Bonachela JA, De Franciscis S, Torres JJ, Muñoz MA. Self-organization without conservation: are neuronal avalanches generically critical? *J Stat Mech* 2010 (2010) P02015. doi:10.1088/1742-5468/2010/02/P02015
7. Buendía V, di Santo S, Bonachela JA, Muñoz MA. Feedback mechanisms for self-organization to the edge of a phase transition. *Front Phys* 8 (2020) 333. doi:10.3389/fphy.2020.00333
8. Palmieri L, Jensen HJ. The emergence of weak criticality in soc systems. *Epl* 123 (2018) 20002. doi:10.1209/0295-5075/123/20002
9. Palmieri L, Jensen HJ. The forest fire model: the subtleties of criticality and scale invariance. *Front Phys* 8 (2020) 257. doi:10.3389/fphy.2020.00257
10. Turing AM. I.-computing machinery and intelligence. *Mind* LIX (1950) 433. doi:10.1093/mind/lix.236.433
11. Usher M, Stemmler M, Olami Z. Dynamic pattern formation leads to1fnoise in neural populations. *Phys Rev Lett* (1995) 74:326. doi:10.1103/PhysRevLett.74.326
12. Corral Á, Pérez CJ, Díaz-Guilera A, Arenas A. Synchronization in a lattice model of pulse-coupled oscillators. *Phys Rev Lett* (1995) 75:3697. doi:10.1103/PhysRevLett.75.3697
13. Bottani S. Pulse-coupled relaxation oscillators: from biological synchronization to self-organized criticality. *Phys Rev Lett* (1995) 74:4189. doi:10.1103/PhysRevLett.74.4189
14. Chen D-M, Wu S, Guo A, Yang ZR. Self-organized criticality in a cellular automaton model of pulse-coupled integrate-and-fire neurons. *J Phys Math GenJ Phys A Math Gen* (1995) 28:5177. doi:10.1088/0305-4470/28/18/009
15. Herz AVM, Hopfield JJ. Earthquake cycles and neural reverberations: collective oscillations in systems with pulse-coupled threshold elements. *Phys Rev Lett* (1995) 75:1222. doi:10.1103/PhysRevLett.75.1222
16. MiddletonTang C. Self-organized criticality in nonconserved systems. *Phys Rev Lett* 74 (1995) 742. doi:10.1103/PhysRevLett.74.742
17. Beggs JM, Plenz D. Neuronal avalanches in neocortical circuits. *J Neurosci* 23 (2003) 11167–77. doi:10.1523/JNEUROSCI.23-35-11167.2003
18. Stassinopoulos D, Bak P. Democratic reinforcement: a principle for brain function. *Phys Rev E* (1995) 51:5033. doi:10.1103/physreve.51.5033
19. Chialvo DR, Bak P. Learning from mistakes. *Neuroscience* (1999) 90:1137–48. doi:10.1016/S0306-4522(98)00472-2
20. Bak P, Chialvo DR. Adaptive learning by extremal dynamics and negative feedback. *Phys Rev E* (2001) 63:031912. doi:10.1103/PhysRevE.63.031912
21. Chialvo DR. Emergent complex neural dynamics. *Nat Phys* (2010) 6:744–50. doi:10.1038/nphys1803
22. Hesse J, Gross T. Self-organized criticality as a fundamental property of neural systems. *Front Syst Neurosci* (2014) 8:166. doi:10.3389/fnsys.2014.00166
23. D Plenz E Niebur, editors. *Criticality in neural systems*. Hoboken: John Wiley & Sons (2014)
24. Cocchi L, Gollo LL, Zalesky A, Breakspear M. Criticality in the brain: a synthesis of neurobiology, models and cognition. *Prog Neurobiol Prog Neurobiol* (2017) 158:132–52. doi:10.1016/j.pneurobio.2017.07.002
25. Muñoz MA. Colloquium: criticality and dynamical scaling in living systems. *Rev Mod Phys* (2018) 90:031001. doi:10.1103/RevModPhys.90.031001
26. Wilting J, Priesemann V. 25 years of criticality in neuroscience—established results, open controversies, novel concepts. *Curr Opin Neurobiol* (2019) 58:105–11. doi:10.1016/j.conb.2019.08.002
27. Zeraati R, Priesemann V, Levina A. Self-organization toward criticality by synaptic plasticity. *arXiv* (2020) 2010.07888.
28. Haldeman C, Beggs JM. Critical branching captures activity in living neural networks and maximizes the number of metastable states. *Phys Rev Lett* (2005) 94:058101. doi:10.1103/PhysRevLett.94.058101
29. Kinouchi O, Copelli M. Optimal dynamical range of excitable networks at criticality. *Nat Phys* (2006) 2:348–351. doi:10.1038/nphys289
30. Copelli M, Campos PRA. Excitable scale free networks. *Eur Phys J B* (2007) 56:273–78. doi:10.1140/epjb/e2007-00114-7
31. Wu A-C, Xu X-J, Wang Y-H. Excitable Greenberg-Hastings cellular automaton model on scale-free networks. *Phys Rev E* (2007) 75:032901. doi:10.1103/PhysRevE.75.032901
32. Assis VRV, Copelli M. Dynamic range of hypercubic stochastic excitable media. *Phys Rev E* (2008) 77:011923. doi:10.1103/PhysRevE.77.011923
33. Beggs JM. The criticality hypothesis: how local cortical networks might optimize information processing. *Phil Trans R Soc A* 366 (2008) 29–343. doi:10.1098/rsta.2007.2092
34. Ribeiro TL, Copelli M. Deterministic excitable media under Poisson drive: Power law responses, spiral waves, and dynamic range. *Phys Rev E* (2008) 77:051911. doi:10.1103/PhysRevE.77.051911
35. Shew WL, Yang H, Petermann T, Roy R, Plenz D. Neuronal avalanches imply maximum dynamic range in cortical networks at criticality. *J Neurosci* (2009) 29:15595–600. doi:10.1523/JNEUROSCI.3864-09.2009
36. Larremore DB, Shew WL, Restrepo JG. Predicting criticality and dynamic range in complex networks: effects of topology. *Phys Rev Lett* (2018) 106:058101. doi:10.1103/PhysRevLett.106.058101
37. Shew WL, Yang H, Yu S, Roy R, Plenz D. Information capacity and transmission are maximized in balanced cortical networks with neuronal avalanches. *J Neurosci* (2011) 31:55–63. doi:10.1523/JNEUROSCI.4637-10.2011
38. Shew WL, Plenz D. The functional benefits of criticality in the cortex. *Neuroscientist* (2013) 19:88–100. doi:10.1177/1073858412445487
39. Mosqueiro TS, Maia LP. Optimal channel efficiency in a sensory network. *Phys Rev E* (2013) 88:012712. doi:10.1103/PhysRevE.88.012712
40. Wang C-Y, Wu ZX, Chen MZQ. Approximate-master-equation approach for the Kinouchi-Copelli neural model on networks. *Phys Rev E* (2017) 95:012310. doi:10.1103/PhysRevE.95.012310
41. Zierenberg J, Wilting J, Priesemann V, Levina A. Tailored ensembles of neural networks optimize sensitivity to stimulus statistics. *Phys Rev Res* (2020) 2:013115. doi:10.1103/physrevresearch.2.013115
42. Galera EF, Kinouchi O. *Physics of psychophysics: two coupled square lattices of spiking neurons have huge dynamic range at criticality*. arXiv (2020) 11254.
43. Dickman R., Vespignani A, Zapperi S. Self-organized criticality as an absorbing-state phase transition. *Phys Rev E* (1998) 57:5095. doi:10.1103/PhysRevE.57.5095
44. Muñoz MA, Dickman R, Vespignani A, Zapperi S. Avalanche and spreading exponents in systems with absorbing states. *Phys Rev E* (1999) 59:6175. doi:10.1103/PhysRevE.59.6175
45. Dickman R, Muñoz MA, Vespignani A, Zapperi S. Paths to self-organized criticality. *Braz J Phys* (2000) 30:27–41. doi:10.1590/S0103-97332000000100004
46. Buendía V., di Santo S., Villegas P., Burioni R, Muñoz MA. Self-organized bistability and its possible relevance for brain dynamics. *Phys Rev Res* (2020) 2:013318. doi:10.1103/PhysRevResearch.2.013318
47. Hernandez-Urbina V, Herrmann JM. Self-organized criticality via retro-synaptic signals. *Front Phys* (2017) 4:54. doi:10.3389/fphy.2016.00054
48. Lübeck S. Universal scaling behavior of non-equilibrium phase transitions. *Int J Mod Phys B* (2004) 18:3977–4118. doi:10.1142/s0217979204027748
49. Markram H, Tsodyks M. Redistribution of synaptic efficacy between neocortical pyramidal neurons. *Nature* (1996) 382:807–10. doi:10.1038/382807a0
50. Tsodyks M, Pawelzik K, Markram H. Neural networks with dynamic synapses. *Neural Comput* (1998) 10:821–35. doi:10.1162/089976698300017502
51. Levina A., Herrmann K, Geisel T. Dynamical synapses causing self-organized criticality in neural networks. *Nat Phys* (2007a) 3:857–860. doi:10.1038/nphys758
52. Levina A, Herrmann M. Dynamical synapses give rise to a power-law distribution of neuronal avalanches. *Adv Neural Inf Process Syst* (2006) 771–8.
53. Levina A., Herrmann M, Geisel T. Phase transitions towards criticality in a neural system with adaptive interactions. *Phys Rev Lett*(2009) 102:118110. doi:10.1103/PhysRevLett.102.118110
54. Wang SJ, Zhou C. Hierarchical modular structure enhances the robustness of self-organized criticality in neural networks. *New J Phys* (2012) 14:023005. doi:10.1088/1367-2630/14/2/023005
55. Brochini L, de Andrade Costa A, Abadi M, Roque AC, Stolfi J, Kinouchi O. Phase transitions and self-organized criticality in networks of stochastic spiking neurons. *Sci Rep* (2016) 6:35831. doi:10.1038/srep35831

56. Gerstner W, van Hemmen JL. Associative memory in a network of 'spiking' neurons. *Netw Comput Neural SystNetw Comput Neural Syst* (1992) 3:139–64. doi:10.1088/0954-898X_3_2_004
57. Galves A, Löcherbach E. Infinite systems of interacting chains with memory of variable length-A stochastic model for biological neural nets. *J Stat Phys* (2013) 151:896–921. doi:10.1007/s10955-013-0733-9
58. Kinouchi O, Brochini L, Costa AA, Campos JGF, Copelli M. Stochastic oscillations and dragon king avalanches in self-organized quasi-critical systems. *Sci Rep* (2019) 9:1–12. doi:10.1038/s41598-019-40473-1
59. Grassberger P, Kantz H. On a forest fire model with supposed self-organized criticality. *J Stat Phys* (1991) 63:685–700. doi:10.1007/BF01029205
60. Costa AdA, Copelli M, Kinouchi O. Can dynamical synapses produce true self-organized criticality? *J Stat Mech* (2015) 2015:P06004. doi:10.1088/1742-5468/2015/06/P06004
61. Campos JGF, Costa AdA, Copelli M, Kinouchi O. Correlations induced by depressing synapses in critically self-organized networks with quenched dynamics. *Phys Rev E* (2017) 95:042303. doi:10.1103/PhysRevE.95.042303
62. Kinouchi O. *Self-organized (quasi-)criticality: the extremal Feder and Feder model*. arXiv (1998) 9802311.
63. Hsu D, Beggs JM. Neuronal avalanches and criticality: a dynamical model for homeostasis. *Neurocomputing* 69 (2006) 1134–36. doi:10.1016/j.neucom.2005.12.060
64. Hsu D, Tang A, Hsu M, Beggs JM. Simple spontaneously active Hebbian learning model: homeostasis of activity and connectivity, and consequences for learning and epileptogenesis. *Phys Rev E* 76 (2007) 041909. doi:10.1103/PhysRevE.76.041909
65. Shew WL, Clawson WP, Pobst J, Karimipanah Y, Wright NC, Wessel R. Adaptation to sensory input tunes visual cortex to criticality. *Nature Phys* 11 (2015) 659–663. doi:10.1038/nphys3370
66. Levina A., Ernst U, Michael Herrmann JM. Criticality of avalanche dynamics in adaptive recurrent networks. *Neurocomputing* 70 (2007b) 1877–1881. doi:10.1016/j.neucom.2006.10.056
67. Peng J, Beggs JM. Attaining and maintaining criticality in a neuronal network model. *Physica A Stat Mech Appl* (2013) 392:1611–20. doi:10.1016/j.physa.2012.11.013
68. Hebb DO. *The organization of behavior: a neuropsychological theory*. Hoboken: J. Wiley; Chapman & Hall (1949).
69. Turrigiano GG, Nelson SB. Hebb and homeostasis in neuronal plasticity. *Curr Opin Neurobiol* (2000) 10:358–64. doi:10.1016/S0959-4388(00)00091-X
70. Kuriscak E, Marsalek P, Stroffek J, Toth PG. Biological context of Hebb learning in artificial neural networks, a review. *Neurocomputing* (2015) 152:27–35. doi:10.1016/j.neucom.2014.11.022
71. de Arcangelis L, Perrone-Capano C, Herrmann HJ. Self-organized criticality model for brain plasticity. *Phys Rev Lett* (2006) 96:028107. doi:10.1103/PhysRevLett.96.028107
72. Lombardi F, Herrmann HJ, de Arcangelis L. Balance of excitation and inhibition determines 1/f power spectrum in neuronal networks. *Chaos* (2017) 27:047402. doi:10.1063/1.4979043
73. Pellegrini G. L., de Arcangelis L., Herrmann HJ, Perrone-Capano C. Activity-dependent neural network model on scale-free networks. *Phys Rev E* (2007) 76:016107. doi:10.1103/PhysRevE.76.016107
74. de Arcangelis L. Are dragon-king neuronal avalanches dungeons for self-organized brain activity? *Eur Phys J Spec Top* (2012) 205:243–57. doi:10.1140/epjst/e2012-01574-6
75. de Arcangelis L, Herrmann HJ. Activity-dependent neuronal model on complex networks. *Front Physiol* (2012) 3:62. doi:10.3389/fphys.2012.00062
76. Lombardi F, Herrmann HJ, Perrone-Capano C, Plenz D, De Arcangelis L. Balance between excitation and inhibition controls the temporal organization of neuronal avalanches. *Phys Rev Lett* (2012) 108:228703. doi:10.1103/PhysRevLett.108.228703
77. de Arcangelis L, Lombardi F, Herrmann HJ. Criticality in the brain. *J Stat Mech* (2014) 2014:P03026. doi:10.1088/1742-5468/2014/03/P03026
78. Lombardi F, Herrmann HJ, Plenz D, De Arcangelis L. On the temporal organization of neuronal avalanches. *Front Syst Neurosci* (2014) 8:204. doi:10.3389/fnsys.2014.00204
79. Lombardi F, de Arcangelis L. Temporal organization of ongoing brain activity. *Eur Phys J Spec Top* (2014) 223:2119–2130. doi:10.1140/epjst/e2014-02253-4
80. Van Kessenich LM, De Arcangelis L, Herrmann HJ. Synaptic plasticity and neuronal refractory time cause scaling behaviour of neuronal avalanches. *Sci Rep* (2016) 6:32071. doi:10.1038/srep32071
81. Çiftçi K. Synaptic noise facilitates the emergence of self-organized criticality in the caenorhabditis elegans neuronal network. *Netw Comput Neural Syst* (2018) 29:1–19. doi:10.1080/0954898X.2018.1535721
82. Uhlig M, Levina A, Geisel T, Herrmann JM. Critical dynamics in associative memory networks. *Front Comput Neurosci* (2013) 7:87. doi:10.3389/fncom.2013.00087
83. Rabinovich M, Huerta R, Laurent G. Neuroscience: transient dynamics for neural processing. *Science* (2008) 321:48–50. doi:10.1126/science.1155564
84. Rubinov M., Sporns O., Thivierge JP, Breakspear M. Neurobiologically realistic determinants of self-organized criticality in networks of spiking neurons. *PLoS Comput Biol* (2011) 7:e1002038. doi:10.1371/journal.pcbi.1002038
85. Del Papa B., Priesemann V, Triesch J. Criticality meets learning: criticality signatures in a self-organizing recurrent neural network. *PLoS One* (2017) 12:e0178683. doi:10.1371/journal.pone.0178683
86. Levina A, Herrmann JM, Geisel T. Theoretical neuroscience of self-organized criticality: from formal approaches to realistic models. In D Plenz E Niebur, editors. *Criticality in neural systems*. Hoboken: Wiley Online Library (2014) 417–36. doi:10.1002/9783527651009.ch20
87. Stepp N, Plenz D, Srinivasa N. Synaptic plasticity enables adaptive self-tuning critical networks. *PLoS Comput Biol* (2015) 11:e1004043. doi:10.1371/journal.pcbi.1004043
88. Delattre V, Keller D, Perich M, Markram H, Muller EB. Network-timing-dependent plasticity. *Front Cell Neurosci* (2015) 9:220. doi:10.3389/fncel.2015.00220
89. Kossio FYK, Goedeke S, van den Akker B, Ibarz B, Memmesheimer RM. Growing critical: self-organized criticality in a developing neural system. *Phys Rev Lett* (2018) 121:058301. doi:10.1103/PhysRevLett.121.058301
90. Tetzlaff C, Okujeni S, Egert U, Wörgötter F, Butz M. Self-organized criticality in developing neuronal networks. *PLoS Comput Biol* (2010) 6, e1001013. doi:10.1371/journal.pcbi.1001013
91. Costa A., Brochini L, Kinouchi O. Self-organized supercriticality and oscillations in networks of stochastic spiking neurons. *Entropy* (2017) 19:399. doi:10.3390/e19080399
92. Zierenberg J., Wilting J, Priesemann V. Homeostatic plasticity and external input shape neural network dynamics. *Phys Rev X* (2018) 8:031018. doi:10.1103/PhysRevX.8.031018
93. Girardi-Schappo M., Brochini L., Costa AA, Carvalho TT, Kinouchi O. Synaptic balance due to homeostatically self-organized quasicritical dynamics. *Phys Rev Res* (2020) 2:012042. doi:10.1103/PhysRevResearch.2.012042
94. Brunel N Dynamics of sparsely connected networks of excitatory and inhibitory spiking neurons. *J Comput Neurosci* (2000) 8:183–208. doi:10.1023/A:1008925309027
95. Bienenstock E, Lehmann D. Regulated criticality in the brain? *Advs Complex Syst* (1998) 01:361–84. doi:10.1142/S0219525998000223
96. Bornholdt S, Rohlf T. Topological evolution of dynamical networks: global criticality from local dynamics. *Phys Rev Lett* (2000) 84:6114. doi:10.1103/PhysRevLett.84.6114
97. Bornholdt S, Röhl T. Self-organized critical neural networks. *Phys Rev E* (2003) 67:066118. doi:10.1103/PhysRevE.67.066118
98. Rohlf T. Self-organization of heterogeneous topology and symmetry breaking in networks with adaptive thresholds and rewiring. *Europhys Lett* (2008) 84:10004. doi:10.1209/0295-5075/84/10004
99. Gross T, Sayama H. *Adaptive networks*. Berlin: Springer (2009) 1–8. doi:10.1007/978-3-642-01284-6_1
100. Rohlf T, Bornholdt S. *Self-organized criticality and adaptation in discrete dynamical networks. Adaptive Networks*. Berlin: Springer (2009). 73–106.
101. Meisel C, Gross T. Adaptive self-organization in a realistic neural network model. *Phys Rev E* 80 (2009) 061917. doi:10.1103/PhysRevE.80.061917
102. Min L, Gang Z, Tian-Lun C. Influence of selective edge removal and refractory period in a self-organized critical neuron model. *Commun Theor Phys* 52 (2009) 351. doi:10.1088/0253-6102/52/2/31
103. Rybarsch M, Bornholdt S. Avalanches in self-organized critical neural networks: a minimal model for the neural soc universality class. *PLoS One* (2014) 9:e93090. doi:10.1371/journal.pone.0093090

104. Cramer B, Stöckel D, Kreft M, Wibral M, Schemmel J, Meier K, et al. Control of criticality and computation in spiking neuromorphic networks with plasticity. *Nat Commun* (2020) 11:1–11. doi:10.1038/s41467-020-16548-3
105. Droste F., Do AL, Gross T. Analytical investigation of self-organized criticality in neural networks. *J R Soc Interface* (2013) 10:20120558. doi:10.1098/rsif.2012.0558
106. Kuehn C. Time-scale and noise optimality in self-organized critical adaptive networks. *Phys Rev E* (2012) 85:026103. doi:10.1103/PhysRevE.85.026103
107. Zeng H-L, Zhu C-P, Guo Y-D, Teng A, Jia J, Kong H, et al. Power-law spectrum and small-world structure emerge from coupled evolution of neuronal activity and synaptic dynamics. *J Phys: Conf Ser* (2015) 604: 012023. doi:10.1088/1742-6596/604/1/012023
108. Mejias JF, Kappen HJ, Torres JJ. Irregular dynamics in up and down cortical states. *PLoS One* (2010) 5:e13651. doi:10.1371/journal.pone.0013651
109. Millman D, Mihalas S, Kirkwood A, Niebur E. Self-organized criticality occurs in non-conservative neuronal networks during 'up' states. *Nat Phys* (2010) 6:801–05. doi:10.1038/nphys1757
110. di Santo S, Burioni R, Vezzani A, Muñoz MA. Self-organized bistability associated with first-order phase transitions. *Phys Rev Lett* (2016) 116:240601. doi:10.1103/PhysRevLett.116.240601
111. Di Santo S, Villegas P, Burioni R, Muñoz MA. Landau–Ginzburg theory of cortex dynamics: scale-free avalanches emerge at the edge of synchronization. *Proc Natl Acad Sci USA* (2018) 115:E1356–65. doi:10.1073/pnas.1712989115
112. Cowan JD, Neuman J, Kiewiet B, Van Drongelen W. Self-organized criticality in a network of interacting neurons. *J Stat Mech*(2013) 2013:P04030. doi:10.1088/1742-5468/2013/04/p04030
113. Magnasco MO, Piro O, Cecchi GA. Self-tuned critical anti-Hebbian networks. *Phys Rev Lett* (2009) 102:258102. doi:10.1103/PhysRevLett.102.258102
114. Khoshkhou M, Montakhab A. Spike-timing-dependent plasticity with axonal delay tunes networks of izhikevich neurons to the edge of synchronization transition with scale-free avalanches. *Front Syst Neurosci* (2019) 13:22–7. doi:10.3389/fnsys.2019.00073

Conflict of Interest: The authors declare that the research was conducted in the absence of any commercial or financial relationships that could be construed as a potential conflict of interest.

frontiers in Physics

MINI REVIEW
published: 21 April 2021
doi: 10.3389/fphy.2020.616408

Self-Organized Criticality in Economic Fluctuations: The Age of Maturity

Claudio Tebaldi *

Department of Finance, IGIER and Baffi Carefin, Università Bocconi, Milan, Italy

Self-Organized Criticality (SOC) has been proposed as a paradigm that may rationalize the emergence of macrofinancial fluctuations. The wave of innovative thinking sparked by this proposal continues to produce interesting contributions in many areas of economics, ranging from macroeconomics to finance. In this review, we propose a guided tour to these achievements, highlighting that analysis of SOC equilibria is a promising avenue to establish a nexus between i) a statistical equilibrium characterized by the spontaneous emergence of dynamic critical fluctuations and ii) a strategic equilibrium concept modeling a large number of interacting players. The critical state is the stable outcome arising from a trade-off between cooperation and competition.

Keywords: self-organized critical behavior, macroeconomics and financial markets, econometrics, critical phenomena, renorm group equation

OPEN ACCESS

Edited by:
Subhrangshu Sekhar Manna, S. N. Bose National Centre for Basic Sciences, India

Reviewed by:
Attilio L. Stella, University of Padua, Italy
Bikas K. Chakrabarti, Saha Institute of Nuclear Physics (SINP), India

***Correspondence:**
Claudio Tebaldi
claudio.tebaldi@unibocconi.it

Specialty section:
This article was submitted to Interdisciplinary Physics, a section of the journal Frontiers in Physics

Received: *12 October 2020*
Accepted: *21 December 2020*
Published: *21 April 2021*

Citation:
Tebaldi C (2021) Self-Organized Criticality in Economic Fluctuations: The Age of Maturity. Front. Phys. 8:616408. doi: 10.3389/fphy.2020.616408

1 INTRODUCTION

The interaction between economic and physical sciences is so rich that a new interdisciplinary field has emerged, econophysics. While its cultural appealing is undisputable, contributions that are considered relevant and well disciplined by both economists and physicists are rare. It is fair to say that the self-organized critical (SOC) paradigm for economic and financial fluctuations put forward in the seminal contributions [1–3] is one of them.

While many are sympathetic with the proposal that an SOC paradigm underlies financial and macroeconomic fluctuations, the introduction of a common language and of analytic tools useful to make this proposal effective at both the descriptive and normative level are still underway. In fact, the virtue and the sin of the early SOC proposal lie in the use of a simple toy model to exemplify a number of characteristics that are expected to play a paradigmatic role.

It is virtually impossible to produce a systematic discussion of the overall state of the art, given the relevance of the topic and the number of research contributions in this area. Hence, in this short review, I propose a guided tour through the research spillover originating from those seminal proposals and argue that the SOC paradigm is an important building block of an emerging interdisciplinary paradigm suitable for framing a notion of statistical equilibrium relevant for both social and natural sciences.

In writing this contribution, I will take a purely subjective point of view with the deliberate goal of highlighting not only the strengths but also the open issues that are to be clarified to make the notion of the SOC state a more disciplined and useful instrument of economic analysis.

The review is organized as follows: we will start focusing in the next **Section 2** on those common misconceptions and cultural differences that have so far limited the interaction among researchers with such different backgrounds. Then, we dedicate a section to each one of the following three themes that we consider SOC—"identitarian." In **Section 3**, we revisit the original model trying to clarify why the notion of "spontaneous emergence of a critical state" fits well in the traditional economic debate about the origin of macroeconomic fluctuations. In **Section 4**, we review the

interdisciplinary attempts to improve the econometric description of financial and economic fluctuations. In particular, we focus on those that analyze financial time series borrowing the conventional tools used to analyze critical phenomena in physics: scaling, universality, and renormalization. In **Section 5**, we review the growing body of literature focusing on the notion of "avalanche" that we interpret as a correlated sequence of spatiotemporal events. We conclude with a focus on those research directions that in our opinion should be targeted by the coming research efforts in order to complete our understanding of the SOC paradigm with the provision of effective policy instruments.

2 ECONOMIC EQUILIBRIUM *VERSUS* STATISTICAL (NON)-EQUILIBRIUM

While the use of probability and statistics is common in both natural and social sciences, its theoretical foundations are radically different [4]; the contribution written by L. Hansen on occasion of the attribution of the Nobel Prize for economic sciences offers a key insight that clarifies the critical challenges underlying the quantification of uncertainty in a dynamic stochastic economy. The line of attack to macrofinancial modeling proposed in Ref. [4] fits nicely within a nonequilibrium statistical mechanics analysis of open systems: "Exogenous shocks repeatedly perturb a dynamic equilibrium through the model's endogenous transmission mechanisms" [4] (page 946). As Hansen points out, macrofinancial modeling poses two challenges. The first one has a descriptive focus: to describe what is called "uncertainty outside the model," that is, to best reproduce statistical features and impulse response of measured real-world time series. This challenge fits well within a conventional statistical mechanical approach. The second challenge faced in economic modeling is that the model also describes *inside uncertainty*: "... agents inside our model, be it consumers, entrepreneurs, or policymakers, must also confront uncertainty as they make decisions. I refer to this as inside uncertainty ...." This second aspect is intimately related to the normative focus of economics: "The modeler's choice regarding insiders' perspectives on an uncertain future can have significant consequences for each model's equilibrium outcomes." It is this second objective that poses a formidable hurdle to the statistical mechanical description of economic fluctuations. This second requirement changes the description at the microlevel of the system qualitatively: description of individual economic behavior requires the introduction of a set of control variables to describe actions at the individual and collective levels. So the conventional mechanical description of a particle must be replaced by the micro-description of individual decision-making. While the emphasis in physics is more focused on the descriptive content, these considerations explain why economists often consider acceptable a poor description of *outside uncertainty* as an acceptable price to pay in order to achieve a better description of *inside uncertainty* that is necessary to account for the policy reaction of individuals.

At first sight, these fundamental issues look completely unrelated and far from the SOC paradigm. On the contrary, they have a strict connection. Intuitively, the SOC automata microscopic rules are those that describe the rational behavior of individuals. The choice of an individual depends crucially on the inference process that the decision-maker adopts to frame observed data in a model. The authors of Ref. [5] provide a thorough information theoretic analysis of the relationship between inference and emergence of critical behavior within an abstract statistical information theory framework. They show that inference procedures are likely to yield models which are close to singular values of parameters, akin to critical points in physics where phase transitions occur. Hence, following this argument, when inside uncertainty is taken into account, the emergence of critical behavior will look like the rule rather than the exception.

A similar, yet simpler example of a microfunded process is proposed in Ref. [6]. They model a game of strategic network formation where agents must collectively form a network in the face of the following trade-off: each agent receives benefits from the direct links it forms with others, but these links expose it to the risk of being hit by a cascading failure that might spread over multistep paths. They prove that the resulting optimal networks are, in a precise sense, situated just beyond a (percolation type) phase transition in the behavior of the cascading failures.

It is worth observing that in this economic detour, we touched statistical equilibrium physics in relation to not only the definition of a second-order critical point corresponding to the critical point for percolation but also the notion of a cascading failure that intrinsically requires the nonequilibrium dynamics. An economy is fundamentally an open system where the *endogenous* reaction is induced from the agents that re-optimize their decisions. This makes the overall response highly nonlinear and certainly not amenable to a standard equilibrium statistical physics treatment.

In light of these considerations, it is striking and puzzling that the SOC paradigm may often provide an effective and accurate description of many empirical stylized properties of a competitive (economic) equilibrium.

3 SELF-ORGANIZATION AND THE "INVISIBLE HAND"

During the early 1990s, many authors have emphasized the role of complexity and nonlinearity in economics and the potential interaction with the analysis of complex phenomena in natural sciences (for a review, see, e.g., [7]). It is within this framework that [1, 2] formulate the proposal that a SOC state may explain business cycle fluctuations in the level of economic activity indicators. In the original model, sharing many characteristics of the directed sandpile [8] and the stochastic failure sharing [9] models, critical fluctuations are driven by local interaction between customers and suppliers, forming a network of producers with non-convex technologies. One key original aspect of the SOC approach to the analysis of macrofinancial fluctuations is the role played by what is called the "large-economy limit" (see, e.g., [2]); "...we argue that aggregate

fluctuations in production continue to occur in the large-economy limit . . ."

From a statistical mechanical point of view, this statement may seem quite natural. It mimics the necessity to consider the so-called thermodynamic limit to match a model with the relevant observables. As discussed in the previous section, the extension of this argument to the analysis of macrofinancial fluctuations is far from trivial; it is the problem of aggregation that has to be analyzed more carefully. A more recent strand of research has highlighted the main role that the network of firm interaction plays in the propagation of shocks in production economies (see, e.g., [10, 11]). Ref. [12] provides an extensive review and proposes a model calibrated on real data. An undisputable merit of these approaches is their compliance at both micro- and macro-levels with the basic economic principles that regulate the firm and consumer actions.

From the point of view of statistical mechanics, they are not completely satisfactory: a more disciplined approach to the analysis of the large-economy limit is proposed in Ref. [13], relying on random matrix theory. In this case, the authors show explicitly that a network economy triggered toward the critical point generates power-tail size distributions of firms. The authors conjecture that evolutionary and behavioral forces conspire to drive the economy toward marginal stability.

In a different economic context, the authors of Ref. [14] offer an important example, to our knowledge the first one, of a properly microfunded "snowball effect" that drives the spontaneous emergence of critical behavior in the large-economy limit; Ref. [14] presents a state-dependent pricing model that describes the inflation fluctuations driven by idiosyncratic shocks hitting the cost of price changes of individual firms. Firms' pricing behavior in equilibrium exhibits complementarity: the critical cascading effect is sparked by firms' repricing that reduces all the competitors' relative prices, thus inducing more of them to reprice. They model the cascade process relying on the classical theory of critical branching processes. Following a trend common to most of the mean field approaches to SOC models, see also [15].

4 SOC AND ECONOMETRICS

One of the strongest arguments in favor of the approach pursued by econophysics is the inadequacy of linear stationary models in providing a reliable description of the basic properties of macrofinancial time series models.

From an empirical point of view, a "minimalist" characterization of SOC models requires the spontaneous emergence of power-law distributions and scaling relationships (in particular, see, e.g., [9, 16]); it postulates that the size of the response (the avalanche) to an exogenous idiosyncratic shock (the addition of a grain in the sandpile) follows a law satisfying a finite-size scaling ansatz:

$$P_s(s,L) := s^{-\tau_s} F_s\left(\frac{s}{L^{D_s}}\right).$$

Then, assuming that $F_s(x)$ has an exponential decay for $x \gg 1$, L is a fundamental cutoff to the scale-invariant behavior. Furthermore, the scale-invariant critical behavior also requires that the size of the response is related to its spatial extension a and to its lifetime T by homogeneous relations, that is, $s \sim a^{\gamma}$ and $s \sim T^{\beta}$. This implies that the finite-size scaling relation holds also for the distributions of a and T:

$$\begin{aligned} &P_a(a,L) := a^{-\tau_a} F_a\left(\frac{a}{L^{D_a}}\right),\ P_T(T,L) := T^{-\tau_T} F_T\left(\frac{T}{L^{D_T}}\right) \\ &\frac{D_s}{D_a} = \frac{\tau_s - 1}{\tau_a - 1} = \gamma,\quad \frac{D_s}{D_T} = \frac{\tau_s - 1}{\tau_T - 1} = \beta. \end{aligned} \tag{1}$$

Scaling Invariance is hardwired in the parametric description of the impulse response and are difficult if not impossible to derive within the class of linear stationary models. Reference to the SOC paradigm appears in all the early contributions [17–20]. One important debatable question is whether, beyond power laws, macrofinancial fluctuations show consistency with the full articulated set of observable implications that characterize dynamic critical phenomena in physics.

In fact, a joint test of power-law behavior, finite-size scaling and universality within a properly defined renormalization group fixed point, is still missing. In the following, we review the interesting results that are suggestive of the possibility that an attracting fixed point may underlie the SOC state properties of financial time series.

4.1 Universality

The emergence of universal scaling relations in financial markets has a relatively long history in relation to return data. It is a relatively more recent acknowledgment in relation to the market microstructure behavior; Ref. [21] formulates the so-called market microstructure invariance hypothesis. It claims and verifies the existence of a universal invariant quantity I representing the average cost of a single bet. It is expressed in dollars, independent of the asset, and constant over time. Dimensional analysis suggests a relation of the form

$$\frac{PQ}{I} = f\left(\sigma_{\mathrm{d}}^2 \frac{Q}{V}\right), \tag{2}$$

where p is the share price in dollars, σ_{d}^2 denotes the square daily volatility, V denotes the total daily amount traded with *bets*, and Q denotes the average volume of an individual *bet*. Invoking the Modigliani–Miller capital structure irrelevance principle yields $f(x) \sim x^{-1/2}$, which implies up to a numerical factor that

$$I = \frac{\sigma_{\mathrm{d}} P Q^{3/2}}{V^{1/2}} := \frac{\mathcal{R}}{N^{3/2}}, \tag{3}$$

where $\mathcal{R} := \sigma_{\mathrm{d}} PV$ measures the total dollar amount of risk traded per day (also referred to as total exchanged risk or trading activity), while $N := V/Q$ represents the number of daily *bets* for a given contract; Ref. [22] proposes a reformulation of the hypothesis that improves the finite-size scaling collapse. A thorough discussion of the potential role played by the SOC state in explaining market microstructure liquidity dynamics is given in Ref. [23]. In classical critical phenomena, universality finds its explanation in the simple observation that macroscopic

(aggregate) properties will depend only on the stochastic limiting properties of a model that are not removed by a progressive integration (averaging) of micro-fluctuations. The progressive averaging procedure is part of the so-called renormalization group transformation.

4.2 Renormalization Group

A natural bridge between critical phenomena and stochastic modeling of financial time series is offered by the probabilistic interpretation of the renormalization group transformation proposed in Ref. [24]. In this formulation, the RG theory is nothing else than a stochastic limit theory for possibly correlated random variables. Fixed points for the semigroup generated iterating the RG transformation represent the achievable limit distributions. Only properties that survive to the iteration and are relevant to define the fixed point are macroscopically observable; Ref. [25] includes an "econometrics -friendly" introduction to RG transformations in time series analysis. They formalize an extension of the (real space) RG transformation introducing an RG operator, the $\mathcal{R}$ operator in paper's notation, that acts on the classical space of stationary square integrable time series.

The most flexible operational approach to stochastic modeling of financial return time series relying on the renormalization group approach is originally proposed in Ref. [26] and systematically exposed in Ref. [27]. It is grounded on a "fine-graining" procedure obtained "inverting" the real space renormalization group (RG hereafter) flow in the space of return probability distributions. In this case, the starting point of the procedure is the fixed point equation that characterizes the scale-invariant distribution. Recovery of the observed ones occurs considering a "cascading procedure" that tracks backward the conventional RG coarse-graining procedure. The merits and challenges of this approach are extensively discussed in Ref. [27]. This approach seems to offer the best setup to frame the probabilistic analysis of (possibly self-organized) critical behavior in time series. The key ingredients that in our opinion are necessary to characterize a SOC *ensemble* (a set of counterfactuals) are essentially two: i) an endogenous propagation dynamics that preserves scale invariance of conditional moments and ii) a random rescaling factor designed to embody exogenous influences also. The fine-graining procedure has found application in a number of interesting declinations (see [28–30]) that witness the applicative content of the theory.

One crucial observation, noticed in Ref. [16] for the SOC abelian sandpile and explored also in relation to the fine graining by the authors in Ref. [27], is that statistical description of impulse-response functions may require a multiscaling framework, an extension of the conventional finite-size scaling framework. In this case, the probability distribution can be seen as a superposition of scale-invariant clusters with heterogeneous fractal properties. Multifractal formalism requires that the scaling properties of $P_s(s, L)$ are described by the spectrum:

$$f(\alpha) := \frac{\log\left(\int_{L^\alpha}^{+\infty} P_s(x, L)dx\right)}{\log(L)},\ \alpha := \frac{\log(s)}{\log(L)} \text{ for } L \to +\infty.$$

Then, in the limit $L \to +\infty$, asymptotic moment scaling functions are determined by:

$$\langle s^q \rangle \overset{L\to+\infty}{\approx} L^{\sigma(q)},\ \sigma(q) := \sup_\alpha [\alpha q + f(\alpha)].$$

These equations are consistent with a multiplicative decomposition of the random propagation effects and cast a direct connection with the analysis of financial markets building on the similarity of volatility fluctuations with energy dissipation cascades in turbulence. Early contributions by the authors of Refs. [31, 32] established a strong analogy between turbulent cascades and volatility clustering. A new generation of refined multiscale models, like, for example, the multifractal random walk model [33], is capable of matching empirical properties of observed time series volatility.

Beyond scale invariance, characterization of the SOC behavior relies also on property ii), that is, the existence of random correlated sequences of micro-events (an avalanche in the SOC dictionary) that generate a breakdown of time translation invariance. Statistical description of dynamic clustering within a scale-invariant model is analyzed in Ref. [34]. This class of models is able to reproduce the stylized behavior of volatility intermittent decay after a main financial shock. As observed in Ref. [35], it parallels the Omori law in geophysics for the seismic activity after an earthquake of exceptional magnitude.

5 AVALANCHE DYNAMICS

We dedicate the last concluding section to the paradigmatic role played by the concept of avalanche that is as intuitive as difficult to formalize within a macrofinancial model. Along this review, we encountered already many notions that are close friends of the notion of avalanche: the reorganization of the supply chain economy in a competitive equilibrium that is hit by a shock, the sequence of correlated orders that is determined by a single trade decision, and the random rescaling factor in the "fine-grained" model. Last but not least, recent macrofinancial research has shown that propagation of financial shocks across financial institutions interconnected by the web of financial claims plays a major role in the unfolding of financial crises (see, e.g., [36]). Consideration of the financial system as a SOC state has provided great insight into the economic collapse following the subprime crises of 2008 and the following sovereign credit crisis in Europe. The authors of Ref. [37] provide an extensive and interdisciplinary review.

Despite the large amount of interesting empirical evidence and modelization efforts, research has not yet reached a consensus on a precise, empirically testable definition of avalanche dynamics. Intuitively, it is meant to be a dynamic counterpart to the self-similar ensemble of clusters that characterizes fluctuations in an

equilibrium system close to the critical point, where susceptibility diverges. Here is where the tension between the equilibrium and nonequilibrium description of avalanche statistics is more evident. Consider, for example, the "Ising model" of the SOC paradigm, the abelian sandpile. In this case, the steady-state model has an exact characterization in terms of the $q \to 0$ limit of the equilibrium Potts model, and critical properties can be derived from its conformal invariance (see [38]). Attempts to extend the mapping and characterize the dynamic (nonequilibrium) scaling properties of avalanche clusters have so far not been successful.

In conclusion, the previous considerations highlighted that the search of a satisfactory SOC model for macrofinancial fluctuations after thirty years is far from the end. Indeed, the SOC paradigm is still a promising avenue toward a truly effective interdisciplinary paradigm to characterize critical statistical fluctuations arising in strategic equilibria of interacting rational individuals.

AUTHOR CONTRIBUTIONS

The author confirms being the sole contributor of this work and has approved it for publication.

FUNDING

This research gratefully acknowledges the support of the MIUR-PRIN Bando 2017-prot. 2017TA7TYC.

REFERENCES

1. Bak P, Chen K, Scheinkman J, and Woodford M. Aggregate fluctuations from independent sectoral shocks: self-organized criticality in a model of production and inventory dynamics. *Res Econ* (1993) 47(1):3–30. doi:10.1016/0035-5054(93)90023-V
2. Scheinkman JA, and Woodford M. Self-organized criticality and economic fluctuations. *Am Econ Rev* (1994) 84(2):417–21.
3. Bak P, Tang C, and Wiesenfeld K. Self-organized criticality: an explanation of the 1/f noise. *Phys Rev Lett* (1987) 59(4):381. doi:10.1103/PhysRevLett.59.381
4. Hansen LP. Nobel lecture: uncertainty outside and inside economic models. *J Political Econ* (2014) 122(5):945–87. doi:10.1086/678456
5. Mastromatteo I, and Marsili M. On the criticality of inferred models. *J Stat Mech: Theory Exp* (2011) 10:P10012. doi:10.1088/1742-5468/2011/10/P10012
6. Blume L, Easley D, Kleinberg J, Kleinberg R, and Tardos É. Network formation in the presence of contagious risk. In: Proceedings of the 12th ACM conference on electronic commerce; 2011 Jun 5–9; San Jose, CA. New York, NY: ACM (2011). p. 1–10.
7. Anderson PW. *The economy as an evolving complex system*. Cleveland, OH: CRC Press (2018).
8. Dhar D, and Ramaswamy R. Exactly solved model of self-organized critical phenomena. *Phys Rev Lett* (1989) 63(16):1659. doi:10.1103/PhysRevLett.63.1659
9. Manna S. Two-state model of self-organized criticality. *J Phys A Math Theor* (1991) 24(7):L363. doi:10.1088/0305-4470/24/7/009
10. Carvalho V, and Gabaix X. The great diversification and its undoing. *Am Econ Rev* (2013) 103(5):1697–727. doi:10.1257/aer.103.5.1697
11. Acemoglu D, Akcigit U, and Kerr W. Networks and the macroeconomy: an empirical exploration. *NBER Macroecon Annu* (2016) 30(1):273–335. doi:10.1073/pnas.1613559113
12. Taschereau-Dumouchel M. Cascades and fluctuations in an economy with an endogenous production network (2019). Available from: https://papers.ssrn.com/sol3/papers.cfm?abstract_id=3115854 (Accessed February 1, 2021).
13. Moran J, and Bouchaud J-P. Will a large economy be stable (2019). Available from: https://papers.ssrn.com/sol3/papers.cfm?abstract_id=3324209 (Accessed February 1, 2021).
14. Nirei M, and Scheinkman J. *Self-organization of inflation volatility*. Tokyo, Japan: Institute for Monetary and Economic Studies (2019).
15. Zapperi S, Lauritsen KB, and Stanley HE. Self-organized branching processes: mean-field theory for avalanches. *Phys Rev Lett* (1995) 75:4071–4. doi:10.1103/PhysRevLett.75.407110.1103/PhysRevLett.75.4071
16. Tebaldi C, De Menech M, and Stella AL. Multifractal scaling in the bak-tang-wiesenfeld sandpile and edge events. *Phys Rev Lett* (1999) 83(19):3952. doi:10.1103/PhysRevLett.83.3952
17. Mantegna RN, and Stanley HE. *Introduction to econophysics: correlations and complexity in finance*. Cambridge, United Kingdom: Cambridge University Press (1999).
18. Gabaix X, Gopikrishnan P, Plerou V, and Stanley HE. A theory of power-law distributions in financial market fluctuations. *Nature* (2003) 423(6937):267–70. doi:10.1038/nature01624
19. Gabaix X. Power laws in economics and finance. *Annu Rev Econ* (2009) 1(1):255–94. doi:10.1146/annurev.economics.050708.142940
20. Cont R, and Bouchaud J-P. Herd behavior and aggregate fluctuations in financial markets. *Macroecon Dyn* (1997) [arXiv preprint cond-mat/9712318].
21. Kyle AS, and Obizhaeva AA. Market microstructure invariance: empirical hypotheses. *Econometrica* (2016) 84(4):1345–404. doi:10.3982/ECTA10486
22. Bucci F, Lillo F, Bouchaud J-P, and Benzaquen M. Are trading invariants really invariant? trading costs matter. *Quant Finance* (2020) 20:1059–68. doi:10.1080/14697688.2020.1741667
23. Fosset A, Bouchaud J-P, and Benzaquen M. Endogenous liquidity crises. *J Stat Mech Theory Exp* (2020) 6:063401. doi:10.1088/1742-5468/ab7c64
24. Jona-Lasinio G. Renormalization group and probability theory. *Phys Rep* (2001) 352(4-6):439–58. doi:10.1016/S0370-1573(01)00042-4
25. Ortu F, Severino F, Tamoni A, and Tebaldi C. A persistence-based wold-type decomposition for stationary time series. *Quant Econ* (2020) 11(1):203–30. doi:10.3982/QE994
26. Baldovin F, and Stella AL. Scaling and efficiency determine the irreversible evolution of a market. *Proc Natl Acad Sci USA* (2007) 104(50):19741–4. doi:10.1073/pnas.0706046104
27. Zamparo M, Baldovin F, Caraglio M, and Stella AL. Scaling symmetry, renormalization, and time series modeling: the case of financial assets dynamics. *Phys Rev E* (2013) 88(6):062808. doi:10.1103/PhysRevE.88.062808
28. Andreoli A, Caravenna F, Dai Pra P, and Posta G. Scaling and multiscaling in financial series: a simple model. *Adv Appl Probab* (2012) 44(4):1018–51. doi:10.1239/aap/1354716588
29. Baldovin F, Caporin M, Caraglio M, Stella AL, and Zamparo M. Option pricing with non-Gaussian scaling and infinite-state switching volatility. *J Econom* (2015) 187(2):486–97. doi:10.1016/j.jeconom.2015.02.033
30. Peirano PP, and Challet D. Baldovin-stella stochastic volatility process and wiener process mixtures. *Eur Phys J B* (2012) 85(8):276. doi:10.1140/epjb/e2012-30134-y
31. Mandelbrot BB, Fisher AJ, and Calvet LE. A multifractal model of asset returns (1997). Available from: https://papers.ssrn.com/sol3/papers.cfm?abstract_id=78588 (Accessed February 1, 2021).
32. Ghashghaie S, Breymann W, Peinke J, Talkner P, and Dodge Y. Turbulent cascades in foreign exchange markets. *Nature* (1996) 381(6585):767–70. doi:10.1038/381767a0

33. Bacry E, Delour J, and Muzy J-F. Multifractal random walk. *Phys Rev E* (2001) 64(2):026103. doi:10.1103/PhysRevE.64.026103
34. Baldovin F, Camana F, Caraglio M, Stella AL, and Zamparo M. Aftershock prediction for high-frequency financial markets' dynamics In: *Econophysics of systemic risk and network dynamics*. Berlin, Germany: Springer (2013). p. 49–58.
35. Lillo F, and Mantegna RN. Power-law relaxation in a complex system: Omori law after a financial market crash. *Phys Rev E* (2003) 68(1):016119. doi:10.1103/PhysRevE.68.016119
36. Haldane AG, and May RM. Systemic risk in banking ecosystems. *Nature* (2011) 469(7330):351–5. doi:10.1038/nature09659
37. Roukny T, Bersini H, Pirotte H, Caldarelli G, and Battiston S. Default cascades in complex networks: topology and systemic risk. *Sci Rep* (2013) 3:2759. doi:10.1038/srep02759
38. Dhar D. Theoretical studies of self-organized criticality. *Physica A* (2006) 369(1):29–70. doi:10.1016/j.physa.2006.04.004

Conflict of Interest: The author declares that the research was conducted in the absence of any commercial or financial relationships that could be construed as a potential conflict of interest.

frontiers in Physics

REVIEW
published: 22 April 2021
doi: 10.3389/fphy.2021.619661

Self-Organization Toward Criticality by Synaptic Plasticity

Roxana Zeraati[1,2], *Viola Priesemann*[3,4] *and Anna Levina*[2,5,6]*

[1]International Max Planck Research School for the Mechanisms of Mental Function and Dysfunction, University of Tübingen, Tübingen, Germany, [2]Max Planck Institute for Biological Cybernetics, Tübingen, Germany, [3]Max Planck Institute for Dynamics and Self-Organization, Göttingen, Germany, [4]Department of Physics, University of Göttingen, Göttingen, Germany, [5]Department of Computer Science, University of Tübingen, Tübingen, Germany, [6]Bernstein Center for Computational Neuroscience Tübingen, Tübingen, Germany

Self-organized criticality has been proposed to be a universal mechanism for the emergence of scale-free dynamics in many complex systems, and possibly in the brain. While such scale-free patterns were identified experimentally in many different types of neural recordings, the biological principles behind their emergence remained unknown. Utilizing different network models and motivated by experimental observations, synaptic plasticity was proposed as a possible mechanism to self-organize brain dynamics toward a critical point. In this review, we discuss how various biologically plausible plasticity rules operating across multiple timescales are implemented in the models and how they alter the network's dynamical state through modification of number and strength of the connections between the neurons. Some of these rules help to stabilize criticality, some need additional mechanisms to prevent divergence from the critical state. We propose that rules that are capable of bringing the network to criticality can be classified by how long the near-critical dynamics persists after their disabling. Finally, we discuss the role of self-organization and criticality in computation. Overall, the concept of criticality helps to shed light on brain function and self-organization, yet the overall dynamics of living neural networks seem to harnesses not only criticality for computation, but also deviations thereof.

Keywords: self-organized criticality, neuronal avalanches, synaptic plasticity, learning, neuronal networks, homeostasis, synaptic depression, self-organization

OPEN ACCESS

Edited by:
Attilio L. Stella,
University of Padua, Italy

Reviewed by:
Ignazio Licata,
Institute for Scientific Methodology (ISEM), Italy
Jae Woo Lee,
Inha University, South Korea
Samir Suweis,
University of Padua, Italy

***Correspondence:**
Anna Levina
anna.levina@uni-tuebingen.de

Specialty section:
This article was submitted to Interdisciplinary Physics, a section of the journal Frontiers in Physics

Received: *20 October 2020*
Accepted: *09 February 2021*
Published: *22 April 2021*

Citation:
Zeraati R, Priesemann V and Levina A (2021) Self-Organization Toward Criticality by Synaptic Plasticity. Front. Phys. 9:619661. doi: 10.3389/fphy.2021.619661

INTRODUCTION

More than 30 years ago, Per Bak, Chao Tang, and Kurt Wiesenfeld [1] discovered a strikingly simple way to generate scale-free relaxation dynamics and pattern statistic, that had been observed in systems as different as earthquakes [2, 3], snow avalanches [4], forest fires [5], or river networks [6, 7]. Thereafter, hopes were expressed that this self-organization mechanism for scale-free emergent phenomena would explain how any complex system in nature worked, and hence it did not take long until the hypothesis sparked that brains should be self-organized critical as well [8].

The idea that potentially the most complex object we know, the human brain, self-organizes to a critical state was explored early on by theoretical studies [9–12], but it took more than 15 years until the first scale-free "neuronal avalanches" were discovered [8]. Since then, we have seen a continuous, and very active interaction between experiment and theory. The initial, simple and optimistic idea that the brain is self-organized critical similar to a sandpile has been refined and diversified. Now we have a multitude of neuroscience-inspired models, some showing classical self-organized critical

dynamics, but many employing a set of crucial parameters to switch between critical and non-critical states [12–16]. Likewise the views on neural activity have been extended: We now have the means to quantify the distance to criticality even from the very few neurons we can record in parallel [17]. Overall, we have observed in experiments, how developing networks self-organize to a critical state [18–20], how states may change from wakefulness to deep sleep [21–25], under drugs [26] or in a disease like epilepsy [27–30]. Criticality was mainly investigated in *in vivo* neural activity during the resting state dynamics [31–34], but there are also some studies during task-induced changes and in presence of external stimuli [35–39]. These results show how criticality and the deviations thereof can be harnessed for computation, but can also reflect cases where self-organization fails.

Parallel to the rapid accumulation of experimental data, models describing the complex brain dynamics were developed to draw a richer picture. It is worthwhile noting that the seminal sandpile model [40] already bears a striking similarity with the brain: The distribution of heights at each site of the system beautifully corresponds to the membrane potential of neurons, and in both systems, small perturbations can lead to scale-free distributed avalanches. However, whereas in the sandpile the number of grains naturally obeys a conservation law, the number of spikes or the summed potential in a neural network does not.

This points to a significant difference between classical SOC models and the brain: While in the SOC model, the conservation law fixes the interaction between sites [40–44], in neuroscience, connections strengths are ever-changing. Incorporating biologically plausible interactions is one of the largest challenges, but also the greatest opportunity for building the neuronal equivalent of a SOC model. Synaptic plasticity rules governing changes in the connections strengths often couple the interactions to the activity on different timescales. Thus, they can serve as the perfect mechanism for the self-organization and tuning the network's activity to the desired regime.

Here we systematically review biologically plausible models of avalanche-related criticality with plastic connections. We discuss the degree to which they can be considered SOC proper, quasi-critical, or hovering around a critical state. We examine how they can be tuned toward and away from the classical critical state, and in particular, what are the biological control mechanisms that determine self-organization. Our main focus is on models that exhibit scale-free dynamics as measured by avalanche size distributions. Such models are usually referred to as critical, although the presence of power laws in avalanches properties is not a sufficient condition for the dynamics to be critical [45–48].

MODELING NEURAL NETWORKS WITH PLASTIC SYNAPSES

Let us briefly introduce the very basics of neural networks, modeling neural circuits and synaptic plasticity. Most of these knowledge can be found in larger details in neuroscience textbooks [49–51]. The human brain contains about 80 billion neurons. Each neuron is connected to thousands of other neurons. The connections between the neurons are located on fine and long trees of "cables". Each neuron has one such tree to collect signals from other neurons (*dendritic tree*), and a different tree to send out signals to another set of neurons (*axonal tree*). Biophysically, the connections between two neurons are realized by *synapses*. These synapses are special: Only if a synapse is present between a dendrite and an axon can one neuron activate the other (but not necessarily conversely). The strength or weight w_{ij} of a synapse determines how strongly neuron j contributes to activating neuron i. If the summed input to a neuron exceeds a certain threshold within a short time window, the receiving neuron gets activated and fires a *spike* (a binary signal). If a synapse w_{ij} allows neuron j to send signals to neuron i, it does not mean that the reverse synapse, w_{ji} is also present. Thus, unlike classical physics systems, interactions between units are not symmetric but determined by a sparse, non-symmetric weight matrix W. Moreover, interactions are not continuous but pulse-like (*spike*), and they are time-delayed by a few milliseconds: It takes a few milliseconds for a spike to travel along an axon, cross the synapse, and reach the cell body of the receiving neuron. Most interestingly, the synaptic weights w_{ji} change over time. This is termed *synaptic plasticity* and is the core mechanism behind learning.

Before we turn to studying synaptic plasticity in a model, the complexity of a living brain has to be reduced into a simplified model. Typically, neural networks are modeled with a few hundred or thousand of neurons. These neurons are either spiking, or approximated by "rate neurons" which represent the joint activity of an ensemble of neurons. Such rate neurons also exist *in vivo*, e.g., in small animals, releasing graded potentials instead of spikes. Of all neurons in the human cortex, 80% are often modeled as excitatory neurons; when active, excitatory neurons contribute to activating their *post-synaptic* neurons (i.e., the neurons to whom they send their signal). The other 20% of neurons are inhibitory, bringing their post-synaptic neurons further away from their firing threshold. Effectively, an inhibitory neuron is modeled as having negative outgoing synaptic weights w_{ij}, whereas excitatory neurons have positive outgoing weights. In many simplified models, only one excitatory population is considered, and inhibition is implicitly assumed to be contributing to activity propagation probability that is already included in the excitatory connections. The connectivity matrix W between the neurons is typically sparse, since most of the possible synapses are not realized. In models, the connectivity and initial strength of synapses are often drawn from some random distribution. In some studies, however, the impact of specific choices for connectivity and topology is explicitly explored, as outlined in this review (*Network Rewiring and Growth*). Finally, the model neurons often receive some external activation or input in addition to the input generated from the network connections to keep the network going and avoid an absorbing (quiescent) state.

Numerous types of plasticity mechanisms shape the activity propagation in neuronal systems. One type of plasticity acts at the synapses regulating their creation and deletion, and determining changes in their weights w_{ij}. Thereby, regulating postsynaptic

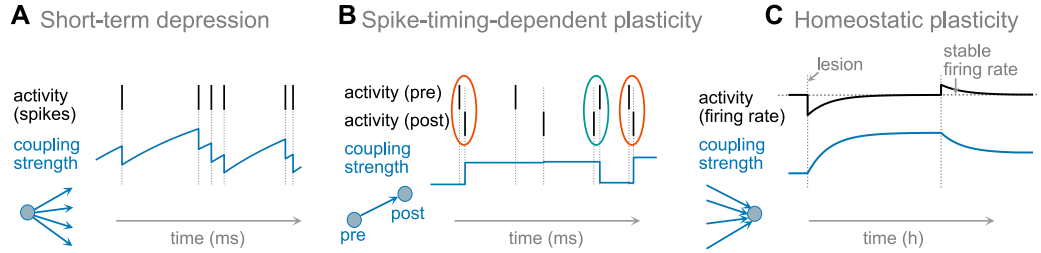

FIGURE 1 | Schematic examples of synaptic plasticity. **(A)** short-term synaptic depression acts on the timescale of spiking activity, and does not generate long-lasting changes. **(B)** For spike-timing dependent plasticity (STDP), a synapse is potentiated upon causal pairing of pre- and postsynaptic activity (framed orange) and depressed upon anti-causal pairing (framed green), forming long-lasting changes after multiple repetitions of pairing. **(C)** Homeostatic plasticity adjusts presynaptic weights (or excitability) to maintain a stable firing rate. After reduction of a neuron's firing rate (e.g., after a lesion and reduction of input), the strengths of incoming excitatory synapses are increased to re-establish the neuron's target firing rate. In contrast, if the actual firing rate is higher than the target rate, then synapses are weakened, and the neuron returns to its firing rate–on the timescales of hours or days.

potentials, which govern the ability of the sending neuron to contribute to the activation of the receiving neuron and thus to activity propagation in the network. The other types of plasticity mechanisms regulate the overall excitability of the neuron, for example, by changing the spiking (activation) threshold or by adaptation currents.

The reasons and mechanisms of changing synaptic strength and neural excitability differ broadly. Changes of the synaptic strengths and excitability in the brain occur at different timescales that might be particularly important for maintaining the critical dynamics. Some are very rapid acting within tens of milliseconds, or associated with every spike; others only make changes on the order of hours or even slower. For this review we simplified the classification in three temporally and functionally distinct classes, **Figure 1**.

The timescale of a plasticity rule influences how it contributes to the state and collective dynamics of brain networks. At the first level, we separate short-term plasticity acting on the timescale of dozens milliseconds, from the long-term plasticity acting with a time constant of minutes to days. As an illustration for short-term plasticity, we present prominent examples of short-term depression (see *Short-Term Synaptic Plasticity*). Among the long-term plasticity rules, we separate two distinct classes. First, plasticity rules that are explicitly associated with learning structures for specific activity propagation such as Hebbian and spike-timing-dependent plasticity (STDP, **Figure 1**, middle). Second, homeostatic plasticity that maintains stable firing rate by up or down regulating neuronal excitability or synaptic strength to achieve a stable target firing rate over long time. This plasticity rule is particularly active after sudden or gradual changes in input to a neuron or neural network, and aims at re-establishing the neuron's firing rate (**Figure 1**, right).

Criticality in Network Models

Studying the distributions of avalanches is a common way to characterize critical dynamics in network models. Depending on the model, avalanches can be defined in different ways. When it is meaningful to impose the separation of timescales (STS), an avalanche is measured as the entire cascade of events following a small perturbation (e.g., activation of a single neuron) - until the activity dies out. However, the STS cannot be completely mapped to living neural systems due to the presence of spontaneous activity or external input. The external input and spontaneous activation impedes the pauses between avalanches and makes an unambigous separation difficult [52]. In models, such external input can be explicitly incorporated to make them more realistic. To extract avalanches from living networks or from models with input, a pragmatic approach is often chosen. If the recorded signal can be approximated by a point process (e.g., spikes recorded from neurons), the data is summed over all signal sources (e.g., electrodes or neurons) and then binned in small time bins. This way, we obtain a single discrete time-series representing a number of events in all time-bins. An avalanche is then defined as a sequence of active bins between two silent bins. If the recorded signal is continuous (like EEG, fMRI, and LFP), it is first thresholded at a certain level and then binned in time [8]. For each signal source (e.g., each electrode or channel), an individual binary sequence is obtained: one if the signal in the bin is larger than the threshold and zero otherwise. After that, the binary data is summed up across all the signal sources, and the same definition as above is applied. Another option to define avalanches in continuous signals is to first sum over the signals across different sources (e.g., electrodes) and then threshold the compound continuous signal. In this method, the beginning of an avalanche is defined as a crossing of the threshold level by the compound activity process from below, and the end is defined as the threshold crossing from above [53, 54]. In this case the proper measure of the avalanche sizes would be the integral between two crossings of the threshold-subtracted compound process [55].

While both binning and thresholding methods are widely used, concerns were raised that depending on the bin size [8, 21, 52, 56], the value of the threshold [55], or the intensity of input [57] distribution of observed avalanches and estimated power-law exponents might be altered. Therefore, to characterize critical dynamics using avalanches it is important to investigate the fundamental scaling relations between the exponents of avalanche size, duration and shapes to avoid misleading results [58, 59], or instead use approaches to assess criticality that do not

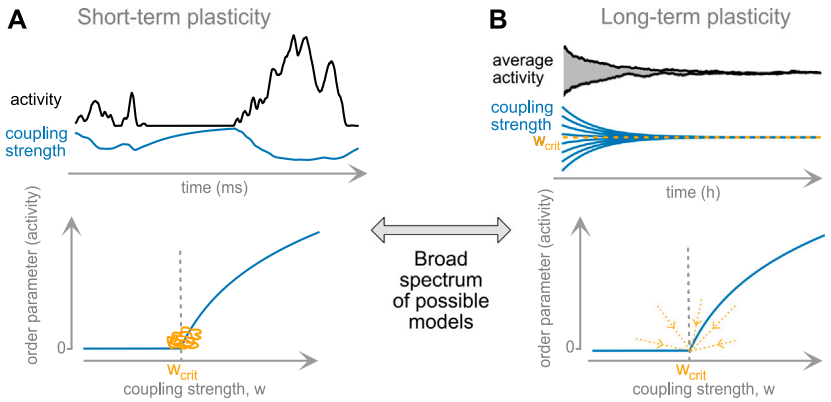

FIGURE 2 | Classical plasticity rules and set-points of network activity. **(A)** Short-term plasticity serves as immediate feedback **(top)**. The resulting long-term behavior of the network hovers near the critical point (orange trace, bottom panel). **(B)** Long-term plasticity results in slow (timescale of hours or longer) convergence to the fixpoint of global coupling strength. In some settings, this fixpoint may correspond to the second-order phase-transition point **(bottom)**, rendering the critical point a global attractor of dynamics.

require the definition of avalanches [17, 60]. We elaborate on these challenges and bias-free solutions in a review book chapter [61]; for the remainder of this review, we assume that avalanches can be assessed unambiguously.

The timescale of a plasticity rule might play a deciding role for the plasticity's ability of reaching and maintaining closeness to criticality. While short-term plasticity acts very quickly, it does not generate long-lasting, stable modifications of the network; and it can clearly serve as a feedback between activity and connection strength. Long-term plasticity, on the other side, takes longer to act, but can result in a stable convergence to critical dynamics, **Figure 2**. To summarize their properties:

- Long-term plasticity is timescale-separated from activity propagation, whereas short-term plasticity evolves at similar timescales.
- Long-term plasticity can self-organize a network to a critical state.
- Short-term plasticity constitutes an inseparable part of the network dynamics. It generates critical statistics in the data, working as a negative feedback.
- The core difference: long-term plasticity, after convergence, can be switched off and the system will remain at criticality. Switching off short-term plasticity will almost surely destroy apparent critical dynamics.
- There is a continuum of mechanisms on different timescales between these two extremes. Rules from this continuum can generate critical states that persist for varying time after rule-disabling, potentially even infinitely.

Short-Term Synaptic Plasticity

The short-term plasticity (STP) describes activity-related changes in connection strength at a timescale close to the timescale of activity propagation, typically on the order of hundreds to thousands of milliseconds. There are two dominant contributors to the short-term synaptic plasticity: the depletion of synaptic resources used for synaptic transmission, and the transient accumulation of the Ca^{2+} ions that are entering the cell after each spike [62].

At every spike, a synapse needs resources. In more detail, at the presynaptic side, vesicles from the readily-releasable pool are fused with the membrane; once fused, the vesicle is not available until it is replaced by a new one. This fast fusion, and slow filling of the readily releasable pool leads to synaptic depression, i.e., decreasing coupling strength after one or more spikes (**Figure 1A**). Synapses whose dynamics is dominated by depletion are called *depressing synapses* [63]. At the same time, for some types of synapses, recent firing increases the probability of release for the vesicles in a readily-releasable pool. This mechanism leads to the increase of the coupling strength for a range of firing frequencies. Synapses with measurable contributions from it are called *facilitating synapses* [64]. Hence, depending on their past activity, some synapses lower their release (i.e., activation) probability, others increase it, leading effectively to a weakening or strengthening of the synaptic strength.

Short-term plasticity (STP) appears to be an inevitable consequence of synaptic physiology. Nonetheless, numerous studies found that it can play an essential role in multiple brain functions. The most straightforward role is in the temporal filtering of inputs, i.e., short-term depression will result in low-pass filtering [65] that can be employed to reduce redundancy in the incoming signals [66]. Additionally, it was shown to explain aspects of working memory [67].

We consider a network of neurons (in the simplest case, non-leaky threshold integrators) that interact by exchanging spikes. The state $V_i \geq 0$ of neuron $i = 1, \ldots, N$ represents the membrane potential and obeys the following equation:

$$\dot{V}_i = \delta_{i,\zeta_\tau(t)} I + C_N \sum_{j=1}^{N} w_{ij}\left(t_{\mathrm{sp}}^j\right)\delta\left(t - t_{\mathrm{sp}}^j - \tau_d\right), \qquad (1)$$

where t_{sp}^j is the time of the spike of presynaptic neuron j, $w_{ij}\left(t_{\mathrm{sp}}^j\right)$ is the strength of synapse between neuron j and i at time t_{sp}^j. Each

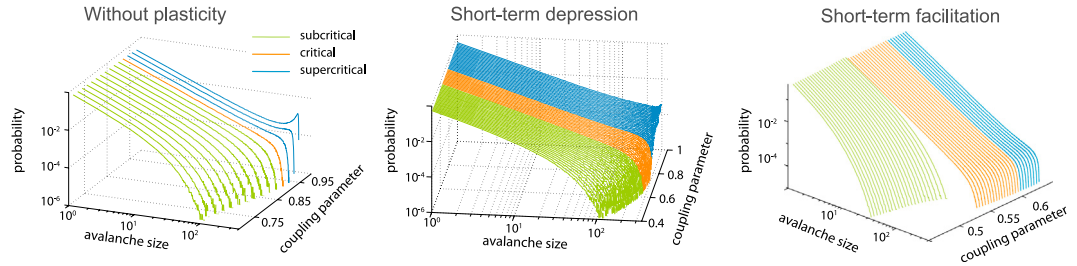

FIGURE 3 | Short-term plasticity increases the range of the near critical regime. Left: model without plasticity reaches critical point only for single coupling parameter, $w_i(t) = w$. Middle: short-term depression extends the range of parameters resulting in the critical dynamics. Fraction u_i of synaptic resources for each spike: $u_i = u = 0.2$, coupling parameter represents resting synaptic strength $w_{rest} = uJ_{rest} = 0.2J_{rest}$. An actual connection strength at time t is $w_i(t) = uJ_i(t)$, where $J_i(t)$ is described by **Eq. 2**. Different lines correspond to different values of $J_{rest} \in [2, 5]$. Right: short-term facilitation and depression together generate a discontinuous (first order - like) phase transition. Resting state fraction of synaptic resources $u_{rest} = 0.1$, coupling parameter is resting state synaptic strength $w_{rest} = u_{rest}J_{rest}$, connection strength $w_i(t) = u_i(t)J_i(t)$ is given by **Eqs 2,3**. Different lines correspond to different values of $J_{rest} \in [4.5, 6.5]$. For all simulations, network size $N = 300$, $\tau_u = \tau_J = 10N\tau$, where τ is a timescale of external drive.

neuron integrates inputs until it reaches a threshold θ. As soon as $V_i(t) > \theta$, the neuron emits a spike and delivers excitatory postsynaptic potentials to every connected neuron in the network after a fixed delay τ_d. The neurons receive external input defined by a random process $\zeta_\tau(t) \in \{1, \ldots, N\}$ that acts on a very slow timescale $\tau \gg \tau_d$ (timescale separation) by selecting a random neuron and increasing its membrane potential by an amount I. The timescale τ defines a time-step in the discrete simulation between the avalanches.

To model the changes in the connection strength associated with short-term synaptic plasticity, it is sufficient to introduce two additional dynamic variables: J_i indicates the number of synaptic resources (i.e., vesicles) available in neuron i, and u_i the fraction of these resources that is used for one spike. Coupling strength is captured by $w_i(t) = J_i(t)u_i(t)$. Each time when neuron i emits a spike at time t^i_{sp}, J_i is reduced by $J_i(t^i_{sp})u_i(t^i_{sp})$. This reflects the use of one or more vesicles to transmit the spike. After a spikes, the resources recover (i.e., the readily-releasable vesicle pool is filled again), and J_i approaches its resting value J_{rest} at a time scale τ_J.

$$\dot{J}_i = \frac{1}{\tau_J}(J_{rest} - J_i) - u_i J_i \delta\left(t - t^i_{sp}\right), \tag{2}$$

with δ denoting Dirac delta function. To add synaptic facilitation, we equip u_i with temporal dynamics, increasing it at each spike and decreasing between the spikes:

$$\dot{u}_i = \frac{1}{\tau_u}(u_{rest} - u_i) + (1 - u_i)u_{rest}\delta\left(t - t^i_{sp}\right). \tag{3}$$

Including depressing synapses (**Eq. 2**) in the integrate-and-fire neuronal network was shown to increase the range of coupling parameters leading to the power-law scaling of avalanche size distribution [68] as compared to the network without synaptic dynamics (**Figure 3**). If facilitation (**Eq. 3**) is included in the model, an additional first-order transition arises [69] (**Figure 3**). Both models have an analytical mean-field solution. In the limit of the infinite network size, the critical dynamics is obtained for any large enough coupling parameter. It was later suggested that the state reached by the system equipped with depressing synapses is not SOC, but self-organized quasi-criticality [70], as it is not locally energy preserving.

The mechanism of the near-critical region extension with depressing synapses is rather intuitive. If there is a large event propagating through the network, the massive usage of synaptic resources effectively decouples the network. This in turn prevents the next large event for a while, until the resources are recovered. At the same time, series of small events allow to build up connection strength increasing the probability of large avalanche. Thus, for the coupling parameters above the critical values, the negative feedback generated by the synaptic depression allows to bring the system closer to the critical state. Complimentary, short-term facilitation can help to shift slightly subcritical systems to a critical state.

A network with STD is essentially a two-dimensional dynamical system (with one variable corresponding to activity, and other to momentary coupling strength). Critical behavior is observed in the activity-dimension, over a long period of time while the coupling is hovering around the mean value as response to the changing activity. If the plasticity is "switched off", the system may be close to–or relatively far from the critical point of the networks. The probability that the system happens to be precisely at its critical state when plasticity is switched off goes to zero, because 1) criticality only presents one point in this one-dimensional phase transition, and 2) for the large system size, already the smallest parameter deviation results in a big difference in the observed avalanche distribution, rendering the probability to switch off plasticity at the moment of critical coupling strength effectively 0.

In critical systems, not only the avalanche size distribution, but also the absence or presence of correlation between the avalanches are of interest. Already in the classical Bak-Tang-Wiesenfeld model [40], subsequent avalanche sizes are not statistically independent, whereas in the branching process they are. Hence, the correlation structure of subsequent avalanche sizes allows inference about the underlying model and self-organization mechanisms. In the presence of such correlations, fitting the avalanche distributions and

investigating power-law statistics should also be applied properly [71]. For models with short-term plasticity, both the avalanche sizes and inter-avalanche intervals are correlated, and similar correlations were observed in the neuronal data *in vitro* [72].

After the first publication [73], short-term depression was employed in multiple models discussing other mechanisms or different model for individual neurons. To name just a few: in binary probabilistic networks [74], in networks with long-term plasticity [75, 76], in spatially pre-structured networks [77, 78]. In one of the few studies using leaky integrate-and-fire neurons, short term depression was also found to result in critical dynamics if neuronal avalanches are defined by following the causal activation chains between the neurons [79]. However, it was shown later that the causal definition of avalanches will lead to power-law statistics even in clearly non-critical systems [80]. In all cases, the short-term plasticity contributes to the generation of a stable critical regime for a broad parameter range.

Long-Term Synaptic Plasticity and Network Reorganization

Long-term modifications in neuronal networks are created by two mechanisms: long-term synaptic plasticity and structural plasticity (i.e., changes of the topology). With long-term synaptic plasticity, synaptic weights change over a timescale of hours or slower, but the adjacency matrix of the network remains unchanged. However, with structural plasticity, new synapses are created or removed. Both these mechanisms can contribute to self-organizing the network dynamics toward or away from criticality.

Three types of long-term synaptic plasticity have been proposed as possible mechanisms for SOC: Hebbian plasticity, Spike-timing-dependent plasticity (STDP) and homeostatic plasticity. In Hebbian plasticity connections between near-synchronously active neurons are strengthened. In STDP, a temporally asymmetric rule is applied, where weights are strengthened or weakened depending on the order of pre- and post-synaptic spike-times. Last, homeostatic plasticity adapts the synaptic strength as a negative feedback, decreasing excitatory synapses if the firing rate is too high, and increasing it otherwise. Thereby, it stabilizes the network's firing rate. In the following, we will discuss how each of these mechanisms can contribute to creating self-organized critical dynamics and deviations thereof.

Hebbian-Like Plasticity

Hebbian plasticity is typically formulated in a slogan-like form: Neurons that fire together, wire together. This means that connections between neurons with similar spike-timing will be strengthened. This rule can imprint stable attractors into the network's dynamics, constituting the best candidate mechanism for memory formation. Hebbian plasticity in its standard form does not reduce coupling strength, thus without additional stabilization mechanisms Hebbian plasticity leads to runaway excitation. Additionally, presence of stable attractors makes it hard to maintain the scale-free distribution of avalanche sizes.

The first papers uniting Hebbian-like plasticity and criticality came from Lucilla de Arcangelis' and Hans J. Herrmann's labs [81–83]. In a series of publications, they demonstrated that a network of non-leaky integrators, equipped with plasticity and stabilizing synaptic scaling develops both power-law scaling of avalanches (with exponent 1.2 or 1.5 depending on the external drive) and power-law scaling of spectral density [81, 82]. In the follow up paper, they realized multiple logical gates using additional supervised learning paradigm [83].

Using Hebbian-like plasticity to imprint patterns in the network and simultaneously maintain critical dynamics is a very non-trivial task. Uhlig et al. [84] achieved it by alternating Hebbian learning epochs with the epochs of normalizing synaptic strength to return to a critical state. The memory capacity of the trained network was close to the maximal possible capacity and remain close to criticality. However, the network without homeostatic regulation toward a critical state achieved better retrieval. This might point to the possibility that classical criticality is not an optimal substrate for storing simple memories as attractors. However, in the so-far unstudied setting of storing memories as dynamic attractors, the critical system's sensitivity might make it the best solution.

Spike-timing-dependent Plasticity

Spike-timing-dependent plasticity (STDP) is a form of activity-dependent plasticity in which synaptic strength is adjusted as a function of timing of spikes in pre- and post-synaptic neurons. It can appear both in the form of long-term potentiation (LTP) or long-term depression (LTD) [85]. Suppose the post-synaptic neuron fires shortly after the pre-synaptic neuron. In that case, the connection from pre-to the post-synaptic neuron is strengthened (LTP), but if the post-synaptic neuron fires after the pre-synaptic neuron, the connection is weakened (LTP), **Figure 1B**. Millisecond temporal resolution measurements of pre- and postsynaptic spikes experimentally by Markram et al. [86–88] together with theoretical model proposed by Gerstner et al. [89] put forward STDP as a mechanism for sequence learning. Shortly after that other theoretical studies [90–94] incorporated STDP in their models as a local learning rule.

Different functional forms of STDP are observed in different brain areas and across various species (for a review see [95]). For example, STDP in hippocampal excitatory synapses appear to have equal temporal windows for LTD and LTP [86, 96, 97], while in neocortical synapses it exhibits longer LTD temporal windows [98, 99]. Interestingly, an even broader variety of different STDP kernels were observed for inhibitory connections [100].

The classical STDP is often modeled by modifying the synaptic weight w_{ij} from pre-synptic neuron j to post-synaptic neuron i as

$$\Delta w_{ij} = \begin{cases} A_+\left(w_{ij}\right)\exp\left(\dfrac{t_j - t_i}{\tau_+}\right) & t_j < t_i \\ -A_-\left(w_{ij}\right)\exp\left(\dfrac{t_j - t_i}{\tau_-}\right) & t_j \geq t_i \end{cases} \tag{4}$$

where t_i and t_j are latest spikes of neurons i and j and τ_+ and τ_- are LTP and LTD time constants. Weight dependence functions $A_+(w_{ij})$ and $A_-(w_{ij})$ control the synaptic weights to stay between 0 and w_{max}, which is required from the biological point of view. Two families of weight dependence functions have been

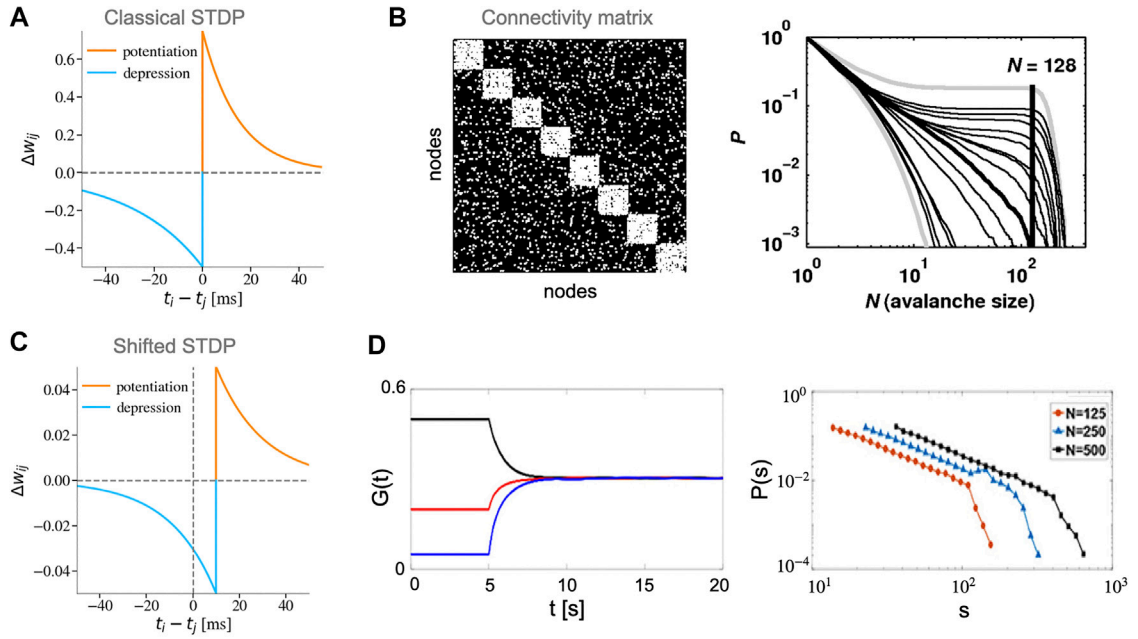

FIGURE 4 | Different STDP rules and their role in creating SOC. **(A)** Classical STDP rule with asymmetric temporal windows (STDP parameters: $\tau_+ = 15$ ms, $\tau_- = 30$ ms, $w_{max} = 1$, $\eta_+ = 0.75$, $\eta_- = 0.5$). **(B)** A modular network that is rewired to create particular inter- and intra-modules connections (left) combined with classical STDP gives rise to dynamics characterized by power-law avalanche-size distribution (right, thick line). Non-power-law avalanche-size distributions correspond to other rewiring probabilities with the gray lines showing the two extremes of ordered and random networks (reproduced from [101] under CC BY license). **(C)** Shifted STDP rule (STDP parameters: $\tau_+ = \tau_- = 20$ ms, $w_{max} = 0.6$, $\eta_+ = \eta_- = 0.05$, time-shift = 10 ms). **(D) (left)** Average coupling strength G(t) in a network with shifted STDP will converge to a steady state value. **(right)** Setting the STDP time-shift to $\tau = 10$ ms (equal to axonal delay time-constant) leads to emergence of power-law avalanche-size distributions that scale with the system size (reproduced from [102] under CC BY license). N indicates the network size.

introduced: 1) soft weight bounds (multiplicative weights) [103], 2) hard weight bounds (additive weights) [89]. Soft weight bounds are implemented as

$$A_+(w_{ij}) = (w_{max} - w_{ij})\eta_+, \quad A_-(w_{ij}) = w_{ij}\eta_-, \tag{5}$$

where $\eta_+ < 1$ and $\eta_- < 1$ are positive constants. Weight dependence functions with hard bounds are defined using a Heaviside step function $H(x)$ as

$$A_+(w_{ij}) = H(w_{max} - w_{ij})\eta_+, \quad A_-(w_{ij}) = H(-w_{ij})\eta_-. \tag{6}$$

There are two types of critical points that can be attained by networks with STDP. The first transition type is characterized by statistics of weights in the converged network. For instance, at this point synaptic coupling strengths [104] or the fluctuations in coupling strengths [105] follow a power-law distribution. The second transition type is related to network's dynamics, it is characterized by presence of scale-free avalanches [101, 102, 106]. In these models STDP is usually accompanied by fine-tuning of some parameters or properties of the network to create critical dynamics. This suggests that STDP alone might not be sufficient for SOC.

Rubinov et al. [101] developed a leaky integrate-and-fire (LIF) network model with modular connectivity (**Figures 4A,B**). In their model, STDP only gives rise to power-law distributions of avalanches when the ratio of connection between and within modules is tuned to a particular value. Their results were unchanged for STDP rules with both soft and hard bounds. However, they reported that switching off the STDP dynamics leads to the deterioration of the critical state, which disappears completely after a while. This property places the model in-between truly long-term and short-term mechanisms. Additionally, avalanches were defined based on the activity of modules (simultaneous activation of a large number of neurons within a module). In this modular definition of activity, SOC is achieved by potentiating within-module synaptic weights during module activation and depression of weights in-between module activations. While the module-based definition of avalanches could be relevant to the dynamics of cell-assemblies in the brain or more coarse-grained activity such as local field potentials (LFP), further investigation of avalanches statistics based on individual neurons activity is required.

Observation of power-law avalanche distributions was later extended to a network of Izhikevich neurons with a temporally shifted soft-bound STDP rule [102] (**Figures 4C,D**). The shift in the boundary between potentiation and depression reduces the immediate synchronization between pre- and post-synaptic neurons that eventually stabilizes the synaptic weights and the post-synaptic firing rate similar to a homeostasis regulation [107]. In the model, the STDP time-shift is set to be equal to the axonal delay time constant that also acts as a control parameter for the state of dynamics in the network. The authors showed that for a physiologically plausible time constant ($\tau = 10$ ms) network dynamics self-organizes to the edge of synchronization

transition point. At this transition point, distribution of size and duration of avalanches follow a power-law-like distribution. They showed that the power-law exponents can be approximately fitted in the standard scaling relation required for a critical system [59]. However, since they defined avalanches based on thresholding of the global network firing, estimated avalanche distributions and fitted exponents might be generated by the thresholding [55].

Homeostatic Regulations

Homeostatic plasticity is a mechanism that regulates neural activity on a long timescale [108–113]. In a nutshell, one assumes that every neuron has some intrinsic target activity rate. Homeostatic plasticity then presents a negative feedback loop that maintains that target rate and thereby stabilize network dynamics. In general, it reduces (increases) excitatory synaptic strength or neural excitability if the spike rate is above (below) a target rate, **Figure 1C**. This mechanism can stabilize a potentially unconstrained positive feedback loop through Hebbian-type plasticity [114–121]. The physiological mechanisms of homeostatic plasticity are not fully disentangled yet. It can be implemented by a number of physiological candidate mechanisms, such as redistribution of synaptic efficacy [63, 122], synaptic scaling [108–110, 123], adaptation of membrane excitability [112, 124], or through interactions with glial cells [125, 126]. Recent results highlight the involvement of homeostatic plasticity in generating robust yet complex dynamics in recurrent networks [127–129].

In models, homeostatic plasticity was identified as one of the primary candidates to tune networks to criticality. The mechanism of it is straightforward: taking the analogy of the branching process, where one neuron (or unit) on average activates m neurons in the subsequent time step, the stable sustained activity that is the goal function of the homeostatic regulation requires $m = m_c = 1$ which is precisely the critical value [130]. In 2007, Levina and colleagues made use of this principle. They devised a homeostasis-like rule, where all outgoing weights were normalized such that each neuron in the fully connected network activated on average $m = 1$ neurons in the next time step [131, 132]. Thereby, the network tuned itself to a critical state.

Similar ideas have been proposed and implemented first in simple models [133] and later also in more detailed models. In the latter, homeostatic regulation tunes the ratio between excitatory and inhibitory synaptic strength [53, 129, 134–136]. It then turned out that due to the diverging temporal correlations, which emerge at criticality, the time-scale of homeostasis would also have to diverge [135]. If the time-scale of the homeostasis is faster than the timescale of the dynamics, then the network does not converge to a critical point, but hovers around it, potentially resembling supercritical dynamics [14, 135]. It is now clear that a self-organization to a critical state (instead of hovering around a critical state) requires that the timescale of homeostasis is slower than that of the network dynamics [14, 135].

Whether a system self-organizes to a critical state, or to a sub- or supercritical one is determined by a further parameter, which has been overlooked for a while: The rate of external input. This rate should be close to zero in critical systems to foster a separation of time scales [52, 137]. Hence, basically all models that studied criticality were implemented with a vanishing external input rate. In neural systems, however, sensory input, spontaneous activation, and other brain areas provide continuous drive, and hence a separation of timescales is typically not realized [52]. As a consequence, avalanches merge, coalesce, and separate [51, 56, 137]. It turns out that under homeostatic plasticity, the external input strength can become a control parameter for the dynamics [14]: If the input strength is high, the system self-organizes to a subcritical state (**Figure 5**, right). With weaker input, the network approaches a critical state (**Figure 5**, middle). However when the input is too weak, pauses between bursts get so long that the timescale of the homeostasis again plays a role - and the network does not converge to a single state but hovers between sub- and supercritical dynamics (**Figure 5**, left). This study shows that under homeostasis the external input strength determines the collective dynamics of the network.

Assuming that *in vivo*, cortical activity is subject to some level of non-zero input, one expects a sightly subcritical state - which is indeed found consistently across different animals [14, 17, 30, 139, 140]. *In vitro* systems, however, which lack external input, are expected to show bursty avalanche dynamics, potentially hovering around a critical point with excursions to supercriticality [14, 136]. Such burst behavior is indeed characteristic for *in vitro* systems [8, 14, 19, 59].

Recently, Ma and colleagues characterized in experiments how homeostatic scaling might re-establish close-to-critical dynamics *in vivo* after perturbing sensory input [139] (**Figure 6**). The past theoretical results would predict that after blocking sensory input in a living animal, the spike rate should diminish, and with the time-scale of homeostatic plasticity, a state close to critical or even super-critical would be obtained [14, 136]. In a recent experiment, however, the behavior is more intricate. Soon after blocking visual input, the network became subcritical (branching ratio m smaller than one [17, 130]) and not supercritical. It then recovered to a close-to-critical state again within two days, potentially compensating the lack of input by coupling stronger to other brain areas. The avalanche size distributions agree with the transient deviation to subcritical dynamics. This deviation to subcriticality is the opposite of what one might have expected under reduced input, and apparently cannot be attributed to concurrent rate changes (which otherwise can challenge the identification of avalanche distributions [47]): The firing rate only started to decrease one day after blocking visual input. The authors attribute this delay in rate decay to excitation and inhibition reacting with different time constants to the blocking of visual input [139].

Overall, although the exact implementation of the homeostatic plasticity on the pre- and postsynaptic sides of excitatory and inhibitory neurons remains a topic of current research, the general mechanism allows for the long-term convergence of the system to the critical point, **Figure 1B**. Homeostasis importantly contributes to many models including different learning mechanisms, stabilizing them.

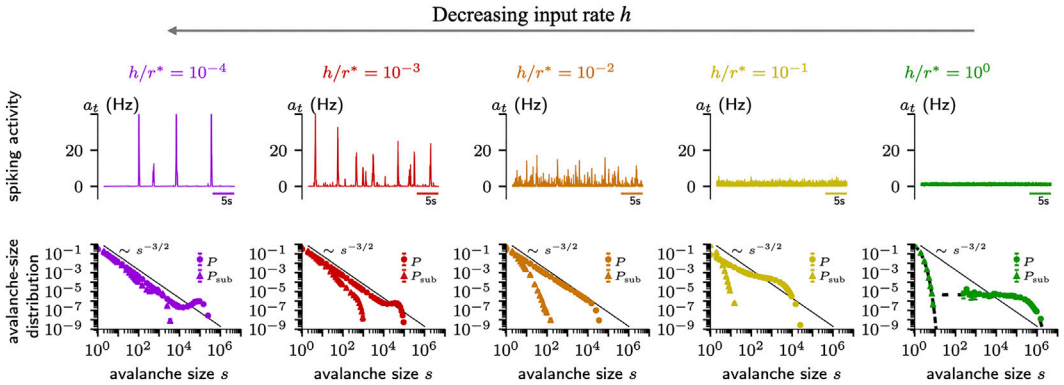

FIGURE 5 | Homeostatic plasticity regulation can create different types of dynamics in the network depending on input strength h, target firing rate r^* and recurrent interactions. **(top)** example spiking activity traces. **(bottom)** full-sampled (circles) and subsampled (triangles) avalanche size distributions averaged over 12 independent simulations. From left to right: network generates supercritical bursting ($m > 1$, $h/r^* \leq 10^{-3}$, purple-red), fluctuating ($m \approx 0.99$, $h/r^* \approx 10^{-2}$ and $m \approx 0.9$, $h/r^* \approx 10^{-1}$, orange-yellow) and irregular ($m \approx 0$, $h/r^* = 1$, green) activity. Solid lines show the critical branching process avalanche-size distribution $P(s) \propto s^{-3/2}$ [130] and dashed line is the analytical avalanche-size distribution of a Poisson process [47] (reproduced from [14] by permission).

Network Rewiring and Growth

Specific network structures such as small-world [68, 81, 141, 142] or scale-free [75, 83, 143–146] networks were found to be beneficial for the emergence of critical dynamics. These network structures are in particular interesting since they have been also observed in both anatomical and functional brain networks [147–150]. To create such topologies in neural networks long-term plasticity mechanisms have been used. For instance, scale-free and small-world structures emerge as a consequence of STDP between the neurons [105]. In addition, Hebbian plasticity can generate small-world networks [151].

Another prominent form of network structures are hierarchical modular networks (HMN) that can sustain critical regime for a broader range of control parameters [77, 101, 152]. Unlike a conventional critical point where control parameter at a single value leads to scale-free avalanches, in HMNs power-law scaling emerges for a wide range of parameters. This extended critical-like region can correspond to a Griffits phase in statistical mechanics [152]. Different rewiring algorithms have been proposed to generate HMN from an initially randomly connected [77] or a fully connected modular network [101, 152].

Experimental observations in developing neural cultures suggest that connections between neurons grow in a way such that the dynamics of the network eventually self-organizes to a critical point (i.e., observation of scale-free avalanches) [18, 19]. Motivated by this observation, different models have been developed to explain how neural networks can grow connections to achieve and maintain such critical dynamics using homeostatic structural plasticity [19, 153–158] (for a review see [159]). In addition to homeostatic plasticity, other rewiring rules inspired by Hebbian learning were also proposed to bring the network dynamics toward criticality [160–162]. However, implementation of such network reorganizations seems to be less biologically plausible.

In most of the models with homeostatic structural plasticity, the growth of neuronal axons and dendrites is modeled as an expanding (or shrinking) circular neurite field. The growth of the neurite field for each neuron is defined based on the neuron's firing rate (or internal Ca^{2+} concentration). A firing rate below the homeostatic target rate (f_{target}) expands the neurite field, and a firing rate above the homeostatic target rate shrinks it. In addition, when neurite fields of two neurons overlap a connection between them will be created with a strength proportional to the overlapped area. Kalle Kossio et al. [156] showed analytically that if the homeostatic target rate is significantly larger than the spontaneous firing rate of the network, such growth mechanism would bring the network dynamics to a critical point with scale-free avalanches (**Figure 7**). However, for a small target rate subcritical dynamics will arise.

Tetzlaff et al. [19] proposed a slightly different mechanism where two neurites fields are assigned separately for axonal growth and dendritic growth to each neuron. While changes in the size of dendritic neurite fields follows the same rule as explained above, neurite fields of axons follow an exact opposite rule. The model simulations start with all excitatoryry neurons, but in the middle phase 20% of the neurons are changed into inhibitory ones. This switch is motivated by the transformation of GABA neurotransmitters from excitatory to inhibitory during development [163]. They showed that when the network dynamics converge to a steady-state regime, avalanche-size distributions follow a power-law.

HYBRID MECHANISMS OF LEARNING AND TASK PERFORMANCE

In living neural networks, multiple plasticity mechanisms occur simultaneously. The joint contribution of diverse mechanisms has been studied in the context of criticality in a set of models [75, 164, 165]. A combination with homeostatic-like regulation is typically necessary to stabilize Hebbian or spike-timing-dependent plasticity (STDP), e.g., learning binary tasks such as an XOR rule with Hebbian plasticity [75] or sequence learning

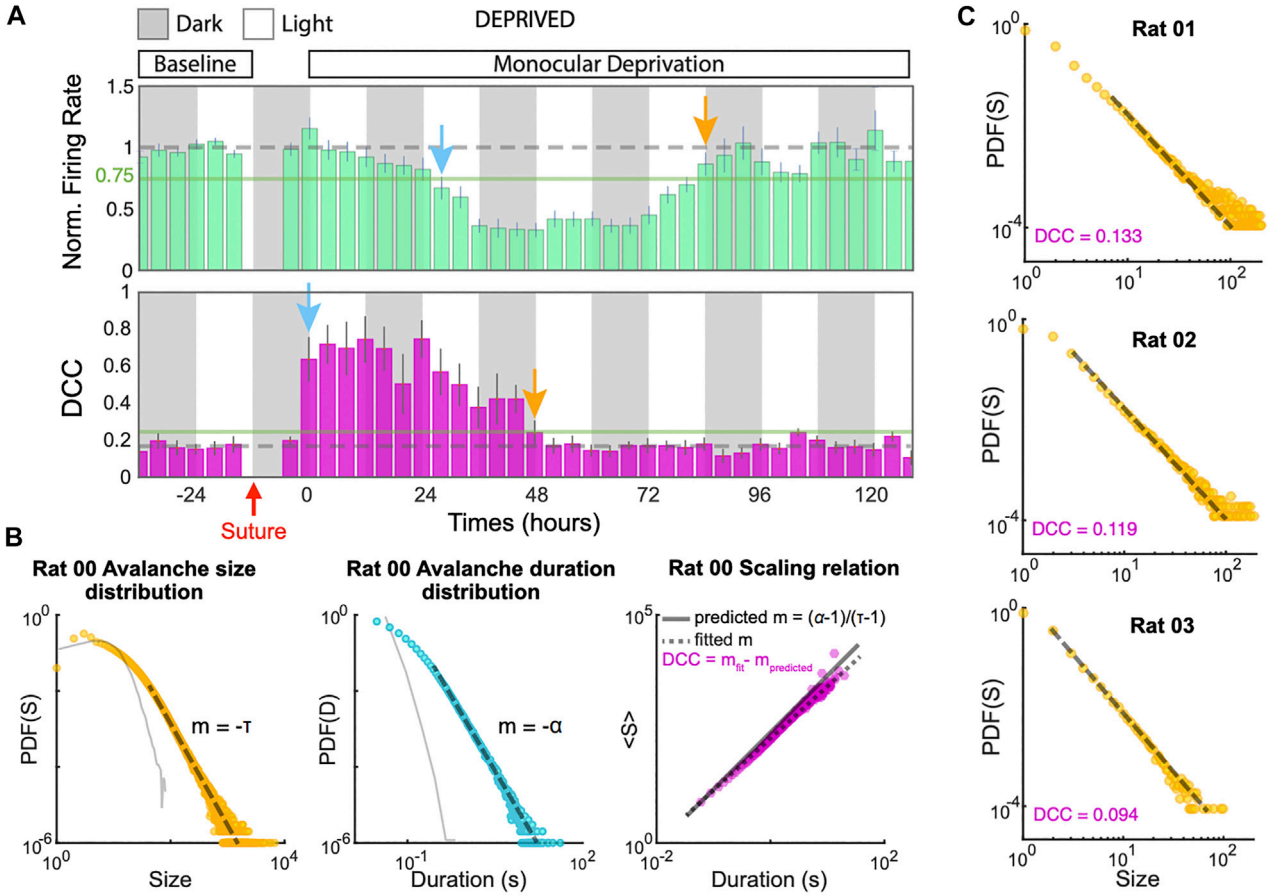

FIGURE 6 | Homeostatic regulations in visual cortex of rats tune the network dynamics to near criticality. **(A) (top)** Firing rate of excitatory neurons during 7 days of recording exhibit a biphasic response to monocular deprivation (MD). After 37 h following MD firing rates were maximally suppressed (blue arrow) but came back to baseline by 84 h (orange arrow). Rates are normalized to 24 h of baseline recordings before MD. **(bottom)** Measuring the distance to criticality coefficient (DCC) in the same recordings. The mean DCC was significantly increased (blue arrow) upon MD, but was restored to baseline levels (near-critical regime) at 48 h (orange arrow). **(B)** An example of estimation of DDC **(right)** using the power-law exponents from the avalanche-size distribution **(left)** and the avalanche-duration distribution (middle). Solid gray traces show avalanche distributions in shuffled data. DCC is defined as the difference between the empirical scaling (dashed gray line) and the theoretical value (solid gray line) predicted from the exponents for a critical system as the displayed formula [59]. **(C)** Avalanche-size distributions and DCCs computed from 4 h of single-unit data in three example animals show the diversity of experimental observations (reproduced from the bioRxiv version of [139] under CC-BY-NC-ND 4.0 international license).

with STDP [166–170]. These classic plasticity rules have been paired with regulatory normalization of synaptic weights to avoid a self-amplified destabilization [119–121]. Additionally, short-term synaptic depression stabilizes the critical regime, and if it is augmented with meta-plasticity [164] the stability interval is increased even further, possibly allowing for stable learning.

In a series of studies, Scarpetta and colleagues investigated how sequences can be memorized by STDP, while criticality is maintained [166–168]. By controlling the excitability of the neurons, they achieved a balance between partial replays and noise resulting in power-law distributed avalanche sizes and durations [166]. They later reformulated the model and used the average connection strength as a control parameter, obtaining similar results [167, 168]. Whereas STDP fosters the formation of sequence memory, Hebbian plasticity is known to form assemblies (associations), and in the Hopfield network enables memory completion and recall [171]. A number of studies showed that the formation of such Hebbian ensembles is also possible while maintaining critical dynamics [84, 168, 172]. These studies show that critical dynamics can be maintained in networks, which are learning classical tasks.

The critical network can support not only memory but also real computations such as performing logical operations (OR, AND or even XOR) [75, 83]. To achieve this, the authors build upon the model with Hebbian-like plasticity that previously shown to bring the network to a critical point [81]. They added the central learning signal [173], resembling dopaminergic neuromodulation. Authors demonstrated both with [75] and without [83] short-term plasticity that the network can be trained to solve XOR-gate task.

These examples lead to the natural question of whether criticality is always optimal for learning. The criticality hypothesis attracted much attention, precisely because models at criticality show properties supporting optimal task

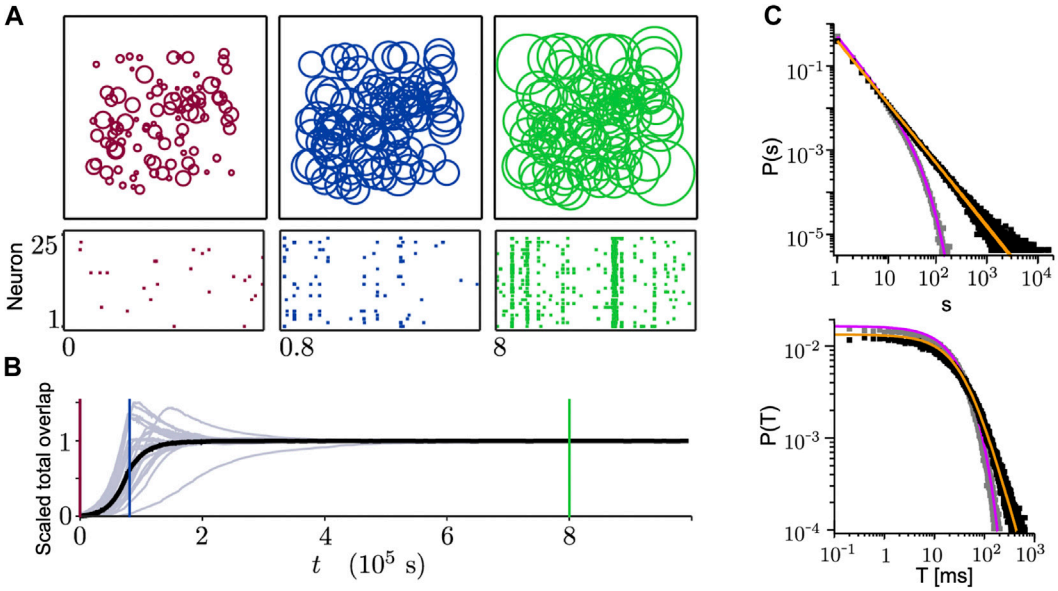

FIGURE 7 | Growing connections based on the homeostatic structural plasticity in a network model leads to SOC. **(A)** Size of neurite fields **(top)** and spiking activity **(bottom)** change during the network growth process (from 25 sample neurons). From left to right: initial state (red), state with average growth (blue), stationary state reaching the homeostatic target rate (green). **(B)** Corresponding scaled total overlaps of 25 sample neurons (gray) and the population average (black) to the three different time points in **(A)**. **(C)** Avalanche-size **(top)** and avalanche-duration **(bottom)** distributions. If the homeostatic target rate (f_{target} = 2 HZ) is significantly larger than the spontaneous rate (f_0 = 0.01 HZ) both distributions follow a power-law (black: simulation, orange: analytic). Small homeostatic target rate (f_{target} = 0.04 HZ) leads to subcritical dynamics (gray: simulation, pink: analytic) (reproduced from [156] with permission).

performance. A core properties of criticality is a maximization of the dynamic range [174, 175], the sensitivity to input, and diverging spatial and temporal correlation lengths [176, 177]. In recurrent network models and experiments, such boost of input sensitivity and memory have been demonstrated by tuning networks systematically toward and away from criticality [174, 178–182].

When not explicitly incorporating a mechanism that drives the network to criticality, learning networks can be pushed away from criticality to a subcritical regime [15, 16, 170, 183, 184]. This is in line with the results above that networks with homeostatic mechanisms become subcritical under increasing network input (**Figure 5**). Subcritical dynamics might indeed be favorable when reliable task performance is required, as the inherent variability of critical systems may corroborate performance variability [52, 185–190].

Recently, the optimal working points of recurrent neural networks on a neuromorphic chip were demonstrated to depend on task complexity [15, 16]. The neuromorphic chip implements spiking integrate-and-fire neurons with STDP-like depressive plasticity and slow homeostatic recovery of synaptic strength. It was found that complex tasks, which require integration of information over long time-windows, indeed profit from critical dynamics, whereas for simple tasks the optimal working point of the recurrent network was in the subcritical regime [15, 16]. Criticality thus seems to be optimal particularly when a task makes use of this large variability, or explicitly requires the long-range correlation in time or space, e.g., for active memory storage.

DISCUSSION

We summarized how different types of plasticity contribute to the convergence and maintenance of the critical state in neuronal models. The short-term plasticity rules were generally leading to hovering around the critical point, which extended the critical-like dynamics for an extensive range of parameters. The long-term homeostatic network growth and homeostatic plasticity, for some settings, could create a global attractor at the critical state. Long-term plasticity associated with learning sequences, patterns or tasks required additional mechanisms (i.e., homeostasis) to maintain criticality.

The first problem with finding the best recipe for criticality in the brain is our inability to identify the brain's state from the observations we can make. We are slowly learning how to deal with strong subsampling (under-observation) of the brain network [17, 20, 56, 191–193]. However, even if we obtained a perfectly resolved observation of all activity in the brain, we would face the problem of constant input and spontaneous activation that renders it impossible to find natural pauses between avalanches, and hence makes avalanche-based analyses ambiguous [52]. Hence, multiple avalanche-independent options were proposed as alternative assessments of criticality in the brain: 1) detrended fluctuation analysis [60] allows to capture the scale-free behavior in long-range temporal correlations of EEG/MEG data, 2) critical slowing down [194] suggests a closeness to a bifurcation point, 3) divergence of susceptibility in the maximal entropy model fitted to the neural data [195], divergence of Fisher information [196], or

the renormalization group approach [197] indicates a closeness to criticality in the sense of thermodynamic phase-transitions, and 4) estimating the branching parameter directly became feasible even from a small set of neurons; this estimate returns a quantification of the distance to criticality [17, 39]. It was recently pointed out that the results from fitting the maximal entropy models [198, 199] and coarse-graining [200, 201] based on empirical correlations should be interpreted with caution. Finding the best way to unite these definitions, and select the most suitable ones for a given experiment remains largely an open problem.

Investigating the criticality hypothesis for brain dynamics has strongly evolved in the past decades, but is far from being concluded. On the experimental side, sampling limits our access to collective neural dynamics [20, 202], and hence it is not perfectly clear yet how close to a critical point different brain areas operate. For cortex in awake animals, evidence points to a close-to-critical, but slightly subcritical state [30, 139, 140]. The precise working point might well depend on the specific brain area, cognitive state and task requirement [15, 16, 32, 35, 36, 179, 188, 190, 203–206]. Thus instead of self-organizing precisely to criticality, the brain could make use of the divergence of processing capabilities around the critical point. Thereby, each brain area might optimize its computational properties by tuning itself toward and away from criticality in a flexible, adaptive manner [188]. In the past decades, the community has revealed the local plasticity rules that would enable such a tuning and adaption of the working point. Unlike classical physics systems, which are constrained by conservation laws, the brain and the propagation of neural activity is more flexible and hence can adhere in principle a large repertoire of working points - depending on task requirements.

Criticality has been very inspiring to understand brain dynamics and function. We assume that being perfectly critical is not an optimal solution for many brain areas, during different task epochs. However, studying and modeling brain dynamics from a criticality point of view allows to make sense of the high-dimensional neural data, its large variability, and to formulate meaningful hypothesis about dynamics and computation, many of which still wait to be tested.

AUTHOR CONTRIBUTIONS

RZ, VP, and AL designed the research. RZ and AL prepared the figures. All authors contributed to writing and reviewing the manuscript.

FUNDING

This work was supported by a Sofja Kovalevskaja Award from the Alexander von Humboldt Foundation, endowed by the Federal Ministry of Education and Research (RZ, AL), Max Planck Society (VP), **SMART***START* 2 program provided by Bernstein Center for Computational Neuroscience and Volkswagen Foundation (RZ). We acknowledge the support from the BMBF through the Tübingen AI Center (FKZ: 01IS18039B).

ACKNOWLEDGMENTS

We are very thankful to SK, MG, and SA for reading the initial version of the manuscript and their constructive comments. The authors thank the International Max Planck Research School for the Mechanisms of Mental Function and Dysfunction (IMPRS-MMFD) for supporting RZ. We acknowledge support by Open Access Publishing Fund of University of Tübingen.

REFERENCES

1. Bak P, Tang C, and Wiesenfeld K. Self-organized criticality. *Phys Rev A* (1988) 38:364–74. doi:10.1103/PhysRevA.38.364
2. Gutenberg B, and Richter C. *Seismicity of the earth*. New York: Geological Society of America (1941), p. 1–126.
3. Gutenberg B, and Richter CF. Earthquake magnitude, intensity, energy, and acceleration(Second paper). *Bull Seismol Soc Am* (1956) 46:105–45.
4. Birkeland KW, and Landry CC. Power-laws and snow avalanches. *Geophys Res Lett* (2002) 29:49 1–49 3. doi:10.1029/2001GL014623
5. Malamud BD, Morein G, and Turcotte DL. Forest fires: an example of self-organized critical behavior. *Science* (1998) 281:1840–2. doi:10.1126/science.281.5384.1840
6. Scheidegger A. A complete thermodynamic analogy for landscape evolution. *Bull Int Assoc Sci Hydrol* (1967) 12:57–62. doi:10.1080/02626667709493550
7. Takayasu H, and Inaoka H. New type of self-organized criticality in a model of erosion. *Phys Rev Lett* (1992) 68:966–9. doi:10.1103/PhysRevLett.68.966
8. Beggs J, and Plenz D. Neuronal avalanches in neocortical circuits. *J Neurosci* (2003) 23:11167–77. doi:10.1523/JNEUROSCI.23-35-11167.2003
9. Chen DM, Wu S, Guo A, and Yang ZR. Self-organized criticality in a cellular automaton model of pulse-coupled integrate-and-fire neurons. *J Phys A: Math Gen* (1995) 28:5177–82. doi:10.1088/0305-4470/28/18/009
10. Corral Á, Pérez CJ, Diaz-Guilera A, and Arenas A. Self-organized criticality and synchronization in a lattice model of integrate-and-fire oscillators. *Phys Rev Lett* (1995) 74:118–21. doi:10.1103/PhysRevLett.74.118
11. Herz AVM, and Hopfield JJ. Earthquake cycles and neural reverberations: collective oscillations in systems with pulse-coupled threshold elements. *Phys Rev Lett* (1995) 75:1222–5. doi:10.1103/PhysRevLett.75.1222
12. Eurich CW, Herrmann JM, and Ernst UA. Finite-size effects of avalanche dynamics. *Phys Rev E* (2002) 66:066137. doi:10.1103/PhysRevE.66.066137
13. Haldeman C, and Beggs J. Critical branching captures activity in living neural networks and maximizes the number of metastable states. *Phys Rev Lett* (2005) 94:058101. doi:10.1103/PhysRevLett.94.058101
14. Zierenberg J, Wilting J, and Priesemann V. Homeostatic plasticity and external input shape neural network dynamics. *Phys Rev X* (2018) 8:031018. doi:10.1103/PhysRevX.8.031018
15. Cramer B, Stöckel D, Kreft M, Wibral M, Schemmel J, Meier K, et al. Control of criticality and computation in spiking neuromorphic networks with plasticity. *Nat Commun* (2020) 11:2853. doi:10.1038/s41467-020-16548-3
16. Prosi J, Khajehabdollahi S, Giannakakis E, Martius G, and Levina A. The dynamical regime and its importance for evolvability, task performance and generalization. *arXiv* [preprint arXiv:2103.12184] (2021).
17. Wilting J, and Priesemann V. Inferring collective dynamical states from widely unobserved systems. *Nat Commun* (2018) 9:2325. doi:10.1038/s41467-018-04725-4

18. Yada Y, Mita T, Sanada A, Yano R, Kanzaki R, Bakkum DJ, et al. Development of neural population activity toward self-organized criticality. *Neuroscience* (2017) 343:55–65. doi:10.1016/j.neuroscience.2016.11.031
19. Tetzlaff C, Okujeni S, Egert U, Wörgötter F, and Butz M. Self-organized criticality in developing neuronal networks. *PLoS Comput Biol* (2010) 6: e1001013. doi:10.1371/journal.pcbi.1001013
20. Levina A, and Priesemann V. Subsampling scaling. *Nat Commun* (2017) 8: 15140. doi:10.1038/ncomms15140
21. Priesemann V, Valderrama M, Wibral M, and Le Van Quyen M. Neuronal avalanches differ from wakefulness to deep sleep–evidence from intracranial depth recordings in humans. *PLoS Comput Biol* (2013) 9:e1002985. doi:10.1371/journal.pcbi.1002985
22. Lo CC, Chou T, Penzel T, Scammell TE, Strecker RE, Stanley HE, et al. Common scale-invariant patterns of sleep–wake transitions across mammalian species. *Proc Natl Acad Sci* (2004) 101:17545–8. doi:10.1073/pnas.0408242101
23. Allegrini P, Paradisi P, Menicucci D, Laurino M, Piarulli A, and Gemignani A. Self-organized dynamical complexity in human wakefulness and sleep: different critical brain-activity feedback for conscious and unconscious states. *Phys Rev E* (2015) 92:032808. doi:10.1103/PhysRevE.92.032808
24. Bocaccio H, Pallavicini C, Castro MN, Sánchez SM, De Pino G, Laufs H, et al. The avalanche-like behaviour of large-scale haemodynamic activity from wakefulness to deep sleep. *J R Soc Interf* (2019) 16:20190262. doi:10.1098/rsif.2019.0262
25. Lombardi F, Gómez-Extremera M, Bernaola-Galván P, Vetrivelan R, Saper CB, Scammell TE, et al. Critical dynamics and coupling in bursts of cortical rhythms indicate non-homeostatic mechanism for sleep-stage transitions and dual role of VLPO neurons in both sleep and wake. *J Neurosci* (2020) 40: 171–90. doi:10.1523/JNEUROSCI.1278-19.2019
26. Meisel C., 117. Antiepileptic drugs induce subcritical dynamics in human cortical networks. *Proc Natl Acad Sci* (2020). p. 11118–25. ISBN: 9781911461111. doi:10.1073/pnas.1911461117
27. Scheffer M, Bascompte J, Brock WA, Brovkin V, Carpenter SR, Dakos V, et al. Early-warning signals for critical transitions. *Nature* (2009) 461:53–9. doi:10.1038/nature08227
28. Meisel C, Storch A, Hallmeyer-Elgner S, Bullmore E, and Gross T. Failure of adaptive self-organized criticality during epileptic seizure attacks. *PLoS Comput Biol* (2012) 8:e1002312. doi:10.1371/journal.pcbi.1002312
29. Arviv O, Medvedovsky M, Sheintuch L, Goldstein A, and Shriki O. Deviations from critical dynamics in interictal epileptiform activity. *J Neurosci* (2016) 36: 12276–92. doi:10.1523/JNEUROSCI.0809-16.2016
30. Hagemann A, Wilting J, Samimizad B, Mormann F, and Priesemann V. No evidence that epilepsy impacts criticality in pre-seizure single-neuron activity of human cortex. *arXiv: 2004.10642 [physics, q-bio]* (2020).
31. Deco G, and Jirsa VK. Ongoing cortical activity at rest: criticality, multistability, and ghost attractors. *J Neurosci* (2012) 32:3366–75. doi:10.1523/JNEUROSCI.2523-11.2012
32. Tagliazucchi E, von Wegner F, Morzelewski A, Brodbeck V, Jahnke K, and Laufs H. Breakdown of long-range temporal dependence in default mode and attention networks during deep sleep. *Proc Natl Acad Sci* (2013) 110(38): 15419–24. doi:10.1073/pnas.1312848110
33. Hahn G, Ponce-Alvarez A, Monier C, Benvenuti G, Kumar A, Chavane F, et al. Spontaneous cortical activity is transiently poised close to criticality. *PLoS Comput Biol* (2017) 13:e1005543. doi:10.1371/journal.pcbi.1005543
34. Petermann T, Thiagarajan TC, Lebedev MA, Nicolelis MA, Chialvo DR, and Plenz D. Spontaneous cortical activity in awake monkeys composed of neuronal avalanches. *Proc Natl Acad Sci USA* (2009) 106:15921–6. doi:10.1073/pnas.0904089106
35. Yu S, Ribeiro TL, Meisel C, Chou S, Mitz A, Saunders R, et al. Maintained avalanche dynamics during task-induced changes of neuronal activity in nonhuman primates. *eLife Sci* (2017) 6:e27119. doi:10.7554/eLife.27119
36. Shew WL, Clawson WP, Pobst J, Karimipanah Y, Wright NC, and Wessel R. Adaptation to sensory input tunes visual cortex to criticality. *Nat Phys* (2015) 11:659–63. doi:10.1038/nphys3370
37. Gautam SH, Hoang TT, McClanahan K, Grady SK, and Shew WL. Maximizing sensory dynamic range by tuning the cortical state to criticality. *PLoS Comput Biol* (2015) 11:e1004576. doi:10.1371/journal.pcbi.1004576
38. Stephani T, Waterstraat G, Haufe S, Curio G, Villringer A, and Nikulin VV. Temporal signatures of criticality in human cortical excitability as probed by early somatosensory responses. *J Neurosci* (2020) 40:6572–83. doi:10.1523/JNEUROSCI.0241-20.2020
39. de Heuvel J, Wilting J, Becker M, Priesemann V, and Zierenberg J. Characterizing spreading dynamics of subsampled systems with nonstationary external input. *Phys Rev E* (2020) 102:040301. doi:10.1103/PhysRevE.102.040301
40. Bak P, Tang C, and Wiesenfeld K. Self-organized criticality: an explanation of noise. *Phys Rev Lett* (1987) 59:381–4. doi:10.1103/PhysRevLett.59.381
41. Dhar D, and Ramaswamy R. Exactly solved model of self-organized critical phenomena. *Phys Rev Lett* (1989) 63:1659–62. doi:10.1103/PhysRevLett.63.1659
42. Manna S. Two-state model of self-organized criticality. *J Phys A: Math Gen Phy* (1991) 24:L363. doi:10.1088/0305-4470/24/7/009
43. Drossel B, and Schwabl F. Self-organized criticality in a forest-fire model. *Physica A: Stat Mech its Appl* (1992) 191:47–50. doi:10.1016/0378-4371(92)90504-J
44. Munoz MA. Colloquium: criticality and dynamical scaling in living systems. *Rev Mod Phys* (2018) 90:031001. doi:10.1103/RevModPhys.90.031001
45. Touboul J, and Destexhe A. Power-law statistics and universal scaling in the absence of criticality. *Phys Rev E* (2017) 95:012413. doi:10.1103/PhysRevE.95.012413
46. Faqeeh A, Osat S, Radicchi F, and Gleeson JP. Emergence of power laws in noncritical neuronal systems. *Phys Rev E* (2019) 100:010401. doi:10.1103/PhysRevE.100.010401
47. Priesemann V, and Shriki O. Can a time varying external drive give rise to apparent criticality in neural systems? *PLOS Comput Biol* (2018) 14: e1006081. doi:10.1371/journal.pcbi.1006081
48. Newman MEJ. Power laws, pareto distributions and zipf's law. *Contemp Phys* (2005) 46:323. doi:10.1080/00107510500052444
49. Kandel ER, Schwartz JH, and Jessell TM. *Principles of neural science*. 3 edn. New York: Elsevier Science Publishing Co Inc (1991).
50. Dayan P, and Abbott L. *Theoretical neuroscience*. Cambridge: MIT Press (2001).
51. Gerstner W, and Kistler WM. *Spiking neuron models. Single neurons, populations, plasticity*. Cambridge: Cambridge University Press (2002).
52. Priesemann V, Wibral M, Valderrama M, Pröpper R, Le Van Quyen M, Geisel T, et al. Spike avalanches *in vivo* suggest a driven, slightly subcritical brain state. *Front Syst Neurosci* (2014) 8:108. doi:10.3389/fnsys.2014.00108
53. Poil SS, Hardstone R, Mansvelder HD, and Linkenkaer-Hansen K. Critical-state dynamics of avalanches and oscillations jointly emerge from balanced excitation/inhibition in neuronal networks. *J Neurosci* (2012) 32:9817–23. doi:10.1523/JNEUROSCI.5990-11.2012
54. Larremore DB, Shew WL, Ott E, Sorrentino F, and Restrepo JG. Inhibition causes ceaseless dynamics in networks of excitable nodes. *Phys Rev Lett* (2014) 112:138103. doi:10.1103/PhysRevLett.112.138103
55. Villegas P, di Santo S, Burioni R, and Muñoz MA. Time-series thresholding and the definition of avalanche size. *Phys Rev E* (2019) 100:012133. doi:10.1103/PhysRevE.100.012133
56. Priesemann V, Munk M, and Wibral M. Subsampling effects in neuronal avalanche distributions recorded *in vivo*. *BMC Neurosci* (2009) 10:40. doi:10.1186/1471-2202-10-40
57. Das A, and Levina A. Critical neuronal models with relaxed timescale separation. *Phys Rev X* (2019) 9:021062. doi:10.1103/PhysRevX.9.021062
58. Muñoz MA, Dickman R, Vespignani A, and Zapperi S. Avalanche and spreading exponents in systems with absorbing states. *Phys Rev E* (1999) 59:6175–9. doi:10.1103/physreve.59.6175
59. Friedman N, Ito S, Brinkman BAW, Shimono M, DeVille REL, Dahmen KA, et al. Universal critical dynamics in high resolution neuronal avalanche data. *Phys Rev Lett* (2012) 108:208102. doi:10.1103/PhysRevLett.108.208102
60. Linkenkaer-Hansen K, Nikouline VV, Palva JM, and Ilmoniemi RJ. Long-range temporal correlations and scaling behavior in human brain oscillations. *J Neurosci* (2001) 21:1370–7. doi:10.1002/anie.201106423
61. Priesemann V, Levina A, and Wilting J. Assessing criticality in experiments. In: N Tomen, JM Herrmann, and U Ernst., editors. *The functional role of*

critical dynamics in neural systems. Springer Series on Bio- and Neurosystems. Cham: Springer International Publishing (2019). p. 199–232. doi:10.1007/978-3-030-20965-0_11

62. Zucker RS, and Regehr WG. Short-term synaptic plasticity. *Annu Rew Physiol* (2002) 64:355–405. doi:10.1146/annurev.physiol.64.092501.114547
63. Markram H, and Tsodyks M. Redistribution of synaptic efficacy between pyramidal neurons. *Nature* (1996) 382:807–10. doi:10.1038/382807a0
64. Tsodyks M, Pawelzik K, and Markram H. Neural networks with dynamic synapses. *Neural Comput* (1998) 10:821–35. doi:10.1162/089976698300017502
65. Abbott LF, Varela JA, Sen K, and Nelson SB. Synaptic depression and cortical gain control. *Science* (1997) 275:220–4. doi:10.1126/science.275.5297.221
66. Goldman MS, Maldonado P, and Abbott L. Redundancy reduction and sustained firing with stochastic depressing synapses. *J Neurosci* (2002) 22:584–91. doi:10.1523/JNEUROSCI.22-02-00584.2002
67. Mongillo G, Barak O, and Tsodyks M. Synaptic theory of working memory. *Science* (2008) 319:1543–6. doi:10.1126/science.1150769
68. Levina A, Herrmann JM, and Geisel T. Dynamical synapses causing self-organized criticality in neural networks. *Nat Phys* (2007a) 3:857–60. doi:10.1038/nphys758
69. Levina A, Herrmann JM, and Geisel T. Phase transitions towards criticality in a neural system with adaptive interactions. *Phys Rev Lett* (2009) 102:118110. doi:10.1103/PhysRevLett.102.118110
70. Bonachela JA, De Franciscis S, Torres JJ, and Munoz MA. Self-organization without conservation: are neuronal avalanches generically critical? *J Stat Mech Theor Exp* (2010) 2010:P02015. doi:10.1088/1742-5468/2010/02/P02015
71. Gerlach M, and Altmann EG. Testing statistical laws in complex systems. *Phys Rev Lett* (2019) 122:168301. doi:10.1103/PhysRevLett.122.168301
72. Lombardi F, Herrmann HJ, Plenz D, and de Arcangelis L. Temporal correlations in neuronal avalanche occurrence. *Scientific Rep* (2016) 6:1–12. doi:10.1038/srep24690
73. Levina A, Herrmann JM, and Geisel T. Dynamical synapses give rise to a power-law distribution of neuronal avalanches. In: Y Weiss, B Schölkopf, and J Platt., editors. *Advances in neural information processing systems*. Cambridge, MA: MIT Press (2006), 18. p. 771–8.
74. Kinouchi O, Brochini L, Costa AA, Campos JGF, and Copelli M. Stochastic oscillations and dragon king avalanches in self-organized quasi-critical systems. *Sci Rep* (2019) 9:1–12. doi:10.1038/s41598-019-40473-1
75. Michiels van Kessenich L, Luković M, de Arcangelis L, and Herrmann HJ. Critical neural networks with short- and long-term plasticity. *Phys Rev E* (2018) 97:032312. doi:10.1103/PhysRevE.97.032312
76. Zeng G, Huang X, Jiang T, and Yu S. Short-term synaptic plasticity expands the operational range of long-term synaptic changes in neural networks. *Neural Networks* (2019) 118:140–7. doi:10.1016/j.neunet.2019.06.002
77. Wang SJ, and Zhou C. Hierarchical modular structure enhances the robustness of self-organized criticality in neural networks. *New J Phys* (2012) 14:22. doi:10.1088/1367-2630/14/2/023005
78. Jung N, Le QA, Lee KE, and Lee JW. Avalanche size distribution of an integrate-and-fire neural model on complex networks. *Chaos: Interdiscip J Nonlinear Sci* (2020) 30:063118. doi:10.1063/5.0008767
79. Millman D, Mihalas S, Kirkwood A, and Niebur E. Self-organized criticality occurs in non-conservative neuronal networks during 'up' states. *Nat Phys* (2010) 6:801–5. doi:10.1038/nphys1757
80. Martinello M, Hidalgo J, Maritan A, Di Santo S, Plenz D, and Muñoz MA. Neutral theory and scale-free neural dynamics. *Phys Rev X* (2017) 7:041071. doi:10.1103/PhysRevX.7.041071
81. de Arcangelis L, Perrone-Capano C, and Herrmann HJ. Self-organized criticality model for brain plasticity. *Phys Rev Lett* (2006) 96(2):028107. doi:10.1103/PhysRevLett.96.028107
82. Pellegrini GL, de Arcangelis L, Herrmann HJ, and Perrone-Capano C. Activity-dependent neural network model on scale-free networks. *Phys Rev E* (2007) 76:016107. doi:10.1103/PhysRevE.76.016107
83. de Arcangelis L, and Herrmann HJ. Learning as a phenomenon occurring in a critical state. *Proc Natl Acad Sci* (2010) 107(9):3977–81. doi:10.1073/pnas.0912289107
84. Uhlig M, Levina A, Geisel T, and Herrmann JM. Critical dynamics in associative memory networks. *Front Comput Neurosci* (2013) 7:87. doi:10.3389/fncom.2013.00087
85. Sjöström J, and Gerstner W. Spike-timing dependent plasticity. *Scholarpedia* (2010) 5:1362. doi:10.4249/scholarpedia.1362
86. Bi G, and Poo M. Synaptic modifications in cultured hippocampal neurons: dependence on spike timing, synaptic strength, and postsynaptic cell type. *J Neurosci* (1998) 18:10464–72. doi:10.1523/JNEUROSCI.18-24-10464.1998
87. Markram H, Helm PJ, and Sakmann B. Dendritic calcium transients evoked by single back-propagating action potentials in rat neocortical pyramidal neurons. *J Physiol* (1995) 485:1–20. doi:10.1113/jphysiol.1995.sp020708
88. Markram H. Regulation of synaptic efficacy by coincidence of postsynaptic APs and EPSPs. *Science* (1997) 275:213–5. doi:10.1126/science.275.5297.213
89. Gerstner W, Kempter R, van Hemmen JL, and Wagner H. A neuronal learning rule for sub-millisecond temporal coding. *Nature* (1996) 383:76–8. doi:10.1038/383076a0
90. Kempter R, Gerstner W, and van Hemmen JL. Hebbian learning and spiking neurons. *Phys Rev E* (1999) 59:4498–514. doi:10.1103/PhysRevE.59.4498
91. Roberts PD, and Bell CC. Computational consequences of temporally asymmetric learning rules: II. Sensory image cancellation. *J Comput Neurosci* (2000) 9:67–83. doi:10.1023/A:1008938428112
92. Guyonneau R, VanRullen R, and Thorpe SJ. Neurons tune to the earliest spikes through STDP. *Neural Comput* (2005) 17:859–79. doi:10.1162/0899766053429390
93. Farries MA, and Fairhall AL. Reinforcement learning with modulated spike timing–dependent synaptic plasticity. *J Neurophysiol* (2007) 98:3648–65. doi:10.1152/jn.00364.2007
94. Costa RP, Froemke RC, Sjöström PJ, and van Rossum MC. Unified pre- and postsynaptic long-term plasticity enables reliable and flexible learning. *eLife* (2015) 4:e09457. doi:10.7554/eLife.09457
95. Sjöström PJ, Rancz EA, Roth A, and Häusser M. Dendritic excitability and synaptic plasticity. *Physiol Rev* (2008) 88:769–840. doi:10.1152/physrev.00016.2007
96. Nishiyama M, Hong K, Mikoshiba K, Poo M, and Kato K. Calcium stores regulate the polarity and input specificity of synaptic modification. *Nature* (2000) 408:584–8. doi:10.1038/35046067
97. Zhang YC. Scaling theory of self-organized criticality. *Phys Rev Lett* (1989) 63:470–3. doi:10.1103/PhysRevLett.63.470
98. Feldman DE. Timing-based LTP and LTD at vertical inputs to layer II/III pyramidal cells in rat barrel cortex. *Neuron* (2000) 27:45–56. doi:10.1016/S0896-6273(00)00008-8
99. Sjöström PJ, Turrigiano GG, and Nelson SB. Rate, timing, and cooperativity jointly determine cortical synaptic plasticity. *Neuron* (2001) 32:1149–64. doi:10.1016/S0896-6273(01)00542-6
100. Hennequin G, Agnes EJ, and Vogels TP. Inhibitory plasticity: balance, control, and codependence. *Annu Rev Neurosci* (2017) 40:557–79. doi:10.1146/annurev-neuro-072116-031005
101. Rubinov M, Sporns O, Thivierge JP, and Breakspear M. Neurobiologically realistic determinants of self-organized criticality in networks of spiking neurons. *PLoS Comput Biol* (2011) 7:e1002038. doi:10.1371/journal.pcbi.1002038
102. Khoshkhou M, and Montakhab A. Spike-timing-dependent plasticity with axonal delay tunes networks of Izhikevich neurons to the edge of synchronization transition with scale-free avalanches. *Front Syst Neurosci* (2019) 13:73. doi:10.3389/fnsys.2019.00073
103. Van Rossum MC, Bi GQ, and Turrigiano GG. Stable hebbian learning from spike timing-dependent plasticity. *J Neurosci* (2000) 20(23):8812–21. doi:10.1523/JNEUROSCI.20-23-08812.2000
104. Meisel C, and Gross T. Adaptive self-organization in a realistic neural network model. *Phys Rev E* (2009) 80:061917. doi:10.1103/PhysRevE.80.061917
105. Shin CW, and Kim S. Self-organized criticality and scale-free properties in emergent functional neural networks. *Phys Rev E* (2006) 74:045101. doi:10.1103/PhysRevE.74.045101
106. Hernandez-Urbina V, and Herrmann JM. Self-organized criticality via retro-synaptic signals. *Front Phys* (2017) 4. doi:10.3389/fphy.2016.00054

107. Babadi B, and Abbott LF. Intrinsic stability of temporally shifted spike-timing dependent plasticity. *PLoS Comput Biol* (2010) 6:e1000961. doi:10.1371/journal.pcbi.1000961
108. Turrigiano GG, Leslie KR, Desai NS, Rutherford LC, and Nelson SB. Activity-dependent scaling of quantal amplitude in neocortical pyramidal neurons. *Nature* (1998) 391:892–6. doi:10.1038/36103
109. Lissin DV, Gomperts SN, Carroll RC, Christine CW, Kalman D, Kitamura M, et al. Activity differentially regulates the surface expression of synaptic AMPA and NMDA glutamate receptors. *Proc Natl Acad Sci* (1998) 95:7097–102. doi:10.1073/pnas.95.12.7097
110. O'Brien RJ, Kamboj S, Ehlers MD, Rosen KR, Fischbach GD, and Huganir RL. Activity-dependent modulation of synaptic AMPA receptor accumulation. *Neuron* (1998) 21:1067–78. doi:10.1016/S0896-6273(00)80624-8
111. Turrigiano GG, and Nelson SB. Homeostatic plasticity in the developing nervous system. *Nat Rev Neurosci* (2004) 5:97–107. doi:10.1038/nrn1327
112. Davis GW. Homeostatic control OF neural activity: from phenomenology to molecular design. *Annu Rev Neurosci* (2006) 29:307–23. doi:10.1146/annurev.neuro.28.061604.135751
113. Williams AH, O'Leary T, and Marder E. Homeostatic regulation of neuronal excitability. *Scholarpedia* (2013) 8:1656. doi:10.4249/scholarpedia.1656
114. Bienenstock EL, Cooper LN, and Munro PW. Theory for the development of neuron selectivity: orientation specificity and binocular interaction in visual cortex. *J Neurosci* (1982) 2:32–48. doi:10.1523/JNEUROSCI.02-01-00032.1982
115. Miller KD, and MacKay DJC. The role of constraints in hebbian learning. *Neural Comput* (1994) 6:100–26. doi:10.1162/neco.1994.6.1.100
116. Abbott LF, and Nelson SB. Synaptic plasticity: taming the beast. *Nat Neurosci* (2000) 3:1178–83. doi:10.1038/81453
117. Turrigiano GG, and Nelson SB. Hebb and homeostasis in neuronal plasticity. *Curr Opin Neurobiol* (2000) 10:358–64. doi:10.1016/S0959-4388(00)00091-X
118. Tetzlaff C, Kolodziejski C, Timme M, and Wörgötter F. Synaptic scaling in combination with many generic plasticity mechanisms stabilizes circuit connectivity. *Front Comput Neurosci* (2011) 5:47.
119. Zenke F, Hennequin G, and Gerstner W. Synaptic plasticity in neural networks needs homeostasis with a fast rate detector. *PLOS Comput Biol* (2013) 9:e1003330. doi:10.1371/journal.pcbi.1003330
120. Keck T, Toyoizumi T, Chen L, Doiron B, Feldman DE, Fox K, et al. Integrating Hebbian and homeostatic plasticity: the current state of the field and future research directions. *Philos Trans R Soc B: Biol Sci* (2017) 372:20160158. doi:10.1098/rstb.2016.0158
121. Zenke F, and Gerstner W. Hebbian plasticity requires compensatory processes on multiple timescales. *Philos Trans R Soc B: Biol Sci* (2017) 372:20160259. doi:10.1098/rstb.2016.0259
122. Tsodyks MV, and Markram H. The neural code between neocortical pyramidal neurons depends on neurotransmitter release probability. *Proc Natl Acad Sci USA* (1997) 94:719–23. doi:10.1073/pnas.94.2.719
123. Fong M, Newman JP, Potter SM, and Wenner P. Upward synaptic scaling is dependent on neurotransmission rather than spiking. *Nat Commun* (2015) 6:6339. doi:10.1038/ncomms7339
124. Pozo K, and Goda Y. Unraveling mechanisms of homeostatic synaptic plasticity. *Neuron* (2010) 66:337–51. doi:10.1016/j.neuron.2010.04.028
125. De PittÃ M, Brunel N, and Volterra A. Astrocytes: orchestrating synaptic plasticity? *Neuroscience* (2016) 323:43–61. doi:10.1016/j.neuroscience.2015.04.001
126. Virkar YS, Shew WL, Restrepo JG, and Ott E. Feedback control stabilization of critical dynamics via resource transport on multilayer networks: how glia enable learning dynamics in the brain. *Phys Rev E* (2016) 94:042310. doi:10.1103/PhysRevE.94.042310
127. Naudé J, Cessac B, Berry H, and Delord B. Effects of cellular homeostatic intrinsic plasticity on dynamical and computational properties of biological recurrent neural networks. *J Neurosci* (2013) 33:15032–43. doi:10.1523/JNEUROSCI.0870-13.2013
128. Gjorgjieva J, Evers JF, and Eglen SJ. Homeostatic activity-dependent tuning of recurrent networks for robust propagation of activity. *J Neurosci* (2016) 36:3722–34. doi:10.1523/JNEUROSCI.2511-15.2016
129. Hellyer PJ, Jachs B, Clopath C, and Leech R. Local inhibitory plasticity tunes macroscopic brain dynamics and allows the emergence of functional brain networks. *NeuroImage* (2016) 124:85–95. doi:10.1016/j.neuroimage.2015.08.069
130. Harris TE. *The Theory of Branching Processes. Grundlehren der mathematischen Wissenschaften*. Berlin Heidelberg: Springer-Verlag (1963).
131. Levina A, Ernst U, and Herrmann JM. Criticality of avalanche dynamics in adaptive recurrent networks. *Neurocomputing* (2007b) 70:1877–81. doi:10.1016/j.neucom.2006.10.056
132. Levina A, Herrmann JM, and Denker M. Critical branching processes in neural networks. *PAMM* (2007c) 7:1030701–2. doi:10.1002/pamm.200700029
133. Rocha RP, Koçillari L, Suweis S, Corbetta M, and Maritan A. Homeostatic plasticity and emergence of functional networks in a whole-brain model at criticality. *Sci Rep* (2018) 8:15682. doi:10.1038/s41598-018-33923-9
134. Girardi-Schappo M, Brochini L, Costa AA, Carvalho TTA, and Kinouchi O. Synaptic balance due to homeostatically self-organized quasicritical dynamics. *Phys Rev Res* (2020) 2:012042. doi:10.1103/PhysRevResearch.2.012042
135. Brochini L, de Andrade Costa A, Abadi M, Roque AC, Stolfi J, and Kinouchi O. Phase transitions and self-organized criticality in networks of stochastic spiking neurons. *Scientific Rep* (2016) 6:35831. doi:10.1038/srep35831
136. Costa AA, Brochini L, and Kinouchi O. Self-organized supercriticality and oscillations in networks of stochastic spiking neurons. *Entropy* (2017) 19:399. doi:10.3390/e19080399
137. Dickman R, Muñoz MA, Vespignani A, and Zapperi S. Paths to self-organized criticality. *Braz J Phys* (2000) 30:27–41. doi:10.1590/S0103-97332000000100004
138. Zierenberg J, Wilting J, Priesemann V, and Levina A. Description of spreading dynamics by microscopic network models and macroscopic branching processes can differ due to coalescence. *Phys Rev E* (2020a) 101:022301. doi:10.1103/PhysRevE.101.022301
139. Ma Z, Turrigiano GG, Wessel R, and Hengen KB. Cortical circuit dynamics are homeostatically tuned to criticality InÂ vivo. *Neuron* (2019) 104:655–64.e4. doi:10.1016/j.neuron.2019.08.031
140. Wilting J, and Priesemann V. Between perfectly critical and fully irregular: a reverberating model captures and predicts cortical spike propagation. *Cereb Cortex* (2019a) 29:2759–70. doi:10.1093/cercor/bhz049
141. Lin M, and Chen T. Self-organized criticality in a simple model of neurons based on small-world networks. *Phys Rev E* (2005) 71:016133. doi:10.1103/PhysRevE.71.016133
142. de Arcangelis L, and Herrmann HJ. Self-organized criticality on small world networks. *Physica A: Stat Mech its Appl* (2002) 308:545–9. doi:10.1016/S0378-4371(02)00549-6
143. Fronczak P, Fronczak A, and Hołyst JA. Self-organized criticality and coevolution of network structure and dynamics. *Phys Rev E* (2006) 73:046117. doi:10.1103/PhysRevE.73.046117
144. Bianconi G, and Marsili M. Clogging and self-organized criticality in complex networks. *Phys Rev E* (2004) 70:035105. doi:10.1103/PhysRevE.70.035105
145. Hughes D, Paczuski M, Dendy RO, Helander P, and McClements KG. Solar flares as cascades of reconnecting magnetic loops. *Phys Rev Lett* (2003) 90:131101. doi:10.1103/PhysRevLett.90.131101
146. Paczuski M, and Hughes D. A heavenly example of scale-free networks and self-organized criticality. *Physica A: Stat Mech its Appl* (2004) 342:158–63. doi:10.1016/j.physa.2004.04.073
147. Bassett DS, and Bullmore E. Small-world brain networks. *The Neuroscientist* (2006) 12:512–23. doi:10.1177/1073858406293182
148. Bullmore E, and Sporns O. Complex brain networks: graph theoretical analysis of structural and functional systems. *Nat Rev Neurosci* (2009) 10:186–98. doi:10.1038/nrn2575
149. He BJ. Scale-free brain activity: past, present, and future. *Trends Cogn Sci* (2014) 18:480–7. doi:10.1016/j.tics.2014.04.003
150. Eguíluz VM, Chialvo DR, Cecchi GA, Baliki M, and Apkarian AV. Scale-free brain functional networks. *Phys Rev Lett* (2005) 94:018102. doi:10.1103/PhysRevLett.94.018102
151. Siri B, Quoy M, Delord B, Cessac B, and Berry H. Effects of Hebbian learning on the dynamics and structure of random networks with inhibitory and excitatory neurons. *J Physiol-Paris* (2007) 101:136–48. doi:10.1016/j.jphysparis.2007.10.003

152. Moretti P, and Muñoz MA. Griffiths phases and the stretching of criticality in brain networks. *Nat Commun* (2013) 4:2521. doi:10.1038/ncomms3521
153. van Ooyen A, and van Pelt J. Activity-dependent outgrowth of neurons and overshoot phenomena in developing neural networks. *J Theor Biol* (1994) 167:27–43. doi:10.1006/jtbi.1994.1047
154. van Ooyen A, and van Pelt J. Complex periodic behaviour in a neural network model with activity-dependent neurite outgrowth. *J Theor Biol* (1996) 179: 229–42. doi:10.1006/jtbi.1996.0063
155. Abbott LF, and Rohrkemper R. A simple growth model constructs critical avalanche networks. *Prog Brain Res* (2007) 165:13–9. doi:10.1016/S0079-6123(06)65002-4
156. Kalle Kossio FY, Goedeke S, van den Akker B, Ibarz B, and Memmesheimer RM. Growing critical: self-organized criticality in a developing neural system. *Phys Rev Lett* (2018) 121(5):058301. doi:10.1103/PhysRevLett.121.058301
157. Droste F, Do AL, and Gross T. Analytical investigation of self-organized criticality in neural networks. *J R Soc Interf* (2013) 10:20120558. doi:10.1098/rsif.2012.0558
158. Landmann S, Baumgarten L, and Bornholdt S. Self-organized criticality in neural networks from activity-based rewiring. *arXiv:2009.11781 [cond-mat, physics:nlin, q-bio]* (2020).
159. van Ooyen A, and Butz-Ostendorf M. Homeostatic structural plasticity can build critical networks. In: N Tomen, JM Herrmann, and U Ernst., editors. *The functional role of critical dynamics in neural systems. Springer series on bio- and neurosystems*. Cham: Springer International Publishing (2019). p. 117–37. doi:10.1007/978-3-030-20965-07
160. Bornholdt S, and Rohlf T. Topological evolution of dynamical networks: global criticality from local dynamics. *Phys Rev Lett* (2000) 84:6114–7. doi:10.1103/PhysRevLett.84.6114
161. Bornholdt S, and Röhl T. Self-organized critical neural networks. *Phys Rev E* (2003) 67:066118. doi:10.1103/PhysRevE.67.066118
162. Rybarsch M, and Bornholdt S. Avalanches in self-organized critical neural networks: a minimal model for the neural soc universality class. *PLoS one* (2014) 9:e93090. doi:10.1371/journal.pone.0093090
163. Ben-Ari Y, Khalilov I, Kahle KT, and Cherubini E. The GABA excitatory/inhibitory shift in brain maturation and neurological disorders. *The Neurosci* (2012) 18:467–86. doi:10.1177/1073858412438697
164. Peng J, and Beggs JM. Attaining and maintaining criticality in a neuronal network model. *Physica A: Stat Mech its Appl* (2013) 392:1611–20. doi:10.1016/j.physa.2012.11.013
165. Stepp N, Plenz D, and Srinivasa N. Synaptic plasticity enables adaptive self-tuning critical networks. *PLoS Comput Biol* (2015) 11:e1004043. doi:10.1371/journal.pcbi.1004043
166. Scarpetta S, Giacco F, Lombardi F, and de Candia A. Effects of Poisson noise in a IF model with STDP and spontaneous replay of periodic spatiotemporal patterns, in absence of cue stimulation. *Biosystems* (2013) 112:258–64. doi:10.1016/j.biosystems.2013.03.017
167. Scarpetta S, and de Candia A. Alternation of up and down states at a dynamical phase-transition of a neural network with spatiotemporal attractors. *Front Syst Neurosci* (2014) 8:88. doi:10.3389/fnsys.2014.00088
168. Scarpetta S, Apicella I, Minati L, and de Candia A. Hysteresis, neural avalanches, and critical behavior near a first-order transition of a spiking neural network. *Phys Rev E* (2018) 97:062305. doi:10.1103/PhysRevE.97.062305
169. Loidolt M, Rudelt L, and Priesemann V. Sequence memory in recurrent neuronal network can develop without structured input. *bioRxiv* (2020). doi:10.1101/2020.09.15.297580
170. Papa BD, Priesemann V, and Triesch J. Criticality meets learning: criticality signatures in a self-organizing recurrent neural network. *PLoS One* (2017) 12: e0178683. doi:10.1371/journal.pone.0178683
171. Hopfield JJ. Neural networks and physical systems with emergent collective computational abilities. *Proc Natl Acad Sci USA* (1982) 79:2554–8. doi:10.1073/pnas.79.8.2554
172. Scarpetta S, and Candia A. Neural avalanches at the critical point between replay and non-replay of spatiotemporal patterns. *PLOS ONE* (2013) 8: e64162. doi:10.1371/journal.pone.0064162
173. Bak P, and Chialvo DR. Adaptive learning by extremal dynamics and negative feedback. *Phys Rev E* (2001) 63:031912. doi:10.1103/PhysRevE.63.031912
174. Kinouchi O, and Copelli M. Optimal dynamical range of excitable networks at criticality. *Nat Phys* (2006) 2:348–51. doi:10.1038/nphys289
175. Zierenberg J, Wilting J, Priesemann V, and Levina A. Tailored ensembles of neural networks optimize sensitivity to stimulus statistics. *Phys Rev Res* (2020b) 2:013115. doi:10.1103/PhysRevResearch.2.013115
176. Stanley HE. Introduction to phase transitions and critical phenomena. *Am J Phys* (1972) 40:927–8. doi:10.1119/1.1986710
177. Sethna J. *Statistical mechanics: entropy, order parameters, and complexity*. Oxford, United Kingdom: Oxford University Press (2021).
178. Shew WL, Yang H, Petermann T, Roy R, and Plenz D. Neuronal avalanches imply maximum dynamic range in cortical networks at criticality. *J Neurosci* (2009) 29:15595–600. doi:10.1523/JNEUROSCI.3864-09.2009
179. Shew WL, and Plenz D. The functional benefits of criticality in the cortex. *Neuroscientist* (2013) 19:88–100. doi:10.1177/1073858412445487
180. Boedecker J, Obst O, Lizier JT, Mayer NM, and Asada M. Information processing in echo state networks at the edge of chaos. *Theor Biosci* (2012) 131:205–13. doi:10.1007/s12064-011-0146-8
181. Boedecker J, Lampe T, and Riedmiller M. Modeling effects of intrinsic and extrinsic rewards on the competition between striatal learning systems. *Front Psychol* (2013) 4:739. doi:10.3389/fpsyg.2013.00739
182. Bertschinger N, and Natschläger T. Real-time computation at the edge of chaos in recurrent neural networks. *Neural Comput* (2004) 16:1413–36. doi:10.1162/089976604323057443
183. Lazar A, Pipa G, and Triesch J. SORN: a self-organizing recurrent neural network. *Front Comput Neurosci* (2009) 3:23. doi:10.3389/neuro.10.023.2009
184. Del Papa B, Priesemann V, and Triesch J. Fading memory, plasticity, and criticality in recurrent networks. In: N Tomen, JM Herrmann, and U Ernst., editors. *The functional role of critical dynamics in neural systems. Springer series on bio- and neurosystems*. Cham: Springer International Publishing (2019). p. 95–115. doi:10.1007/978-3-030-20965-0_6
185. Cocchi L, Gollo LL, Zalesky A, and Breakspear M. Criticality in the brain: a synthesis of neurobiology, models and cognition. *Prog Neurobiol* (2017) 158: 132–52. doi:10.1016/j.pneurobio.2017.07.002
186. Nolte M, Reimann MW, King JG, Markram H, and Muller EB. Cortical reliability amid noise and chaos. *Nat Commun* (2019) 10:3792. doi:10.1038/s41467-019-11633-8
187. Gollo LL. Coexistence of critical sensitivity and subcritical specificity can yield optimal population coding. *J R Soc Interf* (2017) 14:20170207. doi:10.1098/rsif.2017.0207
188. Wilting J, Dehning J, Pinheiro Neto J, Rudelt L, Wibral M, Zierenberg J, et al. Operating in a reverberating regime enables rapid tuning of network states to task requirements. *Front Syst Neurosci* (2018) 12. doi:10.3389/fnsys.2018.00055
189. Wilting J, and Priesemann V. 25 years of criticality in neuroscience â€" established results, open controversies, novel concepts. *Curr Opin Neurobiol* (2019b) 58:105–11. doi:10.1016/j.conb.2019.08.002
190. Tomen N, Rotermund D, and Ernst U. Marginally subcritical dynamics explain enhanced stimulus discriminability under attention. *Front Syst Neurosci* (2014) 8:1–15. doi:10.3389/fnsys.2014.00151
191. Ribeiro TL, Copelli M, Caixeta F, Belchior H, Chialvo DR, Nicolelis MA, et al. Spike avalanches exhibit universal dynamics across the sleep-wake cycle. *PLoS One* (2010) 5:e14129. doi:10.1371/journal.pone.0014129
192. Spitzner FP, Dehning J, Wilting J, Hagemann A, Neto JP, Zierenberg J, et al. MR. Estimator, a toolbox to determine intrinsic timescales from subsampled spiking activity. *arXiv:2007.03367 [physics, q-bio]* (2020).
193. Zeraati R, Engel TA, and Levina A. Estimation of autocorrelation timescales with approximate bayesian computations. *bioRxiv* (2020). doi:10.1101/2020.08.11.245944
194. Meisel C, Klaus A, Kuehn C, and Plenz D. Critical slowing down governs the transition to neuron spiking. *PLoS Comput Biol* (2015) 11:e1004097. doi:10.1371/journal.pcbi.1004097
195. Tkacik G, Mora T, Marre O, Amodei D, Palmer SE, and Bialek W. Thermodynamics and signatures of criticality in a network of neurons. *PNAS* (2015) 112:11508–13. doi:10.1073/pnas.1514188112
196. Hidalgo J, Grilli J, Suweis S, Munoz MA, Banavar JR, and Maritan A. Information-based fitness and the emergence of criticality in living systems. *Proc Natl Acad Sci* (2014) 111:10095–100. doi:10.1073/pnas.1319166111

197. Meshulam L, Gauthier JL, Brody CD, Tank DW, and Bialek W. Coarse graining, fixed points, and scaling in a large population of neurons. *Phys Rev Lett* (2019) 123:178103. doi:10.1103/PhysRevLett.123.178103
198. Nonnenmacher M, Behrens C, Berens P, Bethge M, and Macke JH. Signatures of criticality arise from random subsampling in simple population models. *PLoS Comput Biol* (2017) 13:e1005718. doi:10.1371/journal.pcbi.1005718
199. Mastromatteo I, and Marsili M. On the criticality of inferred models. *J Stat Mech Theor Exp* (2011) 2011:P10012. doi:10.1088/1742-5468/2011/10/P10012
200. Nicoletti G, Suweis S, and Maritan A. Scaling and criticality in a phenomenological renormalization group. *Phys Rev Res* (2020) 2:023144. doi:10.1103/PhysRevResearch.2.023144
201. Morrell MC, Sederberg AJ, and Nemenman I. Latent dynamical variables produce signatures of spatiotemporal criticality in large biological systems. *arXiv preprint arXiv:2008.04435* (2020).
202. Neto JP, Spitzner FP, and Priesemann V. A unified picture of neuronal avalanches arises from the understanding of sampling effects. *arXiv: 1910.09984 [cond-mat, physics:nlin, physics:physics, q-bio]* (2020).
203. Shriki O, Alstott J, Carver F, Holroyd T, Henson RN, Smith ML, et al. Neuronal avalanches in the resting meg of the human brain. *J Neurosci* (2013) 33:7079–90. doi:10.1523/JNEUROSCI.4286-12.2013
204. Clawson WP, Wright NC, Wessel R, and Shew WL. Adaptation towards scale-free dynamics improves cortical stimulus discrimination at the cost of reduced detection. *PLoS Comput Biol* (2017) 13:e1005574. doi:10.1371/journal.pcbi.1005574
205. Carhart-Harris RL, Muthukumaraswamy S, Roseman L, Kaelen M, Droog W, Murphy K, et al. Neural correlates of the LSD experience revealed by multimodal neuroimaging. *Proc Natl Acad Sci* (2016) 113:4853–8. doi:10.1073/pnas.1518377113
206. Simola J, Zhigalov A, Morales-Muñoz I, Palva JM, and Palva S. Critical dynamics of endogenous fluctuations predict cognitive flexibility in the Go/NoGo task. *Sci Rep* (2017) 7:2909. doi:10.1038/s41598-017-02750-9

Conflict of Interest: The authors declare that the research was conducted in the absence of any commercial or financial relationships that could be construed as a potential conflict of interest.

frontiers in Physics

REVIEW
published: 04 May 2021
doi: 10.3389/fphy.2021.641233

Time-Dependent Properties of Sandpiles

*Punyabrata Pradhan**

Department of Theoretical Sciences, S. N. Bose National Centre for Basic Sciences, Kolkata, India

Bak, Tang, and Wiesenfeld (BTW) proposed the theory of self-organized criticality (SOC), and sandpile models, to connect "$1/f$" noise, observed in systems in a diverse natural setting, to the fractal spatial structure. We review some of the existing works on the problem of characterizing time-dependent properties of sandpiles and try to explore if the BTW's original ambition has really been fulfilled. We discuss the exact hydrodynamic structure in a class of conserved stochastic sandpiles, undergoing a non-equilibrium absorbing phase transition. We illustrate how the hydrodynamic framework can be used to capture long-ranged spatio-temporal correlations in terms of large-scale transport and relaxation properties of the systems. We particularly emphasize certain interesting aspects of sandpiles—the transport instabilities, which emerge through the threshold-activated nature of the dynamics in the systems. We also point out some open issues at the end.

Keywords: self-organized criticality, scale invariance, time-dependent correlation, transport coefficients, absorbing phase transitions

OPEN ACCESS

Edited by:
Jürgen Vollmer,
Universität Leipzig, Germany

Reviewed by:
Reinaldo Roberto Rosa,
National Institute of Space Research (INPE), Brazil
Manish Dev Shrimali,
Central University of Rajasthan, India
Raissa D'Souza,
University of California, Davis, United States

***Correspondence:**
Punyabrata Pradhan
punyabrata@gmail.com

Specialty section:
This article was submitted to Interdisciplinary Physics, a section of the journal Frontiers in Physics

Received: *13 December 2020*
Accepted: *22 March 2021*
Published: *04 May 2021*

Citation:
Pradhan P (2021) Time-Dependent Properties of Sandpiles. Front. Phys. 9:641233. doi: 10.3389/fphy.2021.641233

1. INTRODUCTION

More than three decades ago, Bak, Tang, and Wiesenfeld (BTW) proposed the theory of "self-organized criticality" (SOC) [1], and sandpile models [2, 3], as an explanation of the physical origin of the spatio-temporal scale invariance in natural systems found around us [4–6]. Indeed, in nature scale invariance is rather a rule, than an exception [7, 8]. One abundantly finds fractal spatial structures, such as mountain ranges, coastlines and river basins [9, 10], etc., which can be characterized by power-law correlations. For example, consider the height-height correlation function $[h(\mathbf{x}) - h(\mathbf{x}')]^2 \sim |\mathbf{x} - \mathbf{x}'|^{2\chi}$ in a mountain range, where $h(\mathbf{x})$ and $h(\mathbf{x}')$ are heights at position $\mathbf{x}$ and $\mathbf{x}'$. Clearly, the correlation function varies with the distance $|\mathbf{x} - \mathbf{x}'|$ as a power law, characterized by an exponent $0 < \chi < 1$. In other words, upon varying the length scale, mountain ranges would appear a "self-similar" object: if one zooms in or out, a picture of a mountain would look almost the same. Likewise, the bird's eye view of the structures at the delta area of a river, such as the Ganges can look quite similar to the eyes if one changes the length scales (simply by broadening the horizon); similarly, the satellite picture of a country's coastline could well appear self-similar at different length scales. Indeed, such self-similarities indicate that these natural objects generate long-ranged power-law correlations in space.

Similar nontrivial structures can be observed also in the time (or, equivalently, frequency) domain, where many natural phenomena exhibit scale-invariant behaviors, implying the existence of long-ranged temporal correlations in the systems. For example, consider voltage fluctuations across a resistor in a current-carrying conductor, operating in a non-equilibrium steady-state condition. Due to the inherent noise in the system, the voltage $V(t)$ across the resistor randomly fluctuates as a function of time t, however has a steady value $\langle V(t) \rangle = V_0$. Now let us consider

the voltage power spectrum, i.e., the Fourier transform $S(f) \sim \int e^{-i2\pi ft} C(t)dt$ of the voltage autocorrelation function $C(t) = \langle V(t)V(0)\rangle - V_0^2$. Indeed, in a broad range of frequencies (10^{-7} Hz $< f < 10^4$ Hz) and independent of any specific nature of the systems, the power spectrum has a power-law form as $S(f) \sim 1/f^{\alpha}$ with the exponent generally lying in the range $1 \lesssim \alpha \lesssim 1.4$; for a review of the $1/f$ noise in solids (see [11]). This low-frequency noise is called in the literature the "flicker" or, simply, the "$1/f$" noise, where the exponent can in principle be in the range $0 < \alpha < 2$ (the case with $\alpha = 0$ corresponds to the white or delta-correlated noise; on the other hand, $\alpha < 0$ implies anti-correlation in a time-signal). Notably, the $1/f$ noise is different from the Johnson-Nyquist noise [12], which does not depend on frequency ($\alpha = 0$ in that case) and occurs in equilibrium systems; it is different from the shot noise, which is also independent of frequency and happens near equilibrium. While it is less erratic than the white noise, the $1/f$ noise is somewhat more erratic than the $1/f^2$ noise. Quite remarkably, the $1/f$ noise has been observed in a diverse range of apparently unrelated *non-equilibrium* phenomena, such as in traffic movements [13], flow of sand in hour glasses [14], and solar flare [15], etc. Not surprisingly, the origin of the subtle long-time correlations in $1/f$ noise has lacked a general theoretical understanding so far.

In their original paper [1], BTW attempted to provide a universal mechanism of the $1/f$ noise through the interplay between scale-invariant spatial and temporal structures, which can develop in slowly driven spatially extended dynamical systems observed in nature. There were two key ingredients in their theory: *threshold-activated* dynamics and *slow driving*. Bak, Tang, and Wiesenfeld argued that these systems, being highly non-linear, are governed by dynamics where there are dynamical activities only when the value of a certain local quantity crosses a threshold value; the system dissipates energy to maintain itself in a non-equilibrium steady state. According to BTW, under slow driving, such systems would "self-organize" to a "minimally stable" state, which is highly sensitive to perturbations and can create fast relaxation activities, called avalanches. The activities can occur at all length scales, implying a critical state for the system. Here the "slow" driving essentially refers to the separation of time scales in the systems: on the time scale of the driving, the systems relax instantaneously through avalanches. BTW dubbed this particular mechanism of achieving a critical state as the "self-organized criticality" (SOC). That is, apparently it does not require fine-tuning of any external parameter(s) to maintain the criticality; this is unlike any equilibrium critical phenomena, which are achieved only by tuning, say, temperature, and chemical potential (or, magnetic field in a magnetic system).

To demonstrate the mechanism of SOC, BTW proposed a model, called the BTW sandpile [1, 16], which is nothing but simply a metaphor for a real sandpile, made on a finite base and driven to the edge of its stability through slow addition of grains and dissipation (loss of grains) at the boundary. On a two dimensional square lattice, the model is defined as follows. At any site (x, y), a height variable $h(x, y, t)$ at time t is defined as the number of grains at the site. If $h(x, y, t) \geq h_c = 2d$ (dimension $d = 2$ here), $2d$ grains topple and each of the neighboring sites get one grain each, i.e.,

$$\begin{aligned} h(x, y, t+1) &= h(x, y, t) - 4, \\ h(x \pm 1, y, t+1) &= h(x \pm 1, y, t) + 1, \\ h(x, y \pm 1, t+1) &= h(x, y \pm 1, t) + 1. \end{aligned} \tag{1}$$

All sites are updated in parallel and the dissipation is incorporated through the boundary condition by keeping $h(x, y, t) = 0$ at the boundary. Note that the number of grains are conserved in the bulk; grains are dissipated only at the boundary. As the toppling condition depends on the height variable, in this article we shall refer to this class of models as critical *height-type* one. The model can be straightforwardly generalized to higher (and lower) dimension. Later several stochastic variants of the BTW model, such as the two celebrated models—the Manna sandpile [17] and the Oslo ricepile [18], with stochastic toppling rules, were introduced.

It has been debated whether the SOC systems can be thought of as ones spontaneously evolving, or "self-organizing." toward criticality, especially when the driving rate itself is "tuned" to zero [19]. (Nevertheless, one could simply take a view that such slowly driven systems exist in nature and are worth exploring for their interesting properties.) To elucidate this issue of "self-organization" vs. "fine tuning", the *fixed-energy* variants of the BTW sandpiles were introduced [20–22]. In the fixed-energy sandpiles, there is no dissipation of grains and the total mass in the systems remains conserved. Upon tuning the density below a critical density, the system is observed to undergo an absorbing phase transition (APT) [23], where all dynamical activities in the system ceases to exist. Indeed, in the stochastic fixed-energy sandpiles, the critical density is found to be the same as the steady-state density in the corresponding slowly driven dissipative sandpiles [24]; however, the situation can be complicated in the case of deterministic sandpiles, such as the BTW model, due to the ergodicity breaking [25, 26].

Despite the fact that the original motivation of BTW was to connect the long-ranged spatial and temporal correlations observed in natural phenomena, much attention has been drawn in the past toward characterizing the spatial structures of sandpiles, mainly through the avalanches statistics [27]. Indeed, there is a vast body of experimental [28, 29], simulation [17, 21, 22, 30–42] and exact [16, 43–50] results available in the literature; for reviews, see [19, 51]. The time-dependent properties, on the other hand, have not been explored as much. In this article, we review some of the past works, which attempted, and achieved to a certain extent, dynamical characterization of sandpiles, through studies of simple models, which are amenable to analytic calculations and easy to simulate on computers. However, the task of large-scale hydrodynamic characterization of relaxation and transport properties of sandpiles is still incomplete. This review would perhaps give some hints of the possible directions in which one could proceed.

Organization of the article is as follows. In section 2, we discuss the nature of the long-range temporal correlations present in sandpiles, through studies of power spectrum of various time-dependent quantities, which have been measured in the experiments and simulations in the past. In this context,

we also discuss the theories, which have been developed to capture these long-time correlations in the system. In section 3, we review some of the other interesting aspects of time-dependent correlations in the context of particle transport, i.e., that of tagged-particle diffusion in sandpiles. We then address the large-scale relaxation and the transport instabilities in sandpiles through an exact hydrodynamical framework. We end the article with concluding remarks and some open issues.

2. NOISE SPECTRUM IN SANDPILES: EXPERIMENTS, SIMULATIONS, AND THEORIES

2.1. Experiments

After the concept of SOC was introduced, it was quite natural to ask whether a pile of real sand, or any other granular material for that matter, exhibits SOC or not. This question was addressed by Jaeger et al. in an experiment [28] on a pile of granular materials (glass beads and aluminum-oxides grains) driven in a slowly rotating drum, which tilts the surface of the pile and thus generates avalanches of grains down the slope of the pile. The outflux of the grains (i.e., particle-current at the boundary) as a function of time, and the power-spectrum of the corresponding time-signal, were calculated by measuring the change of capacitance (which is related to the particle flow-rate) in a parallel-plate capacitor through which the particles passed. The power-spectrum was observed to have a broadened peak with a subsequent $1/f^3$ decay for large frequencies; the peak in the power-spectrum corresponds to the average interval between two successive avalanches and the large-frequency power-law decay essentially arose from the short-time correlations in the particle currents. In other words, the non-trivial $1/f^{\alpha}$ spectrum with $1 \lesssim \alpha < 2$ was not observed in the experiment.

For a real granular pile, the $1/f$ noise is perhaps not expected to occur, due to the dominant effects of inertia of grains, which tend to roll down the slope under gravity. In the presence of dissipation, the inertia essentially introduces a crossover length scale, beyond which the dissipative regime takes over. This cross over length scale could however be large in a typical experimental set up. To reduce the inertial effects, the Oslo group [29] studied avalanches in a pile of long-grained rice in a specially designed experiment. The pile was made between two vertical plates kept on a plane base, where the separation between the plates is small compared to the length of the base. One end of the pile is closed and the other end is open; the grains are added slowly through the closed end and the grains go out of the system through the open end. Large anisotropy of the grains stops the grains from rolling too far down the surface of the pile. In this particular set up, SOC was indeed observed in the avalanche statistics, where avalanche sizes were observed to follow a power-law distribution, implying events at all length scales and hence criticality. Here avalanche size is defined as the spatial extent of activities generated in the system when the system is perturbed by addition of a single grain (in experiment, the avalanche size can be measured, e.g., through the number of displaced grains in response to a perturbation localized in space and time). The ricepile experiment shows that SOC may not be that generic a feature of systems having a threshold activated dynamics, rather depends on various other details (e.g., shapes and sizes of grains and what materials they are made of, etc.). In the ricepile experiment, in addition to the avalanche statistics, another important aspect of SOC systems, i.e., transport properties of sandpiles, was studied through the distribution of residence times (the times spent by the grains inside the pile). Interestingly, the distribution was observed to have a power-law tail and is discussed later.

2.2. Simulations

Kertesz and Kiss revisited the BTW's original question of long-time correlations in the toppling activity (avalanche) in the BTW sandpile models by carefully analysing the power-spectrum of the activity time-signal [52]. Kertesz and Kiss showed that the average power spectrum of activity,

$$S(\omega) = \int dsP(s)\frac{s^2}{(1+\omega^2\tau_s^2)}, \tag{2}$$

can be obtained by averaging over the distribution $P(s) \sim s^{-\tau}$ of individual avalanche sizes s. Here it is assumed that an individual avalanche of size s have a Lorentzian power spectrum $s^2/(1+\omega^2\tau_s^2)$, with τ_s being the mean time-duration of the avalanche of size s; note that we have written the spectrum in terms of the angular frequency $\omega = 2\pi f$. Provided the power-law dependence of the mean avalanche time duration $\tau_s \sim s^x$ on avalanche size s, one has $S(\omega) \sim \int^{\omega\tau_L} u^{(3-x-\tau)/x}/(1+u^2)du$ where τ_L is the upper cut-off to the avalanche duration. Now, depending on the actual values of the two exponents τ and x, there are two possibilities for the low-frequency behavior of the power spectrum: (i) for $2x+\tau > 3$, $S(\omega) \sim 1/\omega^{(3-\tau)/x}$ and (ii) for $2x+\tau \leq 3$, $S(\omega) \sim 1/\omega^2 \sim 1/f^2$. In simulations, the exponents were found to be $\tau \simeq 1.1$ and $x \simeq 0.68$, implying that the low-frequency behavior of the power-spectrum is actually $1/f^2$ [52]. The theoretical form of the spectrum was verified in direct measurement of the power-spectrum in simulations, which are in fair agreement with $1/f^2$. However, here one should note that the noise spectrum measured in the experiment by Jaeger et al. [28] and that by Kertesz and Kiss [52] (and by BTW in [1]) are in principle two different quantities as the former was related to the outflux at the boundary while the latter to the time-signal of toppling activities in the bulk. In a related work, Jensen et al. [53] pointed out this difference and calculated the power-spectrum of the particle-flow at the boundary. From these studies, one could conclude that the BTW sandpile, though having long-ranged spatio-temporal correlations which are manifest in the power-law distributed avalanche size and avalanche duration, apparently does not exhibit the $1/f$ noise spectrum. The reason because the BTW sandpile does not have $1/f$-type spectrum is that the distribution of avalanche duration has a long tail; indeed, if the distribution of avalanche time decays faster, there would have been a possibility of $1/f$ noise [e.g., provided $\tau + x = 3$, the power spectrum is given by $S(f) \sim 1/f$]. Manna and Kertesz [54] studied the time series of total mass in the two-dimensional BTW sandpile in the slow driving limit; unlike in the studies in [1, 52], here the time unit was chosen as the interval between the addition

of two successive grains. The steady-state two-point temporal correlation $C(t) = \langle M(t)M(0)\rangle - \langle M(0)\rangle^2 \sim \exp(-t/T_M)$, where $M(t)$ is the total mass at time t, has an exponential decay, with the correlation time T_M scaling with system size L as $T_M \sim L^2$. Therefore, the power spectrum of mass fluctuation in the system has a Lorentzian form and essentially has a $1/f^2$ decay in the frequency domain $f \gg 1/L^2$. Therefore, the noise activity in the BTW sandpile is less "erratic," and more correlated, than what was perhaps expected by BTW in their original paper.

In simulations of the BTW sandpiles by Kertesz and Kiss [52], the power spectrum was actually obtained by randomly superposing the activity time-signals during the individual avalanches. As each grain is added only after the system becomes stable (i.e., no unstable site is present), the avalanches created at different positions do not interact, or overlap, with each other. Hwa and Kardar [55] argued that the $1/f$ noise could arise in the system when the individual avalanches, which are created at different space points, are allowed to overlap with each other and to develop nontrivial correlations in that process. This scenario is possible only when the system is driven at a finite rate, as opposed to the slow driving limit proposed in the theory of SOC. Therefore, according to Haw and Kardar, the BTW sandpile could well exhibit the $1/f$ noise when the system is driven at a finite rate. Indeed, in many of the observed phenomena, such as voltage fluctuations in conductors, the $1/f$ noise actually appears at a finite driving rate. If that is the case, presumably one cannot apply the SOC to explain the $1/f$ spectrum in those situations. Sandpiles driven with a finite addition rate should be applicable to much broader range of phenomena and, moreover, can in principle exhibit interesting long-time correlations. Furthermore, from the physical point of view, another troubling point is that the time unit in the slow driving limit is not quite well defined as the grains are added in unequal time intervals (on the microscopic time scale of the elementary toppling events). Finite driving of the system removes these difficulties and introduces a well defined external time scale in the problem.

Following the update rules of the variants of the BTW sandpiles proposed by Kadanoff et al. [3], Hwa and Kardar considered a one dimensional critical *slope-type* sandpiles (toppling condition depends on a threshold value of the slope), called "running sandpiles." The system is driven with finite rate where one adds a grain at a site i, i.e., $h(i, t+1) = h(i,t) + 1$, with a small probability $p = J_{in}/L$, where $h(i,t)$ is the height at site i, J_{in} is the average deposition rate and L is the system size. The evolution rules are given by

$$h(i, t+1) = h(i,t) - n_f, \tag{3}$$

$$h(i+1, t+1) = h(i+1,t) + n_f, \tag{4}$$

provided that the slope $h(i,t) - h(i+1,t) > \Delta$ (in simulations, $n_f = 2$ and $\Delta = 8$) and with the boundary condition that the left boundary is closed, i.e., $h(0,t) = h(1,t)$ and the right boundary dissipates grains, i.e., $h(L+1,t) = 0$. The quantities of interest are the power spectrum of the instantaneous output current $J(t)$ (outflux at the boundary site $i = L$), which is the number of grains leaving the system at time t, and that of the instantaneous activity or energy dissipation $E(t)$, which is the total number of toppling in the system at time t. In the steady state, the input current balances the average outflux, i.e., $J_{in} = \langle J\rangle$; note that the model has a maximum output capacity of n_f grains per unit time so that $J_{in} \leq n_f$. The power spectra are found to have the following power-law form $S_J(\omega) \sim \omega^{-\alpha_J}$ and $S_E(\omega) \sim \omega^{-\alpha_E}$ for the outflux and the activity time-signals, respectively. The system is observed to have three distinct scaling regimes, characterized by the different values of the exponents α_J and α_E: high-frequency single-avalanche regime I, intermediate-frequency interacting-avalanche regime II and low-frequency system-wide discharge regime III; each of the regimes are separated from each other by L-dependent time scales [55]. Regime I is dominated by single avalanches and arises in the time range of the typical avalanche duration (as studied in [52], for example). In the simulations, the exponents in the power spectrum are observed to be $\alpha_J \approx 2$ and $\alpha_E \approx 4$. Regime II is dominated by the interacting avalanches and happens on the time scale L^z, where z is the dynamic exponent. The exponents in the power spectrum in this regime are given by $\alpha_J \approx 1$ and $\alpha_E \approx 1$, confirming the presence of the $1/f$ noise in the system. As we see later, this is the regime (also called hydrodynamic regime), which can be captured by a large-scale hydrodynamic theory [55]. Regime III is dominated by system-wide discharge processes, which happen on the time scales of L^2, during which the macroscopic slope of the pile changes. Interestingly, the exponents in the power spectrum are negative in this regime and are given by $\alpha_J \approx -1$ and $\alpha_E \approx -1$. The negative exponents suggest anti-correlations in outflux and activity time-signals.

It is quite interesting to note that, in a recent study by Garcia-Millan et al. [56], similar anti-correlations, albeit in avalanche time-signals, have been observed in the boundary driven one dimensional Oslo ricepile model [18] in the slow driving limit (grains are added with unit rate and only after the system becomes stable). Here one constructs a time-series of avalanches, where $s(t)$ denotes avalanche size at time step t. Then the variance $\sigma_T^2 = \langle S_T^2\rangle - \langle S_T\rangle^2$ of the sum of T consecutive avalanches $S_T = \sum_{t=1}^{T} s(t)$ is observed to be highly suppressed. That is, avalanche time series have hyper-uniform fluctuation, characterized by $\sigma_T^2 \sim T^{\lambda}$ with $\lambda = 0$. (Normal fluctuations correspond to $\lambda = 1$.) In fact, steady-state two-time correlation function $C(t) = \langle s(t)s(0)\rangle - \langle s(t)\rangle\langle s(0)\rangle$ is negative for any nonzero $t > 0$. Such anti-correlations in time possibly plays a crucial role in determining transport properties of sandpiles and it would be quite interesting to further explore their connections in future.

2.3. Theories

At this stage, one would be interested to explore whether some of the above observations can be captured in a unified theoretical framework. Hwa and Kardar [55, 57] addressed this issue in developing a large-scale hydrodynamic framework, based on symmetries and conservation laws. Later on, more refined field theories were set up [58], especially in the context of absorbing phase transition with a conserved field, which is associated with the fixed-energy version of sandpiles [20–22, 37, 38, 59, 60]. However, the studies by Hwa and Kardar

made the basis for the standard field theoretical techniques applied to sandpiles, particularly in characterizing the long-time correlations and the corresponding power spectra in various time-signals, such as toppling activities. As we discuss next, the following hydrodynamic theory provides simple predictions of the power spectra of various time-dependent quantities, which could be directly tested in simulations.

Motivated by the experiments on granular piles [28] and the observed power spectra of outflux and toppling-activity in simulations of running sandpiles, Hwa and Kardar [55, 57] proposed a drift-diffusion equation for height field $h(\mathbf{x}, t)$ in sandpiles, which are written in the leading order of non-linearities,

$$\frac{\partial h(\mathbf{x}, t)}{\partial t} = D_{||}\partial_{||}^2 h + D_{\perp}\nabla_{\perp}^2 h - \frac{\lambda}{2}\partial_{||}(h^2) + \eta(\mathbf{x}, t), \qquad (5)$$

where $\mathbf{x}_{||} = (\mathbf{x}.\hat{\mathbf{n}})\hat{\mathbf{n}}$ and $\mathbf{x}_{\perp} = \mathbf{x} - \mathbf{x}_{||}$ are the position vector along the transport direction $\hat{\mathbf{n}}$ and perpendicular to the transport direction; $\eta(\mathbf{x}, t)$ is a zero-mean non-conserved noise, having $\langle \eta(\mathbf{x}, t)\eta(\mathbf{x}', t')\rangle = 2\Gamma\delta^d(\mathbf{x} - \mathbf{x}')\delta(t - t')$ (d is the dimension), and physically represents random addition of grains; in the conserved case, noise satisfies $\langle \eta(\mathbf{x}, t)\eta(\mathbf{x}', t')\rangle = 2\Gamma\nabla^2\delta^d(\mathbf{x} - \mathbf{x}')\delta(t - t')$. Note that, due to the specific nature of the boundary condition where the grains are added at the one end (say, left) and are dissipated through the other end (say, right) of the pile, the grains tend to flow in a particular direction $\hat{\mathbf{n}}$. To obtain the above hydrodynamic equation, the local current $\mathbf{J}(h)$ is expanded in height variable h and its gradient,

$$\mathbf{J}(h) \simeq -(D_{||}\partial_{||}h)\hat{\mathbf{n}} - D_{\perp}\nabla_{\perp}h + \frac{\lambda}{2}(h^2)\hat{\mathbf{n}}, \qquad (6)$$

where higher order non-linearities, though some of them (e.g., ∇h^n and h^n, etc. for integer $n > 0$) permitted by the symmetries, are ignored by assuming the fluctuations are small. It is immediately not clear if the non-linear terms such as h^2 should be allowed as such terms do not obey simple translation in h, i.e., $h \to h + c$. However, Grinstein and Lee [61] later provided a mechanism for generating such terms in the hydrodynamic equations. The absence of this translation symmetry in height can also be seen as the consequence of the boundary condition [e.g., $h(x_{||} = L) = 0$ at the right end], due to which one cannot translate the height profile arbitrarily. It should be noted here though that the non-linear terms (e.g., that involving λ) are in fact not necessary to generate scale invariance in a system; anisotropic diffusion can be sufficient for that purpose [61–64]. Provided the stochastic non-linear hydrodynamics Equation (5), one can use dynamic renormalization group and $\epsilon = 4 - d$ expansion technique (upper critical dimension $d_c = 4$ in this case) to calculate the fundamental exponents χ, ζ and z, which characterize spatio-temporal fluctuations of the height variable: upon change of length and time scales $x_{||} \to bx_{||}$, $\mathbf{x}_{\perp} \to b^{\zeta}\mathbf{x}_{\perp}$ and $t \to b^z t$, the height variable should then transform as $h \to b^{\chi}h$. Using simple dimensional analysis, one can obtain the scaling properties of various time-dependent correlation functions in terms of the height correlations and the scaling dimensions (χ, ζ and z) of the systems. For example, one has the outflux and the activity correlations $C_J(t) = \langle J(t)J(0)\rangle - \langle J(t)\rangle\langle J(0)\rangle \sim t^{[4\chi+(d-1)\zeta]/z}$ and $C_E(t) = \langle E(t)E(0)\rangle - \langle E(t)\rangle\langle E(0)\rangle \sim t^{[4\chi+(d-1)\zeta+1]/z}$, respectively, where $J(t)$ and $E(t)$ are the outflux and the number of toppling at time t. The corresponding power spectra, which are the corresponding Fourier transforms of the time-correlation functions, are given by $S_J(\omega) \sim \omega^{-\alpha_J}$ with $\alpha_J = 1/z$ and $S_E(\omega) \sim \omega^{-\alpha_E}$ with $\alpha_E = 2/z$; in two dimensions ($z = 6/5$), the numerical values of the exponents can be obtained as $\alpha_J \simeq 0.83$ and $\alpha_E \simeq 1.67$, implying the existence of the $1/f$-type power spectra in the system corresponding to the anisotropic drift-diffusion Equation (5). For isotropic case (as in the BTW sandpile), one has the simplest non-linear hydrodynamic equation,

$$\frac{\partial h(\mathbf{x}, t)}{\partial t} = D\nabla^2 h - \frac{\lambda}{2}\nabla^2(h^2) + \eta(\mathbf{x}, t), \qquad (7)$$

which, in the absence of noise term $\eta(\mathbf{x}, t)$, is a non-linear diffusion equation, where the local current has the form up to the leading order non-linearities,

$$\mathbf{J}(h) = -(D - \lambda h)\nabla h. \qquad (8)$$

As mentioned previously, depending on the situation, the noise term can be either nonconservative or conservative. Interestingly, in the above equation for local current, one can see that the bulk-diffusion coefficient ($D - \lambda h$) can have a clustering instability (the diffusivity reduces for larger value of h). As we see later, the nature of the above diffusive instability is different from that in sandpiles. However, unlike the anisotropic case, the parameters D and Γ in the isotropic case can get normalized in a nontrivial way and calculation of the exponents are difficult [58, 65]. From an overall point of view, in the dynamic renormalization group analysis, it is not obvious how the renormalized diffusivity could give rise to singular diffusion in the system (the renormalization group theory does predict though "super-diffusive" behavior as $z < 2$).

Hwa and Kardar attempted to provide a large-scale hydrodynamic theory of sandpiles, which could capture scale invariant spatio-temporal structures of the systems having the same symmetries as in sandpiles. The theory was indeed successful in calculating various time-dependent properties of the SOC-like systems, such as the $1/f$-type noise spectrum and height correlations, etc. However, the theory remains somewhat unsatisfactory as it cannot explain the precise nature of the transport instability, a unique characteristic of sandpiles, which, as we discuss later, is present in the form of a near-critical singular bulk-diffusion coefficient as well as singular conductivity. Possibly, the large non-linearity due to the threshold-activated dynamics in the SOC systems invalidates the gradient expansion of the local current as given in Equation (6). The current is truncated at the lowest-order non-linearities in height and height gradient, and cannot capture the singular diffusion in sandpiles.

3. INSTABILITIES IN SANDPILES: SINGULAR TRANSPORT

It is important to characterize instabilities, which can be present in a system near criticality and thus govern the large-scale transport and fluctuations. For example, one could see such an instability in the flow structure of grains in a Hele-Shaw cell where a pile of grains is formed and grown between a confined space and there can be a transition from a continuous flow regime to an intermittent one upon varying certain parameters [66]. In the context of the threshold-activated model systems like sandpiles operating near criticality, the power-law spatio-temporal correlations, as reflected in the avalanche statistics, are strongly indicative of the existence of instabilities in particle transport. However, the precise nature of the transport instability was not clear until Carlson et al. [67] demonstrated the existence of the singular diffusion in a two-state sandpile-like model. Indeed, the bulk-diffusion coefficient in the model was shown to diverge when the system is slowly driven (or, "tuned," in the sense of fixed-energy sandpiles) toward criticality. But, before we go into this topic, let us first discuss another set of related works, which explored tagged-particle diffusion (also called self-diffusion) to characterize transport properties of sandpiles.

3.1. Tagged-Particle Correlations

In sandpiles, particle transport happens through avalanches. One would therefore expect a close relationship between local toppling activities and transport in the system. As discussed in the previous section, the existence of such a relationship is quite apparent through the emergence of long-time correlations in both outflux and toppling activities (as evident in the respective power spectra), which can be closely related through the height fluctuations in the system (they have similar power spectra with exponents $\alpha_J \approx \alpha_E \approx 1$). Another way to characterize the time-dependent correlations in the system would be to directly connect the toppling activities and the particle transport. This could be done by probing tagged-particle correlations in the systems, e.g., through the distribution of tagged-particle residence times or through characterization of the self-diffusion.

The residence time is defined as the time spent by a tagged particle inside the system. If a particle is added in the system, say, at t_{in} and the particle leaves the system at time t_{out}, the residence time is defined as $T = t_{out} - t_{in}$. One could ask whether the distribution of residence time is described by a power law and, if so, whether the distribution is any way related to the power-law statistics of avalanches in the system. It turns out that the distribution of residence time, though governed by local toppling activities and can exhibit power-law tails, does not depend on the avalanche exponents. However, the distributions are not universal in the sense that it can depend on the details of particle addition as well as the toppling (or particle-transfer) rules in the systems.

In the Oslo ricepile experiment [29] discussed in the previous section, the distribution of residence times $P(T, L)$ of tracer particles in a system of size L was measured. The tracers were tracked since the time they have been added till the time they leave the system, and the residence times were measured. The distribution was observed to have a power-law tail, $P(T, L) \sim 1/T^{\alpha}$, with the exponent $\alpha \simeq 2.4$ and the mean residence time $\langle T \rangle \sim L^{\nu}$ with $\nu \simeq 1.5$. To explain the experimental findings, Boguna and Corral proposed a continuous-time random walk model, having a power-law distribution $\psi(t) \sim 1/t^{\alpha'}$ of trapping time t - the time a grain is trapped or buried in the pile; here the exponent α' is an undetermined parameter in the model. The analysis showed that the exponent α in the distribution of residence time is determined by the exponent α' in the trapping-time distribution, $\alpha = \alpha'$. Later, using the ricepile model proposed in Christensen et al. [18], it was argued [68] that the power-law tail of the distribution $P(T, L)$ should be dominated by the grains, which are deeply buried in the pile and take a very long time to come out due to the rare height fluctuations. Indeed, the cut-off time T_{max} to the trapping-time distribution is related to the hight fluctuation of the pile and was estimated to be exponentially large $T_{max} \sim \exp(\kappa L^3)$ [69], where L is the system size. Moreover, the mean residence time $\langle T \rangle$ was exactly shown to be equal to the average mass of the pile, i.e., $\langle T \rangle \sim L^2$. The cumulative probability distributions of both trapping times T_{tr} and residence times T have a power-law scaling $\text{Prob.}(T_{tr} \geq t) \sim L^{\omega_1}/[t\{\ln(t/L^{\omega_1})\}^{\delta_1}]$ and $\text{Prob.}(T \geq t) \sim L^{\omega}/[t\{\ln(t/L^{\omega})\}^{\delta}]$, with a logarithmic corrections where ω_1, δ_1, ω, and δ are model dependent exponents. Therefore, one obtains $\alpha = 2$, which also holds in other critical *slope-type* sandpiles (toppling depends on the threshold value of the slope) as long as one implements "first-in-last-out" rule, i.e., an incoming grain at any site sits on the top, while the topmost grain at the site leaves first [68]. Note that, in the Oslo ricepile experiment, the measured value of α being slightly >2 is possibly because the logarithmic correction was not considered in the experimental data fitting. Though the distribution of residence times in slope-type sandpiles have a universal power-law scaling $1/T^2$ (with a non-universal logarithmic correction), the distribution in critical *height-type* sandpiles (threshold condition is on the height variable) can be a power law or an exponential function [70], depending on the details of the grain addition. Indeed, one can show that the probability distribution (density) function $P(\mathbf{x}, t)$ of position $\mathbf{x}$ of a tagged particle at time t is governed by a space-dependent diffusion equation,

$$\frac{\partial P(\mathbf{x}, t)}{\partial t} = \frac{1}{2}\nabla^2[D(\mathbf{x})P(\mathbf{x}, t)], \tag{9}$$

where local diffusivity $D(\mathbf{x})$ of a tagged particle is proportional to $n(\mathbf{x})$, the average number of toppling at position $\mathbf{x}$ per unit time; the initial condition can be specified as $P(\mathbf{x}, t = 0) = r(\mathbf{x})$ where $r(\mathbf{x})$ is the addition rate at site $\mathbf{x}$ [70]. Therefore, unlike in slope-type models where distributions of residence times are determined by the power-law trapping time distributions, the distributions of residence times in height-type models are governed by the space-dependent diffusivity, which is directly related to the local toppling activity in the systems. We note here that somewhat surprisingly, in both slope- and height-type sandpiles, the exponents characterizing the distributions of residence times are not related to the critical avalanche exponents.

The tagged-particle correlations have also been explored by da Cunha et al. [39, 71] in several variants of the conserved Manna sandpiles and both in one and two dimensions, directly through the studies of the self-diffusion coefficient $\mathcal{D}(\rho)$ of a tagged particle. Here one considers a stochastic steady-state trajectory of a particle, i.e., position $X_i(t)$ of, say, i-th particle at time t. Then the mean-square displacement of the particle up to time t has the following asymptotic form for large t: $\langle [X_i(t) - X_i(0)]^2 \rangle \simeq 2\mathcal{D}(\rho)t$, where the self-diffusion coefficient $\mathcal{D}(\rho)$ depends on the number density ρ. Interestingly, it was observed that the self-diffusion coefficient is proportional to the activity in the system. As the activity $a(\rho)$ in the conserved Manna sandpiles has singular behavior near the critical density, the tagged-particle diffusion is also singular in this regime and can be characterized by the same exponent as in the activity (there is no rigorous proof yet though). Indeed, this particular feature is expected to be quite generic in the fixed energy sandpiles undergoing an absorbing phase transition; however, the issue is not settled yet.

3.2. Hydrodynamics of Sandpiles

The hydrodynamic equations, and the corresponding dynamic renormalization group (RG) theory, proposed by Hwa and Kardar [55, 57] was successful to some extent in explaining the emergence of scale invariance, and in extracting the critical exponents of sandpiles in a general hydrodynamic framework, based on symmetries and conservation laws. Though scope and applicability of this theory is quite broad, the theory cannot really explain the mechanism, which gives rise to the singularity (pole-type) in the diffusion coefficient. The possible reason for the failure to capture the singular diffusion is that the proposed hydrodynamic equations (Equations 5 and 7) do not actually take into account the threshold-activated nature of the local dynamics in the theory. In this scenario, the rigorous derivation of hydrodynamics of the simple two-state model put forward by Carlson et al. [67, 72, 73] provided not only the much needed impetus into the theory of SOC, but also some useful insights into the possible large-scale structures of sandpiles in general. We discuss below a few examples of simple model systems, where large-scale hydrodynamic time evolution can be obtained and, in some of the systems, the transport can indeed become singular. For simplicity, in the following discussions, we confine ourselves to one dimensional models and conserved (fixed-energy) versions; the models can be suitably generalized to higher dimensions and open boundaries. Such a hydrodynamic framework [74, 75] not only provides the insights into the relaxation properties, but can also determine in principle the fluctuation properties of these systems [76–79].

3.2.1. A Two-State Model of Sandpile

Carlson et al. [67, 72] considered a model of lattice gas, consisting of hardcore particles diffusing on a lattice. The occupation variable η_i at site i can be at most one: $\eta_i = 1$ if the site is occupied by a particle, otherwise $\eta_i = 0$. For simplicity, let us consider the fixed-energy version of the model on a periodic lattice of L sites, where the number of particles is conserved; we denote the number density as $\rho = N/L$. The model can be appropriately generalized to that with an open boundary and a slow drive. Any particle hops to its nearest vacancy, with a unit rate and symmetrically to its right or the left; the dynamical rules are unlike that in a simple symmetric exclusion process, where a particle can hop only to its vacant nearest-neighbor site. For example, consider the following hopping event $\{\ldots 01\hat{1}110\ldots\} \rightarrow \{\ldots 010111\ldots\}$, where "$\hat{1}$" denotes the hopping particle; note that the reverse process also happens with the same rate. Consequently, the hopping dynamics satisfy detailed balance with respect to Bernoulli product measure, where any site is occupied with probability ρ and is vacant with probability $(1-\rho)$. Precisely due to the time-reversibility and the product-measure steady state, the model is amenable to a rigorous derivation of hydrodynamics [72], which governs the large-scale relaxation in the system. Here we only present a sketch of the derivation, which will illustrate the procedure of deriving hydrodynamics in a general context. Notably, the model has a long-ranged hopping (avalanche-like) mechanism built into it and, in this way, it mimics the threshold-activated dynamics of sandpiles. Indeed, one can immediately see that, depending on the density ρ, the average jump length $\langle l \rangle$ of a particle in one hopping event is given by $\langle l \rangle = \sum_{l=1}^{\infty} l\rho^{l-1}(1-\rho) = 1/(1-\rho)$, which diverges as the density approaches (from below) the critical density $\rho_c = 1$ (i.e., as $\rho \rightarrow 1^-$). The model is not defined for $\rho > 1$ and one of its variant is discussed in the next section.

To calculate the density-dependent bulk-diffusion coefficient $D(\rho)$, let us consider net local bond-current $J(i, i+1)$ between i-th and $(i+1)$-th sites,

$$J(i,i+1) = \sum_{r=1}^{\infty} \left(\left\langle \prod_{r'=1}^{r} \eta_{i+r'-r} \right\rangle - \left\langle \prod_{r'=1}^{r} \eta_{i+r'} \right\rangle \right) = \sum_{r} \left[\mathcal{A}^{(r)}(i) - \mathcal{A}^{(r)}(i+r) \right]. \quad (10)$$

Here we have denoted the r-point correlation as $\mathcal{A}^{(r)}(i) \equiv \langle \prod_{r'=1}^{r} \eta_{i+r'-r} \rangle$, which is the probability that the consecutive r number of sites to the left of site i are occupied. As one would expect, on hydrodynamic scales, the local density $\rho(i,t) = \langle \eta_i(t) \rangle$ is assumed to be a slowly varying function of space and time, and thus the current in the system is small $[\mathcal{O}(1/L)]$. Now, by scaling space $x = i/L$ and expanding $\mathcal{A}^{(r)}(i+r) \equiv \mathcal{A}^{(r)}(\rho(x+r/L))$ in the Taylor series around the local density $\langle \eta_i(t) \rangle = \rho_i(t) \equiv \rho(x,t)$, we have

$$\mathcal{A}^{(r)}(i+r) \simeq \mathcal{A}^{(r)}(\rho(x,t)) + \frac{r}{L} \frac{\partial \mathcal{A}^{(r)}(\rho(x,t))}{\partial x}. \quad (11)$$

Similarly, the local current can be written using Equation (10),

$$J(i,i+1) \simeq -\sum_{r} \frac{r}{L} \frac{\partial \mathcal{A}^{(r)}(\rho(x,t))}{\partial x} = -\frac{1}{L} \sum_{r} r \frac{\partial (\rho(x,t))^r}{\partial x}, \quad (12)$$

where, in the last step, we have written the correlation $\mathcal{A}^{(r)} = \rho^r$ by using the product-measure (local) steady-state. Therefore, the rescaled local current $J(x) \equiv LJ(i, i+1)$ is proportional to the density gradient (rescaled) $\partial\rho/\partial x$ and can be written as

$$J(\rho(x,t)) = -\sum_{r} r^2 \rho^{r-1} \frac{\partial \rho(x,t)}{\partial x} \equiv -D(\rho) \frac{\partial \rho(x,t)}{\partial x}, \quad (13)$$

where the proportionality constant, which is called the bulk-diffusion coefficient, is given by

$$D(\rho) = \sum_{r=1}^{\infty} r^2 \rho^{r-1} = \frac{1+\rho}{(1-\rho)^3}. \tag{14}$$

Note that the bulk-diffusion coefficient is in general a non-linear function of density ρ and, in this case, has a third-order pole at density $\rho = 1$. The time evolution of density at site i is given by $\partial\rho_i(t)/\partial t = -[J(i,i+1) - J(i-1,i)] \simeq -(1/L)\partial J/\partial x$, which can be written, by rescaling space $x = i/L$ and time $\tau = t/L^2$ (called diffusive scaling limit) and in terms of the rescaled or the coarse-grained density field $\rho(x,\tau)$,

$$\frac{\partial\rho(x,\tau)}{\partial\tau} = \frac{\partial}{\partial x}\left[D(\rho(x,\tau))\frac{\partial\rho(x,\tau)}{\partial x}\right]. \tag{15}$$

Provided an initial condition $\rho_{in}(x) \equiv \rho(x, \tau = 0)$, the long-wavelength density relaxation in the system is exactly described by the above hydrodynamic time-evolution (Equation 15).

Carlson et al. [72] also studied tagged-particle correlations, which can provide information about the singularity in the particle transport. Let us denote the position of the i-th tagged particle at time t as $X_i(t)$. Then the mean square displacement $(\Delta X_i(t))^2 = \langle (X_i(t) - X(0))^2 \rangle$ of the tagged particle has a limiting behavior, where the scaled variance $\lim_{t\to\infty}(\Delta X_i(t))^2/t = \sum_{l=1}^{\infty} l^2\rho^{l-1}(1-\rho) = (1-\rho)D(\rho) \sim 1/(1-\rho)^2$. The scaled variance of the displacement of a tagged particle has the order of pole singularity one less than that for the bulk-diffusion coefficient in Equation (14). The bulk and the self diffusivities are in principle two different quantities, but, as discussed above, both of them can be a good indicator of the instability of the particle transport in a system. In fact, we mentioned in the previous section how the tagged-particle diffusion can be used to probe activity in sandpiles. However, it remains to be seen how one can actually connect activity and tagged-particle diffusion on a hydrodynamic level.

3.2.2. Fixed-Energy Sandpiles and Absorbing Phase Transition

3.2.2.1. A Simple Example

The two-state model discussed in the previous section is not defined above density $\rho = 1$. Note that, during any hopping move in the model, a particle gets transported to its nearest vacant site instantaneously, introducing possibly an unwanted feature of long-range hopping in the system. Alternatively, to bypass the difficulty, one can introduce a microscopic hopping time-scale into the problem and restrict to only nearest-neighbor hopping [80]. For example, if the number of particles $n_i(t)$ at a site i is greater than 1, there is a toppling at unit rate and one particle gets transferred symmetrically to one of its two nearest neighbors. That is, when $n_i(t) > 1$, $n_i(t+1) = n_i(t) - 1$ and $n_j(t+1) = n_j(t) + 1$ where $j = i \pm 1$ is one of the two nearest neighbors of site i. In the modified model, we have relaxed the hardcore constraint on the particle occupancies of the sites. Although this particular model has a trivial scaling behavior, it would illustrate how the relationship between the activity and transport on hydrodynamic scales arise quite naturally in sandpiles.

In fact, given the simple dynamical rules, the model can be treated analytically and the transport coefficients can be calculated exactly as the steady-state, for density $\rho > 1$, has again a product-measure, with the probability distribution Prob.$[n_i = n] = P(n) = \frac{1}{\rho}\left(\frac{\rho-1}{\rho}\right)^{n-1}$ of single-site particle-number $n = 1, 2, \ldots$. The above result can be easily obtained by mapping steady-state dynamics of the model (i.e., in the space of steady-state configurations), to that of a zero range process [81]. Indeed, for density $\rho > 1$, the configurations with $n_i = 0$ are non-recurrent and does not appear in the steady state; however, in the space of recurrent configurations, the model still satisfies a detailed balance with respect to the steady-state (product) measure. On the other hand, for density $\rho \leq 1$, system goes into an absorbing state, devoid of any dynamical activity in the system. One can define an order parameter, called activity, $a(\rho) = \langle N_a \rangle/L$, where N_a is the number of active sites in the system. It is easy to see that the activity $a(\rho)$ is nonzero for $\rho > \rho_c = 1$ and zero otherwise. For $\rho > 1$, the activity is obtained exactly as $a(\rho) = \sum_{n=2}^{\infty} P(n) = 1 - P(n=1) = (\rho-1)/\rho$, implying $a(\rho) \sim (\rho - \rho_c)^{\beta}$ as $\rho \to \rho_c^+$ where order parameter exponent $\beta = 1$.

In the presence of a single conserved quantity such as local particle-number, the coarse-grained density field is governed by two transport coefficients—the bulk-diffusion coefficient $D(\rho)$ and the conductivity $\chi(\rho)$; both transport coefficients are in general non-linear functions of density ρ. In the context of this simple model, it would be quite instructive to discuss a general theoretical framework to calculate transport coefficients following a linear response theory [77, 78, 82, 83]. The framework provides, in the diffusive scaling limit, an exact hydrodynamic theory of relaxation and fluctuation in the system. As done in the previous section, to calculate the bulk-diffusion coefficient, one has to apply a bias in the form of a small density gradient $\partial\rho/\partial x$ and calculate the local diffusive current

$$J_{diff} = -D(\rho)\frac{\partial\rho}{\partial x}, \tag{16}$$

which is analogous to the Fick's law of diffusion. Likewise, to calculate the conductivity, one has to apply a small external force field of magnitude F, which couples to the local particle-number and thus bias the particle-hopping rates in the direction of the biasing force. The biased or the modified particle-hopping rate $c^F_{i\to j}$, from site i to $j = i \pm 1$, is determined using a local detailed balance condition [82, 83] as following,

$$\begin{aligned} c^F_{i\to j} &= c_{i\to j}\exp\left[\frac{1}{2}\Delta m_{i\to j}F(j-i)\delta x\right] \\ &\simeq c_{i\to j}\left[1 + \frac{1}{2}\Delta m_{i\to j}F(j-i)\delta x\right], \end{aligned} \tag{17}$$

where $c_{i\to j}$ is the original hopping rate in the absence of the biasing force, $\Delta m_{i\to j} = 1$ is the number of particles transferred

from site i to j, and $\delta x = 1$ is the lattice spacing. The biasing force gives rise to a small drift current

$$J_{drift} = \chi(\rho)F, \tag{18}$$

which is analogous to the Ohm's law for the electrical conductivity in a current carrying wire. The time-evolution of density $\rho_i(t) = \langle n_i(t)\rangle$ can be straightforwardly obtained using the stochastic update rules for particle number $n_i(t)$ in an infinitesimal time interval between t and $t + dt$ as given below,

$$n_i(t+dt) = \begin{cases} n_i(t) - 1 & \text{prob. } \hat{a}_i dt, \\ n_i(t) + 1 & \text{prob. } \hat{a}_{i-1}\left(1 + \frac{F\delta x}{2}\right)\frac{dt}{2}, \\ n_i(t) + 1 & \text{prob. } \hat{a}_{i+1}\left(1 - \frac{F\delta x}{2}\right)\frac{dt}{2}, \\ n_i(t) & \text{prob. } 1 - \Sigma_1 dt, \end{cases} \tag{19}$$

where $\hat{a}_i$ is an indicator function for occupancy of ith site ($\hat{a}_i = 1$ if $n_i > 0$ and $\hat{a}_i = 0$ otherwise), $\delta x = 1$ is the lattice spacing and

$$\Sigma_1 = \left[\hat{a}_i + \frac{1}{2}\left\{\hat{a}_{i-1}\left(1 + \frac{F\delta x}{2}\right) + \hat{a}_{i+1}\left(1 - \frac{F\delta x}{2}\right)\right\}\right]. \tag{20}$$

The local density evolves according to the equation,

$$\frac{\partial \rho_i(t)}{\partial t} = \frac{1}{2}\left(\langle \hat{a}_{i+1}\rangle + \langle \hat{a}_{i-1}\rangle - 2\langle \hat{a}_i\rangle\right) + \frac{F}{4}\left(\hat{a}_{i-1} - \hat{a}_{i+1}\right), \tag{21}$$

which, in the diffusive scaling limit $x = i/L$, $\tau = t/L^2$ and biasing force $F \to F/L$, leads to the desired hydrodynamic evolution of the scaled density field $\rho(x, \tau)$,

$$\frac{\partial \rho(x,\tau)}{\partial \tau} = \frac{1}{2}\frac{\partial^2 a(\rho(x,\tau))}{\partial x^2} - \frac{1}{2}F\frac{\partial a(\rho(x,\tau))}{\partial x} \equiv -\frac{\partial J}{\partial x}, \tag{22}$$

where $a(\rho) = (\rho - 1)/\rho$ is the activity, i.e., the probability that a site is active and the local current $J(\rho(x,\tau)) = J_{diff} + J_{drift}$. Now using Equations (16) and (18), we arrive at the expressions of the bulk-diffusion coefficient

$$D(\rho) = \frac{1}{2}\frac{da(\rho)}{d\rho} = \begin{cases} \frac{1}{2\rho^2} & \text{for } \rho > 1 \\ 0 & \text{otherwise,} \end{cases} \tag{23}$$

and the conductivity

$$\chi(\rho) = \frac{a(\rho)}{2}. \tag{24}$$

Note that the bulk-diffusion coefficient and the conductivity both vanish below critical density; however, the diffusivity approaches a constant value while one approaches the critical density from above ($\rho \to \rho_c^+$). On the other hand, the conductivity is proportional to the activity in the system and vanishes as density approaches the critical density, and remains zero below critical density. Indeed, as we see next in the conserved Manna sandpiles, vanishing of the conductivity near critical point seems to be a generic feature in conserved stochastic sandpiles, which undergoes an absorbing phase transition. At this stage, one could perhaps recognize the connection to the class of facilitated (or restricted) exclusion processes [84–86], where particles hop symmetrically to one of its vacant neighbors, only if the other neighbor is occupied. These facilitated exclusion processes also have similar features in the transport coefficients.

The model discussed above serves as probably the simplest possible example of an absorbing phase transition (APT) [87] in the presence of a conserved quantity. In fact, due to the non-singular behavior of the order parameter (the order parameter exponent $\beta = 1$), the bulk-diffusion coefficient, which is the derivative of the activity w.r.t. density, does not have any divergence. However, as we see below, the situation changes drastically when one modifies the dynamical rules slightly by introducing time-irreversibility (violation of detailed balance) in the steady state, leading to a nontrivial exponent $\beta < 1$ and thus singular particle transport in the system.

3.2.2.2. The Conserved Manna Sandpile

We now consider the conserved Manna sandpile [17], which serves as the paradigm for non-equilibrium absorbing phase transition [23] in a broad class of models with conserved mass, collectively called conserved stochastic sandpiles [32, 33, 88, 89]. Unlike the deterministic bulk dynamics in the BTW sandpile, the update rules in the conserved Manna sandpile, though still governed by a threshold-activated dynamics (critical height-type), are stochastic in nature. In the conserved version of the Manna sandpile, the total mass in the system remains conserved and the system undergoes an absorbing phase transition below a critical density ρ_c. We consider here the continuous-time variant of the Manna sandpile [32], where a site i is selected randomly and, if particle number $n_i > 1$, there is a toppling. During a toppling event, two particles (instead of one particle in the previous model) are transferred stochastically, and independently, to one of its neighboring sites. The hopping move, where two particles go in the opposite directions, is not reversible. As the system undergoes an absorbing phase transition below a critical density ρ_c, which in this case is strictly less than 1, the activity has nontrivial behavior as a function of density ρ: while $a(\rho)$ is nonzero for $\rho > \rho_c$, it has a power law decay $a(\rho) \sim (\rho - \rho_c)^\beta$, with $\beta < 1$, as ρ approaches the critical density from above ($\rho \to \rho_c^+$). Clearly, as opposed to the unbounded model considered previously, the activity now develops a singularity as a function of density as the derivative of the activity diverges near criticality. As we see below, the singularity in the activity leads to singular diffusion (as well as singular conductivity) in the system.

To calculate the conductivity, we follow the linear response theory of Chatterjee et al. [78]. We apply a constant external biasing force of magnitude F, which couples to the local particle number and bias the motion in the direction of force according to local detailed balance condition given in Equation (17). In the presence of the biasing force, the stochastic update rules for particle number at a site i can be written as

$$n_i(t+dt) = \begin{cases} n_i(t) - 2 & \text{prob. } \hat{a}_i(c^F_{i,0} + c^F_{i,+} + c^F_{i,-})dt, \\ n_i(t) + 1 & \text{prob. } \hat{a}_{i-1}c^F_{i-1,0}dt, \\ n_i(t) + 1 & \text{prob. } \hat{a}_{i+1}c^F_{i+1,0}dt, \\ n_i(t) + 2 & \text{prob. } \hat{a}_{i-1}c^F_{i-1,+}dt, \\ n_i(t) + 2 & \text{prob. } \hat{a}_{i+1}c^F_{i+1,-}dt, \\ n_i(t) & \text{prob. } [1 - \Sigma dt], \end{cases} \tag{25}$$

where $\Sigma = [\hat{a}_i(c^F_{i,0} + c^F_{i,+} + c^F_{i,-}) + \hat{a}_{i-1}c^F_{i-1,0} + \hat{a}_{i+1}c^F_{i+1,0} + \hat{a}_{i-1}c^F_{i-1,+} + \hat{a}_{i+1}c^F_{i+1,-}]$; according to Equation (17), the modified hopping rates $c^F_{i,0} = 1/2$, $c^F_{i,+} = (1+F)/4$ and $c^F_{i,-} = (1-F)/4$ correspond to transfer of one particle to the left and one to the right, that of both particles to the right and that of both particles to the left, respectively. The case with biasing force $F = 0$ corresponds to the unbiased conserved Manna sandpile. The local density satisfies the following time-evolution equation,

$$\frac{\partial \rho_i(t)}{\partial t} = (a_{i-1} - 2a_i + a_{i+1}) + F\frac{a_{i-1} - a_{i+1}}{2}. \tag{26}$$

Now by scaling space $x = i/L$, time $\tau = t/L^2$ and biasing force $F \to F/L$, and by assuming a local-steady state [90, 91], where activity $a_i(t) \equiv a[\rho(x,\tau)]$ can be written as a function of local density field $\rho_i(t) \equiv \rho(x,\tau)$, one obtains the desired hydrodynamic time-evolution of density field $\rho(x,\tau)$,

$$\frac{\partial \rho(x,\tau)}{\partial \tau} = \frac{\partial^2 a(\rho)}{\partial x^2} - F\frac{\partial a(\rho)}{\partial x} \equiv -\frac{\partial J}{\partial x}, \tag{27}$$

where local current $J(\rho) = -\partial a/\partial x + a(\rho)F$. Comparing with Equations (16) and (18), we get the bulk-diffusion coefficient

$$D(\rho) = \frac{da(\rho)}{d\rho}, \tag{28}$$

and the conductivity

$$\chi(\rho) = a(\rho), \tag{29}$$

for the conserved Manna sandpile. One can immediately obtain the near-critical behavior of the bulk-diffusion coefficient using the power-law form of the activity $a(\rho) \simeq \text{Const.}(\rho - \rho_c)^\beta$ near criticality, where critical exponent $\beta < 1$. Using Equation (28), we indeed get a diverging bulk-diffusion coefficient $D(\rho) \sim 1/(\rho - \rho_c)^{1-\beta} \to \infty$ as $\rho \to \rho_c^+$ [78, 92]. On the other hand, the conductivity in the system vanishes as one approaches criticality. Diverging diffusivity and vanishing conductivity near criticality are a unique kind of transport instability, which are usually not seen in equilibrium critical phenomena and could well be the signature of the fixed-energy sandpiles in general.

4. CONCLUDING REMARKS

We have come a long way since the introduction of self-organized criticality (SOC), and the sandpile model, by Bak, Tang, and Wiesenfeld; it has been an exciting journey, which have opened a new horizon. Indeed, in the past three decades or so, SOC and sandpiles have generated "avalanche-like" activities in the literature, in terms of plethora of exact, experimental and numerical results. Undoubtedly, these studies have helped to shape our understanding of scale invariance in general, and non-equilibrium absorbing phase transition in particular, in a new light. One may however recall the original motivation of BTW, which was to connect the long-ranged temporal correlations observed in nature in the form of the "$1/f$" noise to the long-ranged spatial correlations in these systems. In retrospect, it seems that perhaps the BTW's great ambition has not been really fulfilled and the success of achieving the goal of explaining the $1/f$ noise has been mixed at best. As we have discussed in this article, while, under suitable driving condition, sandpiles do generate $1/f$ power spectra in time-signal of various transport quantities, in the slow driving limit though it usually generates $1/f^2$-type power spectra.

However, it does not mean in any way that the time-dependent correlations in sandpiles are not interesting. On the contrary, sandpiles possess extremely rich spatio-temporal structures, which have some unique aspects in their transport properties and would be worth pursuing for understanding their nontrivial structures better. In the past, the scale-invariant spatial structure in sandpiles have attracted a lot of attention and they have been characterized mainly through avalanche statistics. But, the time-dependent properties are much less explored and the studies in the literature have been perhaps a little scattered. Particularly, our knowledge of the exact hydrodynamic structure of sandpiles concerning long wavelength relaxations is still quite limited, primarily due to the lack of knowledge of the steady (quasi) state measure, which could be partly attributed to the absence of time-reversibility in the systems. Indeed, a comprehensive characterization of the temporal correlations, particularly in terms of the transport properties of the systems, though daunting, would be certainly desirable and could lead to a better theoretical understanding of sandpiles in general.

Moreover we should now emphasize more on the problem of characterizing one of the most interesting aspects—the transport instabilities in sandpiles, which are present in the system near criticality. As demonstrated in the past through the studies of simple model systems, the bulk-diffusion coefficient, which governs the long wavelength density relaxation in the system, diverges near criticality [67, 92]. This particular feature, as opposed to that near an equilibrium critical point, where the bulk diffusivity vanishes (known as "critical slowdown"; [93]), is presumably associated with the unique nature of the threshold-activated dynamics in sandpiles. However, at this stage, it is not quite clear whether the near-critical diverging diffusivity, along with the vanishing conductivity, is a generic feature of sandpiles undergoing an absorbing phase transition and, if so, in what ways the transport instabilities can affect the behavior of the systems near criticality. Understanding of these features can have a far reaching consequence in resolving the long-standing issue of determining the universality classes in sandpiles, which have been hotly debated in recent times [41, 60, 78, 89, 94–100]. Indeed, apart from the conserved Manna sandpiles, it would be useful to explore the exact hydrodynamic structure in other variants of conserved sandpiles, such as the restricted-height models [88], the conserved threshold-transfer process (CTTP) [34–36] or the conserved lattice gases (CLG), etc. [31]; this would help one to check if these models too possess similar instabilities in particle transport and thus to classify a rather diverse set of models accordingly. Moreover, an exact hydrodyanamic characterization of sandpiles can provide insights not only into the relaxation properties, but also the fluctuation properties of the systems [78].

Clearly, sandpiles still remain relevant, have many aspects yet unexplored, and have much more to offer in future!

AUTHOR CONTRIBUTIONS

The author confirms being the sole contributor of this work and has approved it for publication.

ACKNOWLEDGMENTS

I thank Deepak Dhar, who introduced me to the world of sandpiles and, since then, has enriched my understanding through discussions, critical comments and suggestions. I thank Arti Garg and Dhiraj Tapader for reading the manuscript and for their useful comments.

REFERENCES

1. Bak P, Tang C, Wiesenfeld K. Self-organized criticality: an explanation of the 1/f noise. *Phys Rev Lett.* (1987) 59:381. doi: 10.1103/PhysRevLett.59.381
2. Bak P, Tang C, Wiesenfeld K. Self-organized criticality. *Phys Rev A.* (1988) 38:364. doi: 10.1103/PhysRevA.38.364
3. Kadanoff LP, Nagel SR, Wu L, Zhou S. Scaling and universality in avalanches. *Phys Rev A.* (1989) 39:6524. doi: 10.1103/PhysRevA.39.6524
4. Bak P. *How Nature Works: The Science of Self-Organised Criticality*. New York, NY: Copernicus (1996).
5. Nagel SR. Instabilities in a sandpile. *Rev Mod Phys.* (1992) 64:321. doi: 10.1103/RevModPhys.64.321
6. Kardar M. Avalanche theory in rice. *Nature.* (1996) 379:22. doi: 10.1038/379022a0
7. Mandelbrot BB. *The Fractal Geometry of Nature*. San Francisco, CA: Freeman (1982).
8. Barabasi AL, Stanley HE. *Fractal Concepts in Surface Growth*. New York, NY: Cambridge University Press (1995).
9. Kirkby MJ. The fractal geometry of nature. *Earth Surf Process Landf.* (1983) 8:406.
10. Scheidegger AE. International association of scientific hydrology. *Bulletin* (1967) 12:57. doi: 10.1080/02626666709493550
11. Dutta P, Horn PM. Low-frequency fluctuations in solids: 1/f noise. *Rev Mod Phys.* (1981) 53:497. doi: 10.1103/RevModPhys.53.497
12. Callen HB, Welton TA. Irreversibility and generalized noise. *Phys Bev.* (1951) 83:34. doi: 10.1103/PhysRev.83.34
13. Mandelbrot BB, Van Ness JW. Fractional Brownian motions, fractional noises and applications. *SIAM Rev.* (1968) 10:422. doi: 10.1137/1010093
14. Schick KL, Vereen AA. Flow of sand in an hourglass. *Nature.* (1974) 251:599. doi: 10.1038/251599a0
15. Press WH. Flicker noises in astronomy and elsewhere. *Comments Mod Phys Part C.* (1978) 7:103.
16. Dhar D. Self-organized critical state of sandpile automaton models. *Phys Rev Lett.* (1990) 64:161. doi: 10.1103/PhysRevLett.64.1613
17. Manna SS. Two-state model of self-organized criticality. *J Phys A.* (1991) 24:L363. doi: 10.1088/0305-4470/24/7/009
18. Christensen K, Corral A, Frette V, Feder J, Jossang T. Tracer dispersion in a self-organized critical system. *Phys Rev Lett.* (1996) 77:107. doi: 10.1103/PhysRevLett.77.107
19. Dickman R, Munoz MA, Vespignani A, Zapperi S. Paths to self-organized criticality. *Braz J Phys.* (2000) 30:27. doi: 10.1590/S0103-97332000000100004
20. Vespignani A, Dickman R, Munoz MA, Zapperi S. Driving, conservation, and absorbing states in sandpiles. *Phys Rev Lett.* (1998) 81:5676. doi: 10.1103/PhysRevLett.81.5676
21. Vespignani A, Dickman R, Munoz MA, Zapperi S. Absorbing-state phase transitions in fixed-energy sandpiles. *Phys Rev E.* (2000) 62:4564. doi: 10.1103/PhysRevE.62.4564
22. Dickman R, Vespignani A, Zapperi S. Self-organized criticality as an absorbing-state phase transition. *Phys Rev E.* (1998) 57:5095. doi: 10.1103/PhysRevE.57.5095
23. Marro J, Dickman R. *Nonequilibrium Phase Transitions in Lattice Models*. Cambridge, UK: Cambridge University Press (1999).
24. Poghosyan SS, Poghosyan VS, Priezzhev VB, Ruelle P. Numerical study of the correspondence between the dissipative and fixed-energy abelian sandpile models. *Phys Rev E.* (2011) 84:066119. doi: 10.1103/PhysRevE.84.066119
25. Fey A, Levine L, Wilson DB. Driving sandpiles to criticality and beyond. *Phys Rev Lett.* (2010) 104:145703. doi: 10.1103/PhysRevLett.104.145703
26. Fey A, Levine L, Wilson DB. Approach to criticality in sandpiles. *Phys Rev E.* (2010) 82:031121. doi: 10.1103/PhysRevE.82.031121
27. Pruessner G. *Self-Organized Criticality, Theory, Models, and Characterisation*. Cambridge, MA: Cambridge University Press (2012).
28. Jaeger HM, Liu C, Nagel SR. Relaxation at the angle of repose. *Phys Rev Lett.* (1989) 62:40. doi: 10.1103/PhysRevLett.62.40
29. Frette V, Christensen K, Malthe-Sorenssen A, Feder J, Jossang T, Meakin P. Avalanche dynamics in a pile of rice. *Nature.* (1996) 49:379. doi: 10.1038/379049a0
30. Paczuski M, Boettcher S. Universality in sandpiles, interface depinning, and earthquake models. *Phys Rev Lett.* (1996) 77:111. doi: 10.1103/PhysRevLett.77.111
31. Rossi M, Pastor-Satorras R, Vespignani A. Universality class of absorbing phase transitions with a conserved field. *Phys Rev Lett.* (2000) 85:1803. doi: 10.1103/PhysRevLett.85.1803
32. Dickman R, Alava M, Munoz MA, Peltola J, Vespignani A, Zapperi S. Critical behavior of a one-dimensional fixed-energy stochastic sandpile. *Phys Rev E.* (2001) 64:056104. doi: 10.1103/PhysRevE.64.056104
33. Dickman R, Tome T, de Oliveira MJ. Sandpiles with height restrictions. *Phys Rev E.* (2002) 66:016111. doi: 10.1103/PhysRevE.66.016111
34. Lubeck S. Scaling behavior of the conserved transfer threshold process. *Phys Rev E.* (2002) 66:046114. doi: 10.1103/PhysRevE.66.046114
35. Lubeck S, Heger PC. Universal finite-size scaling behavior and universal dynamical scaling behavior of absorbing phase transitions with a conserved field. *Phys Rev E.* (2003) 68:056102. doi: 10.1103/PhysRevE.68.056102
36. Lubeck S, Heger PC. Universal scaling behavior at the upper critical dimension of nonequilibrium continuous phase transitions. *Phys Rev Lett.* (2003) 90:230601. doi: 10.1103/PhysRevLett.90.230601
37. Bonachela JA, Munoz MA. Confirming and extending the hypothesis of universality in sandpiles. *Phys Rev E.* (2008) 78:041102. doi: 10.1103/PhysRevE.78.041102
38. Menon G, Ramaswamy R. Universality class of the reversible-irreversible transition in sheared suspensions. *Phys Rev E.* (2009) 79:061108. doi: 10.1103/PhysRevE.79.061108
39. da Cunha SD, da Silva LR, Viswanathan GM, Dickman R. Activity, diffusion, and correlations in a two-dimensional conserved stochastic sandpile. *J Stat Mech.* (2014) 8:P08003. doi: 10.1088/1742-5468/2014/08/P08003
40. Hexner D, Levine D. Hyperuniformity of critical absorbing states. *Phys Rev Lett.* (2015) 114:110602. doi: 10.1103/PhysRevLett.114.110602
41. Grassberger P, Dhar D, Mohanty PK. Oslo model, hyperuniformity, and the quenched Edwards-Wilkinson model. *Phys Rev E.* (2016) 94:042314. doi: 10.1103/PhysRevE.94.042314
42. Hexner D, Levine D. Noise, diffusion, and hyperuniformity. *Phys Rev Lett.* (2017) 118:020601. doi: 10.1103/PhysRevLett.118.020601
43. Dhar D, Ramaswamy R. Exactly solved model of self-organized critical phenomena. *Phys. Rev. Lett.* (1989) 63:1659. doi: 10.1103/PhysRevLett.63.1659
44. Priezzhev VB, Dhar D, Dhar A, Krishnamurthy S. Eulerian walkers as a model of self-organized criticality. *Phys Rev Lett.* (1996) 77:5079. doi: 10.1103/PhysRevLett.77.5079
45. Priezzhev VB, Ktitarev DV, Ivashkevich EV. Formation of avalanches and critical exponents in an Abelian sandpile model. *Phys Rev Lett.* (1996) 76:2093. doi: 10.1103/PhysRevLett.76.2093
46. Priezzhev VB. Structure of two-dimensional sandpile. I. Height probabilities. *J Stat Phys.* (1994) 74:955. doi: 10.1007/BF02188212

47. Ivashkevich EV. Boundary height correlations in a two-dimensional Abelian sandpile. *J Phys A*. (1994) 27:3643. doi: 10.1088/0305-4470/27/11/014
48. Ktitarev DV, Lubeck S, Grassberger P, Priezzhev VB. Scaling of waves in the Bak-Tang-Wiesenfeld sandpile model. *Phys Rev E*. (2000) 61:81. doi: 10.1103/PhysRevE.61.81
49. Levine L, Murugan M, Peres Y, Ugurcan BE. The divisible sandpile at critical density. *Ann Henri Poincare*. (2016) 17:1677–711. doi: 10.1007/s00023-015-0433-x
50. Levine L, Peres Y. Scaling limits for internal aggregation models with multiple sources. *J Anal Math*. (2010) 111:151. doi: 10.1007/s11854-010-0015-2
51. Dhar D. Theoretical studies of self-organized criticality. *Phys A*. (2006) 369:29. doi: 10.1016/j.physa.2006.04.004
52. Kertesz J, Kiss LB. The noise spectrum in the model of self-organised criticality. *J Phys A*. (1990) 23:L433. doi: 10.1088/0305-4470/23/9/006
53. Jensen HJ, Christensen K, Fogedby HC. 1/f noise, distribution of lifetimes, and a pile of sand. *Phys Rev B*. (1989) 40:7425. doi: 10.1103/PhysRevB.40.7425
54. Manna SS, Kertesz J. Correlations and scaling in the outflow statistics of a sandpile automaton. *Phys A*. (1991) 173:49. doi: 10.1016/0378-4371(91)90250-G
55. Hwa T, Kardar M. Avalanches, hydrodynamics, and discharge events in models of sandpiles. *Phys Rev A*. (1992) 45:7002. doi: 10.1103/PhysRevA.45.7002
56. Garcia-Millan R, Pruessner G, Pickering L, Christensen K. Correlations and hyperuniformity in the avalanche size of the Oslo model. *EPL*. (2018) 122:50003. doi: 10.1209/0295-5075/122/50003
57. Hwa T, Kardar M. Dissipative transport in open systems: an investigation of self-organized criticality. *Phys Rev Lett*. (1989) 62:1813. doi: 10.1103/PhysRevLett.62.1813
58. Corral A, Diaz-Guilera A. Symmetries and fixed point stability of stochastic differential equations modeling self-organized criticality. *Phys Rev E*. (1997) 55:2434. doi: 10.1103/PhysRevE.55.2434
59. Ramasco JJ, Munoz MA, da Silva Santos CA. Numerical study of the Langevin theory for fixed-energy sandpiles. *Phys Rev E*. (2004) 69:045105(R). doi: 10.1103/PhysRevE.69.045105
60. Le Doussal P, Wiese KJ. Exact mapping of the stochastic field theory for manna sandpiles to interfaces in random media. *Phys Rev Lett*. (2015) 114:110601. doi: 10.1103/PhysRevLett.114.110601
61. Grinstein G, Lee DH. Generic scale invariance and roughening in noisy model sandpiles and other driven interfaces. *Phys Rev Lett*. (1991) 66:177. doi: 10.1103/PhysRevLett.66.177
62. Garrido PL, Lebowitz JL, Maes C, Spohn H. Long-range correlations for conservative dynamics. *Phys Rev A*. (1990) 42:1954. doi: 10.1103/PhysRevA.42.1954
63. Dorfman JR, Kirkpatrick TR, Sengers JV. Generic long-range correlations in molecular fluids. *Annu Rev Chem*. (1994) 45:213. doi: 10.1146/annurev.pc.45.100194.001241
64. Grinstein G, Lee DH, Sachdev S. Conservation laws, anisotropy, and "self-organized criticality" in noisy nonequilibrium systems. *Phys Rev Lett*. (1990) 64:1927. doi: 10.1103/PhysRevLett.64.1927
65. Obukhov S. *Random Fluctuations and Pattern Growth*. Dordrecht: Kluwer (1988).
66. Alonso-Llanes L, Domínguez-Rubio L, Martínez E, Altshuler E. Intermittent and continuous flows in granular piles: effects of controlling the feeding height. *Rev Cubana Física*. (2017) 34:133–5
67. Carlson JM, Chayes JT, Grannan ER, Swindle GH. Self-orgainzed criticality and singular diffusion. *Phys Rev Lett*. (1990) 65:2547. doi: 10.1103/PhysRevLett.65.2547
68. Pradhan P, Dhar D. Probability distribution of residence times of grains in models of rice piles. *Phys Rev E*. (2006) 73:021303. doi: 10.1103/PhysRevE.73.021303
69. Pradhan P, Dhar D. Sampling rare fluctuations of height in the Oslo ricepile model. *J Phys A*. (2007) 40:2639. doi: 10.1088/1751-8113/40/11/003
70. Dhar D, Pradhan P. Probability distribution of residence-times of grains in sandpile models. *J Stat Mech*. (2004) 5:P05002. doi: 10.1088/1742-5468/2004/05/P05002
71. da Cunha SD, Vidigal RR, da Silva LR, Dickman R. Diffusion in stochastic sandpiles. *Eur Phys B*. (2009) 72:441. doi: 10.1140/epjb/e2009-00367-0
72. Carlson JM, Grannan ER, Swindle GH, Tour J. Singular diffusion limits of a class of reversible self-organizing particle systems. *Ann Prob*. (1993) 21:1372. doi: 10.1214/aop/1176989122
73. Carlson JM, Swindle GH. Self-organized criticality: sandpiles, singularities, and scaling. *Proc Natl Acad Sci USA*. (1995) 92:6712. doi: 10.1073/pnas.92.15.6712
74. Guo MZ, Papanicoiaou GC, Varadhan SRS. Nonlinear diffusion limit for a system with nearest neighbor interactions. *Commun Math Phys*. (1988) 118:31. doi: 10.1007/BF01218476
75. Kipnis C, Landim C. *Scaling Limits of Interacting Particle Systems*. Berlin: Springer (1999).
76. Chatterjee S, Pradhan P, Mohanty PK. Gammalike mass distributions and mass fluctuations in conserved-mass transport processes. *Phys Rev Lett*. (2014) 112:030601. doi: 10.1103/PhysRevLett.112.030601
77. Das A, Kundu A, Pradhan P. Einstein relation and hydrodynamics of nonequilibrium mass transport processes. *Phys Rev E*. (2017) 95:062128. doi: 10.1103/PhysRevE.95.062128
78. Chatterjee S, Das A, Pradhan P. Hydrodynamics, density fluctuations, and universality in conserved stochastic sandpiles. *Phys Rev E*. (2018) 97:062142. doi: 10.1103/PhysRevE.97.062142
79. Das A, Chatterjee S, Pradhan P. Spatial correlations, additivity, and fluctuations in conserved-mass transport processes. *Phys Rev E*. (2016) 93:062135. doi: 10.1103/PhysRevE.93.062135
80. Carlson JM, Grannan ER, Swindle GH. Self-organizing systems at finite driving rates. *Phys Rev E*. (1993) 47:93. doi: 10.1103/PhysRevE.47.93
81. Evans MR, Hanney T. Nonequilibrium statistical mechanics of the zero-range process and related models. *J Phys A*. (2005) 38:R195. doi: 10.1088/0305-4470/38/19/R01
82. Bertini L, Sole AD, Gabrielli D, Jona-Lasinio G, Landim C. Fluctuations in stationary nonequilibrium states of irreversible processes. *Phys Rev Lett*. (2001) 87:040601. doi: 10.1103/PhysRevLett.87.040601
83. Bertini L, De Sole A, Gabrielli D, Jona-Lasinio G, Landim C. Macroscopic fluctuation theory. *Rev Mod Phys*. (2015) 87:593. doi: 10.1103/RevModPhys.87.593
84. Basu U, Mohanty PK. Active-absorbing-state phase transition beyond directed percolation: a class of exactly solvable models. *Phys Rev E*. (2009) 79:041143. doi: 10.1103/PhysRevE.79.041143
85. Gabel A, Krapivsky PL, Redner S. Facilitated asymmetric exclusion. *Phys Rev Lett*. (2010) 105:210603. doi: 10.1103/PhysRevLett.105.210603
86. Gabrielli D, Krapivsky PL. Gradient structure and transport coefficients for strong particles. *J Stat Mech*. (2018) 2018:043212 doi: 10.1088/1742-5468/aab858
87. Henkel M, Hinrichsen H, Lubeck S. *Non-Equilibrium Phase Transitions Vol. I: Absorbing Phase Transitions*. Dordrecht: Springer (2008).
88. Dickman R. Critical exponents for the restricted sandpile. *Phys Rev E*. (2006) 73:036131. doi: 10.1103/PhysRevE.73.036131
89. Dickman R, da Cunha SD. Particle-density fluctuations and universality in the conserved stochastic sandpile. *Phys Rev E*. (2015) 92:020104(R). doi: 10.1103/PhysRevE.92.020104
90. Eyink G, Lebowitz JL, Spohn H. Hydrodynamics of stationary non-equilibrium states for some stochastic lattice gas models. *Commun Math Phys*. (1990) 132:253. doi: 10.1007/BF02278011
91. Eyink G, Lebowitz JL, Spohn H. Lattice gas models in contact with stochastic reservoirs: local equilibrium and relaxation to the steady state. *Commun Math Phys*. (1991) 140:119. doi: 10.1007/BF02099293
92. Tapader D, Pradhan P, Dhar D. Density relaxation in conserved Manna sandpiles. *Phys Rev E*. (2021) 103:032122. doi: 10.1103/PhysRevE.103.032122
93. Hohenberg PC, Halperin BJ. Theory of dynamic critical phenomena. *Rev Mod Phys*. (1977) 49:435. doi: 10.1103/RevModPhys.49.435
94. Ben-Hur A, Biham O. Universality in sandpile models. *Phys Rev E*. (1996) 53:R1317. doi: 10.1103/PhysRevE.53.R1317
95. Mohanty PK, Dhar D. Generic sandpile models have directed percolation exponents. *Phys Rev Lett*. (2002) 89:104303. doi: 10.1103/PhysRevLett.89.104303

96. Bonachela JA, Chate H, Dornic I, Munoz MA. Absorbing states and elastic interfaces in random media: two equivalent descriptions of self-organized criticality. *Phys Rev Lett.* (2007) 98:155702. doi: 10.1103/PhysRevLett.98.155702
97. Basu M, Basu U, Bondyopadhyay S, Mohanty PK, Hinrichsen H. Fixed-energy sandpiles belong generically to directed percolation. *Phys Rev Lett.* (2012) 109:015702. doi: 10.1103/PhysRevLett.109.015702
98. Lee SB. Comment on "Fixed-energy sandpiles belong generically to directed percolation". *Phys Rev Lett.* (2013) 110:159601. doi: 10.1103/PhysRevLett.110.159601
99. Lee SB. Critical behavior of absorbing phase transitions for models in the Manna class with natural initial states. *Phys Rev E.* (2014) 89:062133. doi: 10.1103/PhysRevE.89.062133
100. Lee SB. Universality class of the conserved Manna model in one dimension. *Phys Rev E.* (2014) 89:060101. doi: 10.1103/PhysRevE.89.060101

Conflict of Interest: The author declares that the research was conducted in the absence of any commercial or financial relationships that could be construed as a potential conflict of interest.

frontiers in Physics

REVIEW
published: 02 June 2021
doi: 10.3389/fphy.2021.641966

Sandpile Models in the Large

Philippe Ruelle *

Institut de Recherche en Mathématique et Physique, Université catholique de Louvain, Louvain-la-Neuve, Belgium

This contribution is a review of the deep and powerful connection between the large-scale properties of critical systems and their description in terms of a field theory. Although largely applicable to many other models, the details of this connection are illustrated in the class of two-dimensional Abelian sandpile models. Bulk and boundary height variables, spanning tree–related observables, boundary conditions, and dissipation are all discussed in this context and found to have a proper match in the field theoretic description.

Keywords: critical systems, scaling limit, sandpile models, conformal field theory, symplectic fermions

1 INTRODUCTION

In statistical mechanics, critical points are very special points in the space of external parameters which control the state of a system. At such a point, the system is scale-invariant, and its thermodynamic functions and correlations are characterized by critical exponents and power laws. In many cases, physical systems have a finite number of critical points, most often only one. Typical examples include the endpoint of the liquid–gas coexistence line or the Curie point for ferromagnetic materials. In these cases, a system is brought to its critical point by tuning very precisely a few external parameters to their critical values.

In nature, however, power laws are commonplace and can be found in a large variety of different phenomena, like avalanches, earthquakes, solar flares, droplet formation. In all these cases, it is certainly not clear what parameters should be tuned, and even if they are perfectly tuned, it is unlikely that they would stay so over large periods of time. To solve this apparent paradox, Bak, Tang, and Wiesenfeld suggested in the 80s that the external parameters would tune themselves dynamically: even if the system is not initially in a critical state, its own dynamics will ineluctably drive it to criticality and maintain it in that state [1]. This attractive idea has led to the concept of self-organized criticality (SOC).

To support this idea, these authors proposed the sandpile model as a prototypical example of a system which shows a form of self-organized criticality. Since then, many other models showing SOC have been proposed, as abundantly illustrated in this volume and in introductory books and reviews [2–5].

The present review will be exclusively concerned with specific versions of two-dimensional sandpile models, formulated by Dhar [6], called Abelian sandpile models. Even though there are among the simplest and easiest sandpile models to handle, they show a large spectrum of interesting and difficult problems which have attracted considerable attention, in both the physical and mathematical communities. From the point of view taken here (like their scaling limit and the emerging conformal field theory), they are, to our knowledge, the only ones to have been studied. Yet, compared to many other equilibrium statistical models, a fair statement is that our present understanding of them is still very poor.

Our primary purpose is two-fold, namely, to give the unfamiliar reader an introduction of why and how the neighborhood of a critical point can be described by a Euclidean field theory, which, at first sight, appears to be a rather obscure statement, and also to show how this description can be

OPEN ACCESS

Edited by:
Lev Shchur,
Landau Institute for Theoretical Physics, Russia

Reviewed by:
Sergio Caracciolo,
University of Milan, Italy
Mikko Alava,
Aalto University, Finland

***Correspondence:**
Philippe Ruelle
philippe.ruelle@uclouvain.be

Specialty section:
This article was submitted to Interdisciplinary Physics, a section of the journal Frontiers in Physics

Received: *15 December 2020*
Accepted: *19 January 2021*
Published: *02 June 2021*

Citation:
Ruelle P (2021) Sandpile Models in the Large. Front. Phys. 9:641966. doi: 10.3389/fphy.2021.641966

worked out in practical terms. The second part will be illustrated in sandpile models, which lend themselves very well to this kind of analysis: they are simple enough that one can follow the steps in a clear and transparent way, yet they are rich enough to show the difficulties one sometimes has to face but also the elegance and the power of the approach. Understanding how of a field theory emerges from a stochastic lattice model enables to gain a probabilistic and intuitive view of what a field theory is in this context.

It turns out that the field theories which appear when analyzing critical systems are conformal field theories. The simple reason for this is that their large conformal symmetry integrates the fact that critical systems have a local scale invariance. Conformal theories in two dimensions have been tremendously successful since the 80s and have led to a deep understanding of the two-dimensional critical phenomena. It is certainly not our purpose to give an introduction to conformal field theories, and we will not go very deep into its technicalities, referring to the vast literature. We restrict to their most basic features, in the hope that these will be sufficient and useful to understand how conformal theories are so well suited for our study.

Section 2 starts with a brief review of the Abelian sandpile models, where the most basic features of the models are recalled. **Section 3** is a general description, valid beyond the sandpile models, of what is called the scaling limit, which allows establishing the connection between the large-distance regime of a critical system and the associated field theory. A brief tour of conformal theories, and specifically logarithmic conformal theories, is presented in **Section 4**. The application of the conceptual ingredients is illustrated in the next three sections. **Section 5** focuses on the bulk observables in the sandpile models, computes the first correlators, and explains how these should be understood in terms field theoretic quantities. Boundary conditions and boundary observables are examined in **Section 6** as well as the way they should be thought of in conformal theories. **Section 7** discusses a dissipative variant of the sandpile models and their description by a massive field theory, and also some universality aspects of the sandpile models. The last section summarizes the present status of the conformal theory at work in sandpile models.

The present text has some overlap with [7]. The latter was more concerned with the sandpile models as being described specifically by a logarithmic conformal field theory. Intended to a potentially wider readership, the present review is more devoted to the general connection between critical systems and field theories, illustrated in a specific class of models. The two are somehow complementary and, if combined, may provide a more complete overview.

2 ABELIAN SANDPILE MODELS

The models we discuss are discrete stochastic dynamical systems. Their microscopic variables are attached to the vertices of a finite connected graph $\Gamma = (V,E)$ (with V the set of vertices, or sites, and E the set of simple, unoriented edges) and evolve in discrete time as a random process. We label the vertices of Γ by Latin indices $i, j, \ldots$ and denote the microscopic variables by h_i. These are called height variables and simply give the height of the sandpile at vertex i (i.e., count the number of sand grains at i); they are integer-valued, with $h_i \geqslant 1$. A height configuration C is a set of height values $\{h_i\}_{i\in V}$.

We are not quite ready to define the dynamics. For reasons that will become clear in a moment, we need to extend Γ by adding one special vertex, noted s and called the sink, as well as a number of edges connecting s to the vertices of a non-empty subset $D \subset V$. Vertices in D are called dissipative or open, while those in $V\backslash D$ are conservative or closed. If $\Gamma^\star = (V^\star, E^\star)$ denotes the extended graph in an obvious notation, we define z_i to be the coordination number of i in Γ (the number of edges in E incident to i, or the number of its nearest neighbors in Γ) and, similarly, $z_i^\star$ its coordination number in $\Gamma^\star$. Thus, $z_i^\star = z_i$ if i is closed and $z_i^\star > z_i$ if i is open. Finally, we say that a site i of V is stable[1] if its height satisfies $1 \leqslant h_i \leqslant z_i^\star$. A height configuration is stable if all sites are stable. Clearly, the number of stable configurations is equal to $\prod_{i\in V} z_i^\star$.

The discrete, stochastic dynamics of the sandpile model is defined as follows. Assume that $C_t = \{h_i\}$ is a stable configuration at time t. The stable configuration C_{t+1} is obtained from the following two steps.

1) *Deposition*: One grain of sand is dropped on a random site j of V, selected with probability p_j, producing therefore a new configuration C^{new} with heights $h_i^{\text{new}} = h_i + \delta_{i,j}$. If $h_j^{\text{new}} \leqslant z_j^\star$, then C^{new} is stable and defines C_{t+1}; if not, we proceed to step (ii).
2) *Relaxation*: If $h_j^{\text{new}} > z_j^\star$ (it is in fact equal to $z_j^\star + 1$), we let the site j topple: its height is decreased by $z_j^\star$, each of its neighbors in Γ receives one grain, and the remaining $z_j^\star - z_j$ grains go to the sink. After this, one or more neighbors of j in Γ may become unstable, in which case they topple in the way explained above for the site j. The toppling process is pursued for all unstable sites until a stable configuration is obtained. That configuration defines C_{t+1}.

It is useful to introduce the toppling matrix Δ as it will play an important role in what follows:

$$\Delta_{i,j} = \begin{cases} z_i^\star & \text{for } i = j, \\ -1 & \text{if } i \text{ and } j \text{ are neighbours (i.e. connected)}, \\ 0 & \text{otherwise}, \end{cases} \qquad (1)$$

for $i, j \in V$. The sand redistribution occurring when a site j topples can then be written as the update $h_i \to h_i - \Delta_{j,i}$ for all $i \in V$. The matrix Δ is like a Laplacian on Γ, with mixed boundary conditions dictated by the open and closed sites, which induce, respectively, Dirichlet and Neumann boundary conditions (see **Section 6**).

The above dynamics is well-defined. We see that the total number of sand grains is conserved under the toppling of a closed

[1]There is no need to keep track of the number of sand grains in the sink, and so we do not assign it a height variable.

site, whereas a nonzero number of grains are transferred to the sink under the toppling of an open site. The existence of at least one open site guarantees that the relaxation process terminates after a finite number of topplings and motivates the necessity of the extension of the graph Γ by the sink site. Moreover, if several sites are unstable during the relaxation process, the order in which they are toppled does not matter. More generally, one may define the operator a_i for each $i \in V$, whose action on a stable configuration returns the stable configuration resulting from the relaxation process after the deposition of a sand grain at i. One can then prove that the operators a_i commute [6], explaining the qualifier "Abelian" used to designate the models satisfying this property.

The dynamics described above is a discrete Markov chain on a finite configuration space: at each time step, one applies the operator a_i with probability p_i (it is the only stochastic element of the dynamics), going from C_t to $C_{t+1} = a_i C_t$. An important question concerns the invariant measures, since they control the behavior of the model in the long run.

If there is no strong reason to favor certain sites, one takes all probabilities p_i equal (uniform distribution). In this case,[2] Dhar [6] has shown that there is unique invariant measure $\mathbb{P}_\Gamma$, which is uniform on its support. In the Markov chain terminology, the configurations in the support of $\mathbb{P}_\Gamma$ are called recurrent; the others are called transient. Being in the support of the unique invariant measure means that the recurrent configurations are those which are in the repeated image of the operators a_i. The transient ones either never appear (depending on the initial configuration) or cease to appear after some finite time.

If indeed the unique invariant measure is uniform, the situation appears to be deceptively simple. Not so. What makes the sandpile models nontrivial, fascinating, and rich is the support of the invariant measure. A generic recurrent configuration is really complicated because the height values are delicately correlated over the entire graph. In the general case, there is no simpler criterion characterizing the recurrent configurations than the following. Let C be a stable configuration, and let C_F be its restriction to a subgraph $F \subset \Gamma$ (F can be assumed to be connected). We say that C_F is a forbidden subconfiguration if each vertex of F has a height smaller or equal to the number of its neighbors in F. It can be shown [8] that a forbidden subconfiguration cannot be in the repeated image of the dynamics (of the operators a_i). It follows that a configuration is recurrent if and only if it contains no forbidden subconfiguration. The simplest example of a forbidden subconfiguration is when F contains just two neighboring vertices with height values equal 1. The criterion also implies that the maximal configuration with heights $h_i = z_i^\star$ is recurrent since a vertex i with height $h_i > z_i$ cannot be in a forbidden subconfiguration. It is also clearly in the image of the iterated dynamics since it can be reached from any other stable configuration by an appropriate sequence of a_i's.

The characterizing condition for recurrence shows that the heights of a recurrent configuration are not at all independent. They are not only correlated locally (think of two neighboring 1's) but also globally because asserting that a given configuration is recurrent generally requires scanning the entire graph. For instance, the configuration having $h_i = z_i$ for all i is not recurrent and possesses no other forbidden subconfiguration than the whole configuration itself. Moreover, the recurrent status is very sensitive to local changes and can be lost or gained by the change of a single height (for the configuration just discussed, the increase by one unit of the height at a single open site makes it recurrent). However, the increase in any height in a recurrent configuration preserves the recurrence.

The burning algorithm [8] (see also the review [5]) provides a convenient way to test whether a given stable configuration is recurrent. In addition to providing a completely automatic procedure, more importantly, it establishes a bijection between the set of recurrent configurations on Γ and the set of rooted spanning trees on $\Gamma^\star$, rooted at the sink site s. Let us recall that a spanning tree is a loopless connected subgraph $(V^\star, F) \subset \Gamma^\star = (V^\star, E^\star)$ with $F \subset E^\star$. This bijection is important and useful as most of the actual calculations use the spanning tree formulation. Interestingly, there is no canonical bijection between the two sets in the sense that there are in fact many burning algorithms (the detailed definition requires a certain prescription that is largely arbitrary), each giving rise to a different bijection. This freedom in the choice of a definite algorithm, a sort of huge gauge symmetry, has remained unexploited so far.

If the notion of recurrence remains somewhat elusive in the generic case, simple arguments lead to a remarkably simple and general formula for the number of recurrent configurations [6], naturally identified as the partition function Z since the invariant measure is uniform:

$$Z = \#\{\text{recurrent configs}\} = \det \Delta, \tag{2}$$

for Δ the toppling matrix introduced in **(1)**. It is a standard result in combinatorics (Kirchhoff's matrix-tree theorem) that $\det \Delta$ also counts the number of spanning trees on Γ (see **Section 5.7** for a proof). The previous formula usually implies that the recurrent configurations form an exponentially small fraction of the set of stable configurations (whose number is equal to $\prod_i \Delta_{i,i}$). On a large grid in $\mathbb{Z}^2$, for instance, for which the density of dissipative sites goes to 0 in the infinite volume limit, the effective number of degrees of freedom per site in a recurrent configuration is roughly 3.21 (as compared to 4 in a stable configuration), meaning that $\det \Delta \simeq e^{\frac{4G}{\pi} N} = (3.21\ldots)^N$, with N the total number of sites and G the Catalan constant.

The definition of recurrence implies that all the operators a_i map recurrent configurations to recurrent configurations, implying that once the dynamics has brought the sandpile into a recurrent configuration, all subsequent configurations are recurrent. Therefore, the invariant measure is appropriate to study the long-term behavior of the sandpile.

The sandpile models summarized above have raised a large number of interesting and difficult questions. In the context of this review, most if not all of them focus on the stationary regime and study the statistical behavior of the sandpile when it runs over the recurrent configurations. In other words, all the probabilities

[2]The result holds in the more general case where $p_i \neq 0$ for every i.

we are interested in are induced by the invariant measure $\mathbb{P}_\Gamma$. The use of $\mathbb{P}_\Gamma$ is what makes most of the calculations fairly hard[3] because as noted earlier, that measure is nonlocal in terms of the (local) height variables (equivalently the recurrence criterion is nonlocal).

We should remark that the measure $\mathbb{P}_\Gamma$ fully depends on all the minute details which are necessary in order to completely specify the sandpile model under study. Not only the graph Γ itself but also the number and relative positions of closed and open vertices, and the values of the local thresholds $z_i^\star$ affect the invariant measure. Many features which directly depend on these data will change if any of these parameters is modified, like the number of recurrent configurations, the structure of the sandpile group,[4] the geometric structure of the identity configuration,[5] or the average height at a given site for instance. All these features are mathematically interesting and challenging (hence interesting) but very sensitive to the underlying details.

One should however expect that more robust features would be shared by sandpile models that are "close enough." The same situation prevails for other statistical models which, although having different microscopic descriptions, are considered to be essentially equivalent and grouped together to form a single universality class. Models belonging to the same universality class have identical behaviors "in the large," a point of view made technically more precise by the renormalization group analysis.

In order to identify these common behaviors, one should not look at small scales as these are more likely to be determined by the local details. The probability that two vertices next to each other have a height 2, for instance, is not really interesting; in addition, it is a pure number, different for each different model. Robust behaviors are expected to be found at large scales as they are much less affected by the microscopic details. One convenient method to access the large-distance behaviors is by taking the scaling limit. (Readers familiar with the scaling limit and the ideas of the renormalization group can safely go straight to the next sections.)

3 THE SCALING LIMIT AND CONTINUUM FIELD THEORIES

The simple idea underlying the scaling limit is this: if we want to concentrate on the large-scale behavior of a system, let us look at it from far away! The further away we look at the system, the larger our horizon is and the larger the distances we keep in sight. At the same time, when looking from a distance, the details get blurred and disappear: one can no longer recognize the type of graph, and its connectivities are no longer visible. What we see seems to become independent of the microscopic details of the model.

Rather than stepping back, an equivalent but more convenient way to proceed is to shrink the discrete structure (graph or grid or lattice) on which the microscopic variables live. This will involve a (real) small parameter ε such that the graph can be embedded in $\varepsilon\mathbb{Z}^d$ (or another shrinked regular lattice). For smaller and smaller ε, fixing a macroscopic distance $\vec{x} = \varepsilon\vec{m} \in \varepsilon\mathbb{Z}^d$ amounts to probe larger and larger scales $\vec{m}$ in terms of lattice units and at the same time, allows to keep a macroscopic distance $r = |\vec{x}|$ under control. The scaling limit corresponds[6] to take $\varepsilon \to 0$.

We note that since the scaling limit is a way to focus on asymptotically large distances, we have to make sure that the system does have such asymptotic distances! Indeed the scaling limit requires that we also take the infinite volume limit, by allowing the system to remain finite but of increasing size, the growth being at least of order $1/\varepsilon$.

The scaling limit has interesting consequences. The first most apparent one is that the substrate of the rescaled model goes to a continuum, either $\mathbb{R}^d$ or a part of $\mathbb{R}^d$, which may be bounded.[7] This is the first sign that a continuum description ought to emerge in the scaling limit. This is confirmed by a second observation: the microscopic variables—the heights in the sandpile models—, which were attached to the vertices of a graph, or a grid, should, in some sense, converge to variables defined on a continuum. If indeed this is expected to happen, exactly what happens is quite subtle. To realize this, one may note that all the microscopic variables attached to sites contained in a ball of radius $o(1/\varepsilon)$ will actually collapse to the same point in the scaling limit. Thus, every point in the continuum is the convergence point of an infinite number of vertices in the original discrete setting. The infinity of microscopic variables carried by these vertices will supposedly mix and fuse to generate some kind of degree of freedom located *at a single point in the continuum*. What is then the nature of the emerging continuum degree of freedom at that point, and how is it related to the lattice variables supposed to collectively generate it? The conceptual answer is provided by the renormalization group. It roughly goes as follows.[8]

The scaling limit, as explained at the beginning of this section, was carried out in one stroke: all distances are scaled by ε, which is then taken to 0. This limit was only designed to show how the large-distance behaviors can be assessed but is too rough to answer the question raised in the previous paragraph. The renormalization group is much better designed conceptually as it organizes the scaling limit scale by scale and keeps track, at each scale, of the degrees of freedom present in the system.

Let us suppose that we start with a statistical model defined on very large graph, or, to simplify and fix the ideas, on an infinite

[3]A notable exception concerns the linear or almost linear graphs, for which the recurrence property usually takes a simpler form and allows for a larger number of explicit results (see f.i., [9, 10]).

[4]We have mentioned that the operators a_i generate an Abelian algebra. But when acting on recurrent configurations, they are invertible and therefore generate an Abelian group, called the sandpile group. The sandpile group, of order equal to $\det\Delta$, has been determined for a number of finite graphs.

[5]Recurrent configurations form an Abelian group under the site-wise addition of the heights, followed by relaxation. This group is isomorphic to the sandpile group. In particular, one of the recurrent configurations is the identity in the group and shows remarkable geometric patterns [11–14].

[6]For the scaling to be nontrivial, some external parameters may need to be appropriately scaled with ε. One example of this is discussed in **Section 7.1**.

[7]It is bounded if all the linear sizes of the finite systems in the sequence defining the infinite volume limit grow exactly like $1/\varepsilon$.

[8]Among the many books and reviews on the renormalization group in statistical mechanics, see, for instance, the book by Cardy [15].

lattice. We fix a convenient scale $\Lambda > 1$, partition the lattice into boxes of size Λ, and shrink the lattice by a factor Λ. Each box is now of linear size 1 and contains of the order of Λ^d microscopic variables. Within each box, we associate an effective, coarse-grained degree of freedom which takes into account the overall behavior of the microscopic variables inside the box (it could be, f.i., their average value), and we then compute the sum over the microscopic variables conditioned by the values of the coarse-grained variables. The result is a statistical model for the coarse-grained variables, defined on a lattice similar to the original one. Once this is done (!), we iterate the process by defining a second generation of coarse-grained variables out of those of the first generation, and so on.

After the first iteration, each group of roughly Λ^d microscopic variables has collapsed to a single coarse-grained variable of the first generation; the statistical model obtained for these can be interpreted as the original model in which the fluctuations of scale smaller than Λ have been integrated out. The second iteration yields a statistical model for the coarse-grained variables of the second generation, each of which has integrated the fluctuations of Λ^{2d} microscopic variables over scales smaller than Λ^2, and so on, for the next iterations. In this way, each iteration, also called renormalization, yields a model where more small-scale fluctuations have been integrated out, and whose large-scale behavior should be identical to that of the original model, since the large-scale fluctuations have been preserved.

The continuum degrees of freedom we were asking about are what the coarse-grained variables of higher and higher generation should converge to when the number of iterations goes to infinity. Each of them is indeed what is left of the infinite collection of the microscopic variables that were located around it. Because the coarse-grained variables of one generation are representative of those of the previous generation, the continuum degrees of freedom should similarly carry the same characteristics as the original microscopic variables. In particular, the long-distance correlations should be identical, at dominant order.

The continuum degrees of freedom emerging in the scaling limit are called *fields*. Unlike their lattice ancestors, they usually take continuous values. Fields are all what remains when the short-ranged degrees of freedom have been integrated out: they form the complete set of variables which are relevant as far as the long-distance properties of the original model are concerned. It means that only the lattice degrees of freedom which have long range correlations, namely, with diverging correlation lengths, will survive the scaling limit and eventually give rise to a field; all the others progressively disappear in the renormalization process.

The microscopic variables in terms of which the discrete statistical model is defined usually give rise to fields, but they are not the only ones. Any lattice observable, that is, any function of the microscopic variables, can potentially give rise to a field in the scaling limit[9] so that one is typically left with an infinite number of different fields. Each field has its own specific properties and should be interpreted as the scaling limit of one particular lattice observable (it may also happen that different lattice observables converge to fields with the same characteristics).

One last question must be addressed. The original statistical model was not only defined by its microscopic variables but also by a probability measure on the configuration space. That measure, which is a joint distribution for the (nonindependent) random microscopic variables, is usually given by a Gibbs measure and written, up to normalization, as $\mathbb{P}(C) \sim \exp(-H[C])$, where H is the Hamiltonian of the system, that is, some given function of the microscopic variables which determines the relative probability of a configuration C. What is the equivalent of the Gibbs measure for the fields?

According to the discussion above, one starts from the original model and its Hamiltonian $H_0 \equiv H$. The first renormalization yields the coarse-grained variables of the first generation and a corresponding Hamiltonian H_1, computed (at least in principle) by summing $\exp(-H_0)$ over the microscopic variables inside the boxes. Similarly, the kth iteration will produce a Hamiltonian H_k, defining the statistical model for the coarse-grained variables of the kth generation. The appropriate measure for the fields should therefore be something like the formal limit $\lim_{k\to\infty} \exp(-H_k)$. Physicists like to denote this formal object by $\exp(-S)$, where S, called the action, is a certain functional of the fields.

Thus, if the description of a statistical model is given, in the discrete lattice setting, in terms of a set of microscopic variables $(h_i^1, h_i^2, \dots)$ and a Hamiltonian $H(h_i^1, h_i^2, \dots)$, it is given in the scaling limit by a set of continuous fields $(\phi_1(\vec{x}), \phi_2(\vec{x}), \dots)$ and an action $S[\phi_1, \phi_2, \dots]$. The pair $\{(\phi_1(\vec{x}), \phi_2(\vec{x}), \dots), S\}$ is referred to as a *continuum field theory*.[10] More precisely, specifying a set of fields and their action S is only *one* way to present a field theory; it is also the most comfortable one because it allows to compute the correlators of the various fields, at least in principle.

Needless to say, working out the successive renormalizations along with the Hamiltonians $H_0, H_1, \dots$ is a formidable task that is, for all practical purposes, impossible to carry out explicitly, except on extremely rare occasions (and for tailored examples). As a consequence, the field theory describing the large distances of a statistical model cannot be obtained in a deductive way.

The situation however is not hopeless. Experience, heuristic arguments, or results obtained on the lattice can often give definite hints about the nature of the seeked field theory. More importantly, and even if one has no clue of what the correct field theory is, the relevance of a trial field theory, perhaps suggested by an educated guess, can be firmly tested by comparing correlation functions. If the lattice microscopic variable $h_{i=\frac{x}{\varepsilon}}$ (at site i) converges in the scaling limit to the field $\phi(x)$, it must be true that the scaling limit of the lattice correlators is equal to field theoretic correlators, as follows:

$$\lim_{\varepsilon\to 0} \varepsilon^{-n\Delta} \left\langle h_{\frac{x_1}{\varepsilon}} h_{\frac{x_2}{\varepsilon}} \dots h_{\frac{x_n}{\varepsilon}} \right\rangle_{\text{lattice}} = \left\langle \phi(x_1)\, \phi(x_2) \dots \phi(x_n) \right\rangle_{\text{FT}}, \quad (3)$$

[9]For instance, the energy density in the Ising model, namely, the product of two neighboring spins, gives rise to a field that is different from the one obtained from the spin variable itself. Later, we will give examples of this in the sandpile models (cluster variables).

[10]One should add "Euclidean" field theory because it is formulated on a Euclidean space $\mathbb{R}^d$.

where the exponent Δ is determined so that the limits on the left hand side exist: as shown below, it will eventually be related to the scale dimension of the field ϕ to which the lattice variable h_i converges. The previous identity must be satisfied for all n-point correlators, but also for any correlator of any number of lattice observables provided that for each observable $O(i)$ around the site i inserted in the lattice correlator, the corresponding field $\Phi(x)$ to which it converges is inserted in the field theoretic correlator:

$$\lim_{\varepsilon\to 0} \varepsilon^{-\sum_i \Delta_i} \left\langle O_1\left(\frac{x_1}{\varepsilon}\right) O_2\left(\frac{x_2}{\varepsilon}\right) \dots O_n\left(\frac{x_n}{\varepsilon}\right)\right\rangle_{\text{lattice}} = \langle \Phi_1(x_1)\, \Phi_2(x_2) \dots \Phi_n(x_n)\rangle_{\text{FT}}. \tag{4}$$

So, we can write the convergence of a lattice observable to a field as the formal identity:

$$\lim_{\varepsilon\to 0} \varepsilon^{-\Delta} O\left(\frac{x}{\varepsilon}\right) = \Phi(x), \tag{5}$$

meant to be valid inside correlators.

If both types of correlators can be separately computed, the potential infinity of identities similar to the previous one will put very strong constraints on the field theory proposed and allow to validate it or, on the contrary, to discard it. The more identities we are able to test, the higher the level of confidence we gain for the conjectural field theory.

At this stage, we seem to be running in a vicious circle: we want to test the proposed field theory by comparing its correlators with the lattice quantities, but we cannot compute the field correlators if we do not know the field theory! If one thinks of a field theory as being given by a set of fields and an action S, this is indeed a serious problem because the action cannot be easily guessed, and even worse, there are many cases for which one has no clue as to what the action is. However, the action is just one convenient (and usually not simple) way to compute correlators. One could think of other ways to determine correlators, and one of them is the presence of symmetry: enough symmetry allows determining the correlators. It is precisely the principle underlying the conformal field theories, which therefore provides a field theoretic framework where no action is necessary. They are discussed in the next section.

Knowing the details of the field theory describing the long-distance properties of a statistical model is at the same time extremely powerful and immensely complicated. On the one hand, it is indeed powerful because it captures the very essential behavior of the statistical model without being cluttered with the many irrelevant lattice effects which make the lattice model so much more complex. On the other hand, it is also immensely complicated because every single element in the lattice model which affects the long distances must have a match in the field theory. Such elements include,

- of course, the bulk observables as discussed above;
- the boundary conditions, the changes of boundary conditions, and the boundary observables;
- the nonlocal observables (like disorder lines in the Ising model);
- the algebra of all the observables;
- the specific effects arising when the lattice is embedded in topologically nontrivial geometries (cylinder, torus, etc.);
- the symmetry, finite or other, that may be present in the model,

and possibly many others. All this represents a huge amount of information that must be present and known in the field theory, and which can be only very rarely contemplated in full. A renown exception is when we consider critical statistical models, as we do here, which are in addition formulated on two-dimensional domains ($d = 2$).

4 CONFORMAL FIELD THEORIES

Critical systems are primarily characterized by a scale invariance. The correlation lengths of the observables surviving the scaling limit diverge in the infinite volume limit so that there is no intrinsic length scale left: the fluctuation patterns appear to be the same at all scales. As a consequence, the correlation functions of those observables decay algebraically rather than exponentially. The large-distance 2-point correlator of a typical lattice observable O_i located around the site i takes the following form:

$$\langle O_i\, O_j\rangle = \frac{A}{|i-j|^{2\Delta}} + \dots, \tag{6}$$

where A is a normalization, Δ is the exponent controlling the decay, and the dots indicate lower order terms.

The field theory emerging in the scaling limit inherits the scale invariance. Further assuming translation and rotation symmetries, the scale invariance is enhanced to the invariance under a larger group, namely, the group of conformal transformations, that is, the coordinate transformations which preserve angles.[11] In d dimensions, the conformal transformations include the transformations mentioned above, namely, the translations (d real parameters), dilations (1 parameter), and rotations ($d(d-1)/2$ parameters), and the so-called special conformal transformations (or conformal inversions) which depend on an arbitrary vector $\vec{b}$ (d additional parameters) take the following general form:

$$\frac{\vec{x}'}{|\vec{x}'|^2} = \frac{\vec{x}}{|\vec{x}|^2} + \vec{b} \quad \Leftrightarrow \quad \vec{x}' = \frac{\vec{x} + |x|^2\, \vec{b}}{1 + 2\vec{b}\cdot\vec{x} + |\vec{b}|^2\, |\vec{x}|^2}. \tag{7}$$

Together these transformations form a finite Lie group isomorphic to $\mathrm{SO}(d+1,1)$. They are all global conformal transformations because they are defined everywhere on $\mathbb{R}^d \cup \{\infty\}$ and bijective. In dimension $d > 2$, a conformal transformation defined locally can be extended to a global transformation.

Typical spinless (i.e., rotationally invariant) fields transform tensorially under conformal transformations as follows:

$$\Phi(\vec{x}) \to \left|\frac{\partial x'^i}{\partial x^j}\right|^{\Delta/d} \Phi(\vec{x}'), \tag{8}$$

[11]The material recalled in this section is completely standard; useful references include Ref [16] (rather comprehensive) and [17] (more focused on critical statistical systems).

for some number Δ. Fields transforming that way under global conformal transformations are called *quasi-primary*. Global conformal invariance then fixes the average value of a quasi-primary field,

$$\langle \Phi(\vec{x}) \rangle = 0, \qquad \text{if } \Delta \neq 0, \tag{9}$$

(a constant for $\Delta = 0$ by translation invariance) and the 2-point correlator of two quasi-primary fields is given as follows:

$$\langle \Phi_1(\vec{x}_1)\, \Phi_2(\vec{x}_2) \rangle = \begin{cases} \dfrac{A_{12}}{|\vec{x}_1 - \vec{x}_2|^{2\Delta_1}} & \text{if } \Delta_1 = \Delta_2, \\ 0 & \text{if } \Delta_1 \neq \Delta_2. \end{cases} \tag{10}$$

Specializing (8) to a dilation, $\vec{x}' = \alpha\vec{x}$, we have $\Phi(\vec{x}) \to \alpha^{\Delta}\, \Phi(\alpha\vec{x})$ so that Δ can be identified with the dimension of the field Φ (in units of inverse length).

Global conformal invariance also completely determines the correlator $\langle \Phi_1(\vec{x}_1)\, \Phi_2(\vec{x}_2)\, \Phi_3(\vec{x}_3) \rangle$ of three (and not more) quasi-primary fields as follows:

$$\langle \Phi_1(\vec{x}_1)\, \Phi_2(\vec{x}_2)\, \Phi_3(\vec{x}_3) \rangle = \frac{A_{123}}{|\vec{x}_1 - \vec{x}_2|^{\Delta_1+\Delta_2-\Delta_3}\, |\vec{x}_1 - \vec{x}_3|^{\Delta_1+\Delta_3-\Delta_2}\, |\vec{x}_2 - \vec{x}_3|^{\Delta_2+\Delta_3-\Delta_1}}. \tag{11}$$

We see that the lattice 2-correlator (6) is consistent with the convergence of the observable O_i to a quasi-primary field $\Phi(\vec{x})$ of dimension Δ upon setting $i = \vec{x}/\varepsilon$ since the matching identity (3) is satisfied as follows:

$$\lim_{\varepsilon \to 0} \varepsilon^{-2\Delta} \left\langle O_{\vec{x}_1/\varepsilon}\, O_{\vec{x}_2/\varepsilon} \right\rangle_{\text{lattice}} = \frac{A}{|\vec{x}_1 - \vec{x}_2|^{2\Delta}} = \langle \Phi(\vec{x}_1)\, \Phi(\vec{x}_2) \rangle_{\text{FT}}. \tag{12}$$

We note that all subdominant terms in the lattice correlator (6) drop out when taking the limit $\varepsilon \to 0$, confirming once more that a field theory captures the large-distance behavior of a critical lattice model.

What has been just recalled is valid in any dimension $d \geqslant 2$ but is only the beginning of the story for $d = 2$. The global conformal group discussed above remains but is more conveniently presented in complex coordinates as the $\mathrm{SL}(2, \mathbb{C})$ group of Möbius transformations $w = \frac{az+b}{cz+d}$, for $a, b, c, d \in \mathbb{C}$ satisfying $ad - bc = 1$.

The two-dimensional world has however many more conformal transformations in store. Indeed, it is a well-known fact that any *analytic map* $w(z)$ of the complex plane is conformal. Surely, an analytic function requires an infinite number of parameters to fix it (f.i., the coefficients of its Laurent expansion in some neighborhood) so that the conformal "group" is certainly infinite-dimensional. The term *group* is not really appropriate because the composition of analytic maps is generally not defined everywhere on the complex plane: unless it is a Möbius transformation, an analytic map is either not defined everywhere or its image is not the whole complex plane. For instance, the map $w = \frac{L}{2\pi \mathrm{i}} \log z$ maps the complex plane to a cylinder of circumference L. The discussion of the two-dimensional conformal group is thus usually carried out at the level of its algebra, for which infinitesimal transformations of the form $w = z + \epsilon\, z^{n+1}$ are considered. The corresponding generators satisfy the famous infinite-dimensional *Virasoro algebra*,

$$[L_m, L_n] = (m-n) L_{m+n} + \frac{c}{12}\, m\left(m^2 - 1\right) \delta_{m+n,0}, \qquad m, n \in \mathbb{Z}, \tag{13}$$

a central extension of the Witt algebra. The real number c is the central charge and is one of the most important data of a two-dimensional conformal field theory (CFT). The modes L_0 and $L_{\pm 1}$, whose algebra is unaffected by the central charge, are the infinitesimal generators of the Möbius group, with L_{-1} and L_0 corresponding to translations and dilations, respectively. As it turns out, a second commuting copy of the Virasoro algebra, with modes $\overline{L}_n$, can formally be considered for the conformal transformations of the antiholomorphic variable $\overline{z}$.

It is not our purpose to give an introduction to the CFT, but one can easily conceive the huge difference between a finite symmetry algebra and an infinite one. A field theory that is to be invariant under an infinite algebra is immensely more constrained and therefore much more rigid, leaving the hope that one should be able to say a lot more about it. It is indeed the case.

For one thing, the field content of a CFT must be organized into representations of the Virasoro algebra, which are all infinite dimensional, and this opens up the possibility that an infinite number of fields be in fact accommodated in a finite number of representations (such CFTs are called rational). In this respect, the *primary fields* are particularly important. They are the strengthened version of quasi-primary fields in the sense that they transform tensorially under any conformal transformation. A primary field is an eigenfield of L_0 and $\overline{L}_0$ with real eigenvalues h and $\overline{h}$ and, more importantly, is annihilated by all positive modes $L_{n>0}, \overline{L}_{n>0}$. It is in particular characterized by a total weight $\Delta = h + \overline{h}$ (its eigenvalue under $L_0 + \overline{L}_0$, the real dilation generator) and is, of course, quasi-primary. The action of any string of negative Virasoro modes $L_{n<0}, \overline{L}_{n<0}$ on a primary field produces infinitely many new fields, called *descendant fields*, which include all derivatives of the primary field, since $L_{-1} = \partial_z$ and $\overline{L}_{-1} = \partial_{\overline{z}}$ act as derivatives on any field. All of them are eigenfields of L_0 and $\overline{L}_0$. Together, they form a highest weight representation of the Virasoro algebra whose structure is similar to highest weight representations of simple Lie algebras, the primary field playing the role of the highest weight state.

Like in higher dimensions, the forms of the 1-, 2-, and 3-point of quasi-primary fields are completely fixed by their invariance under Möbius transformations. They are more easily written in complex coordinates ($z_{ij} = z_i - z_j$) as follows:

$$\langle \Phi(z, \overline{z}) \rangle = A\, \delta_{h,0} \delta_{\overline{h},0}, \tag{14}$$

$$\langle \Phi_1(z_1, \overline{z}_1)\, \Phi_2(z_2, \overline{z}_2) \rangle = \frac{A_{12}}{z_{12}^{h_1+h_2}\, \overline{z}_{12}^{\overline{h}_1+\overline{h}_2}} \delta_{h_1,h_2} \delta_{\overline{h}_1,\overline{h}_2}, \tag{15}$$

$$\langle \Phi_1(z_1, \overline{z}_1)\, \Phi_2(z_2, \overline{z}_2)\, \Phi_3(z_3, \overline{z}_3) \rangle = \frac{A_{123}}{z_{12}^{h_1+h_2-h_3}\, z_{13}^{h_1+h_3-h_2}\, z_{23}^{h_2+h_3-h_1}\, \overline{z}_{12}^{\overline{h}_1+\overline{h}_2-\overline{h}_3}\, \overline{z}_{13}^{\overline{h}_1+\overline{h}_3-\overline{h}_2}\, \overline{z}_{23}^{\overline{h}_2+\overline{h}_3-\overline{h}_1}}. \tag{16}$$

These forms suggest that the conformal weights $h_i, \overline{h}_i$ are positive so that the correlators decrease with the separation distances, as seems natural from a physical point of view. We will nonetheless encounter physical fields with negative weights, for which the correlators have a different meaning.

Occasionally, we will consider *chiral correlators* for which we only retain the dependence in the z_i variables of the full correlators (equivalently the action of the holomorphic modes L_n). Chiral correlators are appropriate for observables living on a boundary, like the real line bordering the upper-half plane, since a boundary is one-dimensional. In this case, only one copy of the Virasoro algebra remains so that the fields are characterized by a single conformal weight. Chiral correlators are also useful to compute the correlators of bulk variables on surfaces with boundaries (see **Section 6**).

The precise structure of a Virasoro highest weight representation (c, Δ) based on a primary field of weight Δ is crucial. In the good cases, it determines the properties of the primary field (and of its descendants) by fixing its correlators with itself or with other fields. The 2-point correlator of a primary field has the form **(15)** since it is quasi-primary, and the same is true for the 3-point correlator. To go beyond, the global conformal invariance is not enough.[12] It turns out to be often the case that the structure of a Virasoro highest weight representation implies that the correlators $\langle \Phi(z,\overline{z}) \dots \rangle$ involving the primary field Φ obey differential equations. Four-point functions can be routinely computed in this way. All correlators can then be determined, at least in principle, without knowing anything of a possible Lagrangian realization of the underlying field theory (through its action).

The miracle of 2-dimensional CFTs can be paraphrased in the following way: to completely solve a CFT, that is, compute all its correlation functions, and thereby to know everything there is to know of the large-distance limit of a critical model; it is sufficient to know enough of the Virasoro representations making up that CFT. This methodology has been immensely successful since the mid-80's and has led to a profound understanding of the many aspects of critical models listed at the end of the previous section. The Ising model is the prominent example of a model that can be treated that way, but the same is true of more general statistical models involving local interactions between the microscopic variables.

More recently, models showing some form of nonlocality have been examined at the conformal light. Sandpile models are in this class, since, as we have seen earlier, the height variables are in strong interaction over the entire domain to form global recurrent configurations. Other models with nonlocal interactions and/or nonlocal degrees of freedom include percolation, critical polymers, and more general loop models. It may sound surprising, but the conclusion seems to be that the conformal approach is still relevant. However, the CFTs underlying these models are more complex essentially because the representations of the Virasoro algebra that appear have a far more complicated structure. These special CFTs are called *logarithmic conformal field theories* (LCFTs). What follows is a very basic introduction to the salient features of the LCFT; various reviews and applications may be found in the special issue [18]. Let us also mention [19] which reviews the extension to the LCFT of the calculational tools used in CFT.

For the highest weight representations discussed above, the operators $L_0, \overline{L}_0$ are diagonalizable. LCFTs have the distinct feature to include Virasoro representations for which L_0 and $\overline{L}_0$ are no longer diagonalizable, but instead contain (infinitely many) Jordan blocks of finite rank. To have a rough idea of what these representations look like, one can think of a highest weight representation for which the highest weight is not a single primary field, but a pair of fields (Φ, Ψ), of which only Φ is primary. The action of L_0 on them would be typical of a rank 2 Jordan cell as follows:

$$L_0\Phi = h\Phi, \qquad L_0\Psi = h\Psi + \lambda\Phi, \tag{17}$$

where Ψ is called the *logarithmic partner* of the primary field Φ and a similar action of $\overline{L}_0$ (with $\overline{h}$). Under the action of the negative Virasoro modes, the Jordan block structure will propagate among the descendant fields. The presence of Jordan blocks is a sort of minimal ingredient to make a representation logarithmic; many mathematical complications can and do arise (see, f.i., [20]). Higher rank Jordan blocks can also appear.

A immediate consequence of the presence of Jordan blocks explains the use of the word "logarithmic": the correlators of fields in an LCFT contain logarithmic terms in addition to the power laws encountered before. For instance, the 2-point correlators of the logarithmic pair $\{\Phi, \Psi\}$, both of weights $(h, \overline{h})$, read

$$\langle \Phi(z_1,\overline{z}_1)\,\Phi(z_2,\overline{z}_2)\rangle = 0,$$
$$\langle \Phi(z_1,\overline{z}_1)\,\Psi(z_2,\overline{z}_2)\rangle = \frac{B}{(z_1-z_2)^{2h}(\overline{z}_1-\overline{z}_2)^{2\overline{h}}}, \tag{18a}$$
$$\langle \Psi(z_1,\overline{z}_1)\,\Psi(z_2,\overline{z}_2)\rangle = \frac{C-2\lambda B\log|z_1-z_2|^2}{(z_1-z_2)^{2h}(\overline{z}_1-\overline{z}_2)^{2\overline{h}}}. \tag{18b}$$

For rank r Jordan blocks, the 2-point correlators would involve up to $(r-1)$th powers of logarithms. The parameter λ is not intrinsic as it can be observed in the normalization of Φ or of Ψ; likewise, the logarithmic partner Ψ is defined up to a multiple of Φ without affecting the defining relations (17). The chiral version of the above 2-point functions reads

$$\langle \Phi(z_1)\,\Phi(z_2)\rangle = 0, \qquad \langle \Phi(z_1)\,\Psi(z_2)\rangle = \frac{B}{(z_1-z_2)^{2h}}, \tag{19a}$$
$$\langle \Psi(z_1)\,\Psi(z_2)\rangle = \frac{C-2\lambda B\log(z_1-z_2)}{(z_1-z_2)^{2h}}, \tag{19b}$$

It should not be too surprising that Jordan blocks and logarithms go hand in hand. Under dilation by a factor α, a logarithmic term transforms inhomogeneously $\log z \to \log z + \log\alpha$, reflecting the inhomogeneous action of the dilation generator L_0 on Ψ. Under a finite dilation $w = \alpha z$, the transformation laws of Φ and Ψ read

$$\Phi'(w,\overline{w}) = |\alpha|^{-\Delta}\,\Phi(z,\overline{z}),$$
$$\Psi'(w,\overline{w}) = |\alpha|^{-\Delta}\left\{\Psi(z,\overline{z}) - \lambda\log|\alpha|^2\,\Phi(z,\overline{z})\right\}. \tag{20}$$

[12] A general 3-point correlator $\langle \Phi_1(z_1)\,\Phi_2(z_2)\,\Phi_3(z_3)\rangle$ is a function of three complex numbers; if all three fields are quasi-primary, that function can be determined by trading z_1, z_2, and z_3 for the three complex parameters of a general Möbius transformation.

One may check that the form of the correlators (18) is indeed invariant under the replacement $\Phi(z,\overline{z}) \to \Phi'(w,\overline{w})$ and $\Psi(z,\overline{z}) \to \Psi'(w,\overline{w})$. Let us also note that the scaling (5) must be redefined for the lattice observables described by logarithmic fields since it involves a dilation by a factor $1/\varepsilon$, to which the field responds by an inhomogeneous term.

Despite all the efforts spent, LCFTs are generally much less understood than their non-logarithmic cousins, although a number of general features are known. On the statistical side, few models have been thoroughly studied as their nonlocal features make it hard to carry out exact calculations on the lattice. On the field theoretic side, it is not known what a generic LCFT looks like. The simplest of all (but nontrivial) and probably the only LCFT to be fully under control is the symplectic fermion theory with central charge $c = -2$, also called the triplet theory. It has been introduced in [21] and then investigated in greater detail in [22, 23]. It has the following Lagrangian realization in terms of a pair of free, massless, Grassmannian scalar fields $\theta, \tilde{\theta}$,

$$S = \frac{1}{\pi}\int \mathrm{d}z\mathrm{d}\overline{z}\ \partial\theta\overline{\partial}\tilde{\theta}\,, \qquad \partial = \partial_z,\ \overline{\partial} = \partial_{\overline{z}}. \tag{21}$$

Several fields in this theory form logarithmic pairs, like the identity $\mathbb{I}$ and the composite field $\theta\tilde{\theta}$. We note that (18) then implies the somewhat unusual relation $\langle \mathbb{I} \rangle = 0$, which indeed follows, using the rules of integration over Grassmannian variables, from the fact that the above action does not depend on the constant modes of θ and $\tilde{\theta}$. Since this is a free scalar theory, all correlators of fields that are local (i.e., product of derivatives) in $\theta, \tilde{\theta}$ are polynomials in the derivatives of the Green function (the kernel of the inverse Laplacian $-4\partial\overline{\partial}$) given in complex coordinates by $G(z, w) = -\log|z - w|$.

To finish, let us note that the statistical models which have a non-diagonalizable transfer matrix (when there is a proper one) are the natural candidates for being described by LCFTs in their scaling regime. Indeed, such a transfer matrix gives rise to a non-diagonalizable Hamiltonian, which itself is the lattice version of the field theoretic operator $L_0 + \overline{L}_0$. As said above, the non-diagonalizability of $L_0, \overline{L}_0$ is the hallmark of LCFTs. The logarithmic minimal models form an infinite series of such lattice models [24].

The rest of this review is devoted to discussing the variables of the 2-dimensional sandpile models which have been successfully (i.e., with enough confidence) identified in the corresponding LCFT. These elements reveal *some* facets of the field theory at work in sandpile models: the big and complete picture is well out of reach for the moment.

5 BULK VARIABLES

The height variables are certainly the first and most natural variables to look at as they are the microscopic variables in terms of which the models are defined. The introduction we gave in **Section 2** was for the Abelian sandpile on an arbitrary graph. If large-distance properties should be rather robust against local modifications of a graph, they are not expected to be the same on a graph with a high degree of connectivity (the extreme example being the complete graphs), a regular graph with a moderate degree of connectivity or a graph with a strong hierarchical structure (like Cayley trees). Most of the results reviewed here are obtained when the graph is a rectangular portion of the square lattice $\mathbb{Z}^2$; varying the size of the grid is an easy way to approach the infinite volume limit, and this choice ensures that conservative sites away from the boundary have height variables taking the same number of values (namely, 4). The triangular and honeycomb lattices, for which the number of height values is, respectively, 6 and 3, will be briefly discussed as well in order to address universality issues (see **Section 7.2**).

In most cases, the only dissipative sites will be located on the boundary,[13] except when we discuss the insertion of isolated dissipation. With one exception, we will exclusively consider open and closed boundary conditions, by which we mean that whole stretches of boundary sites are either dissipative or conservative, respectively. The choice of boundary conditions not only has an effect at finite volume but also in the infinite volume limit if some of the boundaries are kept at finite distance (e.g., on the upper-half plane or on a strip of finite width, see **Section 6**).

On a finite grid Γ, the heights assigned to the vertices form stable configurations, but only the recurrent ones have a nonzero (and uniform) weight with respect to the invariant measure $\mathbb{P}_\Gamma$. So far, we have no clear idea of what a generic recurrent configuration looks like. Answers to questions like "What is the proportion of sites having height 1, height 2, . . .?" can certainly help figure out. Also, the heights must be correlated within a recurrent configuration. Can one characterize these correlations? Are they exponential or power-lawed? The computation of multisite height probabilities answers these questions and helps understand the statistics of recurrent configurations.

To be definite, let us consider Γ as an $L \times M$ rectangular grid in $\mathbb{Z}^2$, with open boundary conditions: the non-boundary sites are conservative and have a maximal height value equal to $z_i^\star = z_i = 4$, whereas the boundary sites have a maximal height value chosen to be $z_i^\star = 4 > z_i$ (boundary and corner sites dissipate 1 resp. 2 grains of sand under toppling; both types are connected to the sink). Thus, the toppling matrix is four times the identity minus the adjacency matrix of the grid, and the height at every site takes values in {1, 2, 3, 4}. In this section, all boundaries are sent off to infinity in the scaling limit so that the domain converges to $\mathbb{R}^2$; in that limit, all multisite probabilities are fully invariant under translations.

5.1 One-Site Height Probabilities

As a warm up for what has to come, we ask the following: what is the probability $\mathbb{P}_\Gamma(h_i = a)$ that in a recurrent configuration, a given site i has height equal to a, between 1 and 4? Because we are interested in the infinite volume limit of these numbers, we take i to be deep in the middle of the grid, well away from the boundaries.

If we pause for a while and ponder over that simple question, we feel a bit at a loss on how to handle it because the only means

[13] For rectangular grids $\Gamma \subset \mathbb{Z}^2$, the notion of boundary is clear: when Γ is embedded in $\mathbb{Z}^2$, the boundary sites are those which are connected to sites of $\mathbb{Z}^2$ not in Γ.

we have is the general criterion of recurrence, namely, the nonexistence of forbidden subconfigurations. Let us start with the height 1.

Since the total number of recurrent configuration is equal to $\det \Delta_\Gamma$ (see **Section 2**), we can write

$$\mathbb{P}_\Gamma(h_i = 1) = \frac{\#\{\text{recurrent configs with } h_i = 1\}}{\det \Delta_\Gamma}. \tag{22}$$

For $h_i = 1$ to be in a recurrent configuration C, the height of none of its neighbors N, E, S, or W can be equal to 1 (as they would form a forbidden subconfiguration). Following the clever trick proposed in [25], we consider a new grid $\tilde{\Gamma}_i$ by deleting from Γ the vertex i and the four edges incident to it. We also define from C a new configuration $\tilde{C}$ on $\tilde{\Gamma}_i$ by setting

$$\tilde{h}_j = \begin{cases} h_j & \text{for } j \notin \{i, \mathrm{N}, \mathrm{E}, \mathrm{S}, \mathrm{W}\}, \\ h_j - 1 \geqslant 1 & \text{for } j \in \{\mathrm{N}, \mathrm{E}, \mathrm{S}, \mathrm{W}\}. \end{cases} \tag{23}$$

Looking back at the criterion of recurrence for an arbitrary graph, it is not difficult to see that a configuration C with $h_i = 1$ is recurrent on Γ if and only if $\tilde{C}$ is recurrent on $\tilde{\Gamma}_i$. We thus obtain

$$\mathbb{P}_\Gamma(h_i = 1) = \frac{\det \Delta_{\tilde{\Gamma}_i}}{\det \Delta_\Gamma} = \frac{\det[\Delta_{\tilde{\Gamma}_i} \oplus 1_{ii}]}{\det \Delta_\Gamma}, \tag{24}$$

where the matrix in the numerator has been extended by a one-dimensional diagonal block labeled by the vertex i, without changing the value of the determinant. One then can write

$$\Delta_{\tilde{\Gamma}_i} \oplus 1_{ii} = \Delta_\Gamma + B(i), \tag{25}$$

with $B(i)$, the defect matrix is given by

$$B(i)_{k,k'} = \begin{pmatrix} -3 & 1 & 1 & 1 & 1 \\ 1 & -1 & 0 & 0 & 0 \\ 1 & 0 & -1 & 0 & 0 \\ 1 & 0 & 0 & -1 & 0 \\ 1 & 0 & 0 & 0 & -1 \end{pmatrix}, \qquad k, k' \in \{i, \mathrm{N}, \mathrm{E}, \mathrm{S}, \mathrm{W}\}, \tag{26}$$

and $B(i)$ is zero everywhere else. We obtain

$$\mathbb{P}_\Gamma(h_i = 1) = \frac{\det[\Delta_\Gamma + B(i)]}{\det \Delta_\Gamma} = \det\left[\mathbb{I} + \Delta_\Gamma^{-1} B(i)\right]. \tag{27}$$

It reduces to the computation of a finite determinant since $B(i)$ has finite rank. In the infinite volume limit (both $L, M \to \infty$), this probability converges to a constant $\mathbb{P}_1$ (by translation invariance). As the matrix Δ_Γ becomes the discrete Laplacian on $\mathbb{Z}^2$ in that limit,[14] standard results yield [25]

$$\mathbb{P}_1 \equiv \lim_{|\Gamma| \to \infty} \mathbb{P}_\Gamma(h_i = 1) = \frac{2(\pi - 2)}{\pi^3} \simeq 0.073\,63. \tag{28}$$

[14]The reader will legitimately point out that the Laplacian on $\mathbb{Z}^2$ has a zero mode and is therefore not invertible. A closer look at the determinants (27) however reveals that they only depend on differences of the inverse matrix entries, which are perfectly well-defined.

It also means that a recurrent configuration has an average of about 7% of sites with a height equal to 1.

What about higher heights? We know for sure that the inequalities $\mathbb{P}_4 > \mathbb{P}_3 > \mathbb{P}_2 > \mathbb{P}_1$ hold because adding one grain of sand to a recurrent configuration, at a site where $h_i = a$, yields a recurrent configuration if $a < 4$. However, to actually compute these numbers, can one use the same trick as for the height 1? The answer is definitely negative: no local modification of Γ like what we did above will allow computing the corresponding probabilities. To understand this, we turn to the description in terms of spanning trees.

As was briefly mentioned in **Section 2**, the burning algorithm yields a one-to-one correspondence between a recurrent configuration and a spanning tree rooted at the sink site s and growing into the interior of Γ. In a given spanning tree $\mathcal{T}$, a site j is called a *predecessor* of i if the unique path in $\mathcal{T}$ from j to the root passes through i. Let us also denote by $X_k(i)$ the fraction of all spanning trees for which the site i has k predecessors *among its nearest neighbors*, for $0 \leqslant k \leqslant 3$. A careful analysis of the burning algorithm shows the following [26]:

$$\mathbb{P}_\Gamma(h_i = a) = \mathbb{P}_\Gamma(h_i = a - 1) + \frac{X_{a-1}(i)}{5 - a}, \qquad 1 \leqslant a \leqslant 4. \tag{29}$$

For $a = 1$, we see that $\mathbb{P}_\Gamma(h_i = 1)$ is related to $X_0(i)$, namely, the fraction of spanning trees on Γ for which the site i is a leaf. All such trees can be obtained from arbitrary spanning trees on $\tilde{\Gamma}_i$ by adding one edge between one neighbor of i and i itself (four different possibilities). Thus, both points of view coincide and lead to the same local modification $\Gamma \to \tilde{\Gamma}_i$.

The next case is $\mathbb{P}_\Gamma(h_i = 2)$, related to $X_1(i)$. Here, the situation is dramatically different because the condition that i has only one predecessor among its nearest neighbors is highly nonlocal. The reason for this is that there are two manners for a neighbor of i to be a predecessor of i in a given tree. The first one is that the tree includes the edge between the two sites so that the neighbor of i is directly connected to i. In the second manner, the tree contains a potentially long chain of edges that forms a path between the two sites. The first one is a local connection and is easy to check, and the second one is nonlocal and more difficult. The same remark applies to the fractions $X_2(i)$ and $X_3(i)$ and makes the calculation of the corresponding probabilities much more complicated.

In fact, this first natural and simple-looking question we have raised, namely, the value of $\mathbb{P}(h_i = a)$, turned into a fairly long warming up exercise as it took about twenty years before the completely explicit probabilities could be found. By using a rather heavy graph theoretical technology, Priezzhev [26] obtained the first expressions for $\mathbb{P}_2, \mathbb{P}_3$, and $\mathbb{P}_4$, but these were given in the form of multivariate integrals. The problem was reconsidered in [27], where the following explicit values were conjectured:

$$\mathbb{P}_2 = \frac{1}{4} - \frac{1}{2\pi} - \frac{3}{\pi^2} + \frac{12}{\pi^3} \simeq 0.173\,90, \tag{30a}$$

$$\mathbb{P}_3 = \frac{3}{8} + \frac{1}{\pi} - \frac{12}{\pi^3} \simeq 0.306\,29, \tag{30b}$$

$$\mathbb{P}_4 = \frac{3}{8} - \frac{1}{2\pi} + \frac{1}{\pi^2} + \frac{4}{\pi^3} \simeq 0.446\,17. \tag{30c}$$

A few years later, three independent proofs were given. The first one was based on a relation with the probability of a loop-erased random walk (LERW) to visit a fixed nearest neighbor of its starting point, which was then computed in terms of dimer arrangements [28]. The second proof also used the relation with LERW passage probabilities but within a much more general approach [29]. Finally the third one [30] carried out the direct computation of the multiple integrals left open in [26]. Let us mention that the technique developed in [29] to enumerate the so-called cycle-rooted groves (which generalize spanning trees to spanning forests with marked points) currently provides by far the most efficient way to compute height probabilities, reducing the calculation of $\mathbb{P}_2, \mathbb{P}_3$ to just a few lines (see Ref [31]). Most of the height correlators presented below have been computed using this technique. Also noteworthy in this context is the work [32] which presents a direct and elementary derivation of the average height $\langle h \rangle = \sum_a a\,\mathbb{P}_a$ on planar lattices (from the formulas above, it is equal to $\frac{25}{8}$ on $\mathbb{Z}^2$) without computing the individual height probabilities.

Ironically, the four numbers $\mathbb{P}_a$ are not very useful for a comparison with a field theory because they will have to be subtracted in correlators (see below). And indeed, some of the correlators have been determined exactly before the 1-site probabilities $\mathbb{P}_a$ were found.

Even though the explicit expressions for $\mathbb{P}_a$'s have the same level of simplicity, the far larger complexity of the combinatorial problem posed by the calculation of $\mathbb{P}_{a\geqslant 2}$ hints at a striking difference of nature between the height 1 and the higher heights: the height 1 is essentially local, and the others are nonlocal. This will soon be confirmed.

5.2 Height Cluster Probabilities

Cluster height probabilities are a rather obvious generalization of one-site probabilities, by which we ask for the probability that a specific connected subconfiguration occurs in recurrent configurations, away from the boundaries and in the infinite volume limit. Examples of height clusters are shown below.

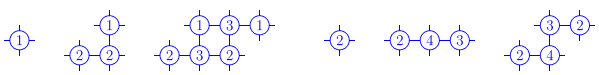

(31)

The three clusters on the left belong to the family of *weakly allowed subconfigurations*, or minimal height clusters, first introduced in [25], which contains the cluster made of a single height equal to 1. They are minimal subconfigurations in the sense that if one decreases any of its heights by 1, the clusters become (or contain) forbidden subconfigurations. As was done in the previous subsection for single height 1, their occurrence probabilities around position i can be computed by cutting off appropriate lattice sites and edges. They take the form of finite determinants $\mathbb{P}_S(i) = \det[\mathrm{I} + \Delta_\Gamma^{-1} B_S(i)]$, where the defect matrix $B_s(i)$ depends on the cluster S considered [25, 33].

The three clusters on the right of (31) are not minimal and generalize the simple cluster made of a single height larger or equal to 2. Their level of complexity is comparable to the latter and is best computed using the methods of [29]. Explicit calculations become fairly tedious as the size of the cluster increases.

5.3 Height Correlations

In terms of the subtracted height variables,[15]

$$h_a(i) \equiv \delta_{h(i),a} - \mathbb{P}_a, \tag{32}$$

the n-point correlation functions are given by

$$\sigma_{a_1,a_2,\ldots,a_n}(i_1, i_2, \ldots, i_n) = \mathbb{E}\big[h_{a_1}(i_1)\, h_{a_2}(i_2) \ldots h_{a_n}(i_n)\big]. \tag{33}$$

These are the functions we are primarily interested in for a future comparison with a conformal field theory. To make the comparison sensible, we have to take the infinite volume limit *and* the limit of large separations $|i_k - i_l| \to +\infty$. In addition, to avoid the boundary effects—they will be studied later on, all insertion points i_k are to stay (infinitely) far from the boundaries. In practice, one first replaces Δ_Γ by the Laplacian Δ on $\mathbb{Z}^2$ and then expand the Green matrix (i.e., the inverse Laplacian) for large separations.

The computation of correlations of heights 1 (or indeed any weakly allowed subconfigurations, see below) poses no particular problem. The argument used in **Section 5.1** leading to consider new configurations $\tilde{C}$ on a locally modified lattice $\tilde{\Gamma}$ is simply repeated for the neighborhood of each cluster. Thus, the probability to find a height $h(i_1) = 1$ at site i_1, a height $h(i_2) = 1$ at site i_2, and so on, is equal to

$$\begin{aligned}\mathbb{P}_\Gamma\big(h(i_1) = 1,\, h(i_2) = 1, \ldots\big) &= \frac{\det[\Delta_\Gamma + B(i_1) + B(i_2) + \ldots]}{\det \Delta_\Gamma} \\ &= \det\big[\mathbb{I} + \Delta_\Gamma^{-1}\{B(i_1) + B(i_2) + \ldots\}\big].\end{aligned} \tag{34}$$

The correlators $\sigma_{1,1,\ldots,1}$ are obtained by taking appropriate subtractions and the limits discussed above.

The first few n-point correlators can be easily computed for arbitrary configurations of insertion points [31, 33]. By construction, the 1-point function vanishes, $\sigma_1(i_1) = 0$ (the relation (9) is indeed the main motivation for the subtraction). The 2-point function is found to be ($i_1 - i_2 = \vec{r} = re^{i\varphi}$)

$$\sigma_{1,1}(i_1, i_2) = -\frac{\mathbb{P}_1^2}{2r^4} - \frac{4(\pi - 2)\big[1 + (\pi - 2)\cos 4\varphi\big]}{\pi^6\, r^6} + \ldots \tag{35}$$

where the dots stand for lower order terms.

This first result is instructive for several reasons. First, for large separation distances, the dominant term indicates that the correlation decay is algebraic, which shows that the model is critical and makes room for a conformal field theoretic description. Second, choosing the scale dimension $\Delta = 2$, the scaling limit (12) indeed retains the first term only, the form of which is the expected one (note that the

[15] In order to make contact with fields, we slightly change the notation $h_i \to h(i)$ for the height at site i.

second term, like all other subdominant ones, has only the lattice rotation invariance and is therefore not expected to survive the scaling limit). And third, the dominant term is negative, indicating an anticorrelation between heights 1. This is consistent with the fact that the presence of many heights 1 in a configuration makes it more likely to be nonrecurrent. Interestingly, the calculation can be carried out in $\mathbb{Z}^d$, with the result that the correlation decays like r^{-2d}, giving a dimension $\Delta = d$ [25].

The mixed correlator of a height 1 and a height 2, 3, or 4 is harder. They have first been obtained in [34, 35] by using classical graph theoretic techniques, and then reconsidered and extended in Ref [31] using the results of Ref [29]. Whatever the method used, one has to evaluate the fractions $\tilde{X}_k(i_1)$ of spanning trees, as defined in **Section 5.2**, but on a lattice modified around the site i_2 where height 1 is located. This modification affects the toppling (Laplacian) matrix and its inverse and, consequently, the whole computation, heavily based on these two matrices. The result for a height 1 and a height 2 reads, at dominant order,

$$\sigma_{2,1}(i_1, i_2) = -\frac{\mathbb{P}_1^2}{2r^4}\left\{\log r + \left(\gamma + \frac{3}{2}\log 2 + \frac{16 - 5\pi}{2(\pi - 2)}\right)\right\} + \dots \quad (36)$$

where $\gamma = 0.577216\ldots$ is the Euler constant. The first subdominant correction is of order r^{-6} and contains a nontrivial angular dependence, like in **(35)**, but also a $\log r$ term [31]. The expressions of $\sigma_{3,1}$ and $\sigma_{4,1}$ are similar, with different coefficients.

The expressions $\sigma_{a,1}$ for $a > 1$ definitely establish the logarithmic character of the CFT underlying the sandpile model. The expressions (35) and (36) are strongly reminiscent of those in (18) but do not quite match. If in the scaling limit, heights 1 and 2 were to converge to a logarithmic pair $\{h_1(z), h_2(z)\}$, one would think that $\sigma_{1,1}$ and $\sigma_{2,1}$ ought to go over to the 2-point functions $\langle h_1(z_1)h_1(z_2)\rangle$ and $\langle h_2(z_1)h_1(z_2)\rangle$, respectively. However, conformal invariance implies that the former vanishes identically, whereas the latter is not logarithmic. We could think of computing $\sigma_{2,2}$ to see what comes out, but large-distance correlators with several heights strictly larger than 1 are far beyond our present computational capabilities. Let us add that the calculation of $\sigma_{a,b}(i_1, i_2)$ for $a, b > 1$ does not merely reduce to the evaluation of numbers like $X_{a-1,b-1}(i_1, i_2)$ which would generalize the numbers $X_{a-1}(i)$ defined earlier and enumerate the spanning trees with fixed numbers of predecessors among the nearest neighbors of i_1 resp. i_2. Indeed, the possibility that neighbors of i_1 are predecessors of i_2, or vice versa, substantially complicates the matter. Details on how to perform the correct counting have been given in [31].

To reconcile the previous lattice results and the LCFT predictions, we pause for a while to examine the effects of a seemingly unrelated observable.

5.4 Isolated Dissipation

In the previous section, the calculation of height probabilities started on a finite grid Γ, where the only dissipative sites are boundary sites. We did not pay too much attention to exactly which boundary sites are dissipative; in fact, since the infinite volume limit sends the boundaries off to infinity, there is no need to know precisely which boundary conditions are used (this is what we meant when we said that Δ_Γ becomes the Laplacian on $\mathbb{Z}^2$). We show now that the situation changes if we make some of the bulk sites dissipative [36]. It is not difficult to understand why this is so in terms of spanning trees. We remember that dissipative sites are sites that are connected to the sink, the root of the trees, from which the branches of the tree are growing. Therefore, the existence of dissipative sites in the bulk makes it possible that branches grow from the middle of the grid, thereby affecting the macroscopic structure of the spanning trees.

To make a bulk site i_1 dissipative, one simply has to connect it to the sink. In the notations of **Section 2**, this amounts to increase the value $z_{i_1}{}^\star$, for instance, from $z_{i_1} = 4$ (on $\mathbb{Z}^2$) to 5 (a higher value would not make much difference). In turn, this changes by 1 the diagonal entry $(\Delta\Gamma)_{i_1,i_1}$ of the toppling matrix, that is, $\Delta_\Gamma \to \Delta_\Gamma + D_{i_1}$, with $(D_{i_1})_{i,j} = \delta_{i,i_1}\delta_{j,i_1}$. More generally, the new toppling matrix $\tilde{\Delta}_n \equiv \Delta_\Gamma + D_{i_1} + D_{i_2} + \ldots + D_{i_n}$ defines a new model in which several bulk sites i_k are dissipative. As a consequence, the height variables at these sites take values in the set {1, 2, 3, 4, 5}.

A simple and natural way to evaluate the effect of inserting isolated dissipation is to consider the change in the number of recurrent configurations, by computing the ratio $\det\tilde{\Delta}_n/\det\Delta_\Gamma$, first at finite volume and then in the infinite volume limit.

We start by inserting dissipation at the single site i, far from the boundaries. The ratio is easy to compute since the defect matrix D_i has rank 1,

$$\frac{\det\tilde{\Delta}_1}{\det\Delta_\Gamma} = \det\left(\mathbb{I} + \Delta_\Gamma^{-1}D_i\right) = 1 + \left(\Delta_\Gamma^{-1}\right)_{i,i}. \quad (37)$$

It is a finite number at finite volume but diverges in the infinite volume limit, no matter where the site i is located. The divergence reflects the fact that the extra value $h_i = 5$ allows enormously more recurrent configurations in the modified model.[16]

The *same* divergence is present in the ratio $\det\tilde{\Delta}_n/\det\Delta_\Gamma$, which suggests to change the normalization and compare the effect of inserting n dissipative sites with respect to the situation where there is only one dissipative site, that is, to consider instead the ratio $\det\tilde{\Delta}_n/\det\tilde{\Delta}_1$, which is perfectly well-defined. Let us also remark that in the infinite volume limit, the denominator does not depend on the location of the (only) dissipative site so that the ratios are fully symmetric in the insertion points i_k and translation invariant.

The first two ratios read, with $r = |i_1 - i_2|$ for $n = 2$,

$$\frac{\det\tilde{\Delta}_1}{\det\tilde{\Delta}_1} = 1, \qquad \frac{\det\tilde{\Delta}_2}{\det\tilde{\Delta}_1} = \frac{1}{\pi}\log r + 2\gamma_0 + \mathcal{O}\left(r^{-2}\right), \quad (38)$$

[16]We note that the inverse ratio $\det\Delta_\Gamma/\det\tilde{\Delta}_1$ is equal to $\mathrm{Prob}[\text{all } h_j \leqslant 4] = \mathrm{Prob}[h_i \leqslant 4] = 1 - \mathrm{Prob}[h_i = 5]$ where the probabilities are evaluated in the modified model. The divergence mentioned in the text therefore implies that $h_i = 5$ with probability 1.

where $\gamma_0 = \frac{1}{2\pi}(\gamma + \frac{3}{2}\log 2) + 1$. If we denote by $\omega(z,\overline{z})$ the field that describes, in the scaling limit, the insertion of dissipation at a bulk site, the previous two equations would imply

$$\langle \omega(z,\overline{z})\rangle = 1, \qquad \langle \omega(z_1,\overline{z}_1)\,\omega(z_2,\overline{z}_2)\rangle = \frac{1}{\pi}\log|z_1 - z_2| + 2\gamma_0. \tag{39}$$

Interestingly, they exactly match the last two equations of (18), with the logarithmic pair $\{\Phi, \Psi\}$ identified with $\{\mathbb{I}, \omega\}$, both fields having the weights $h = \overline{h} = 0$ (the identity field is primary). Moreover, the logarithmic term in the 2-point correlation fixes the coefficient λ of the logarithmic pair $(\mathbb{I}, \omega)$ equal to $\lambda = -\frac{1}{4\pi}$ so that $L_0\,\omega = \overline{L}_0\,\omega = -\frac{1}{4\pi}\mathbb{I}$. The relation $\langle \mathbb{I}\rangle = 0$, as noted for the free symplectic fermion theory, is here understood as being given by the inverse of the divergent quantity in **(37)**.

The lattice calculation of $\det\tilde{\Delta}_3/\det\tilde{\Delta}_1$, corresponding to the insertion of three dissipative sites, is not difficult and yields the following 3-point correlation, with $z_{ij} \equiv z_i - z_j$,

$$\langle \omega(1)\,\omega(2)\,\omega(3)\rangle = 3\gamma_0^2 + \frac{\gamma_0}{2\pi}\log|z_{12}z_{13}z_{23}|^2 + \frac{1}{16\pi^2}\left[\log|z_{12}|^2 \log\left|\frac{z_{13}z_{23}}{z_{12}}\right|^2 + \text{cyclic}\right]. \tag{40}$$

It is fully consistent with the general 3-point correlators of fields in a logarithmic pair [19]. Many additional checks have been carried out [36] which all confirm the consistency of the above field assignment. It has been shown [27] that the bulk dissipation field can be realized in terms of symplectic free fermions as

$$\omega(z,\overline{z}) = \frac{1}{2\pi}\theta\tilde{\theta} + \gamma_0, \tag{41}$$

in the sense that the correlators of this composite field, computed in the symplectic fermion theory, reproduce the above expressions.

5.5 Height Correlations Continued

The multisite height probabilities computed in **Section 5.3** were obtained by taking the limit over a sequence of grids of increasing size. Because of the dissipation along the boundaries, the probabilities are well-defined for each finite grid and properly converge. On the field theoretic side, the CFT supposedly describing the scaling limit is defined right away on the infinite continuum and does not know about the dissipation of the finite systems. To make the CFT connect with the lattice description, we have to insert by hand the required dissipation in the correlators. Since on the lattice side, the boundary dissipation is pushed off to infinity when we take the infinite volume limit, the previous section suggests that we insert the additional field $\omega(\infty)$ in the correlators. Thus, the proposal, first made in Ref [27], is that a lattice n-point height correlator is described in the scaling limit by an $(n+1)$-point field correlator as follows:

$$\sigma_{a_1,a_2,\ldots,a_n}(i_1,i_2,\ldots,i_n) \xrightarrow{\text{scalim}} \langle h_{a_1}(z_1)\,h_{a_2}(z_2)\ldots h_{a_n}(z_n)\,\omega(\infty)\rangle. \tag{42}$$

It turns out that the proposed field correlations exactly reproduce the form of the lattice results obtained in **Section 5.3**. If $\{\Phi, \Psi\}$ are fields of weights $h = \overline{h}$ forming a logarithmic pair such that $(L_0 - h)\Psi = (\overline{L}_0 - h)\Psi = \lambda\Phi$, one finds with $\Delta = 2h$ [27] the following equations:

$$\langle \Phi(z_1,\overline{z}_1)\,\Phi(z_2,\overline{z}_2)\,\omega(\infty)\rangle = \frac{A}{|z_{12}|^{2\Delta}}, \tag{43a}$$

$$\langle \Phi(z_1,\overline{z}_1)\,\Psi(z_2,\overline{z}_2)\,\omega(\infty)\rangle = \frac{B - \lambda A\log|z_{12}|^2}{|z_{12}|^{2\Delta}},$$

$$\langle \Psi(z_1,\overline{z}_1)\,\Psi(z_2,\overline{z}_2)\,\omega(\infty)\rangle = \frac{C - 2\lambda B\log|z_{12}|^2 + \lambda^2 A\log^2|z_{12}|^2}{|z_{12}|^{2\Delta}}. \tag{43b}$$

Comparing with equation (18), we see that the insertion of dissipation at infinity through $\omega(\infty)$ allows a nonzero value of A and solves the problem encountered in **Section 5.3**.

From the dominant terms in equations **(35)** and **(36)** for the lattice correlations $\sigma_{1,1}(i_1, i_2)$ and $\sigma_{2,1}(i_1, i_2)$, we infer that the (subtracted) bulk lattice height 1 and height 2 variables converge to fields $h_1(z)$ and $h_2(z)$ that form a logarithmic pair of weight $\Delta = 2$. Moreover, if we assign them the same normalization as their lattice companions $(A = -\frac{\mathbb{P}_1^2}{2})$, we find the parameter of the logarithmic pair (h_1, h_2) equal to $\lambda = -\frac{1}{2}$. The explicit results for $\sigma_{3,1}(i_1, i_2)$ and $\sigma_{4,1}(i_1, i_2)$ [35] show that the fields $h_3(z)$ and $h_4(z)$ are also logarithmic partners of $h_1(z)$, albeit of different normalizations and for different values of λ. As noted in **Section 4**, it means that they can be written as linear combinations[17] of $h_1(z)$ and $h_2(z)$ with known coefficients,

$$h_a(z) = \alpha_a h_2(z) + \beta_a h_1(z), \qquad \alpha_1 = 0,\ \alpha_2 = 1,\ \alpha_3 = \frac{8-\pi}{2(\pi-2)},\ \alpha_4 = -\frac{\pi+4}{2(\pi-2)}, \tag{44}$$

and other values for β_a [27]. These field assignments predict that the lattice correlation of heights larger or equal to 2 behaves asymptotically as follows:

$$\sigma_{a,b}(i_1,i_2) \simeq -\alpha_a\alpha_b\frac{\mathbb{P}_1^2}{2}\frac{\log^2 r}{r^4} + \mathcal{O}\left(\frac{\log r}{r^4}\right), \qquad a,b \geqslant 2. \tag{45}$$

Because α_4 is the only negative coefficient among α_a, the height variables are all anticorrelated, except the height 4 which has a positive correlation with the other three heights. Numerical simulations have successfully confirmed the behavior (45) [27]. A lattice proof however remains one of the greatest challenges in the sandpile models.

The lattice 2-point correlators discussed above correspond to 3-point functions in the CFT. They are therefore completely generic, depending only on the weights of the fields involved and a few

[17]The four height fields $h_a(z)$ also satisfy the trivial identity $h_1(z) + h_2(z) + h_3(z) + h_4(z) = 0$.

assumptions about their global conformal transformations. Higher correlators are not generic and depend on finer details of the nature of the fields and of the specific CFT at work, in particular its central charge. In this regard, the first hint for the value of the central charge was given in Ref [8] by looking at the finite-size corrections of the partition function (i.e., the number of recurrent configurations); the analysis yields the value $c = -2$.

The simplest higher correlators to consider on the lattice are the 3- and 4-point height 1 correlators. They have been computed in Ref [33] with the following results. Since the height 1 variable has weight $\Delta = 2$ in the scaling limit, one would expect the dominant contribution to the 3-point correlator to be homogeneous of degree −6 in the separation distances. Surprisingly, the first nonzero term has degree −8,

$$\sigma_{1,1,1}(i_1,i_2,i_3) = 0 + \dots \tag{46}$$

implying that its scaling limit, corresponding to the CFT 4-point function $\langle h_1(z_1)\, h_1(z_2)\, h_1(z_3)\, \omega(\infty)\rangle$, vanishes identically.

The lattice 4-point correlator has the expected dominant degree −8,

$$\begin{aligned}\sigma_{1,1,1,1}(i_1,i_2,i_3,i_4) = \frac{\mathbb{P}_1^4}{8}\Bigg\{&\frac{1}{|z_{12}\, z_{34}|^4} + \frac{1}{|z_{13}\, z_{24}|^4} + \frac{1}{|z_{14}\, z_{23}|^4}\\ &- \frac{1}{(z_{12}\, z_{34}\, \overline{z}_{13}\, \overline{z}_{24})^2} - \frac{1}{(z_{13}\, z_{24}\, \overline{z}_{14}\, \overline{z}_{23})^2}\\ &- \frac{1}{(z_{14}\, z_{23}\, \overline{z}_{12}\, \overline{z}_{34})^2} + \text{c.c.}\Bigg\} + \dots\end{aligned} \tag{47}$$

and is much more instructive: it is precisely the expression we obtain for the 5-point CFT correlation function $\langle h_1(z_1)\, h_1(z_2)\, h_1(z_3)\, h_1(z_4)\, \omega(\infty)\rangle$ if we assume that the height 1 field $h_1(z)$ is a primary field of dimensions $(h, \overline{h}) = (1, 1)$ in a CFT with central charge $c = -2$ and that it satisfies a certain degeneracy condition at level 2. This last condition furnishes a differential equation [16], from which the correlator can be fully determined, the result being exactly the function (47)! From this result, one can actually infer that the previous correlator $\langle h_1(z_1)\, h_1(z_2)\, h_1(z_3)\, \omega(\infty)\rangle$ must vanish if it is to be symmetrical in the three insertion points [31].

The lattice 3-point correlators $\sigma_{a,1,1}(i_1,i_2,i_3)$, $a \geqslant 2$, have been computed more recently in [31]. For simplicity, the three points were assumed to be aligned horizontally in the plane, with real separations x_{ij}. The following result was obtained to dominant order:

$$\sigma_{a,1,1}(i_1,i_2,i_3) = \alpha_a \frac{\mathbb{P}_1^3}{8}\frac{1}{x_{21}^3 x_{31}^3} + \dots, \qquad (a \geqslant 2), \tag{48}$$

where the coefficients α_a are those given in **(44)**. In addition to being very simple, this expression is surprisingly non-logarithmic. Because its scaling limit should be given by $\langle h_a(z_1)\, h_1(z_2)\, h_1(z_3)\, \omega(\infty)\rangle$, it is particularly important to understand it from the CFT point of view. Indeed, the computation of such a correlator requires additional information on the height fields $h_{a\geqslant 2}$ as logarithmic partners of h_1. Since h_3 and h_4 can be regarded as linear combinations of h_1 and h_2, it is sufficient to consider h_2.

Inspired by the conformal representations appearing in the bosonic sector of the symplectic theory [22], the following proposal has been made in Ref [27] regarding the conformal nature of $h_2(z,\overline{z})$. A more complete account will be presented in **Section 8**.

The field $h_2(z,\overline{z})$ is not primary since it transforms into $h_1(z,\overline{z})$ under dilations. It is also not quasi-primary because its L_1 and $\overline{L}_1$ transforms generate two new fields $\rho(z,\overline{z})$ and $\overline{\rho}(z,\overline{z})$, respectively, with weights (0,1) and (1,0). Moreover, the field $\rho(z,\overline{z})$ is left primary, and its $\overline{L}_1$ transform is equal to $\kappa\mathbb{I}$; likewise, $\overline{\rho}(z,\overline{z})$ is right primary, and its L_1 transform is also equal to $\kappa\mathbb{I}$. All this results in the following transformation law of $h_2(z,\overline{z})$ under a general conformal transformation $z \to w(z)$ and $\overline{z} \to \overline{w}(\overline{z})$ as follows:

$$\begin{aligned}h_2(z,\overline{z}) = \left|\frac{\mathrm{d}w}{\mathrm{d}z}\right|^2 &\left[h_2(w,\overline{w}) + \log\left|\frac{\mathrm{d}w}{\mathrm{d}z}\right|^2 h_1(w,\overline{w})\right]\\ &+\frac{1}{2}\left(\frac{\mathrm{d}^2 w}{\mathrm{d}z^2}\Big/\frac{\mathrm{d}w}{\mathrm{d}z}\right)\frac{\mathrm{d}\overline{w}}{\mathrm{d}\overline{z}}\,\rho(w,\overline{w})\\ &+\frac{1}{2}\frac{\mathrm{d}w}{\mathrm{d}z}\left(\frac{\mathrm{d}^2\overline{w}}{\mathrm{d}\overline{z}^2}\Big/\frac{\mathrm{d}\overline{w}}{\mathrm{d}\overline{z}}\right)\overline{\rho}(w,\overline{w})\\ &+\frac{\kappa}{4}\left(\frac{\mathrm{d}^2 w}{\mathrm{d}z^2}\Big/\frac{\mathrm{d}w}{\mathrm{d}z}\right)\left(\frac{\mathrm{d}^2\overline{w}}{\mathrm{d}\overline{z}^2}\Big/\frac{\mathrm{d}\overline{w}}{\mathrm{d}\overline{z}}\right), \quad \kappa = -\frac{\mathbb{P}_1}{4}.\end{aligned} \tag{49}$$

This conformal transformation law of h_2 is sufficient to compute correlators involving h_2, but substantially complicates the calculations. Using this transformation and the left and right level 2 degeneracies of $h_1(z,\overline{z})$, the required correlator can be nonetheless determined. The result reads [31]

$$\langle h_2(z_1)\, h_1(z_2)\, h_1(z_3)\, \omega(\infty)\rangle = \frac{\mathbb{P}_1^3}{16}\frac{1}{|z_{12}z_{13}|^2}\left[\frac{1}{z_{13}\overline{z}_{12}} + \frac{1}{z_{12}\overline{z}_{13}}\right]. \tag{50}$$

When the three points z_i are aligned horizontally, it exactly reproduces the lattice result (48) for $a = 2$. The cases $a = 3, 4$ follow by multiplying by the proper coefficient α_a since $\langle h_1(z_1)\, h_1(z_2)\, h_1(z_3)\, \omega(\infty)\rangle = 0$.

5.6 Minimal Height Cluster Correlations

The calculation of occurrence probabilities of minimal subconfigurations has been briefly discussed in **Section 5.2**. Their correlations can be computed very much like those of heights 1 by using a defect matrix. The calculation of mixed 2-point correlators for about a dozen different minimal subconfigurations has been reported in Ref [33]. It turns out that each such cluster S can be specified by a triplet (a, b_1, b_2) of real numbers.

We define as before subtracted variables

$$h_S(i) = \delta_{S(i)} - \mathbb{P}_S, \tag{51}$$

where $\delta_{S(i)}$ denotes the event "a minimal subconfiguration S is found around site i" and $\mathbb{P}_S(i) = \mathbb{E}[\delta_{S(i)}]$ is the probability of such an event. The mixed correlator of two such variables takes the form

$$\sigma_{S,S'}(i_1,i_2) = \mathbb{E}\big[h_S(i_1)\,h_{S'}(i_2)\big] = -\frac{1}{2r^4}\{aa' + (b_1b_1' - b_2b_2')\cos 4\varphi\} + \dots \qquad (52)$$

We see that the dominant contribution retains an angular dependence, which in this case is not surprising since the minimal clusters are generally not rotationally invariant. As a matter of illustration, the cluster reduced to a single height 1 is characterized by the triplet $(a, b_1, b_2) = (\mathbb{P}_1, 0, 0)$, while for the second one in equation (31), one has

$S =$  $: \; a = \frac{(4-\pi)(72-19\pi)(3\pi-8)^2}{18\pi^5},\; b_1 = 0,\; b_2 = -\frac{(4-\pi)(32-9\pi)(3\pi-8)^3}{18\pi^6}.$ (53)

In the scaling limit, the subtracted cluster variables give rise to the fields $h_S(z)$, whose mixed correlators are given by the terms displayed in equation **(52)**. Interestingly, it has been observed [33] that these fields have a realization in terms of the symplectic free fermions, which is discussed at the end of **Section 4**. Indeed, one may check that the explicit fields given by

$$h_S(z,\overline{z}) = -\Big\{a\Big(\partial\theta\,\overline{\partial}\,\tilde{\theta} + \overline{\partial}\,\theta\,\partial\tilde{\theta}\Big) + (b_1 + \mathrm{i}b_2)\,\partial\theta\,\partial\tilde{\theta} + (b_1 - \mathrm{i}b_2)\,\overline{\partial}\,\theta\,\overline{\partial}\,\tilde{\theta}\Big\}, \qquad (54)$$

reproduce the above 2-point correlators, as well as the higher order correlators computed in Ref [33], provided the dissipation field ω, proportional to $\theta\tilde{\theta}$, is inserted in the correlators, as explained earlier. In particular, the height 1 field $h_1(z,\overline{z})$ is recovered upon setting $a = \mathbb{P}_1$ and $b_1 = b_2 = 0$. Let us note a generic field $h_S(z,\overline{z})$ is a linear combination of three fields with different conformal weights, namely, (1,1), (2,0), and (0,2) and therefore different conformal transformations; the last two are responsible for inducing an angular dependence in the correlators. The field realization (54) has been proved in a much greater generality in Ref [37]: any lattice observable based on a conservative local bond modification[18] converges in the scaling limit to a field of the form **(54)**.

On general grounds, this should not be surprising. On the one hand, the multisite probabilities for minimal clusters can be computed by using defect matrices which implement the local bond modifications. On the other hand, defect matrices always yield contributions that are given by finite determinants of discrete Green matrix entries. In the limit of large separations, the determinants converge to polynomial expressions in the Green function and its derivatives. It is therefore not a complete surprise that the associated fields can be constructed out from the symplectic free fermions $\theta, \tilde{\theta}$. Indeed, because the 2-point correlators of $\theta, \tilde{\theta}$ are given by the Green function, the correlators of any fields that are local in $\theta, \tilde{\theta}$ and their derivatives are necessarily polynomials in the Green function and its derivatives (Wick's theorem). We expect this observation to extend to all the observables that correspond to local perturbations of the toppling matrix. Isolated dissipation and minimal cluster variables are among them; the arrow variables discussed in the next section are in this class too. These general remarks apply to the massive extension of the sandpile model (see **Section 7.1**).

What about the height 2, 3, and 4 variables? Can they also be accommodated in the free symplectic fermion theory? As explained earlier, these three variables cannot be handled with finite rank perturbations of the toppling matrix because they involve nonlocal constraints on the nearest neighbors (some of them should not be predecessors). Using the technique developed in Ref [29], the 1-site probabilities $\mathbb{P}_{a\geqslant 2}$ can be efficiently computed. Surprisingly, the details show that the explicit values are given in terms of a few entries of the lattice Green matrix (at short distances), which explains why the values of $\mathbb{P}_{a\geqslant 2}$ quoted in (**30**) are not much more complicated than for $\mathbb{P}_1$. This is no longer the case for large-distance correlations $\sigma_{a\geqslant 2,1}(i_1,i_2)$. The analysis of Ref [31] shows that those correlators are expressed in terms of sums of the product of Green matrix entries over a path connecting i_1 to i_2 and thus in terms of quantities that are not local in the Green matrix. It supports the view that the height fields $h_{a\geqslant 2}$ do not belong to the free symplectic fermion theory. A detailed analysis of this question has been carried out in Ref [27] and has reached the same conclusion. **Section 8** below summarizes this somewhat strange situation.

5.7 Spanning Tree–Related Variables

A recurrent configuration of the sandpile model can be specified as a set of height values or as a spanning tree; the former has the local heights as natural variables, the latter has local connectivities as natural variables, namely, the existence or absence of specific bonds in the spanning tree.

We recall that a spanning tree is a connected subgraph with no loop which contains all vertices, including the sink. The latter is chosen to be the root of the tree, implying that there is a unique path connecting any vertex to the root and therefore any vertex to any other vertex. A rooted spanning tree can then naturally be oriented by deciding that the edges of the tree all point toward the root. As a consequence, in any rooted spanning tree, there is exactly one outgoing edge at each vertex but the root; there may however be more (or less) ingoing edges (a vertex with no ingoing edge is a leaf). A site j is then a predecessor of i if the unique path from j to i is consistently oriented (equivalently if the unique path form j to i does not pass through the root). As we have seen, the question of being predecessor is a nonlocal problem, even if i and j are close to each other, even nearest neighbors [38].

Connectivities between neighboring sites can be handled in much the same way as height 1 or minimal height cluster variables. To see this, we must first understand why the determinant of the toppling matrix on a graph counts the number of spanning trees on that graph. In the perspective of this section, we generalize the matrix by assigning arbitrary weights to the oriented

[18]The qualifier "conservative" means that the defect matrix that implements the bond modifications has zero row and column sums. The defect matrix used in **Section 5.1** to compute the height 1 probability does not have this property. It can however be replaced by another one that does have it [33]. An example of a nonconservative bond modification is given in **Section 5.7**.

edges of the graph $\Gamma^\star = (V^\star, E^\star)$. We define x_{ij} as the weight carried by the edge from the vertex i to the vertex j ($x_{ij} = 0$ means that there is no edge from i to j), and we set, for $i, j \in V$,

$$\Delta_{i,j} = \begin{cases} y_i = x_{i^\star} + \sum_{j \neq i} x_{ij} & \text{for } i = j, \\ -x_{ij} & \text{for } i \neq j, \end{cases} \tag{55}$$

In the context of the sandpile model, the difference $x_{i^\star} = y_i - \sum_{j \neq i} x_{ij}$ can be viewed as the weight of the oriented edge from i to the sink $\star$ so that the conservative vertices have this difference equal to 0 (no connection to the root).

If $N = |V|$ is the number of vertices in the graph, let us write the determinant of Δ as a sum over the permutations σ of the symmetric group S_N, which we partition according to the number k of proper cycles they contain, that is, the cycles of length strictly larger than 1 as follows:

$$\begin{aligned} \det \Delta &= \sum_{\sigma \in S_N} \varepsilon_\sigma \, \Delta_{1,\sigma(1)} \Delta_{2,\sigma(2)} \dots \Delta_{N,\sigma(N)} \\ &= \sum_{k=0}^{[N/2]} (-1)^k \sum_{\substack{\sigma \text{ has } k \\ \text{proper cycles}}} \Delta^+_{1,\sigma(1)} \dots \Delta^+_{N,\sigma(N)} \end{aligned} \tag{56}$$

where the matrix Δ^+ is Δ without the minus signs in the non-diagonal part. The second equality follows by combining the signs in the non-diagonal entries of Δ with the parity of σ: every cycle of length $\ell \geqslant 2$ in a permutation σ brings a sign $(-1)^{\ell-1}$ coming from the parity ε_σ and another sign $(-1)^\ell$ from the product of non-diagonal entries of Δ, resulting in an overall sign -1 per proper cycle. A cycle of length $\ell = 1$, corresponding to a vertex left invariant by σ, brings no sign.

The term $k = 0$ is simply equal to $\prod_i y_i$ as the only permutation with no proper cycle is the identity. In combinatorial terms, the product $\prod_i y_i$ is the weighted sum over all configurations of N arrows, where each vertex has exactly one arrow pointing to one of the other vertices or to the root, each configuration being weighted by the product of the weights carried by the arrows. The generic term $k \neq 0$, apart for the sign $(-1)^k$, is a weighted sum of arrow configurations which contain at least k oriented loops. Indeed, the k cycles contained in a fixed σ give rise to k loops, and the arrows attached to the vertices left invariant by σ are unconstrained and possibly form more loops.

By using the inclusion–exclusion principle, one can see that the above alternating sum has the effect to subtract from the term $k = 0$ the weights of all the arrow configurations which contain at least one loop [26, 39]. Thus, $\det \Delta$ is the sum over the oriented spanning trees on $\Gamma^\star$, each tree being weighted by the product of the weights of the oriented edges present in the tree (Kirchhoff's theorem). These oriented trees are also rooted spanning trees because one vertex at least must have its arrow oriented to the sink (a configuration of N arrows on N vertices necessarily contains a loop). When all weights x_{ij} are equal to 0 or 1, $\det \Delta$ is simply the number of spanning trees.

Let us come back to the question of local connectivities on a rectangular grid in $\mathbb{Z}^2$ and compute the probability that the outgoing arrow from the site i is oriented to its right neighbor. This amounts to compute the fraction of spanning trees with such an arrow given as follows:

$$\mathbb{P}_{\rightarrow}(i) = \mathbb{P}\big(\text{right arrow at } i\big) = \frac{\{\#\text{ trees with right arrow at } i\}}{\det \Delta}, \tag{57}$$

where Δ is the discrete Laplacian. We take i to be a conservative, non-boundary site.

According to the general discussion above, in order to force an arrow from i to its right neighbor E, one could simply set to 0 the weights between i and its three neighbors S, W, and N. It is however computationally more efficient to set the weight from i to its right neighbor to x and take the limit $x \to +\infty$ so as to give the edges to the other three neighbors a relative weight equal to 0. This implies that we define a new matrix $\tilde{\Delta}$ which coincides with Δ, except on two entries, namely, $\tilde{\Delta}_{i,i+\widehat{e_1}} = -x$ and $\tilde{\Delta}_{i,i} = x + 3$. As before, we write $\tilde{\Delta} = \Delta + B_{\rightarrow}(i)$ for the defect matrix $B_{\rightarrow}(i)$ which is zero everywhere, except on the two sites $i, i + \hat{e}_1$, where it reduces to $\left(\begin{smallmatrix} x-1 & 1-x \\ 0 & 0 \end{smallmatrix}\right)$. Since x is in any case large, we can simply set that part of $B_{\rightarrow}(i)$ to $\left(\begin{smallmatrix} x & -x \\ 0 & 0 \end{smallmatrix}\right)$. From Kirchhoff's theorem, we obtain

$$\mathbb{P}_{\rightarrow}(i) = \lim_{x \to +\infty} \frac{1}{x} \det\big[\mathbb{I} + \Delta^{-1} B_{\rightarrow}(i)\big], \tag{58}$$

which reduces to a 2-by-2 determinant. In the infinite volume limit, one finds $\mathbb{P}_{\rightarrow}(i) = \frac{1}{4}$, as expected. If we want to have the arrow at i oriented to its neighbor j, other than E, we use similar defect matrices $B_{\uparrow}, B_{\downarrow}, B_{\leftarrow}$, which look the same as $B_{\rightarrow}$ but with the nonzero 2-by-2 block $\left(\begin{smallmatrix} x & -x \\ 0 & 0 \end{smallmatrix}\right)$ placed on the sites i and j. The four orientations of the arrow at i yield the same result $\frac{1}{4}$.

Multipoint arrow probabilities can be computed in the now usual way, placing appropriate defect matrices at the different sites. For instance, the probability to find a right arrow at two sites i_1 and i_2 is given as follows:

$$\sigma_{\rightarrow,\rightarrow}(i_1, i_2) = \lim_{x \to +\infty} \frac{1}{x^2} \det\big[\mathbb{I} + \Delta^{-1}\{B_{\rightarrow}(i_1) + B_{\rightarrow}(i_2)\}\big]. \tag{59}$$

In the infinite volume limit and for a large distance, the following two-point probabilities are found at dominant order:

$$\sigma_{\rightarrow,\rightarrow}(i_1, i_2) - \frac{1}{16} = \frac{1}{16\pi^2} \frac{(z + \overline{z})^2}{|z|^4} + \dots \tag{60a}$$

$$\sigma_{\uparrow,\uparrow}(i_1, i_2) - \frac{1}{16} = -\frac{1}{16\pi^2} \frac{(z - \overline{z})^2}{|z|^4} + \dots \tag{60b}$$

$$\sigma_{\rightarrow,\uparrow}(i_1, i_2) - \frac{1}{16} = -\frac{\mathrm{i}}{16\pi^2} \frac{z^2 - \overline{z}^2}{|z|^4} + \dots \tag{60c}$$

Looking for symplectic fermion realizations of fields $\rho_{\rightarrow}$ and $\rho_{\uparrow}$ which reproduce these two-point correlators, one quickly sees that these have to include two parts with respective weights (1,0) and (0,1), leading in a natural way to the following forms:

$$\rho_{\rightarrow}(z, \overline{z}) = \frac{1}{2\pi}\big(\theta \partial\tilde{\theta} + \theta \overline{\partial}\tilde{\theta}\big), \qquad \rho_{\uparrow}(z, \overline{z}) = \frac{\mathrm{i}}{2\pi}\big(\theta \partial\tilde{\theta} - \theta \overline{\partial}\tilde{\theta}\big), \tag{61}$$

in agreement with the fact that $\rho_{\uparrow}(z,\overline{z})$ is formally the rotated form of $\rho_{\rightarrow}(z,\overline{z})$ (under $z \to -\mathrm{i}z$). The first two correlators are indeed related by rotation. This observation also suggests that the other two orientations are described by fields which are the opposite of the previous two, $\rho_{\leftarrow}(z,\overline{z}) = -\rho_{\rightarrow}(z,\overline{z})$ and $\rho_{\downarrow}(z,\overline{z}) = -\rho_{\uparrow}(z,\overline{z})$. Explicit calculations confirm it.

In a similar way, probabilities that edges belong to a random spanning tree, irrespective of their orientation, can be computed. The probability that a single, fixed edge belonging to a tree is the sum of the probabilities to find it in either of the two possible orientations, and is thus equal to $\frac{1}{2}$.

Likewise, the probability to find m edges in a tree is the sum of the probabilities to find them in all possible orientations and so is the sum of 2^m probabilities of m oriented edges. That sum can however be obtained in one go by replacing the block $\left(\begin{smallmatrix} x & -x \\ 0 & 0 \end{smallmatrix}\right)$ used for the oriented edges by $\left(\begin{smallmatrix} x & -x \\ -x & x \end{smallmatrix}\right)$ and dividing as above the determinant by x^m. Because two arrows with opposite orientations cannot occupy the same edge (as they would form a loop), the summation over the 2^m terms is correctly realized.

Correlations of unoriented edges should decay faster than those of oriented edges because the sum of the two orientations is zero, in view of the relations $\rho_{\leftarrow} = -\rho_{\rightarrow}$ and $\rho_{\downarrow} = -\rho_{\uparrow}$, at least at the order that was dominant for the oriented edges (r^{-2}). Indeed, explicit calculations yield a r^{-4} decay:

$$\sigma_{\leftrightarrow,\leftrightarrow}(i_1,i_2) - \frac{1}{4} = \sigma_{\updownarrow,\updownarrow}(i_1,i_2) - \frac{1}{4} = -\frac{1}{16\pi^2}\frac{\left(z^2+\overline{z}^2\right)^2}{|z|^8} + \dots \tag{62a}$$

$$\sigma_{\leftrightarrow,\updownarrow}(i_1,i_2) - \frac{1}{4} = \frac{1}{16\pi^2}\frac{\left(z^2-\overline{z}^2\right)^2}{|z|^8} + \dots \tag{62b}$$

From these correlators, the associated fields $\phi_{\leftrightarrow}$ and $\phi_{\updownarrow}$ must have components with conformal weights (2,0), (1,1), and (0,2). One finds the same form as the fields associated to the minimal clusters, in agreement with a previous remark since the defect matrix $\left(\begin{smallmatrix} x & -x \\ -x & x \end{smallmatrix}\right)$ is conservative. More precisely, the following fermionic expressions reproduce the above correlations:

$$\begin{aligned}\phi_{\leftrightarrow}(z,\overline{z}) &= \frac{1}{2\pi}\left(\partial\theta\,\overline{\partial}\tilde{\theta} + \overline{\partial}\theta\,\partial\tilde{\theta} + \partial\theta\,\partial\tilde{\theta} + \overline{\partial}\theta\,\overline{\partial}\tilde{\theta}\right)\\ &= \left(\partial+\overline{\partial}\right)\rho_{\rightarrow} - \frac{1}{2\pi}\left(\theta\partial^2\tilde{\theta} + \theta\overline{\partial}^2\tilde{\theta}\right),\end{aligned} \tag{63a}$$

$$\begin{aligned}\phi_{\updownarrow}(z,\overline{z}) &= \frac{1}{2\pi}\left(\partial\theta\,\overline{\partial}\tilde{\theta} + \overline{\partial}\theta\,\partial\tilde{\theta} - \partial\theta\,\partial\tilde{\theta} - \overline{\partial}\theta\,\overline{\partial}\tilde{\theta}\right)\\ &= \mathrm{i}\left(\partial-\overline{\partial}\right)\rho_{\uparrow} - \frac{1}{2\pi}\left(\theta\partial^2\tilde{\theta} + \theta\overline{\partial}^2\tilde{\theta}\right).\end{aligned} \tag{63b}$$

In fact, given that an unoriented edge is a sum of two oriented edges with opposite orientation, or, from what we said above, a difference of two oriented edges with the same orientation, one would expect that the fields describing a horizontal resp. vertical unoriented edge are proportional to the horizontal resp. vertical derivative of the fields describing the oriented edges, namely, $\phi_{\leftrightarrow} \sim (\partial+\overline{\partial})\rho_{\rightarrow}$ and $\phi_{\updownarrow} \sim \mathrm{i}(\partial-\overline{\partial})\rho_{\uparrow}$. It turns out not to be quite the case.

6 BOUNDARIES, BOUNDARY CONDITIONS, AND BOUNDARY VARIABLES

Formulating the sandpile model on a surface with boundaries is important to see how they affect the statistics of the model. The multisite correlations discussed in the previous section are likely to be modified by the presence of a boundary, and by the associated boundary conditions. Moreover, the microscopic variables on a boundary or very close to it will surely have a different behavior from their bulk versions. In the field theoretic description, the boundary fields have to be properly identified, and the way changes of boundary conditions are implemented must be clarified. All this adds to the known set of bulk fields a number of boundary-related fields and offers the opportunity to further test the consistency of their identification by computing mixed correlations combining both types of variables.

Surfaces with boundaries arise in the thermodynamic limit when some of the boundaries of the finite system are not sent off to infinity, unlike the situation considered in the previous section. The simplest case is when only one boundary of the rectangular grid is kept at finite distance, leading to a domain converging to the upper-half plane $\mathbb{H} = \{(x,y) \in \mathbb{R}^2 \colon y \geqslant 0\}$. There is only one boundary to care about, and the invariance under horizontal translations is preserved.

From our earlier discussion of conservative vs. dissipative sites, we have already defined two possible boundary conditions: open and closed. Let us recall that the boundary condition is open resp. closed if the boundary sites are dissipative resp. conservative. As before, a boundary open site has $z_i^\star = 4$, while a boundary closed site has $z_i^\star = z_i = 3$. In the scaling limit, it endows $\mathbb{H}$ with a homogeneous boundary condition, open or closed. We also can (and will) consider inhomogeneous boundary conditions, by alternating open and closed stretches on a single boundary.

In terms of height variables, the open boundary condition is equivalent[19] to fix all the boundary heights to 4, whereas the closed condition amounts to constrain the boundary heights not to take the value 4. The fixed boundary condition with boundary heights equal to 1 is not possible (two neighboring 1's form a forbidden subconfiguration); the fixed boundary conditions with boundary heights equal to 2 and/or 3 should be possible but seem to be difficult to handle in practice.

Two more boundary conditions, defined in the spanning tree description and previously called windy boundary conditions will be discussed at the end of this section (as we will see, they are not so far from the possibility just mentioned, namely, that of having height variables being equal to 2 or 3). No other boundary condition has been considered so far, though it would be very surprising that no other exist.[20]

[19]Indeed, the burning algorithm implies that the boundary sites, all with a height equal to 4, will burn at the first step of the burning process. The sites on the next layer all have $z_i^\star = 4$, corresponding to the open condition.

[20]Of course, we talk here of no other universality class of boundary conditions. Many boundary conditions may differ in the way they are microscopically defined on the lattice and nevertheless renormalize to the same continuum boundary condition in the scaling limit.

6.1 Bulk Variables With Homogeneous Open or Closed Boundary

In this section, we would like to reconsider the multisite height probabilities but on a domain with a boundary, the upper-half plane (UHP) being the simplest case. The principle underlying the calculations on the UHP stays the same as on the full plane. The most essential difference is that the toppling matrix becomes in the thermodynamic limit the Laplacian matrix on the discrete UHP with the appropriate boundary condition, open or closed. In this section, we consider homogeneous boundary conditions only.

To be specific, we choose the boundary row of sites to be located on the horizontal line $y = 1$ so that the discrete UHP we consider is $\{(x,y) \in \mathbb{Z}^2 \,|\, y \geqslant 1\}$. For either boundary condition, the Laplacian matrix Δ^{op} or Δ^{cl} is minus the adjacency matrix of the discrete UHP plus a diagonal matrix, everywhere equal to 4 for the open condition, equal to 4 and 3, respectively, for the bulk and boundary sites for the closed condition. By the method of images, the Green matrices $G^{\mathrm{op/cl}} = (\Delta^{\mathrm{op/cl}})^{-1}$ can be easily computed in terms of that on the full plane as follows:

$$G^{\mathrm{op}}_{(x_1,y_1),(x_2,y_2)} = G_{(x_1,y_1),(x_2,y_2)} - G_{(x_1,y_1),(x_2,-y_2)}, \tag{64a}$$

$$G^{\mathrm{cl}}_{(x_1,y_1),(x_2,y_2)} = G_{(x_1,y_1),(x_2,y_2)} + G_{(x_1,y_1),(x_2,1-y_2)}, \tag{64b}$$

for y_1 and $y_2 > 0$. As anticipated, we verify that G^{op} satisfies the Dirichlet condition, namely, it is odd under the reflection through the line $y = 0$ and therefore vanishes on it, and that G^{cl} satisfies the Neumann condition, namely, it is even under the reflection through the line $y = \frac{1}{2}$, inducing a vanishing normal derivative in the scaling limit. The calculations of the previous section can then be generalized to the UHP geometry by using these Green matrices. For height 1 and for the cluster variables, one merely has to use the appropriate Green matrix. For higher heights, the presence of a boundary makes the calculations more complicated because the combinatorics involved is heavier.

The simplest case is the 1-site height probability $\mathbb{P}_1^{\mathrm{op/cl}}(y)$ to find a height equal to 1 at a distance y from the boundary. It can be computed by using **eq. (27)**, where Δ_Γ^{-1} is replaced, in the infinite volume limit, by one of the two Green matrices given above. This was historically the first calculations of boundary effects in sandpile models [40], with the result

$$\begin{aligned} \sigma_1^{\mathrm{op}}(y) &= \mathbb{P}_1^{\mathrm{op}}(y) - \mathbb{P}_1 = \frac{\mathbb{P}_1}{4y^2} + \ldots, \\ \sigma_1^{\mathrm{cl}}(y) &= \mathbb{P}_1^{\mathrm{cl}}(y) - \mathbb{P}_1 = -\frac{\mathbb{P}_1}{4y^2} + \ldots \end{aligned} \tag{65}$$

The analogous results for higher heights were obtained somewhat later [27, 41] and were the first to firmly establish their logarithmic nature. They take the following form, valid for $a \geqslant 1$,

$$\begin{aligned} \sigma_a^{\mathrm{op}}(y) &= \frac{1}{y^2}\left(c_a + \frac{d_a}{2} + d_a \log y\right) + \ldots, \\ \sigma_a^{\mathrm{cl}}(y) &= -\frac{1}{y^2}\left(c_a + d_a \log y\right) + \ldots \end{aligned} \tag{66}$$

up to terms of order $\mathcal{O}(y^{-4}\log y)$, which have since been explicitly computed [31], as they enter the calculations of $\sigma_{a,1}^{\mathrm{op/cl}}$ given below. The coefficients are explicitly known and are shown in **Table 1**. One may check that the relations (44) expressing h_3 and h_4 linearly in terms of h_1 and h_2 are confirmed. The distinctive change of sign between the two boundary conditions and the fact that for fixed a, both are controlled by the same constants c_a and d_a and the equality $d_2 = c_1$ are striking. As will be explained below and in one of the next sections, all three features will follow from the CFT picture.

Let us mention that these lattice calculations have been carried out on another lattice realization of the UHP, namely, on the diagonal upper-half plane $\{(x,y) \in \mathbb{Z}^2 \,|\, y > x\}$, for which the method of images allows to explicitly compute the Green matrices for the two boundary conditions. As expected, the dominant terms are exactly the same as above in terms of the Euclidean distance between height 1 and the diagonal boundary, while the subdominant terms are different [31].

The 2-site height correlators in the bulk of the UHP, at sites $i_1 = (x_1, y_1)$ and $i_2 = (x_2, y_2)$, and which involve the same subtractions as before,

$$\begin{aligned} \sigma_{a,1}^{\mathrm{op/cl}}(x; y_1, y_2) = \mathbb{P}_{a,1}^{\mathrm{op/cl}}(i_1, i_2) - \mathbb{P}_a^{\mathrm{op/cl}}(i_1)\,\mathbb{P}_1 \\ - \mathbb{P}_a\,\mathbb{P}_1^{\mathrm{op/cl}}(i_2) + \mathbb{P}_a\,\mathbb{P}_1, \end{aligned} \tag{67}$$

have been computed in [31] when the two sites are far from the boundary and far from each other, again using the technique developed in [29]. They depend on three real variables, the horizontal distance $x = x_1 - x_2$ between the two sites and their vertical positions y_1 and y_2. For simplicity however, the lattice calculations have been carried out for two vertically aligned sites, that is, for $x = 0$.

Defining the two bivariate functions,

$$\begin{aligned} P(u,v) &= \frac{1}{8u^2v^2} - \frac{1}{(u-v)^4} - \frac{1}{(u+v)^4}, \\ Q(u,v) &= \frac{1}{(u-v)^4} - \frac{1}{(u+v)^4}, \end{aligned} \tag{68}$$

the results for $a = 1, 2$ take the following form, at dominant order:

$$\sigma_{1,1}^{\mathrm{op}}(0; y_1, y_2) = \sigma_{1,1}^{\mathrm{cl}}(0; y_1, y_2) = \frac{\mathbb{P}_1^2}{2} P(y_1, y_2) + \ldots, \tag{69a}$$

$$\begin{aligned} \sigma_{2,1}^{\mathrm{op/cl}}(0; y_1, y_2) = \frac{\mathbb{P}_1^2}{2}\Bigg[P(y_1, y_2)\left(\log y_1 + \gamma + \frac{5}{2}\log 2\right) \\ + Q(y_1, y_2)\log\left|\frac{y_2 + y_1}{y_2 - y_1}\right|\Bigg] + \frac{H^{\mathrm{op/cl}}(y_1^2, y_2^2)}{y_1^2 y_2^2 \left(y_1^2 - y_2^2\right)^4} + \ldots, \end{aligned} \tag{69b}$$

where $H^{\mathrm{op}}(u,v)$ and $H^{\mathrm{cl}}(u,v)$ are homogeneous polynomials of degree 4 in u, v, with explicitly known coefficients. The results for

TABLE 1 | Numerical coefficients for one-site height probabilities on the UHP, with $\tilde{\gamma} = \gamma + \frac{5}{2}\log 2$. They satisfy the relation $\sum_a c_a = \sum_a d_a = 0$.

	$a = 1$	$a = 2$	$a = 3$	$a = 4$
c_a	$\frac{\mathbb{P}_1}{4} = \frac{\pi-2}{2\pi^3}$	$\frac{\pi-2}{2\pi^3}\tilde{\gamma} + \frac{34-11\pi}{8\pi^3}$	$\frac{8-\pi}{4\pi^3}\tilde{\gamma} + \frac{-88+5\pi+2\pi^2}{16\pi^3}$	$-\frac{\pi+4}{4\pi^3}\tilde{\gamma} + \frac{36+9\pi-2\pi^2}{16\pi^3}$
d_a	0	$\frac{\mathbb{P}_1}{4} = \frac{\pi-2}{2\pi^3}$	$\frac{8-\pi}{4\pi^3}$	$-\frac{\pi+4}{4\pi^3}$

$a = 3, 4$ take the same form with different coefficients and confirm once more the linear relations (44).

Let us discuss these results in the CFT picture, using what we already know about the height fields $h_a(z,\overline{z})$. For a homogeneous boundary condition like here, boundary CFT prescribes to compute bulk correlators on the UHP by viewing a field $\phi(z,\overline{z})$ with conformal weights $(h,\overline{h})$ as the product $\phi_h(z)\phi_{\overline{h}}(\overline{z})$ of two chiral fields of weights h and $\overline{h}$, respectively, located at the points z and $\overline{z}$ (the latter being in the lower-half plane) [42]. A correlation function of n bulk (non-chiral) fields on the UHP can then be computed as a correlation of $2n$ chiral fields on the full plane; the correlation appropriate for the boundary condition under consideration is accordingly selected in the solution space of these 2n-correlators.

The above prescription must however be adapted in the case of logarithmic fields because the chiral factorization is not consistent with the non-diagonal action of L_0. Indeed, let us consider a logarithmic pair $(\Phi(z,\overline{z}), \Psi(z,\overline{z}))$. If we factorize the logarithmic partner as $\Psi(z,\overline{z}) = \psi_h(z)\psi_{\overline{h}}(\overline{z})$, we find from the action of L_0,

$$L_0\Psi = \big(L_0\psi_h\big)\psi_{\overline{h}} = \big(h\psi_h + \lambda\,\phi_h\big)\psi_{\overline{h}} = h\Psi + \lambda\,\phi_h\psi_{\overline{h}}, \tag{70}$$

That the chiral factorization of the primary partner is $\Phi = \phi_h\psi_{\overline{h}}$. The same argument with $\overline{L}_0$ shows that an equally good factorization is $\Phi = \psi_h\phi_{\overline{h}}$.

Let us first see how this works for $\sigma_a^{\mathrm{op}}(y)$. Their dominant terms, made explicit in relations **(65)** and **(66)**, should correspond to $\langle h_a(z,\overline{z})\rangle_{\mathrm{op}}$. Note that unlike the correlations on the plane discussed in **Section 5**, we do not insert dissipation at infinity since the whole boundary is open and therefore dissipative. From the prescription recalled above, these 1-point functions should have the general form of chiral 2-point functions. If ψ and ϕ denote chiral versions of the height 2 and height 1 fields, respectively, with $h = \overline{h} = 1$, the chiral factorizations of the height fields h_1 and h_2 read $h_1(z,\overline{z}) = \psi(z)\phi(\overline{z})$ and $h_2(z,\overline{z}) = \psi(z)\psi(\overline{z})$. The CFT formalism gives the general forms (19) as follows:

$$\begin{aligned}\langle h_1(z,\overline{z})\rangle_{\mathrm{op}} &= \big\langle\phi(z)\psi(\overline{z})\big\rangle = \frac{B}{(z-\overline{z})^2},\\ \langle h_2(z,\overline{z})\rangle_{\mathrm{op}} &= \big\langle\psi(z)\psi(\overline{z})\big\rangle = \frac{C - 2\lambda B\log(z-\overline{z})}{(z-\overline{z})^2}.\end{aligned} \tag{71}$$

With the value $\lambda = -\frac{1}{2}$ noted in **Section 5**, these forms exactly reproduce the lattice results (66), including the relation $d_2 = c_1 = B$.

For $\sigma_a^{\mathrm{cl}}(y)$ and since the closed boundary is not dissipative, we insert by hand dissipation at infinity so that $\sigma_a^{\mathrm{op}}(y)$ should be given by $\langle h_a(z,\overline{z})\omega(\infty)\rangle_{\mathrm{cl}}$. Using the same chiral factorization as above leads to a 3-point function. The selection of a physically sensible solution leads to the same general form as for the open boundary condition [27].

The conformal calculations required to account for $\sigma_{a,1}^{\mathrm{op}}$ are only technically more involved. The needed chiral correlators are $\langle\phi(z_1)\psi(\overline{z}_1)\phi(z_2)\psi(\overline{z}_2)\rangle$ for $a = 1$ and $\langle\psi(z_1)\psi(\overline{z}_1)\phi(z_2)\psi(\overline{z}_2)\rangle$ for $a = 2$. Both can be computed from the primary nature of the chiral field ϕ, as established in **Section 5**, by solving a second-order differential equation and selecting the appropriate solution. As the details are given in [31], we merely give the results, valid for any relative positions of the two heights, $z_1 = (x_1, y_1)$ and $z_2 = (x_2, y_2)$

$$\begin{aligned}\langle h_1(z_1,\overline{z}_1)h_1(z_2,\overline{z}_2)\rangle_{\mathrm{op}} = \frac{\mathbb{P}_1^2}{2}\Bigg\{&\frac{2}{(z_1-\overline{z}_1)^2(z_2-\overline{z}_2)^2}\\ &-\frac{1}{|z_1-z_2|^4}-\frac{1}{|z_1-\overline{z}_2|^4}\Bigg\},\end{aligned} \tag{72}$$

and

$$\begin{aligned}&\langle h_2(z_1,\overline{z}_1)h_1(z_2,\overline{z}_2)\rangle_{\mathrm{op}}\\ &\quad= \frac{\mathbb{P}_1}{32y_1^2y_2^2}\,\frac{t^4-2t^3+4t-2}{(1-t)^2}\\ &\qquad\times\left[\frac{3(3\pi-10)}{2\pi^3} - \mathbb{P}_1\Big(\log y_1+\gamma+\frac{5}{2}\log 2\Big)\right]\\ &\qquad+\frac{\mathbb{P}_1^2}{64y_1^2y_2^2}\left[\frac{t^3(t-2)}{(1-t)^2}\left(\log(1-t)+\frac{y_1}{2y_2}\right)-\frac{t^2}{1-t}\right],\\ &\qquad t = -\frac{4y_1y_2}{|z_1-z_2|^2}.\end{aligned} \tag{73}$$

One can check that setting $x_1 = x_2$ exactly reproduces the lattice results $\sigma_{1,1}^{\mathrm{op}}(0;y_1,y_2)$ and $\sigma_{2,1}^{\mathrm{op}}(0;y_1,y_2)$ reported above.

The analogous calculation for the closed boundary has been carried out in the case $a = 1$, yielding the same expression as for the open boundary. No calculation however has been successful for $a = 2$ as it involves a nontrivial 5-point chiral correlator (in this case, the dissipation field ω must be added).

Similar calculations with isolated bulk dissipation, instead of height variables, have been considered in [36]; it was found in all cases that the CFT predictions compare successfully with the lattice results.

6.2 Changing the Boundary Condition

We have considered so far two different boundary conditions, the open and closed conditions. This allows addressing a fundamentally new issue, namely, how to think of a change of boundary condition, both on the lattice and in the emerging field theory. Like in the previous section, we consider the UHP.

We have seen that the calculation of correlations on the UHP, of height or dissipation variables, involves the use of the appropriate Laplacian (toppling) matrix and its inverse. On the lattice, the way we can change the boundary condition at a boundary site i is thus fairly clear: since an open boundary site has $\Delta_{i,i} = z_i^\star = 4$ and a closed one has $\Delta_{i,i} = z_i^\star = 3$, we simply lower by 1 the diagonal entry $\Delta_{i,i}$ to close an open site, and we increase it by 1 to open a closed site (as we did in **Section 5.4** to introduce dissipation at bulk sites). We do it either way for n consecutive boundary sites to change the boundary condition on an interval I of length n, that is, we do the following change on the toppling matrix $\Delta \to \Delta \pm D_I$, where D_I implements the diagonal shifts described above.

Let us examine the effect of closing n consecutive sites in an otherwise open boundary. We decide to measure this effect as in **Section 5.4**, namely, by comparing the number of recurrent configurations before and after the closing of n sites. So, we want to compute the ratio $Z_{\rm op}(n)/Z_{\rm op}$. At finite volume, the two partition functions can be computed as determinants of the corresponding toppling matrices on rectangular grids, with say four open boundaries in the case of $Z_{\rm op}$, and with n closed sites inserted on the lower boundary for $Z_{\rm op}(n)$. As usual, we can readily write the infinite volume limit of the ratio as follows:

$$\frac{Z_{\rm op}(n)}{Z_{\rm op}} = \frac{\det \Delta^{\rm op}(n)}{\det \Delta^{\rm op}} = \frac{\det\left[\Delta^{\rm op} - D_{I_n}\right]}{\det \Delta^{\rm op}} = \det\left[\mathbb{I} - G^{\rm op} D_{I_n}\right] = \det\left[\mathbb{I} - G^{\rm op}\right]_{i,j\in I_n}, \tag{74}$$

where $(D_{I_n})_{i,j} = \delta_{i,j}$ for $i,j \in I_n$ is zero elsewhere, and $I_n = \{(\ell,1) : 1 \leqslant \ell \leqslant n\}$ is the set of sites being closed. Using the relation (64a) expressing $G^{\rm op}$ in terms of the Green matrix on the full plane $\mathbb{Z}^2$, the matrix in the determinant reads

$$(\mathbb{I} - G^{\rm op})_{i,j\in I} = \left(\delta_{\ell,\ell'} - G_{(\ell,1),(\ell',1)} + G_{(\ell,1),(\ell',-1)}\right)_{1\leqslant \ell,\ell' \leqslant n}. \tag{75}$$

By the horizontal translation invariance of $G^{\rm op}$, this is a Toeplitz matrix of the form $a_{\ell-\ell'}$. Using standard results on the Green matrix on the plane, one finds that the entries a_m are the Fourier coefficients of the following symbol, which has a so-called Fisher–Hartwig singularity,

$$\sigma^{\rm op}(k) = \sqrt{1-\cos k}\cdot\left\{\sqrt{3-\cos k} - \sqrt{1-\cos k}\right\}. \tag{76}$$

For large n, the asymptotics of such Toeplitz determinants is well-known (see f.i., [43]) and leads to the following result [44]:

$$\frac{Z_{\rm op}(n)}{Z_{\rm op}} \simeq A\, n^{1/4}\, {\rm e}^{-\frac{2\rm G}{\pi} n}, \qquad n \gg 1, \tag{77}$$

with G = 0.915965, the Catalan constant. The proportionality constant A is explicitly known but is unimportant here.

What if we consider the opposite situation in which we open n consecutive sites of a closed boundary? Reasoning as above, we quickly get the corresponding ratio,

$$\frac{Z_{\rm cl}(n)}{Z_{\rm cl}} = \frac{\det \Delta^{\rm cl}(n)}{\det \Delta^{\rm cl}} = \frac{\det\left[\Delta^{\rm cl} + D_{I_n}\right]}{\det \Delta^{\rm cl}} = \det\left[\mathbb{I} + G^{\rm cl}\right]_{i,j\in I_n}, \tag{78}$$

which is also a Toeplitz determinant. However, this one is infinite—each entry is infinite—for the same reason we have pointed out in **Section 5.4**. Adopting the same point of view, we similarly evaluate the effect of opening n sites with respect to the situation where only one site is open. One therefore considers instead the ratio $\frac{Z_{\rm cl}(n)}{Z_{\rm cl}(1)}$, which one can write as

$$\frac{Z_{\rm cl}(n)}{Z_{\rm cl}(1)} = \frac{1}{b_0}\det\left(b_{\ell-\ell'}\right)_{1\leqslant \ell,\ell' \leqslant n}, \tag{79}$$

where the entries b_m are the Fourier coefficients of a symbol $\sigma^{\rm cl}(k)$ given by

$$\sigma^{\rm cl}(k) = \frac{1}{2}(1-\cos k)^{\alpha}\cdot\left\{\sqrt{3-\cos k} + \sqrt{1-\cos k}\right\}, \qquad \alpha = -\frac{1}{2}. \tag{80}$$

Its Fourier coefficients are well-defined for $\alpha > -\frac{1}{2}$, diverge in the limit $\alpha \to -\frac{1}{2}$, but nonetheless keep the ratio (79) finite. Remarkably, for large n, it takes the form [44].

$$\frac{Z_{\rm cl}(n)}{Z_{\rm cl}(1)} \simeq A\, n^{1/4}\, {\rm e}^{\frac{2\rm G}{\pi}(n-1)}, \qquad n \gg 1, \tag{81}$$

for the same constant A as above.

Before discussing the CFT side, let us remark that the exponential factors in equations **(77)** and **(81)** are expected. On a finite $N \times N$ grid, all four partition functions (numerators and denominators) are asymptotically dominated by the bulk free energy, given by ${\rm e}^{\frac{4\rm G}{\pi}N^2}$, as mentioned in **Section 2**. These terms drop out in the ratios. The next correction is related to the boundary free energy $f_{\rm b}$ (per site) and takes the form ${\rm e}^{4Nf_{\rm b}}$ in case the boundary condition b is the same at all boundary sites. For the partition functions considered above, the boundary conditions only differ on the lower edge of the grid so that for large $N \gg n \gg 1$, the ratios are asymptotic to

$$\frac{Z_{\rm op}(n)}{Z_{\rm op}} \simeq \frac{{\rm e}^{(N-n)f_{\rm op}+nf_{\rm cl}}}{{\rm e}^{Nf_{\rm op}}} = {\rm e}^{-n(f_{\rm op}-f_{\rm cl})},$$
$$\frac{Z_{\rm cl}(n)}{Z_{\rm cl}(1)} \simeq \frac{{\rm e}^{(N-n)f_{\rm cl}+nf_{\rm op}}}{{\rm e}^{(N-1)f_{\rm cl}+f_{\rm op}}} = {\rm e}^{(n-1)(f_{\rm op}-f_{\rm cl})}. \tag{82}$$

The free energies f_{op} and f_{cl} represent (the logarithm of) the effective number of values taken by the boundary heights in the set of recurrent configurations. The number of possible values taken by the height at an open boundary site is 4, and is 3 at a closed site. If these numbers of values get effectively reduced in the set of recurrent configurations, one should expect that the number of values at an open boundary site remains larger than that at a closed site, implying $f_{\rm op} - f_{\rm cl} > 0$. An explicit calculation [44] confirms this and yields $f_{\rm op} - f_{\rm cl} = \frac{2\rm G}{\pi}$, in agreement with the above results. To fix the ideas, the effective number of values taken by a boundary height is ${\rm e}^{f_{\rm op}} = 3.70$ at an open site, and ${\rm e}^{f_{\rm cl}} = 2.07$ at a closed site.

In the CFT approach, a change of the boundary condition at x, from condition a to condition b, is implemented by the insertion in the correlators of a specific field $\phi^{\rm a,b}(x)$. Such boundary condition changing fields[21] are usually expected to be chiral primary fields and satisfy $\phi^{\rm a,b}(x) = \phi^{\rm b,a}(x)$ when the boundary conditions a and b do not carry an intrinsic orientation (see **Section 6.4** for counterexamples). The insertion of the product $\phi^{\rm a,b}(x_1)\phi^{\rm b,a}(x_2)$ accounts for the

[21]In the correspondence between statistical system and field theory, the boundary condition changing fields are somehow special. They describe the effects of a change of the boundary condition but are not associated with a lattice observable, unlike the height fields h_a, for instance.

change at x_1 from condition a to condition b and then back from b to a at x_2 but does *not* account for the exponential terms related to the difference of boundary free energies of condition a vs. condition b, namely, the terms we have just discussed in the previous paragraph. These are clearly nonuniversal, that is, depend on the specific model under consideration, and cannot be accounted for by the underlying CFT, which itself applies to all the models in the universality class to which the sandpile model belongs.

It follows that the effect of changing the boundary condition given above, in which we omit the exponential terms, should correspond to the 2-point function $\langle \phi^{\mathrm{op,cl}}(0)\, \phi^{\mathrm{cl,op}}(n)\rangle = \langle \phi^{\mathrm{cl,op}}(0)\, \phi^{\mathrm{op,cl}}(n)\rangle$. The two are indeed equal on the lattice and asymptotic to $n^{\frac{1}{4}}$, and from this, we infer that the boundary condition changing field $\phi^{\mathrm{op,cl}}(x) = \phi^{\mathrm{cl,op}}(x)$ is a chiral conformal field of weight $h = -\frac{1}{8}$, with a correlator given by

$$\left\langle \phi^{\mathrm{op,cl}}(x_1)\, \phi^{\mathrm{cl,op}}(x_2)\right\rangle_{\mathrm{op}} = A\,|x_1 - x_2|^{1/4}. \tag{83}$$

For physical reasons, we might worry about having a correlator that actually increases with the distance, suggesting somehow the existence of a strange interaction that would get stronger at larger distances. There is nothing strange however as it does not really correspond to the physical correlation of two observables. As said above, the field $\phi^{\mathrm{op,cl}}$ is expected to be primary. As usual, this conjecture can be put to test: the consequences of this statement must have a match in the lattice properties of the model.

One of the strongest consequence of the primary nature of $\phi^{\mathrm{op,cl}}$ and the assumed structure of the conformal module that contains it is that any correlator where this field appears must satisfy a second-order partial differential equation,[22] the precise form of which depends on the other fields involved. A first and simple test is to look at a 4-point function,[23] for instance $\langle \phi^{\mathrm{op,cl}}(x_1)\phi^{\mathrm{cl,op}}(x_2)\, \phi^{\mathrm{op,cl}}(x_3)\, \phi^{\mathrm{cl,op}}(x_4)\rangle$, which should describe the effect of closing the sites on two disjoint interval $[x_1, x_2]$ and $[x_3, x_4]$ in the otherwise open boundary of the UHP. Using the global conformal invariance, one can reduce the partial differential equation to a second-order ordinary differential equation. In the two-dimensional solution space, we select the only solution which reduces to the product $\langle \phi^{\mathrm{op,cl}}(x_1)\, \phi^{\mathrm{cl,op}}(x_2)\rangle \langle \phi^{\mathrm{op,cl}}(x_3)\, \phi^{\mathrm{cl,op}}(x_4)\rangle$ when the two intervals are infinitely distant. This unique solution reads (with $x_{ij} = x_i - x_j$)

$$\begin{aligned}&\left\langle \phi^{\mathrm{op,cl}}(x_1)\, \phi^{\mathrm{cl,op}}(x_2)\, \phi^{\mathrm{op,cl}}(x_3)\, \phi^{\mathrm{cl,op}}(x_4)\right\rangle_{\mathrm{op}}\\ &\quad = \frac{2A^2}{\pi}(x_{12}\,x_{34})^{1/4}\,(1-t)^{1/4}\,K(t), \quad t \equiv \frac{x_{12}x_{34}}{x_{13}x_{24}},\end{aligned} \tag{84}$$

where $K(t) = \int_0^{\frac{\pi}{2}} \frac{\mathrm{d}\theta}{\sqrt{1-t\sin^2\theta}}$ is the complete elliptic integral.

To compare with a lattice calculation, we take x_i integers, with x_{21}, x_{32}, and x_{43} all large, and try to compute the determinant in eq. **(74)** with $I = I_1 \cup I_2$, the union of the two intervals $[x_1, x_2]$ and $[x_3, x_4]$. This determinant is no longer Toeplitz, which makes it difficult to compute its asymptotics analytically. Dividing it by the prefactor $(x_{12}\,x_{34})^{1/4}$, it can however be evaluated numerically as a function of t by varying the lengths of the intervals and their separation distance. The agreement with eq. **(84)** is more than satisfactory [44].

The opposite situation—two open intervals in a closed boundary—has also been considered. The appropriate 4-point function can be obtained from eq. **(84)** by making a simple cyclic permutation $(x_1, x_2, x_3, x_4) \to (x_4, x_1, x_2, x_3)$, with the result that $K(t)$ gets replaced by $K(1 - t)$. An equally successful agreement was observed [36]. Many other cross-checks have been done, confirming that the open/closed boundary condition changing field is indeed a primary field with conformal weight $h = -\frac{1}{8}$. One of them, particularly convincing, is presented in the next section.

6.3 Bulk Variables With Inhomogeneous Boundary

In **Section 6.1**, we have computed the lattice 1- and 2-site height probabilities on the UHP, with either the open or the closed boundary condition. Here, we would like to revisit these results in light of what we have learned of the boundary condition field, in terms of which one should be able to relate the probabilities for the two boundary conditions. In particular, we would like to understand the 1-site probabilities $\sigma_a^{\mathrm{op}}(y)$ and $\sigma_a^{\mathrm{cl}}(y)$,

$$\begin{aligned}\sigma_a^{\mathrm{op}}(y) &= \frac{1}{y^2}\left(c_a + \frac{d_a}{2} + d_a \log y\right) + \ldots,\\ \sigma_a^{\mathrm{cl}}(y) &= -\frac{1}{y^2}\,(c_a + d_a \log y) + \ldots\end{aligned} \tag{85}$$

One can do this by computing, on the CFT side, a more general probability, namely, we look for the probability to find a height equal to a at a distance y from the boundary, when the boundary condition is mixed, namely, open everywhere, except on the interval $[x_1, x_2]$ where the condition is closed. The two homogeneous open and closed conditions can be recovered in the limits $x_1 \to x_2$ and $x_1 \to -\infty$, $x_2 \to \infty$. Let us denote by $\langle h_a(z,\overline{z})\rangle_{\mathrm{mix}}$ the corresponding quantity in the CFT, given by

$$\langle h_a(z,\overline{z})\rangle_{\mathrm{mix}} = \frac{\left\langle \phi^{\mathrm{op,cl}}(x_1)\, \phi^{\mathrm{cl,op}}(x_2)\, h_a(z,\overline{z})\right\rangle_{\mathrm{op}}}{\left\langle \phi^{\mathrm{op,cl}}(x_1)\, \phi^{\mathrm{cl,op}}(x_2)\right\rangle_{\mathrm{op}}}, \tag{86}$$

where the division by $\langle \phi^{\mathrm{op,cl}}(x_1)\, \phi^{\mathrm{cl,op}}(x_2)\rangle_{\mathrm{op}}$ comes from the fact that we want to evaluate the probability to have a height 1 in front of a mixed boundary condition and not the combined effects of having a height 1 and the closing the boundary between x_1 and x_2. The denominator is known from **eq. (83)**.

[22] Again, the technical assumption is that the field $\phi^{\mathrm{op,cl}}$ is degenerate at level 2, similarly to the height 1 field h_1 (see **Section 5.5**).

[23] The CFT is really defined on the UHP plus the point at infinity. The boundary must therefore be thought of as the real line plus the two points $\pm\infty$ identified, and forming a loop closing at infinity. Any change of the boundary condition thus involves an even number of insertions of $\phi^{\mathrm{op,cl}}$. For instance, $\langle \phi^{\mathrm{op,cl}}(0)\, \phi^{\mathrm{cl,op}}(\infty)\rangle$ changes the boundary condition from open to closed on the positive real axis.

To compute the numerator, we represent the height fields in terms of the chiral fields as $h_1(z,\overline{z}) = \phi(z)\psi(\overline{z})$ and $h_2(z,\overline{z}) = \psi(z)\psi(\overline{z})$ (as usual, considering the heights $a = 1, 2$ is enough) and write the differential equation satisfied by the two ensuing 4-point correlators, as a consequence of the primary nature of $\phi^{\mathrm{op,cl}}$. Because ψ is the chiral logarithmic partner of ϕ, the general solution for $\langle \phi^{\mathrm{op,cl}}(x_1)\,\phi^{\mathrm{cl,op}}(x_2)\,\psi(z)\,\psi(\overline{z})\rangle_{\mathrm{op}}$ in fact depends on that of $\langle \phi^{\mathrm{op,cl}}(x_1)\,\phi^{\mathrm{cl,op}}(x_2)\,\phi(z)\,\psi(\overline{z})\rangle_{\mathrm{op}}$.

All calculations done, one finds that they depend on two integration constants c_2 and d_2 in such a way that the ratios in **eq. (86)** take the following forms, where $y = \mathrm{Re}\, z$ [27]:

$$\langle h_1(z,\overline{z})\rangle_{\mathrm{mix}} = \frac{d_2}{2y^2}\frac{1+t}{\sqrt{t}}, \qquad t = \frac{(x_1-\overline{z})(x_2-z)}{(x_1-z)(x_2-\overline{z})}, \tag{87a}$$

$$\langle h_2(z,\overline{z})\rangle_{\mathrm{mix}} = \frac{1}{2y^2}\frac{1+t}{\sqrt{t}}\left\{c_2 + \frac{d_2}{8}\frac{(1+\sqrt{t}\,)^2}{\sqrt{t}} + d_2\log y - d_2\frac{\mathrm{i}y(1-t)}{(x_1-x_2)}\left[\frac{1}{1+t} - \frac{1}{2\sqrt{t}}\right]\right\}. \tag{87b}$$

Although t is complex, both expressions are real on account of $t^* = 1/t$.

Let us now discuss the above two limits $x_1 \to x_2$ and $x_1 \to -\infty$, $x_2 \to \infty$. For convenience, we set $x_1 = -x_2$ and examine the limits $x_2 \to 0^+$ and $x_2 \to +\infty$. To compute the two limits, the important thing to notice is that the complex variable t, now equal to

$$t = \frac{(x_2+\overline{z})(x_2-z)}{(x_2+z)(x_2-\overline{z})}, \tag{88}$$

has complex norm equal to 1 and loops anticlockwise around the origin as x_2 varies from 0^+ to $+\infty$, starting from 1+ 0i to 1 − 0i. It follows that t itself goes to 1 in both limits, but $\sqrt{t}$ goes to +1 when $x_2 \to 0^+$ and goes to −1 when $x_2 \to +\infty$. The actual limits yield

$$\begin{aligned}\langle h_1(z,\overline{z})\rangle_{\mathrm{op}} &= \lim_{x_2\to 0^+}\langle h_1(z,\overline{z})\rangle_{\mathrm{mix}} = \frac{d_2}{y^2},\\ \langle h_1(z,\overline{z})\rangle_{\mathrm{cl}} &= \lim_{x_2\to +\infty}\langle h_1(z,\overline{z})\rangle_{\mathrm{mix}} = -\frac{d_2}{y^2},\end{aligned} \tag{89a}$$

$$\begin{aligned}\langle h_2(z,\overline{z})\rangle_{\mathrm{op}} &= \frac{1}{y^2}\left(c_2 + \frac{d_2}{2} + d_2\log y\right),\\ \langle h_2(z,\overline{z})\rangle_{\mathrm{cl}} &= -\frac{1}{y^2}\left(c_2 + d_2\log y\right),\end{aligned} \tag{89b}$$

in complete agreement with the lattice results: the change of the overall sign between the open and closed boundary conditions, the specific dependence on the two coefficients c_2 and d_2, and the equality $c_1 = d_2$ are all accounted for! The conformal approach however cannot fix the two coefficients c_2 and d_2; these must be determined by lattice calculations.

The expressions (87) can also be tested in situations where the boundary condition along the real axis is no longer homogeneous. A particularly instructive case is when the boundary condition is closed on the negative part of the real axis and open on the positive part, corresponding to the limits $x_1 \to -\infty$ and $x_2 \to 0$. The conformal transformation $w = \frac{L}{\pi}\log z$ can be used to map the UHP onto an infinite strip of width L, with open boundary condition on the left side and closed on the right side. The conformal transformation rules of the fields involved being known, the expressions (87) can be transformed to the strip and compared with numerical simulations on a truncated (and large) strip (exact calculations on the lattice are not available). It was found [27] that the conformal predictions and the numerical plots match remarkably well, thereby confirming once more all the field identifications made so far.

6.4 Wind on the Boundary

The open and closed boundary conditions are very natural as the very definition of the sandpile model uses dissipative and conservative sites. One may wonder what other type of boundary condition could be thought of. Perhaps, we could think of alternating open and closed boundary sites; we expect however that such a boundary condition would flow to the open condition in the scaling limit, as numerical experiments confirm. We have already commented on the possibility to uniformly fix the boundary heights. Fixing the boundary heights to 2 or to 3, or even to 2 or 3, seems difficult. The two boundary conditions, different from open and closed, which have been considered in [45], are in fact closely related, but not quite identical, to the third possibility. They are fixed boundary conditions but in the language of spanning trees.

We recall that in a rooted spanning tree, there is exactly one outgoing arrow at each vertex. The two new boundary conditions, noted ← and →, force the outgoing arrows at the boundary sites to be uniformly left or uniformly right.[24] In terms of height values, either condition means that none of the boundary sites has height 1 (because each boundary site has an ingoing arrow) or height 4 (because the burning algorithm would imply that the arrow is pointing down, toward the root). The converse is however not true: recurrent configurations with height values equal to 2 or 3 on the boundary do not necessarily have boundary arrows uniformly oriented.

The way the orientation of an edge can be forced has been briefly discussed in **Section 5.7**. This allows evaluating the effects of inserting a stretch of left or right arrows into an open or a closed boundary, similarly to what we did in **Section 6.2**. We refer the reader to Ref [45] for details of the analysis and restrict here to a summary of the results.

An obvious but unusual feature of the boundary conditions ← and → is that they are intrinsically oriented. It implies that the boundary condition changing field $\phi^{\mathrm{a},\rightarrow}$ turning the boundary condition from a to → may not be the same as the field $\phi^{\rightarrow,\mathrm{a}}$ implementing the opposite change. With $\mathrm{a},\mathrm{b} \in \{\mathrm{op},\mathrm{cl},\leftarrow,\rightarrow\}$, this makes potentially twelve distinct fields $\phi^{\mathrm{a,b}}$ (the fields $\phi^{\mathrm{a,a}}$ are just the identity). We already know $\phi^{\mathrm{op,cl}} = \phi^{\mathrm{cl,op}}$, and likewise, if $\mathrm{a} \in \{\mathrm{op},\mathrm{cl}\}$ is unoriented and $\mathrm{b} \in \{\leftarrow,\rightarrow\}$ is oriented, we expect the identifications $\phi^{\mathrm{a},\rightarrow} = \phi^{\leftarrow,\mathrm{a}}$ and $\phi^{\mathrm{a},\leftarrow} = \phi^{\rightarrow,\mathrm{a}}$ on the basis of a left–right reflection symmetry. These identifications have been confirmed and reduce the number of distinct fields to seven.

[24] In contrast, the outgoing arrow of a closed boundary site of the UHP can point left, up, or right, while that of an open boundary site can point in any of the four directions, a down arrow pointing to the root.

There is an additional subtlety for the field that changes the orientation from $\rightarrow$ to $\leftarrow$. Indeed the right and left arrows $\circ\!\!\rightarrow\bullet\leftarrow\!\!\circ$ point to the same boundary site (in black), and whether that site is open or closed may be relevant. Indeed, if it is open, the flow of arrows, which eventually terminates at the root, can go directly to the root; if it is closed, it must necessarily go upward into the bulk of the UHP. In the two cases, the macroscopic configurations of arrows are different. Thus, we should distinguish two different fields, $\phi^{\rightarrow,\leftarrow}_{\text{op}}$ and $\phi^{\rightarrow,\leftarrow}_{\text{cl}}$. The detailed analysis confirms that they are distinct fields as their conformal weights are different.

We therefore have eight distinct boundary condition changing fields. A mix of analytical calculations and numerical simulations has been used to determine the conformal weights of these eight fields. The results are given in **Table 2**.

The more delicate question of the exact nature of all these fields has been addressed by considering the fusion of the representations to which they belong. Loosely speaking, the fusion rules implement the composition law $\phi^{a,b}\star\phi^{b,c}\simeq\phi^{a,c}$ of boundary condition changing fields in the limit where the insertion points coincide. The ensuing consistency conditions suggest that all of them are primary fields, except two, which could belong to logarithmic representations (i.e., reducible indecomposable with Jordan cells). Also, the fields of weight 0 are nontrivial, that is, not equal to the identity (they are found to be degenerate at level 3). Relying on these proposals, various 4-point correlators have been computed and successfully compared with numerical simulations. We refer the readers to Ref [45] for more details on these specific points.

6.5 Boundary Height Variables

The boundary condition changing fields are not the only ones to live on a boundary. The lattice model includes observables in the bulk as well as on the boundaries. Those in the bulk have been discussed at length and give rise in the scaling limit to non-chiral fields $\Phi(z,\overline{z})$, characterized by a pair of conformal weights $(h,\overline{h})$; those on the boundaries give rise to boundary, chiral fields $\Phi^{a}(x)$, characterized by a single conformal dimension h_a. In general, the nature of the boundary field associated with a boundary observable and its conformal weight depend on the boundary condition.

In the Abelian sandpile model, only the boundary fields arising from the height variables and from the insertion of isolated dissipation have been studied on the UHP. In both cases, only open and closed boundaries have been considered.

The case of isolated dissipation is simpler and has been examined in detail in Ref [36], where isolated dissipation has been considered on a closed boundary only. The calculation proceeds much like that for the bulk, reviewed in **Section 5.4**, for which the same regularization is used. The results are similar: the dissipation field $\omega^{\text{cl}}(x)$ turns out to be a chiral field with conformal weight $h_{\text{cl}}=0$ and is a logarithmic partner of the identity. The multipoint correlators involve various combinations of logarithms like their bulk versions. On an open boundary, already dissipative, the dissipation field $\omega^{\text{op}}(x)$ is expected to be a descendant of the identity. Isolated dissipation is the simplest observable that can be associated and computed in terms of a local defect matrix. This, from what we have said in **Section 5.6** of the minimal clusters, suggests that both ω^{cl} and ω^{op} can be realized as local fields in the symplectic fermions. It was indeed shown that $\omega^{\text{cl}}\sim\theta\tilde{\theta}$ [36] and $\omega^{\text{op}}\sim\partial\theta\partial\tilde{\theta}$ [46] reproduce all known correlations. We note that the latter is proportional to the boundary stress–energy tensor $T(x)$ of the symplectic theory, a non-primary chiral field of weight $h_{\text{op}}=2$ and a descendant of the identity since $T(x)\sim(L_{-2}\mathbb{I})(x)$.

Boundary height variables are more complicated than dissipation but simpler than the bulk height variables. The first results have been derived by Ivashkevich in Ref [47], where the one- and two-site height probabilities on open and closed boundaries were obtained. The probabilities involving heights 1 only are no more complicated than in the bulk and can be easily obtained by using a defect matrix. As could be expected, probabilities for higher heights are more difficult.

On a boundary, heights larger or equal to 2 are characterized as in the bulk, namely, in terms of the number of predecessors among their nearest neighbors. So, it leads essentially to the same problems of computing nonlocal contributions. Both in the bulk and on a boundary, one can write linear identities expressing combinations of nonlocal contributions in terms of local ones, themselves calculable with a defect matrix. In turn, the nonlocal contributions can be used to calculate probabilities. In the bulk, the linear system is underdetermined and cannot be inverted to provide the required nonlocal contributions and then the probabilities themselves. The main observation made in Ref [47] was that on a boundary, the linear system can be inverted and therefore allows computing the height probabilities and correlations in terms of local contributions only. The following results were obtained.

The 1-site height probabilities on the boundary, open and closed, of the infinite UHP were computed exactly. For comparison purposes, we reproduce here their numerical values (the exact values can be found in Ref [47]) and recall those in the bulk, as given in **Section 5.1**:

$$\mathbb{P}_1=0.073\,63,\quad \mathbb{P}_2=0.173\,90,\quad \mathbb{P}_3=0.306\,29,\quad \mathbb{P}_4=0.446\,17, \tag{90}$$

$$\mathbb{P}^{\text{op}}_1=0.103\,82,\quad \mathbb{P}^{\text{op}}_2=0.216\,57,\quad \mathbb{P}^{\text{op}}_3=0.316\,23,\quad \mathbb{P}^{\text{op}}_4=0.363\,38, \tag{91}$$

$$\mathbb{P}^{\text{cl}}_1=0.113\,38,\quad \mathbb{P}^{\text{cl}}_2=0.318\,31,\quad \mathbb{P}^{\text{cl}}_3=0.568\,31. \tag{92}$$

TABLE 2 | Conformal weights of the fields $\phi^{a,b}$ which implement a change of boundary condition from a (row label) to b (column).

$h[\phi^{a,b}]$	Open	Closed	→	←
Open		$-\frac{1}{8}$	0	0
Closed	$-\frac{1}{8}$		$-\frac{1}{8}$	$\frac{3}{8}$
→	0	$\frac{3}{8}$		0 (center op) 1 (center cl)
←	0	$-\frac{1}{8}$	0	

On the open boundary, for which the comparison makes more sense, lower heights are thus more likely.

Mixed 2-site correlators $\tau^{\rm op}_{a,b}(x_1,x_2)$ and $\tau^{\rm cl}_{a,b}(x_1,x_2)$ on an open or a closed boundary were also computed in Ref [47]; all of them were found to decay like $|x_1-x_2|^{-4}$. Although logarithmic conformal field theory was in its infancy at the time, it indicates in hindsight that unlike their bulk cousins, boundary height fields are not logarithmic. This is also in agreement with the fact explained above that boundary height correlations can be fully computed in terms of local contributions.

The decay of the 2-site correlators strongly suggest that all boundary height fields, whatever the boundary condition, have a conformal dimension equal to $h_{\rm op}=h_{\rm cl}=2$. But like for the other observables discussed so far, we are interested to know the precise nature of the associated fields. Since the multisite boundary height probabilities appear to be calculable in terms of local contributions using defect matrices, it suggests again to look for field candidates constructed out from the symplectic free fermions $\theta,\tilde\theta$. This was done independently in Ref [46] and in Ref [48], following however two different approaches: the former computed various 3-point correlators, whereas the latter considered 2-point correlators only but in the massive extension of the sandpile model (see **Section 7.1**). The massive extension indeed allows distinguishing more efficiently different fields which would otherwise have the same 2-point correlators in the non-massive (critical) limit.

The results are as follows. The four height fields on an open boundary are all proportional to a single field,

$$h^{\rm op}_a(x)=O_a\,\partial\theta\,\partial\tilde\theta,\qquad 1\leqslant a\leqslant 4, \tag{93}$$

with explicit normalization constants O_a and where the $\theta,\tilde\theta$ fields satisfy the Dirichlet boundary condition. Thus, on an open boundary, the four height fields and the dissipation field turn out to be all proportional to each other. On a closed boundary, the three height fields are distinct and given by

$$\begin{aligned} &h^{\rm cl}_1(x)=C_1\,\partial\theta\,\partial\tilde\theta,\quad h^{\rm cl}_2(x)=C_2\,\partial\theta\,\partial\tilde\theta+\frac{1}{2\pi}\theta\,\partial\partial\tilde\theta,\\ &h^{\rm cl}_3(x)=C_3\,\partial\theta\,\partial\tilde\theta-\frac{1}{2\pi}\theta\,\partial\partial\tilde\theta, \end{aligned} \tag{94}$$

where the $\theta,\tilde\theta$ fields now satisfy the Neumann boundary condition. In both cases, the boundary condition means that the correlators are computed using the Wick theorem with the Wick contractions given by the Green functions $G^{\rm op}$ or $G^{\rm cl}$ (see **eqs. (64a)** and **(64b)**). Let us point out that for both boundary conditions, the 3-site correlations of three heights 1 do not vanish, unlike their bulk version.

The question of the nature of the height fields on the windy boundary conditions discussed in the previous section is definitely interesting but has not been considered so far.

6.6 Duality

This long section on boundaries has been largely devoted to a discussion of the open and closed boundary conditions, the best known and most studied ones. To finish, it is worth pointing out that a duality exists between these two boundary conditions, which has not been fully investigated nor exploited. This duality follows from a duality relation for planar graphs, well-known in graph theory, and acquires in the framework of the sandpile model an interesting flavor. It has been considered and discussed in [39, 49] in the dimer model, intrinsically related, like the sandpile model, to spanning trees.

Let us consider a rectangular portion of $\mathbb{Z}^2$, that is, the graph Γ made of a rectangular array of vertices, in which two adjacent vertices are linked by a single edge. The boundary conditions chosen for the boundary vertices determine the extended graph $\Gamma^\star$, obtained from Γ by adding the sink vertex and the edges connecting the open boundary sites to the sink. The graph $\Gamma^\star$ corresponding to a 3×3 grid with three open edges and one closed edge is shown in **Figure 1**.

Once the graph $\Gamma^\star$ is embedded in the plane,[25] the faces of $\Gamma^\star$ are the connected components of its complementary in the plane (for a finite graph, there is thus a large outer face, encircling the graph). The definition of the dual graph $(\Gamma^\star)^*$ is standard: the vertices of $(\Gamma^\star)^*$ are associated with the faces of $\Gamma^\star$, and two such vertices are connected if their corresponding two faces are separated from each other by an edge of $\Gamma^\star$. The dual graph of the example above is also shown in **Figure 1**.

By comparing the two graphs, one immediately notices that the boundary conditions are exchanged: if a boundary is homogeneously open resp. closed in $\Gamma^\star$, it becomes homogeneously closed resp. open in $(\Gamma^\star)^*$. In addition, the dual graph $(\Gamma^\star)^*$ is the extension $(\Gamma^*)^\star$ by a sink of a dual rectangular grid Γ^*, of size slightly different from the original grid Γ.

A classical result states that the number of spanning trees on $\Gamma^\star$ is equal to the number of spanning trees on its dual $(\Gamma^\star)^*$. In fact, for every spanning tree $\mathcal{T}$ on $\Gamma^\star$, there is a unique dual spanning tree $\mathcal{T}^*$ on $(\Gamma^\star)^*$ such that the two are perfectly interdigitating: the edges of $\mathcal{T}^*$ are exactly those of $(\Gamma^\star)^*$ which cross the edges of $\Gamma^\star$ not used in $\mathcal{T}$, and vice versa. An example of this is given in **Figure 1**.

This dual picture implies that the recurrent configurations for the sandpile model defined using $\Gamma^\star$ can be isomorphically described by those on $(\Gamma^*)^\star$. As far as the counting goes, the equality of their partition functions can be explicitly written for rectangular grids. If Γ is an $L_1\times L_2$ rectangular grid with k of its four boundaries being open, the other $4-k$ being closed, the dual Γ^* is an $L_1'\times L_2'$ rectangular grid with swapped boundary conditions, and the following identity holds,

$$Z_{k\,{\rm op}\,|\,(4-k)\,{\rm cl}}\,(L_1,L_2)=Z_{(4-k)\,{\rm op}\,|\,k\,{\rm cl}}\,\big(L_1',L_2'\big). \tag{95}$$

The dimensions are related as follows: $L_i'=L_i+1$ resp. L_i-1 if the opposites sides of length L_i of Γ are both open resp. closed, and $L_i'=L_i$ otherwise. If $k=4$, the dual rectangle has all its boundaries closed with a single boundary site open.

[25] This requires $\Gamma^\star$ to be planar and therefore excludes that some of the bulk vertices *and* some of the boundary vertices be open (dissipative) at the same time, except in a few very special cases.

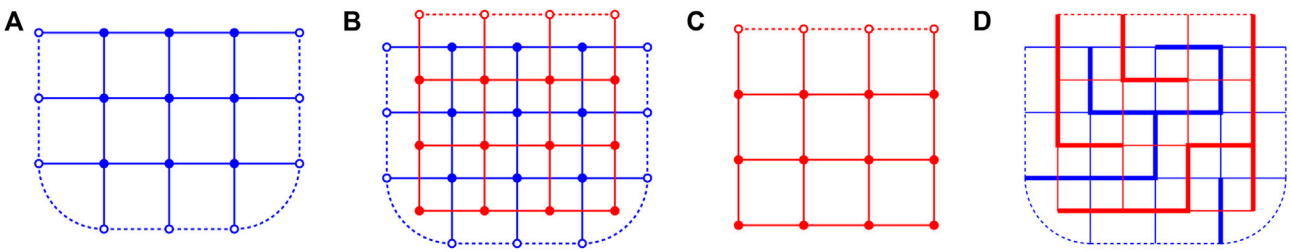

FIGURE 1 | Drawing codes for the three figures are as follows. The open circle stands for the sink vertex, while the solid circles stand for the non-sink vertices. The solid lines represent true edges of the extended graphs, unlike the dashed lines connecting the open circles which indicate that these should be identified as the unique sink vertex. Let us note that the corner vertices which lie at the intersection of an open and a closed boundary have a single edge to the sink; those at the intersection of two open boundaries have two such edges. **(A)** The left figure shows the extended graph of a 3×3 grid with open boundary conditions on the left, lower, and right boundaries, and closed boundary condition on the upper boundary. **(B)** The second panel shows how the dual of the blue graph, in red, is constructed. The red sink is the vertex associated with the outer face of the blue graph. **(C)** For a better readability, the dual graph alone is reproduced on the third panel. **(D)** Two dual spanning trees are drawn on the far right.

The isomorphism of the two descriptions may be hard to formulate in concrete terms for the height variables as it is defined for the associated trees. Its practical utility remains to be seen.

7 MORE DEVELOPMENTS

We would like to add a few more considerations about two further features of the sandpile model, namely, the dissipative sandpile model and some aspects of universality.

7.1 The Massive Sandpile Model

In the standard sandpile we have studied so far, the sites in the bulk of the grid, that is, the vast majority of sites, are conservative. This means that when such a site topples, it loses a certain number of sand grains which are all redistributed to its nearest neighbors. Sand moves in the grid but remains conserved. Dissipative sites must be present for the dynamics of the model to be well-defined; however, the dissipative sites were located most of the time on the boundaries.

The mostly conservative nature of the model is what drives it dynamically to a critical state: when enough sand is stored in the system, large avalanches become likely and span macroscopic parts of it, inducing strong correlations between distant heights. In the long run, the system enters a critical state described by the invariant measure $\mathbb{P}$, characterized by infinite correlation lengths in the infinite volume limit, and algebraic decays of the correlation functions. The field theory emerging in the scaling limit is conformal and consequently massless.

From the above point of view, a natural way to take the sandpile model out of criticality is to introduce a fair amount of dissipation so as to make the range of the avalanches shorter. It is not completely clear what *a fair amount* means as there are several ways to introduce dissipation. In the most common version, every site is made dissipative, with a dissipation rate controlled by an external parameter. In this case, it has been argued that indeed criticality is broken, resulting in an exponential decay of the correlations [33, 50, 51]. A mathematically rigorous proof that all correlations decay exponentially has been provided in Ref [52, 53]. Presumably, a nonzero density of dissipative sites could be sufficient to break criticality, but to our knowledge, this possibility has not been investigated. In any case, the field theory emerging from the dissipative sandpile model must be massive, with mass(es) inversely proportional to the lattice correlation length(s).

To make all sites dissipative, one can simply add to the toppling matrix of the standard model an integer multiple of the identity matrix, $\Delta \to \Delta(t) = \Delta + t\,\mathbb{I}$ with t an integer, while leaving all non-diagonal entries unchanged. According to the update of the heights after the toppling of site j, namely, $h_i \to h_i - \Delta_{j,i}(t)$, a toppled site loses t sand grains more than what it used to lose (whether or not the toppled site is on a boundary). That this change makes the correlation functions decay exponentially should be clear, for the following simple reason.

The new toppling matrix $\Delta(t)$ is a massive Laplacian matrix. It is well-known that the inverse Laplacian $\Delta^{-1}(t)$ has a kernel given at large distances by $G_{i_1,i_2}(t) \simeq \frac{1}{2\pi} K_0(|i_1 - i_2|\sqrt{t}\,) + \dots$ and decays exponentially like $e^{-r\sqrt{t}}$ at large distances (K_0 is the modified Bessel function). Thus, all multisite probabilities examined in the earlier sections, for observables like minimal cluster variables, arrow variables, isolated dissipation, or boundary heights, will similarly decay exponentially. Though technically less clear for bulk heights equal to 2, 3, or 4, the same decay is expected for the reason explained above: there is a loss of sand each time a site topples, which makes the typical avalanches short-ranged, which in turn induces correlations of heights on local scales only.

To take a concrete example, let us look at the correlation of two heights 1 in the dissipative model. The technique explained in **Section 5.3** in terms of defect matrices goes through. At dominant order, the result, which is the off-critical extension of **(35)**, reads [33]

$$\sigma_{1,1}(i_1, i_2; t) = -t^2 \frac{\mathbb{P}_1^2}{2} \left\{ K_0''^2 - K_0\, K_0'' + \frac{1}{\pi} K_0'^2 + \frac{1+\pi^2}{2\pi^2} K_0^2 \right\} + \dots \tag{96}$$

where the argument of the Bessel functions is $r\sqrt{t}$ and $\mathbb{P}_1$ on the right hand side is the critical probability; the dots stand for higher orders in t. We see that the correlation decays exponentially, with a correlation length proportional to $\xi \sim t^{-1/2}$.

How do we compute the scaling limit in the massive model? The general discussion in **Section 3** suggested that setting $i = \frac{\vec{x}}{\varepsilon}$ in

the lattice correlator and taking the limit over ε (after multiplying the correlator by a suitable power of ε) yields the field theoretic correlator. This cannot be the right way to proceed in the dissipative model. Because the correlators decay exponentially, the limit for ε going to zero of $\exp(-|\vec{x}_1 - \vec{x}_2|\sqrt{t}\,/\varepsilon)$ vanishes whatever the power of ε it is multiplied by.

The only way to get a nontrivial limit is to take a double limit: as we take the large distance limit by setting $i = \frac{\vec{x}}{\varepsilon}$, we simultaneously take the large correlation length limit by accordingly adjusting the dissipation rate. In the present case, we should take the latter proportional to ε^2: we therefore set $t = M^2\varepsilon^2$, with M playing the role of a mass (inverse correlation length in the continuum field theory).

Looking at the lattice correlator (96), we see that the factor t^2 carries the overall dimension of the fields involved: t^2 is proportional to M^4 and thus inversely proportional to a distance to the fourth power. It replaces the explicit dependence in r^{-4} in the non-dissipative model. Eventually, we find that the scaling limit of the correlator (96) is

$$\lim_{\varepsilon\to 0}\ \varepsilon^{-4}\,\sigma_{1,1}\left(\frac{z}{\varepsilon},\frac{w}{\varepsilon};\varepsilon^2M^2\right) = -M^4\,\frac{\mathbb{P}_1^2}{2}\left\{K_0''^2 - K_0\,K_0'' + \frac{1}{\pi}K_0'^2 + \frac{1+\pi^2}{2\pi^2}K_0^2\right\}, \tag{97}$$

where the argument of the Bessel function is now $M|z - w|$. It is straightforward to check that the $M \to 0$ limit of the previous expression is equal to $-\mathbb{P}_1^2/2|z-w|^4$, obtained in **Section 5**.

The last question is: the expression above is: the correlator of what field and in what field theory? The most obvious guess turns out to be correct: let us look into the massive extension of the free symplectic fermion theory. It contains the same two fields as before, which simply acquire a mass through a mass term in the action,

$$S = \frac{1}{\pi}\int \mathrm{d}z\mathrm{d}\overline{z}\left(\partial\theta\overline{\partial}\,\tilde{\theta} + \frac{M^2}{4}\theta\tilde{\theta}\right). \tag{98}$$

The 2-point correlators of the two fundamental fields are now given by

$$\begin{aligned}\langle\theta(z,\overline{z})\theta(w,\overline{w})\rangle &= \left\langle\tilde{\theta}(z,\overline{z})\tilde{\theta}(w,\overline{w})\right\rangle = 0,\\ \left\langle\theta(z,\overline{z})\tilde{\theta}(w,\overline{w})\right\rangle &= K_0(M|z-w|).\end{aligned} \tag{99}$$

Using Wick's theorem, it is a simple matter to check that the following local field,

$$h_1(z,\overline{z};M) = -\mathbb{P}_1\left[\partial\theta\,\overline{\partial}\,\tilde{\theta} + \overline{\partial}\,\theta\,\partial\tilde{\theta} + \frac{M^2}{2\pi}\theta\tilde{\theta}\right], \tag{100}$$

has a 2-point correlator[26] in the massive fermionic theory that is precisely given by equation **(97)**. The 3- and 4-point correlators of the same field have been checked to reproduce the corresponding lattice results. The field $h_1(z,\overline{z};M)$ is therefore what the height 1 variable in the dissipative sandpile model converges to in the scaling limit.

Similar correlators have been computed for many minimal clusters in Ref [33], with an unexpectedly simple result. The field describing the minimal cluster variable S in the dissipative model appears to be simply given by

$$h_S(z,\overline{z};M) = h_S(z,\overline{z}) - \mathbb{P}_S\,N_S\frac{M^2}{2\pi}\theta\tilde{\theta}, \tag{101}$$

where $\mathbb{P}_S$ is the probability of S in the non-dissipative model and N_s is the size of the cluster S. The field $h_S(z,\overline{z})$ is still given by relation **(54)** in terms in the (now massive) fermions.

Likewise, the mixed 2-point correlators for all boundary heights on open and closed boundaries have been explicitly evaluated in the dissipative model [48]. For them too, it is found that the boundary fields given in **Section 6.5** get additional terms proportional to $M^2\,\theta\tilde{\theta}$.

The nature of the higher height fields remains elusive but is definitely worth investigating as it would add a most valuable and crucial element of understanding of the sandpile model.

7.2 Aspects of Universality

Universality is the statement that the large distance properties of statistical models should only depend on some gross features of the way they are defined; microscopic details which become invisible from large distances should not matter. The statement is admittedly not very precise but, in concrete instances, leads to an expected robustness with respect to local modifications. In sandpile models, these would include the precise way sand is deterministically redistributed among neighbors (provided some form of isotropy is preserved), or, to a certain extent, the specific graph or lattice on which the model is defined. Features that do matter are a substantial introduction of dissipation, as we have seen in the previous section; a directed redistribution of sand after toppling [54]; a dynamics with stochastic toppling rules [55]; the formulation of the model on a hierarchical geometric structure like the Bethe lattice [56]; and, of course, a change of dimensionality of the underlying lattice.

Very early on, universality with respect to the planar lattice on which the sandpile is being formulated has been tested via a renormalization group approach [57, 58] and numerical simulations [59]. More recently, exact calculations of height correlations have been carried out on the honeycomb and triangular lattices.

In Ref [60], all calculations of height 1 correlations presented in the previous sections have been worked out on the hexagonal lattice (in the non-dissipative model). These include the 2-, 3-, and 4-site probabilities for heights 1 in general positions, in the bulk and on open and closed boundaries, as well as 1-site probabilities on the UHP, again for both types of boundary conditions. The results show that although the subdominant contributions differ from those on the square lattice, the dominant terms are exactly identical, up to normalizations. The same distinctive features are found, like the fact that the 3-site bulk correlation vanishes in the scaling limit (the dominant

[26]The insertion by hand of the dissipation field $\omega(\infty)$ at infinity in the field theoretic correlator is not required in the dissipative model as dissipation is present everywhere in the bulk.

term in the lattice result has dimension −7, instead of −8), and the change of sign for the UHP 1-site probabilities when changing the boundary condition from open to closed (see **Section 6.3**). Up to normalization, the field identifications of the height 1 variable in the bulk and on open and closed boundaries have been confirmed.

The results have been extended to higher heights on the honeycomb lattice and to all heights on the triangular lattice [61]. Interestingly, these two regular lattices have coordination numbers different from the square lattice, with the consequence that the height variables take in each case a different number of values: four for the square lattice, three for the honeycomb lattice and six for the triangular lattice. This naturally raises the question of which height variables scale to logarithmic fields and which do not.

The calculations have been carried out by using the technique developed in Ref [29], already used on the square lattice. The 1-site probabilities on the infinite honeycomb lattice are all rational,

$$\mathbb{P}_1 = \frac{1}{12}, \qquad \mathbb{P}_2 = \frac{7}{24}, \qquad \mathbb{P}_3 = \frac{5}{8}, \tag{102}$$

while those on the infinite triangular lattice are somewhat more complicated, like

$$\mathbb{P}_6 = \frac{1175}{864} - \frac{365}{144\sqrt{3}\pi} - \frac{289}{12\pi^2} + \frac{30\sqrt{3}}{\pi^3} + \frac{45}{\pi^4} - \frac{54\sqrt{3}}{\pi^5} \simeq 0.286, \tag{103}$$

and very similar expressions for $\mathbb{P}_{1\leqslant a\leqslant 5}$.

Concerning the nature of the height variables in the scaling limit, the results confirm what the reader has probably already suspected: far from boundaries, the height 1 variable becomes a primary field with conformal weights $(h, \overline{h}) = (1, 1)$, while each of the higher heights scales to a logarithmic partner of the height 1, exactly like on the square lattice. On boundaries, all height fields are non-logarithmic. Moreover, all computed correlations[27] exhibit the same bulk and boundary behaviors as on the square lattice. Thus, for what concerns the type of the underlying lattice, universality has been explicitly and successfully verified.

8 CONFORMAL SUMMARY

This last section is more specifically oriented toward conformal aspects of the sandpile model. We will summarize what we believe is currently known of the conformal picture, and discuss some of the most peculiar issues that are not so well-understood. We will almost exclusively discuss the non-chiral bulk fields, but before coming to those, we briefly comment on the chiral boundary fields encountered so far.

The boundary fields have been somewhat less investigated than the bulk fields. We have encountered two types of boundary fields, those arising from boundary observables and the boundary condition changing fields. In the first class, we have considered the height fields on open and closed boundaries and the dissipation field. Except for the dissipation on a closed boundary, none of them is logarithmic, and no evidence of a logarithmic partner has been found. All can be expressed as local fields in the symplectic fermions.

In the second class, we found primary fields of weights $-\frac{1}{8}$ and $\frac{3}{8}$, which are both standard fields in a $c = -2$ CFT. Due to the values of their conformal weight, they cannot be local in the symplectic fermions but are naturally accommodated[28] in the symplectic fermion theory [22]. The status of the other boundary condition changing fields related to the windy boundary conditions is uncertain and should be further investigated before their exact nature can be reliably stated.

Thus, overall, the boundary fields raise no particular questions. They are fairly simple fields which fit well within the symplectic theory. From this point of view, the bulk fields are somehow more intriguing.

Most of the bulk fields we have encountered seem to have a realization in terms of symplectic fermions, by which we mean that the fermionic expressions reproduce the known correlators. A few have not been realized in this way so far, namely, the height variables $h_{a\geqslant 2}$ not equal to 1, logarithmic partners of the height 1 field h_1, and the two fields ρ and $\overline{\rho}$, to which they transform under L_1 and $\overline{L}_1$, respectively.

Although we have not given any physical interpretation of ρ and $\overline{\rho}$, they appear to be related to the derivatives of the dissipation field ω [31],

$$\rho = \delta\, \overline{L}_{-1}\omega, \qquad \overline{\rho} = \delta\, L_{-1}\omega, \tag{104}$$

where δ is a constant which may depend on the lattice considered and equal to $\delta = \frac{\pi\mathbb{P}_1}{2}$ on the square lattice. In addition, the primary field h_1 may be consistently identified as being proportional to the derivatives of ρ and $\overline{\rho}$,

$$L_{-1}\rho = \overline{L}_{-1}\overline{\rho} = \beta\lambda h_1, \qquad \beta = \frac{1}{2}, \tag{105}$$

where λ is defined from $L_0\, h_2 = \overline{L}_0\, h_2 = h_2 + \lambda h_1$ and depends on the normalizations of h_1 and h_2. Combining these relations with the previous ones yields the somewhat surprising result is that the height 1 field is proportional to the Laplacian of the dissipation field, $h_1 \sim \partial\overline{\partial}\,\omega$. The correlator (40) confirms this: applying $\partial_1\overline{\partial}_1\partial_2\overline{\partial}_2$ on it indeed yields a multiple of $1/|z_1 - z_2|^4$, itself proportional to $\langle h_1(z_1, \overline{z}_1)h_1(z_2, \overline{z}_2)\omega(\infty)\rangle$.

From these observations, it follows that all bulk fields encountered so far, namely,

$$h_{a>1},\ h_1,\ \rho,\ \overline{\rho},\ \rho_{\rightarrow},\ \rho_{\uparrow},\ \phi_S,\ \phi_{\leftrightarrow},\ \phi_{\updownarrow},\ \omega,\ \mathbb{I}, \tag{106}$$

belong to the same conformal representation as they are all related to each other by the action of Virasoro modes L_n or $\overline{L}_n$. Indeed, $\rho_{\rightarrow}$ and $\rho_{\uparrow}$ are not quasi-primary and transform to a

[27] Some of the calculations done on the square lattice could not be worked out. For instance, we could not find a proper method of images to compute the Green matrix on the triangular half-plane with the closed boundary condition and therefore could not investigate that boundary condition.

[28] Very much like the spin field of the Ising model belongs naturally to the free Majorana fermionc theory with $c = \frac{1}{2}$, despite being nonlocal in the fermions.

multiple of $\mathbb{I}$ under L_1 or $\overline{L}_1$, while ϕ_S, $\phi_\leftrightarrow$ and $\phi_\updownarrow$ are linear combinations of h_1 and the chiral and antichiral stress–energy tensors T and $\overline{T}$. In fact, in terms of fermions, all these fields, except $h_{a>1}$, are proportional to or are linear combinations of $\mathbb{I}$, $\theta\tilde{\theta}$, $\theta\partial\tilde{\theta}$, $\theta\overline{\partial}\tilde{\theta}$, $\partial\theta\overline{\partial}\tilde{\theta}$, $\overline{\partial}\theta\partial\tilde{\theta}$, $\partial\theta\partial\tilde{\theta}$ and $\overline{\partial}\theta\overline{\partial}\tilde{\theta}$. Clearly, the main question is: do the fields $h_{a>1}$ also have a realization in terms of symplectic fermions?

In the symplectic fermion theory, the conformal representation which contains the fields quoted above is larger because it contains many other fields, like $\theta\partial\theta$ or $\partial\theta\overline{\partial}\theta$, which have not yet been found in the sandpile model. Among other peculiarities, the fermionic theory also contains four logarithmic pairs $(\phi^{\alpha\beta}, \psi^{\alpha\beta})$ of weight (1,1), given by $\phi^{\alpha\beta} = \partial\theta^\alpha\overline{\partial}\theta^\beta$ for the primary fields, and $\psi^{\alpha\beta} = \theta\tilde{\theta}\partial\theta^\alpha\overline{\partial}\theta^\beta$ for their logarithmic partners, where θ^α and θ^β are independently either θ or $\tilde{\theta}$ (see [22] for more details).

Conformal representations of the above type are called staggered modules and have been first studied in Ref [62] in their chiral version. As far as we know, it has been first noticed in Ref [63] for the case of modules containing rank 2 Jordan blocks that these representations are characterized by an intrinsic complex parameter β, known as a logarithmic coupling, an indecomposability parameter or a beta-invariant. The parameter β is crucial because it specifies the equivalence class of such representations, whose general structure was further studied in Ref [20] in the rank 2 case. The non-chiral staggered modules are far less understood and documented and reflect the difficulty to formulate a consistent and local logarithmic CFT (see however [64, 65]). It is nonetheless believed that the parameter β present in the chiral representations plays the same role of equivalence class label in the non-chiral ones, even if the latter may have more than one such label.

Concentrating on the action of the chiral Virasoro modes, the parameter β arises when we consider the triangular relations satisfied by a generic logarithmic pair (ϕ, ψ) of weights (1,1) and the associated ρ.

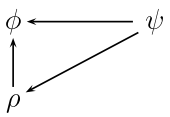

The arrows coming out of ψ indicate the actions $(L_0 - 1)\psi = \lambda\phi$ and $L_1\psi = \rho$. It is important to note that if the normalization of ψ is fixed, those of $\lambda\phi$ and ρ are fixed as well (the value of λ depends on the way ϕ is normalized). The vertical arrow indicates that $L_{-1}\rho$ is proportional to $\lambda\phi$,

$$L_{-1}\rho = \beta(\lambda\phi), \tag{107}$$

the proportionality factor β being intrinsic to the representation as all normalizations have already been fixed. In addition, these relations are invariant under the change $\psi \to \psi + \alpha\phi$ because the field ϕ is primary ($L_1\phi = 0$), and so they do not depend on which logarithmic partner is considered.

To answer the above question thus amounts to check whether the sandpile representation and the symplectic representation have the same value of β. The value of β in the sandpile model has been given above: if the pair (ϕ, ψ) is chosen to be (h_1, h_2), with the same normalization as the height variables on the square lattice, in which case $\lambda = -\frac{1}{2}$, then one finds $\beta = \frac{1}{2}$ [27].

The field h_1 has been already identified in terms of fermions and yields a natural choice for the primary field ϕ on the symplectic side,

$$\phi_\theta = -\mathbb{P}_1\big(\partial\theta\overline{\partial}\tilde{\theta} + \overline{\partial}\theta\partial\tilde{\theta}\big). \tag{108}$$

As mentioned earlier, the lattice results in the scaling limit are consistent with h_1 being degenerate at level 2, namely, $(L_{-1}^2 - 2L_{-2})h_1 = 0$ (see **Section 5.5**). The same equation is satisfied by ϕ_θ.

The only candidate for the logarithmic partner of ϕ_θ is proportional to $\theta\tilde{\theta}\,(\partial\theta\overline{\partial}\tilde{\theta} + \overline{\partial}\theta\partial\tilde{\theta})$ up to an irrelevant multiple of ϕ_θ. By computing its conformal transformations via its OPE with the chiral stress–energy tensor, one finds that the following normalization,

$$\psi_\theta = -\mathbb{P}_1\,\theta\tilde{\theta}\big(\partial\theta\overline{\partial}\tilde{\theta} + \overline{\partial}\theta\partial\tilde{\theta}\big), \tag{109}$$

satisfies $L_0\psi_\theta = \psi_\theta - \frac{1}{2}\phi_\theta$, for the same value $\lambda = -\frac{1}{2}$. The same OPE reveals in addition that

$$\rho_\theta = L_1\psi_\theta = -\frac{\mathbb{P}_1}{2}\big(\theta\overline{\partial}\tilde{\theta} + \overline{\partial}\theta\tilde{\theta}\big), \tag{110}$$

from which, upon using $\partial\overline{\partial}\theta = \partial\overline{\partial}\tilde{\theta} = 0$, one obtains

$$L_{-1}\rho_\theta = \partial\rho_\theta = -\frac{\mathbb{P}_1}{2}\big(\partial\theta\overline{\partial}\tilde{\theta} + \overline{\partial}\theta\partial\tilde{\theta}\big) = \frac{1}{2}\phi_\theta. \tag{111}$$

Comparing with equation **(107)**, the value of the logarithmic coupling is found to be $\beta_\theta = -1$ in the fermionic realization. As a consequence, the symplectic fermion theory cannot accommodate the height fields $h_{a>1}$ and therefore *does not appear to be the correct CFT to describe the scaling limit of the sandpile model*.

As one might suspect, the value of β has strong consequences on correlation functions involving ψ. A detailed comparison between $\beta = \frac{1}{2}$ and the fermionic realization $\beta_\theta = -1$ has been made in Ref [27]; it was shown in particular that the correlations with a trial field h_2 corresponding to a value $\beta = -1$ do not match the lattice results.[29] On general grounds, this can also be understood from the fact that the value of β determines the singular descendant of ψ, which, if set to zero, yields a β-dependent differential equation satisfied by any correlator containing ψ. In the present case, the singular logarithmic field is a combination of a descendant of ψ at level 5 and a descendant of ρ at level 6, with the following explicit dependence on β [20]:

[29] As an example, the correlator $\langle h_2(z,\overline{z})\rangle_{\text{mix}}$ displayed in **(87b)**, and corresponding to the four-point function $\langle\phi^{\text{op,cl}}(x_1)\,\phi^{\text{cl,op}}(x_2)\,h_2(z,\overline{z})\rangle$, can be computed upon assuming that h_2 is a logarithmic partner of h_1 carrying a generic value of $\beta \neq 0$. Its general form is given in Ref [7].

$$\xi = \left(L_{-1}^3 - 8L_{-2}L_{-1} + 12L_{-3}\right)\left(L_{-1}^2 - 2L_{-2}\right)\psi - \frac{1}{\beta}\Big[-\frac{16}{3}(\beta+1)L_{-2}^2L_{-1}^2 + \frac{4}{3}(14\beta+5)L_{-3}L_{-2}L_{-1} - 6\beta L_{-3}^2 - 6(\beta-2)L_{-4}L_{-1}^2 + 8\beta L_{-4}L_{-2} - \frac{2}{3}(5\beta+2)L_{-5}L_{-1} + 4\beta L_{-6}\Big]\rho. \quad (112)$$

Using the relations $L_1\psi = \rho$, $(L_0 - 1)\psi = \lambda\phi$, as well as the degeneracy condition $(L_{-1}^2 - 2L_{-2})\phi = 0$ (and the value $c = -2$), one can verify that the field ξ satisfies $L_1\xi = L_2\xi = 0$, provided the identity $L_{-1}\rho = \beta\lambda\phi$ holds. A rather convincing confirmation for the value of $\beta = \frac{1}{2}$ in the sandpile model is therefore to check that the various correlators involving h_2 indeed satisfy the condition $\xi = 0$ for $\beta = \frac{1}{2}$. It has been done for the correlator **(87b)**.

The situation therefore seems to be the following. The sandpile model contains a conformal logarithmic representation whose structure is very similar to the one appearing in the symplectic fermion theory, but which is nevertheless inequivalent to it. As far as the logarithmic partner ψ is not brought in, the two representations look the same; this explains why some of the fields can be realized in terms of symplectic fermions. However, the fermionic theory does not contain the $\beta = \frac{1}{2}$ representation found in the sandpile model, from which one concludes that it does not describe its scaling limit.

To characterize the CFT that does describe the sandpile model, even if a Lagrangian realization of it cannot be found, remains an enormous challenge. At the moment, this looks to be an extremely ambitious question in view of the (very) small number of fields which has been successfully identified.

AUTHOR CONTRIBUTIONS

The author confirms being the sole contributor of this work and has approved it for publication.

FUNDING

The author is a senior research associate of FRS-FNRS (Belgian Fund for Scientific Research). This work was supported by the Fonds de la Recherche Scientifique (FNRS) and the Fonds Wetenschappelijk Onderzoek-Vlaanderen (FWO) under EOS (project no 30889451).

REFERENCES

1. Bak P, Tang C, and Wiesenfeld K. Self-organized criticality: an explanation of the 1/fnoise. *Phys Rev Lett* (1987) 59:381. doi:10.1103/physrevlett.59.381
2. Bak P. *How nature works: the science of self-organised criticality*. New York: Springer-Verlag (1996).
3. Jensen HJ. *Self-organized criticality*. Cambridge: Cambridge University Press (1998).
4. Pruessner G. *Self-organised criticality: theory, models and characterisation*. Cambridge: Cambridge University Press (2012).
5. Dhar D. Theoretical studies of self-organized criticality. *Physica A: Stat Mech its Appl* (2006) 369:29. doi:10.1016/j.physa.2006.04.004
6. Dhar D. Self-organized critical state of sandpile automaton models. *Phys Rev Lett* (1990) 64:1613. doi:10.1103/physrevlett.64.1613
7. Ruelle P. Logarithmic conformal invariance in the Abelian sandpile model. *J Phys A: Math Theor* (2013) 46:494014. doi:10.1088/1751-8113/46/49/494014
8. Majumdar SN, and Dhar D. Equivalence between the Abelian sandpile model and the q→0 limit of the Potts model. *Physica A: Stat Mech its Appl* (1992) 185:129. doi:10.1016/0378-4371(92)90447-x
9. Ruelle P, and Sen S. Toppling distributions in one-dimensional Abelian sandpiles. *J Phys A: Math Gen* (1992) 25:L1257. doi:10.1088/0305-4470/25/22/006
10. Ali AA, and Dhar D. Breakdown of simple scaling in Abelian sandpile models in one dimension. *Phys Rev E* (1995) 51:R2705. doi:10.1103/physreve.51.r2705
11. Creutz M. Abelian sandpiles. *Comput Phys* (1991) 5:198. doi:10.1063/1.168408
12. Dhar D, Ruelle P, Sen S, and Verma D-N. Algebraic aspects of Abelian sandpile models. *J Phys A: Math Gen* (1995) 28:805. doi:10.1088/0305-4470/28/4/009
13. Le Borgne Y, and Rossin D. On the identity of the sandpile group. *Discrete Math* (2002) 256:775. doi:10.1016/s0012-365x(02)00347-3
14. Caracciolo S, Paoletti G, and Sportiello A. Explicit characterization of the identity configuration in an Abelian sandpile Model. *J Phys A: Math Theor* (2008) 41:495003. doi:10.1088/1751-8113/41/49/495003
15. Cardy J. *Scaling and Renormalization in statistical Physics, cambridge lecture notes in Physics*. Cambridge: Cambridge University Press (1996).
16. Di Francesco P, Mathieu P, and Sénéchal D. *Conformal field theory*. New York: Springer (1997).
17. Henkel M. *Conformal invariance and critical phenomena*. New York: Springer (1999).
18. Gainutdinov A, Ridout D, and Runkel I. Logarithmic conformal field theory. *J Phys A: Math Theor* (2013) 46:490301.
19. Flohr MAI. Bits and pieces in logarithmic conformal field theory. *Int J Mod Phys A* (2003) 18:4497. doi:10.1142/s0217751x03016859
20. Kytölä K, and Ridout D. On staggered indecomposable Virasoro modules. *J Math Phys* (2009) 50:123503. doi:10.1063/1.3191682
21. Gurarie V. Logarithmic operators in conformal field theory. *Nucl Phys B* (1993) 410:535. doi:10.1016/0550-3213(93)90528-w
22. Gaberdiel MR, and Kausch HG. A local logarithmic conformal field theory. *Nucl Phys B* (1999) 538:631. doi:10.1016/s0550-3213(98)00701-9
23. Gaberdiel MR, and Runkel I. The logarithmic triplet theory with boundary. *J Phys A: Math Gen* (2006) 39:14745. doi:10.1088/0305-4470/39/47/016
24. Pearce PA, Rasmussen J, and Zuber J-B. Logarithmic minimal models. *J Stat Mech* (2006) 2006:P11017. doi:10.1088/1742-5468/2006/11/p11017
25. Majumdar SN, and Dhar D. Height correlations in the Abelian sandpile model. *J Phys A: Math Gen* (1991) 24:L357. doi:10.1088/0305-4470/24/7/008
26. Priezzhev VB. Structure of two-dimensional sandpile. I. Height probabilities. *J Stat Phys* (1994) 74:955. doi:10.1007/bf02188212
27. Jeng M, Piroux G, and Ruelle P. Height variables in the Abelian sandpile model: scaling fields and correlations. *J Stat Mech* (2006) 2006:P10015. doi:10.1088/1742-5468/2006/10/p10015
28. Poghosyan VS, Priezzhev VB, and Ruelle P. Return probability for the loop-erased random walk and mean height in the Abelian sandpile model: a proof. *J Stat Mech* (2011) 2011:P10004. doi:10.1088/1742-5468/2011/10/p10004
29. Kenyon RW, and Wilson DB. Spanning trees of graphs on surfaces and the intensity of loop-erased random walk on planar graphs. *J Amer Math Soc* (2015) 28:985. doi:10.1090/S0894-0347-2014-00819-5
30. Caracciolo S, and Sportiello A. Exact integration of height probabilities in the Abelian sandpile model. *J Stat Mech* (2012) 2012:P09013. doi:10.1088/1742-5468/2012/09/p09013
31. Poncelet A, and Ruelle P. Multipoint correlators in the Abelian sandpile model. *J Stat Mech* (2017) 2017:123102. doi:10.1088/1742-5468/aa9a59
32. Kassel A, and Wilson DB. The looping rate and sandpile density of planar graphs. *Amer Math Monthly* (2016) 123:19. doi:10.4169/amer.math.monthly.123.1.19

33. Mahieu S, and Ruelle P. Scaling fields in the two-dimensional Abelian sandpile model. *Phys Rev E Stat Nonlin Soft Matter Phys* (2001) 64:66130. doi:10.1103/PhysRevE.64.066130
34. Poghosyan VS, Grigorev SY, Priezzhev VB, and Ruelle P. Pair correlations in sandpile model: a check of logarithmic conformal field theory. *Phys Lett B* (2008) 659:768. doi:10.1016/j.physletb.2007.12.002
35. Poghosyan VS, Grigorev SY, Priezzhev VB, and Ruelle P. Logarithmic two-point correlators in the Abelian sandpile model. *J Stat Mech* (2010) 2010: P07025. doi:10.1088/1742-5468/2010/07/p07025
36. Piroux G, and Ruelle P. Pre-logarithmic and logarithmic fields in a sandpile model. *J Stat Mech Theor Exp* (2004) 2004:P10005. doi:10.1088/1742-5468/2004/10/p10005
37. Jeng M. Conformal field theory correlations in the Abelian sandpile model. *Phys Rev E Stat Nonlin Soft Matter Phys* (2005) 71:16140. doi:10.1103/PhysRevE.71.016140
38. Poghosyan VS, and Priezzhev VB. The problem of predecessors on spanning trees. *Act Polytech* (2011) 51:59. doi:10.14311/1364
39. Izmailian NS, Priezzehv VB, and Ruelle P. Non-local finite-size effects in the dimer model. *SIGMA* (2007) 3:1. doi:10.3842/SIGMA.2007.001
40. Brankov JG, Ivashkevich EV, and Priezzhev VB. Boundary effects in a two-dimensional Abelian sandpile. *J Phys France* (1993) 3:1729. doi:10.1051/jp1:1993212
41. Piroux G, and Ruelle P. Logarithmic scaling for height variables in the Abelian sandpile model. *Phys Lett B* (2005) 607:188. doi:10.1016/j.physletb.2004.12.045
42. Cardy JL. Conformal invariance and surface critical behavior. *Nucl Phys B* (1984) 240:514. doi:10.1016/0550-3213(84)90241-4
43. Deift P, Its A, and Krasovsky I. Toeplitz matrices and Toeplitz determinants under the impetus of the ising model: some history and some recent results. *Comm Pure Appl Math* (2013) 66:1360. doi:10.1002/cpa.21467
44. Ruelle P. A c=−2 boundary changing operator for the Abelian sandpile model. *Phys Lett B* (2002) 539:172. doi:10.1016/s0370-2693(02)02069-5
45. Ruelle P. Wind on the boundary for the Abelian sandpile model. *J Stat Mech* (2007) 2007:P09013. doi:10.1088/1742-5468/2007/09/p09013
46. Jeng M. Four height variables, boundary correlations, and dissipative defects in the Abelian sandpile model. *Phys Rev E Stat Nonlin Soft Matter Phys* (2005) 71: 036153. doi:10.1103/PhysRevE.71.036153
47. Ivashkevich EV. Boundary height correlations in a two-dimensional Abelian sandpile. *J Phys A: Math Gen* (1994) 27:3643. doi:10.1088/0305-4470/27/11/014
48. Piroux G, and Ruelle P. Boundary height fields in the Abelian sandpile model. *J Phys A: Math Gen* (2005) 38:1451. doi:10.1088/0305-4470/38/7/004
49. Izmailian NS, Priezzehv VB, Ruelle P, and Hu C-K. Logarithmic conformal field theory and boundary effects in the dimer model. *Phys Rev Lett* (2005) 95: 260602. doi:10.1103/physrevlett.95.260602
50. Ghaffari P, Lise S, and Jensen HJ. Nonconservative sandpile models. *Phys Rev E* (1997) 56:6702. doi:10.1103/physreve.56.6702
51. Tsuchiya T, and Katori M. Proof of breaking of self-organized criticality in a nonconservative Abelian sandpile model. *Phys Rev E* (2000) 61:1183. doi:10.1103/physreve.61.1183
52. Maes C, Redig F, and Saada E. The infinite volume limit of dissipative Abelian sandpiles. *Commun Math Phys* (2004) 244:395. doi:10.1007/s00220-003-1000-8
53. Járai A, and Redig F. *Approaching Criticality via the Zero Dissipation Limit in the Abelian Avalanche Model. J Stat Phys* (2015) 159:1369–1407.
54. Dhar D, and Ramaswamy R. Exactly solved model of self-organized critical phenomena. *Phys Rev Lett* (1989) 63:1659. doi:10.1103/physrevlett.63.1659
55. Manna SS. Two-state model of self-organized criticality. *J Phys A: Math Gen* (1991) 24:L363. doi:10.1088/0305-4470/24/7/009
56. Dhar D, and Majumdar SN. Abelian sandpile model on the Bethe lattice. *J Phys A: Math Gen* (1990) 23:4333. doi:10.1088/0305-4470/23/19/018
57. Papoyan VV, and Povolotsky AM. Renormalization group study of sandpile on the triangular lattice. *Physica A: Stat Mech its Appl* (1997) 246:241. doi:10.1016/s0378-4371(97)00347-6
58. Lin CY, and Hu CK. Renormalization-group approach to an Abelian sandpile model on planar lattices. *Phys Rev E Stat Nonlin Soft Matter Phys* (2002) 66: 21307. doi:10.1103/PhysRevE.66.021307
59. Hu C-K, and Lin C-Y. Universality in critical exponents for toppling waves of the BTW sandpile model on two-dimensional lattices. *Physica A: Stat Mech its Appl* (2003) 318:92. doi:10.1016/s0378-4371(02)01411-5
60. Azimi-Tafreshi N, Dashti-Naserabadi H, Moghimi-Araghi S, and Ruelle P. The Abelian sandpile model on the honeycomb lattice. *J Stat Mech* (2010) 2010:P02004. doi:10.1088/1742-5468/2010/02/p02004
61. Poncelet A, and Ruelle P. Sandpile probabilities on triangular and hexagonal lattices. *J Phys A: Math Theor* (2018) 51:15002. doi:10.1088/1751-8121/aa9255
62. Rohsiepe F. On reducible but indecomposable representations of the Virasoro algebra. *arXiv* (1996).
63. Gaberdie MR, and Kausch HG. Indecomposable fusion products. *Nucl Phys B* (1996) 477:293. doi:10.1016/0550-3213(96)00364-1
64. Do A-L, and Flohr M. Towards the construction of local logarithmic conformal field theories. *Nucl Phys B* (2008) 802:475. doi:10.1016/j.nuclphysb.2008.05.001
65. Ridout D. Non-chiral logarithmic couplings for the Virasoro algebra. *J Phys A: Math Theor* (2012) 45:255203. doi:10.1088/1751-8113/45/25/255203

Conflict of Interest: The author declares that the research was conducted in the absence of any commercial or financial relationships that could be construed as a potential conflict of interest.

frontiers in Physics

REVIEW
published: 07 July 2021
doi: 10.3389/fphy.2021.639389

Self-Organized Criticality in the Brain

Dietmar Plenz, Tiago L. Ribeiro, Stephanie R. Miller, Patrick A. Kells, Ali Vakili and Elliott L. Capek*

Section on Critical Brain Dynamics, National Institute of Mental Health, National Institutes of Health, Bethesda, MD, United States

Self-organized criticality (SOC) refers to the ability of complex systems to evolve toward a second-order phase transition at which interactions between system components lead to scale-invariant events that are beneficial for system performance. For the last two decades, considerable experimental evidence has accumulated that the mammalian cortex with its diversity in cell types, interconnectivity, and plasticity might exhibit SOC. Here, we review the experimental findings of isolated, layered cortex preparations to self-organize toward four dynamical motifs presently identified in the intact cortex *in vivo*: up-states, oscillations, neuronal avalanches, and coherence potentials. During up-states, the synchronization observed for nested theta/gamma oscillations embeds scale-invariant neuronal avalanches, which can be identified by robust power law scaling in avalanche sizes with a slope of –3/2 and a critical branching parameter of 1. This precise dynamical coordination, tracked in the negative transients of the local field potential (nLFP) and spiking activity of pyramidal neurons using two-photon imaging, emerges autonomously in superficial layers of organotypic cortex cultures and acute cortex slices, is homeostatically regulated, exhibits separation of time scales, and reveals unique size vs. quiet time dependencies. A subclass of avalanches, the coherence potentials, exhibits precise maintenance of the time course in propagated local synchrony. Avalanches emerge in superficial layers of the cortex under conditions of strong external drive. The balance of excitation and inhibition (E/I), as well as neuromodulators such as dopamine, establishes powerful control parameters for avalanche dynamics. This rich dynamical repertoire is not observed in dissociated cortex cultures, which lack the differentiation into cortical layers and exhibit a dynamical phenotype expected for a first-order phase transition. The precise interactions between up-states, nested oscillations, and avalanches in superficial layers of the cortex provide compelling evidence for SOC in the brain.

Keywords: organotypic cortex culture, acute cortex slice, dissociated cortex culture, neuronal avalanches, oscillations, up-state

OPEN ACCESS

Edited by:
Alex Hansen, Norwegian University of Science and Technology, Norway

Reviewed by:
Ernesto Altshuler, University of Havana, Cuba
Changsong Zhou, Hong Kong Baptist University, Hong Kong

****Correspondence:***
Dietmar Plenz
plenzd@mail.nih.gov

Specialty section:
This article was submitted to Interdisciplinary Physics, a section of the journal Frontiers in Physics

Received: *08 December 2020*
Accepted: *10 June 2021*
Published: *07 July 2021*

Citation:
Plenz D, Ribeiro TL, Miller SR, Kells PA, Vakili A and Capek EL (2021) Self-Organized Criticality in the Brain. Front. Phys. 9:639389. doi: 10.3389/fphy.2021.639389

INTRODUCTION

Brains are inherently complex. Composed of a vast number of cell types, orders of magnitude larger number of connections, and a myriad of structural and functional networks that make up biochemical pathways affecting every spatial and temporal scale of brain organization, brains are deeply challenging to study. Yet, elaborate efforts to assemble the rich and detailed structural evidence on brain circuits have uncovered a rather small set of dynamical features. Highly detailed brain models comprised of thousands of neurons exhibit relatively simple neuronal activity patterns that range from irregular firing to synchronized or oscillatory activity similar to what is measured in real brains [1,2]. Importantly, the major aspect of brain dynamics that has been particularly difficult

to understand thus far is how many neurons in the cortex selectively communicate over long distances with associated characteristic times and level of coherence.

The aspect of many interacting elements leading to relatively few dynamical motifs is also a major appeal of self-organized criticality (SOC) [3]. SOC will drive a system toward a second-order phase transition at which dynamics are dominated by universal properties (for review, see [4–10]). The universal property that is of particular interest to brain functions is scale invariance indicative of system-wide correlations that emerge in a system exhibiting SOC. Such scale invariance could be a hallmark of coordinated, yet adaptive, neuronal activity that incorporates large numbers of brain cells.

For the brain, and specifically the cortex, it is currently an intensive field of research whether certain aspects of brain dynamics are true aspects of SOC. Fortunately, numerous key features of SOC can be addressed experimentally in a number of advanced brain preparations [11]. For example, one would expect cortical tissue, developing autonomously in isolation, i.e., in the absence of any instructive sensory and motor inputs, to exhibit scale-invariant properties in the emergent dynamics. One would expect that the emergence of scale invariance is highly regulated as well. For example, it should be robust to slow driving (i.e., exhibiting a separation of time scales) and it should exhibit homeostatic regulation (i.e., returning to scale invariance after profound perturbations), with these regulations failing when essential circuit components are absent or suppressed.

This review summarizes the experimental findings on the emergent dynamics of immature and mature cortical networks when taken in isolation and, thus, disconnected from any external, structuring input or required outputs. These dynamics from cortical tissue in isolation, i.e., *in vitro*, will be compared to the corresponding dynamical findings in the intact brain, i.e., *in vivo*. It will be argued that the four dynamical motifs of up-states, nested oscillations, neuronal avalanches, and coherence potentials emerge in superficial layers of the cortex as major hallmarks of SOC in the brain.

Structural Motifs of Self-Organization: Cortical Layers, Pyramidal Neurons, Interneurons, and Glial Cells

Until now, the organotypic cortex culture to date represents the most complex *in vitro* model of the cortex. Typically taken from a newborn rodent and grown in isolation for up to several months (**Figure 1**), it captures several core features of cortical organization. First, it exhibits the major division of the mammalian cortex into superficial and deep cortical layers (**Figures 1A,B**) [12–15], which exhibit distinct functional

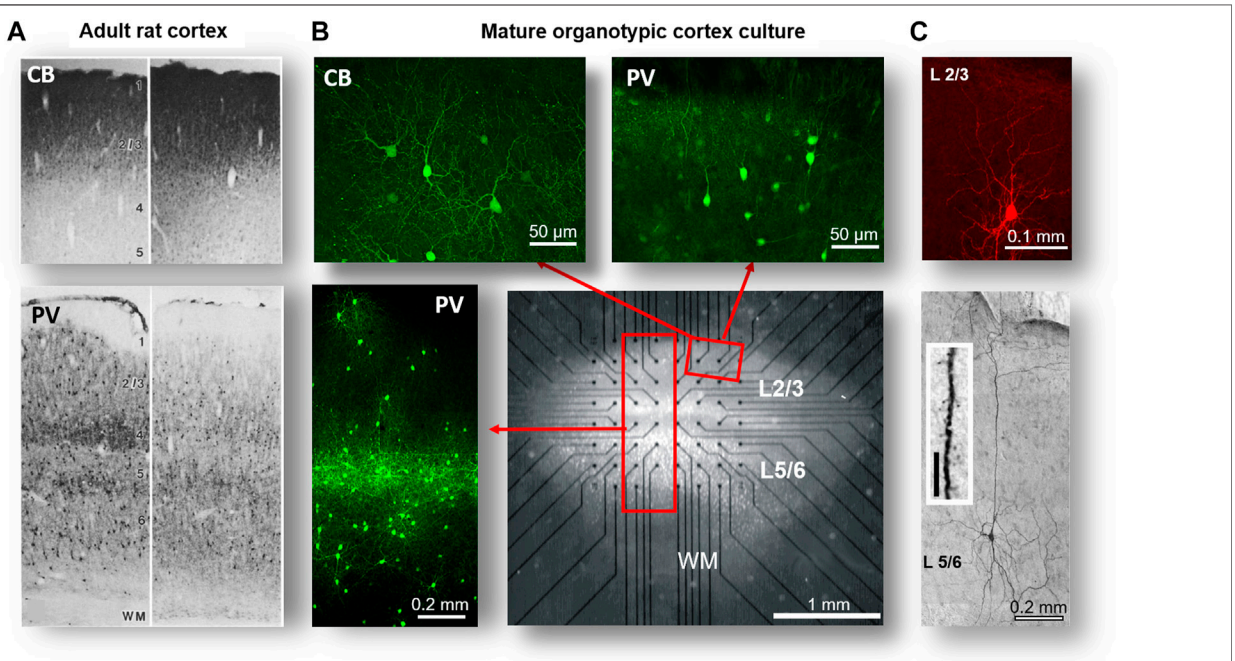

FIGURE 1 | Structural motifs of self-organization: cortical layers, pyramidal neurons, and interneurons in organotypic cortex cultures. **(A)** Coronal sections from the brain in adult rats showing the somatosensory cortex (*left*) and motor cortex (*right*). Note high density of calbindin (*CB*)–positive interneuron stain typical for superficial layers (*top*) and the layer-dependent bands of parvalbumin (*PV*)–positive interneurons in deep layers (*bottom*). **(B)** Organotypic cortex culture after ~4 weeks grown on a planar multielectrode array (MEA). Note transparent healthy neural tissue of ~4 mm^2 covering the array at a thickness of ~100–200 µm and electrodes (*black dots*), conductors of the MEA. Composite images (red rectangles) indicating superficial layers (L2/3) that contain PV and CB-positive interneurons and deep layers (L5/6) with their intense band of PV-positive interneurons. *WM*: white matter region. **(C)** Typical cell body and dendritic morphology of pyramidal neurons from L2/3 and L5, the latter with their characteristically long and branched apical dendrite. *Inset*: spiny dendrite typical for pyramidal neurons (*A* reprinted with permission from [165], *B* modified with permission from [14], and *C* modified with permission from [18]; Copyright 1998 Society for Neuroscience).

properties [16,17]. Superficial layers 2/3, called the associative layers, are composed of pyramidal (excitatory) neurons with reduced branching of their apical dendrites that preferentially connect to other intralaminar pyramidal neurons (**Figure 1C**, *top*). In contrast, pyramidal neurons from deep layers 5/6 typically feature elaborate apical dendrites and, besides selectively connecting with superficial layers, communicate *in vivo* with brain regions outside the cortex (**Figure 1C**, *bottom*; [18]). *In vivo*, layer 4 receives sensory input via the thalamus, a brain structure that conveys sensory information to the cortex; this selective connectivity has been found as well for organotypic cocultures using the thalamus and cortex [19–21]. The second important hallmark in cortical organization is the presence of three major interneuron (inhibitory) classes identified as parvalbumin (PV), somatostatin (SST), and vasoactive intestinal peptide (VIP)–expressing neurons, which exhibit highly selective connectivity and specific firing patterns (for review, see [22,23]). Several of these classes, with their layer-specific distribution and electrophysiology, have been demonstrated in organotypic cortex cultures using various immunochemical markers (**Figure 1B** [14,24,25]). The third and often overlooked hallmark of the cortical microcircuit is the up to 10× higher presence of nonneuronal cells, or glial cells, compared to neurons. Of the three types of glial cells, cortical astrocytes exhibit brain-region–specific control over neuronal excitation and dynamics, among many other functions [26–28]. For organotypic cortex cultures, glial cells have been demonstrated to protect the neuronal tissue from mechanical damage [29,30]. Also, organotypic cortex cultures show clear differences compared to the *in vivo* cortex, such as an overall reduced connectivity due to a reduction in the third dimension when preparing the brain slice taken into culture [31] or a change in glial protein expression [32]. Organotypic cultures are typically prepared from newborn animals. Therefore, the cortical section of the postnatal brain, which is taken for culturing, is still immature, particularly with respect to the development of superficial layers. However, this immature cortex has benefited from structuring input during embryonic development, which has been shown to be important for somatotopic map formation, i.e., establishing a correspondence between body parts and brain regions [33]. Therefore, the organotypic cortex culture should be best thought of as an *in vitro* system that has experienced a robust structural organization during embryogenesis and contains the blueprint for the organization of layered, cortical columns in isolation. The next section will summarize how structural self-organization continues as the cortex further matures in isolation and gives rise to several dynamical motifs of neuronal population activity.

The First and Second Dynamical Motifs of Self-Organization: Up-States and Nested θ/γ-Oscillations

The structural self-organization in organotypic cultures should parallel a self-organization of dynamical motifs found in the fully mature brain. One of these motifs, which is dominant in the electrocorticogram (ECoG) of humans in the awake state, is composed of transient, i.e., up to several seconds lasting, nested oscillations in the theta (θ: 8–12 Hz) and gamma (γ: >25 Hz) range capturing the emergence of population synchrony at many local sites (**Figure 2A**; [34]). The nesting of high-frequency γ-oscillations to each θ-cycle has been proposed to be essential for working memory [35,36] and information transfer from lower to higher cortical areas (e.g., [37,38]). In mature organotypic cortex cultures, detailed intracellular recordings demonstrated the presence of nested θ/γ-oscillations that arise during pronounced depolarizations that can last up to several seconds (**Figures 2B,C**; [25,39,40]). This depolarization establishes the well-known dynamical motif of an "up-state", which is typically defined as a prolonged period of self-sustained network excitation lasting from hundreds of milliseconds to several seconds.

The dominance of up-states supporting nested θ/γ-oscillations has several profound implications when studying SOC in isolated cortex preparations. First, it is well known that up-states, particularly prolonged ones (>0.2 s), require stimulation of both the fast-acting (<30 ms) AMPA-glutamate receptor and the slow-acting (>50 ms) NMDA-glutamate receptor (**Figure 2D**). The prolonged time course of the NMDA-glutamate receptor reduces the precision in action potential timing [41], suggesting that the scaffolding of precise spatiotemporal events requires alternative mechanisms, e.g., interneuron firing. Indeed, pyramidal neurons tend to fire sparsely during up-states, whereas interneurons fire reliably during almost every γ-cycle, a robust finding established in organotypic cortex cultures [25,39,42] and in acute cortex slices [43].

Second, the profound intracellular depolarization found in neurons during up-states indicates an overall increase in network activity. However, the up-state depolarization should not be equated with a higher excitability of individual neurons, which is implicitly assumed in neuronal models that do not take intracellular membrane conductance changes into account, i.e., due to synaptic inputs [44]. On the contrary, individual neurons significantly change in how they respond to additional input during up-states [42,45,46]; this change is effected by a rather expansive combination of a decrease in neuronal input resistance [47], a shortened synaptic integration window [44], transient changes in the balance of excitatory to inhibitory (E/I) synaptic transmission [48], active dendritic conductances [49], a critical slowing down of the threshold to action potential generation [50], and other mechanisms (for further reading, see [51]). Few neuronal simulations take these changes during the buildup of network activity into account [1,2], potentially limiting insights that can be gained into these dynamical motifs from less biophysically oriented modeling.

Third, nested θ/γ-oscillations during the up-state are not blocked by the gap junction blocker carbenoxolone [52] and the activity propagates relatively fast, with a velocity >50 mm/s [53]. These findings support the view that nested θ/γ-oscillations originate in superficial layers from synaptic interactions between local interneurons and pyramidal neurons [39]. These nested oscillations are, therefore, considered to differ from the so-called slow oscillations, which, *in vivo,* can be induced by deep but not superficial layer stimulation [54]. Slow oscillations were shown

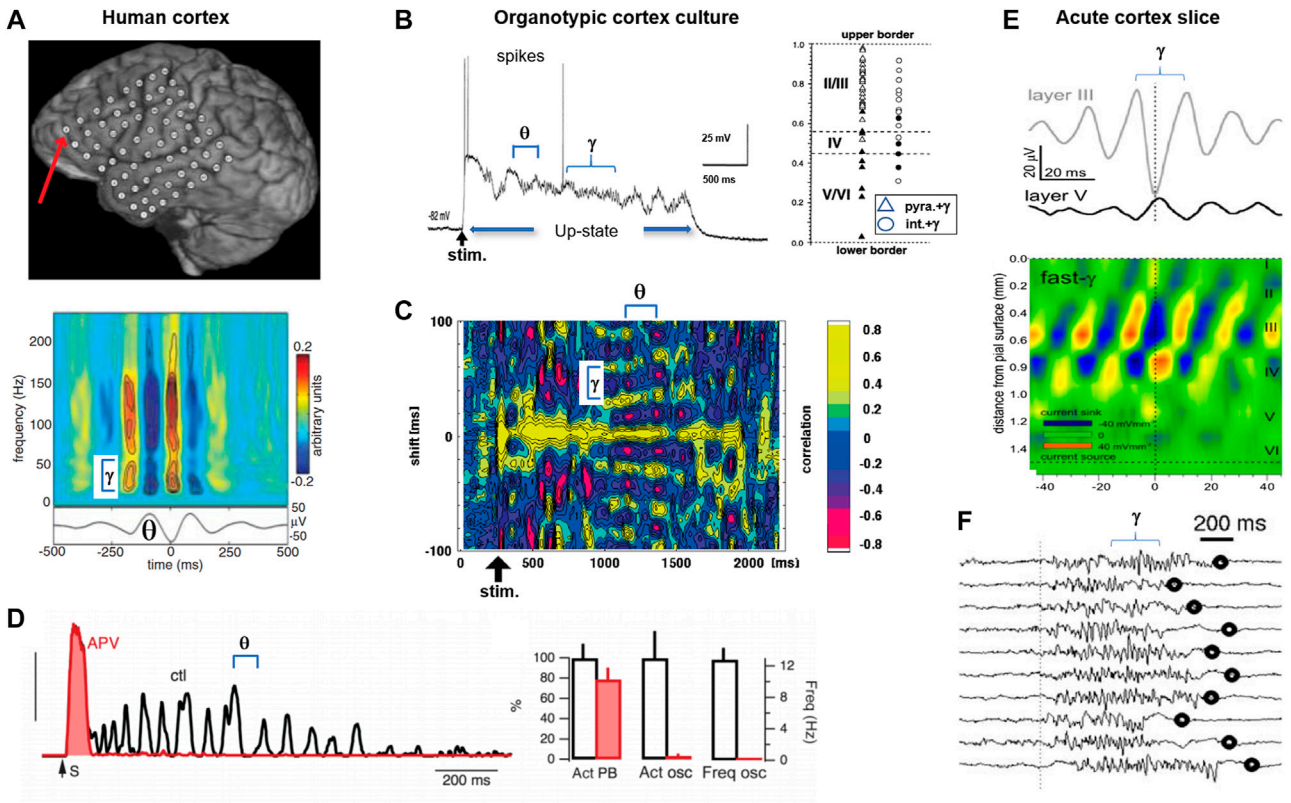

FIGURE 2 | The first and second dynamical motif of dynamical self-organization: up-state and nested θ/γ-oscillations in organotypic cortex cultures and acute cortex slices. **(A)** The human brain displaying distinct periods of nested θ/γ-oscillations at rest and during behavior. *Top*: electrode array on the cortex surface (*circles*) recording the electrocorticogram. *Bottom*: corresponding power spectrum of fast γ-oscillations (>25 Hz; *top*) phase locked over several cycles of a θ-oscillation (*bottom*) (reprinted with permission from [34]). **(B)** In mature organotypic cortex cultures, neuronal activity self-organizes into up-states with nested θ/γ-oscillations in superficial layers. *Left*: time course of the intracellular membrane potential for a pyramidal neuron in response to a microsecond-lasting, electrical shock stimulation (*stim*; *arrow*). Note self-sustained up-state with nested θ/γ-oscillations and sparse occurrence of action potentials (*spikes*). *Right*: γ-oscillations are found in pyramidal neurons (*triangles*) and interneurons (*circles*) of superficial (*open*), but not deep layers (*filled*). **(C)** Cross correlation over time in the membrane potential of two pyramidal neurons in response to electrical shock stimulation (*stim*; *arrow*). Note maintained phase locking of nested θ/γ-oscillations during the up-state with drop in γ-frequency creating a fan-out pattern (subpanels *B* and *C* modified from [39]). **(D)** Self-sustained up-states with θ-oscillations require recurrent, excitatory network connections. Blocking the excitatory NMDA glutamate receptor with the antagonist APV only leaves an initial, short-lasting direct response (organotypic cortex culture) (*red*). *Left*: population activity time course to electric shock stimulation (*S*; arrow). *ctl*: control. *Right*: APV only slightly reduces the number of up-states (*leftmost bars*) but blocks the emergence of oscillations at θ-frequency (*middle and rightmost bars*). *Act*: control (reprinted with permission from [42]). **(E)** In the acute cortex slice, γ-oscillations emerge in superficial layers (CSD analysis) (reprinted with permission from [63]). **(F)** Acute cortex slice from adult ferret with spontaneous, self-sustained period of fast γ-oscillations in the LFP (reprinted with permission from [43]; Copyright 2008 Society for Neuroscience). *Oscillation identifiers* have been added to some subpanels for clarity.

in vitro to originate in deep layers and to propagate significantly slower than θ/γ-oscillations locally, yet they were shown to contribute to up-state initiation in superficial layers [55–57].

The propensity of the isolated cortex to produce up-states and nested oscillations is demonstrated in the acute cortex slice as well, in which tissue is studied within hours after being taken from the adult brain. In the acute slice, synchronized nesting during up-states can be induced by an external, pharmacological stimulation that includes direct neuronal depolarization through excitatory glutamate receptors in combination with the neuromodulator acetylcholine (**Figures 2E,F**; [43,58,59]). Current-source density (CSD) analysis, which tracks the spatial location of neuronal current generation [60–62], demonstrates that nested θ/γ-oscillations originate in superficial layers 2/3 in both the acute cortex slice (**Figure 2E**; [63]) and the organotypic cortex culture (**Figure 3**). Developmentally, these dynamical motifs occur in organotypic cultures with a similar time course compared to *in vivo*, specifically when coculturing the cortex with midbrain regions, which provide the neuromodulator dopamine (**Figure 3**; [52]). In summary, isolated cortex preparations demonstrate the autonomous emergence of two dynamical motifs in superficial layers of the cortex: up-states and nested oscillations.

The Third Dynamical Motif of Self-Organization: Neuronal Avalanches

Until now, the two dynamical motifs of up-states and nested oscillations have been treated from the point of view of averages. In this view, an up-state is approximated as a binary transition between two network states that differ in overall activity and

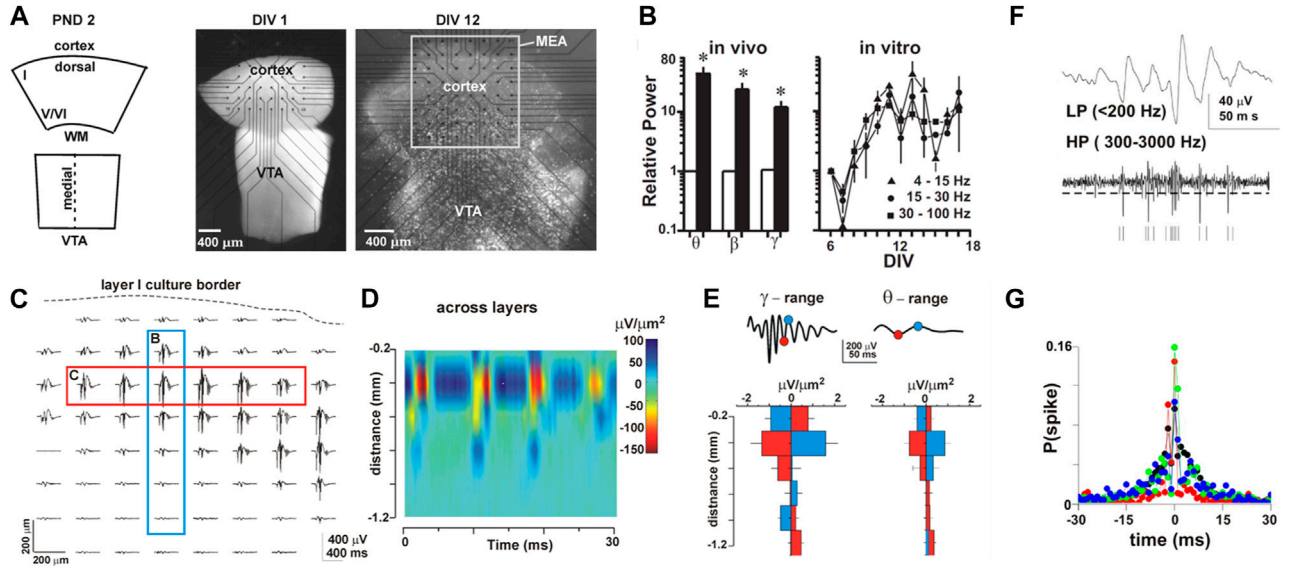

FIGURE 3 | Self-organization into nested θ/γ-oscillations in organotypic cortex cultures during the second week postnatal when superficial layers mature. **(A)** Coronal sections of the cortex and ventral tegmental area (*VTA*) are combined and grown on the MEA over two weeks in culture. *Left*: sketch of the coronal cortex slice and midline crossing midbrain region containing the VTA at postnatal day (*PND*) 1–2, when taken into culture after 1 day *in vitro* (*DIV 1*; *middle*), and about 2 weeks later (*DIV* 12; *right*). Note flattening of the culture visible by the increased transparency and expansion of the dorsal tissue on the MEA as superficial layers develop (light microscopic image). **(B)** Nested oscillations increase in power from first (*white*) to second (*black*) postnatal week *in vivo* (*left*), a developmental time course mirrored in organotypic cortex-VTA cocultures (*right*). **(C)** Spontaneous nested θ/γ-oscillations distribute along the dorsal part of the cortex within superficial layers (*red rectangle*; single culture). **(D)** Corresponding CSD (across *blue rectangle* in C) demonstrates θ/γ-oscillations to originate from synaptic sources (*sinks*) within superficial layers; CSD density with distance from the upper culture border over time. **(E)** Summary of average CSD with distance from the dorsal border for 7 cultures separated into θ- and γ-oscillation activity. **(F)** Separating the broadband LFP into a spike-information–carrying high-frequency band (*HP*) and the population-activity–containing low-frequency band (*LP*) demonstrates local spiking (vertical bars) to be phase locked to γ-oscillations. **(G)** Spike probability is highest at the negative peak of the γ-cycle (nLFP) at $t = 0$ (color code shows 4 cultures) (reprinted with permission from [52]; Copyright 2008 National Academy of Sciences).

oscillations are treated to be spatiotemporally stationary. These views are ill-equipped to capture spatiotemporal propagation in synchronized cortical activity as well as the spatiotemporal variability encountered in spontaneous or evoked instantiation of synchronous activity.

In contrast, the third dynamical motif of self-organization, neuronal avalanches [53], emphasizes both spatiotemporal propagation and variability in cortical synchronization. In that respect, avalanches are related to the spatially compact, wave-like propagation of cortical activity [64–66] as well as the concept of "synfire chains," spatiotemporally selective cascades of neuronal firing proposed by Abeles [67]. Neuronal avalanche dynamics introduces several major concepts with respect to propagation and variability in cortical synchronization. First, avalanche dynamics quantifies synchronization within a period of duration Δt and successive occurrences of synchronization in near future time periods. It, therefore, covers "instantaneous" and propagated synchrony (see **Figure 4**). Second, avalanche dynamics exhibits scale-invariance in space and time, which introduces power laws as the statistical measure of variability and the concept of critical branching (see **Figures 4**, **5**). Third, avalanche dynamics allows for the decomposition of propagated synchrony into "coherence potentials," a previously unknown concept in cortical dynamics for information transfer (**Figure 6**). Fourth, avalanche dynamics lifts the idea of *one* particular spatiotemporal pattern to that of "avalanches of avalanches," which serves as a set of very specific predictions of how spatiotemporal synchronization events in the cortex are linked to each other in sizes and time (see **Figure 11**). Finally, avalanche dynamics introduces quantitative and absolute measures to study optimization in cortical networks (see **Figure 12**). We will elaborate on these major conceptual changes in studying cortical synchronization in the following sections.

We start with the basic definition of avalanches using the comparative *in vivo* and *in vitro* study on the developmental emergence of neuronal avalanches in superficial layers of the cortex (**Figures 3**, **4**). Gireesh and Plenz [52] used multielectrode array (MEA) recordings to demonstrate the embedding of avalanches into ongoing nested oscillations. Using a simple threshold crossing approach, they extracted the time and amplitude of negative peak deflections in the LFP (nLFP) at each electrode in order to identify the location, time, and size of short-lasting, synchronized activity in a local group of neurons (**Figures 3F,G**; **Figure 4A**; [11, 74]). Contiguous time periods with nLFPs were defined as avalanches (**Figure 4A**, *bottom*), which resulted in a large variety of different patterns. The size of these patterns, here defined as the absolute sum of nLFPs distributed according to a power law up to a cutoff, serves as the hallmark of neuronal avalanches (**Figure 4C**). This power law was also found when defining avalanche size by the number of

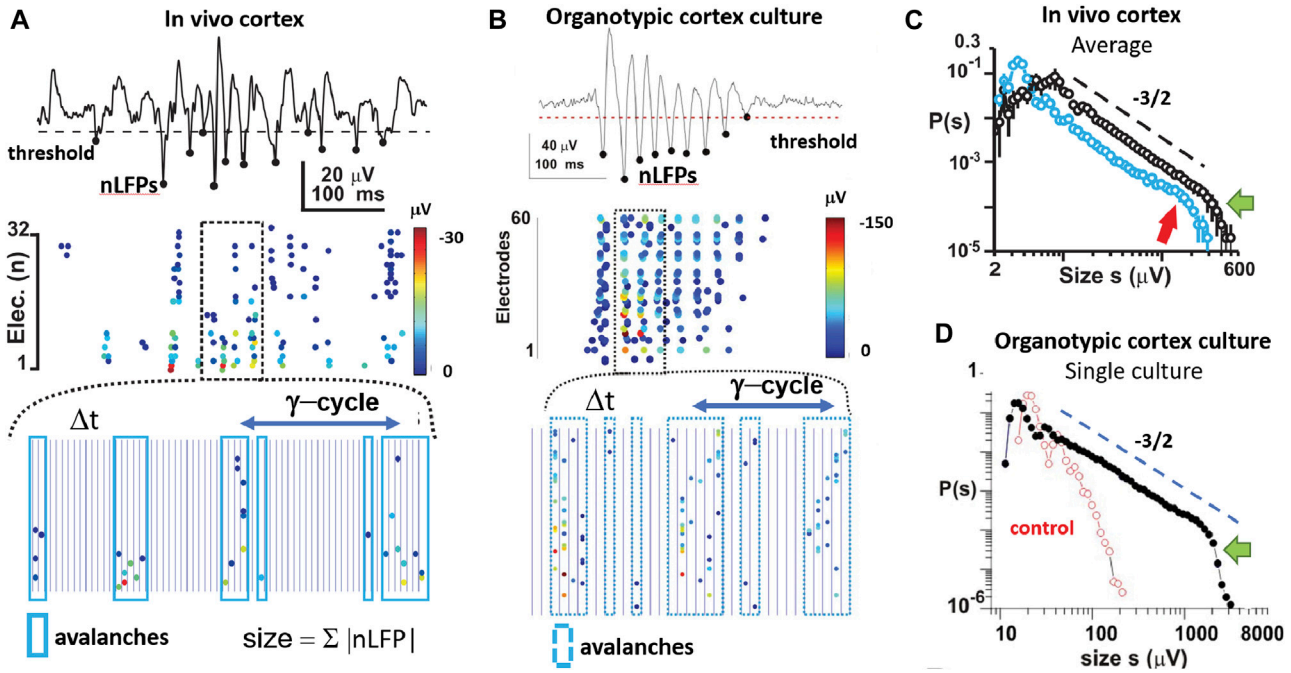

FIGURE 4 | The third dynamical motif of self-organization: neuronal avalanches embedded in nested oscillations. **(A)** Nested θ/γ-oscillations in the superficial layer of a 2-week-old rat *in vivo* organize as neuronal avalanches that predominantly emerge at oscillation cycles. *Top*: single cortical electrode with continuous LFP from which negative peak deflections (nLFP; *filled circles*) are identified after threshold crossing. *Middle*: corresponding raster of nLFPs on the full 32-MEA exhibiting columnar, variable bouts of synchronization in space and time. nLFP peak amplitudes are color coded. *Bottom*: expanded view of identified avalanches (*blue rectangles*) during each γ-oscillation period plotted in discrete time steps of duration Δt (*vertical lines*). Size of an avalanche is defined as the sum of absolute nLFP amplitudes within each avalanche. **(B)** As in *A* but for a transient γ-oscillation in an organotypic culture. **(C)** At the end of the second week postnatal (*black*), avalanches distribute in size from 10 to 300 μV followed by a cutoff (*green arrow*; $n = 7$ animals). *Broken line*: slope of −3/2 as guide to the eye. Size distribution is slightly bimodal (*red arrow*) at the beginning of the second week postnatal (*blue*; $n = 5$ animals). **(D)** Power law in avalanche size distribution for a single culture and exponential size distribution obtained from time-shuffled controls in which spatial and temporal correlations among nLFPs are destroyed (reprinted with permission from [52]; Copyright 2008 National Academy of Sciences).

threshold crossing electrodes [52], which approximates the spatial extent of avalanches [68]. The embedding of avalanches in nested oscillations clearly emerges in cortex-VTA cocultures, with avalanche size distributions exhibiting a precise power law up to the cutoff (**Figures 4C,D**). These findings established that the complex developmental signature of avalanches and nested oscillations *in vivo* develops autonomously in organotypic cortex cultures with a similar developmental time course; i.e., it is established toward the end of the second week postnatal, in the absence of any structuring sensory input or motor output (**Figures 4C,D**). The precise match of the power law in avalanche sizes with a slope of −3/2 that emerges from the variability of nested θ/γ-oscillations is not a statistical coincidence. Besides both dynamical motifs being highly sensitive to fast inhibition via the $GABA_A$ receptor and slow excitation via the NMDA-glutamate receptor, this coexistence requires fine tuning via the dopamine D_1 receptor. Specifically, when the dopamine D_1- but not D_2-receptor was blocked, nested oscillations continued to emerge, yet the resulting nLFP cascades now exhibited a much steeper size distribution [52]. This regulation of avalanche size distributions to a slope of −3/2 as a function of NMDA/D1 receptor costimulation has been confirmed for superficial layers in acute slices of the prefrontal cortex taken from two-month-old adult rats [69,70] (cf. **Figure 11**). Recent analysis *in vivo* in the prefrontal cortex of awake nonhuman primates further confirmed this precise relationship between avalanche dynamics and γ-oscillations [71].

We note that the definition of neuronal avalanches, originally introduced by Beggs and Plenz [53] using the LFP, requires that each local site exceeds a minimal activity threshold. Using a neuronal network model, Poil et al. [72] adopted a scheme in which the summed spiking activity within Δt of the finite-size network is required to exceed a population threshold. This latter definition is very similar to a threshold applied to the LFP, as will be argued in more detail below (cf. **Figure 13**). It potentially introduces linear terms in certain scaling relationships as pointed out by Villegas et al. [73]. As for statistical tests demonstrating the presence of a power law in avalanche size distributions, we refer to the work of Yu et al. [68] for a more detailed discussion.

To summarize, *in vivo* experiments in rodents and nonhuman primates, as well as developmentally well-controlled *in vitro* experiments using organotypic cortex cultures and acute cortex slices, demonstrate a precise regulation between up-states, nested oscillations, and neuronal avalanches that involves fast GABA-mediated inhibition, slow glutamate-mediated excitation, and the neuromodulator dopamine.

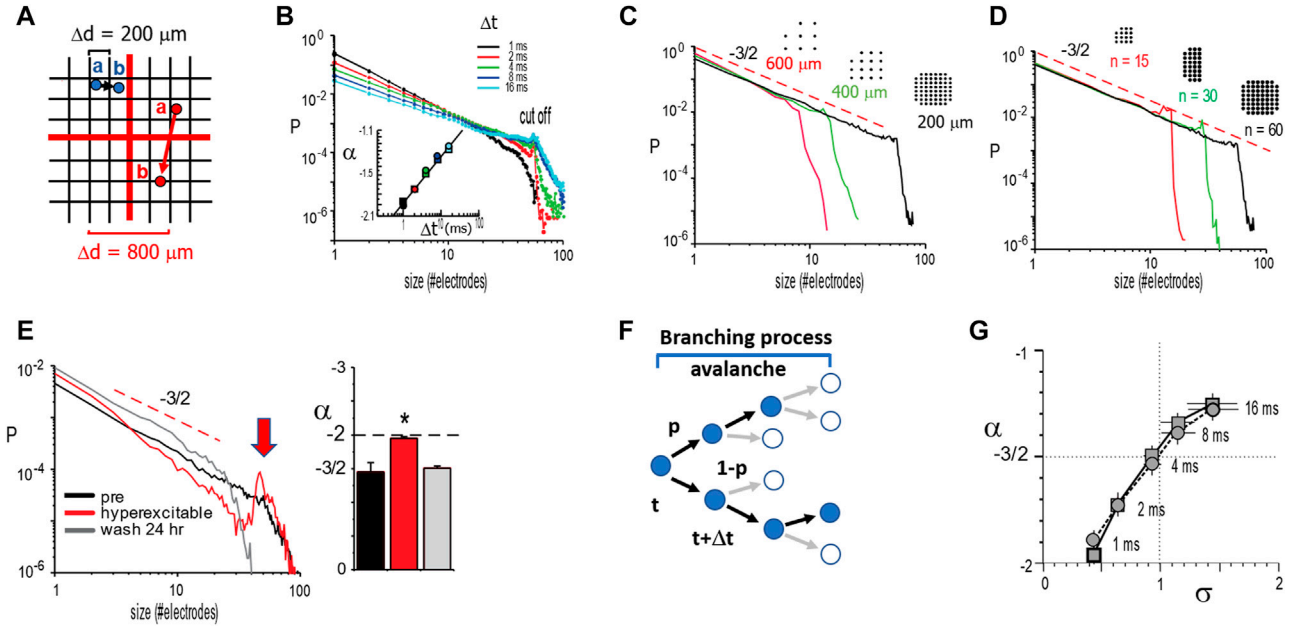

FIGURE 5 | Temporal and spatial scaling links size distribution slope −3/2 to a critical branching parameter for neuronal avalanches. **(A)** When identifying spatial propagation of activity over time (a → b; *blue* and *red* circles), the distances between neighboring electrodes on a multielectrode array introduce a discrete spatial scale Δd. For different spatial scales (grids: *black*: 200 μm; *red*: 800 μm) and a finite propagation velocity <*v*>, the time Δ*t* to wait in order to identify propagation toward an electrode is approximately Δt ≅<v>*Δd. **(B)** In organotypic cortex cultures, at fixed Δd = 200 μm, an *increase* in Δ*t* results in a power law of avalanche size with a *shallower* exponent *α* due to preferential concatenation of avalanches (avalanche size based on the number of active electrodes). Note the absence of any change in the power law form itself. *Inset*: average change in α with Δt over all cultures and size based on electrodes (*circles*) or nLFP amplitudes (*squares*). **(C)** A change in Δ*d* by accordingly omitting electrode rows and columns (*insets*) maintains the size distribution slope of −3/2 (*broken line*) if correspondingly increasing Δt to Δt ≅<v>*Δd. **(D)** Finite-size scaling using compact subarrays (*insets*) only affects the power law cutoff, but not power law slope *α*. *Broken line*: slope of −3/2. **(E)** Reducing inhibition pharmacologically using picrotoxin (PTX) leads to hyperexcitable neuronal cultures, resulting in a "supercritical" phenotype with an initial, steep slope close to ~−2 and a preference for large, i.e., system-wide propagated, population events (*red arrow*). *Right*: quantification of change in *α* from −3/2 → −2 when reducing inhibition. **(F)** The unfolding of an avalanche in a network viewed as a branching process. In this sketch, activity at an initial site at time *t* can induce activity at another site with probability *p* or fails to induce activity at a new site with probability 1−p. Each site exhibits a potential branching to two new sites. **(G)** Experimental demonstration that avalanche dynamics crosses the critical point (σ, α) = (1,−3/2) predicted for a critical branching process with change in Δt at fixed Δd. Avalanche size definition (*squares, circles*) as in *B*, inset (subpanels *B–E*, *G* reprinted with permission from [53]; Copyright 2003 Society for Neuroscience).

Temporal and Spatial Scaling Links Size Distribution Slope −3/2 to a Critical Branching Parameter for Neuronal Avalanches

The identification of avalanches and their implication for SOC has been a particular challenge from an experimental point of view. Besides the structural constraints of superficial layers and developmental period that must be considered, there are additional aspects specific to the emergence of neuronal avalanches themselves that are of importance. These points will be addressed in the following sections. The original identification of neuronal avalanches [53] involved numerous scaling controls to demonstrate that power laws identified in propagated neuronal activity were robust to obvious choices in the experimental setup. Specifically, tracking the spatiotemporal spreading of an avalanche using discrete, spatial sensors such as MEAs requires the appropriate choice of a discrete time interval Δ*t* (**Figure 5A**). This choice of Δ*t* is imposed by the average, finite propagation velocity <*v*> for neuronal activity in the system and the introduction of a discrete sampling distance of Δd by the MEA. Three observations laid the groundwork that established the power law in avalanche sizes with a slope $\alpha = -3/2$. First, increasing Δ*t*, while keeping Δ*d* constant, led to a shallower slope *α* without change in power law shape. This dependency of $\alpha(\Delta t)$ itself is approximated by a power law, allowing for scaling collapse *in vitro* (**Figures 5B,C**) and *in vivo* [74]. Second, when changing Δ*d* and accordingly adjusting Δ*t* =<*v*> * Δ*d*, a robust size exponent of $\alpha = -3/2$ was obtained (**Figure 5C**). Third, the cutoff of the power law was simply a function of the finite MEA size and did not change *α* itself (**Figure 5D**). Importantly, when cultures were made more excitable, by reducing inhibition in the system using pharmacological means, avalanche size distribution changed from a power law to a bimodal distribution exhibiting an initial steep slope close to −2 and a pronounced system size peak indicative of all-or-none, system-wide population events (**Figure 5E**). This latter separation into local, nonpropagated events and large system-wide synchronization exhibits the phenotype of a first-order discontinuous phase transition. We will point out in detail in subsequent sections that these scaling operations are not robustly observed in dissociated culture experiments, where an increase in Δ*t* typically *steepens* the initial slope and uncovers a bimodal cascade size distribution (see below for details; cf. **Figure 13**), which is more in line with a hyperexcitable system.

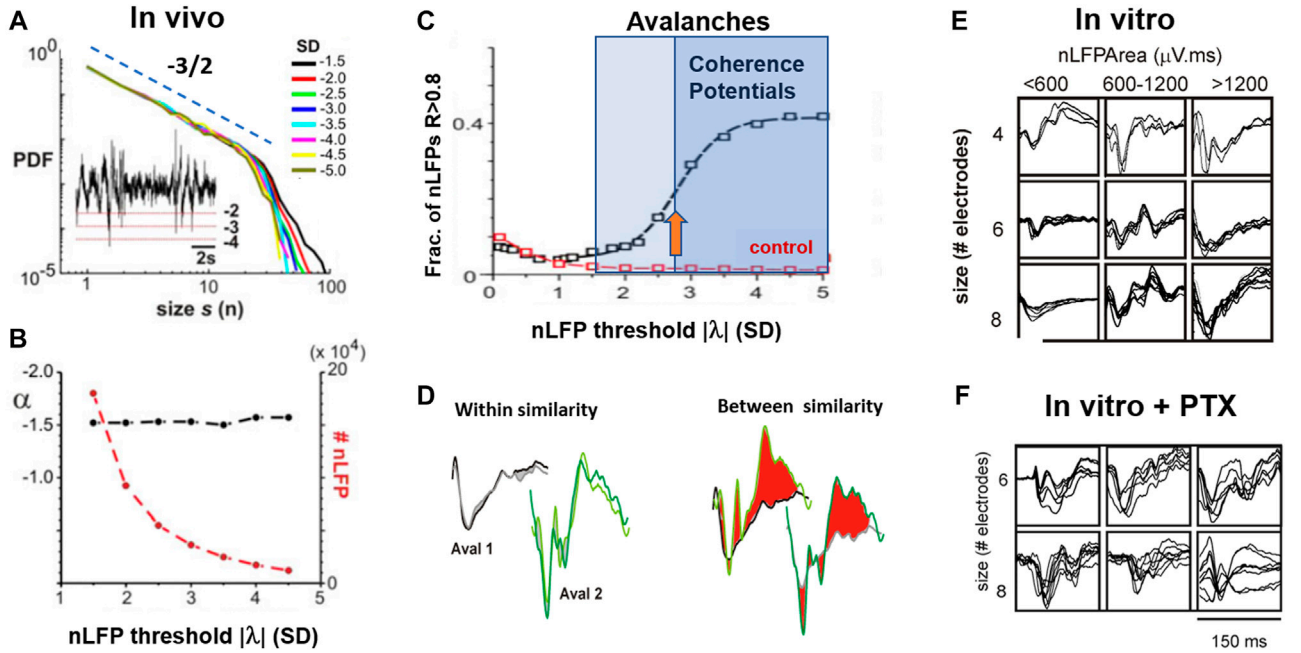

FIGURE 6 | The fourth dynamical motif of self-organization: The coherence potential. **(A)** LFP avalanches from ongoing activity in nonhuman primate show a robust power law in sizes for a range in threshold λ at which nLFPs are detected. *Inset*: example LFP trace and nLFP detection for three different values of λ. *SD*: standard deviation. *Broken line*: slope of −3/2. **(B)** The number of nLFPs >λ drops several orders of magnitude with an increase in λ, while the power law in sizes remains robust with slope α close to −3/2. **(C)** The similarity in nLFP waveforms within avalanches rapidly increases for λ> ~2.7 SD (*orange arrow*). This threshold-dependent sigmoidal increase in within-nLFP similarity identifies a relatively small number (~20%) of nLFPs that constitute coherence potentials (cf. *B*). *Control*: expected change in similarity after random temporal shifts in the LFP. **(D)** Complex nLFP waveforms within a coherence potential are highly similar. Example comparison for two subsequent coherence potentials at two sites. Within similarity (*gray/black*; *light/dark green*) is high for each coherence potential (*CP*), whereas between similarity is very low with large waveform deviations highlighted in *red* for visual contrast. **(E)** Coherence potentials spontaneously form *in vitro* in organotypic cultures. Overplot matrix of waveform examples for coherence potentials of size four to eight for nLFP areas in three size categories. **(F)** Under disinhibited conditions (*PTX*), coherence potentials are absent (reproduced with permission from [11]).

The original work by Beggs and Plenz [53] provided the first insights into a critical branching process as a proxy to understand avalanche dynamics in cortical networks as well. A memoryless branching process captures the probability of an initial event to spawn future events at new sites [75]. The corresponding branching parameter, σ, quantifies the average ratio of next generation to the currently active sites (**Figure 5F**). For random neighbors and $\sigma = 1$, the resulting size distribution from such an unbiased or critical branching process exhibits a power law with a slope of −3/2 and can be analytically linked to the self-organized critical sandpile [76]. In line with these basic expectations, it was found that σ is close to one and $\alpha = -3/2$ for neuronal avalanches at $\Delta t = \langle v \rangle^* \Delta d$ (**Figure 5G**). These findings introduced branching processes as a promising entry point to study avalanche generation.

These original scaling operations for avalanches involved >10 h of continuous recordings *in vitro*, which is difficult to achieve under standard experimental conditions. Recently, Miller et al. [71,77] extended this scaling analysis of LFP-based avalanches. They identified a scaling exponent of two for an avalanche waveform and a mean size vs. duration relationship in line with predictions for a critical branching process. We also note that LFP avalanches show nearest-neighbor propagation and typically involve no loops [68]. The precise identification of scaling exponents for neuronal avalanches and the conditions under which they are robust is currently an intense field of research. Several alternative processes, both critical and noncritical, have been suggested to produce size exponents close to −3/2 (for further reading, see, e.g., [78,79]). In the following sections, we will focus on additional dimensions of neuronal avalanche dynamics that go beyond these basic scaling relationships. Importantly, the presence of a power law in avalanche sizes and a critical branching parameter of one is linked to several distinct aspects in the emergence and propagation of neuronal activity.

The Fourth Dynamical Motif of Self-Organization: The Coherence Potential

In the previous section, the scaling relationship between the temporal and spatial resolution was reviewed. The third free parameter in assessing avalanche dynamics is the threshold, λ, at which a local site is considered to carry significant activity. For LFP-based avalanches, this threshold is typically chosen to be around three SD of the fluctuations in activity at each site and it has been shown in numerous studies that the presence of a power law is rather robust to the threshold chosen, assuming that it is reasonably outside of baseline noise [53,74,80]. Yet, when

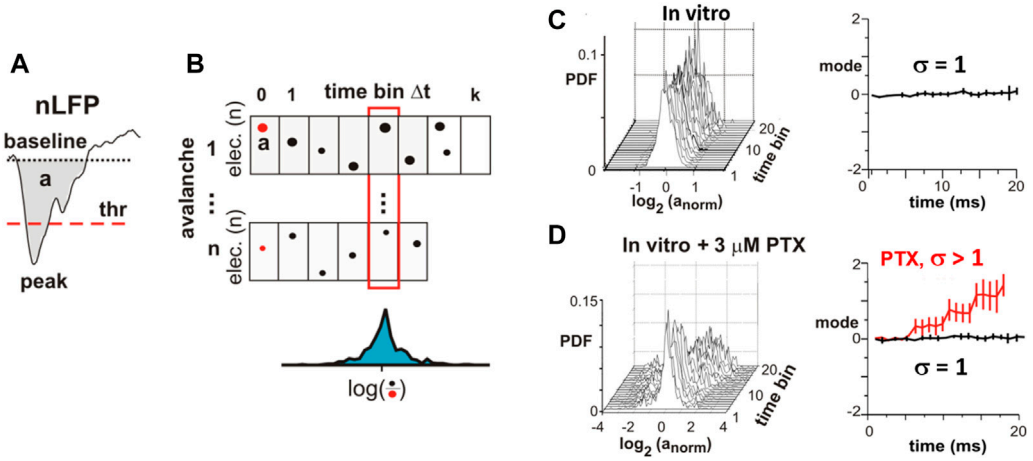

FIGURE 7 | Critical branching parameter estimation for coherence potentials. **(A)** Area *a* and waveform of a local nLFP identified by threshold (*thr*) crossing. **(B)** nLFP areas normalized by the initial nLFP area (*red dots*) distribute around a median value (*blue distribution*) after *n* time bins of duration Δt. **(C)** *In vitro* avalanches reveal distribution around the log(1) = 0 mode demonstrating that, as an avalanche unfolds, nLFPs on average neither grow nor decay in the area in line with expectations for a critical branching process with $\sigma = 1$. **(D)** In organotypic cortex cultures that are made more excitable by slightly reducing inhibition (*PTX*), an expansion of the nLFP area with time from cascade initiation is found in line with the prediction for a supercritical branching process with $\sigma > 1$. These experiments demonstrate that a transition from a power law in sizes to a bimodal size distribution under reduced inhibition changes the system from critical to supercritical dynamics (reproduced with permission from [11]).

systematic evaluations of threshold effects were conducted within a regime of robust power law scaling, it was found that avalanche dynamics implicitly contains a local synchrony threshold that identifies a subclass of avalanches *in vivo* and *in vitro*: the coherence potential (**Figure 6**; [11,81]). Coherence potentials constitute avalanches with nLFPs above a minimal amplitude threshold, typically ~3 SD, of the ongoing LFP fluctuations [82]. Both avalanches and coherence potentials form power laws in size distributions that are indistinguishable by simple thresholding (**Figure 6A**). Only when the waveform of nLFPs is explicitly taken into account is a sigmoidal function identified separating the high-fidelity activity propagation regime that constitutes the relatively small number of coherence potentials from that of all other avalanches (**Figures 6B–D**). The identity of an nLFP waveform correlates with the identity of local spike sequences across different cortical locations [81], suggesting that coherence potentials confer the exact temporal activity of local neuronal firing over wide distances of the cortex. In the human ECoG, coherence potentials were found to initiate finger tapping [83]. The emergence of coherence potentials in cortical networks with avalanche dynamics has been compared to the emergence of "gliders" in cellular automata and hypothesized to be a vehicle of information transfer within the cortex at the network level [11].

The waveform identity in coherence potentials could be expanded to area identity *in vitro* and *in vivo*. By grouping nLFPs in coherence potentials into different size categories, waveform similarity within these categories was established and shown to break down when the network was disinhibited (**Figures 6E,F**). This demonstrates that coherence potentials are actively regulated by the network through the E/I-balance. Coherence potentials were shown to demonstrate initial group size conservation as well. Specifically, it was demonstrated that the area of nLFPs, which participate in a single coherence potential, does not grow nor decay on average as the coherence potential unfolds, a finding that is independent of the size of the initiating nLFP (**Figures 7A–C**). This property of preserving the local group size initiating an avalanche was lost when the cortex was even mildly disinhibited, upon which propagated activity displayed a within-cascade explosive growth (**Figure 7D**). This particular approach extends the original identification of the critical branching parameter [53], which was estimated by the ratio between the number of nLFPs in the second ("descendants") and first ("ancestors") time bins of an avalanche. The analysis in **Figure 7** is more complete by including an nLFP area and waveform and considers all avalanches in their full duration. The critical branching parameter is reflected in the finding that normalized distributions have a stable mode of 1, i.e., log(1) = 0, for up to 20 ms of propagation, which typically covers the full area of recording. The area of the nLFP correlates tightly with the number of neurons firing at the corresponding electrode *in vivo* and *in vitro* [11]. Therefore, the critical branching parameter established for coherence potentials demonstrates a conservation law, specifically in which the initiating group size determines all group sizes that emerge within the coherence potential. This complements the finding that spike sequences at different locations within a coherence potential are similar [11].

Oscillation-Synchronization Transition and Neuronal Avalanches: Simulations

Over the last decade, several models have explored these challenging relationships between oscillations, neuronal avalanches, coherence potentials, and critical dynamics. The group of Linkenkaer-Hansen [72,84] demonstrated the emergence of avalanches with $\alpha \cong -3/2$ embedded in

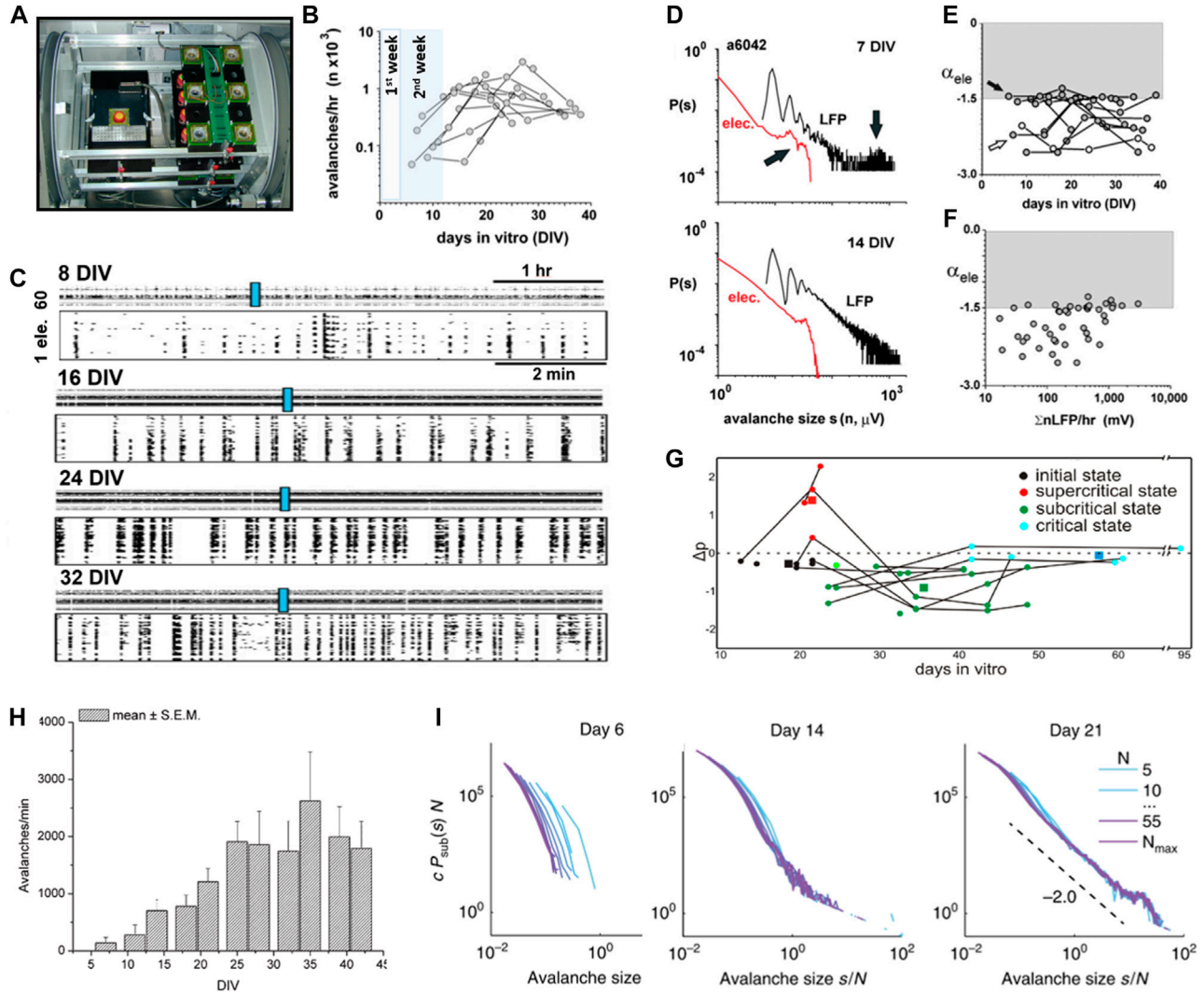

FIGURE 8 | Developmental time course for the self-organization of neuronal avalanches in isolated cortex preparations. **(A)** Overview picture of a custom-made incubator for long-term recordings of individual organotypic cortex cultures on an MEA in a chronic, sterile chamber with head stage (*left*) and off-recording storage racks (*right*). For details, see [166]. (reproduced with permission from [167]). **(B)** In organotypic cortex cultures, avalanches are absent during the first postnatal week *in vitro*, but increase in rate during the second and third postnatal weeks in line with *in vivo* maturation of superficial layers. *Highlighted periods*: equivalent postnatal week *in vivo* when cultures are taken from pups at postnatal day 1–2. **(C)** Raster plots of spontaneous nLFP increase in complexity from the first to fifth week (*rows*) postnatally *in vitro*. *Top of each row*: 5 h raster. *Bottom of each row*: higher temporal resolution for periods indicated by the *blue rectangle*. **(D)** Example of early (7 DIV) bimodal size distribution (*top*) and second week power law size distribution (*bottom*) in a single organotypic cortex culture. Sizes are defined as the number of active electrodes (*red*) or summed nLFP (*black*). **(E)** Most organotypic cortex cultures achieved $\alpha = -3/2$ within 2 - 3 weeks *in vitro* (*arrow*), except for one (*open circle*). Time course in avalanche size distribution slope α for individual organotypic cortex cultures. **(F)** The emergence of slope $\alpha = -3/2$ correlates with a ~10x increase in LFP activity. (*B–F* modified and reproduced with permission from [94]). **(G)** In dissociated cultures taken at PND 0 - 1, power laws tend to be reported after ~4 weeks in culture (reproduced under CC-NY license from [98]). **(H)** Neuronal activity reaches a steady state in dissociated cortex cultures after ~4 weeks *in vitro* (reproduced with permission from [107]). **(I)** Transition of avalanche size distributions from exponential to bimodal in dissociated cortex cultures (reproduced under CC-NY license from [99]).

α-oscillations (~12 Hz) in an E/I-balanced network model. They compared this to a critical parameter of $\kappa = 1$ and the emergence of long-range temporal correlations (see **Figure 12**) in human MEG recordings demonstrating nested oscillations [72] (see also [85]). The coemergence of oscillations and neuronal avalanches has been demonstrated in small systems to result from temporal correlations between large avalanches due to finite-size effects [86]. It is an open question how such boundaries could be established in superficial cortical layers. When neuronal avalanches coemerge with oscillations, neural networks achieve high cost efficiency; that is, they balance their need for moderate synchronization with high information capacity [87]. Recent models have combined system-wide synchronization and hysteresis, i.e., to support an oscillation cycle, with structural heterogeneity, i.e., to capture the variability observed in avalanches, in order to arrive at the coemergence of

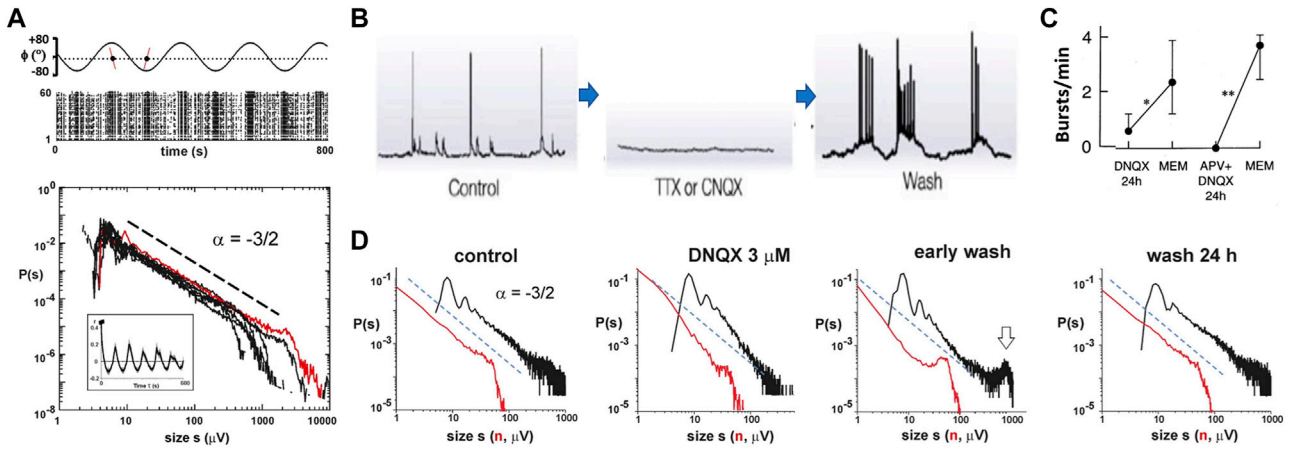

FIGURE 9 | Separation of time scales and homeostatic regulation of neuronal avalanches *in vitro*. **(A)** Power law in avalanche sizes is preserved during externally induced slow changes in neuronal activity. *Top*: periodic tilting (ϕ) of the sealed, sterile chamber, which contains the organotypic culture grown on the MEA, alternates culture exposure to feeding medium or air. This slowly drives the network through the corresponding large changes in nLFP activity visualized in the corresponding raster plot. *Bottom*: power law in avalanche sizes for $n = 7$ cultures under conditions of periodic tilting. *Red*: distribution from single culture shown in the raster plot. *Inset*: average autocorrelation of population activity demonstrating strong correlations from periodic tilting. **(B)** Intracellular recording demonstrating rebound hyperactivity when neuronal activity is suppressed in dissociated cortex cultures (reproduced with permission from [101]). **(C)** Increase in rebound population bursts after 24 h of excitatory glutamate receptor suppression in organotypic cortex cultures (reproduced with permission from [100]). **(D)** Homeostatic regulation of avalanches in organotypic cortex cultures. *Control*: size distribution before manipulation. *DNQX*: size distribution during 24 h of reducing excitatory synaptic transmission. *Early wash*: bimodal size distribution demonstrating hyperexcitability after wash out of DNQX. *Wash 24* h: homeostatic return to avalanche dynamics before pharmacological manipulation. Distributions are based on 1 h recordings each from a single culture (*A*, *D* reproduced with permission from [11]).

oscillations and scale-invariant avalanche statistics (e.g., [88]), while others have added an oscillating extinction rate to a continuous-time branching process using perturbative field theory [89]. Coherence-potential–like activity and its potential computational advantages have been explored by the Gong group [90–92]. The many experimentally established dimensions of neuronal avalanches provide a rich testing ground to study the role of SOC in cortical information processing both experimentally and in network simulations. In the following sections, we will provide additional key experimental aspects of neuronal avalanche dynamics that go beyond size and synchronization scaling aspects.

Developmental Self-Organization of Robust Avalanche Dynamics in Organotypic Cortex Cultures

The previous sections demonstrated the emergence of neuronal avalanches around the second week postnatally in culture and in adult slices when tested in isolation. It is well understood that cortical development *in vivo* involves intrinsically maturing cellular properties and microcircuits in a complex interplay with structuring sensory inputs and motor outputs [17]. Many of these intrinsic embryonic and neonatal dynamics are found to arise autonomously in isolated cortex preparations [16,93]. Yet, so far, only few studies have reliably covered the time course of avalanche emergence during development over prolonged periods. In a first study of postnatal maturation of avalanches *in vitro*, Stewart and Plenz [94] grew individual organotypic cortex cultures on a planar MEA in sterile chambers over many weeks (**Figure 8A**). Spontaneous LFP activity emerged toward the beginning of the second week postnatally with a typical bimodal distribution in cascade sizes (**Figures 8B–D**) indicating a bias toward system-wide population bursts before the time of superficial layer maturation. During the end of the second week, stable power laws in avalanche activity emerged, particularly in those cultures that reached a high level of spontaneous activity and intermittent synchronized activity (**Figures 8B–F**). Given the late development of superficial layers and the well-known preponderance of deep-layer gap–junctions during the first week postnatal [95], the initial bimodal distribution in cascade sizes might reflect system-wide deep-layer synchronization supported by extensive gap–junction coupling [96], in turn potentially facilitated by transient hyperconnectivity that reduces toward the end of the second postnatal week *in vivo* [97]. The ability of the young cortex to express neuronal avalanches toward the end of the second week postnatally was recently confirmed for superficial layers in young acute cortex slices [70].

A second developmental study followed avalanche emergence in dissociated cortex cultures grown on MEAs, starting with neonatal cortex tissue around postnatal day (PND) 0–1 [98]. This study described an initial bimodal size distribution as well, characterized as "supercritical," followed by a pronounced "subcriticality" and, eventually, after more than 5 weeks in culture, a "critical" condition characterized by stable power laws in size distribution (**Figure 8G**). While both organotypic and dissociated cultures capture an initial bimodal activity state, the developmental time course in dissociated cultures appears to be delayed by more than three weeks with respect to the buildup of neuronal activity (**Figure 8H**) and power law formation when compared to *in vivo* [52]. Recently, Levina and Priesemann [99] showed that the bimodal distribution in avalanche sizes is maintained in dissociated cultures over long periods,

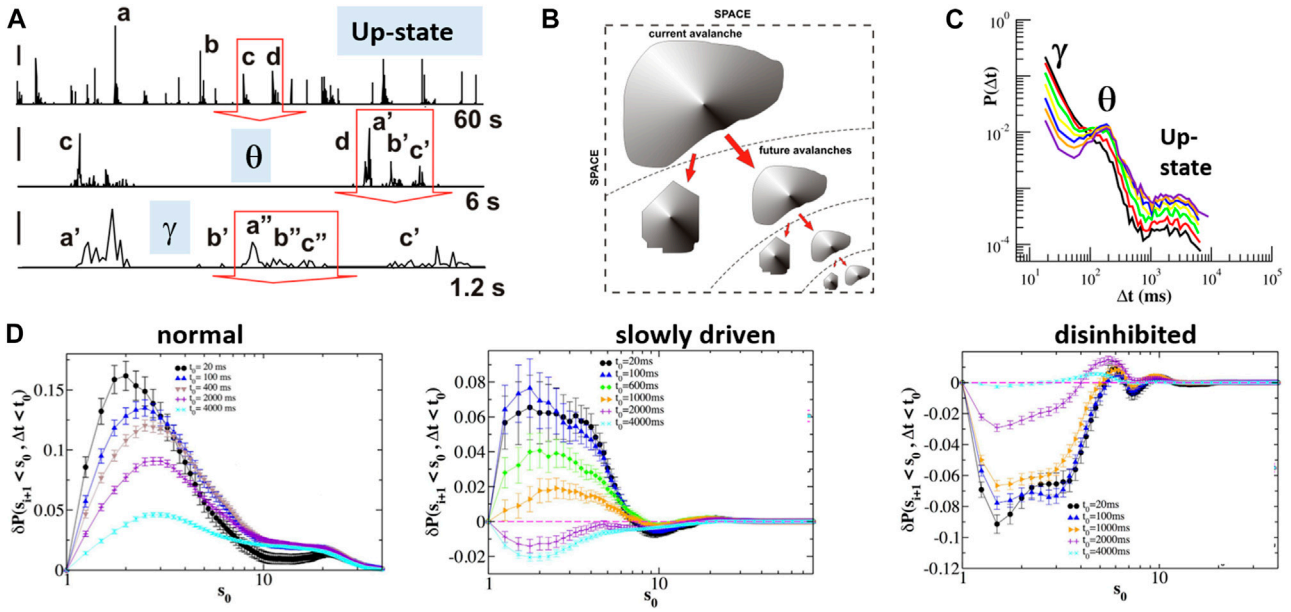

FIGURE 10 | Size-dependent nesting in the temporal self-organization of neuronal avalanches. **(A)** Time course of integrated avalanche activity at three different resolutions. Note the presence of intermittent bursts of successively smaller size [e.g., (*a, b, c, d*)] that are recursively embedded at smaller time scales [e.g., *d*-> (*a′*, *b′*, *c′*); b′-> (a″, b″, c″)]. *Red arrows* indicate the zoomed-in period from larger time scale (single organotypic culture; slowly driven; cf. **Figure 9A**). Labels place each time scale within the corresponding up-state and nested oscillation regimes. **(B)** Sketch of size-dependent nesting of avalanches begetting future avalanches (*A, B* modified and reproduced with permission from [11]). **(C)** Quiet time distribution of avalanches revealing power law decay with θ-oscillation peak and indicated γ-oscillation and up-state regime (organotypic cortex cultures) (modified and reproduced under CC-BY license from [103]). **(D)** Quantification of the dependency in preavalanche size and successive quiet time. Avalanches beget future avalanches (*left*) absent driving and during periodic, slowly driven condition (*middle*). This relationship is reversed in disinhibited cultures (*right*). The *Y*-axis displays the probability that the next avalanche within observation window t_0 is smaller given size s_0 of the current avalanche (reproduced under CC-BY license from [105]).

questioning the robustness of power laws identified by previous studies for that system (**Figure 8I**; see also below).

These developmental studies of cortical tissue in isolation suggest distinct differences in neuronal avalanche emergence between organotypic and dissociated cortex cultures, with the latter demonstrating a delayed maturation time course compared to *in vivo* and a tendency of bimodal size distributions. In contrast, avalanche emergence in organotypic cortex cultures matches that of the *in vivo* development with respect to layer location and robust power law scaling.

Separation of Time Scales and Homeostatic Regulation of Neuronal Avalanches

A separation of time scales, in which the time course of driving the system is slow enough as to not interfere with the fast avalanching process itself, is of essence in some models of SOC (e.g., [8]). This concept was tested in organotypic cortex cultures grown individually in sterile, closed chambers, while the chamber is tilted periodically. This approach periodically submerges the culture in a liquid culture medium ("feeding") followed by exposure to normal air ("breathing") and slowly drives the system through concomitant, large changes in neuronal population activity (**Figure 9A**, *top*; [11]). The resulting avalanche size distributions were power law distributed despite strong common, external triggers from the change in environmental condition (**Figure 9A**, *bottom*). In a second series of experiments, the well-established effect of rebound activity and rebound bursts after prolonged periods of suppression in excitatory synaptic transmission (**Figures 9B,C**; [100,101]) was used to study the robustness of avalanche dynamics. Excitatory synaptic transmission was mildly reduced in organotypic cultures by adding a low amount of the fast glutamate receptor antagonist, DNQX, to the culture medium for 24 h. This reduction in excitatory transmission steepened the distribution in cascade sizes. Importantly, after removing the "brake" on excitatory transmission, cascade size distributions rapidly became bimodal with an initial steep slope close to −2, but autonomously recovered within 24 h toward the power law distribution with a slope of −3/2 observed prior to the perturbation (**Figure 9D**; [11]). These experiments demonstrate homeostatic regulation of avalanche dynamics from a supercritical to a critical state in the absence of any structuring external inputs. A recent study by Ma et al. [102] demonstrated recovery to power-law–distributed avalanches during monocular deprivation *in vivo* over the course of several days, suggesting that recovery can be initiated from the subcritical phase as well.

Size-Dependent Nesting in the Temporal Self-Organization of Neuronal Avalanches

Population activity that spontaneously forms in isolated cortex preparations has been typically described as intermittent bursts of variable length, as well as variable intensity,

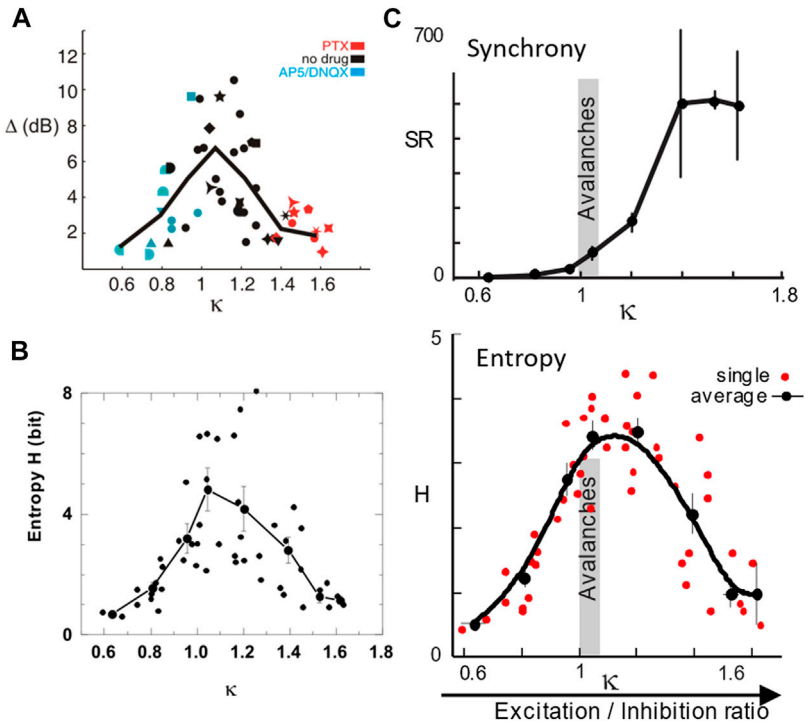

FIGURE 11 | The E/I balance is a control parameter for the emergence of avalanches. **(A)** The dynamic range Δ is maximized when avalanche size distributions are closest to a power law. The parameter κ quantifies the Kolmogorov–Smirnov deviation at 10 equidistant steps of the actual cumulative size distribution from that of a power law [108,109]. When $\kappa = 1$, the distribution is a power law, whereas $\kappa > 1$ for a bimodal distribution and $\kappa < 1$ for an exponential distribution. **(B)** Information capacity is maximized close to $\kappa = 1$. **(C)** Synchronization exhibits a phase transition at $\kappa = 1$ (*top*) where the entropy of synchronization is maximal (*bottom*) and total synchronization is still orders of magnitude lower than that of the hyperexcitable regime for $\kappa > 1$. *A–C* are derived from LFP avalanches measured in organotypic cortex cultures with κ changed pharmacologically as indicated in *A* (reproduced from [108–110], respectively; Copyright 2009, 2011, 2012 Society for Neuroscience).

pauses in between (cf. **Figure 8C**). When analyzing the summed population activity of avalanche activity more closely, the picture of "avalanches within avalanches" readily emerges (**Figures 10A,B**), which dominates periodically driven cultures as well [11]. Based on the observation of an avalanche, the average time to wait before observing a future avalanche is known as the waiting time distribution and was found to reflect the characteristic time scales of θ/γ-oscillations and up-states (**Figure 10C**; [103]). This was true for avalanches independent of minimal size and with strong dependence on the E/I balance [104]. By calculating conditional probabilities, Lombardi et al. [105] obtained precise functions capturing the nesting of avalanches with respect to size and time to the next avalanche. It was generally found that there is a high probability that the next avalanche will be smaller than the currently observed avalanche. This finding was robust to a large range of sizes and time windows of observation as well for periodically driven activity (**Figure 10D**, *left*, *middle*). Importantly, this relationship reverses when reducing inhibition; more specifically, the network becomes hyperexcitable at which point future "avalanches" are likely to be larger than the currently observed activity (**Figure 10D**, *right*; cf. also **Figure 7D**). These experimental findings add an important dimension to the discussion of hyperexcitable network activity beyond the finding of bimodal size distributions.

Control Parameters Identified in the Regulation of Neuronal Avalanches

The core requirement for SOC is the ability for the system to adjust a control parameter, which allows the system to reside near the critical point [8,106]. Given the complexity of cortical microcircuits regarding neurotransmitter categories (excitatory and inhibitory), neuromodulators (e.g., dopamine, acetylcholine, and serotonin), and brain states (e.g., wakefulness, sleep, and attention), there could be many control parameters that are able to tune cortical networks toward or away from criticality, yet few have been experimentally examined so far. Of common focus, the E/I balance establishes an important control parameter, first demonstrated for avalanches in organotypic cortex cultures [53]. Specifically, reducing fast inhibitory synaptic transmission nonselectively by pharmacological means, rapidly destroys the power law in LFP-based avalanches and causes bimodal distributed cascade sizes (cf. **Figure 5E**). Similar results have been obtained in dissociated cultures, in which a power law distribution in avalanches changed to a bimodal distribution when inhibition was blocked (e.g., [107]). In more detailed follow-up studies, a reduction in fast synaptic inhibition or in fast and slow synaptic excitation changes

the dynamics from avalanches to a "supercritical" or "subcritical"-like condition [108–111]. These studies, by quantifying the distance of bimodal or exponential distributions from a power law, demonstrated that numerous network parameters are maximized at the E/I balance at relatively low level of synchronizations, where avalanche dynamics reigns (**Figure 11**).

The neuromodulator dopamine has been identified as a second control parameter for the regulation of neuronal avalanches in the prefrontal cortex (**Figure 12**). Dopamine is crucial for working memory performance, which in turn requires prefrontal cortex functioning [112,113]. Acute prefrontal cortex slices taken from adult rats, exposed to a moderate external excitatory drive, rapidly respond to the presence of dopamine with the emergence of avalanche activity in superficial cortex layers (**Figures 12A,B**; [69]). At intermediate levels, but not low or high levels of dopamine, nLFPs formed a power law in avalanche sizes with a slope of −3/2 (**Figure 12C**). The activity was selective for the dopamine D_1 receptor and required NMDA-glutamate receptor stimulation, thus matching the pharmacological inverted-U profile reported for working memory performance in the prefrontal cortex [114]. Analysis of the intracellular membrane potential in individual pyramidal neurons in the acute slice, as well as extracellular single-unit analysis *in vivo*, demonstrated that even large LFP avalanches engage individual pyramidal neurons selectively and this selectivity breaks down when inhibition is reduced [70]. These results taken together suggest that the control parameter dopamine maximizes the spatial extent and occurrence frequency of system-wide avalanches formed by selective activation of distributed pyramidal neurons in the network.

The high sensitivity of the power law to the reported control parameters suggests that thresholding of the LFP is unlikely to play a major role in the origin of scale-invariant avalanches. The LFP is a continuous time-varying signal, for which avalanche processing requires a threshold operation to convert this signal into point process-like data. Such thresholding preserves essential avalanche information in a discretized spatiotemporal raster, e.g., as shown for human avalanches in the fMRI [80]. Yet, thresholding is a nonlinear operation and can affect scaling regimes, particularly, in the temporal domain [73,115]. On the other hand, if thresholding were the underlying cause to observe avalanches, one would expect power law characteristics in the observed dynamics to be robust to relatively mild pharmacological manipulation, which is not the case.

Changes in network connectivity based on local plasticity rules have been demonstrated to establish SOC in models [116], suggesting that plasticity could function as a control parameter (e.g., [117,118]). Since network connectivity was found to support avalanche dynamics in dissociated cultures, it could be considered a control parameter as well [119]. On the other hand, measurements in organotypic cortex cultures and in nonhuman primates *in vivo* demonstrate that avalanches establish integrative network architectures that are robust to certain plastic changes [77,120,121]. Of note, *in vivo* studies have shown avalanches to be exquisitely sensitive to the sleep/wakefulness transition [122–126], suggesting sleep [127,128] and sleep-arousal transitions [129] as a behavioral state control parameter.

Lack of Scale-Invariant LFP Avalanches in Deep Layers

The results summarized here were based on LFP recordings taken from high-density arrays oriented in a specific manner with

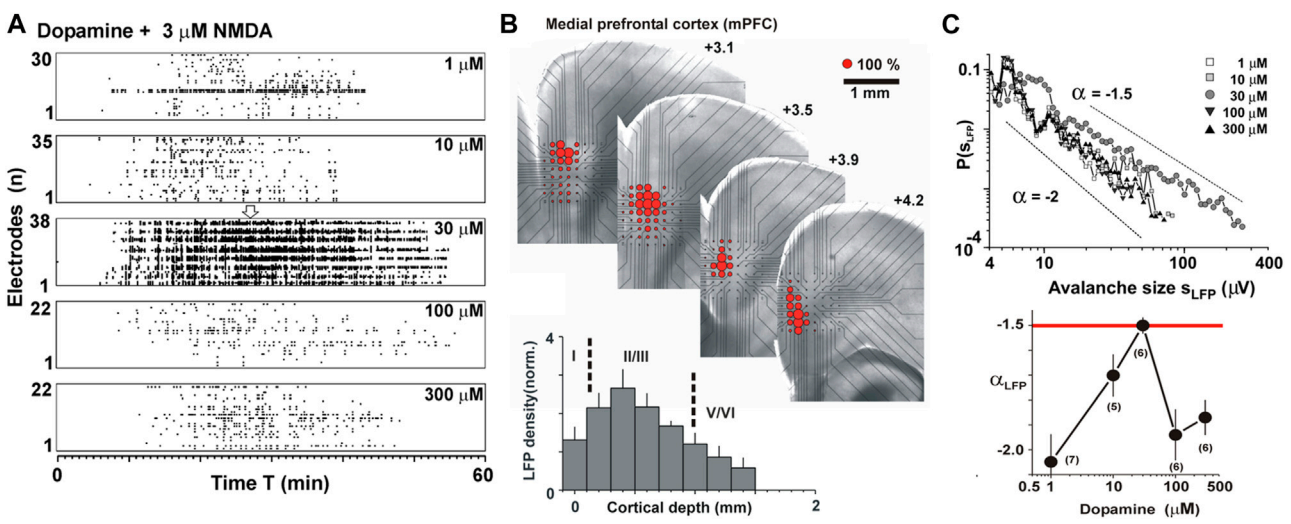

FIGURE 12 | Dopamine is a control parameter for the emergence of neuronal avalanches in superficial layers of the cortex. **(A)** Externally driven acute cortex slice using weak excitatory drive (3 μM NMDA) maximizes avalanche activity at intermediate dopamine concentrations. Raster plots of nLFPs from different slices for increasing dopamine concentrations (*top to bottom*). **(B)** Externally driven neuronal avalanches emerge in superficial layers 2/3. Average nLFP density (*red circle size*) projected onto the light microscopic image of the MEA with the corresponding acute coronal slice from the medial prefrontal cortex. *Lower left*: nLFP density projected along cortical layers demonstrating that most avalanche activity is induced in L2/3. **(C)** Avalanche activity exhibits a power law slope of −3/2 at moderate dopamine concentration. Size distributions (*top*) and corresponding slopes (*bottom*) are a function of dopamine concentration (reprinted with permission from [69]; Copyright 2006 Society for Neuroscience).

respect to the underlying cortical column. The planar projection of the array was aligned in such a way where propagation of activity in all layers of the cortex can be monitored. Even under those carefully chosen projection conditions, deep-layer LFP activity was strikingly absent, e.g., during spontaneous avalanche emergence in organotypic cortex cultures (cf. **Figure 3**) or during external glutamate-mediated depolarization, which induces avalanche activity in superficial layers in the acute cortex slice (**Figure 13**). The absence of LFP-based avalanches in deep layers *in vitro* could have various causes. First, deep layers could mature incompletely in organotypic culture preparations, e.g., due to lack of subcortical inputs from the thalamus or lack of subcortical targets. However, this argument does not apply to the acute cortex slice. Second, deep layers might require the presence of neuromodulators such as acetylcholine and neurotensin, often provided by brain regions outside the cortex, which regulate the amount of bursting in deep-layer pyramidal neurons [130,131]. However, even in the awake nonhuman primate, the LFP activity in deep layers does not establish power laws even when avalanche activity propagates simultaneously in superficial layers (Fig. S4 of [74]). Third, avalanches in deep layers could be composed of spatially distributed neurons that are difficult to track in the LFP. However, local cortical connectivity favors connections between nearby pyramidal neurons [132] such that avalanche activity would be expected to sum in the LFP. Taken together, these arguments suggest that deep layers might not be able to support scale-invariant avalanche dynamics in general. Even advanced recording techniques *in vivo* in the awake rodent demonstrate the absence of avalanches in deep layers. Using two-photon imaging *in vivo*, power laws in spike-based avalanches were identified in cortical layer 2/3 and layer 4 [133], but seem to be absent in deep layers [134].

The Negative Transients of the Local Field Potential is the Avalanche: A Local Reconstruction From Spike Avalanches Using Two-Photon Imaging

In the LFP, the structural and dynamical heterogeneity of the network is summed to form a local point source, which does not allow for the identification of the network elements contributing to the LFP [135]. While many experimental findings on avalanches have utilized spatially expansive MEAs, scale invariance predicts that avalanche dynamics should be observable even within the local neighborhood of a single electrode as the spatial resolution increases. This in turn should allow for a more detailed analysis of the underlying network components contributing to scale invariance. In this scenario, the nLFP amplitude should reflect the local neuronal group activity governed by avalanche dynamics (**Figure 13A**). Accordingly, it was found that the nLFP amplitude distribution at the single-electrode level approximates a power law with a slope of −3/2, which is destroyed when pharmacologically changing the E/I balance (**Figure 13B**; [11]).

The notion that locally summed the activity of neuronal group *firing* constitutes avalanche dynamics was first demonstrated directly with two-photon imaging using the genetically encoded calcium indicator (GECI) YC2.60, which exhibits single-spike sensitivity [124,136]. The indicator was selectively expressed in pyramidal neurons from superficial layers in organotypic cortex cultures by electroporation (**Figure 13C**; [124]). When the coordinated firing in groups of pyramidal neurons was studied, it was found that the highly irregular firing of pyramidal neurons during ongoing spontaneous activity exhibits clear avalanche signatures. We note that these power laws are robust at the temporal scale of Δt = 30 ms (i.e., at an imaging frame rate of 30 Hz) and their slope α is more shallow than −3/2 as predicted from LFP avalanche analysis (cf. **Figures 5B,G**). Importantly, the power law in avalanche sizes was transformed to a bimodal distribution only after pharmacologically reducing inhibition at which the typical hyperexcitable phenotype of an initial steep slope close to −2 and an overabundance of system-wide cascades robustly presents (**Figures 13D–F**). We note in passing that a hypersynchronized phenotype in the size distribution also emerges when mildly reducing excitatory transmission (cf. **Figures 13B,F**, *right*, "Disfacilitated"). Such a reduction increases spontaneous synchronization in the network due to an overall increase in synaptic transmission efficacy when the global rate of activity drops (e.g., [137]). Taken together, these results demonstrate that the nLFP reflects local avalanche activity and should not be equated to single spikes. In this context, the threshold, λ, applied to extract nLFPs is similar to the population threshold applied to summed spiking activity in identifying neuronal avalanches in network models (e.g., [72]). These findings identify pyramidal neuron activity in superficial cortex layers to carry signatures associated with the organization of avalanches, which, since then, has been confirmed *in vivo* [124,133,134,138]. The relationship between firing statistics of single neurons and critical exponents in avalanche dynamics has been a major research topic in neural network dynamics (e.g., [139–142]).

Not All Avalanches Are Self-Organized Criticality Avalanches: The Prevalence of Local and System-Wide Population Events in Dissociated Neuronal Cultures

Dissociated cultures [143] have been used for decades to study the autonomous development in structure and dynamics of cortical microcircuits. As a complementary approach to organotypic cultures [20], dissociated neuronal cultures are prepared from cortical tissue typically taken from an embryo at embryonic days 15–18 (that is, 3–6 days before birth). The tissue is then mechanically and enzymatically disintegrated, and the remaining neuronal cell bodies and precursor cells are reseeded on a glia-feeder layer and grown for up to several months *in vitro* [143]. Dissociated cultures appeal by focusing on the *de novo* formation of neuronal connections, yet they require careful attention to the design of glia-feeder layers and the culture medium composition. They lack cortical layers and a clear classification of pyramidal neurons and interneurons into functional subtypes, which, in contrast, are both well-established *in vivo* and organotypic cortex cultures during various developmental stages (see introductory sections). Synchronized

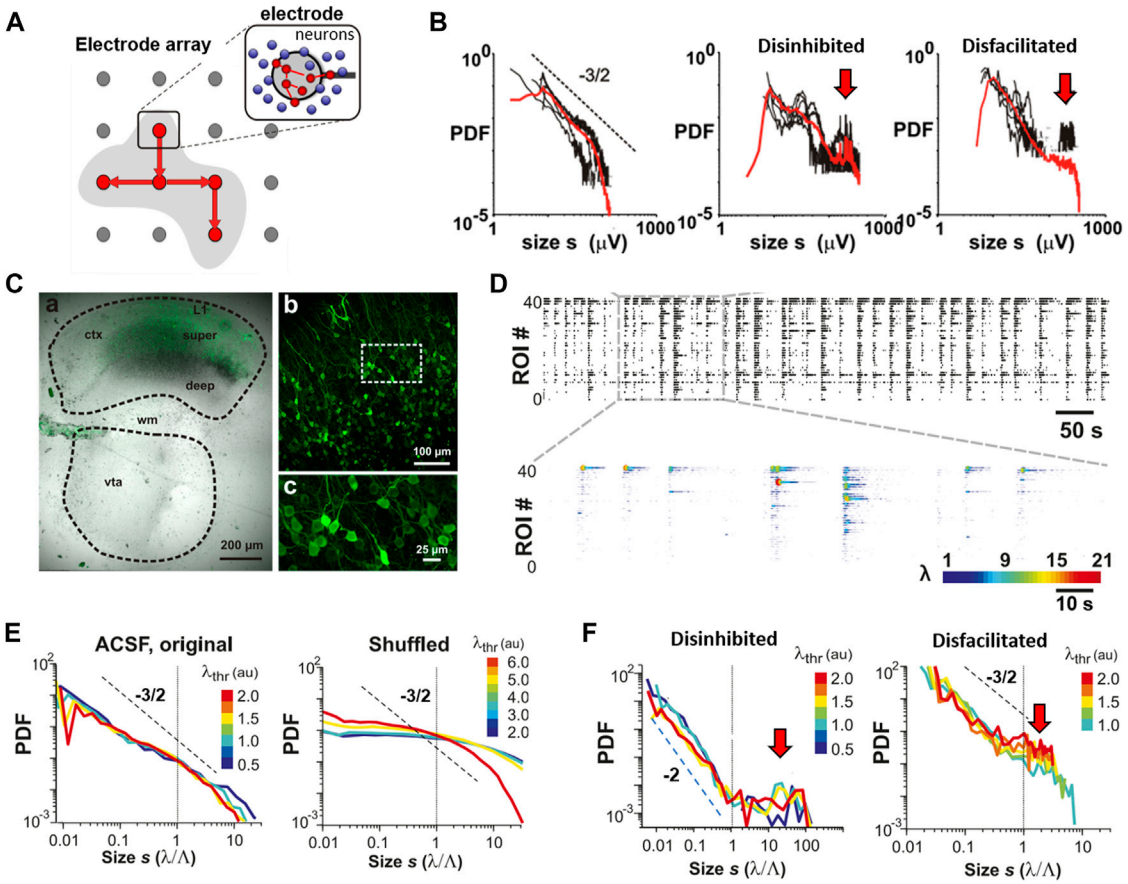

FIGURE 13 | Experimental transition from single-nLFP avalanches to spike avalanches in organotypic cortex cultures using two-photon imaging (2PI). **(A)** Sketch of spatial transformation of propagated nLFPs on the electrode array to propagated spike activity in local neuronal groups (*circles*; *red*: spiking; *blue*: quiet) within the neighborhood of a single electrode (*zoom*). **(B)** Distribution of nLFP amplitudes at single electrodes (*red*: average; *black*: example single electrodes). Power-law–like distributions change into bimodal distributions when reducing inhibition (*disinhibited*) or excitation (*disfacilitated*) (reproduced with permission from [11]). **(C)–(F)** Reconstruction of spike avalanches in an organotypic cortex culture. **(C)** Single organotypic coculture of the cortex (*ctx*) and ventral tegmental area (*VTA*) after ~3 weeks grown postnatal. Electroporation of the embryo at E16.5 leads to expression of the genetically encoded calcium indicator YC2.6 in pyramidal neurons from superficial cortex layers (*b* and *c* are successive zooms from *a*). *Broken lines*: tissue borders. *wm*: white matter. **(D)** Raster of spontaneous spike density monitored with 2PI and obtained through deconvolution ($n = 40$ pyramidal neurons). *Top*: binarized raster. *Bottom*: temporally expanded raster segmented with color coded spike intensity λ for each neuron. **(E)** Spontaneous neuronal activity reveals power laws in spike avalanches that are robust to the threshold λ_{thr} applied at the single neuron level (*left*). Temporal shuffling of spike activity abolishes the power law in avalanche sizes (*right*). **(F)** Mild disinhibition changes the power law to a bimodal distribution with an initial steep slope of −2 and system-wide population events (*red arrow*; cf. **Figure 5E**). System-wide events also become prominent when mildly reducing excitation (*right*). (modified for *C* and *C–F* reproduced under CC0 license from [124]).

bursting has been the hallmark of the developing population activity in dissociated cultures grown on MEAs [144]. Despite the apparent simplicity of this culture system, when systematically studied using a large number of cultures grown on MEAs over many weeks, highly variable outcomes in neuronal synchronization have been documented that depend on plating density, which affects the number of neurons per area and developmental trajectory [145]. Accordingly, the application of avalanche analysis to these synchronized bursts has yielded heterogenous outcomes across and within studies (**Figure 14**). Nevertheless, a consistent finding emerges from these studies, which deviates from results reported for LFP- and spike-based avalanches in organotypic cortex cultures, as detailed below.

Pasquale et al. [107] were the first to report spike avalanches in six dissociated cultures with size distribution of either exponential, bimodal, or power law form. Two out of six cultures displayed the power law in avalanche size, however, only at submillisecond temporal resolution Δt. In fact, increasing Δt to 1 ms steepened the initial slope and rapidly uncovered a bimodal distribution, explained in their model as explosive growth introduced by neuronal hubs (**Figure 14A**). Using neonatal tissue right after birth, Tetzlaff et al. [98] tracked spike avalanche distributions during development and found an initial slope close to −2 for mature cultures and an increase in bimodality with increasing bin size (**Figure 14B**). Similar findings were presented by Levina and Priesemann [99] using dissociated cultures prepared from E18 tissue and grown for ~3 weeks. Spike avalanches revealed a size distribution with a steep slope close to −2 and a preference for large avalanches. Again, an increase in Δt steepened the initial slope further and

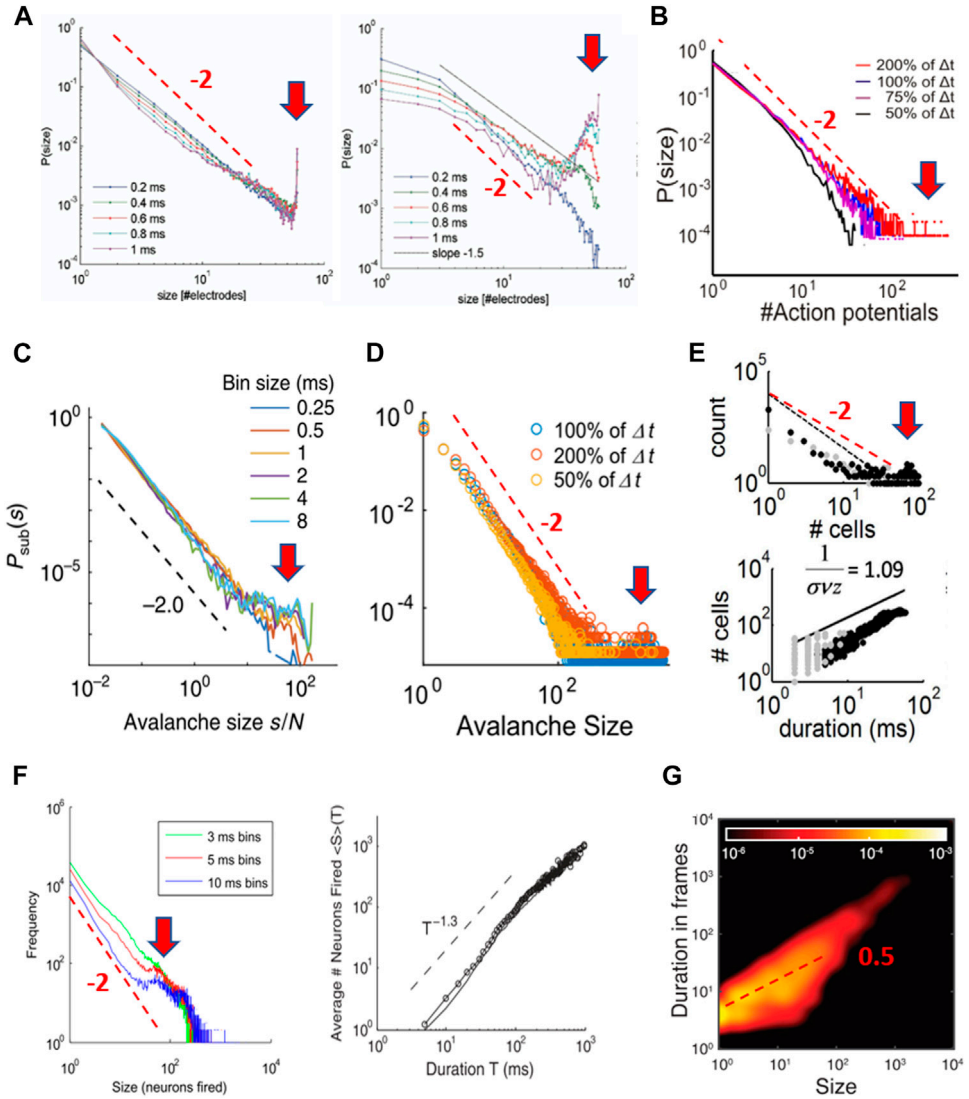

FIGURE 14 | Spike "avalanches" in dissociated cultures display the scaling characteristic of hyperexcitable dynamics. **(A)** Spike avalanches in dissociated cultures exhibit a steeper initial slope and become more bimodal with an increase in Δt. *Left*: cultures; *Right*: model (reproduced with permission from [107]). **(B)** With an increase in Δt, spike avalanches in dissociated culture change from exponential to bimodal size distribution with steep initial slope close to −2 (reproduced under CC-NY license from [98]). **(C)** Initial slope of −2 and bimodality with an increase in Δt in mature dissociated cultures (reproduced under CC-NY license from [99]). **(D)** Bimodal size distributions in dissociated cultures around the mean interspike interval Δt exhibit an initial slope of −2. The mean interspike interval Δt has been used as a proxy at which the size distribution should show a power law with slope $\alpha = -3/2$ (see **Figure 5**) (reproduced with permission from [146]). **(E)** Bimodal size distribution and linear mean-size-to-duration relation at Δt close to the mean interspike interval for dissociated cultures (reproduced under CC-NY license from [147]). **(F)** Spike avalanches of unknown layer origin in organotypic cortex cultures. *Left*: the bimodal size distribution and steepening initial slope with an increase in Δt suggest hyperexcitable culture condition. *Right*: near linear mean-size-vs.-duration scaling similar to spike avalanches from dissociated cultures in *E* suggests deviation from critical branching that predicts a slope of 2 (reproduced under CC-BY license from [157]). **(G)** Duration-to-mean-size slope close to 1/2 in dissociated cultures prepared from *postnatal* tissue in line with prediction for a critical branching process (reproduced under CC-BY license from [163]). Subpanels *A–F* have been modified by adding a *red arrow* emphasizing the bimodal feature in each size distribution and/or a broken red line with a slope of −2 as a guide to the eye. A broken red line with a slope of −0.5 was added to subpanel *G*.

disproportionately increased the probability for large activity events (**Figure 14C**). Even when examining only a small range of bin width, reported results for dissociated culture experiments are more in line with expectations for a hyperexcitable system. Yada et al. [146] tracked the development of spike avalanches in six cultures and reported a bimodal form and an initial steep slope close to −2 that was robust to modest changes in Δt (**Figure 14D**). Similarly, robust bimodality and initial steep slope were reported in [147] (**Figure 14E**).

These experimental findings are in contrast to what has been reported for sizes of LFP and spike avalanches in organotypic cultures, where an increase in Δt leads to a more shallow slope in the size distribution and bimodality only arises when the system is made hyperexcitable (cf. **Figures 5**, **13**). The notion that

dissociated cultures might be characterized better by hyperexcitable dynamics is in line with a recent finding that increasing inhibition by adding a GABA agonist reduces bimodal size distributions in dissociated cultures, bringing them closer to a power law [148]. It is striking that, in some dissociated cultures, power laws were found mainly at submillisecond Δt (e.g., [107]). Given that synaptic integration times between neurons are on the order of 2–3 ms, a submillisecond temporal integration window will prematurely terminate the tracking of propagated activity, thereby randomly partitioning synchronous activity and potentially creating heavy-tail statistics in cascade sizes. Accordingly, at temporal resolutions >3–4 ms, which overlap with synaptic integration times, a strongly bimodal population dynamics of local, nonpropagated activity and global, propagated activity is revealed in these systems. For comparison, temporal resolutions studied in organotypic cultures ranged up to 16 ms (LFP avalanches; **Figures 5B,G**) and 33 ms (spike avalanches; an imaging frame rate of 30 Hz; **Figure 13**). Despite these long integration windows, bimodal distributions were absent, unless the system was made hyperexcitable. These integration windows are about an order of magnitude longer than those at which dissociated cultures show clear bimodal dynamics.

We suggest that the bimodal size distribution in dissociated cultures reflects a predominance of local activity and system-wide propagated activity. Such heterogenous dynamics can arise from several scenarios. The bimodality could reflect different structural networks, potentially including different cell types, that mature in dissociated cultures. For example, Orlandi et al. [149] applied an avalanche algorithm to neuronal activity tracked with intracellular calcium imaging in dissociated cultures grown from embryos for up to three weeks. They separated functional networks of "background" avalanches that established a cascade size distribution steeper than −2 from system-wide avalanches. Alternatively, dissociated cultures could establish a homogenous neural network in which bimodality arises from a discontinuous, first-order phase transition. In this latter case, neuronal activity either remains local and small or, alternatively, propagated and system wide. Increasing Δt in such a system more robustly collects activity into system-wide events, concomitantly reducing smaller-sized events steepening the initial slope in size distributions as observed for dissociated cultures. In fact, the simulation of population activity in dissociated cultures using a first-order phase transition has a long tradition. These dynamics were captured in early models featuring a first-order phase transition of all-or-none propagation [150], as well as recently for up-state generation in deep layers of cortical slices (e.g., [57]). They have been recently revived within the framework of self-organized bistability [151–154] or quasicriticality as well [155].

We note that spatial subsampling of activity, by recording only from a small number of neurons from the full network, is a common technical challenge in avalanche analysis. Yet, this technical constraint cannot explain the uncovering of a bimodal distribution at large Δt. Spatial subsampling decorrelates activity, leading to exponential distributions in cascade sizes [156]. However, in the present cases, a power-law–like or exponential distribution is observed at the outset for spike avalanches at small Δt, which changes to a bimodal distribution with increasing Δt (**Figures 14A–D**). In fact, avalanche analysis under increased spatial sampling in dissociated cultures, e.g., using intracellular calcium imaging, established clear bimodal size distribution [149]. Further support that spike avalanches in dissociated cultures differ from LPF avalanches *in vivo* comes from the mean size vs. duration scaling exponent. This exponent was found to be 2, which is in line with expectations for a critical branching process [71], but ranges between 1–1.5 for spike-based avalanches with bimodal distributions even at large Δt [146,147]. This is more in line with expectations for a noise process wherein size simply grows more linearly with duration [73,79].

We note that, in a study by Friedman et al. [157], spike avalanche distributions were calculated from ten cortex slice cultures, and this study is often used as an introduction of scaling relationships for spike avalanches. Three of those cultures exhibited bimodal, four exponential, and two were reported as "critical," i.e., power-law–like in their size distribution. However, similar to spike avalanches in dissociated cultures, power law distributions in their cultures considered "critical" steepened in initial slope and became bimodal when increasing Δt (**Figure 14F**, *left*). The loss of the power law at low temporal resolution supports the interpretation of this activity to be of a first-order phase transition either from preferentially recording spikes from deep layers or from networks that are hyperexcitable, i.e., "supercritical." This interpretation is further supported by their report of a mean size vs. duration exponent close to 1 (**Figure 14F**, *right*; [157]).

Developmental Differences Between Organotypic Cultures and Dissociated Cultures of the Cortex

Organotypic cortex cultures that are grown from postnatal brains demonstrate up-states and nested θ/γ-oscillations in their superficial layers, which give rise to avalanche scaling (see **Figures 2–7**). The conspicuous absence of these dynamics in dissociated cultures suggests an incomplete maturation of superficial layer circuitry, which is supported by several arguments, with the most obvious one being that the standard protocol for dissociated cortex culture biases toward the formation of deep-layer circuits. Dissociated cultures are typically prepared from the cortex at embryonic day E18 [107], which is dominated by deep-layer neurons known to autonomously generate population burst activity, also called "delta" brushes [158]. In contrast, superficial precursor neurons develop relatively late [16,17] and at E15–16 are still migrating toward the cortex along the periventricular wall, a developmental feature that can be used to selectively transfect superficial cells at that developmental stage [124,159] (cf. **Figure 13**). In addition, late migrating interneurons will be absent in dissociated cultures prepared from the embryonic cortical mantle only. Without an endogenous neurotransmitter such as acetylcholine, which is lacking *in vitro*, deep-layer pyramidal neurons exhibit intrinsic bursting [130,160,161] that can result in network-wide events [55–57]. Importantly, organotypic cortex cultures are typically prepared from the cortex after birth between postnatal day P1 and 2, at which

point most precursor neurons required for establishing superficial pyramidal and interneurons have already arrived in the cortex, allowing an autonomous assembly of superficial layers in the isolated local cortical culture (see above). This sensitivity to the developmental time point of neuronal harvest is further exemplified by cultures of the hippocampus, an evolutionary early part of cortex. Dissociated hippocampus cultures, when taken at E18, reveal an avalanche size distribution slope close to −2 and a supercritical branching parameter at 3 ms bin width [162]. In contrast, dissociated hippocampus cultures made from newborn pups reveal mean size vs. duration scaling exponents of 2, not found for supercritical dynamics (**Figure 14G**; [163]). Similarly, Tetzlaff et al. [98] prepared dissociated cultures from postnatal day P1–2 resulting in relatively mild bimodality with increasing bin width (**Figure 14B**). Preparing dissociated cultures from postnatal tissue, expansion toward three-dimensional scaffolding using microbeads, and coculturing with other brain regions, e.g., the hippocampus, might introduce structural heterogeneity that stabilizes avalanche dynamics in future analysis [119,164].

To summarize, most avalanche analyses in dissociated cortex cultures reveal power laws that change to a bimodal distribution with *steepening* initial slope at longer integration windows. This dependency on the integration time window seems to reflect a first-order phase transition commonly found for predominantly deep layer pyramidal networks. These findings suggest that the activity in dissociated cultures does not compare well with neuronal avalanche dynamics originally described in organotypic cortex cultures and acute cortex slices and further established in awake *in vivo* preparation that features neuronal activity localized to superficial layers of the cortex.

Summary and Conclusion

The experimental evidence for SOC in the brain points to the presence of at least four dynamical motifs, up-states, nested oscillations, neuronal avalanches, and coherence potentials. These motifs have been robustly reported for the intact brain and in the isolated mammalian cortex, with its layered structure and cell type diversity largely preserved, specifically for the organotypic cortex culture and in the acute cortex slice. The coemergence of scale-invariant neuronal avalanches with oscillations during up-states should encourage future work on SOC in the brain at a disorder-synchronization phase transition. Neuronal population activity measured in dissociated cortex cultures typically differs from that reported for layered cortex preparations and is more in line with supercritical dynamics. Identifying the precise structural and dynamical constraints responsible for these differences might provide important insights into the mechanisms supporting SOC in the brain.

AUTHOR CONTRIBUTIONS

DP took the lead in writing the manuscript and in discussions with all other authors.

FUNDING

This research was supported by the Division of the Intramural Research Program of the National Institute of Mental Health (NIMH), United States, ZIAMH002797. This research utilized the computational resources of Biowulf (http://hpc.nih.gov) at the National Institutes of Health (NIH), United States.

ACKNOWLEDGMENTS

We thank Dante R. Chialvo and Patrick Kanold for comments and support during writing of this manuscript.

REFERENCES

1. Markram H, Muller E, Ramaswamy S, Reimann MW, Abdellah M, Sanchez CA, et al. Reconstruction and Simulation of Neocortical Microcircuitry. *Cell* (2015) 163(2):456–92. doi:10.1016/j.cell.2015.09.029
2. Dura-Bernal S, Suter BA, Gleeson P, Cantarelli M, Quintana A, Rodriguez F, et al. NetPyNE, a Tool for Data-Driven Multiscale Modeling of Brain Circuits. *eLife* (2019) 8:e44494. doi:10.7554/eLife.44494
3. Bak P, Tang C, and Wiesenfeld K. Self-organized Criticality: An Explanation of the 1/fnoise. *Phys Rev Lett* (1987) 59(4):381–4. doi:10.1103/PhysRevLett.59.381
4. Jensen HJ. *Self-organized Criticality*.Cambridge: Cambridge University Press (1998). doi:10.1017/cbo9780511622717
5. Chialvo DR. Emergent Complex Neural Dynamics. *Nat Phys* (2010) 6: 744–50. doi:10.1038/NPHYS1803
6. Mora T, and Bialek W. Are Biological Systems Poised at Criticality?. *J Stat Phys* (2011) 144(2):268–302. doi:10.1007/s10955-011-0229-4
7. Pruessner G. *Self-organised Criticality: Theory, Models and Characterisation*. Cambridge: Cambridge University Press (2012). doi:10.1017/cbo9780511977671
8. Hesse J, and Gross T. Self-organized Criticality as a Fundamental Property of Neural Systems. *Front Syst Neurosci* (2014) 8:11. doi:10.3389/fnsys.2014.00166
9. Marković D, and Gros C. Power Laws and Self-Organized Criticality in Theory and Nature. *Phys Rep* (2014) 536(2):41–74. doi:10.1016/j.physrep.2013.11.002
10. Muñoz MA. Colloquium: Criticality and Dynamical Scaling in Living Systems. *Rev Mod Phys* (2018) 90(3):031001. doi:10.1103/RevModPhys.90.031001
11. Plenz D. Neuronal Avalanches and Coherence Potentials. *Eur Phys J Spec Top* (2012) 205(1):259–301. doi:10.1140/epjst/e2012-01575-5
12. Götz M, and Bolz J. Formation and Preservation of Cortical Layers in Slice Cultures. *J Neurobiol* (1992) 23:783–802. doi:10.1002/neu.480230702
13. Plenz D, and Aertsen A. Neural Dynamics in Cortex-Striatum Co-cultures-II. Spatiotemporal Characteristics of Neuronal Activity. *Neuroscience* (1996) 70: 893–924. doi:10.1016/0306-4522(95)00405-X
14. Plenz D, and Aertsen A. Neural Dynamics in Cortex-Striatum Co-cultures-I. Anatomy and Electrophysiology of Neuronal Cell Types. *Neuroscience* (1996) 70:861–91. doi:10.1016/0306-4522(95)00406-8
15. Gorba T, Klostermann O, and Wahle P. Development of Neuronal Activity and Activity-dependent Expression of Brain-Derived Neurotrophic Factor mRNA in Organotypic Cultures of Rat Visual Cortex. *Cereb Cortex* (1999) 9(8):864–77. doi:10.1093/cercor/9.8.864
16. Luhmann HJ, Sinning A, Yang J-W, Reyes-Puerta V, Stüttgen MC, Kirischuk S, et al. Spontaneous Neuronal Activity in Developing Neocortical Networks: from Single Cells to Large-Scale Interactions. *Front NeuralCircuits* (2016) 10(40):29. doi:10.3389/fncir.2016.00040

17. Molnár Z, Luhmann HJ, and Kanold PO. Transient Cortical Circuits Match Spontaneous and Sensory-Driven Activity during Development. *Science* (2020) 370(6514):eabb2153. doi:10.1126/science.abb2153
18. Plenz D, and Kitai ST. Up and Down States in Striatal Medium Spiny Neurons Simultaneously Recorded with Spontaneous Activity in Fast-Spiking Interneurons Studied in Cortex-Striatum-Substantia Nigra Organotypic Cultures. *J Neurosci* (1998) 18:266–83. doi:10.1523/JNEUROSCI.18-01-00266.1998
19. Bolz J, Novak N, Götz M, and Bonhoeffer T. Formation of Target-specific Neuronal Projections in Organotypic Slice Cultures from Rat Visual Cortex. *Nature* (1990) 346:359–62. doi:10.1038/346359a0
20. Gähwiler B, Capogna M, Debanne D, McKinney RA, and Thompson SM. Organotypic Slice Cultures: a Technique Has Come of Age. *Trends Neurosci* (1997) 20(10):471–7. doi:10.1016/s0166-2236(97)01122-3
21. Humpel C. Organotypic Brain Slice Cultures: A Review. *Neuroscience* (2015) 305:86–98. doi:10.1016/j.neuroscience.2015.07.086
22. Tremblay R, Lee S, and Rudy B. GABAergic Interneurons in the Neocortex: From Cellular Properties to Circuits. *Neuron* (2016) 91(2):260–92. doi:10.1016/j.neuron.2016.06.033
23. Lim L, Mi D, Llorca A, and Marín O. Development and Functional Diversification of Cortical Interneurons. *Neuron* (2018) 100(2):294–313. doi:10.1016/j.neuron.2018.10.009
24. Götz M, and Bolz J. Development of Vasoactive Intestinal Polypeptide (VIP)-containing Neurons in Organotypic Slice Cultures from Rat Visual Cortex. *Neurosci Lett* (1989) 107:6–11. doi:10.1016/0304-3940(89)90782-9
25. Klostermann O, and Wahle P. Patterns of Spontaneous Activity and Morphology of Interneuron Types in Organotypic Cortex and Thalamus-Cortex Cultures. *Neuroscience* (1999) 92(4):1243–59. doi:10.1016/s0306-4522(99)00009-3
26. Halassa MM, Fellin T, and Haydon PG. The Tripartite Synapse: Roles for Gliotransmission in Health and Disease. *Trends Mol Med* (2007) 13(2):54–63. doi:10.1016/j.molmed.2006.12.005
27. Fellin T, Halassa MM, Terunuma M, Succol F, Takano H, Frank M, et al. Endogenous Nonneuronal Modulators of Synaptic Transmission Control Cortical Slow Oscillations *In Vivo*. *Proc Natl Acad Sci* (2009) 106(35):15037–42. doi:10.1073/pnas.0906419106
28. Perea G, Sur M, and Araque A. Neuron-glia Networks: Integral Gear of Brain Function. *Front Cel Neurosci.* (2014) 8:112. doi:10.3389/fncel.2014.00378
29. Schultz-Süchting F, and Wolburg H. Astrocytes Alter Their Polarity in Organotypic Slice Cultures of Rat Visual Cortex. *Cel Tissue Res* (1994) 277(3):557–64. doi:10.1007/BF00300229
30. Schmidt-Kastner R, and Humpel C. Nestin Expression Persists in Astrocytes of Organotypic Slice Cultures from Rat Cortex. *Int J Dev Neurosci* (2002) 20(1):29–38. doi:10.1016/S0736-5748(02)00003-5
31. Cäser M, and Schüz A. Maturation of Neurons in Neocortical Slice Cultures. A Light and Electron Microscopic Study on *In Situ* and *In Vitro* Material. *J für Hirnforschung* (1992) 33:429–43.
32. Staal JA, Alexander SR, Liu Y, Dickson TD, and Vickers JC. Characterization of Cortical Neuronal and Glial Alterations during Culture of Organotypic Whole Brain Slices from Neonatal and Mature Mice. *PLoS One* (2011) 6(7):e22040. doi:10.1371/journal.pone.0022040
33. Antón-Bolaños N, Sempere-Ferràndez A, Guillamón-Vivancos T, Martini FJ, Pérez-Saiz L, Gezelius H, et al. Prenatal Activity from Thalamic Neurons Governs the Emergence of Functional Cortical Maps in Mice. *Science* (2019) 364(6444):987–90. doi:10.1126/science.aav7617
34. Canolty RT, Edwards E, Dalal SS, Soltani M, Nagarajan SS, Kirsch HE, et al. High Gamma Power Is Phase-Locked to Theta Oscillations in Human Neocortex. *Science* (2006) 313(5793):1626–8. doi:10.1126/science.1128115
35. Lisman J, and Idiart M. Storage of 7 +/- 2 Short-Term Memories in Oscillatory Subcycles. *Science* (1995) 267:1512–5. doi:10.1126/science.7878473
36. Lisman JE, and Jensen O. The Theta-Gamma Neural Code. *Neuron* (2013) 77(6):1002–16. doi:10.1016/j.neuron.2013.03.007
37. André M, Vezoli J, Conrado R, Oostenveld R, Jarrod L, et al. Visual Areas Exert Feedforward and Feedback Influences through Distinct Frequency Channels. *Neuron* (2015) 85(2):390–401. doi:10.1016/j.neuron.2014.12.018
38. Lundqvist M, Rose J, Herman P, Brincat SL, Buschman TJ, and Miller EK. Gamma and Beta Bursts Underlie Working Memory. *Neuron* (2016) 90(1):152–64. doi:10.1016/j.neuron.2016.02.028
39. Plenz D, and Kitai ST. Generation of High-Frequency Oscillations in Local Circuits of Rat Somatosensory Cortex Cultures. *J Neurophysiol* (1996) 76(6):4180–4. doi:10.1152/jn.1996.76.6.4180
40. Johnson HA, and Buonomano DV. Development and Plasticity of Spontaneous Activity and up States in Cortical Organotypic Slices. *J Neurosci* (2007) 27(22):5915–25. doi:10.1523/JNEUROSCI.0447-07.2007
41. Harsch A, and Robinson HPC. Postsynaptic Variability of Firing in Rat Cortical Neurons: the Roles of Input Synchronization and Synaptic NMDA Receptor Conductance. *J Neurosci* (2000) 20(16):6181–92. doi:10.1523/jneurosci.20-16-06181.2000
42. Czarnecki A, Tscherter A, and Streit J. Network Activity and Spike Discharge Oscillations in Cortical Slice Cultures from Neonatal Rat. *Eur J Neurosci* (2012) 35(3):375–88. doi:10.1111/j.1460-9568.2011.07966.x
43. Compte A, Reig R, Descalzo VF, Harvey MA, Puccini GD, and Sanchez-Vives MV. Spontaneous High-Frequency (10-80 Hz) Oscillations during up States in the Cerebral Cortex *In Vitro*. *J Neurosci* (2008) 28(51):13828–44. doi:10.1523/jneurosci.2684-08.2008
44. Bernander O, Douglas RJ, Martin KA, and Koch C. Synaptic Background Activity Influences Spatiotemporal Integration in Single Pyramidal Cells. *Proc Natl Acad Sci* (1991) 88:11569–73. doi:10.1073/pnas.88.24.11569
45. Petersen CCH, Hahn TTG, Mehta M, Grinvald A, and Sakmann B. Interaction of Sensory Responses with Spontaneous Depolarization in Layer 2/3 Barrel Cortex. *Proc Natl Acad Sci* (2003) 100(23):13638–43. doi:10.1073/pnas.2235811100
46. Reig R, Zerlaut Y, Vergara R, Destexhe A, and Sanchez-Vives MV. Gain Modulation of Synaptic Inputs by Network State in Auditory Cortex *In Vivo*. *J Neurosci* (2015) 35(6):2689–702. doi:10.1523/JNEUROSCI.2004-14.2015
47. Monier C, Fournier J, and Frégnac Y. *In Vitro* and *In Vivo* Measures of Evoked Excitatory and Inhibitory Conductance Dynamics in Sensory Cortices. *J Neurosci Methods* (2008) 169(2):323–65. doi:10.1016/j.jneumeth.2007.11.008
48. Haider B, Duque A, Hasenstaub AR, and McCormick DA. Neocortical Network Activity *In Vivo* Is Generated through a Dynamic Balance of Excitation and Inhibition. *J Neurosci* (2006) 26(17):4535–45. doi:10.1523/JNEUROSCI.5297-05.2006
49. Ness TV, Remme MWH, and Einevoll GT. Active Subthreshold Dendritic Conductances Shape the Local Field Potential. *J Physiol* (2016) 594(13):3809–25. doi:10.1113/JP272022
50. Meisel C, Klaus A, Kuehn C, and Plenz D. Critical Slowing Down Governs the Transition to Neuron Spiking. *Plos Comput Biol* (2015) 11(2):e1004097e1004097. doi:10.1371/journal.pcbi.1004097
51. Fregnac Y, Blatow M, Changeux J-P, DeFelipe J, Lansner A, Maass W, et al. UPs and DOWNs in Cortical Computation. In Dahlem Workshop on Microcircuits (2004). MIT Press. p. 393–433.
52. Gireesh ED, and Plenz D. Neuronal Avalanches Organize as Nested Theta- and Beta/gamma-Oscillations during Development of Cortical Layer 2/3. *Proc Natl Acad Sci* (2008) 105:7576–81. doi:10.1073/pnas.0800537105
53. Beggs JM, and Plenz D. Neuronal Avalanches in Neocortical Circuits. *J Neurosci* (2003) 23(35):11167–77. doi:10.1523/JNEUROSCI.23-35-11167.2003
54. Beltramo R, D'Urso G, Dal Maschio M, Farisello P, Bovetti S, Clovis Y, et al. Layer-specific Excitatory Circuits Differentially Control Recurrent Network Dynamics in the Neocortex. *Nat Neurosci* (2013) 16(2):227–34. doi:10.1038/nn.3306
55. Sanchez-Vives MV, and McCormick DA. Cellular and Network Mechanisms of Rhythmic Recurrent Activity in Neocortex. *Nat Neurosci* (2000) 3:1027–34. doi:10.1038/79848
56. Wester JC, and Contreras D. Columnar Interactions Determine Horizontal Propagation of Recurrent Network Activity in Neocortex. *J Neurosci* (2012) 32(16):5454–71. doi:10.1523/JNEUROSCI.5006-11.2012
57. Capone C, Rebollo B, Muñoz A, Illa X, Del Giudice P, Sanchez-Vives MV, et al. Slow Waves in Cortical Slices: How Spontaneous Activity Is Shaped by Laminar Structure. *Cereb Cortex* (2017) 29(1):319–35. doi:10.1093/cercor/bhx326
58. Buhl EH, Tamas G, and Fisahn A. Cholinergic Activation and Tonic Excitation Induce Persistent Gamma Oscillations in Mouse Somatosensory Cortex *In Vitro*. *J Physiol* (1998) 513(Pt 1):117–26. doi:10.1111/j.1469-7793.1998.117by.x

59. Yamawaki N, Stanford IM, Hall SD, and Woodhall GL. Pharmacologically Induced and Stimulus Evoked Rhythmic Neuronal Oscillatory Activity in the Primary Motor Cortex *In Vitro*. *Neuroscience* (2008) 151(2):386–95. doi:10.1016/j.neuroscience.2007.10.021
60. Nicholson C, and Freeman JA. Theory of Current Source-Density Analysis and Determination of Conductivity Tensor for Anuran Cerebellum. *J Neurophysiol* (1975) 38:356–68. doi:10.1152/jn.1975.38.2.356
61. Mitzdorf U. Current Source-Density Method and Application in Cat Cerebral Cortex: Investigation of Evoked Potentials and EEG Phenomena. *Physiol Rev* (1985) 65:37–100. doi:10.1152/physrev.1985.65.1.37
62. Plenz D, and Aertsen A. Current Source Density Profiles of Optical Recording Maps: a New Approach to the Analysis of Spatio-Temporal Neural Activity Patterns. *Eur J Neurosci* (1993) 5:437–48. doi:10.1111/j.1460-9568.1993.tb00510.x
63. Oke OO, Magony A, Anver H, Ward PD, Jiruska P, Jefferys JGR, et al. (2010). High-frequency Gamma Oscillations Coexist with Low-Frequency Gamma Oscillations in the Rat Visual Cortexin Vitro.*Eur. J. Neurosci.*31(8)**,**1435–45. doi:10.1111/j.1460-9568.2010.07171.x
64. Ermentrout GB, and Kleinfeld D. Traveling Electrical Waves in Cortex. *Neuron* (2001) 29(1):33–44. doi:10.1016/s0896-6273(01)00178-7
65. Rubino D, Robbins KA, and Hatsopoulos NG. Propagating Waves Mediate Information Transfer in the Motor Cortex. *Nat Neurosci* (2006) 9(12): 1549–57. doi:10.1038/nn1802
66. Takahashi K, Saleh M, Penn RD, and Hatsopoulos NG. Propagating Waves in Human Motor Cortex. *Front Hum.Neurosci* (2011) 5:40. doi:10.3389/fnhum.2011.00040
67. Abeles M. *Corticonics: Neural Circuits of the Cerebral Cortex*. New York: Cambridge University Press (1991). doi:10.1017/cbo9780511574566
68. Yu S, Klaus A, Yang H, and Plenz D. Scale-invariant Neuronal Avalanche Dynamics and the Cut-Off in Size Distributions. *PLoS One* (2014) 9(6): e99761. doi:10.1371/journal.pone.0099761
69. Stewart CV, and Plenz D. Inverted-U Profile of Dopamine-NMDA-Mediated Spontaneous Avalanche Recurrence in Superficial Layers of Rat Prefrontal Cortex. *J Neurosci* (2006) 26(31):8148–59. doi:10.1523/JNEUROSCI.0723-06.2006
70. Bellay T, Shew WL, Yu S, Falco-Walter JJ, and Plenz D. Selective Participation of Single Cortical Neurons in Neuronal Avalanches. *Front NeuralCircuits* (2021) 14(90):117.doi:10.3389/fncir.2020.620052
71. Miller SR, Yu S, and Plenz D. The Scale-Invariant, Temporal Profile of Neuronal Avalanches in Relation to Cortical γ-oscillations. *Scientific Rep* (2019) 9:16403. doi:10.1101/757278
72. Poil S-S, Hardstone R, Mansvelder HD, and Linkenkaer-Hansen K. Critical-state Dynamics of Avalanches and Oscillations Jointly Emerge from Balanced Excitation/inhibition in Neuronal Networks. *J Neurosci* (2012) 32(29): 9817–23. doi:10.1523/jneurosci.5990-11.2012
73. Villegas P, Di Santo S, Burioni R, and Muñoz MA. Time-series Thresholding and the Definition of Avalanche Size. *Phys Rev E* (2019) 100(1). doi:10.1103/PhysRevE.100.012133
74. Petermann T, Thiagarajan TC, Lebedev MA, Nicolelis MAL, Chialvo DR, and Plenz D. Spontaneous Cortical Activity in Awake Monkeys Composed of Neuronal Avalanches. *Pnas* (2009) 106(37):15921–6. doi:10.1073/pnas.0904089106
75. Harris TE. *The Theory of Branching Processes*. Berlin: Springer-Verlag (1963). doi:10.1007/978-3-642-51866-9
76. Christensen K, and Olami Z. Sandpile Models with and without an Underlying Spatial Structure. *Phys Rev E* (1993) 48(5):3361–72. doi:10.1103/physreve.48.3361
77. Miller SR, Yu S, Pajevic S, and Plenz D. Long-term Stability of Avalanche Scaling and Integrative Network Organization in Prefrontal and Premotor Cortex. *Netw Neurosci* (2021). 13:155. doi:10.1101/2020.11.17.386615
78. Martinello M, Hidalgo J, Maritan A, di Santo S, Plenz D, and Muñoz MA. Neutral Theory and Scale-free Neural Dynamics. *Phys Rev X* (2017) 7(4): 041071. doi:10.1103/physrevx.7.041071
79. Touboul J, and Destexhe A. Power-law Statistics and Universal Scaling in the Absence of Criticality. *Phys Rev E* (2017) 95:113.doi:10.1103/PhysRevE.95.012413
80. Tagliazucchi E, Balenzuela P, Fraiman D, and Chialvo DR. Criticality in Large-Scale Brain fMRI Dynamics Unveiled by a Novel point Process Analysis. *Front Physio* (2012) 3(15):27. doi:10.3389/fphys.2012.00015
81. Thiagarajan TC, Lebedev MA, Nicolelis MA, and Plenz D. Coherence Potentials: Loss-Less, All-Or-None Network Events in the Cortex. *Plos Biol* (2010) 8(1):e1000278. doi:10.1371/journal.pbio.1000278
82. Yu S, Yang H, Nakahara H, Santos GS, Nikolic D, and Plenz D. Higher-order Interactions Characterized in Cortical Activity. *J Neurosci* (2011) 31(48): 17514–26. doi:10.1523/JNEUROSCI.3127-11.2011
83. Parameshwaran D, Crone NE, and Thiagarajan TC. Coherence Potentials Encode Simple Human Sensorimotor Behavior. *PLoS One* (2012) 7(2): e30514. doi:10.1371/journal.pone.0030514
84. Poil S-S, Van Ooyen A, and Linkenkaer-Hansen K. Avalanche Dynamics of Human Brain Oscillations: Relation to Critical Branching Processes and Temporal Correlations. *Hum Brain Mapp* (2008) 29:770–7. doi:10.1002/hbm.20590
85. Dalla Porta L, and Copelli M. Modeling Neuronal Avalanches and Long-Range Temporal Correlations at the Emergence of Collective Oscillations: Continuously Varying Exponents Mimic M/EEG Results. *Plos Comput Biol* (2019) 15(4):e1006924. doi:10.1371/journal.pcbi.1006924
86. Wang S-J, Ouyang G, Guang J, Zhang M, Wong KM, and Zhou C. Stochastic Oscillation in Self-Organized Critical States of Small Systems: Sensitive Resting State in Neural Systems. *Phys Rev Lett* (2016) 116(1):133. doi:10.1103/physrevlett.116.018101
87. Yang D-P, Zhou H-J, and Zhou C. Co-emergence of Multi-Scale Cortical Activities of Irregular Firing, Oscillations and Avalanches Achieves Cost-Efficient Information Capacity. *Plos Comput Biol* (2017) 13(2):e1005384. doi:10.1371/journal.pcbi.1005384
88. di Santo S, Villegas P, Burioni R, and Muñoz MA. Landau–Ginzburg Theory of Cortex Dynamics: Scale-free Avalanches Emerge at the Edge of Synchronization. In: Proceedings of the National Academy of Sciences (2018). p. 201712989.
89. Pausch J, Garcia-Millan R, and Pruessner G. *Time-dependent Branching Processes: A Model of Oscillating Neuronal Avalanches*. Berlin: Springer (2019).
90. Gong P, and van Leeuwen C. Distributed Dynamical Computation in Neural Circuits with Propagating Coherent Activity Patterns. *Plos Comput Biol* (2009) 5(12):e1000611. doi:10.1371/journal.pcbi.1000611
91. Gong P, and Robinson PA. Dynamic Pattern Formation and Collisions in Networks of Excitable Elements. *Phys Rev E* (2012) 85(5):055101. doi:10.1103/PhysRevE.85.055101
92. Chen G, and Gong P. Computing by Modulating Spontaneous Cortical Activity Patterns as a Mechanism of Active Visual Processing. *Nat Commun* (2019) 10(1):4915. doi:10.1038/s41467-019-12918-8
93. Allene C, and Cossart R. Early NMDA Receptor-Driven Waves of Activity in the Developing Neocortex: Physiological or Pathological Network Oscillations?. *J Physiol* (2010) 588(1):83–91. doi:10.1113/jphysiol.2009.178798
94. Stewart CV, and Plenz D. Homeostasis of Neuronal Avalanches during Postnatal Cortex Development *In Vitro*. *J Neurosci Meth* (2007) 169: 405–16.doi:10.1016/j.jneumeth.2007.10.021
95. Dupont E, Hanganu IL, Kilb W, Hirsch S, and Luhmann HJ. Rapid Developmental Switch in the Mechanisms Driving Early Cortical Columnar Networks. *Nature* (2006) 439(7072):79–83. doi:10.1038/nature04264
96. Kandler K, and Katz LC. Coordination of Neuronal Activity in Developing Visual Cortex by gap junction-mediated Biochemical Communication. *J Neurosci* (1998) 18(4):1419–27. doi:10.1523/JNEUROSCI.18-04-01419.1998
97. Meng X, Solarana K, Bowen Z, Liu J, Nagode DA, Sheikh A, et al. Transient Subgranular Hyperconnectivity to L2/3 and Enhanced Pairwise Correlations during the Critical Period in the Mouse Auditory Cortex. *Cereb Cortex* (2019) 30(3):1914–30. doi:10.1093/cercor/bhz213
98. Tetzlaff C, Okujeni S, Egert U, Wörgötter F, and Butz M. Self-organized Criticality in Developing Neuronal Networks. *Plos Comput Biol* (2010) 6(12): e1001013. doi:10.1371/journal.pcbi.1001013
99. Levina A, and Priesemann V. Subsampling Scaling. *Nat Commun* (2017) 8: 15140. doi:10.1038/ncomms15140
100. Corner MA, van Pelt J, Wolters PS, Baker RE, and Nuytinck RH. Physiological Effects of Sustained Blockade of Excitatory Synaptic Transmission on Spontaneously Active Developing Neuronal Networks-

An Inquiry into the Reciprocal Linkage between Intrinsic Biorhythms and Neuroplasticity in Early Ontogeny. *Neurosci Biobehavioral Rev* (2002) 26(2): 127–85. doi:10.1016/S0149-7634(01)00062-8

101. Turrigiano GG, and Nelson SB. Homeostatic Plasticity in the Developing Nervous System. *Nat Rev Neurosci* (2004) 5(2):97–107. doi:10.1038/nrn1327
102. Ma Z, Turrigiano GG, Wessel R, and Hengen KB. Cortical Circuit Dynamics Are Homeostatically Tuned to Criticality *In Vivo*. *Neuron* (2019) 104:655–64. doi:10.1016/j.neuron.2019.08.031
103. Lombardi F, Herrmann HJ, Plenz D, and de Arcangelis L. On the Temporal Organization of Neuronal Avalanches. *Front Syst Neurosci* (2014) 8:204. doi:10.3389/fnsys.2014.00204
104. Lombardi F, Herrmann HJ, Perrone-Capano C, Plenz D, and de Arcangelis L. Balance between Excitation and Inhibition Controls the Temporal Organization of Neuronal Avalanches. *Phys Rev Lett* (2012) 108(22): 228703. doi:10.1103/PhysRevLett.108.228703
105. Lombardi F, Herrmann HJ, Plenz D, and de Arcangelis L. Temporal Correlations in Neuronal Avalanche Occurrence. *Sci Rep* (2016) 6:24690. doi:10.1038/srep24690
106. Chialvo DR, Cannas SA, Grigera TS, Martin DA, and Plenz D. Controlling a Complex System Near its Critical point via Temporal Correlations. *Sci Rep* (2020) 10(1):12145. doi:10.1038/s41598-020-69154-0
107. Pasquale V, Massobrio P, Bologna LL, Chiappalone M, and Martinoia S. Self-organization and Neuronal Avalanches in Networks of Dissociated Cortical Neurons. *Neuroscience* (2008) 153(4):1354–69. doi:10.1109/EMBC.2015.731945210.1016/j.neuroscience.2008.03.050
108. Shew WL, Yang H, Petermann T, Roy R, and Plenz D. Neuronal Avalanches Imply Maximum Dynamic Range in Cortical Networks at Criticality. *J Neurosci* (2009) 29(49):15595–600. doi:10.1523/JNEUROSCI.3864-09.2009
109. Shew WL, Yang H, Yu S, Roy R, and Plenz D. Information Capacity and Transmission Are Maximized in Balanced Cortical Networks with Neuronal Avalanches. *J Neurosci* (2011) 31:55–63. doi:10.1523/JNEUROSCI.4637-10.2011
110. Yang H, Shew WL, Roy R, and Plenz D. Maximal Variability of Phase Synchrony in Cortical Networks with Neuronal Avalanches. *J Neurosci* (2012) 32(3):1061–72. doi:10.1523/JNEUROSCI.2771-11.2012
111. Shew WL, and Plenz D. The Functional Benefits of Criticality in the Cortex. *Neuroscientist* (2013) 19(1):88–100. doi:10.1177/1073858412445487
112. Durstewitz D, and Seamans JK. The Dual-State Theory of Prefrontal Cortex Dopamine Function with Relevance to Catechol-O-Methyltransferase Genotypes and Schizophrenia. *Biol Psychiatry* (2008) 64(9):739–49. doi:10.1016/j.biopsych.2008.05.015
113. Arnsten AFT. Catecholamine Influences on Dorsolateral Prefrontal Cortical Networks. *Biol Psychiatry* (2011) 69(12):e89–e99. doi:10.1016/j.biopsych.2011.01.027
114. Cai J, and Arnsten A. Dose-dependent Effects of the Dopamine D1 Receptor Agonists A77636 or SKF81297 on Spatial Working Memory in Aged Monkeys. *J Pharmacol Exp Ther* (1997) 283(1):183–9.
115. Francesc F-C, Gunnar P, Nicholas RM, and Anna D. The Perils of Thresholding. *New J Phys* (2015) 17(4):043066. doi:10.1088/1367-2630/17/4/043066
116. Bornholdt S, and Rohlf T. Topological Evolution of Dynamical Networks: Global Criticality from Local Dynamics. *Phys Rev Lett* (2000) 84(26):6114–7. doi:10.1103/PhysRevLett.84.6114
117. de Arcangelis L, and Herrmann HJ. Learning as a Phenomenon Occurring in a Critical State. *Proc Natl Acad Sci* (2010) 107(9):3977–81. doi:10.1073/pnas.0912289107
118. Michiels van Kessenich L, Luković M, de Arcangelis L, and Herrmann HJ. Critical Neural Networks with Short- and Long-Term Plasticity. *Phys Rev E* (2018) 97(3):032312. doi:10.1103/PhysRevE.97.032312
119. Massobrio P, Pasquale V, and Martinoia S. Self-organized Criticality in Cortical Assemblies Occurs in Concurrent Scale-free and Small-World Networks. *Sci Rep* (2015) 5(1):10578. doi:10.1038/srep10578
120. Pajevic S, and Plenz D. Efficient Network Reconstruction from Dynamical Cascades Identifies Small-World Topology of Neuronal Avalanches. *Plos Comput Biol* (2009) 5(1):e1000271. doi:10.1371/journal.pcbi.1000271
121. Pajevic S, and Plenz D. The Organization of strong Links in Complex Networks. *Nat Phys* (2012) 8(5):429–36. doi:10.1038/NPHYS2257
122. Ribeiro TL, Copelli M, Caixeta F, Belchior H, Chialvo DR, Nicolelis MAL, et al. Spike Avalanches Exhibit Universal Dynamics across the Sleep-Wake Cycle. *PLoS One* (2010) 5(11):e14129. doi:10.1371/journal.pone.0014129
123. Scott G, Fagerholm ED, Mutoh H, Leech R, Sharp DJ, Shew WL, et al. Voltage Imaging of Waking Mouse Cortex Reveals Emergence of Critical Neuronal Dynamics. *J Neurosci*(2014) 34(50):16611–20. doi:10.1523/JNEUROSCI.3474-14.2014
124. Bellay T, Klaus A, Seshadri S, and Plenz D. Irregular Spiking of Pyramidal Neurons Organizes as Scale-Invariant Neuronal Avalanches in the Awake State. *eLife* (2015) 4:e07224. doi:10.7554/eLife.07224
125. Fagerholm ED, Scott G, Shew WL, Song C, Leech R, Knöpfel T, et al. Cortical Entropy, Mutual Information and Scale-free Dynamics in Waking Mice. *Cereb Cortex* (2016) 26:3945–52. doi:10.1093/cercor/bhw200
126. Ribeiro TL, Ribeiro S, and Copelli M. Repertoires of Spike Avalanches Are Modulated by Behavior and novelty. *Front NeuralCircuits* (2016) 10:16. doi:10.3389/fncir.2016.00016
127. Meisel C, Olbrich E, Shriki O, and Achermann P. Fading Signatures of Critical Brain Dynamics during Sustained Wakefulness in Humans. *J Neurosci* (2013) 33(44):17363–72. doi:10.1523/JNEUROSCI.1516-13.2013
128. Meisel C, Bailey K, Achermann P, and Plenz D. Decline of Long-Range Temporal Correlations in the Human Brain during Sustained Wakefulness. *Sci Rep* (2017) 7(1):11825. doi:10.1038/s41598-017-12140-w
129. Lombardi F, Gómez-Extremera M, Bernaola-Galván P, Vetrivelan R, Saper CB, Scammell TE, et al. Critical Dynamics and Coupling in Bursts of Cortical Rhythms Indicate Non-homeostatic Mechanism for Sleep-Stage Transitions and Dual Role of Vlpo Neurons in Both Sleep and Wake. *J Neurosci* (2020) 40(1):171–90. doi:10.1523/jneurosci.1278-19.2019
130. McCormick DA, and Prince DA. Mechanisms of Action of Acetylcholine in the guinea-pig Cerebral Cortex *In Vitro*. *J Physiol (London)* (1986) 375: 169–94. doi:10.1113/jphysiol.1986.sp016112
131. Case L, Lyons DJ, and Broberger C. Desynchronization of the Rat Cortical Network and Excitation of white Matter Neurons by Neurotensin. *Cereb Cortex* (2016) 27(4):bhw100–2685. doi:10.1093/cercor/bhw100
132. Braitenberg V, and Schüz A. *Anatomy of the Cortex: Statistics and Geometry*. Berlin, Heidelberg, New York: Springer-Verlag (1991). doi:10.1007/978-3-662-02728-8
133. Bowen Z, Winkowski DE, Seshadri S, Plenz D, and Kanold PO. Neuronal Avalanches in Input and Associative Layers of Auditory Cortex. *Front Syst Neurosci* (2019) 13, 137.doi:10.3389/fnsys.2019.00045
134. Ma Z, Liu H, Komiyama T, and Wessel R. Stability of Motor Cortex Network States during Learning-Associated Neural Reorganizations. *J Neurophysiol* (2020) 124(5):1327–42. doi:10.1152/jn.00061.2020
135. Buzsáki G, Anastassiou CA, and Koch C. The Origin of Extracellular fields and Currents - EEG, ECoG, LFP and Spikes. *Nat Rev Neurosci* (2012) 13(6): 407–20. doi:10.1038/nrn3241
136. Yamada Y, Mikoshiba K, Hashimoto M, Horikawa K, Nagai T, Miyawaki A, et al. Quantitative Comparison of Novel GCaMP-type Genetically Encoded Ca2+ Indicators in Mammalian Neurons. *Front Cel Neurosci.* (2011) 6:18. doi:10.3389/fncel.2012.00041
137. O'Donovan MJ. The Origin of Spontaneous Activity in Developing Networks of the Vertebrate Nervous System. *Curr Opin Neurobiol* (1999) 9(1):94–104. doi:10.1016/s0959-4388(99)80012-9
138. Karimipanah Y, Ma Z, Miller J-e. K, Yuste R, and Wessel R. Neocortical Activity Is Stimulus- and Scale-Invariant. *PLoS One* (2017) 12(5): e0177396e0177396. doi:10.1371/journal.pone.0177396
139. Buice MA, and Cowan JD. Field-theoretic Approach to Fluctuation Effects in Neural Networks. *Phys Rev.E.Stat.Nonlin.Soft.Matter Phys* (2007) 75:051919. doi:10.1103/physreve.75.051919
140. Benayoun M, Cowan JD, van Drongelen W, and Wallace E. Avalanches in a Stochastic Model of Spiking Neurons. *Plos Comput Biol* (2010) 6(7): e1000846. doi:10.1371/journal.pcbi.1000846
141. Buice MA, Cowan JD, and Chow CC. Systematic Fluctuation Expansion for Neural Network Activity Equations. *Neural Comput* (2010) 22(2):377–426. doi:10.1162/neco.2009.02-09-960
142. Liang J, Zhou T, and Zhou C. Hopf Bifurcation in Mean Field Explains Critical Avalanches in Excitation-Inhibition Balanced Neuronal Networks: A Mechanism for Multiscale Variability. *Front Syst Neurosci* (2020) 14(87): 155.doi:10.3389/fnsys.2020.580011
143. Dichter MA. Rat Cortical Neurons in Cell Culture: Culture Methods, Cell Morphology, Electrophysiology, and Synapse Formation. *Brain Res* (1978) 149:279–93. doi:10.1016/0006-8993(78)90476-6

144. Maeda E, Robinson H, and Kawana A. The Mechanisms of Generation and Propagation of Synchronized Bursting in Developing Networks of Cortical Neurons. *J Neurosci* (1995) 15:6834–45. doi:10.1523/JNEUROSCI.15-10-06834.1995
145. Wagenaar D, Pine J, and Potter S. An Extremely Rich Repertoire of Bursting Patterns during the Development of Cortical Cultures. *BMC Neurosci* (2006) 7(1):11. doi:10.1186/1471-2202-7-11
146. Yada Y, Mita T, Sanada A, Yano R, Kanzaki R, Bakkum DJ, et al. Development of Neural Population Activity toward Self-Organized Criticality. *Neuroscience* (2017) 343:55–65. doi:10.1016/j.neuroscience.2016.11.031
147. Shaukat A, and Thivierge J-P. Statistical Evaluation of Waveform Collapse Reveals Scale-free Properties of Neuronal Avalanches. *Front Comput Neurosci* (2016) 10:27.doi:10.3389/fncom.2016.00029
148. Heiney K, Ramstad OH, Sandvig I, Sandvig A, and Nichele S. Assessment and Manipulation of the Computational Capacity of *In Vitro*Neuronal Networks through Criticality in Neuronal Avalanches. In IEEE Symposium Series on Computational Intelligence (SSCI). IEEE (2019). p. 247–54.
149. Orlandi JG, Soriano J, Alvarez-Lacalle E, Teller S, and Casademunt J. Noise Focusing and the Emergence of Coherent Activity in Neuronal Cultures. *Nat Phys* (2013) 9(9):582–90. doi:10.1038/nphys2686
150. Giugliano M, Darbon P, Arsiero M, Lüscher H-R, and Streit J. Single-neuron Discharge Properties and Network Activity in Dissociated Cultures of Neocortex. *J Neurophysiol* (2004) 92(2):977–96. doi:10.1152/jn.00067.2004
151. Scarpetta S, and de Candia A. Neural Avalanches at the Critical point between Replay and Non-replay of Spatiotemporal Patterns. *PLoS One* (2013) 8(6): e64162. doi:10.1371/journal.pone.0064162
152. di Santo S, Burioni R, Vezzani A, and Muñoz MA. Self-organized Bistability Associated with First-Order Phase Transitions. *Phys Rev Lett* (2016) 116(24): 240601. doi:10.1103/PhysRevLett.116.240601
153. Scarpetta S, Apicella I, Minati L, and de Candia A. Hysteresis, Neural Avalanches, and Critical Behavior Near a First-Order Transition of a Spiking Neural Network. *Phys Rev E* (2018) 97(6):062305. doi:10.1103/PhysRevE.97.062305
154. Buendía V, di Santo S, Villegas P, Burioni R, and Muñoz MA. Self-organized Bistability and its Possible Relevance for Brain Dynamics. *Phys Rev Res* (2020) 2(1):013318. doi:10.1103/PhysRevResearch.2.013318
155. Kinouchi O, Pazzini R, and Copelli M. Mechanisms of Self-Organized Quasicriticality in Neuronal Network Models. *Front Phys* (2020) 8(530): 113. doi:10.3389/fphy.2020.583213
156. Ribeiro TL, Ribeiro S, Belchior H, Caixeta F, and Copelli M. Undersampled Critical Branching Processes on Small-World and Random Networks Fail to Reproduce the Statistics of Spike Avalanches. *PLoS One* (2014) 9(4):e94992. doi:10.1371/journal.pone.0094992
157. Friedman N, Ito S, Brinkman BAW, Shimono M, DeVille REL, Dahmen KA, et al. Universal Critical Dynamics in High Resolution Neuronal Avalanche Data. *Phys Rev Lett* (2012) 108(20):208102. doi:10.1103/physrevlett.108.208102
158. Khazipov R, and Luhmann HJ. Early Patterns of Electrical Activity in the Developing Cerebral Cortex of Humans and Rodents. *TrendsNeurosciences* (2006) 29(7):414–8. doi:10.1016/j.tins.2006.05.007
159. Saito T. *In Vivo* electroporation in the Embryonic Mouse central Nervous System. *Nat Protoc* (2006) 1(3):1552–8. doi:10.1038/nprot.2006.276
160. Wang Z, and McCormick D. Control of Firing Mode of Corticotectal and Corticopontine Layer V Burst-Generating Neurons by Norepinephrine, Acetylcholine, and 1S,3R- ACPD. *J Neurosci* (1993) 13:2199–216. doi:10.1523/JNEUROSCI.13-05-02199.1993
161. Compte A, Sanchez-Vives MV, McCormick DA, and Wang X-J. Cellular and Network Mechanisms of Slow Oscillatory Activity (. *J Neurophysiol* (2003) 89(5):2707–25. doi:10.1152/jn.00845.2002
162. Pu J, Gong H, Li X, and Luo Q. Developing Neuronal Networks: Self-Organized Criticality Predicts the Future. *Sci Rep* (2013) 3(1):1081. doi:10.1038/srep01081
163. Yaghoubi M, de Graaf T, Orlandi JG, Girotto F, Colicos MA, and Davidsen J. Neuronal Avalanche Dynamics Indicates Different Universality Classes in Neuronal Cultures. *Sci Rep* (2018) 8(1):3417. doi:10.1038/s41598-018-21730-1
164. Brofiga M, Pisano M, Tedesco M, Raiteri R, and Massobrio P. Three-dimensionality Shapes the Dynamics of Cortical Interconnected to Hippocampal Networks. *J Neural Eng* (2020) 17(5):056044056044. doi:10.1088/1741-2552/abc023
165. Van Brederode JFM, Helliesen MK, and Hendrickson AE. Distribution of the Calcium-Binding Proteins Parvalbumin and Calbindin-D28k in the Sensorimotor Cortex of the Rat. *Neuroscience* (1991) 44:157–71. doi:10.1016/0306-4522(91)90258-p
166. Plenz D, Stewart CV, Shew W, Yang H, Klaus A, and Bellay T. Multi-electrode Array Recordings of Neuronal Avalanches in Organotypic Cultures. *JoVE* (2011)11(54) e2949. doi:10.3791/2949
167. Pfeffer L, Ide D, Stewart CV, and Plenz D. A Life Support Systems for Stimulation of and Recording from Rodent Neuron Networks Grown on Multi-Electrode Arrays. In Proceedings. 17th IEEE Symposium on Computer-Based Medical Systems (2012). p. 473–8.

Conflict of Interest: The authors declare that the research was conducted in the absence of any commercial or financial relationships that could be construed as a potential conflict of interest.

Advantages of publishing in Frontiers

OPEN ACCESS
Articles are free to read for greatest visibility and readership

FAST PUBLICATION
Around 90 days from submission to decision

HIGH QUALITY PEER-REVIEW
Rigorous, collaborative, and constructive peer-review

TRANSPARENT PEER-REVIEW
Editors and reviewers acknowledged by name on published articles

Frontiers
Avenue du Tribunal-Fédéral 34
1005 Lausanne | Switzerland

Visit us: www.frontiersin.org
Contact us: frontiersin.org/about/contact

REPRODUCIBILITY OF RESEARCH
Support open data and methods to enhance research reproducibility

DIGITAL PUBLISHING
Articles designed for optimal readership across devices

FOLLOW US
@frontiersin

IMPACT METRICS
Advanced article metrics track visibility across digital media

EXTENSIVE PROMOTION
Marketing and promotion of impactful research

LOOP RESEARCH NETWORK
Our network increases your article's readership